

THE 1997 HST

# Calibration Workshop

**With a New Generation of Instruments**

**Held at the Space Telescope Science Institute  
Baltimore, Maryland**

**September 22-24, 1997**

**Edited by S. Casertano, R. Jedrzejewski, T. Keyes, M. Stevens**





Cover design and artwork by John Godfrey, using a NICMOS Camera 2 parallel image taken for W. Brandner (Program 7412). The processed image is courtesy of C. J. Skinner and L. E. Bergeron.

# The 1997 HST Calibration Workshop

with a new generation of instruments

Proceedings of a Workshop held at the  
Space Telescope Science Institute  
Baltimore, Maryland  
September 22–24, 1997

Edited by Stefano Casertano, Robert Jedrzejewski, Charles D. (Tony) Keyes, and Mark Stevens

Published and distributed by the Space Telescope Science Institute  
3700 San Martin Drive, Baltimore, MD 21218, USA

**Page intentionally left blank**



## Contents

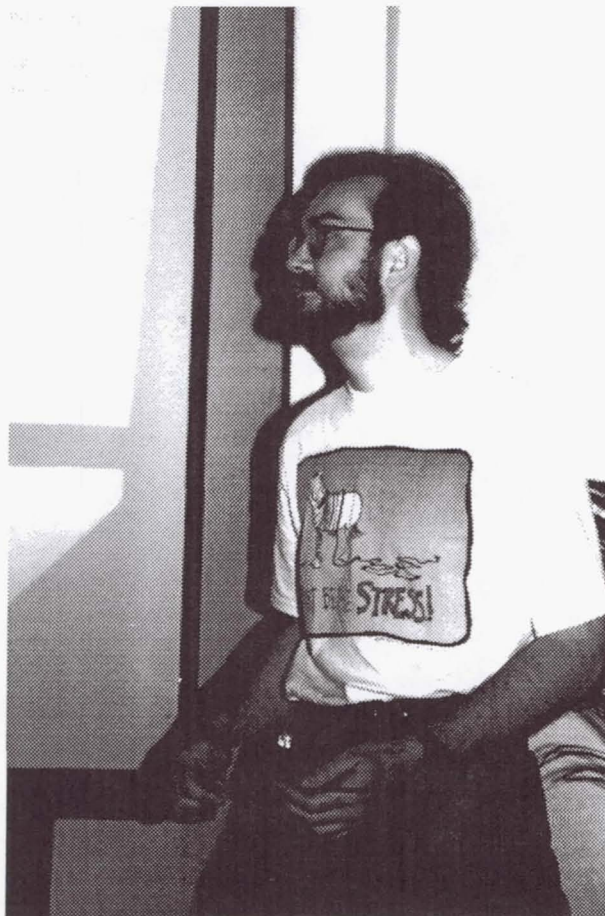
Preface . . . . .	xi
Conference participants . . . . .	xiii
 <b>Part 1. STIS</b>	
STIS Overview; Capabilities and Basic Operations . . . . .	3
<i>S. A. Baum</i>	
The On-Orbit Performance of the STIS Detectors . . . . .	8
<i>R. A. Kimble</i>	
The On-Orbit Optical Performance of STIS . . . . .	18
<i>C. W. Bowers</i>	
The Flat Fielding and Achievable Signal-to-Noise of the MAMA Detectors . . . . .	29
<i>M. E. Kaiser</i>	
STIS Target Acquisition . . . . .	39
<i>S. Kraemer, R. Downes, R. Katsanis, M. Crenshaw, M. McGrath, and R. Robinson</i>	
The STIS Calibration Pipeline . . . . .	47
<i>S. Hulbert and P. Hodge</i>	
The Cycle 7 Calibration Plan for STIS . . . . .	52
<i>P. Goudfrooij, S. A. Baum, H. C. Ferguson, J. J. E. Hayes, S. J. Hulbert, C. Leitherer, M. A. McGrath, K. C. Sahu, and R. A. Shaw</i>	
STIS Capabilities: Current and Future Implementation . . . . .	60
<i>B. Woodgate</i>	
STIS CCD Hot Pixel Annealing . . . . .	65
<i>T. Beck and W. Landsman</i>	
STIS Observations of the Nuclear Ionized Gas in the Elliptical Galaxy M84 . . . . .	70
<i>G. A. Bower, R. F. Green, and D. Lindler</i>	
STIS First-Order Low-Resolution Mode Point-Source Sensitivity Curves . . . . .	77
<i>N. Collins and R. Bohlin</i>	
Simulations of the STIS CCD Clear Imaging Mode PSF . . . . .	84
<i>R. H. Cornett, A. Gruszczak, C. Ftaclos, S. R. Heap, and B. E. Woodgate</i>	
A Test of the STIS CCD Flatfielding Accuracy on Small Scales . . . . .	90
<i>H. Ferguson</i>	
The STIS Parallel Survey: Introduction and First Results. . . . .	94
<i>J. Gardner, R. Hill, S. Baum, N. Collins, H. Ferguson, R. Fosbury, R. Gilliland, R. Green, T. Gull, S. Heap, D. Lindler, E. Malumuth, A. Micol, N. Pirzkal, J. Sandoval, E. Tolstoy, J. Walsh, and B. Woodgate</i>	
Fringe Correction for STIS Near-IR Long-Slit Spectra using Contemporaneous Tungsten Flat Fields . . . . .	100
<i>P. Goudfrooij, S. Baum, and J. Walsh</i>	
Thermal Motion of the STIS Optical Bench . . . . .	106
<i>T. R. Gull, M. J. Taylor, R. Shaw, R. Robinson, and R. S. Hill</i>	

Correction for the STIS Echelle Blaze Function . . . . .	114
<i>S. R. Heap and T. M. Brown</i>	
Cosmic Ray and Hot Pixel Removal from STIS CCD Images . . . . .	120
<i>R. S. Hill, W. B. Landsman, D. Lindler, and R. Shaw</i>	
Laboratory Test Data on the Stability of the STIS MAMAs . . . . .	126
<i>C. L. Joseph</i>	
Scattered Light in the STIS Echelle Modes . . . . .	132
<i>W. Landsman and C. Bowers</i>	
Analysis of STIS Time-Tag Data . . . . .	138
<i>D. J. Lindler, T. R. Gull, S. B. Kraemer, and S. J. Hulbert</i>	
Determination of Geometric Distortion in STIS Images . . . . .	144
<i>E. M. Malumuth and C. W. Bowers</i>	
Fringe Science: Creating a STIS CCD Fringe Flat Field . . . . .	150
<i>P. Plait and R. Bohlin</i>	
Extraction of Point Source Spectra from STIS Long Slit Data . . . . .	156
<i>J. R. Walsh</i>	
 <b>Part 2. NICMOS</b>	
NICMOS Status and Plans . . . . .	163
<i>R. I. Thompson</i>	
Characteristics of the NICMOS Detectors . . . . .	171
<i>C. J. Skinner, L. E. Bergeron, and D. Daou</i>	
The Photometric Performance of NICMOS . . . . .	182
<i>L. Colina and M. J. Rieke</i>	
NICMOS PSF Variations and Tiny Tim Simulations . . . . .	192
<i>J. Krist and R. Hook</i>	
Narrow-Band Emission Line Imaging with NICMOS: Lessons Learned from the Data Reduction of OMC-1 . . . . .	202
<i>S. Stolovy</i>	
The NICMOS Grism Mode . . . . .	207
<i>W. Freudling</i>	
The Polarimetric Capabilities of NICMOS . . . . .	217
<i>D. C. Hines, G. D. Schmidt, and D. Lyer</i>	
The NICMOS CALNICA and CALNICB Pipelines . . . . .	223
<i>H. Bushouse</i>	
Improving on the NICMOS Calibration Pipeline Products . . . . .	233
<i>C. J. Skinner</i>	
Understanding the NICMOS Darks . . . . .	240
<i>L. E. Bergeron and C. J. Skinner</i>	

On October 21, 1997, Chris Skinner passed away while visiting his parents in England. His sudden and untimely death was a great loss for astrophysics and especially for all his colleagues at STScI. Chris was a promising and brilliant scientist, whose recent research included dust around young stars, mass loss from evolved stars, and the origin of planetary nebulae. His paper on the Cygnus Egg Nebula, which appeared posthumously in *Astronomy and Astrophysics*, is a wonderful example of the depth and breadth of his scientific investigations.

Chris's contributions at STScI went beyond his research. He was one of the critical members of the NICMOS instrument team at STScI, and had followed the camera's progress throughout assembly and ground testing, highlighting some of the critical areas early on. He was involved in essentially all areas of the NICMOS calibration, and his work will make a huge difference in how well users will be able to take advantage of the camera's unique capabilities. He was well liked and respected for his exceptional technical skills, dedication, dry sense of humor, and ability to work effectively with other team members. His crucial role in the calibration of NICMOS can be seen in the Proceedings, in which he is involved in no less than six contributions.

This book is dedicated to the memory of Chris, as a modest tribute to his many contributions to the birth of infrared science on HST.



Christopher J. Skinner  
1963–1997



NICMOS Data Processing Software in STSDAS . . . . .	245
<i>I. Busko</i>	
NICMOS Sensitivity to Cosmic Rays . . . . .	250
<i>D. Calzetti</i>	
The NICMOS Data Handbook . . . . .	255
<i>D. Calzetti and H. Bushouse</i>	
NICMOS Cycle7 Calibration Plan and Beyond . . . . .	259
<i>L. Colina and A. Storrs</i>	
Persistence in NICMOS: Results from On-Orbit data . . . . .	263
<i>D. Daou and C. Skinner</i>	
NICMOS Pointed Thermal Background: Results from On-Orbit data . . . . .	267
<i>D. Daou, C. Skinner and D. Axon</i>	
Subtraction of Well-Exposed NICMOS 2 PSFs . . . . .	271
<i>J. Krist</i>	
NICMOS File Formats . . . . .	277
<i>D. Lytle, E. Stobie, A. Ferro, and I. Barg</i>	
NICRED: Reduction of NICMOS MULTIACCUM Data with IRAF . . . . .	281
<i>B. A. McLeod</i>	
NICMOS Data Quality Control and Paper Products . . . . .	287
<i>C. Ritchie, H. Bushouse, L. Colina, D. Calzetti, C. Skinner, and A. Storrs</i>	
Software Tools for NICMOS . . . . .	297
<i>E. Stobie, D. Lytle, A. Ferro, and I. Barg</i>	
Making Maps and Mosaics . . . . .	303
<i>A. Storrs</i>	
Long-Term and Short-Term Variations of NICMOS Foci . . . . .	308
<i>A. A. Suchkov, L. Bergeron, and G. G. Galas</i>	
 <b>Part 3. WFPC2</b>	
WFPC2 Status and Overview . . . . .	317
<i>B. C. Whitmore</i>	
WFPC2 Photometric Calibration . . . . .	327
<i>S. Casertano</i>	
WFPC2 Calibration for Emission Line Images . . . . .	338
<i>G. Dudziak and J. R. Walsh</i>	
HST, uvby Photometry and System Calibration . . . . .	343
<i>P. Linde, A. Ardeberg, T. Bensby, and R. Snel</i>	
Associations of WFPC2 Exposures . . . . .	349
<i>A. Micol, P. Bristow, and B. Pirenne</i>	
Drizzling Dithered WFPC2 Images—A Demonstration . . . . .	355
<i>M. Mutchler and A. Fruchter</i>	

Calibrating the WFPC2 Astrometry for MDS . . . . .	361
<i>K. U. Ratnatunga, E. J. Ostrander, and R. E. Griffiths</i>	
HST Observations of the Gravitational Lens Systems HE 1104–1805 and J03.13 . .	368
<i>M. Remy, J.-F. Claeskens, and J. Surdej</i>	
WFPC2 Photometry from Subtraction of TinyTim PSFs . . . . .	374
<i>M. Remy, J. Surdej, S. Baggett, and M. Wiggs</i>	
Aperture Corrections for WFPC2 Stellar Photometry . . . . .	378
<i>A. Suchkov and S. Casertano</i>	
WFPC2 Photometry from Subtraction of Observed PSFs . . . . .	386
<i>J. Surdej, S. Baggett, M. Remy, and M. Wiggs</i>	
The WFPC2 PSF Library . . . . .	392
<i>M. Wiggs, S. Baggett, J. Surdej, and C. Tullos</i>	
The WFPC2 Clearinghouse . . . . .	398
<i>M. S. Wiggs, B. Whitmore, and I. Heyer</i>	

#### Part 4. Other Instruments

FOC Status and Overview . . . . .	405
<i>R. Jedrzejewski</i>	
F/48 Slit Spectroscopy . . . . .	413
<i>R. Jedrzejewski and M. Voit</i>	
The Closeout State of the Faint Object Spectrograph . . . . .	420
<i>C. D. Keyes</i>	
Average Inverse Sensitivity Recalibration of Pre-COSTAR Faint Object Spectrograph Data and Comparison with International Ultraviolet Explorer Data . . . . .	430
<i>A. Koratkar and I. Evans</i>	
Estimating Scattered Light in the FOS . . . . .	440
<i>J. J. E. Hayes and C. D. Keyes</i>	
The HST/FOS Wavelength Scale . . . . .	443
<i>R. P. van der Marel</i>	
Astrometry with the FGS in POSITION Mode and TRANSFER Mode: Observing Strategies, Pipeline Processing and Data Reduction . . . . .	449
<i>E. Nelan, O. Lupie, and L. Nagel</i>	
FGS1R: Potentially HST's Astrometry Science Workhorse . . . . .	463
<i>O. Lupie, E. Nelan, and L. Nagel</i>	
Maintaining the FGS3 Optical Field Angle Distortion Calibration . . . . .	472
<i>B. McArthur, G. F. Benedict, W. H. Jefferys, and E. Nelan</i>	
Stability of FGS Photometry . . . . .	481
<i>R. Kuschnig, W. W. Weiss, and K. Zwintz</i>	
The Goddard High Resolution Spectrograph . . . . .	486
<i>D. R. Soderblom and L. E. Sherbert</i>	

GHRs Calibration Changes since February 1997 . . . . .	497
<i>L. E. Sherbert</i>	

## Part 5. General

The New HST FITS Format, the FITS Kernel and OpenIRAF . . . . .	505
<i>P. Greenfield</i>	
New Calibration Systems Projects at STScI . . . . .	513
<i>S. Lubow</i>	
A Package for the Reduction of Dithered Undersampled Images . . . . .	518
<i>A. S. Fruchter, R. N. Hook, I. C. Busko, and M. Mutchler</i>	
Deconvolution of Substepped 1-D and 2-D HST Data . . . . .	529
<i>N. Wu and J. Caldwell</i>	
Calibrating Echelle Spectra using Instrument Models . . . . .	533
<i>M. Rosa and P. Ballester</i>	
Author index . . . . .	537
Index . . . . .	539



**Page intentionally left blank**

## Preface

The Second Servicing mission in early 1997 has brought major changes to the Hubble Space Telescope. Two of the original instruments, FOS and GHRS, were taken out, and replaced by completely new instruments, STIS and NICMOS. Two new types of detectors were installed, and for the first time, HST gained infrared capabilities. A new FGS was installed, with an alignment mechanism that could improve substantially both guiding and astrometric capabilities.

With all these changes come new challenges. The characterization of the new instruments has required a major effort, both by their respective Investigation Definition Teams and at the Space Telescope Science Institute. All necessary final calibrations for the retired spectrographs needed to be carried out, and their properties definitively characterized. At the same time, work has continued to improve our understanding of the two instruments that have remained on board.

The results of these activities were discussed in the 1997 HST Calibration Workshop, a three-day meeting held on September 22–24, 1997 at the Space Telescope Science Institute. About 150 astronomers took part in the Workshop, which featured over 30 invited talks and about 50 posters. The main focus of the Workshop was to provide users with the tools and the understanding they need to use HST's instruments and archival data to the best of their possibilities.

This book contains the written record of the Workshop, including both invited talks and poster papers. As such, it should provide a valuable tool to all interested in using existing HST data or in proposing for new observations. Of course, our knowledge and understanding of the HST instruments is continuously evolving (and so are the instruments themselves). In the era of electronic connectivity, obtaining up-to-date information can be as easy as a few mouse clicks, and prospective HST users are urged to obtain the latest information on HST status and calibration from the STScI web pages (at <http://www.stsci.edu>), or by sending electronic mail to [help@stsci.edu](mailto:help@stsci.edu). This book is also available electronically, at the URL <http://www.stsci.edu/meetings/cal97/proceedings.html>.

The Workshop was a great success, and we wish to thank all the participants for their enthusiasm and hard work that made it possible. We are grateful to all the members of the Organizing Committee for their help and support, and especially to Helmut Jenkner for stepping up whenever needed. We thank Knox Long, Helmut Jenkner, Ken Freeman, Ron Gilliland, John Graham, Don Lindler, and Chris Blades for chairing the sessions. The Workshop was sponsored by the Science Support Division of STScI, and enjoyed the support of many people at STScI, especially Jim Jones, Ron Meyers and Jeff Nesbitt. Harry Payne provided many of the latex formatting tools for this book, and the cover design is due to Trish Pengra and John Godfrey. Finally, very special thanks are due to Tawanta Nance and Cheryl Schmidt, who took good care of all administrative and practical details and ensured the smooth preparation and running of the Workshop.

The Editors

### **The Organizing Committee**

David Axon (STScI)  
Stefano Casertano (chair, STScI)  
Wolfram Freudling (ST-ECF)  
Ron Gilliland (STScI)  
Robert Jedrzejewski (STScI)  
Helmut Jenkner (STScI)  
Tony Keyes (STScI)  
Anuradha Koratkar (STScI)  
Melissa McGrath (STScI)  
Tawanta Nance (STScI)  
Michael Rosa (ST-ECF)  
David Soderblom (STScI)



## Participant List

David Axon	STScI	axon@stsci.edu
Sylvia Baggett	STScI	sbaggett@stsci.edu
Pascal Ballester	ESO	pballest@eso.org
Stefi Baum	STScI	sbaum@stsci.edu
Sylvie Beaulieu	Institute of Astronomy, Cambridge	beaulieu@ast.cam.ac.uk
Terry Beck	ACC Inc. / NASA/GSFC	beck@cassini.gsfc.nasa.gov
G. Fritz Benedict	McDonald Observatory	fritz@clyde.as.utexas.edu
Louis E. Bergeron	STScI	bergeron@stsci.edu
Leonard Berkoski	NASA/GSFC	
Chris Blades	STScI	blades@stsci.edu
Kirk Borne	NASA/GSFC	borne@nssdca.gsfc.nasa.gov
Gary Bower	NOAO/KPNO	gbower@noao.edu
Charles W. Bowers	NASA/GSFC	bowers@band2.gsfc.nasa.gov
Art Bradley	HST Program Operations	bradley.art@lmmail.hst.nasa.gov
Larry Bradley	JHU	bradley@valhalla.gsfc.nasa.gov
Fred Bruhweiler	Catholic Univ. of America	hrsfred@hrs.gsfc.nasa.gov
Andrew Bunker	UC Berkeley	bunker@bigz.Berkeley.EDU
Chris Burrows	STScI	burrows@stsci.edu
Howard Bushouse	STScI	bushouse@stsci.edu
Ivo C. Busko	STScI	busko@stsci.edu
John Caldwell	York Univ.	caldwell@nereid.sal.phys.yorku.ca
Daniela Calzetti	STScI	calzetti@stsci.edu
Kenneth Carpenter	NASA/GSFC	
Stefano Casertano	STScI	stefano@stsci.edu
Nancy Chanover	NASA/GSFC	Nancy.Chanover@gsfc.nasa.gov
Hua Chen	Steward Observatory	hchen@as.arizona.edu
Luis Colina	STScI	colina@stsci.edu
Nicholas Collins	Hughes STX/LASP/GSFC	collins@zolo.gsfc.nasa.gov
Michael Corbin	Steward Observatory	mcorbin@as.arizona.edu
Bob Cornett	Hughes STX/NASA/GSFC	cornett@stars.gsfc.nasa.gov
Colin Cox	STScI	cox@stsci.edu
D. Michael Crenshaw	NASA/GSFC	crenshaw@buckeye.gsfc.nasa.gov
Doris Daou	STScI	daou@stsci.edu
Ilana Dashevsky	York Univ.	ilana@aries.phys.yorku.ca
Ron Downes	STScI	downes@stsci.edu
Reginald J. Dufour	Rice University	rjd@rice.edu
Douglas Duncan	Univ. of Chicago	duncan@oddjjob.uchicago.edu

Brian Espey	JHU	espey@pha.jhu.edu
Anthony J. Ferro	Univ. of Arizona	tferro@as.arizona.edu
Pierre Ferruit	Univ. of Maryland	pierre@astro.umd.edu
Donald F. Figer		
Holland Ford	STScI	ford@stsci.edu
Otto G. Franz	Lowell Observatory	ogf@lowell.edu
Kenneth Freeman	Mount Stromlo Obs.	kcf@mso.anu.edu.au
Wolfram Freudling	ST - ECF / ESO	
Scott Friedman	JHU	scott@pha.jhu.edu
Andrew Fruchter	STScI	fruchter@stsci.edu
Jorge F. Garcia	STScI	jpgarcia@stsci.edu
Jonathan P. Gardner	NASA/GSFC	gardner@harmony.gsfc.nasa.gov
Don Garnett	Univ. of Minnesota	garnett@oldstyle.spa.umn.edu
Ron Gilliland	STScI	gillil@stsci.edu
Daniel Golombek	STScI	golombek@stsci.edu
Shireen Gonzaga	STScI	gonzaga@stsci.edu
Paul Goudfrooij	STScI	goudfroo@stsci.edu
John A. Graham	Carnegie Inst. -DTM	graham@jag.ciw.edu
James C. Green	Univ. of Colorado	green@tardis.colorado.edu
Perry Greenfield	STScI	perry@stsci.edu
Theodore R. Gull	NASA/GSFC/LASP	gull@sea.gsfc.nasa.gov
Jeffrey Hayes	STScI	hayes@stsci.edu
Sara R. Heap	NASA/GSFC	hrsheap@stars.gsfc.nasa.gov
Robert S. Hill	Hughes STX Corp.	robert.s.hill@gsfc.nasa.gov
Dean C. Hines	Univ. of Arizona	dhines@as.arizona.edu
Steve Hulbert	STScI	hulbert@stsci.edu
David C. Humm	JHU/APL	David.Humm@jhuapl.edu
Robert Jedrzejewski	STScI	rij@stsci.edu
Helmut Jenkner	STScI	jenkner@stsci.edu
Rachel Johnson	Institute of Astronomy, Cambridge	raj@ast.cam.ac.uk
Charles L. Joseph	Rutgers Univ.	cjoseph@physics.rutgers.edu
Mary Beth Kaiser	JHU/GSFC	kaiser@hunin.gsfc.nasa.gov
Charles D. (Tony) Keyes	STScI	keyes@stsci.edu
Randy Kimble	NASA/GSFC	kimble@stars.gsfc.nasa.gov
Anuradha Koratkar	STScI	koratkar@stsci.edu
Steve Kraemer	Catholic Univ. of America	stiskraemer@yancey.gsfc.nasa.gov
John Krist	STScI	krist@stsci.edu
Varsha Kulkarni	Univ. of Arizona	kulkarni@as.arizona.edu
Rainer Kuschnig	Univ. of Vienna	kuschnig@isaac.ast.univie.ac.at

Lucas Labhardt	Univ. of Basel	labhardt@astro.unibas.ch
Wayne Landsman	Hughes STX	landsman@mpb.gsfc.nasa.gov
Peter Linde	Lund Observatory	peter@astro.lu.se
Don J. Lindler	ACC Inc.	lindler@rockit.gsfc.nasa.gov
Knox Long	STScI	long@stsci.edu
Bruno Lopez	Obs. de la Cote d'Azur	lopez@obs.nice.fr
Stephen Lubow	STScI	lubow@stsci.edu
Olivia Lupie	STScI	lupie@stsci.edu
Dyer Lytle	Univ. of Arizona	dlytle@as.arizona.edu
Eliot M. Malumuth	Hughes STX/STIS/GSFC	eliot@barada.gsfc.nasa.gov
André Martel	STScI	martel@stsci.edu
Barbara McArthur	Univ. of Texas	mca@barney.as.utexas.edu
Stephan McCandliss	JHU	stephan@pha.jhu.edu
Brian McLeod	Smithsonian Astro. Obs.	bmcleod@cfa.harvard.edu
Alberto Micol	ST-ECF	amicol@eso.org
Cherie Miskey	Catholic Univ. of America	miskey@stars.gsfc.nasa.gov
Andrea Moneti	ESA-Villafranca	amoneti@iso.vilspa.esa.es
Edward M. Murphy	JHU	emurphy@jhu.edu
Max Mutchler	STScI	mutchler@stsci.edu
Lauretta Nagel	STScI	nagel@stsci.edu
Joan Najita	Center for Astrophysics	jnajita@cfa.harvard.edu
Edmund Nelan	STScI	nelan@stsci.edu
Chris O'Dea	STScI	odea@stsci.edu
Raymond Ohl	JHU	ohl@pha.jhu.edu
Nino Panagia	STScI	panagia@stsci.edu
Dan Pascu	US Naval Observatory	pas@phobos.usno.navy.mil
Anna Pasquali	ESO	pasquali@stsci.edu
Norbert Pirzkal	ST - ECF / ESO	npirzkal@eso.org
Philip Plait	ACC Inc. / NASA/GSFC	plait@abba.gsfc.nasa.gov
Judith L. Provencal	Univ. of Delaware	jlp@strauss.udel.edu
Chun Shing Jason Pun	NASA/GSFC	pun@congee.gsfc.nasa.gov
Kavan Ratnatunga	Carnegie Mellon Univ.	kavan@astro.phys.cmu.edu
Michael Regan	Carnegie Inst. of Wash.	mregan@dtm.ciw.edu
Michael Rosa	ST - ECF / ESO	mrosa@eso.org
David Sahnaw	JHU	sahnaw@pha.jhu.edu
David Schade	Canadian Astron. Data Ctr.	schade@dao.nrc.ca
Glenn Schneider	Steward Observatory	gschneider@as.arizona.edu
Al Schultz	CSC/STScI	schultz@stsci.edu
Dick Shaw	STScI	shaw@stsci.edu
Lisa E. Sherbert	STScI	lisa@stsci.edu



Chris Skinner	STScI	skinner@stsci.edu
David R. Soderblom	STScI	soderblom@stsci.edu
George Sonneborn	NASA/GSFC	sonneborn@stars.gsfc.nasa.gov
Elizabeth B. Stobie	Univ. of Arizona	bstobie@as.arizona.edu
Susan Stolovy	Univ. of Arizona	sstolovy@as.arizona.edu
Lisa Storrie-Lombardi	Carnegie Observatories	lisa@ociw.edu
Alex Storrs	STScI	storrs@stsci.edu
Anatoly Suchkov	STScI	suchkov@stsci.edu
Jean Surdej	Universite de Liege	surdej@astro.ulg.ac.be
Nial Tanvir	Institute of Astronomy, Cambridge	nrt@ast.cam.ac.uk
Susan Terebey	Extrasolar Research Corp.	terebey@extrasolar.com
Rodger I. Thompson	Steward Observatory	rthompson@as.arizona.edu
Colleen Townsley	NASA/GSFC	
John Trauger	Jet Propulsion Lab	jtt@bb4.jpl.nasa.gov
Calvin Tullis	STScI	tullis@stsci.edu
Monica Valluri	Rutgers Univ.	valluri@physics.rutgers.edu
Roeland van der Marel	STScI	marel@stsci.edu
Mark Voit	STScI	voit@stsci.edu
Jeremy Walsh	ST - ECF	jwalsh@eso.org
Brad Whitmore	STScI	whitmore@stsci.edu
Michael Wiggs	STScI	wiggs@stsci.edu
Bruce E. Woodgate	NASA/GSFC	woodgate@stars.gsfc.nasa.gov
Erick Young	Univ. of Arizona	eyoung@as.arizona.edu
David Zurek	STScI	zurek@stsci.edu

## Part 1. STIS



## STIS Overview; Capabilities and Basic Operations

S. A. Baum

*Space Telescope Science Institute, 3700 San Martin Drive, Baltimore, MD 21218*

**Abstract.** This paper summarizes the basic capabilities of STIS and describes its successful early on-orbit operation for Cycle 7.

### 1. An Overview of STIS

STIS, the Space Telescope Imaging Spectrograph, was built by Ball Aerospace Corporation under the direction of Bruce Woodgate (GSFC), the Principal Investigator for STIS. A description of the instrument and its early on-orbit performance through the Servicing Mission Orbital Verification (SMOV) period is provided by Kimble et al. (1997) and a more detailed description of the instrument and its science operation is available in the STIS Instrument Handbook and the updates to it (contact [help@stsci.edu](mailto:help@stsci.edu) or see the STScI Web pages).

STIS is an extremely diverse instrument which can be used both for spectroscopy and imaging and which operates from the near-infrared through the ultraviolet. In order to accomplish this range of science STIS has the following components.

- A slit wheel which holds the apertures for spectroscopy and filters for imaging
- A grating wheel (called the Mode Select Mechanism, or MSM) which holds and tilts the first order gratings, the cross dispersers for use with the echelles, and the mirrors for imaging. Only specific central wavelength settings can be achieved as continuous tilt selection is not available.
- Three detectors; a CCD for use in the NIR/Optical and two MAMAs, one for use in the Near-UV to roughly 1650 Å and one for use in the Far-UV to roughly 1150 Å.
- Two calibration lamp systems - including line lamps and flat field lamps.
- A smart CPU which enables the flight software to perform onboard target acquisitions (which take roughly 5 min) that are needed for all slitted spectroscopy and coronagraphy and peakups (which take 5-10 min) that are needed only for observations in the smallest slits ( $\leq 0.1$  arcsecond).

### 2. Typical Operations for STIS Spectroscopy

A typical STIS spectroscopic sequence will consist of the following:

- A target acquisition, followed by a peakup if one is observing in the smallest slits (those which are less than or equal to 0.1 arcseconds) to center the target in slit. The target acquisition is performed immediately following the Guide Star Acquisition at the start of visit. Acquisitions and peakups have been shown to be quite robust and accurate for STIS (see Kraemer and Downes, this volume).
- A series of science exposures at a given grating setting or a series of grating settings.



- Automatic wavecalcs inserted by the ground system at 40-60 minute intervals which return zeropoint accuracies of 0.1 to 0.2 pixels or better, for most settings, to account for both the Mode Select Mechanism irrepeatability and the thermal drifts.
- For MAMA observations, only a total of 5 orbits are permitted per visit, since we have been forced to allow operation of the MAMA high voltage only in the SAA-free orbits of each day, in order to avoid upsets of the MAMA Control Electronics due to charged particles triggering the opto-isolators in the circuitry.
- For visits longer than 4 orbits, taken in a small slit, observers may wish to take a second peakup after 4 orbits, to assure that FGS drift does not cause the target to drift off center in the slit

### 3. Parallel Observations

STIS can be used in parallel with other instruments. The STIS MAMAs can be used only in coordinated and not in pure parallels to assure that bright object screening can be done of the observing fields. The early worries over 50CCD (clear) imaging and the impact of UV bright sources on persistence have been shown to be unfounded and today 50CCD is used regularly in the pure parallels program (see Gardner et al., this volume). STIS detectors do not operate in parallel with each other (as they share one optical path) but observations interleaving STIS detectors have no extra overhead.

### 4. STIS Detector Overview

STIS has three large format (1024 x 1024 pixels) detectors. The STIS/CCD (SITE) is used from the NUV through NIR with a spectral range from 2000-11000 Å, a 51x51 arcsecond field of view, 0.05 arcsecond pixels, low read noise (4 electrons at a GAIN=1), low dark current (0.002 electrons/sec), good dynamic range (up to 140,000 electrons at GAIN=4), and high QE. The overhead between identical exposures is roughly 60 sec for full frame, and 20 seconds using subarrays. The performance at wavelengths longward of about 8000 Å is affected by fringing and by an extended halo on the PSF (see Kimble this volume). Small dust motes visible on flats cover a very small fraction of the detector, but can have opacities of 20%. The general performance of the STIS CCD has been excellent to date (see Kimble this volume). The CCD has shown excellent repeatability during early standard star spectroscopic sensitivity monitoring with repeatability to better than 1% (and see also Ferguson, this volume for photometric results in CCD imaging mode).

The STIS MAMA (Multi-Anode Microchannel Array) detectors are used in the UV. They are photon counting detectors and have both an accumulate mode which is the typical mode of observation and a time-tag mode. In the time-tag mode each photon is time-tagged to 125 microsec. The MAMA detectors are subject to damage at high local (per pixel) and global (over the detector) count rates, therefore we have had to set brightness limits for targets to preserve the safety of the detector. While the MAMAs have 1024x1024 pixels, it is possible to use the MAMAs in the so-called 'highres' mode; this allows subsampling of the 1024x1024 pixels, using 3 electrodes per pixel to centroid the incident charge to roughly half-pixel accuracy, thereby producing 2048x2048 array images. This provides a 10-30% increase in resolution for unresolved features at the price of decreased signal-to-noise per pixel due to increased fixed pattern noise from the statistics of charge partition between the electrodes. All data with STIS is taken, by default, in highres mode and the raw data archived as such. However, the calibration pipeline bins the data back to nominal pixel size, so the calibrated data have the native pixel format and are 1024X1024 pixels in size.



The STIS/NUV-MAMA operates in the NUV from roughly 1650-3100 Å, covers a 25x25 arcsecond FOV, has 0.024 arcsecond pixels, no read noise, reasonably low dark current ( $6 \times 10^{-4}$  counts/pix/sec) and is solar insensitive (with a Cs<sub>2</sub>Te photocathode).

The STIS/FUV-MAMA operates in the UV from 1150-1700 Å, also covers a 25x25 arcsecond FOV, has 0.024 arcsecond pixels, no read noise, extremely low dark current ( $7 \times 10^{-6}$  counts/pix/sec), and is solar blind (CsI photocathode).

## 5. What Science Does the Space Telescope Imaging Spectrograph Do?

STIS can be used to perform the following basic science.

- First Order Spectroscopy from 1150 - 11000 Å with a long slit which is 51 arcsecond long in the optical and 25 arcsecond long in the UV. The first order modes include the Low resolution 'L' Gratings which have a resolving power,  $R$ , of roughly 500 - 1400 (where  $R$  is defined as wavelength divided by a spectral resolution element in Å, where a resolution element is nominally taken as two detector pixels) providing roughly 500 km/sec resolution and the Medium resolution 'M' Gratings which have a resolving power of roughly 5000 - 17000, corresponding to 50 km/sec resolution. Slits of varying widths (52x0.1, 52x0.2, 52x0.5, 52x2, slitless) are supported for observations in first order modes.
- Echelle Spectroscopy from 1150 - 3100 Å, optimized for point source observations using small apertures to separate orders ( $\leq 0.2 \times 0.2$  arcseconds). The Medium Resolution Echelles (E230M, E140M) have nominal resolving powers of roughly 30,000 - 45,000 providing roughly 10 km/sec resolution and the High Resolution Echelles (E230H, E140H) have nominal resolving powers of roughly 110,000, providing roughly 2.5 km/sec resolution.
- Objective Prism spectroscopy in the UV from 1200-3100 Å either slitless or with a long slit, providing resolving powers from 1000 at the short wavelength end to 26 at the long wavelengths.
- Imaging with the CCD, NUV-MAMA, and FUV-MAMA. There is a limited filter set. In the optical, the low readnoise, low dark current, high CCD QE, and in particular the wide band pass of the clear CCD imaging mode means STIS can get deeper faster than WFPC2, particularly when color information is not needed. In the UV, the FUV-MAMA is solar blind and much more sensitive (factor of  $>10$ ) than WFPC2 with the Woods filters, opening up new science opportunities there as well.
- High Time Resolution in the UV Time-Tag mode where resolutions of 125 microseconds can be achieved in any of the spectral or imaging modes.
- Coronagraphy, either coronagraphic imaging in the optical and near IR or bar-occulted spectroscopy over the entire spectral range (1150-11000 Å) using the 52x0.2 slit with a 0.5 arcsecond bar.

The principal gains of STIS relative to FOS and GHRS are the spatial coverage provided by long slit spectroscopy and the greatly increased wavelength coverage at high spectral (echelle) resolutions enabled by the full two dimensionality of the detectors. Additionally, STIS provides greatly decreased background for point sources in UV due to the fine plate scale, appreciably higher throughput in the optical/IR due to the use of the CCD, ease and relative time-efficiency of the target acquisitions and peakups due to the smart CPU, and high time resolution spectroscopy and imaging due to the time-tag mode.

## 6. Outstanding Technical Considerations as of Launch and Status

There were a number of outstanding technical considerations as of launch, all of which have been favorably resolved. These are described below.

- Concern existed about the ability to get signal to noise greater than 30 per resolution element in the Near-IR, longward of roughly 8000 Å where fringing and the long wavelength PSF halo set it. It has now been shown that relatively high signal to noise (100 to 1 for point or fully diffuse sources) can be achieved by the taking of contemporaneous flats which can be used to rectify the data in post-observation data processing (see Goudfrooij and Plait, this volume). However, issues do still remain, particularly the long wavelength halo which in conjunction with the fringing, and for complicated source structures, can still make it difficult to remove the fringes (see also Kimble, this volume).
- Concern existed about the ability to get high signal-to-noise observations with the MAMA detectors. This area is still under work as well, but the signs are extremely encouraging with signal-to-noise greater than 150 per resolution element over a point source extraction box having been achieved on sensitivity calibration stars (see Kaiser, this volume) and early results from the test of the FPSPLIT slits showing the ability to achieve signal-to-noise considerable higher than even this (look for ISRs on the WWW in the future). The quoted signal-to-noises refer to the ability to detect faint lines on a continuum; the fidelity of line shapes will depend critically on other factors as well, such as background subtraction and scattered light.
- At launch there remained a flight software problem which prevented taking of data using onboard Doppler correction for the MAMA echelle modes. This was corrected by the GSFC FSW Group (who took over responsibility for the STIS FSW at launch), and uploaded to STIS in early August, along with the target acquisition fixes (see below) and successfully tested on orbit immediately thereafter.

The principal 'discrepancies' uncovered on orbit include the opto-isolator resets which affect the operation of the MAMAs, the rate of hot pixel growth on the CCDs, and the elevated NUV-MAMA dark rate (see Kimble, this volume for details on these three). During the commissioning of target acquisitions it became clear that the FSW could be further optimized to make the acquisitions and pickups more robust and accurate; those FSW fixes were implemented and uplinked in August and demonstrated to work most effectively (see Kraemer and Downes, this volume). Lastly, there exist mostly small, but some important, differences in predicted versus realized sensitivities (see Bowers, this volume).

## 7. STIS Science Examples

The scientific use of STIS science is just starting to pick up for Cycle 7 as of the writing of this contribution. However, excellent STIS science examples exist in the archive and are publically available. They come from the EROs, SMOV and Cycle 7 Calibration Activities, and some early planetary GO science. The full range of STIS science capabilities have now been demonstrated: including the echelles, which have been used for interstellar medium absorption studies and stellar absorption studies, the long slit and slitless first order optical and UV capability - which have been used on black hole studies in a nearby galaxies (see this volume Bowers), emission line regions around active galactic nuclei, SN1987A, comets, and for the pure parallels observations (see Gardner, this volume). Coronagraphic imaging and spectroscopy has been used to observe Beta Pic and a putative brown dwarf, respectively. The remarkable depth of CCD clear imaging (achieving a depth within a magnitude of



the deepest single filter observations of the Hubble Deep Field in only two orbits!), has been demonstrated through observations of a Gamma Ray Burster (see Fruchter, STScI newsletter, July 1997) and high time resolution timetag observations have been taken of the Crab (see Lindler et al., this volume). Many of these data are now public, and others will become public shortly. The EROs and early science results will be featured in a special, January, issue of the ApJ Letters.

Remember all SMOV data, all Cycle 7 Calibration data (some data good for science there!), all of the archival pure parallel data (slitless G750L, 50CCD and longpass filter imaging) as well as the ERO data is public.

## 8. Summary

SMOV is complete, finishing off a successful collaborative effort to commission STIS by STScI and the STIS IDT. All Cycle 7 science is now fully commissioned - and STIS is off and running. The on-orbit performance of STIS has generally been exceptional - very close to ground predictions; while a few things are not as good as predicted, the bulk are right on and others substantially better. For future updates to the STIS on-orbit performance we refer you to the STIS Instrument Page off the Observing with HST Page of STScI. With STIS GOs and GTOs using the broad range of STIS capabilities and STIS performing as well as it is, we look forward eagerly to an exciting cycle full of new astronomical discoveries.

**Acknowledgments.** The instrument and its on-orbit performance herein described owe to many, many individuals, including the STIS Instrument Definition Team led by Bruce Woodgate, Ball Aerospace, the FSW Group at GSFC, and the commanding, scheduling, pipeline, servicing mission, and instrument groups at STScI. Thanks to all for designing and building such a successful instrument and FSW and ground system to operate it and for facilitating its on-orbit characterization, thereby allowing me the pleasure of writing such a positive summary of STIS's capabilities and performance to date with the confident prediction that many STIS science discoveries await us all.

## References

- Baum S. et al., 1996, *STIS Instrument Handbook*, (Baltimore:STScI)  
Kimble R. et al., 1997, ApJ Letters, in press

## The On-Orbit Performance of the STIS Detectors<sup>1</sup>

Randy A. Kimble<sup>2</sup>

Laboratory for Astronomy and Solar Physics, Goddard Space Flight Center,  
Greenbelt, MD 20771

**Abstract.** The Space Telescope Imaging Spectrograph (STIS), successfully installed into the *Hubble Space Telescope* in February 1997, achieves its advances over the first-generation *HST* spectrographs primarily through the use of modern large-format, two-dimensional array detectors. The performance of the STIS detectors, two Multi-Anode Microchannel Arrays (MAMAs) and one CCD, has been evaluated on-orbit as part of the Servicing Mission Orbital Verification (SMOV) program. All three detectors are functioning well. We report highlights of the results to date here.

### 1. Introduction

The Space Telescope Imaging Spectrograph is a versatile spectrograph covering the 115-1000 nm wavelength range in a variety of spectroscopic and imaging modes. (See Woodgate et al. [1992,1998] and the STScI *STIS Instrument Handbook* [Baum et al. 1996] for overviews of the STIS design and operations.) The principal advances offered by STIS stem primarily from the use of large-format two-dimensional array detectors. Two photon-counting Multi-Anode Microchannel Array (MAMA) detectors, each read out in a  $2048 \times 2048$  format, record UV light, and one  $1024 \times 1024$  pixel CCD covers the visible. Compared with the  $1 \times 512$  element linear array detectors employed by the first-generation *HST* spectrographs, these two-dimensional array detectors enable STIS to provide observing modes with large spatial and/or spectral multiplexing gains.

The observing modes of STIS divide its wavelength range into four spectral bands. Figure 1 presents the quantum efficiency of the flight detectors and demonstrates how they combine to cover the instrument's observing range and also how their overlapping sensitivities provide a degree of redundancy. Band 1 (115-170 nm) is covered by a MAMA detector designated as the FUV MAMA, fabricated with an opaque CsI photocathode deposited directly on the front of its single curved-channel microchannel plate (C-plate). Band 2 (165-310 nm) is covered by a similar detector, the NUV MAMA, which utilizes a semi-transparent CsTe photocathode on the inside of the detector window. This detector provides additional coverage down to 115 nm in imaging and prism modes, and it serves as a backup to the FUV MAMA. The MAMAs were developed by Ball Aerospace and are both permanently sealed tubes with  $MgF_2$  entrance windows. See Timothy (1994) and Joseph et al. (1995) for further details about the MAMA design and performance.

Each MAMA detector incorporates a  $1024 \times 1024$  element anode array, but the processing electronics centroid event positions to half the spacing of the anode array, providing improved image sampling and higher resolution (but with larger flat-field variations) in a

---

<sup>1</sup>The results reported here represent the efforts of many people, including the STIS Investigation Definition Team and personnel of the Goddard Space Flight Center, Ball Aerospace, and the Space Telescope Science Institute.

<sup>2</sup>Co-Investigator, STIS Investigation Definition Team



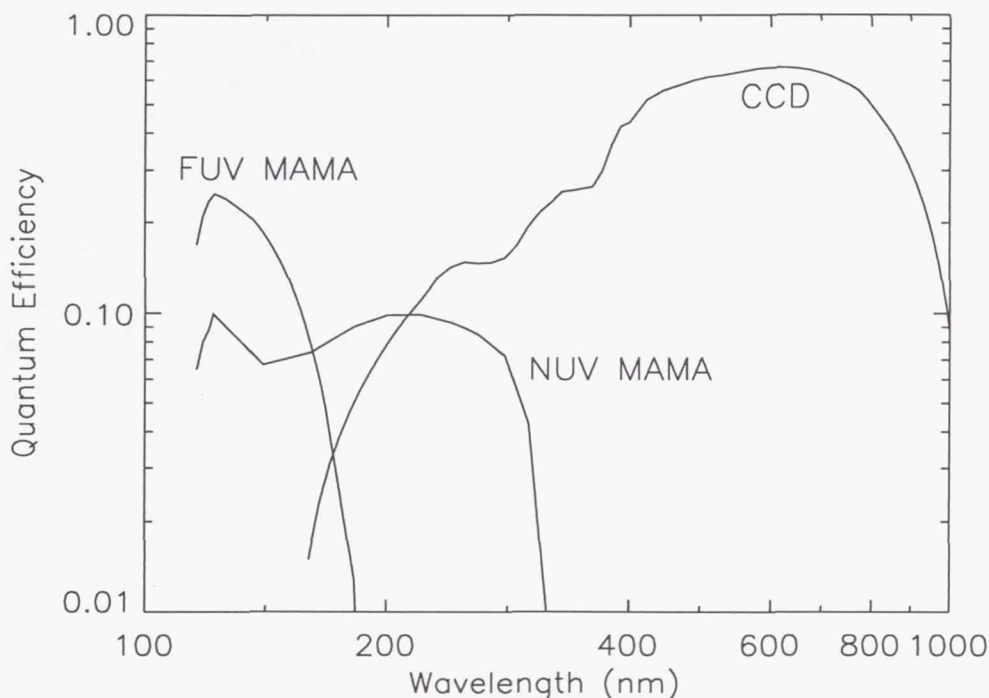


Figure 1. Quantum Efficiency of the STIS Flight Detectors

2048 × 2048 image format (Kasle & Morgan 1991). For historical reasons, this is referred to as the high resolution mode; all generic references to MAMA pixels in this paper (and in most other STIS documentation) refer instead to low-resolution pixels in the 1024 × 1024 format.

Bands 3 and 4 (305-555 nm; 550-1000 nm) are covered by a backside-thinned, UV-enhanced, multi-pinned-phase, 1024 × 1024 pixel CCD developed by Scientific Imaging Technologies (SITe). The CCD also provides backup to the NUV MAMA in the 180-305 nm range. The CCD is cooled to an operating temperature of -83 C using a four-stage thermoelectric cooler (TEC). The CCD and TEC are enclosed within a sealed, evacuated housing whose fused silica window is only slightly cooler than the rest of the instrument, minimizing the condensation of contaminants which could otherwise be deposited directly onto the much colder CCD. See Kimble et al. (1994) for a more comprehensive discussion of the CCD subsystem.

Since launch, a variety of performance and characterization tests have been carried out for STIS as part of the Servicing Mission Orbital Verification (SMOV) program. We report here on the highlights of the detector-related aspects of the SMOV program. For critical parameters that have not yet been or can not be measured directly in flight, we also cite relevant results from the pre-flight calibration.

## 2. CCD Performance

The 1024 × 1024 pixel STIS CCD is a backside-illuminated three-phase device, with 21 μm pixels, multi-pinned-phase implants and operation, and an enhanced UV response. The backside UV-enhancement process was developed by SITe for the STIS program. The resulting quantum efficiency (Figure 1) is stable, does not show QE hysteresis, and does not require a UV flood.

The CCD is fabricated with a readout amplifier in each of the four corners. There is an independent analog signal processing chain for each amplifier, and the STIS flight software supports full-frame, on-chip-binned, or subarray readout with any of the four amplifiers, as well as two and four amplifier readout modes. Initial functional testing on orbit verified that all four amplifier chains were functioning nominally. Observations since that first checkout have been carried out exclusively with the lowest noise amplifier, which was most fully characterized in ground testing. The redundant amplifiers are available as future backups.

Four commandable gain settings are available for the CCD. The noise performance *measured in flight* and the dynamic range for each setting are summarized in Table 1. Rough gain measurements made in flight are consistent with the more precisely determined ground values shown in the table. Two gain settings are recommended for general use: gain=1 for the greatest sensitivity to faint targets and gain=4 for the highest dynamic range and full well.

Table 1. CCD Noise/Dynamic Range.

Nominal Gain e/DN	Measured Gain e/DN	Noise (rms) <i>In-flight data</i>	Linear Range At 1% Rolloff	Single Frame Dynamic Range = Linear Range/Noise
1	0.995	4.0 DN = 4.0 e	33,000 e	8,250
2	2.01	2.7 DN = 5.4 e	86,000 e	16,000
4	4.11	1.7 DN = 7.0 e	144,000 e	20,600
8	8.38	1.3 DN = 10.9 e	144,000 e	13,200

In-flight mean bias levels vary over roughly 10 DN (data numbers in the 16-bit digitized readout) at gain=1 and 3 DN at gain=4 (due to temperature variations in the CCD and processing electronics); however, the *shape* of the bias frames is constant to  $<0.2$  DN, so the bias level is well determined by the serial and parallel overscan data read out with each CCD frame. Under logarithmic stretch, some frames, particularly at gain=4, show “herringbone” noise that can be discerned by the eye. This pattern is low amplitude, however,  $<1$  DN, and does not significantly affect the overall noise statistics in the image.

Charge transfer efficiency (CTE) was measured by both x-ray and edge response techniques in ground calibration, with parallel CTE results of 0.999994 @ 1620 e (x-ray) and 0.999991 @ 200 e, 0.99996 @ 10 e (edge response). Serial CTE’s are higher. Additional ground calibration tests measured the parallel CTE performance under “sparse field” illumination, i.e. as would be encountered when observing the spectrum of a point source or an image of a dilute stellar field with only one or two stars per CCD column. These tests implied a charge loss up to 1.1% from the top of the CCD column to the bottom, for signal levels of 500 e/pixel, operating at the gain=1 voltage settings. For higher signal levels or the gain=4 voltage settings, the derived charge loss across the CCD is lower.

The x-ray CTE measurements can not be duplicated in flight, and the sparse field measurements have not yet been. However, edge response measurements (using onboard flat-field lamps for illumination) show no significant changes from ground measurements.

The median dark current at the CCD operating temperature of -83 C is only  $\sim 0.0015$  electrons/pixel/second, or 5-6 electrons/pixel/hour. Unless significant on-chip binning is employed, the noise from the median dark current is thus negligible compared with the read noise of the system. Of much greater significance are the effects of cosmic rays and radiation-induced hot pixels. With regard to these issues, the performance of the STIS CCD is very similar to that of WFPC2.

The cosmic ray rate observed on the STIS CCD outside of the South Atlantic Anomaly (SAA) is  $\sim 1$  event/cm<sup>2</sup>/second. Roughly 30-40 pixels/second are affected at greater than a 20 electron level. Cosmic rays are most effectively removed from science data by specifying CR-SPLIT exposures to obtain multiple images from which cosmic rays can be vetoed.



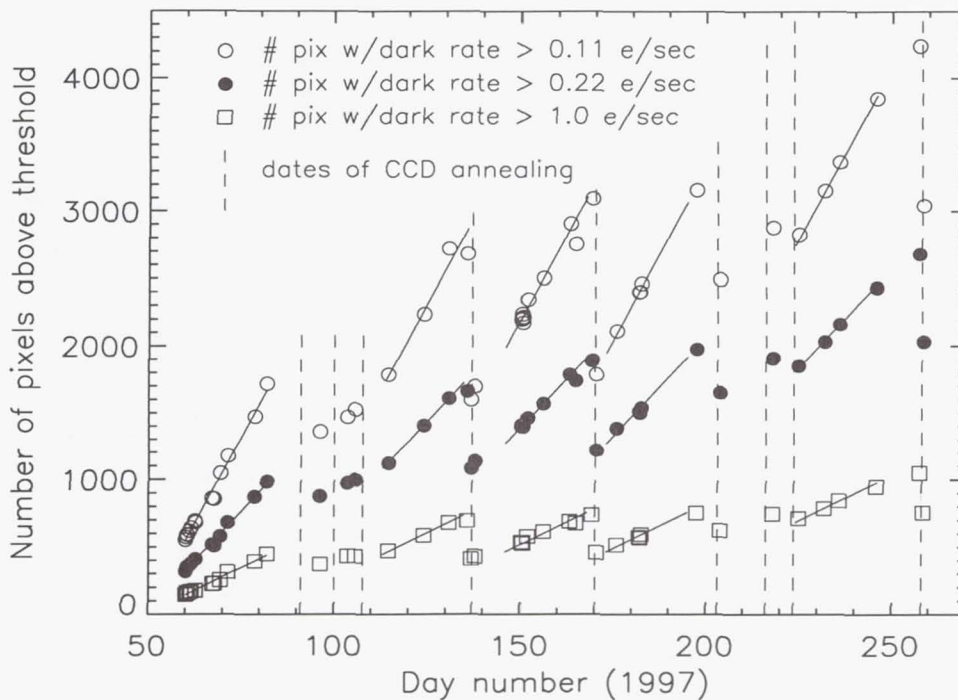


Figure 2. Growth of CCD Hot Pixels in Orbit

As expected for a CCD in space, energetic particle impacts on the STIS CCD produce “hot pixels” with enhanced dark current. As for WFPC2, warming of the CCD by turning off the thermoelectric cooler is effective at “annealing” some portion of the hot pixels. The STIS CCD reaches  $-5^{\circ}\text{C}$  with the TEC off; annealing at this temperature for 12 hours is scheduled monthly. WFPC2 experience suggests that eventually a near steady state is reached in which the number of new hot pixels each month is similar to the number of old hot pixels that “heal” through the annealing process or spontaneously while the CCD is cold; hence the *net* growth rate of hot pixels over several years on orbit for WFPC2 is  $<8\%$  of the instantaneous growth rate (Biretta et al. 1996). After the first few STIS annealing cycles, the net growth rate of hot pixels is down to about 30% of the instantaneous growth rate (see Figure 2); this fraction is expected to decrease as the hot pixel count asymptotically approaches a steady state. CCD dark frames are taken frequently to permit flagging of hot pixels in nearby science exposures. The most effective removal of hot pixels from science data can be accomplished by dithering the pointing between exposures to permit hot pixel vetoing. Additional details regarding the hot pixels and annealing behavior are reported in this volume by Beck & Landsman (1997).

An unpleasant feature of the SITE backside-illuminated devices, discovered during STIS ground testing, is a significant degradation of the CCD point spread function (PSF) at long wavelengths. While the core of the PSF remains sharp at all wavelengths, a substantial halo is seen at wavelengths longer than  $\sim 750\text{ nm}$ , where the CCD silicon begins to become transparent. As an increasing fraction of the incident light reaches the substrate of the backside-illuminated device, scattering in the (unfortunately translucent) substrate material produces an ever larger halo, containing an increasing proportion of the overall energy (see Figure 3). At the longest wavelengths (1000 nm), the halo extends to hundreds of pixels in radius and contains up to  $\sim 40\%$  of the light, though each pixel in the halo of course captures a very small fraction of the peak brightness. This portion of the raw QE of the CCD is

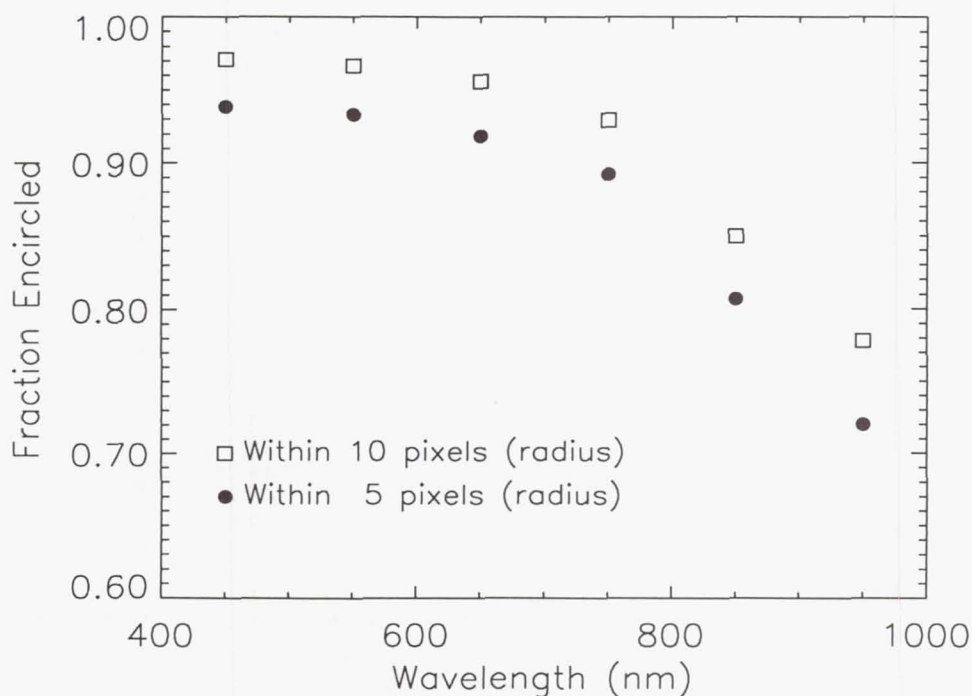


Figure 3. Encircled Energy vs. Wavelength and Extraction Radius for the STIS CCD

thus not useful, as it is not included within practical extraction radii for spectroscopy or imaging. The effect is stable over time, however, and can be appropriately calibrated.

The pixel-to-pixel flat-field behavior of the STIS CCD is also extremely stable. Short term (several hour) pixel-to-pixel stability at better than 0.1% rms was verified over several wavelengths spanning the CCD range in ground testing. In flight, broad-band flat-field exposures spanning a month constrain any changes in the pixel-to-pixel response to be <0.2% rms, and some portion of that variation is attributable to poorly removed hot pixels. Flats constructed using the onboard tungsten continuum lamps thus in general provide high S/N rectification of STIS CCD data.

The most significant issue affecting flat-fielding of STIS CCD data is fringing at the longer wavelengths (where the silicon begins to become transparent), caused by interference between the incident beam and light reflected by the substrate of the device. The fringing is negligible shortward of ~750 nm, but grows to peak-to-peak amplitudes of 25 and 32% at 980 nm for G750L and G750M, respectively.

Rectification of the fringing pattern should be a tractable problem, because the behavior is completely stable with time. However, small shifts in the wavelength mapping onto the detector, caused by grating wheel non-repeatability and thermal drifts, do cause the fringe pattern to shift from exposure to exposure. Therefore, for accurate fringe removal, it is necessary to take contemporaneous spectral flats using the onboard tungsten lamps (at least until a suitable library of flats can be constructed); see Plait & Bohlin (1997) in this volume. Fortunately, the onboard lamps are bright, so the required exposures are short.

The spatial extent of the source along the slit is also an issue in fringe removal. Because of the PSF halo at long wavelengths, an extended source produces a smooth pedestal beneath the fringing modulation that is not present for a point source. However, a judicious combination of short and long-slit flats should serve. In data taken to date, Goudfrooij, Baum, & Walsh (1997, this volume) have successfully removed the fringes to better than



1% to  $\sim 950$  nm for a white dwarf spectrum using a short slit flat and for the extended source Io using a long-slit flat. Development of a systematic fringe removal methodology is a key goal of the in-flight calibration program.

Note that STIS imaging is generally unaffected by the fringing, because no narrow-band filters are used at long wavelengths, and the sky background is continuum zodiacal light, not airglow emission lines (as on the ground). Broadband continuum input smooths over the fringes completely; only a highly monochromatic long wavelength emission-line source would show fringe modulation in imaging mode.

### 3. MAMA Performance

The STIS MAMA detectors began on-orbit operations in late April 1997. Their use was delayed until software and scheduling changes had been made to deal with an unexpected issue of control electronics resets (see Section 4.) Since that time, the MAMA detectors have been performing very well. See Figures 3 and 4 for examples of FUV MAMA echelle spectroscopy and NUV MAMA imaging.

A few key MAMA performance parameters are shown in Table 2. Most of these data are from ground calibration, except for the dark rate, for which in-flight values are shown. While detector-only PSF and quantum efficiency can not be measured directly in flight, the end-to-end STIS performance indicates that the detector resolution and efficiency are nominal.

Table 2. Key MAMA Performance Parameters

	FUV MAMA	NUV MAMA
Wavelength Range	115 - 170 nm	165-310 prime 115 - 170 backup
Low-res Pixel Size	25 $\mu\text{m} \times 25 \mu\text{m}$	25 $\mu\text{m} \times 25 \mu\text{m}$
Spatial Resolution (FWHM) (w/hi-res readout)	22.7 $\mu\text{m}$	29.3 $\mu\text{m}$
Quantum Efficiency	$\sim 21\%$ (142 nm)	$\sim 9.5\%$ (237 nm)
Dark Rate	$5\text{-}10 \times 10^{-6}$ cts/pix/s*	$0.6\text{-}1.5 \times 10^{-3}$ cts/pix/s*
Dynamic Range (10% rolloff)		
Local (MCP limited)	220 cts/pixel/s*	340 cts/pixel/s*
Global (electronics limited)	305,000 cts/s	305,000 cts/s
Flat Field Uniformity (low-res pixels*)	6.4% rms	3.1% rms
Flat Field Stability (changes in 2x2 pixels*)	over 4 months <1% rms	over 21 days <0.68% rms
Visible Light Rejection (QE at 400 nm)	$1.5 \times 10^{-10}$	$2.7 \times 10^{-4}$

\*Note: "Pixel" refers to a low-resolution MAMA pixel here (*i.e.*, the 1024 $\times$ 1024 format).

A positive highlight of the in-flight performance is the extremely low background of the FUV MAMA, 5-10 times lower than the specification. The close agreement of the in-flight dark rate with that seen in ground test confirms the successful rejection of Cherenkov events produced in the detector window. Cherenkov photons produced by passage of energetic particles through the detector windows formed the dominant background in the Digicon detectors of the first-generation spectrographs; because the multiple Cherenkov photons produced by a particle transit are effectively simultaneous, they are rejected by the MAMA event processing logic.

The only performance disappointment with the MAMA detectors in flight is the high dark rate of the NUV MAMA. The specified dark rate for the tube was  $1.25 \times 10^{-4}$



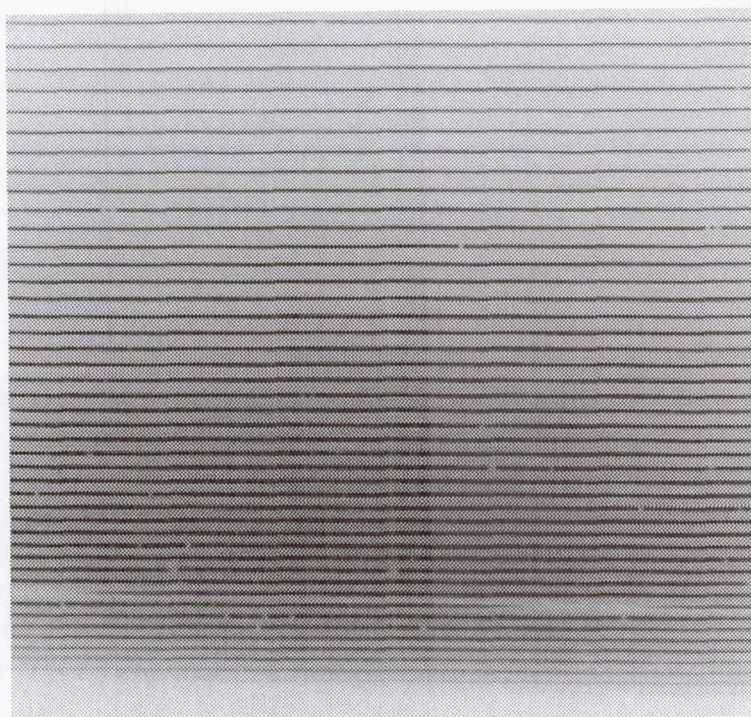


Figure 4. Echelle Spectrum (Mode E130M) of BD+28°4211 with the FUV MAMA. The spectrum shown covers 115-170 nm and shows broad Lyman  $\alpha$  absorption (near the bottom) as well as numerous narrow stellar absorption features.

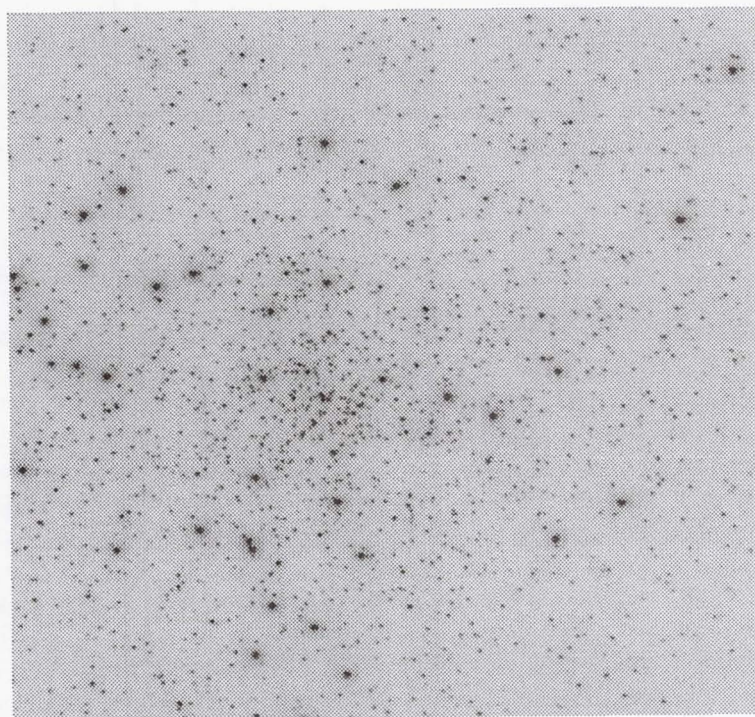


Figure 5. 270 nm Image of the Globular Cluster NGC6681 with the NUV MAMA. All of the features visible in the image are statistically significant detections of stars.



cts/second/pixel, and ground testing led us to expect substantial improvement over that specification in orbit. Unfortunately, in flight, energetic SAA particles excite meta-stable states in impurities in the window of the NUV MAMA; the subsequent phosphorescent decay produces UV photons that are detected by the MAMA photocathode. This phenomenon has long been recognized, and a screening program for phosphorescence was specifically instituted for the STIS detector windows; however, an error in the ground testing of this particular  $\text{MgF}_2$  ingot allowed it to be used despite its poor phosphorescence characteristics.

The observed NUV MAMA background of  $0.6\text{--}1.5 \times 10^{-3}$  cts/second/pixel (the de-excitation rate varies with detector temperature) is roughly an order of magnitude higher than the specification. Over a typical 2000 second single-orbit exposure, the resulting dark count signal in a standard  $2 \times 11$  pixel spectral extraction slit is 26-66 counts. Optimal extraction techniques or the use of a smaller extraction slit reduce the dark contribution below this level. Thus, in short exposure time observing programs, only very low S/N observations are significantly affected. However, long observations or those which are binned spectrally or spatially (such as for extended sources) can be significantly compromised by the unwanted background.

The high S/N potential of MAMA observing is a key issue; accordingly, a separate paper in this volume (Kaiser et al. 1997) is devoted entirely to this topic. Here we briefly summarize the extremely encouraging S/N results described in more detail in the Kaiser et al. paper.

Intrinsic pixel-to-pixel variations in the response of the MAMA detectors are significant: 3.9% and 2.8% rms for the FUV and NUV MAMA, respectively, in the  $1024 \times 1024$  low-res pixel format (which supports the nominal resolution of all STIS modes). Severe odd-even effects in the high-res readout lead to much larger rms variations ( $\sim 45\text{--}50\%$ ) in the  $2048 \times 2048$  format. Nevertheless, high S/N MAMA observations are possible, particularly in spectroscopic modes, for two principal reasons: first, the flat-field behavior is extremely stable over time (as long as the instantaneous local count rate is not too high); second, the illumination pattern on the detector during an exposure provides a significant smoothing of the intrinsic response variations (especially in the high resolution echelle modes, where the Doppler effects of orbital motion shift the spectrum gradually over the detector format).

In first order spectroscopic modes, the raw detector response is smoothed over the cross-dispersion profile produced by the stellar spectrum. Convolution of detector flat-field images with a Gaussian profile of two low-res pixels FWHM (representative of the cross-dispersion profiles in STIS spectroscopy) reduces the rms response variations to 2.5% (FUV) and 1.8% (NUV) per low-res pixel in the dispersion direction, and to 1.4% (FUV) and 0.92% (NUV) per two-pixel wide spectral resolution element. We would therefore expect the MAMAs to support point source spectroscopy up to  $S/N = 70$  (FUV) and 110 (NUV) per resolution element *without applying a flat field calibration at all*. The additional smoothing produced by a typical Doppler amplitude of  $\pm 8$  high-res pixels in the high resolution echelle modes should increase the S/N capability to  $\sim 140$  (FUV) and  $\sim 300$  (NUV) per spectral resolution element, *again, without even using a flat*.

The S/N expectations without Doppler smoothing have been well confirmed in flight by SMOV observations in the low resolution first order modes G140L (FUV MAMA) and G230L (NUV MAMA). The extracted spectra of standard stars observed in these modes are compared with low order spline fits to various regions of the spectra. The rms fluctuations of the actual spectrum divided by the low order fit provide a measure of the S/N achieved. With the FUV MAMA, a spectrum with a count-statistic-limited S/N of 165 yielded an observed S/N of 80 with no flat field applied and 128 using a flat from ground testing. For the NUV MAMA, a spectrum with a count statistic potential of 200 yielded a S/N of 105 with no flat and 150 using a ground flat. Both results are in excellent agreement with predictions. See Kaiser et al. (1997) for details.

As this paper goes to press, preliminary results have just been reported from a STIS test of the "F-P split" technique previously employed to obtain very high S/N data with



the first generation *HST* spectrographs. In this technique, multiple spectra of the target are acquired, offset from each other in the dispersion direction, but overlying each other as closely as possible in the cross-dispersion direction. Iterative analysis of the resulting data then permits a simultaneous solution for the source spectrum and the flat-field response of the instrument. A preliminary analysis of MAMA echelle spectra taken in this manner (in STIS medium resolution echelle modes E140M and E230M) yields S/N of  $>250$  per low-resolution pixel in the spectral direction (integrated over the cross-dispersion profile) and  $>350$  per 2-pixel spectral resolution element. Details of the observations and analysis are presented by Gilliland et al. (1997) and Kaiser et al. (1997).

Thus, between the use of onboard calibration lamps to derive spectral flats, the smoothing effects of the illumination pattern and Doppler shifting, and the use of F-P split techniques, the MAMA detectors should routinely achieve the specified S/N performance of  $>100$  per resolution element (when count statistics permit), and the ultimate S/N capability of STIS MAMA observations appears to be well beyond that level.

STIS also has the ability to perform time-resolved observing with the MAMA detectors, time-stamping the photons detected to an accuracy of  $125\ \mu\text{sec}$  for event rates below 30,000 cts/sec. The most rigorous test of this capability has been the acquisition of time-resolved spectra of the Crab pulsar with the NUV MAMA in mode G230L. The test was completely successful; see Lindler et al. (1997, this volume) for details.

#### 4. Detector Electronics Resets

The biggest surprise encountered in operating STIS in flight has been the response of the detector control electronics to the radiation environment. Digital communication between the STIS control section microprocessor and the MAMA and CCD control electronics is optically coupled in order to eliminate conducted electrical noise and thereby maintain a low noise environment for the detectors. Unfortunately, the detector reset circuitry has been found to respond to transient spikes on the outputs of the optical isolators by partially resetting the detectors. These transients can be produced by the passage of trapped SAA particles or cosmic rays through the optical isolators. Though these components had been properly screened for total radiation dose effects, the transient response of the optical isolator reset-circuit combination was not recognized pre-flight.

In the CCD subsystem, the partial resets are relatively infrequent (roughly one per month of continuous operation) and are quite benign. A few CCD control voltages are set to non-functional but non-harmful values. By scheduling CCD voltage reconfiguration commands at each SAA exit or before CCD observation blocks, the chances of losing data from a CCD reset are rendered negligible.

The MAMA partial resets are both more frequent (approximately one per day per MAMA if the MAMA low voltage power is left on during SAA passages) and more complex. One effect of the partial reset is to turn off the detector high voltage abruptly. Though the detectors can withstand such shutdowns (as they must during the infrequent spacecraft safings), daily shutdowns of this type would be unnecessarily stressful to the high voltage system. In addition, when the partial reset occurs, there is a small but non-zero probability (1 in  $\sim 500$ ) that a high voltage ramp-up to the full power supply rails could be spuriously commanded; this would very likely damage the MAMA tube if allowed to proceed. Once the reset phenomenon was recognized on orbit, the MAMA low voltage power was left off until protective software was installed onboard. This software monitors the MAMA subsystems on 40 msec timescales and is designed to intercept a reset-induced ramp-up before it can reach hazardous voltage levels.

In order to avoid potential stresses and risks to the MAMA detectors, they are now being operated in the following manner. The MAMA low voltage system is cycled off for each SAA crossing, but is powered on the rest of the time to maintain thermal stability

in the instrument. The MAMA high voltage, on the other hand, is ramped up and down at the nominal slow ramp rate once per day, in the block of contiguous non-SAA-crossing orbits, if the MAMA is scheduled for use that day. The MAMAs have been operated under this regimen for approximately 130 days. They have experienced seven resets outside of the SAA in that time. Hence, the best current estimate is that each MAMA will be shut down abruptly by a particle-induced reset approximately every three months (since the MAMA high voltage is on less than half of the time), and the spurious voltage ramp-up is unlikely ever to begin.

The principal effect of the resets, therefore, is to lower the available duty cycle for MAMA observations to about 40% of *HST* orbits. During the current period, when NICMOS observations are being accelerated to maximize its scientific yield before its cryogen is depleted, this duty cycle is more than adequate to schedule MAMA science. More complex, higher duty cycle operating schemes can be considered later if required.

## 5. Summary

The three STIS detectors have been evaluated through a variety of tests in the SMOV program. They are all functioning well. We expect them to support a rich scientific program in the coming years.

**Acknowledgments.** We are grateful to all whose efforts over many years made the development of STIS and the execution of the *HST* Second Servicing Mission so successful. The STIS IDT has been funded in response to NASA Announcement of Opportunity OSSA-4-84 through the *Hubble Space Telescope Project* at the Goddard Space Flight Center. This paper is based on observations with the NASA/ESA *Hubble Space Telescope*, obtained at the Space Telescope Science Institute, which is operated by AURA Inc. under NASA contract NAS5-26555.

## References

- Baum, S. et al. 1996, *STIS Instrument Handbook*, (Baltimore:STScI)  
Beck, T., & Landsman, W. 1997, this volume  
Biretta, J. et al. 1996, *WFPC2 Instrument Handbook*, (Baltimore:STScI)  
Gilliland, R. L., et al. 1997, Instrument Science Report STIS, (Baltimore:STScI), in preparation  
Goudfrooij, P., Baum, S. A., & Walsh, J. R. 1997, this volume  
Joseph, C. L. et al. 1995, Proc. SPIE, 2551, 248  
Kaiser, M. E., Lindler, D. J., Bohlin, R. C., & Gilliland, R. L. 1997, this volume  
Kasle, D. B., & Morgan, J. S. 1991, Proc. SPIE, 1549, 52  
Kimble, R. et al. 1994, Proc. SPIE, 2282, 169  
Lindler, D. J., Gull, T. R., Kraemer, S. B., & Hulbert, S. J. 1997, this volume  
Plait, P., & Bohlin, R. 1997, this volume  
Timothy, J. G. 1994, Proc. SPIE, 2278, 134  
Woodgate, B. et al. 1992, ESO Conf. and Workshop Proc. 44: Science with the Space Telescope, P. Benvenuti & E. Schreier, European Southern Observatory: Munich, 525  
Woodgate, B. et al. 1998, in preparation



## The On-Orbit Optical Performance of STIS<sup>12</sup>

Charles W. Bowers<sup>3</sup>

*Laboratory for Astronomy and Solar Physics, Goddard Space Flight Center,  
Greenbelt, MD 20771*

**Abstract.** The Space Telescope Imaging Spectrograph (STIS) is a versatile, general purpose instrument installed aboard the *Hubble Space Telescope* in February, 1997. During the following Servicing Mission Orbital Verification (SMOV) period, STIS has been made operational and aligned, and initial checkout and calibration completed. The overall optical performance goals have largely been achieved and a summary of these results is presented.

### 1. Introduction

The Space Telescope Imaging Spectrograph (STIS) is a general purpose spectrograph installed aboard the Hubble Space Telescope in February, 1997. Through a number of optical modes, spatially resolved spectroscopy is possible from the ultraviolet to near infrared (115–1000nm) over fields of 25 and 50 arcseconds in the ultraviolet and visible respectively. Spectral resolving powers of 500–1000 may be achieved throughout the wavelength range in low resolution modes, and 10,000–20,000 in medium resolution modes. In the ultraviolet (115–310nm) medium and high resolution echelle spectroscopy may be obtained at resolutions of 30,000–45,000 and about 100,000. Custom manufactured gratings were acquired, tested, and installed to perform these functions (Content et al. 1997). Formats have been designed to provide simultaneous acquisition of spectra over wide bandpasses whenever possible to increase observing efficiency. A wide variety of slits and apertures are available to permit selection of many combinations of resolution and field in all modes. Camera modes are also available throughout the full instrument bandpass for target acquisition and for scientific imagery either in an unfiltered mode or using the small complement of available filters. Photon counting (MAMA) detectors are utilized in the ultraviolet with neutral density filters available to extend their capability for ultraviolet observations of brighter targets. A single CCD is provided for observations longward of 310nm.

Light entering STIS is corrected for the HST spherical aberration and astigmatism at the STIS field point by a two-element corrector system, analogous to the corrector pairs deployed by COSTAR. Following correction, a well focused image is formed at the STIS slit plane at which an appropriate slit, aperture or filter may be inserted in the light path using the slit wheel. Following the slit plane, light passes to an ellipsoidal collimator which redirects the beam toward an element on the mode select mechanism (MSM). Any one of

---

<sup>1</sup>The results reported here represent the efforts of many people, including the STIS Investigation Definition Team and personnel of the Goddard Space Flight Center, Ball Aerospace, and the Space Telescope Science Institute.

<sup>2</sup>Based on observations with the NASA/ESA *Hubble Space Telescope*, obtained at the Space Telescope Science Institute, which is operated by the Association of Universities for Research in Astronomy, Inc. (AURA), under NASA contract NAS5-26555.

<sup>3</sup>Co-investigator, STIS Investigation Definition Team



21 optics mounted on the MSM may be rotated into the collimated beam. The MSM can also tip or tilt the element as necessary for modes which must be scanned to cover the complete bandpass. All first order gratings, echelle cross dispersers and ultraviolet camera mirrors are located on the MSM, as well as several backup mode and transfer optics. Order sorters are mounted as appropriate in front of the MSM gratings. Selection of the particular element of the MSM results in light going toward one of the three detectors, either directly or via an echelle or fold mirror.

Further details of the STIS design and operations may be obtained from Woodgate et al. (1992, 1998) and the STScI *STIS Instrument Handbook* (Baum et al. 1996). The optical performance of STIS in a number of key areas is briefly summarized here based primarily on results obtained in-flight during the Servicing Mission Orbital Verification (SMOV) program.

## 2. Corrector Alignment and Performance

Alignment of STIS consisted of essentially two steps. First, during ground calibration, all optics and detectors were adjusted to properly re-image the STIS slit plane onto each detector. This insured that the nominal spectral resolution could be achieved by selection of the appropriate slit. Secondly, the corrector system was aligned in flight to correct and re-image light from the OTA onto the slit plane, producing the greatest concentration of light at this plane and so maximize the instrument throughput and the spatial resolution along the slit.

STIS incorporates a two mirror corrector system. The first mirror, CM1, is a concave sphere mounted on a mechanism which permits in-flight adjustment in focus and tip/tilt. CM1 produces a nearly collimated beam from the OTA and redirects it toward the second corrector mirror, CM2. CM2 is an anamorphic asphere located at a pupil position which redirects and focuses the beam from CM1 onto the STIS slit plane. Adjustment of CM1 in focus provides a focused image at the STIS slit plane and in tip/tilt provides optimal correction of the image by properly positioning the beam onto CM2.

Ground testing using HST simulators had confirmed the capability of the STIS corrector system. In-flight measurements using on-board calibration lamps confirmed that the spectroscopic modes remained focused to the slit plane following launch. Corrector alignment was accomplished through a series of focus and tip/tilt sweeps, initially in the visible, and finally in the ultraviolet, with the ultimate goal being to maximize the ultraviolet transmission through the  $0''.1 \times 0''.09$  aperture. Spectra obtained in the low resolution modes, G140L and G230L, confirm that following the final setting, slit transmission values measured are very close to expectations, namely 39% (121.6 nm), 50% (160 nm), 55% (200 nm) and 60% (270 nm).

Some additional measurements of slit transmission through a few slits have been completed with the CCD and typically show slightly greater transmission (5-15%) than expected. A similar series of measurements with the MAMA detectors in the ultraviolet will be undertaken shortly.

## 3. Spectral Resolution

Spectral resolution has been measured in all the STIS primary science modes. For scanning modes, in-flight measurements have typically been made at only a few settings so far, with the remainder to be made shortly. These measurements are made using the single on-board Pt-Cr/Ne calibration lamp (LINE) which illuminates the entire slit plane at a focal ratio similar to the OTA. The selected slits for all measurements are those nominal slits which project to about 2 pixels width at the respective detectors. Uniform slit illumination will yield values which are slit limited. Higher resolution may be achievable, even through these

slits, with point sources which are well focused at the slit plane and so underfill the selected slit. Gaussian fits were made to the line profiles and the fwhm values of these fits have been used to specify the resolving power. No significant differences have been measured between these in-flight tests and similarly produced ground tests which confirmed that STIS achieves, and generally surpasses its spectral resolution requirements. The results are presented as resolving power for first order prime modes in Table 1, echelle modes in Table 2 and first order support modes in Table 3. Values in italics are from ground testing.

### 3.1. First order, long slit modes

The  $52'' \times 0''.050$  slit, SL050, was selected for UV measurements (115-310 nm) with the MAMA detectors and the  $52'' \times 0''.10$  slit, SL100, for CCD measurements ( $>310$ nm). The results are shown in Table 1 with ground measurements indicated in italics. The resolving powers indicated include variation over the bandpass and the field for each mode. For the scanning modes, the projection of the slit width at the detector plane is reduced due to the grating anamorphic magnification to about 1.5 pixels for G140M and G230M and about 1.7 pixels for G430M and G750M.

The resolution along the slit length varies  $\leq 10\%$  in bands 2,3 and 4 (165-1000nm). The far-UV modes (G140L, G140M) show more variation:  $\leq 10\%$  over  $\sim 75\%$  of the slit length for G140L, degrading to 70% of the field center value at one end of the slit, and 30% variation over the central half slit length for G140M. Both modes however, meet their pre-flight resolution specifications over  $>70-75\%$  slit length.

Table 1. Spectral Resolving Power, First Order Primary Modes

Mode	Specification	Measured	Name/ $\lambda$	Slit
G140L	770-1130 (115-170nm)	1210-947 (130nm) 1440-1039 (155nm)	P1/143nm	SL050
G140M	$0.86-1.28 \times 10^4$ (115-170nm)	<i>12070-7760 (117nm)</i> 14370-9240 (137nm) <i>19340-12380 (164nm)</i>	P1/117nm P5/137nm I6/164nm	SL050 SL050 SL050
G230L	415-730 (165-310nm)	670-502 (190nm) 950-775 (269nm)	P1/238nm	SL050
G230M	$0.75-1.39 \times 10^4$ (165-310nm)	<i>9800-8180 (169nm)</i> 15810-14440 (234nm) <i>20640-17550 (306nm)</i>	P1/169nm P9/238nm P18/306nm	SL050 SL050 SL050
G430L	445-770 (305-555nm)	540-990	P1/430nm	SL100
G430M	$4.34-7.73 \times 10^3$ (305-555nm)	<i>6200-4940 (317nm)</i> 8002-6460 (445nm) <i>10140-8390 (522nm)</i>	P1/317nm P6/445nm P9/522nm	SL100 SL100 SL100
G750L	425-680 (550-1000nm)	650-560 (610nm) 760-690 (820nm)	P1/775nm	SL100
G750M	$3.76-6.22 \times 10^3$ (550-1000nm)	<i>5490-5150 (573nm)</i> 8420-6490 (780nm) <i>10370-8890 (1036nm)</i>	P1/573nm P5/780nm I1/1036nm	SL100 SL100 SL100

<sup>†</sup>Results in italics are based on ground testing



### 3.2. Echelle modes

Spectral resolution measurements were made with the 0''60 wide (S200X060) and 0''90 wide (S100X090, S200X090) slits for the medium and high dispersion echelle modes respectively. The results are presented in Table 2. The medium resolution echelles exceed their specified resolutions as shown. The E140M echelle used in-flight was a late replacement to the nominal grating which suffered from low efficiency. Used at about 45° instead of the original design 32°, this grating has higher resolution, as indicated, than the companion E230M grating.

The spectral resolving powers of the high resolution echelle modes, E140H and E230H, in Table 2 were measured using the on-board calibration line lamp. While comparable results have been obtained during ground and flight testing, thus confirming the stability of alignment, these modes are capable of much higher resolution. Ground measurements using a mono-isotopic Pt lamp (the on-board lamps are poly-isotopic) with the narrow 0''025 wide slit (S100X025) gave resolving powers of 132,000-170,000 for the E230H mode. To obtain these results, flat field correction was applied to the spectra in the unbinned, high resolution MAMA formats. Even higher resolution (220,000) was obtained in mode E140H by the same methods and additionally, by removing the voltage which establishes a repelling field in the FUV MAMA. This reduces the detector contribution to PSF by more tightly confining emitted photoelectrons.

Table 2. Spectral Resolving Power, Echelle Modes

Mode	Specification	Measured	Name/ $\lambda$	Slit
E140M	24,000-24,200 <sup>a</sup> (115-170nm)	46,000	P1/143nm	S200X060
E140H	100,000 (115-170nm)	99,300-114,200 <sup>b</sup>	P2/142nm	S200X090
E230M	23,900-23,100 (165-310nm)	31,000-32,000	I5/256nm	S200X060
E230H	100,000 (165-310nm)	106,000-116,000 <sup>b</sup> <i>92,300-100,700<sup>b</sup></i>	P4/251nm P6/301nm	S100X090 S200X090

<sup>†</sup>Results in italics are based on ground testing

<sup>a</sup>Resolving power specification is for the original, design grating. For the as-flown echelle, the equivalent specification resolving power is 37,000.

<sup>b</sup>Resolving powers are as measured with the on-board poly-isotopic calibration lamps. Potential mode resolving power is greater - see text.

### 3.3. Support modes

Ground test measurement results of the spectral resolution of the STIS support modes are shown in Table 3. These modes use the echelle mode, cross disperser gratings in first order to produce intermediate resolution in the ultraviolet. A small set of orthogonal slits have been provided to be used with these support modes.

## 4. Spectrograph Spatial Resolution

Measurements have been made of the extent of illumination perpendicular to spectral dispersion in the primary science modes. The data used was mostly obtained for sensitivity



Table 3. Spectral Resolving Power, First Order Support Modes

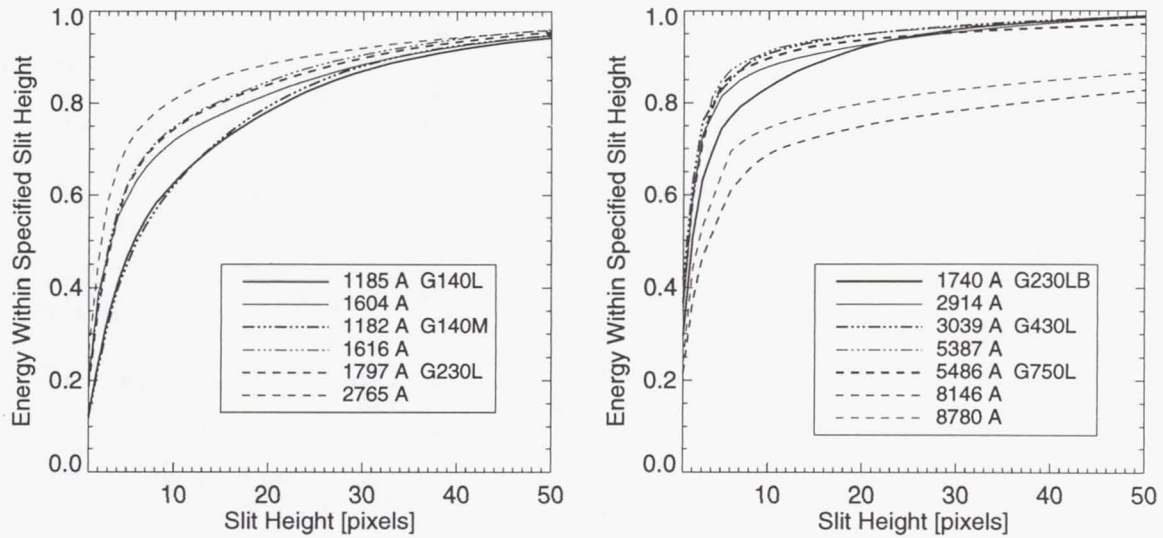
Mode	Specification	Measured	Name/ $\lambda$	Slit
X140M	768-1123 (115-170nm)	<i>880-700 (122nm)</i> <i>1680-1430 (172nm)</i>	P1/143nm	S050X31B
X140H	2735-3446 (115-170nm)	<i>3535-2500 (123nm)</i> <i>4490-3630 (159nm)</i>	P1/123nm P3/159nm	S050X29 S050X29
X230M	838-1504 (165-310nm)	<i>1300-1020 (159-204nm)</i>	P1/198nm	S050X31A
X230H	2437-4391 (165-310nm)	<i>3220-2880 (163-183nm)</i> <i>5400-4420 (239-263nm)</i>	P1/176nm P4/251nm	S050X29 S050X31A

<sup>†</sup>Results in italics are based on ground testing

calibrations with various stellar targets at field center using the  $52'' \times 2''$  slit. Figures 1 and 2 show the fraction of total illumination in the cross dispersion profile for different extraction heights. In table 4 are presented the best Gaussian fit fwhm at selected wavelengths and the fraction of light in the cross dispersion profile within 2 and 11 pixel total extraction heights for the primary, long slit modes. Similar results for the echelle modes are presented in Table 5, where however, the fraction of light is presented, normalized to the value in 11 pixels.

Figure 1 shows that there is a clear and consistent improvement in light concentration with increasing wavelength in the ultraviolet modes. This reflects the improved performance of the OTA as well as within STIS at longer wavelengths, with peak performance near 300 nm. Note that the plate scales differ by about 20% between first order low and medium resolution modes shown in Figure 1. If OTA scatter were the only effect present, one would expect equal enclosed energy in 12 pixels of G140L as 10 pixels of G140M. This is seen near 160nm, but not near 118nm where the low order mode has better performance. Table 4 also shows slight but consistently smaller fwhm for spatial profiles in low compared to medium resolution modes in the ultraviolet. As the medium resolution modes have two additional mirrors within STIS compared to the low resolution modes, this difference may be due to the additional accumulation of wavefront error in STIS most apparent at the shortest wavelengths. However, measurements of the spatial fwhm from repeated observations in modes G140L and G230L show occasional differences as great as 20% presumably due to a combination of OTA "breathing" and possible drift. Interpretation of the cause of differences smaller than this are thus highly uncertain.

Figure 2 shows a similar trend of improved light concentration with wavelength in the CCD modes from 170-300nm with comparable performance to about 550nm. Longward of this however, diffraction, and more significantly, the diffusion of light within the CCD chip ("halo") is evident, lowering the fraction of light within a given extraction height, though as shown in Table 4, the fwhm of the spatial profile is nearly constant (about 2 pixels =  $0''.1$ ) at all CCD wavelengths.



Figures 1 and 2: These figures show the fraction of energy, perpendicular to the dispersion direction, within an indicated extracted, slit height. Results are shown for the MAMA detectors at selected wavelengths in figure 1(left), and for the CCD detector in figure 2(right). Note that the results are expressed in pixels. The MAMA plate scales are about 25mas/pixel and 29mas/pixel for low and medium resolution modes respectively, while the CCD plate scale is about 51mas/pixel.

Table 4. Spatial Resolution - First Order Modes

Mode	FWHM [pixels]	FWHM [arcsecs]	Wavelength [nm]	fld pos	EE 2pix	EE 11 pix	frame
G140L	3.9	0.10	119	ctr	0.24	0.65	1767
	2.4	0.06	160	ctr	0.39	0.73	1767
G140M	4.1	0.12	119	ctr	0.23	0.65	1537
	3.0	0.09	162	ctr	0.37	0.76	1539
G230L	3.2	0.08	180	ctr	0.36	0.76	1742
	2.5	0.06	277	ctr	0.46	0.82	1742
G230M	3.4	0.10	169	ctr	0.31	0.69	1541
	2.6	0.08	298	ctr	0.41	0.74	1547
G430LB	2.1	0.11	174	ctr	0.51	0.85	672
	1.9	0.10	291	ctr	0.60	0.89	672
G430L	1.9	0.10	304	ctr	0.63	0.91	1345
	1.9	0.10	539	ctr	0.59	0.92	1345
G430M	2.0	0.10	309	ctr	0.55	0.89	1358
	1.8	0.09	538	ctr	0.62	0.92	1368
G750L	1.9	0.10	549	ctr	0.60	0.90	676
	2.2	0.11	878	ctr	0.37	0.70	676
G750M	2.1	0.11	754	ctr			1373
	2.0	0.10	10208	ctr			1376



Table 5. Spatial Resolution - Echelle Modes

Mode	FWHM [pixels]	FWHM [arcsecs]	Wavelength [nm]	fld pos	EE 2pix/11pix	EE 11 pix	frame
E140M	2.8-3.3	0.08-0.10	119	ctr	0.47	1.00	4420
	2.2-2.5	0.07	156	ctr	0.60	1.00	4420
E140H	2.6-3.0	0.08-0.09	130	ctr	0.53	1.00	4489
E230M	1.8-2.1	0.05-0.06	287	ctr	0.65	1.00	4416
E230H	2.8-2.9	0.08-0.09	271	ctr	0.53	1.00	3550

## 5. Sensitivity

A companion paper by N. Collins and R. Bohlin (Collins and Bohlin 1997) presents the results of the initial sensitivity calibrations. Here we will concentrate on those areas where there are significant differences from the early estimates as detailed in the STIS Instrument Handbook or pre-launch testing. In general, sensitivities determined on-orbit are within 20-30% of the estimates presented in the Instrument Handbook and based on component build up estimates. Differences are generally due to slightly different grating blaze angles than exact design specifications. Such a difference leads to less sensitivity at one end of the bandpass and greater sensitivity at the other end. At wavelengths where the sensitivity changes rapidly (typically shortward of the grating blaze peak) a small blaze shift can result in a significant sensitivity change. In most cases the greatest difference occurs where the absolute sensitivity was very low already. An example is in mode G230M where the measured sensitivity is about 60% of the handbook value near 170nm, about the same near 230nm, and about 15% greater near 290nm. G430L sensitivity is sufficiently shifted that the flight value is about 50% greater than the handbook value near 310nm and about nominal from 450nm and longward to 550nm. G430M is more sensitive than handbook values throughout the range: about 60% near 310nm, 35% near 450nm, 25% near 520nm. Both long wavelength CCD modes (G750L, G750M) have lower than anticipated sensitivity at the longest wavelengths due to the CCD halo, G750L about 60% of expected and G750M about 70% near 1000 nm. These sensitivities are defined using nominal extraction heights of 11 pixels for all modes except G430L and G750L for which 7 pixel extractions were used. Preliminary comparisons of echelle sensitivities (typically using wider slits than would be used for normal observations) indicate as expected or higher sensitivity throughout their bandpass for the slits used. The high UV transmission measured at the slit suggests that these modes will be as sensitive or greater than anticipated.

Modes, G140L, G230L and G230LB, show about 25% less sensitivity in-flight than ground testing indicated, through the region 140-220 nm. This is a region in which many typical contaminants show significant thin film absorption. Repeated measurements during ground testing showed no change in the UV efficiency of STIS during testing. Continued monitoring of G140L indicates that the sensitivity between 150-170nm may have declined about 2% over 14 weeks, with no change from 128-140nm. No change throughout the bandpass of G230L can be detected in the same time. Ongoing contamination monitoring will allow more firm limits to be placed on any sensitivity instability.

## 6. Camera Performance

Camera modes are provided for each STIS detector, primarily for target acquisition but also for scientific purposes. A small complement of filters are provided as well as clear, full field apertures. (Filter characteristics, including red leak data, may be found in the STIS Instrument Handbook with updates.) The open aperture modes of the CCD and FUV cameras as well as the NUV camera with the SrF<sub>2</sub> or crystal quartz filters, have very broad



bandpasses defined by the detector and system optical response. They have significantly greater grasp than other existing HST instruments. The nominal CCD field of view is  $50'' \times 50''$  (open aperture) or  $25'' \times 50''$  (filtered), and the MAMA detectors have  $25'' \times 25''$  fields.

A limited series of in-flight tests have been performed to assess camera performance. The results are summarized in Table 6. In some cases, initial measurements have been obtained only at field center as indicated. As a performance criterion, the encircled energy in a  $0''.1$  diameter circle is listed (column 5). A reference value (column 6) is the OTA only encircled energy in a  $0''.1$  diameter circle based on interpolations of the information in Figures 11.13 and 11.14 of Schroeder (1987). The STIS detectors alone will reduce these OTA values as will any residual wavefront error, however these reference values provide a useful benchmark of the maximum possible performance with a well corrected OTA. Typically, 70-85% of the corrected OTA light within  $0''.1$  diameter will be contained within the same diameter in the STIS images.

Table 6. STIS Camera Performance Summary

Mode	Filter	Wavelength [nm]	Target	EE(<0.1'')	Reference EE(<0.1'')
MIRCUV	A25	clear	NGC6681	0.32-0.36 over the full field	
MIRFUV	F25LYA	122	BPM16274	0.27 at field center	0.39 (122nm)
	F25SRF2	>130	NGC6681	0.33-0.39 over the full field	0.45 (145nm)
	F25QTZ	>146	NGC6681	0.39-0.43 over the full field	0.49 (155nm)
MIRNUV	F25CN182	182	NGC6681	0.40-0.48 over 2/3, 0.30-0.40 over 1/3	0.56
	F25C3	191	LS749B	0.41 at a single, off-center field point	0.58
	F25CN270	270	NGC6681	0.50-0.54 over 2/3 field 0.40-0.50 over 1/3 field	0.63
	F25MG2	280	BPM16274	0.51 at field center	0.63
	F25SRF2	>130	-	data not yet acquired	
	F25QTZ	>146	-	data not yet acquired	
MIRVIS	A50	clear	Omega Cen	0.47 in 2x2 near field ctr 0.38 < 0.1''	-
	F28X50O2	373	Feige 34	0.50 in 2x2 near field ctr 0.41 < 0.1''	0.60
	F28X50O3	501	Feige 34	0.47 in 2x2 near field ctr 0.36 < 0.1''	0.58
	F28X50LP	548	Omega Cen	0.42 in 2x2 near field ctr 0.34 < 0.1''	0.51 (775nm)

The image quality of the camera modes is illustrated in figures 3-5. Each figure is a set of log-stretched and magnified images from single exposures of the clusters NGC6681 (figures 3 and 5) and Omega Cen (figure 4). The relative positions of the stars are indicated in pixel coordinates below each star. The best fit Gaussian fwhm for profiles extracted horizontally and vertically from each star are shown above and to the left of each star. Figures 3 and 4 also show the horizontally extracted profiles, plotted to the right of the corresponding images.

Figure 3 is of the cluster NGC6681 obtained in a single exposure (1100 seconds) using the far ultraviolet camera without any filter (MIRCUV,A25). Each pixel is about 25mas and the total field around each star shown is  $1''.27 \times 1''.27$ . The horizontal branch stars have temperatures of typically 8000-15000 K; the flux weighted camera response will be toward the lower end of the camera range, near 120 nm. The halo seen around each star is due to a combination of OTA scatter, STIS internal scatter and wavefront error, and detector PSF, all of which increase at shorter wavelengths. In the log-stretched images, this halo is seen to be asymmetric. The profiles show more accurately the relative amount of light in the halo.

Figure 4 shows stellar images in the field of Omega Cen obtained in a single, 64 second, unfiltered exposure using the CCD (MIRVIS,A50). Each pixel in this image is about 51mas, about twice that of the MAMA camera modes. Some small residual asymmetry of the PSF

is still evident in the corners of the field but the image quality is generally good with fwhm of about two pixels or 102mas.

Figure 5 illustrates the effects of OTA "breathing" (secondary mirror motion due to orbital thermal variations) on the STIS ultraviolet camera modes. The image sets shown are from two exposures, 500 seconds long and separated by 2080 seconds. These were extracted from a single time-tagged 2600 second exposure. The target was again the cluster NGC6681 and the camera was the NUV MAMA with the 270nm, continuum filter (MIR-NUV,F25CN270). In the first image set, the image quality degrades on the left side of the detector, but is relatively good (about 2.2 pixels fwhm) over the center and right side. In the second image set, this pattern has switched, with the left side of the field now in good focus and the right side clearly defocused. In both cases, the central, vertical strip stays in relatively good focus. The complement of spectroscopic and camera modes for each MAMA may direct light onto each detector from any of four different directions. The detectors were oriented to optimize the performance in the spectroscopic modes. This results in a tilt between the MAMA camera mode focal planes and the detector plane, creating a cylindrical symmetry to the camera mode field imagery. Movement of the OTA secondary ("breathing") results in a relative defocus of the camera focal planes with respect to the MAMA detectors, the line of best focus sweeping across the detector. With the center of the field at nominal focus, little effect is seen as long as the defocus is less than the depth of focus. However the edges of the camera fields are nominally near the limits of the focal depth so that any further defocus creates a noticeable degradation on one side of the field and improvement on the opposite side. The results seen with STIS are consistent with the typical OTA breathing, secondary displacements of several microns. Values for encircled energy in Table 6 are thus time averages.

The flux transmitted through a spectrographic slit at the field center is relatively insensitive to OTA breathing. Modelling of the PSF at the slit plane at 125nm for a 60mas wide slit shows about 10% lower transmission for a 1" long slit and about 20% loss for a very short, 0".1 slit, for a characteristic maximum secondary excursion of 5 microns. Examination of two time tag spectroscopic observations using the 0".2  $\times$  0".09 slit shows a variation of no more than 10% transmitted flux over 2000 seconds, which loss includes any drift as well as breathing effects.



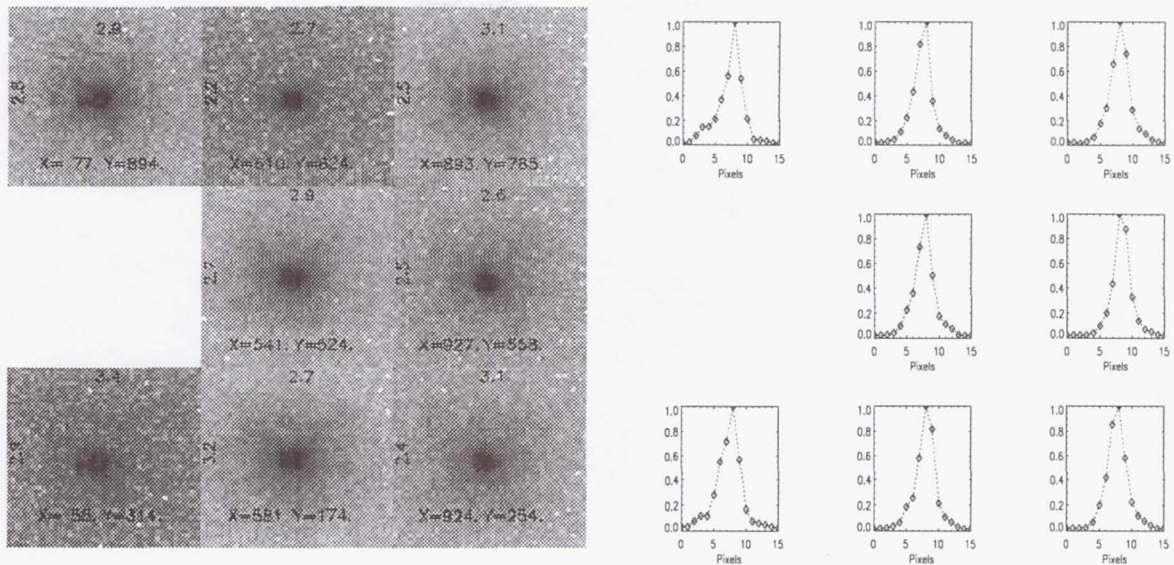


Figure 3: Figure 3a (left) is a log-stretched set of stellar images from an 1100 second exposure of NGC6681 taken with the far-UV MAMA without a filter. Each pixel is about 25mas with a total field around each star of about  $1''.3 \times 1''.3$  (51 pixels). The Gaussian fit fwhm to vertical and horizontal extracted profiles are given in pixels, to the left and above each star. The flux weighted camera response peaks  $<130$  nm, where STIS residual wavefront error and OTA scatter are greatest. These result in the asymmetric images seen near the corners of the field and the halo around each star. Figure 3b (right) shows horizontally extracted profiles of each star in the field indicating the relative flux distribution.

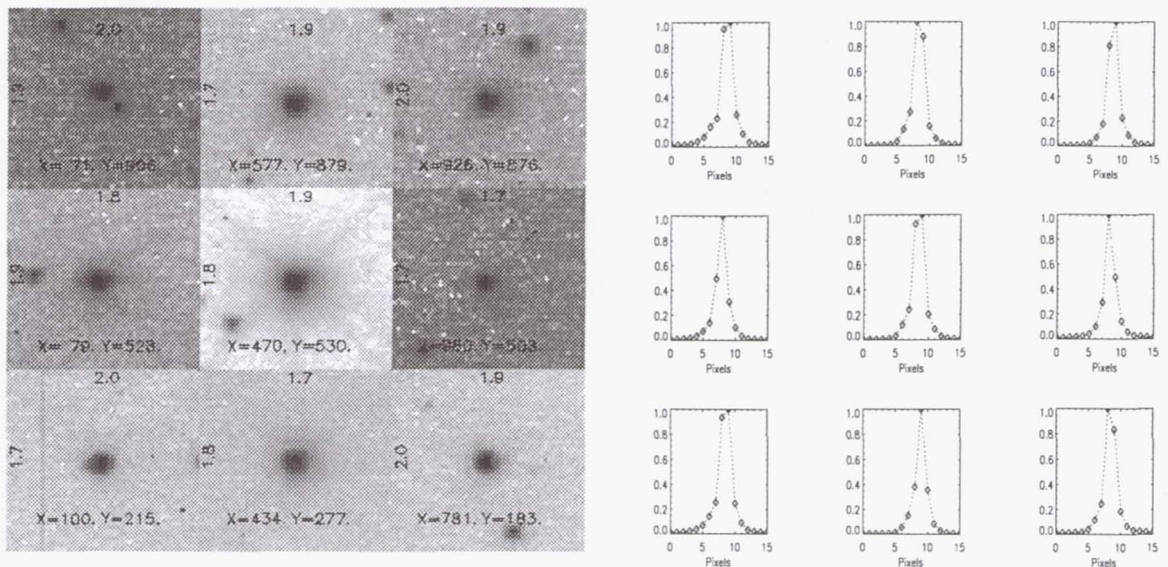


Figure 4: Figure 4a (left) shows a similar set of stellar images from a 64 second exposure of Omega Cen acquired with the unfiltered, CCD camera. The plate scale is about twice that of the ultraviolet images, 51mas/pixel with  $2''.6 \times 2''.6$  field around each star. Corresponding horizontal, extracted profiles are shown in the adjacent figure 4b (right). Image quality is generally uniform across the field, with small asymmetries of the PSF most evident in the field corners.



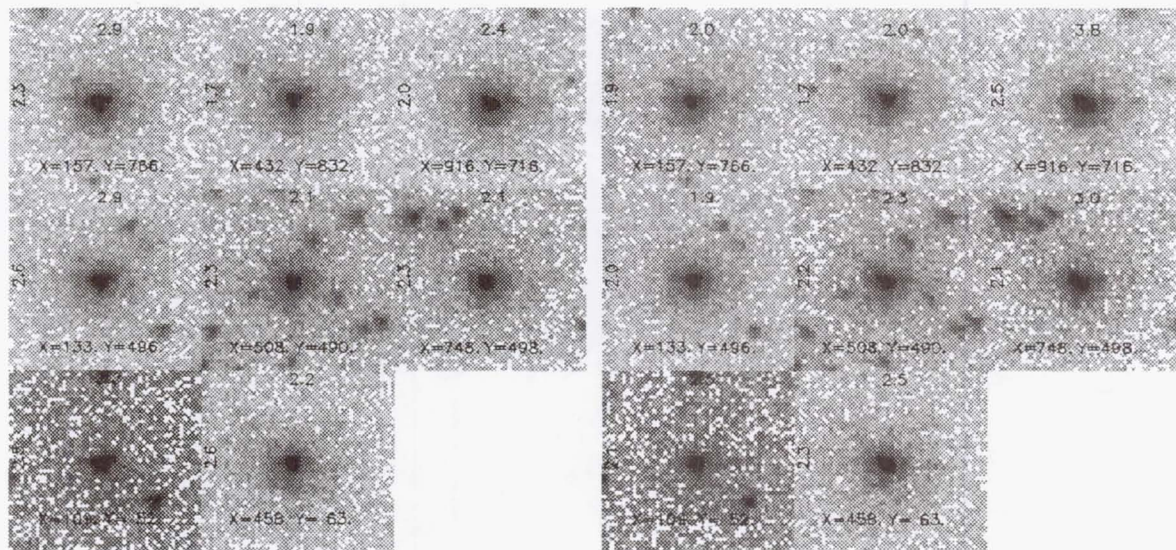


Figure 5: The effects of OTA breathing on STIS imagery are illustrated in these two log-stretched images of stars in the field of NGC6681 acquired with the NUV MAMA using the CN270 filter. The same stars are shown in both image sets, labeled by their X,Y locations in pixels. The best fit Gaussian fwhm to the extracted vertical and horizontal profiles are indicated to the left and above each image (fwhm values in pixels where 1pix = 25mas). Each exposure was 520 seconds long with 2080 seconds separating the two exposures. The first exposure (left) shows degraded performance to the left of center, due to defocus at the detector plane. By the time of the second exposure (right), the OTA secondary had shifted in position causing a corresponding shift in the camera focal plane. Stars on the left side of the field are now in good focus while stars on the right side of the field are now defocused. Images of stars along the vertical, central strip are less sensitive to breathing: the focal shift was approximately within the depth of focus of these images.

**Acknowledgments.** We would like to thank all those whose hard work and perseverance through the years have resulted in the successful construction, testing, installation and commissioning of STIS. The STIS IDT has been funded in response to NASA Announcement of Opportunity OSSA-4-84 through the *Hubble Space Telescope Project* at the Goddard Space Flight Center. This paper is based on observations with the NASA/ESA *Hubble Space Telescope*, obtained at the Space Telescope Science Institute, which is operated by the Association of Universities for Research in Astronomy, Inc. (AURA), under NASA contract NAS5-26555

## References

- Baum, S. et al. 1996, *STIS Instrument Handbook*, STScI: Baltimore
- Collins, N. & Bohlin, R. 1997, this volume
- Content, D. A. et al. 1997, Proc. SPIE, 2807, 267
- Schroeder, D., 1987 in *Astronomical Optics*, San Diego: Academic Press, 216
- Woodgate, B. et al. 1992, ESO Conf. and Workshop Proc. 44: Science with the Space Telescope, P. Benvenuti & E. Schreier, European Southern Observatory: Munich, 525
- Woodgate, B. et al. 1998, in preparation

## The Flat Fielding and Achievable Signal-to-Noise of the MAMA Detectors<sup>1</sup>

Mary Elizabeth Kaiser<sup>2</sup>

*The Johns Hopkins University, Department of Physics and Astronomy, Baltimore,  
MD 21218*

Don J. Lindler

*Advanced Computer Concepts, Inc, Potomac, MD 20805*

Ralph C. Bohlin

*Space Telescope Science Institute, 3700 San Martin Drive, Baltimore, MD 21218*

**Abstract.** The Space Telescope Imaging Spectrograph (STIS) was designed to achieve a signal-to-noise of at least 100:1 per resolution element. MAMA observations during Servicing Mission Orbital Verification (SMOV) confirm that this specification can be met. From analysis of a single spectrum of GD153, with counting statistics of  $\sim 165$  a S/N of  $\sim 125$  is achieved per spectral resolution element in the FUV over the spectral range of 1280Å to 1455Å. Co-adding spectra of GRW+70D5824 to increase the counting statistics to  $\sim 300$  yields a S/N of  $\sim 190$  per spectral resolution element over the region extending from 1347Å to 1480Å in the FUV. In the NUV, a single spectrum of GRW+70D5824 with counting statistics of  $\sim 200$  yields a S/N of  $\sim 150$  per spectral resolution element over the spectral region extending from 2167 to 2520Å. Details of the flat field construction, the spectral extraction, and the definition of a spectral resolution element will be described in the text.

### 1. Introduction

The first generation HST instruments spent considerable effort to devise flat field calibrations for their detectors in the UV. As areal detectors, this was a problem for FOC and WFPC in particular. Time was spent generating streak flats by observing the bright earth limb, but despite heroic efforts the method did not work well and the S/N suffered. Having witnessed the efforts expended to obtain in-flight flat fields, UV flat field calibration lamps were installed in STIS. Acquiring both the pre- and post-launch data and the subsequent derivation of a flat for each of the MAMA detectors has been a very iterative and time consumptive process. The end results of these endeavors are contained in section 4 on signal-to-noise.

In the ultraviolet, STIS employs a less familiar detector technology to achieve relatively high throughput over this bandpass. For this reason and the difficulty in obtaining large-area UV flat fields, the achievable signal-to-noise has been a key issue for the UV bands.

---

<sup>1</sup>Based on Observations with the NASA/ESA *Hubble Space Telescope*, obtained at the Space Telescope Science Institute, which is operated by the Association of Universities for Research in Astronomy, Inc. (AURA), under NASA contract NAS5-26555.

<sup>2</sup>Co-Investigator, STIS Investigation Definition Team



In the FUV (1150-1700Å), STIS employs a  $1024 \times 1024$  Multi-anode Microchannel Array (MAMA) with an inclined, planar window and a CsI photocathode deposited directly on the microchannel plate (MCP). The NUV (1650-3100Å) MAMA has a CsTe photocathode deposited directly on the inside of its non-inclined window. Due to the tilt of the window on the front of the FUV MAMA, the flat fields for this bandpass are more susceptible to variations as a function of angle of incidence. Consequently, the FUV flat fields may be optical mode dependent.

Both detectors are read-out in high-res mode, whereby the processing electronics centroid event positions to half the spacing of the  $1024 \times 1024$  element anode array. This high-resolution readout mode provides higher resolution, but unfortunately flat field variations are much larger, exhibiting a pronounced ( $\sim 45$ -50%) odd-even amplitude variation. Except where noted, the results in this paper will refer to the low-resolution pixels in the  $1024 \times 1024$  format (Kimble et al. 1998).

Intrinsic pixel-to-pixel variations are 3.9% and 2.8% rms for the FUV and NUV MAMA, respectively, in the  $1024 \times 1024$  low-res pixel format. Ground flat fields for both flight MAMA detectors have shown excellent long term stability, particularly in the low-res mode:  $< 1.0\%$  rms variations over time scales of weeks to months. The pixel-to-pixel flat-field variations of the NUV MAMA show little dependence on wavelength or angle of incidence. Consequently, flat fields have been constructed at a  $S/N > 300$  per resolution element ( $2 \times 2$  low-res pixels) that can be applied to all NUV modes (Bohlin, Lindler, and Kaiser 1997).

In the FUV, there is also little dependence on wavelength. However, due to the inclined window on the FUV MAMA detector, the angle of incidence effects are not as negligible as in the NUV. As a consequence of the mode dependence of the flats detected during the ground-based calibration program, FUV flat fields were taken in the echelle modes as well as the first order spectroscopic modes.

Construction of the FUV and NUV flats are similar in principle but differ in practice. The NUV flat field has been installed in both the IDT and STScI calibration pipelines, whereas the FUV flat is still undergoing test and refinement. Pipeline delivery is expected in the near future.

In section 2, we describe the acquisition of flat-field calibration data in ground-testing. Section 3 presents the detailed methodology for construction of the final flats. Section 4, of greatest interest to the general observer, presents the  $S/N$  achieved in actual in-flight observations with and without applying the ground-based flats.

## 2. Ground Flat Field Calibrations

Contemporaneous analysis of the NUV flat fields during ground-based calibration verified that the flat field construction method outlined in Bohlin, Lindler, and Baum 1996 (hereafter BLB) was valid. Mode G230M exposures of the internal deuterium calibration lamp were acquired in addition to exposures with an external deuterium continuum lamp.

Internal lamp use was limited to a sufficient number of exposures to confirm the flat field stability and to acquire a pixel-to-pixel detector flat (requiring a  $S/N$  of 100:1 per pixel) as a baseline comparison for in-flight pixel-pixel flats. The NUV flat field currently in the pipeline consists solely of this ground based data set.

It should be noted that acquisition of flat fields with large format, count-rate limited detectors requires a significant investment of time. Acquiring a pixel-pixel flat, composed of 13 consecutive exposures, to yield a total  $S/N$  of 100:1 per pixel at a single grating position ( $\lambda 2659$ ) consumed 13 hours. This is a best case result: a mode with uniform illumination of the detector, a count-rate well-matched to the limits imposed during ground calibrations ( $300,000 \text{ counts s}^{-1}$ ), and with minimal exposure overheads.

Due to the detection of angle of incidence effects in the FUV flats during the latter period of the ground calibration, the strategy for acquiring FUV flats was modified. A



campaign of acquiring flats at the required S/N of 100:1 per resolution element for each mode with the external UV lamps was initiated. Since the Kr lamp continuum spans a limited spectral range (1280-1700Å), where the flux beyond 1500Å is dropping rapidly, additional exposures were required using an external argon lamp at the short end of the bandpass and an external xenon lamp at the longest wavelengths.

Furthermore, illumination of the nominal inter-order format on the echelle detectors required additional exposures with the cross-dispersion grating tipped slightly from the nominal position to illuminate the inter-order pixels. The FUV flat field exposures used to construct the FUV super-flat are the set of E140M and E230M ground-based data taken with the external argon, krypton, and xenon lamps, in addition to the in-flight G140L and G140M ( $\lambda 1272$  and  $\lambda 1518$ ) data.

### 3. Flat Field Construction

Algorithms have been defined (BLB) for deriving the STIS MAMA flats. We employ the terminology defined in that document here. The overall strategy is to separate the illuminating lamp signature from the high frequency structure of the MAMA flat itself. However, one major modification to the initial formalism was required due to the presence of irregularities ( $>1\%$ ) in the slit widths for the long slits. The introduction of a correction  $W$  for slit width variations can correct all but the largest defects in the NUV to 1% precision.  $W$  is an average over wavelength and is a function of pixel position along the slit. The 1-D function  $W$  is the raw flat data image collapsed along the spectral direction and is analogous to the orthogonal correction,  $R_L(\lambda)$ , which is the average lamp spectrum collapsed along the slit direction and is used to correct the flat field images for narrow emission lines.

In addition to the illumination variation resulting from the lamp spectral and spatial response and the slit non-uniformity, there is also a contribution due to the HST Optical Telescope Assembly(OTA)+STIS vignetting. This low frequency correction awaits analysis of post-launch calibration data. In practice the flats are constructed by geometrically correcting the original co-added image to make the dispersion and spatial axes parallel to the  $x$  and  $y$  axes of the rotated image. Then the corrected image is collapsed along the separate axes to obtain the spectral S-flat and the W-flat averages. Following this, the inverse geometric distortion correction is applied to transform the WS-flat product image back to the original distorted space. The original image,  $R_L$  is then divided by the transformed WS-flat template. Fiducials, the long-slit occulting bars near the detector edge in the nominal position, are filled in the non-dithered flats and other problem regions are then masked. Filtering is then applied to the flat to obtain the overall 2-D illumination function (L-flat) for that mode. Division of the flat by the L-flat yields the pixel-pixel detector response (P-flat). Thus the P-flat is simply obtained by removing the lamp signature from the original co-added  $R_L$  image and then dividing by the L-flat as rebinned to the original  $2048 \times 2048$  high-res size. The L-flat and the P-flat are both normalized to unity in the central region.

#### 3.1. NUV Flat Fields

Table 1 compares each of the first 11 P-flats to the extreme wavelength 2977Å flat with the best statistics. The entries are the one sigma values for ratios of images. Image ratios test the similarity of the flat fields at different wavelengths. The first row for each of the three image sizes is the expected sigma from counting statistics, the second row is the actual scatter in the ratio images, and the third row measures the actual difference between the two ratioed images. In other words, these third rows of each set are the actual scatter with the Poisson uncertainty removed in quadrature. The results are consistent with no wavelength dependence and little MAMA contribution to the scatter per low-res pixel or per resolution element. There is a residual scatter of a few percent in the high-res ratios,

which demonstrates the nearly complete removal of the large 60% pixel-to-pixel scatter of the high-res flats. Since the tabulated Poisson statistics utilize the average counts, the Poisson entries for the high-res case are underestimates of sigma because of the large change in sensitivity between adjacent pixels due to the odd-even effect in the MAMA electronics. The corresponding high-res residuals are overestimates.

Table 1. Statistics for the Ratio of NUV Flat Fields to the 2977Å Flat

	1769	1933	2176	2419	2419	2419	2659	2659	2659	2659	2977
P FLATS (512x512)											
Poisson (%)	1.23	1.38	1.33	2.05	1.50	1.99	1.05	1.65	2.09	1.25	2.07
Actual sigma (%)	1.24	1.41	1.33	2.04	1.50	2.02	1.07	1.64	2.07	1.33	2.06
Resid. sigma (%)	0.20	0.27	0.00	0.00	0.02	0.38	0.19	0.00	0.00	0.46	0.00
P FLATS (1024x1024)											
Poisson (%)	2.45	2.77	2.67	4.09	2.99	3.98	2.10	3.29	4.18	2.50	4.14
Actual sigma (%)	2.47	2.80	2.67	4.02	2.99	4.01	2.12	3.31	4.17	2.63	4.13
Resid. sigma (%)	0.29	0.42	0.12	0.00	0.11	0.56	0.34	0.31	0.00	0.80	0.00
P FLATS (2048x2048)											
Poisson (%)	4.91	5.53	5.33	8.18	5.98	7.95	4.19	6.59	8.35	5.00	8.28
Actual sigma (%)	5.72	6.47	6.15	8.96	6.89	12.18	4.87	7.25	9.63	11.01	9.55
Resid. sigma (%)	2.95	3.34	3.05	3.66	3.42	9.22	2.48	3.04	4.79	9.81	4.75

Ground-based NUV flats were obtained during two time intervals. The first data set was obtained during August and September 1996 while in thermal vacuum at Ball Aerospace. After shipping the instrument to GSFC, a second set of flats was acquired under nitrogen purge during November 1996. The two sets of flats exhibit residual structure as illustrated most strongly in the high-res residual of 9.81% in the last row of Table 1. The other P-flat data obtained in November 1996 is at 2419Å and also has a high residual of 9.22% per high-res pixel at image center.

Since the 1769 and 1933Å flats have illumination along only the central third of the slit, the superflat is the combination of the Ball data at the G230M central wavelengths of 2176, 2419, 2659, and 2977Å and is shown in Figure 1. The Poisson statistic of 0.30% per resolution element for the superflat correspond to a S/N=333 in regions without fiducial or slit defect masks. On-orbit flats are required to quantify changes, which degrade S/N achieved when this superflat is applied to flight data.



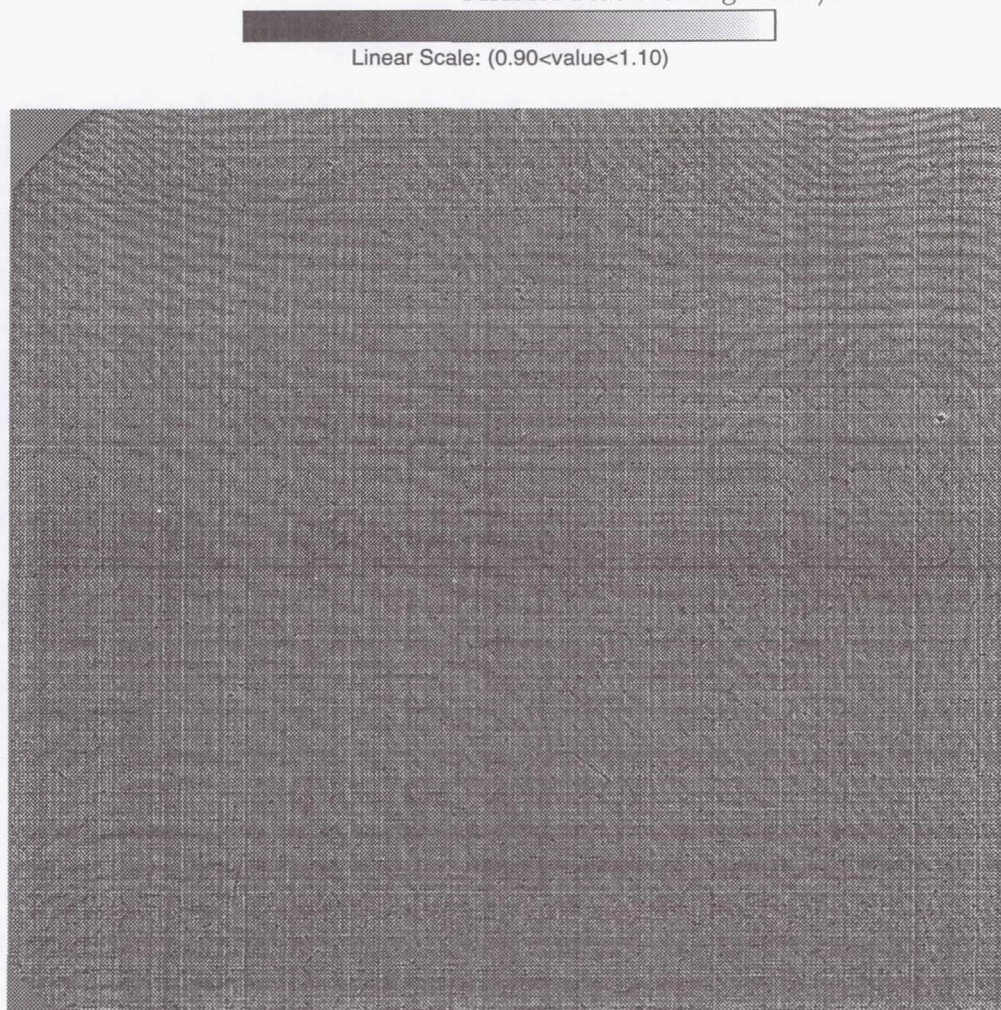


Figure 1: Combined NUV Flat Field

### 3.2. FUV Flat Fields

The formalism applied for the FUV mirrors the NUV procedure. However, all the images except the G140M ( $\lambda 1518$ ) exposure had limited spectral coverage which required masking large regions of unilluminated regions on the flat. In addition, the echelle images with the argon and xenon lamps were taken with the  $0.5'' \times 0.5''$  arcsec slit, thus broadening emission lines from these lamps which required masking prior to removal of the illumination signature from the data. From the set of echelle images, a flat has been created which is illuminated over nearly the full field. A few unilluminated regions of limited extent remain. These are the result of inter-order rows which remain unilluminated despite the slight offset of the cross-disperser grating position, or the repeller wire (an electrode above the MCP which prevents photoelectrons created by the MCP from escaping) shadow in the echelle modes which requires masking but this region of the detector will be fully illuminated with a more complete set of first order flats. A few isolated emission line regions persist, but will also be illuminated by either a more complete set of first order flats or echelle flats with the internal krypton lamp.

The addition of the post-launch G140L and G140M flat field images also provides nearly complete illumination of the detector. However, a  $52'' \times 0.05''$  ND filtered slit was used to acquire the G140M data set. Residuals from filtering this slit's prominent features



were masked. Pending command development, the slit wheel was used solely at the nominal setting thus leaving regions shadowed by the fiducials unilluminated.

In the spectral direction, the G140L and G140M( $\lambda 1272$ ) images are unilluminated for wavelengths below  $\sim 1280\text{\AA}$ . Thus the G140M( $\lambda 1272$ ) image provides illumination of the longest wavelength pixels in the G140L image where the flux is rapidly decreasing. The G140M( $\lambda 1518$ ) image provides illumination at pixels corresponding to the shortest wavelengths in the G140L image.

Combination of the G140L and G140M data sets provides nearly complete illumination of the detector at a S/N, derived purely from counting statistics, of 150 per  $2 \times 2$  pixel resolution element at the longest wavelengths where the counting statistics are poorest. Masked fiducial shadows in the G140M flats can be filled by the proposed commanding to move the slit from its nominal position in the spatial direction when acquiring flats with the fiducial slits.

In constructing the echelle flats, for the addition of each set of images at a unique central wavelength, the ratio of the new composite flat to a single flat was calculated. In all instances, the image ratio errors decreased as the data were combined. The image ratio test was then executed for flats in different modes; the results are presented in Tables 2 and 3. Table 2 presents the results for a single flat field image in mode G140L relative the remaining G140L images. The subset of G140L flats are then combined with flats in the remaining modes. Table 3 presents the image ratio results for the combined G140L flat relative to the other modes.

Table 2. Statistics for the Ratio of a single FUV G140L 1425 $\text{\AA}$  Flat Field to the Composite Flats

	G140L	(G140L + G140M)	(G140L + G140M + E140M)	(G140L + G140M + E140M + E140H)
P FLATS (1024x1024)				
Poisson (%)	2.30	2.53	2.17	1.94
Actual sigma (%)	2.70	3.02	2.85	2.76
Resid. sigma (%)	1.40	1.65	1.84	1.96
P FLATS (2048x2048)				
Poisson (%)	5.05	5.58	5.14	4.87
Actual sigma (%)	5.64	5.98	8.18	9.02
Resid. sigma (%)	2.50	2.15	6.37	7.59

Table 3. Statistics for the Ratio of the FUV G140L Flat Field to the Flats from Other Modes

	G140M	E140M	E140H
P FLATS (1024x1024)			
Poisson (%)	3.23	2.20	1.49
Actual sigma (%)	4.02	3.16	2.47
Resid. sigma (%)	2.39	2.27	1.96
P FLATS (2048x2048)			
Poisson (%)	7.14	5.16	3.63
Actual sigma (%)	11.23	11.65	9.07
Resid. sigma (%)	8.67	10.45	8.31

From a visual inspection of the flat ratios it is apparent that there is  $\leq 5\%$  residual effect in removing an overall fringe pattern in the FUV flats. This fringe pattern can



be seen in both the NUV (Figure 1) and FUV flats (Figure 2). Despite this residual, a flat field composite of all the prime FUV observing modes (G140L, G140M, E140M and E140H) can be constructed and used to improve the achievable S/N for a given spectrum. The improvements attainable will be described further in the S/N section. Further in-orbit flats are required to monitor the FUV flat field stability and to improve the counting statistics in poorly illuminated regions (i.e. under fiducials, masked emission line regions). In addition, the use of one mode to correct another mode limits the achievable S/N. More data is required to isolate the dependence of this effect on post versus pre launch data versus mode dependence.

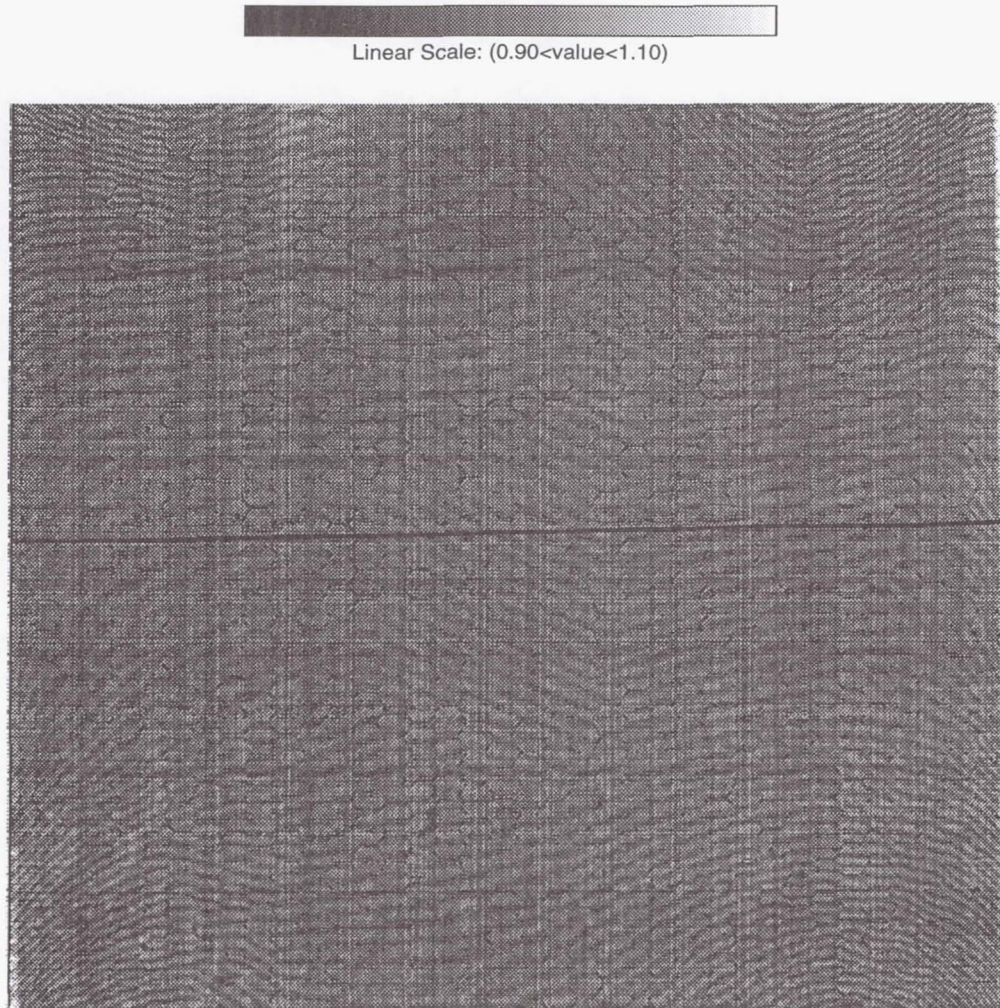


Figure 2: Combined FUV Flat Field

#### 4. Signal-to-Noise

Spectra of GD153 in mode G140L and GRW+70D58 in mode G140M were flat fielded to determine the realizable S/N. In practice, the IDT calibration pipeline employs a spectral extraction height of 11 pixels (spatial direction) and the spectral resolution is nominally two pixels. Therefore the S/N quoted for a point source in the first order modes, as defined in this paper, is per spectral resolution element ( $11 \times 2$  pixels).

Initially the data is background subtracted, then extracted, and binned in the spectral direction. The 1-D spectrum is then partitioned into segments composed of 20 bins each

which are fit with a cubic spline. Each segment is divided by its fit; the mean and standard deviation are calculated and ratioed to determine the S/N for each segment. The average of the S/N over the spectral segments contained within the specified spectral range is tabulated in Table 4 for the NUV and Table 5 for the FUV. For the NUV MAMA, the GRW+70D58 spectrum has a peak potential S/N, corresponding to pure counting statistics, of  $\sim 200$  per spectral resolution element. The realized S/N is  $\sim 105$  *without the application of a flat field* and  $\sim 150$  after application of the NUV flat field. For the FUV MAMA, the GD153 spectrum has a peak potential S/N, corresponding to pure counting statistics, of  $\sim 165$  per spectral resolution element. The realized S/N is  $\sim 85$  *without the application of a flat field* and  $\sim 130$  after application of the FUV flat field.

Table 4. NUV Signal-to-Noise Capabilities for a G230L Point Source Spectrum

Star	Spectral Class (B Mag)	Exposure Time	Flat Composition	Spectral Range	S/N (Counting Statistics)	S/N
GRW+70D58	DA3 (12.63)	636.0	NO Flat	1698 - 2167	<165>	<100>
				2167 - 2520	<204>	<101>
				2520 - 3050	<163>	<102>
			G230M	1698 - 2167	<165>	<154>
				2167 - 2520	<204>	<149>
				2520 - 3050	<163>	<152>

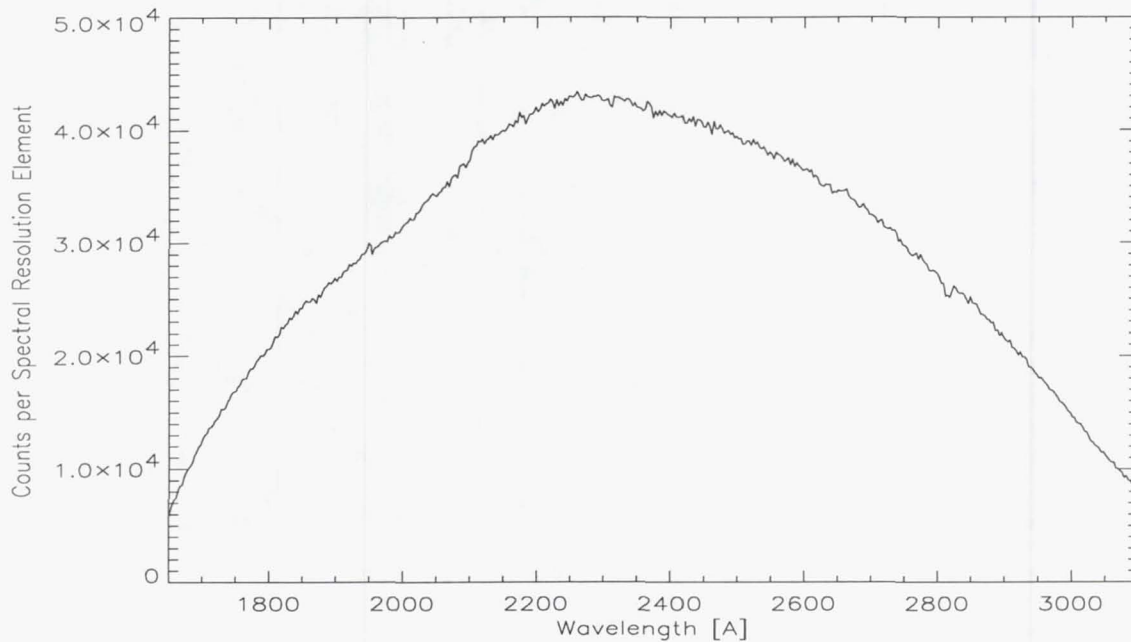


Figure 3: NUV Flat Fielded Single Spectrum of GRW+70D58

To test the S/N limit in the FUV, six G140L spectra of GD+70D58 were coadded. No shifts were applied to align the spectra. Over the region extending from 1347-1502Å the S/N of the composite spectrum is  $\sim 180$ , with S/N  $\sim 300$  from pure counting statistics. It should be cautioned however that these spectra are neither spatially nor spectrally coincident, exhibiting an offset of  $\sim 10$  pixels spectrally and  $\sim 4$  pixels spatially. Consequently a single spectrum of comparable count statistics may yield a slightly lower S/N. These results are also presented in Table 5.



Table 5. FUV Signal-to-Noise Capabilities for a G140L Point Source Spectrum

Star	Spectral Class (B Mag)	Exposure Time	Flat Composition	Spectral Range	S/N (Counting Statistics)	S/N
GD153	DA1 (13.07)	187.1	NO Flat	1280 - 1458	<165>	<85>
				1502 - 1657	<75>	<65>
			G140L	1280 - 1458	<165>	<113>
				1502 - 1657	<75>	<50>
			G140L + G140M	1280 - 1458	<165>	<116>
				1502 - 1657	<75>	<73>
			E140M + E140H	1280 - 1458	<165>	<127>
				1502 - 1657	<75>	<74>
			G140L + G140M + E140M + E140H	1280 - 1458	<165>	<128>
				1502 - 1657	<75>	<75>
GRW+70D58	DA3 (12.63)	1260.0	NO Flat	1347 - 1502	<295>	<93>
				1502 - 1657	<172>	<81>
			G140L	1347 - 1502	<295>	<184>
				1502 - 1657	<172>	<92>
			G140L + G140M	1347 - 1502	<295>	<189>
				1502 - 1657	<172>	<130>
			E140M + E140H	1347 - 1502	<295>	<168>
				1502 - 1657	<172>	<150>
			G140L + G140M + E140M + E140H	1347 - 1502	<272>	<182>
				1502 - 1657	<172>	<155>

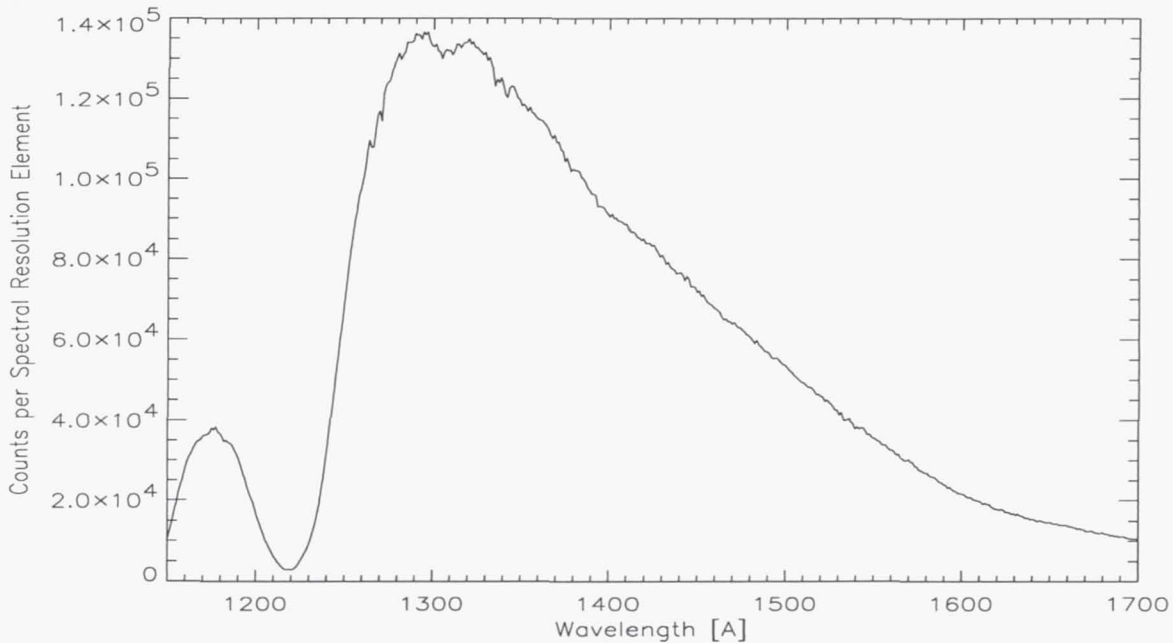


Figure 4: FUV Flat Fielded Combined Spectra of GRW+70D58

Further inspection of the results indicates that at S/N  $\sim 180$  the composition of the flat becomes important. To achieve a S/N in excess of this, it may be required to use a flat composed solely from the same mode as the observations to eliminate residual angle of incidence effects in the flat. It is also possible that the pre-launch data (E140M and E140H) does not flatten the observations as well as the post launch flats. Note: at the pixels corresponding to longer wavelengths in the G140L observations, the counting statistics in the (G140L + G140M) flat are poorer than the counting statistics in the (E140M + E140H)

flat; this is why the S/N is poorer with the (G140L + G140M) flat over the spectral range from 1502-1657Å.

Even higher S/N ratios are possible if the FP split slit methodology is employed to acquire the observations. Using this technique, exposures are taken through a special set of apertures which offset the spectrum in a purely spectral direction on the detector. Iterative analysis of the data permits solving for both the target spectrum and the flat field response of the instrument. Preliminary analysis of the data (Gilliland et al.) acquired to test this method with STIS indicates that a S/N of >250 per low resolution pixel and >350 per spectral resolution element can be achieved in modes E140M and E140H by employing this technique. The FP split slit results were not presented at the conference because the proposal was executed the same day as the talk.

## 5. Conclusion

STIS is capable of achieving a S/N well in excess of 100:1 in the UV observing modes. In the first order modes, the NUV S/N of ~150 is probably limited by count statistics. Limitations of the existing ground-based flat are much less stringent, in principle a S/N exceeding ~250 could be achieved with sufficient counting statistics and if the flat has been stable to this limit. In the FUV, we have obtained a S/N ~190 by coadding spectra. This method incorporates some additional smoothing, but also does not approach the S/N limit derived from pure counting statistics. Therefore it is the quality of the FUV flat field that is currently limiting the S/N to  $\leq 190$  for the first order FUV modes. Using the FP split slit methodology, the S/N limit is unknown. Preliminary results indicate that the S/N (per low-res pixel) of ~260 in the NUV and ~270 in the FUV is comparable to the counting statistics.

## References

- Bohlin, R. C., Lindler, D. J., Baum, S. 1996, Instrument Science Report STIS 96-015 (Baltimore:STScI)
- Bohlin, R. C., Lindler, D. J., Kaiser, M. E. 1997, Instrument Science Report STIS 97-07 (Baltimore:STScI)
- Gilliland, R. et al., Instrument Science Report STIS, (Baltimore:STScI), in preparation
- Joseph, C. J. et al. 1995, Proc. SPIE, 1549, 52
- Kimble, R. A., et al. 1998, ApJ, in press
- Timothy, J. G. 1994, Proc. SPIE, 2278, 134
- Woodgate, B. et al. 1998, PASP, submitted



## STIS Target Acquisition

Steve Kraemer<sup>1,2</sup>, Ron Downes<sup>3</sup>, Rocio Katsanis<sup>3</sup>, Mike Crenshaw<sup>1</sup>, Melissa McGrath<sup>3</sup>, and Rich Robinson<sup>1</sup>

**Abstract.** We describe the STIS autonomous target acquisition capabilities. We also present the results of dedicated tests executed as part of Cycle 7 calibration, following post-launch improvements to the STIS flight software. The residual pointing error from the acquisitions are  $< 0.5$  CCD pixels, which is better than preflight estimates. Execution of peakups show clear improvement of target centering for slits of width  $0''.1$  or smaller. These results may be used by Guest Observers in planning target acquisitions for their STIS programs.

### 1. Introduction

Target acquisition for STIS is required if an observer wishes to observe through one of the STIS spectroscopic slits. The method of target acquisition will depend on the type of target observed and the dimensions of the chosen spectroscopic slit. There are several types of autonomous STIS target acquisition, controlled by software executing in the STIS control section microprocessor. All modes of target acquisition will use images taken with one of the STIS detectors. Currently, only the STIS CCD is used for acquisition. The details of target acquisition are presented by Downes, Clampin, McGrath, & Shaw (1997). The paper presented here is intended to be a high level review of STIS target acquisition capability and a report of the results of acquisition tests executed during SMOV and as part of the Cycle 7 Calibration program.

### 2. Target Acquisition Modes

Autonomous target acquisition for STIS is divided into two modes: target location, which is used to place the target into a spectroscopic slit, and peakups, which are used to center the target within the slit. Both modes of acquisition execute the following set of functions: image taking, correction of the images for defects and cosmic ray hits, bias level subtraction, and the request to the HST main computer (NSSC-1) for correction maneuvers.

Two types of target locate are available to the GO's. The first is "point source" location. For a point source acquisition the STIS software will execute the following sequence:

1. After slew to STIS aperture, take two images of a  $5'' \times 5''$  subarray, through one of the STIS imaging apertures. Perform corrections listed above. Find brightest  $3 \times 3$  pixel "checkbox" and calculate target position via flux-weighted centroid.
2. Look up position of reference slit in on-board table. The reference slit is always the  $0''.2 \times 0''.2$  slit.

---

<sup>1</sup>Catholic University of America, NASA/Goddard Space Flight Center

<sup>2</sup>STIS IDT Member

<sup>3</sup>Space Telescope Science Institute

3. Request correction slew to place target where slit will project.
4. Retake image and find target as above.
5. Move slit wheel to reference slit. Illuminate slit with calibration lamp and find center of light pattern via threshold centroid (a flux-weighted centroid algorithm modified to eliminate errors due to non-uniform illumination).
6. Request final correction slew to center target in reference slit.
7. Slew to requested slit using aperture offset table (maintained in the ground system).

Images are taken in steps 1), 4) and 5). There will be no final confirmation image unless the GO includes it as a separate exposure.

The other type of target location is the "diffuse acquisition". The steps are identical to those for a point source, but the GO may adjust the size of the "checkbox" to acquire a diffuse or extended source, and can either use a flux-weighted centroid or take the center pixel of the brightest checkbox (geometric-center) as the target location.

The other mode of autonomous acquisition is the pickup. The sequence will begin with the desired spectroscopic slit in place. The STIS software will execute a dwell scan, taking images at each point. The software will sum the flux in the subarray image at each dwell point. The software will determine the target location either by performing a flux-weighted centroid of the set of dwell point fluxes or, simply taking the dwell point with maximum flux. For a flux-weighted centroid, the minimum flux will be subtracted from each image, which effectively performs a bias subtraction and eliminates read noise. A correction slew is then requested and a confirmation image (the only one saved for downlink in this process) is taken.

The scan pattern used for the peak is tailored for the dimensions of the science slit. For example, a linear scan in the slit width direction is used for the long slits, linear scans in both dimensions for shorter slits, and spiral searches for the smallest echelle slits. Peakups can be executed in either undispersed light or, if there is sufficient flux, in dispersed light, but only in spectral modes that are available for the CCD. Finally, in addition to the pickup, a "peakdown" can be executed to center targets behind occulting bars. The method is essentially identical to that outlined above.

In the next section, we will review the results of target acquisition tests run to date; see also Katsanis et al. (1997) for early SMOV results.

### 3. The Results of On-orbit Target Acquisition Tests

The cycle 7 calibration program 7605, "TA checkout", included tests of the basic target acquisition capabilities described in section II. Although these have all been demonstrated in earlier SMOV programs, 7605 was executed after a set of flight software modifications were installed. These modifications included the elimination of a set of bad columns in CCD subarray images (an artifact of the readout software) from the area checked for the target, the revised bias/darknoise subtraction algorithm for peakups mentioned earlier, and a change in the NSSC-1 software to avoid truncation of commanded offsets, which had affected the dwell scan pattern used in peakups. Therefore, the results of 7605 are the best way to assess the accuracy of STIS autonomous target acquisition.

Three point source acquisitions were executed. Two on a bright target (G93-48) and one on a faint target (the BL Lac PKS1255-316). The accuracy of the results were determined by measuring the target position in a confirmation image taken through the 6"x6" aperture, and a corresponding correction was made to determine the position of the target within the slit. As noted above, GO's will not get confirmation images unless they add a



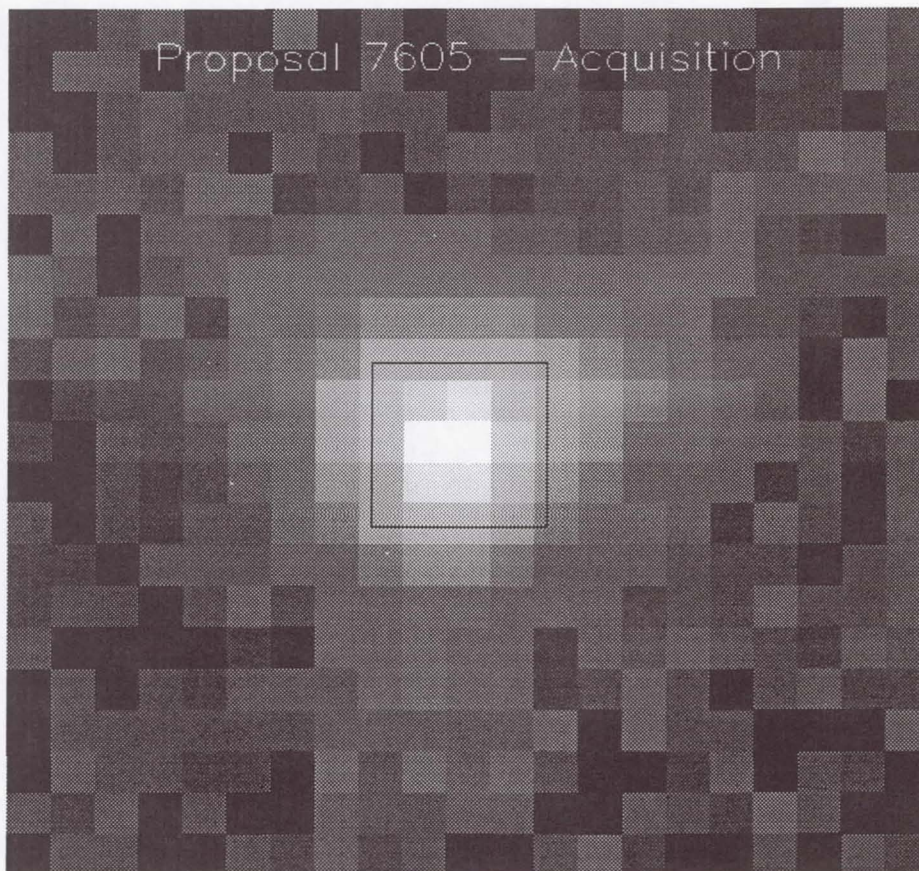


Figure 1. Confirmation image after acquisition of the target into a  $0''.2 \times 0''.2$  slit. The position of the slit is drawn on the image. First order dispersion is in the horizontal, or "X", direction.

separate exposure after the acquisition. The results are as follows. Positions are given in CCD detector coordinates.

1) For the faint target acq (PKS1255-316):

total counts in brightest checkbox:	641	
	X	Y
position of reference aperture:	534.4	517.0
position of target in slit:	534.3	517.0
(corrected for 6x6 aperture)		
error in acquisition:	0.1	0.0 (pixels)
	0.005	0.0 (arcseconds)

The result of this acquisition are shown in Figure 1, in which we have superimposed the outline of the slit on the confirmation image taken in the  $6'' \times 6''$  aperture. As one can see, this pictorial demonstration confirms the analysis shown above.

## 2) For the bright target acq (G93-48):

total counts in brightest checkbox:	9082	
	X	Y
position of reference aperture:	535.0	517.3
position of target in slit:	535.0	517.5
(corrected for 6x6 aperture)		
error in acquisition:	0.0	-0.2 (pixels)
	0.0	-0.01 (arcseconds)

## 3) For the bright target acq, second visit (G93-48):

total counts in brightest checkbox:	9018	
	X	Y
position of reference aperture:	534.8	516.8
position of target in slit:	534.6	516.6
(corrected for 6x6 aperture)		
error in acquisition:	0.2	0.2 (pixels)
	0.010	0.010 (arcseconds)

Two diffuse source acquisitions were executed. These both had the galaxy RXJ1347.5 as the target and were taking with exposure times of 250 and 30 seconds, respectively, to see how the acquisition would work at the nominal S/N and with low counts. Both used the flux-weighted centroid algorithm. Note that the accuracy of diffuse acquisitions tends to be lower than for the point source, due to the flatter image profile of the target and size of the checkbox used. The results were as follows.

## 1) At the nominal exposure time:

total counts in brightest checkbox:	5040	
	X	Y
position of reference aperture:	533.4	516.3
position of target in slit:	534.7	516.9
(corrected for 6x6 aperture)		
error in acquisition:	-1.3	-0.6 (pixels)
	-0.066	-0.031 (arcseconds)

2) At low counts. Note that this had failed earlier in SMOV due to the bright column problem mentioned above.

total counts in brightest checkbox:	465	
	X	Y
position of reference aperture:	533.4	516.3
position of target in slit:	534.7	517.6
(corrected for 6x6 aperture)		
error in acquisition:	-1.3	-1.3 (pixels)
	-0.065	-0.065 (arcseconds)

Several different pickups were executed as part of this program. The error in the final pointing can be estimated by fitting a gaussian to the set of data points, determining the position of maximum flux and finding where the flux in the confirmation image would fall. The difference gives the error.

Some examples:

## 1) target - PKS1255-316



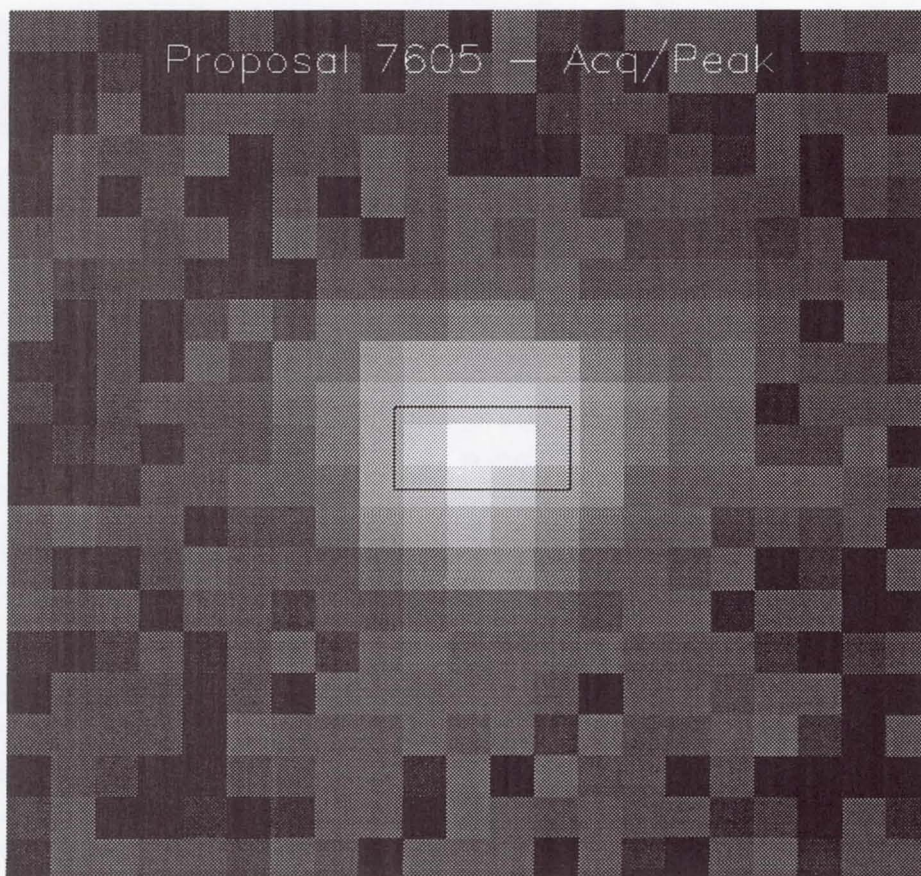


Figure 2. Confirmation image after acquisition/peakup of the target into a  $0''.1 \times 0''.2$  slit. The position of the slit is drawn on the image.

- peakup in  $52'' \times 0''.1$  slit, in undispersed light, using 5 step scan with stepsize = 75 milliarcsec.
- initial flux (after target locate) = 4437
- flux after centering = 5086
- error, from comparison to gaussian fit = 0.016 pixels (0.0008'')

2) target - PKS1255-316

- peakup in  $0''.1 \times 0''.2$  slit, in undispersed light, using 5 step scan with stepsize = 75 milliarcsec.
- initial flux (after target locate) = 5079
- flux after centering = 5165
- error, from comparison to gaussian fit = 0.082 pixels (0.004'')

In Figure 2, we show the outline of the  $0''.1 \times 0''.2$  slit superimposed on the confirmation image. Comparison with Figure 1 gives a qualitative measure of the improvement in pointing offered by the peakup mode.



Another way to measure the accuracy of the pickup is to measure the flux of the target through the slit and compare it to the flux in a wider aperture, taking the relative throughput into account. This was done for 7605 by comparing the flux of the target in the pickup confirmation image to the flux in a post-acq image taken through the  $6'' \times 6''$  aperture. The predicted relative throughputs are given in Robinson (1997). For example, the results of two pickups of the star GS93-48 in undispersed light were as follows: for a pickup in the  $0''.1 \times 0''.2$  slit, the throughput ratio was 0.66, compared to a predicted ratio of 0.60, while for a pickup in the  $0''.1 \times 0''.09$  slit, the ratio was 0.64, compared to a prediction of 0.49. Although this measurement is sensitive to the amount of background included (we used a  $20 \times 20$  pixel area in both cases), it does show that the pickup can be used to maximize throughput, and helps confirm the analysis done using a Gaussian fit.

Pickups may also be executed in dispersed light. In the three cases that were run in this mode during the execution of 7605, the fluxes in the confirmation images were equal to those at the end of the target locate, within Poisson statistical error. We confirm that the pickup did not degrade the pointing accuracy. Since, we did not have confirmation images taken through wider slits to get a measure of the relative throughput, we cannot tell if improved centering were achieved. It should be noted that before the flight software upgrade that made the bias subtraction more robust, this mode routinely failed.

In SMOV proposal 7073, we demonstrated the capability to center a target behind an occulting bar, using a "peakdown" routine. The results are shown in Figures 3 and 4. Qualitatively, we can state that the method worked as planned, and the target is well centered behind the occulting bar.

Finally, it does not appear that pickups are effective if the slit width is  $\geq 0''.2$ . Early in SMOV, pickups in slits of this width did improve pointing, but the improvement was due to the elimination of a systematic offset related to the refractive properties of filters used during the target locate. Once the systematic error was eliminated, the target locate became sufficiently accurate to abrogate the need for a pickup in  $0''.2$  wide slits. Note that including the pickup for these slits does not significantly change the centering, either for the better or the worse. It is, rather, unnecessary.

#### 4. Conclusions

STIS possess accurate and robust autonomous target acquisition capabilities. Target locate and pickup processes have been demonstrated for a variety of targets and optical modes, and the results show that the instrument can be used to center targets in small spectroscopic slits required for high resolution spectroscopy. The improvements in the flight software made during SMOV have addressed early problems with image quality that made the acquisition of faint targets less reliable.

An observer can decide which mode of target acquisition is required to support their science, based on observing mode and type of target. The target locate process, both for point and extended sources, is highly accurate and may suffice for most types of STIS science. For example, for slits of width  $0''.2$  or greater, it will be unnecessary to perform a pickup, since the locate will already provide the maximum centering accuracy. It should also be noted that point source acquisitions may work as well for extended targets, as long as the light profile possesses a central peak. The diffuse locate is preferable for targets whose surface brightness varies unevenly. An observer may determine the best mode to use by using the STScI target acquisition software available on-line (see STIS site at <http://www.stsci.edu>).

There are still improvements to be made for STIS target acquisition. New methods for the flagging of hot pixels that may affect an acquisition are being discussed, and will be included during cycle 7. Although these will be transparent for the observer, they will result in fewer acquisition failures, particularly for faint targets.



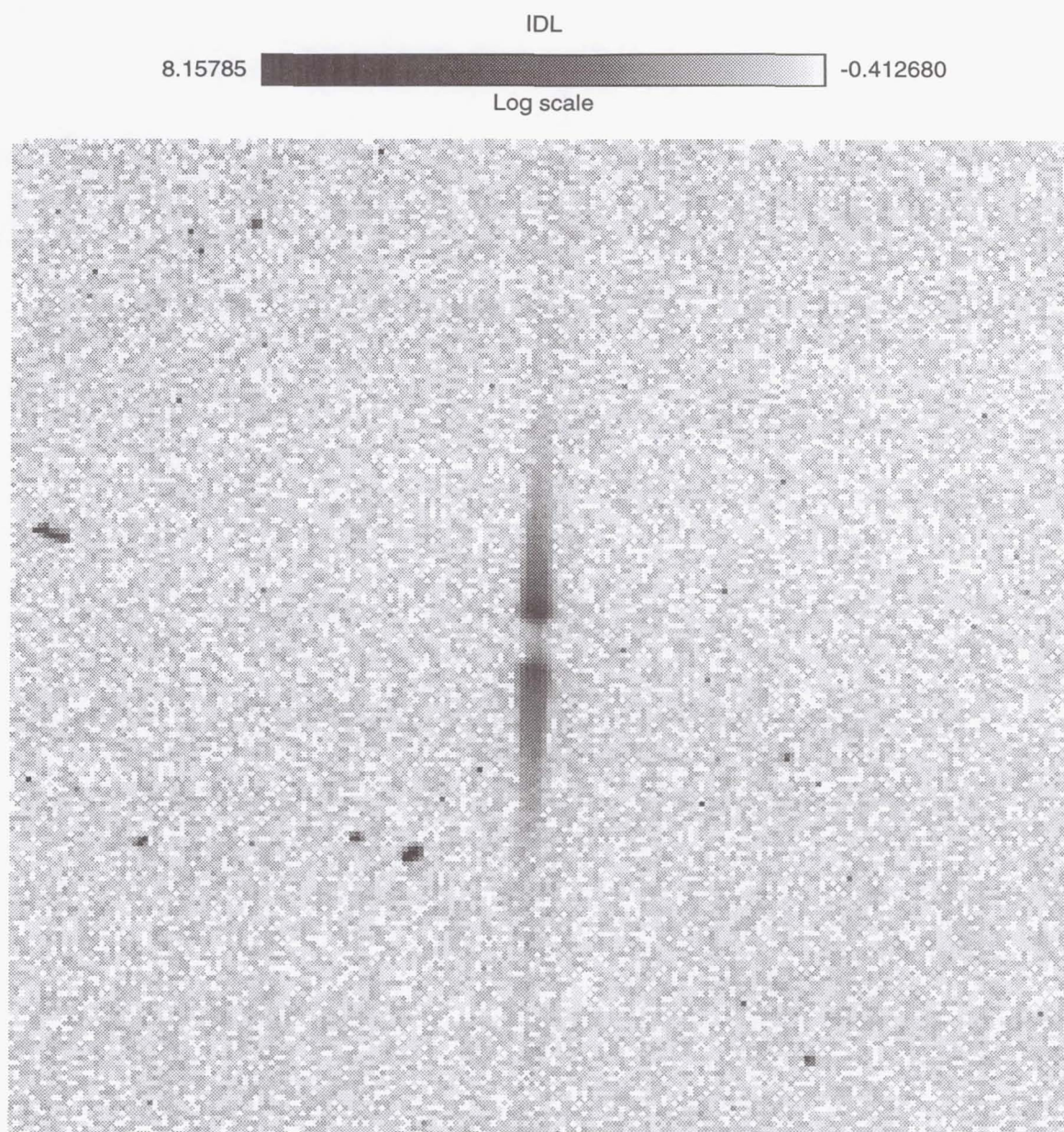


Figure 3. STIS CCD (undispersed) image of a star after acquisition and peak-down into into an occulting bar in a 52''x0''.2 slit.

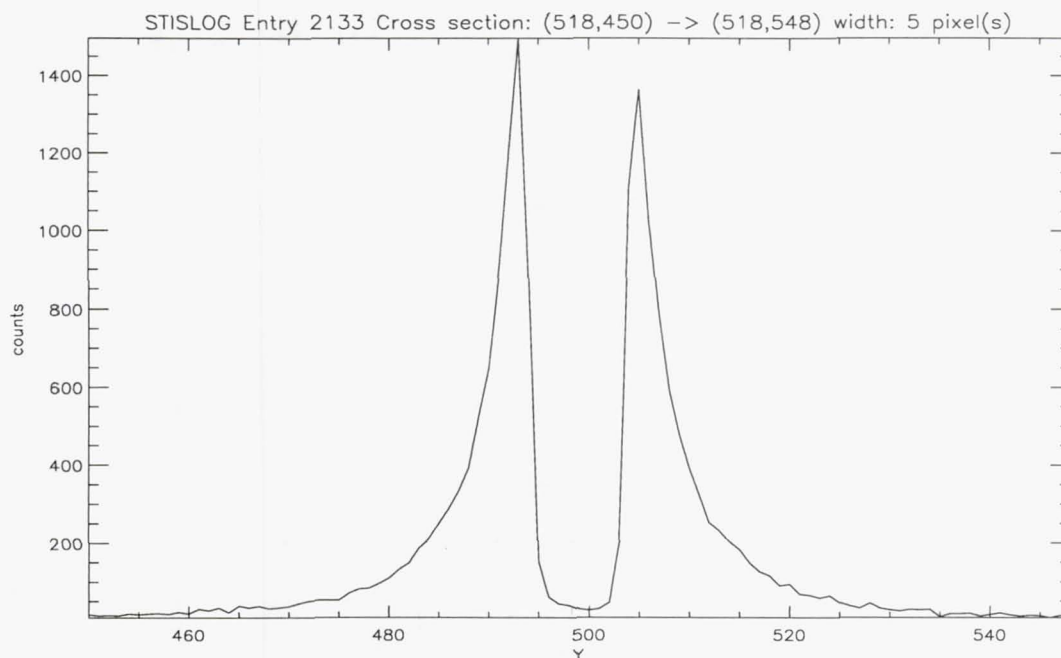


Figure 4. Plot along the length of the slit (in the "Y" direction) in Figure 3.

Also, the results of peakups in slits of size  $0''.2$  show no pointing improvement, and therefore they should be deleted in cases where they are included as part of the default method.

## References

- Downes, R., Clampin, M. McGrath, M. & Shaw, R. 1997, Instrument Science Report STIS 97-03 (Baltimore:STScI)
- Katsanis, R. Downes, R., Hartig, G., & Kraemer, S. 1997, Instrument Science Report STIS 97-12 (Baltimore:STScI)
- Robinson, R. 1997, Quick-Look Post-Launch STIS Calibration Report, No. 44



## The STIS Calibration Pipeline

S.J. Hulbert and P.E. Hodge

*Space Telescope Science Institute, 3700 San Martin Drive, Baltimore, MD 21218*

**Abstract.** The STIS calibration pipeline is a complex collection of software tasks and processes managed by many groups at STScI. The current pipeline for STIS differs in several significant ways from previous pipelines at STScI including data structures and software implementation. CALSTIS can be run both under the IRAF environment and completely outside of IRAF as the user chooses. The STIS pipeline is up and running with all of the basic capabilities for processing STIS data.

### 1. The STIS Calibration Pipeline Is More than CALSTIS

The collection of software, processes, and personnel that are responsible for the routine calibration of STIS data is quite extensive. Typically, the calibration pipeline is most strongly associated with CALSTIS, the software that actually performs the science calibration of the STIS data. In fact, the pipeline is much more. The complexity of the pipeline process is shown schematically in Figure 1. This figure details the various groups within STScI that are responsible for some portion of the pipeline process as well as the interactions among the groups. Missing from the diagram, but not missing from the process, is the STIS group at STScI. The instrument group monitors, provides specifications, and supports troubleshooting for STIS-related issues with the pipeline.

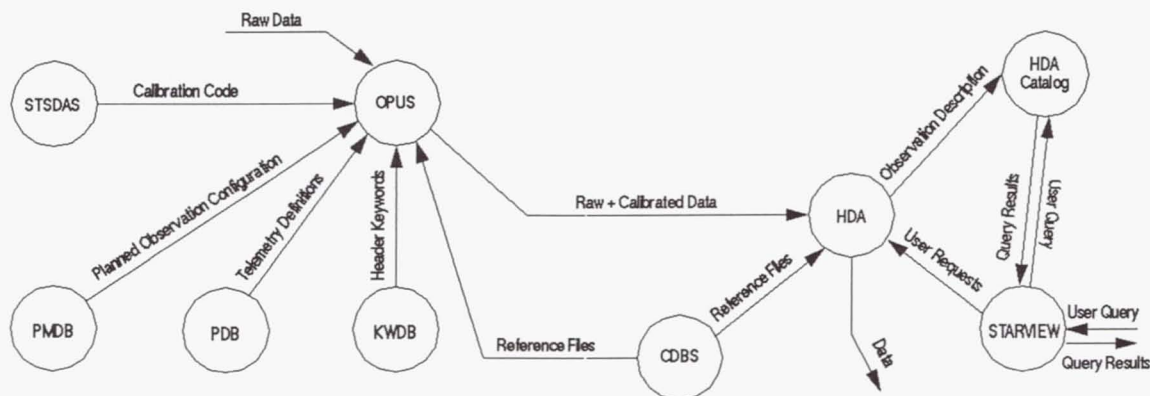


Figure 1. Interactions among STScI groups that form the STIS calibration pipeline.

## 2. Differences from Previous Pipelines

The current implementation of the routine calibration pipeline for STIS differs from previous pipelines in significant (albeit) technical ways. For example:

- Separate STIS exposures can be (and are) associated in a single file (e.g., WAVECALs, CRSPLITS and REPEATs)
- FITS file I/O is used rather than GEIS. Thus the science, error estimates, and data quality data are image extensions in a single FITS file (this collection of extensions is called an *imset*) instead of residing in separate files.
- CALSTIS, the software that actually calibrates the data, uses a new interface (*hstio*) for FITS I/O. Additionally, a FITS kernel for images has been added to IRAF and most of the *ttools* have been updated to use the HEASARC FITSIO routines to permit easy access to the new data structures.
- CALSTIS (usually) reads the entire image set into memory making CALSTIS a memory intensive program.
- The CALSTIS code is written in ANSI C and linked with IRAF.
- CALSTIS uses a new C interface (*cvos*) to IRAF routines.
- CALSTIS tasks can be run as either host programs or IRAF tasks. This simply means the tasks can be run within IRAF or completely outside of IRAF at the unix operating system level.

## 3. Running CALSTIS

A single executable is used to perform all calibration steps in the operation pipeline (OPUS). This single executable is also the "parallel" pipeline version available in the STIS package of STSDAS running under IRAF. The single task version of CALSTIS reads calibration switches from the header. We also provide individual executables to perform subsets of the calibration processing. These tasks have pipeline functions but are called individually. In this case, each executable takes switches from the command line. The major components of the calibration software are described in Table 1.

Examples for data processing by the pipeline software are shown in a series of three figures, highlighting important modes of reduction: cosmic ray removal, 2-D rectification and 1-D spectral extraction. Figure 2 shows the processing of CRSPLIT data wherein three raw frames are combined in such a way as to remove the cosmic rays. Figure 3 shows the rectification of a two-dimensional long slit exposure. Figure 4 shows the extraction of the multiple orders of an echelle spectrum and the production of calibrated spectra.

Table 1. Major tasks in the STIS package

Task Name	Processing
CALSTIS	all processing steps
BASIC2D	bias and dark subtraction, flat-fielding
OCRREJECT	cosmic-ray rejection
WAVECAL	WAVECAL processing
X2D	2-D spectral rectification
X1D	1-D spectral extraction
INTTAG	Convert TIMETAG event stream to ACCUM image



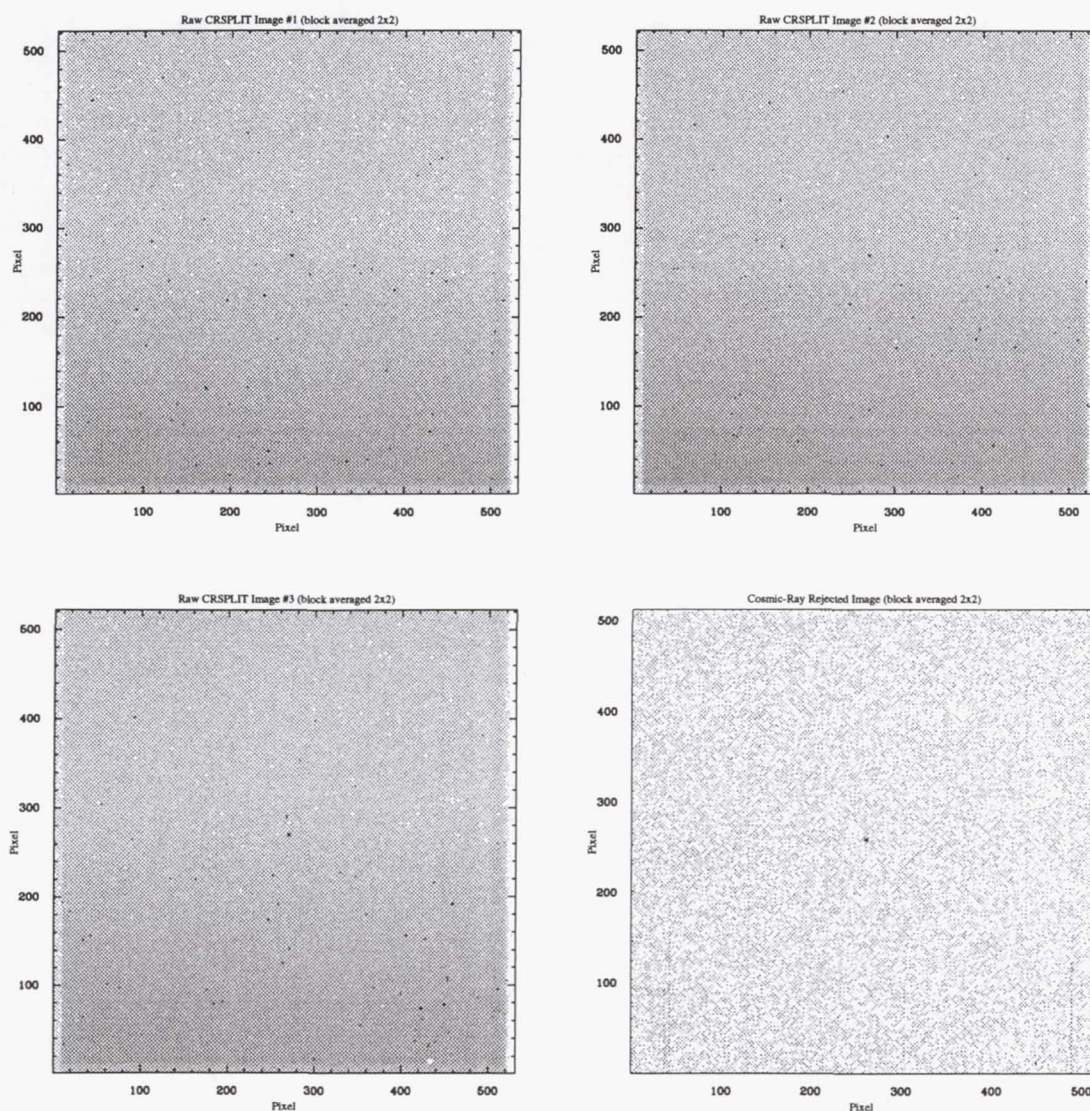


Figure 2. Removal of cosmic rays from a set of STIS imaging exposures. The top two and bottom left images show the raw frames complete with cosmic rays. Can you find the target? The bottom left image shows the corrected image with cosmic rays removed. Now can you see the target?



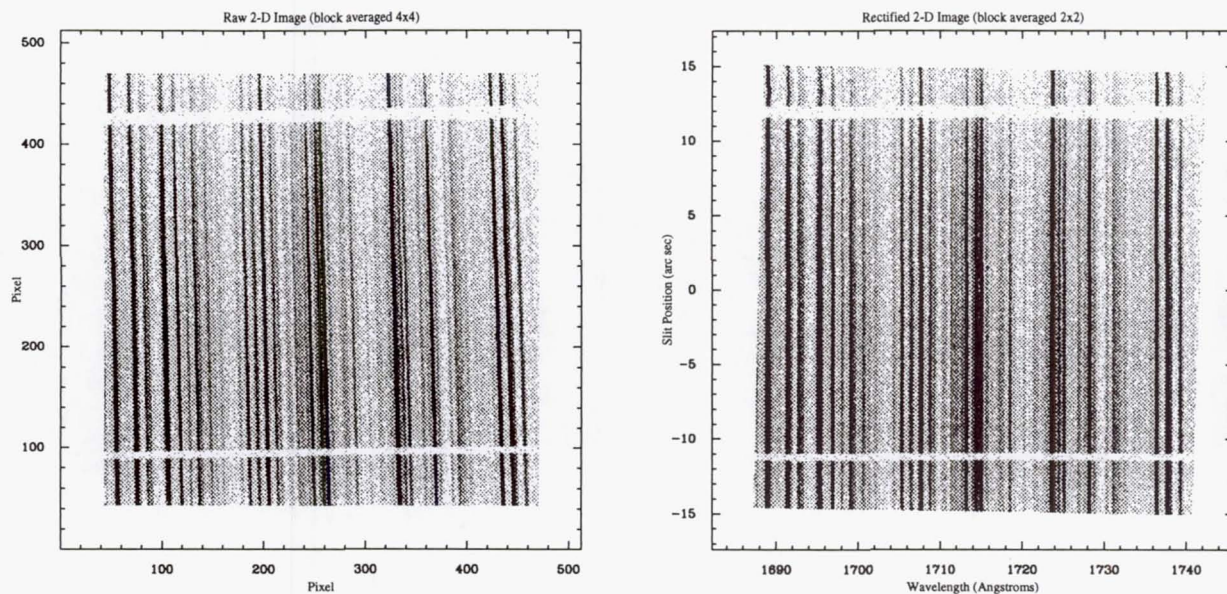


Figure 3. 2-D rectification of a STIS longslit exposure. The raw data are shown in the image on the left. The processed data are shown on the right. In the rectified image, the data have been interpolated onto linear wavelength and spatial scales.

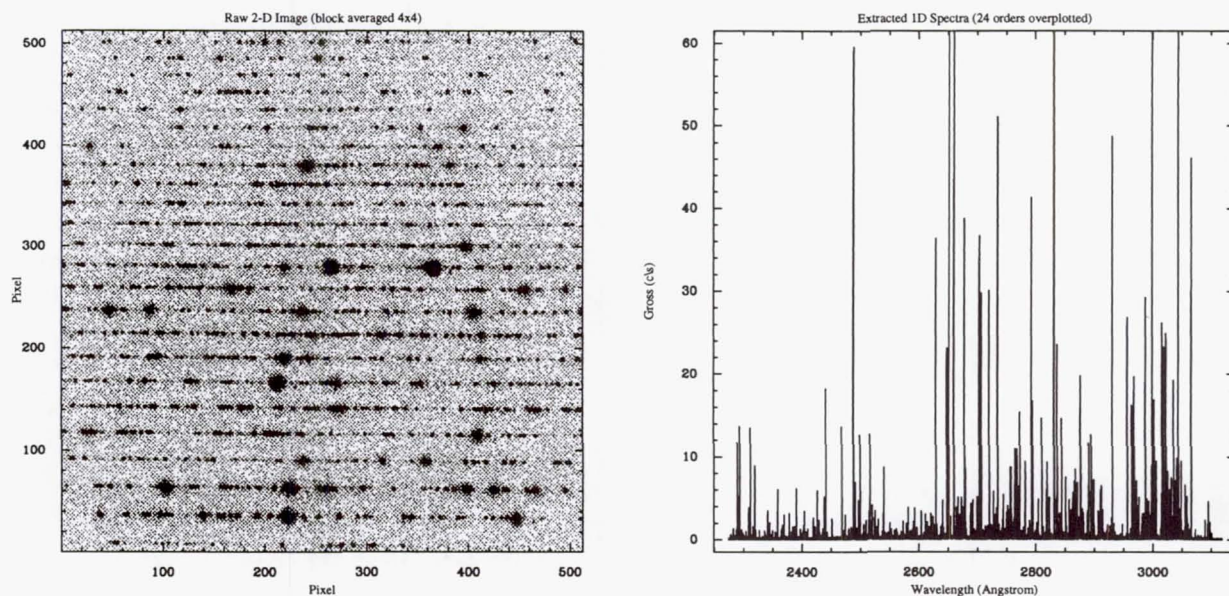


Figure 4. 1-D spectral extraction of multiple orders of an echelle exposure. Raw data on the left; extracted spectra on the right. A total of 24 orders were extracted and overplotted in the line plot. In this case the wavelength scales have not been linearized.



#### 4. Calibration Pipeline Status

The current capabilities of the pipeline include: creation of (associated) STIS data files in FITS format, tracking of STIS calibration reference files, 1-D extraction of echelle observations by CALSTIS, 2-D rectification of longslit observations by CALSTIS and archiving and retrieval of STIS observations. Currently, observations processed through CALSTIS using SMOV (and ground) calibrations have relative wavelengths good to 0.2-1.0 pixels (from dispersion solution), wavelength zeropoints accurate to less than 8 pixels without a WAVECAL and to 0.1-0.2 pixels with a WAVECAL, spatial zeropoints good to 0.2-0.5 pixels and fluxes good to  $\pm 50\%$ . Please note that the flux accuracies are quite setting dependent; a sensitivity update is planned by the beginning of 1998 after which we expect flux accuracies of  $\pm 10\%$ .

The best way to keep informed of the status of the STIS calibration pipeline is to regularly visit the STIS web page at [http://www.stsci.edu/ftp/instrument\\_news/STIS](http://www.stsci.edu/ftp/instrument_news/STIS)

#### 5. Planned Enhancements to STIS pipeline

Future enhancements to CALSTIS in the planning stages are primarily expected to be changes to 1-D extraction of spectra. These changes will include: improved background subtraction using the cross dispersion profiles of the spectral orders to properly model the background, flux corrections for point sources for different 1-D extraction boxes and support for optimal extraction. Additionally, the capability to extract 1-D spectra for 1st order grating/longslit observations will be implemented.

**Acknowledgments.** The following individuals have contributed to bringing the STIS calibration online (and to keeping it running smoothly): Faith Abney, John Baum, Stefi Baum, Mike Bielefeld, Ralph Bohlin, Mike Boyer, Ivo Busko, Colin Cox, Jen Christensen, Bob Dempsey, Dorothy Fraquelli, Anne Gonnella, Paul Goudfrooij, Perry Greenfield, Forrest Hamilton, Helen Hart, Al Holm, Ed Hopkins, J.C. Hsu, Lee Hurt, Rocio Katsanis, Susan Keener, Debby Kenny, Mark Kuchte, Ray Kutina, Don Lindler, Steve Lubow, Melissa McGrath, Warren Miller, Sid Parsons, Joe Pollizzi, Lloyd Rawley, Michael Rosa, Jim Rose, John Sandoval, John Scott, Dick Shaw, Steve Slowinski, Dan Steinberg, Daryl Swade, Mike Swam, Jay Travisano, Calvin Tullos, Jeremy Walsh, Ray Williamson and others that we may have inadvertently and unintentionally not included in this list.

## The Cycle 7 Calibration Plan for STIS

Paul Goudfrooij<sup>1</sup>, Stefi A. Baum, Henry C. Ferguson, Jeffrey J. E. Hayes, Steve J. Hulbert, Claus Leitherer, Melissa A. McGrath, Kailash C. Sahu, and Richard A. Shaw

*Space Telescope Science Institute, 3700 San Martin Drive, Baltimore, MD 21218*

**Abstract.** We give a short overview of the Cycle 7 calibration plan for STIS, discussing its challenge, its general goals and philosophy, the expected calibration accuracies after Cycle 7, and the way the GO and GTOs will be informed on the progress of the calibration efforts. A list of all calibration proposals with a brief description of each is also included.

### 1. Introduction

As already noted by the review of Stefi Baum in this volume, the Space Telescope Imaging Spectrograph (STIS) is an extremely versatile instrument. It has three detectors on board (1 CCD, 2 MAMAs) by means of which it covers a very large wavelength range (from the far-UV to beyond 1  $\mu\text{m}$ ); it allows both imaging and imaging spectroscopy (including long-slit and echelle spectroscopy); there are several operational *modes* (ACQ, ACQ/PEAK, ACCUM, DOPPLER, CORONOGRAPH; there are 44 supported *apertures* (filters + slits), a total of 133 supported primary and secondary wavelength settings for the spectroscopic modes, not even mentioning the numerous available modes of STIS that are not (yet) supported.

This great versatility presents a real challenge for the STIS support group at STScI to provide all calibrations associated with both imaging and spectroscopy (e.g., dark correction, flat fielding, photometric calibrations for all settings, geometric distortions, Point Spread Functions (PSFs), Line Spread Functions (LSFs), etc.) in an accurate and timely way. In the following sections, we describe our plan on how to handle the calibration effort in cycle 7.

### 2. Goals and Philosophy of the Cycle 7 Calibration Program

#### 2.1. General Goals

The general goals for the Cycle 7 calibration program of STIS are as follows:

1. The highest priority calibrations in the near term are those that will acquire missing calibration data from ground testing, or those that will likely provide a new understanding of the performance of the instrument that will be important to a significant number of observers. Most of the crucial tests and calibrations have been carried out successfully on-orbit in the *Servicing Mission Orbital Verification* (SMOV); however, there are a few still outstanding issues that are needed to support STIS Cycle 7 science. These issues are listed below:
  - The flatfielding accuracy around the “dust motes” that are present on the CCD (early results are shown in Ferguson 1997)

---

<sup>1</sup>Affiliated with the Astrophysics Division, Space Science Department, European Space Agency



- The accuracy of fringe removal for wavelengths  $\geq 700$  nm in CCD spectroscopy (gratings G750L and G750M) (early results on this issue can be found in the contributions by Goudfrooij et al. 1997 and Plait et al. 1997)
  - The limiting Earth-limb avoidance angle beyond which the influence of scattered light becomes important
  - The memory effect of the CCD after (heavy) saturation
  - The characteristics of the red light which is scattered within the CCD substrate
  - Missing dispersion solutions for some wavelength settings (mostly in the far-UV medium-dispersion modes)
  - Confirmation of correctness of flight software updates for Target Acquisitions (*now confirmed*)
  - Grating scatter (Red light into UV gratings, especially important in the case of the G230LB and G230MB (CCD) gratings)
  - Flatfielding accuracy for the MAMA's (see Kaiser et al. 1997)
  - Out-of-band transmissions (red leaks) for MAMA filters
  - Sensitivities of a number of medium-dispersion MAMA grating modes
2. Establish the on-orbit performance of STIS with respect to that found during Ground Calibration;
  3. Monitor the on-orbit performance of STIS on a timely basis, with timescales as appropriate for a given calibration issue, both to keep track of the health & safety of the instrument and to establish the stability in time of a given calibration solution;
  4. Finally, if time allows it: Commission new capabilities of STIS.

## 2.2. Philosophy during Cycle 7

In view of the limited amount of manpower available within the STIS support group, it is necessary to find a suitable compromise between what is ultimately needed from a calibration program and what can be reasonably observed and analyzed within the duration of Cycle 7. We therefore have to assign priorities to our calibration analysis efforts. These priorities come in two different lists. The first one shows the overall, mode independent, priorities for instrument calibration, whereas the second one shows a hierarchy of the importance of the different instrument modes (determined by the Cycle 7 usage statistics).

In broad terms we will employ the following overall calibration priorities:

1. First priority is the regular health and safety monitoring of the detectors, mechanisms, lamps, window contamination and basic operations, so that we can, at any time, attest to the acceptable performance of STIS and to its longterm stability.
2. Regular updating of reference files (e.g., biases, darks, delta flats) for use in the STIS pipeline and for a-posteriori reduction, and keeping GO updated with the latest information on our calibration experience.
3. Basic sensitivity calibration of all spectroscopic modes, and monitoring its stability in time as well as that of the flat field calibrations.
4. Optical performance (e.g., PSFs, LSFs, Geometric distortion, etc.)
5. Characterization of miscellaneous specific peculiarities (e.g., detector non-linearity, Charge Transfer Efficiency (CTE), long-wavelength halo, fringing and scattered light).

Within each of these priority groups, our calibration priority will be in the following order of observing modes:

1. First-order low-resolution *prime* grating modes (G140L, G230L, G430L, G750L).
2. Echelle spectroscopy.
3. First-order medium-dispersion grating modes.
4. CCD imaging (broad-band first, then narrow-band).
5. MAMA imaging (broad-band first, then narrow-band).
6. First-order low-resolution *backup* grating modes (G230LB, G230MB), including the analysis of its grating scatter.

In addition to this, on-axis calibrations have higher priority than do off-axis calibrations. I.e., we will first establish the calibrations at the *center* of the field or slits and expand the calibration to two dimensions thereafter.

In view of these analysis priorities, it is unavoidable that not all data taken by GOs will have the available calibration data fully analyzed yet by the time their observations are taken, especially if it concerns data taken in a mode that has a low "analysis priority". In any case, we would like to stress that *all calibration data in the archive is immediately non-proprietary upon archival*, and can thus be retrieved by the GO to perform his/her own calibration at any time.

### 2.3. Expected Calibration Accuracies

Tables 1 and 2 summarize the calibration accuracies we aim to achieve by the end of cycle 7 for the different spectroscopic and imaging attributes, respectively.

Table 1. Spectroscopic Accuracies to be reached in Cycle 7

Attribute	Accuracy: CCD	Accuracy: MAMA	Limiting Factor(s)
Relative wavelengths (within exposure)	0.1 – 0.25 pixels	0.25 – 0.5 pixels	Optical & geometric distortion
Absolute wavelengths (across exposures)	$\leq 1.0$ pixel	$\leq 1.0$ pixel	Thermal stability; Internal vs. external illumination; wavecal zeropoint
Absolute photometry	10%	15%	Instrument stability; photometric calibration
Relative photometry (within exposure)	5%	5 – 10%	Instrument stability; photometric calibration

Table 2. Imaging Accuracies to be reached in Cycle 7

Attribute	Accuracy: CCD	Accuracy: MAMA	Limiting Factor(s)
Relative astrometry (within image)	0.1 pixels	0.25 pixels	Stability of optical distortion
Absolute photometry	5 – 10%	15%	Instrument stability; photometric calibration
Relative photometry (within image)	5%	10%	Flat fields; external illumination

Some of the indicated accuracies are already reached (e.g., relative imaging photometry for the CCD), while others will still take a while to be reached (e.g., far-UV MAMA flatfielding).



### 3. Specifics on the Calibration Programs

In this Section, we inform the reader with specific, but brief, information about the individual STIS calibration programs that are being executed in Cycle 7. Different goals of the calibration program are individually listed in subsections.

#### 3.1. Monitoring for Health and Safety

Our approach to monitoring for health and safety issues is to start off with fairly intense monitoring for about 6 months, after which it will be less frequently as dictated by the first 6 months worth of data.

In the following we denote the different Cycle 7 calibration program designations in sans serif font, followed by a short description.

**7600: CCD Performance Monitor**

Measures the baseline performance and commandability of the CCD. Measurements of bias structure, dark current, flat field structure, and CTE.

**7659: Daily Darks for ACQ Hot Pixels**

For updating hot pixel list for Target Acquisitions.

**7635: Hot Pixel Annealing**

Anneal out CCD hot pixels, and test for window contamination.

**7604: MAMA Dark Monitor**

Monitoring of dark noise which is the primary means of checking the health of the MAMA detectors.

**7643: MAMA Fold Distribution**

Basic monitor of performance of MAMA microchannel plates.

#### 3.2. Monitoring for Calibration Stability

**7601: CCD Dark and Bias Monitor**

Weekly monitor of CCD darks and biases to update reference files, including hot pixel lists

**7634: CCD Flat Fielding Monitor**

Monitor appearance of flat field (as well as the intensity of the tungsten lamp)

**7672: CCD Sensitivity Monitor at Field Center**

Monitor sensitivity of all supported low-resolution settings of the CCD gratings (wide-slit spectra of a HST spectrophotometric standard)

**7639: CCD Sensitivity over full field**

Take CCD images of photometric standard star field in  $\omega$  Cen every few months to monitor throughput as well as measure the CTE (and the PSF)

**7638: CCD PSF Monitor**

Monitor PSF in different filter passbands (*deferred to 1998*)

**7711: CCD Fringe Flats**

Build library of CCD fringe flats in the G750L and G750M settings at central wavelengths  $\geq 700$  nm for different slits.

**7644: NUV-MAMA Monitoring flats**

Monitor NUV-MAMA flat field to construct bi-monthly delta flats

**7728: FUV-MAMA Monitoring flats**

Monitor FUV-MAMA flat field to construct delta flats for every three months

**7673: MAMA Sensitivity Monitor**

Monitor sensitivity of all supported low-resolution settings of the MAMA gratings (wide-slit spectra of a HST spectrophotometric standard)

**7720: MAMA Sensitivity over full field**

Take MAMA images of photometric standard star field in NGC 6681 every few months to monitor throughput (as well as the PSF)

**3.3. Major Calibration Programs***A. Flat Fielding***7636: Spectroscopic CCD Flatfielding**

Build up a library of flats for all CCD grating settings during the course of cycle 7

**7664: CCD External Flats, Earth Streak**

Take Earth-streak flats to build up a high signal-to-noise external flat field, to be used as intermediate-order illumination correction to the internal flats

**7658: CCD External Flats, Sky**

Take images of the sky, to be merged together later on to form low-order illumination correction to the flat field. These exposures will be taken in parallel with an equivalent NICMOS calibration program

**7645: MAMA FUV Flats**

Build up a library of flats for all MAMA FUV grating settings during the course of cycle 7

**7647: MAMA NUV Flats**

Build up a library of flats for all MAMA NUV grating settings during the course of cycle 7

*B. Sensitivities***7656: Spectroscopic and Imaging Sensitivity, CCD**

Basic sensitivity measurement for all supported CCD imaging and spectroscopic modes; running once a year

**7657: Spectroscopic and Imaging Sensitivity, MAMA**

Basic sensitivity measurement for all supported MAMA imaging and spectroscopic modes; running once a year

*C. Dispersion Solutions***7650: Dispersion Solution Monitor, CCD**

Wavelength dispersion solutions will be determined for each CCD grating on a yearly basis as part of a long-term monitoring program. Only central and extreme wavelength settings are observed

**7651: Dispersion Solution Monitor, MAMA**

Wavelength dispersion solutions will be determined for each MAMA grating on a yearly basis as part of a long-term monitoring program. Only central and extreme wavelength settings are observed



### 3.4. Special CCD Calibrations

#### 7603: Optimizing Removal of NIR Fringing

Test accuracy of using contemporaneous spectral flats in G750L and G750M settings with  $\lambda \geq 700$  nm to correct for fringes (*Already finished; see first results in Goudfrooij, Walsh & Baum 1997*)

#### 7605: Target Acquisition Workout

Test Flight Software Changes that were linked up in August 1997 (*Already finished*)

#### 7637: Residual Images after Overillumination

Overexpose the CCD by taking a slitless spectrum of a bright star. Take dark frames afterwards to study the residual effect over time. Repeat the experiment, now taking bias frames instead of dark frames to study the effect of read-outs. Do this whole procedure using three different gratings, one in the UV (G230LB), one in the blue (G430L) and one in the red (G750L) to check for any dependence on color.

#### 7641: CCD External Flats, Stellar

Take images of dense stellar field and step across the field with small offsets to map out the throughput at the dust "motest". Also a test for the accuracy of relative photometry within exposures. (*Already finished*)

#### 7642: Red Halo of Light Scattered within CCD Substrate

Observe red star through [OIII] filter (which has a red leak at  $\lambda > 1\mu\text{m}$ ) to characterize the red halo. Repeat observation with long-pass 28X50LP filter, and take spectrum with G750L grating to characterize wavelength dependence of the halo

#### 7646: Scattered Light near Earth Limb

Measure the scattered light from the Earth background at low limb angle with the CCD, both during bright and dark Earth conditions, to determine its effect to the background intensity.

#### 7648: Missed Dispersion Solutions, CCD

Take arc lamp spectra in the CCD grating settings which were missing from Ground and SMOV calibrations

#### 7652: LSF Measure, CCD

Measure LSF of emission lines of young Planetary Nebula (of which the FWHM of the lines is  $\sim 8 \text{ km s}^{-1}$ ) as a function of  $\lambda$  and compare with LSF of arc lines

#### 7654: Slitless Spectroscopy, CCD

Determine dispersion solution as a function of position on the CCD by taking slitless spectra of a star with known radial velocity and numerous narrow absorption lines, and moving it around on the CCD

#### 7660: STIS to FGS Alignment Check

Re-verify the STIS aperture and slit locations, and check the transformation of the STIS CCD detector reference frame to the FGS reference frame, after the FGS-FGS update

#### 7665: Geometric Distortion, CCD

Step star along wide slit and step along slit to map out the geometric distortion in three residual CCD grating settings that were missed in Ground Calibration

#### 7666: CCD Linearity and Shutter Stability Test

Use Tungsten and relatively bright star to test linearity at high and low intensities, as well as the stability of shutter delay time for CCD

**7668: Missing Incidence Angle Corrections, CCD**

Measure corrections to dispersion solutions for non-concentric slits with respect to the reference slit (up to first order)

**7723: Red Scattered Light with CCD UV Gratings**

Determine influence of red scattered light to spectra taken with the G230LB and G230MB CCD gratings by comparing spectra of a red star with those taken with the equivalent MAMA gratings (G230L and G230M).

**3.5. Special MAMA Calibrations****7649: Missed Dispersion Solutions, MAMA**

Take arc lamp spectra in the MAMA grating settings which were missing from Ground and SMOV calibrations

**7653: LSF Measure, MAMA**

Measure LSF of emission lines of young Planetary Nebula (of which the FWHM of the lines is  $\sim 8 \text{ km s}^{-1}$ ) as a function of  $\lambda$  and compare with LSF of arc lines (*deferred*)

**7655: Slitless Spectroscopy, MAMA**

Determine dispersion solution as a function of position on the MAMA by taking slitless spectra of a star with known radial velocity and numerous narrow absorption lines, and moving it around on the MAMA

**7661: MAMA Filter Red Leak Measurement**

Measure out-of-band throughput for MAMA filters with the CCD

**7667: MAMA Geometric Distortion**

Step star along wide slit and step along slit to map out the geometric distortion in the MAMA grating settings that were missed in Ground Calibration

**7669: Missing Incidence Angle Corrections, MAMA**

Measure corrections to dispersion solutions for non-concentric slits with respect to the reference slit (up to first order)

**7671: External to Internal Wavelength Scale Corrections**

Observe emission-line object with known radial velocity to check dispersion solution from arc lamp (*deferred*)

**7721: Slit Throughputs**

Measure relative slit throughputs for a variety of commonly used slits as a function of wavelength (using one and the same star)

**7774: High S/N PSF Measurement**

Deep images of isolated point sources are taken in MAMA imaging modes (NUV and FUV) using selected narrow-band filters to establish a (central) PSF with  $S/N = 100$  in the near wings

**7724: Doppler Checkout**

Check automatic Doppler correction for MAMA ACCUM measurements (*deferred*)

**3.6. Total Orbit Summary**

The total amount of orbits needed for execution of the full Cycle 7 calibration plan for STIS is shown in Table 3, subdivided into the different goals of the program.

The total number of external orbits needed for STIS calibrations is about 10% of the total STIS (external) observing time, both for the CCD and the MAMA.



Table 3. Orbit Summary for Cycle 7 STIS Calibrations

	External Orbits		Internal Orbits
	Prime	Parallel	
CCD, Total	84	154	1334
Monitoring	22	4	1149
Major	25	150	124
Special	37	0	61
MAMA, Total	167	0	1401
Monitoring	115	0	1374
Special	52	0	17

#### 4. Keeping the GO/GTO Community Informed

The status of the STIS Calibrations in Cycle 7 is kept up to date on the World Wide Web through the "calibration resources" WWW page that can be accessed through the STIS home page ([http://www.stsci.edu/ftp/instrument\\_news/STIS/topstis.html](http://www.stsci.edu/ftp/instrument_news/STIS/topstis.html)). On the "STIS Calibration Resources" are

1. Pages on the Cycle 7 Calibration Program: A table of all programs (sorted by either topic or execution date) with links to their phase I and phase II proposal texts. If you have comments or suggestions on the calibration plan, please email them to [help@stsci.edu](mailto:help@stsci.edu) with a clear title, such as "Comments on STIS cycle-7 calibration plan." We will certainly welcome your input.
2. A page on the STIS On-Orbit Performance, containing various summaries and examples of the on-orbit performance of STIS, obtained from analysis of data from SMOV and early Cycle 7 calibration proposals.
3. UNDER CONSTRUCTION: Page on calibration accuracies reached to date in the different observing modes of STIS (this page will be available by November 1, 1997, and regularly updated thereafter).

#### References

- Baum, S. A., et al., 1997, this volume.  
 Ferguson, H. C., 1997, this volume.  
 Goudfrooij, P., Walsh, J. R., & Baum, S. A., 1997, this volume.  
 Kaiser, M. B., et al., 1997, this volume.  
 Plait, P., & Lindler, D., 1997, this volume.

## STIS Capabilities: Current and Future Implementation

Bruce E. Woodgate

*Goddard Space Flight Center, Greenbelt, MD*

**Abstract.** Capabilities of STIS currently supported and those going beyond the subset available at the start of Cycle 7 are described. The latter are candidates for later implementation.

### 1. Introduction

At the beginning of Cycle 7, many of the modes of STIS are activated, and "Available" to be used, and a large subset of those are "Supported" with pipeline calibration. Some others are not available yet for command development or other ground system reasons. Some of them are candidates for future development. I point out some capabilities we hope will become more available in the future. Table 1 shows some of these capabilities, and some which are already supported and are particularly sensitive.

General descriptions of STIS are available: the design in Woodgate et al, 1997, the in-orbit performance in Kimble et al (1997), and operational access in the STScI STIS Handbook by Baum et al (1996). Also see the STScI Web page

[http://www.stsci.edu/ftp/instrument\\_news/STIS/topstis.html](http://www.stsci.edu/ftp/instrument_news/STIS/topstis.html)

and the IDT STIS Web page

<http://hires.gsfc.nasa.gov/stis/stispage.html>

### 2. QSO spectroscopy

The currently supported STIS capability for UV spectroscopy of faint QSOs, via the modes G140L and G230L, does not fully replace the nearest equivalent GHRS and FOS modes. The resolving powers, 415-1130, are lower than the GHRS low resolution modes. Consequently studies of QSOs too faint for the echelle modes, but with the ability to distinguish absorption lines as well as GHRS are not currently possible.

This problem can be partly alleviated by using modes X140M and X230M, with resolving powers 3500-4500, and a range of 20nm in the band 115-170nm, and 27.6nm in the band 165-310nm respectively. The sensitivity of the X140M mode is 62% of the STIS G140L mode, and 80% of the GHRS mode G140L. These modes use cross-disperser gratings, and their dispersions and slits are orthogonal to the prime modes. They were withheld from use partly because each spectral format also crossed the other MAMA detector, and checking for Bright Object Protection was more complicated. Now that the MAMA detectors must be cycled around the radiation belts, rather than being kept on all the time, the other MAMA could remain off during the use of these modes, removing the problem.

A comparison of QSO magnitudes reachable in the FUV modes is shown in Table 2, for an exposure of 10 orbits (24,000 sec) with S/N = 10 at 140 nm.

For all of these modes, for exposures longer than an orbit, effective sensitivities are enhanced compared to GHRS and FOS because of the lower background of the MAMAs compared to the digicons. This is particularly true for the FUV, but even the NUV, with its particle phosphorescence, has a factor 2.5 lower background than the digicons for point source spectra.



Table 1. Current and future STIS performance					
Performance goal	Mode	Aperture	Technical feature	Supported?	Command development needed?
Spectral resolution					
R=220,000	E140H	0.1X0.03	Repeller off	N	Y - HV control
R=167,000	E230H	0.1X0.03		N	N
R=4000	X140M	Any	NUV off	N	N- ground system?
FUV background					
- imaging	MAMA/FUV	F25SRF2	BOP	Not parallel	N
- spectra	G140L	52X2	BOP	Not parallel	N
Faint spectra					
- NUV	PRISM	6X6	BOP	N	Wavecalcs?
- Vis line	G430L	52X2		Y	N
- NIR line	G750L	52X2		Y	N
Faint images					
- CCD	CCD	50CCD		Y	N
- NUV				Not parallel	N
- FUV				Not parallel	N
High S/N					
- R<100,000	Except E...H	0.2X0.06FP	FP-split	N	Ground system?
Timing	Any UV	Any	Time tag	Y	N
Coronagraphy					
- Vis/NIR	Imaging	Wedge, etc	Combine rolls	Y	N
UV	Spectra	Bar		Off-center only	N
	Imaging	Wedge, etc	Local BOP, Combine rolls	N	Screening?
	Spectra	Bar		N	Screening?

A new reason for use of the X230M mode for NUV faint sources is that very long exposures with the E230M mode are background limited because of the phosphorescence, and spectral binning to improve S/N is less effective.

As well as QSO studies, faint stellar spectroscopy can benefit from these intermediate resolving power modes, particularly for studies of time variable lines, where increasing the exposure time does not help.

Table 2. Magnitudes reachable in FUV modes, S/N=10/resel, 10 orbits			
Spectral mode	Spectral resolving power	Spectral coverage (nm)	Magnitude
G140L	770-1130	55	20.0
X140M	3500-4500	20	18.0
E140M	35,000	55	14.3
GHRSG140L	1800-2800	30	18.8

### 3. Very faint object spectroscopy

The prism mode, nominally in the NUV, but in fact covering both the NUV and FUV using the NUV MAMA, provides the highest spectroscopic sensitivity. This is particularly true in the NUV where the dispersion is lowest, and for detecting continuum edges. An important current use would be for detecting the Lyman continuum break in Gamma Ray Burst afterglows, in the range  $0.5 < z < 2$ , to obtain their redshifts and other properties.

This mode is currently supported when used with  $25 \times 25$  arcsec apertures with various filters, most usefully  $\text{SrF}_2$  with a cutoff at 125 nm ( $T = 1\%$ ) to exclude the Lyman alpha geocorona, and with the  $2 \times 2$  arcsec aperture. Use of the  $6 \times 6$  arcsec aperture would allow rejection of other sky lines for much of the spectrum, such as the 247 nm line, while allowing point and shoot operations without prior HST image analysis if the position is known to  $\pm 3$  arcsec from ground observations. This enables spectroscopic observations with HST of the GRB afterglow much sooner after its discovery, while it is still bright enough.

A S/N of 5 per 2 nm band could be obtained in 10,000s for  $V=23$  at 180 nm and  $V=24$  for 270 nm.

A narrow compact Lyman alpha emission line of  $5 \times 10^{-17} \text{ erg cm}^{-2} \text{ s}^{-1}$  at 250 nm ( $z=1$ ) would be detected at  $S/N=5$  in the same time. This is 6 times fainter than the faintest of a group of 3 Lyman alpha galaxies at  $z=2.4$  that we have found.

### 4. Compact emission line galaxies

Very high redshift galaxies may be detected spectroscopically if they are compact and have emission lines. Their redshifts may be measured. Line ratios can indicate whether they are formed by star formation or AGNs. Line broadening and extended emission may indicate dynamics.

The low resolution modes of any of the 4 bands may be used, depending on the redshifts searched for. Lyman alpha may be searched for between redshifts zero to 7. For the NUV band, either the MAMA (G230L) mode or the CCD (G230LB) mode may be used, depending whether sensitivity above or below 250 nm is emphasized. For specific known objects, a slit may be used, but to search a suspect cluster or a random field, a slitless mode may be used. Slitless observing requires a small proportion of the time be spent in direct imaging to act as a position reference to determine the wavelength scale.

The current initial GO pure parallel program uses slitless G750L to measure compact galaxy redshifts. Several emission line galaxies have been found (see Gardner et al. poster in this volume). For objects in the center of the field, the wavelength range is 550-1000 nm. A compact emission line at 700 nm, for example Lyman alpha at  $z=4.7$ , with a flux of  $4 \times 10^{-17} \text{ erg cm}^{-2} \text{ s}^{-1}$  would be detected at  $S/N=5$  in one orbit. This would correspond to a dust free star formation rate of  $3\text{--}12 M_\odot \text{ yr}^{-1}$  ( $H_0=65 \text{ km s}^{-1} \text{ Mpc}^{-1}$ ,  $Q_0=0.02$ ).

### 5. High resolution spectroscopy

The highest spectral resolution measured with STIS in test is  $R=220,000$ . This was obtained in Mode E140H using the  $0.1 \times 0.03$  arcsec slit, the FUV MAMA repeller off, hi-res ( $2048 \times 2048$ ) data analysis, and illuminating with a mono-isotopic Pt lamp to avoid hyper-fine structure broadening. The  $2048 \times 2048$  data mode is the normal raw data mode from the spacecraft, the  $0.1 \times 0.03$  arcsec slit is an Available Mode requiring special justification, but the Repeller-off requires command development not yet available.

The same measurement with the normal Repeller-on would yield  $R=190,000$ , and with also the  $0.2 \times 0.09$  arcsec slit, to return to the nearest Supported mode, would yield  $R=114,000$ .



The NUV MAMA does not have a repeller. The highest resolution NUV mode, E230H, using the 0.1x0.03 arcsec slit would provide  $R = 167,000$ .

Results using STIS for ISM spectroscopy with the supported 0.09 arcsec wide slit are found in Jenkins et al (1997), and results illustrating the need for the highest resolving powers obtainable, showing ISM b-values less than 0.5 km/s, are found in Welty et al (1996).

These capabilities are summarized in Table 3.

Table 3. Highest spectral resolving powers			
Spectral mode	Slit width (arcsec)	Repeller	Resolving power ( $\lambda/\partial\lambda$ )
E140H	0.03	OFF	220,000
E140H	0.03	ON	190,000
E140H	0.09	ON	115,000
E230H	0.03	N/A	167,000

## 6. Special capabilities

Several other forefront capabilities of STIS that should be mentioned, are being covered at this meeting.

The ability to do high S/N spectroscopy above  $S/N = 100$  is being explored and is reported on by Kaiser. For modes other than the high resolution echelle modes (E140H and E230H), for which Doppler smoothing will permit very high S/N, the use of the FP-split slits will extend the S/N capability.

Timing of photon arrival times using the time-tag readout has been demonstrated using the Crab pulsar, and a timing accuracy of at least 1 in  $10^6$  shown, limited by the current calibration of the spacecraft clock. See the poster by Lindler et al. in this volume.

A reduction in stray light from stellar images may be obtained by using the coronagraph stops (Cornett et al. poster in this volume). This is mostly due to preventing the light from the image core reaching the CCD and scattering within the CCD backing and reflecting from the CCD window. This is initially being used for the detection of protoplanetary disks around nearby stars with the CCD. Spectroscopic use of the coronagraphic bars in the UV, when permitted, will allow the detection of faint extended emission, particularly in emission lines, around bright objects without getting swamped by the haloes produced in the detectors by the bright objects, and without saturating the detectors. Applications include material around galaxy nuclei and stellar winds.

Direct imaging with STIS is very sensitive, particularly when broad or no filters are used. CCD imaging with no filter can go 3 to 6 times fainter than WFPC2, largely because it covers 200 to 1000 nm, but it also has somewhat higher DQE and lower noise. NUV imaging with the Quartz filter covers 150 - 310 nm. FUV imaging with the  $\text{SrF}_2$  filter covers 130 to 170 nm, avoiding the Lyman alpha geocorona.

## References

- Baum, S. et al., 1996, *STIS Instrument Handbook* Version 1.0, (Baltimore, STScI)
- Cornett, R. 1997, this volume
- Gardner, J. et al., 1997, this volume
- Jenkins, E. B. et al., 1997, ApJ, Nov HST special issue
- Kaiser, M. E. 1997, this volume
- Kimble, R. A. et al, 1997, ApJ, Nov HST special issue
- Lindler, D. et al., 1997, this volume

Welty, D. E., Morton, D. C. and Hobbs, L. M. 1996, *ApJS*, 106,533

Woodgate, B. E. et al., 1997, in preparation



## STIS CCD Hot Pixel Annealing

T. Beck

*Advanced Computer Concepts, Inc. Potomac, Maryland*

W. Landsman

*Hughes STX Corp. Lanham, Maryland*

### 1. Introduction

In an effort to reduce the number of "hot" pixels in the CCD array, an annealing process was used that allowed the CCD to warm up to about 0C for approximately 12 hours. The effectiveness of the procedure was tested by measuring the dark current behavior before and after annealing.

### 2. Observations

Data for this test (SMOV proposal 7107) was taken on May 17-18, 1997 and again on June 19-20, 1997 and consist of five 1200-second dark frames taken before and after each annealing cycle. All observations were executed using CCD amplifier "D" at GAIN=1.

### 3. Data Reduction

For each group of 5 dark frames, the STIS IDL procedure CALSTIS\_OVERSCAN was used to remove the overscan and trim each dark frame. Routine iraf\$darkcombine was used to create a cosmic-ray rejected combined dark.

### 4. Analysis

For each combined dark frame, pixels above three different threshold rates (1.0, 0.5, and 0.1 electrons/sec) were counted using the IDL WHERE function. The ratio of the values of these pixels was then computed (post/pre). A ratio of less than 1.0 indicates that the pixel had annealed. Table 1 summarizes the results for the May 17/18 test. Table 2 shows the results for the June 19/20 annealing.

Table 1. Annealing Cycle for 17-18 May 1997.

Count Rate e-/sec	Hot Pixels				Percent of pre-annealing hot pixels with a ratio of			
	pre	post	common	new	< 1.0	< 0.5	< 0.1	< 0.01
1.0	720	427	362	65	80.9	52.6	24.9	5.8
0.5	1084	684	600	84	79.7	51.9	22.6	5.0
0.1	3222	1811	1620	191	84.2	59.6	17.0	2.4

Table 2. Annealing Cycle for 19-20 June 1997.

Count Rate e-/sec	Hot Pixels				Percent of pre-annealing hot pixels with a ratio of			
	pre	post	common	new	< 1.0	< 0.5	< 0.1	< 0.01
1.0	758	476	405	71	80.2	54.1	26.9	8.0
0.5	1211	782	642	140	80.6	55.1	27.3	8.1
0.1	4594	3482	1846	1636	86.1	66.4	36.0	18.2

Note that in each case approximately 80% of the hot pixels identified in the pre-annealing combined darks annealed to some degree. The three panels of Figures 1 and 2 show the histograms of the pixel value ratios at each threshold rate.

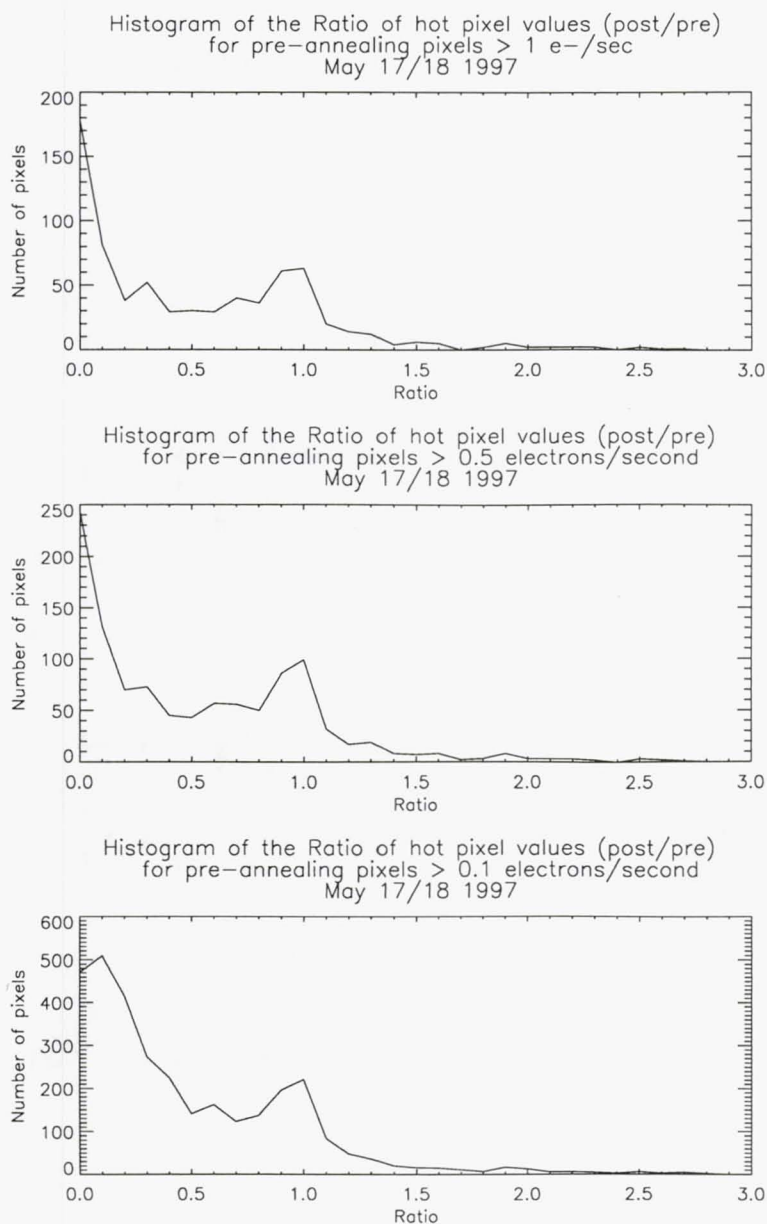


Figure 1. Ratio Histograms for May 17/18



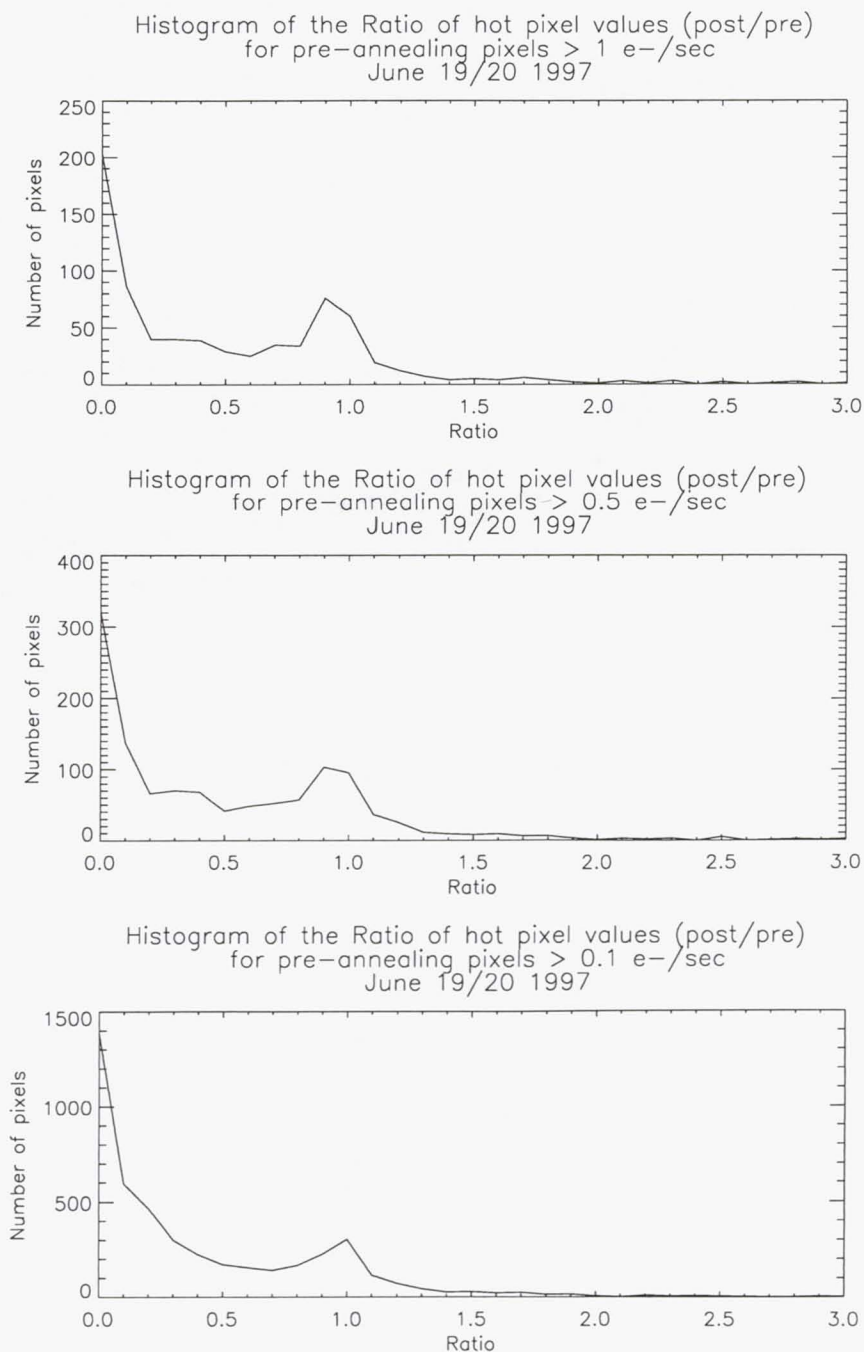


Figure 2. Ratio Histograms for June 19/20

Cumulative histograms of each combined dark frame (overplotted) show the drop in the number of hot pixels at low count rates. See Figure 3.

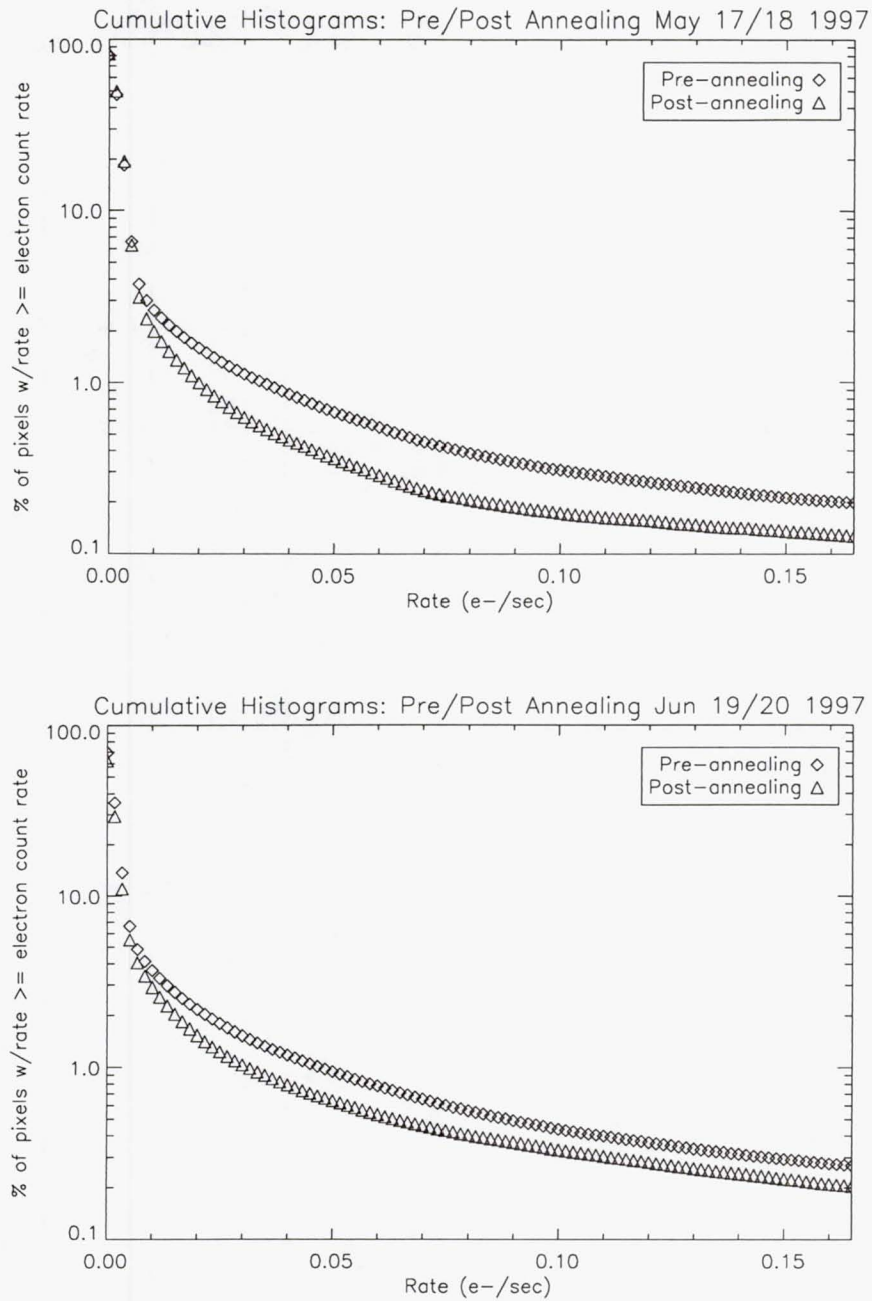


Figure 3. Cumulative Histograms

The hottest pixels in the sample ( $>25$  electrons/sec) appear to either anneal to a high degree (ratio  $<0.1$ ) or not all (ratio  $\approx 1.0$ ), with few pixels in between. See Histogram in Figure 4.



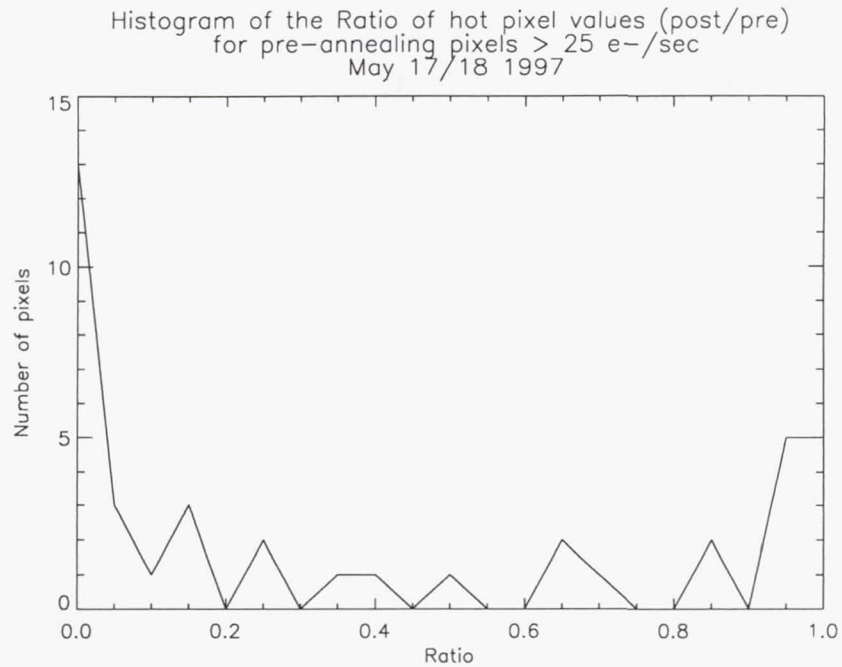


Figure 4.

## 5. Conclusion

In each annealing test approximately 80% of the hot pixels annealed to some degree. The ratio distribution of the hottest pixels appears to be somewhat polarized.

## STIS Observations of the Nuclear Ionized Gas in the Elliptical Galaxy M84

G. A. Bower<sup>1</sup>, R. F. Green<sup>1</sup>, D. Lindler<sup>2</sup>, The STIS IDT

**Abstract.** We present optical long-slit spectroscopy of the nucleus of the nearby radio galaxy M84 (NGC 4374 = 3C 272.1) obtained with STIS aboard HST. Our spectra reveal that the nuclear gas disk seen in WFPC2 imaging by Bower et al. (1997, ApJ, 483, L33) is rotating rapidly. The velocity curve has an S-shape with a peak amplitude of  $400 \text{ km s}^{-1}$  at  $0''.1 = 8 \text{ pc}$  from the nucleus. To model the observed gas kinematics, Bower et al. (1997, ApJL, in press) fit a thin Keplerian disk model to these data, leading to the conclusion that a  $\approx 1.5 \times 10^9 M_{\odot}$  dark compact mass (most likely a supermassive black hole) resides in the nucleus of M84.

### 1. Introduction

M84 is an E1 galaxy in the Virgo Cluster with an active galactic nucleus and hosts the F-R I (Fanaroff & Riley 1974) radio source 3C 272.1. Bower et al. (1997a; hereafter Paper I) obtained images of M84 with WFPC2 aboard HST, showing that the ionized gas within the central kpc has three components: a nuclear gas disk, outer filaments, and an 'ionization cone'. The nuclear gas disk has diameter  $\approx 1''$  (82 pc) and a major axis P.A.  $\approx 58^\circ$  that is tilted by  $\approx 25^\circ$  with respect to the major axis P.A. of the outer filamentary emission. This outer filamentary emission had been seen in ground-based imaging (e.g., Hansen et al. 1985; Baum et al. 1988). Its major axis is approximately perpendicular to the axis of the radio jets (Laing & Bridle 1987; Jones et al. 1981).

The presence of a nuclear gas disk in M84 is especially interesting. If the gas exhibits Keplerian motion about the nucleus, then a straightforward application of Newton's laws to the dynamics of this gas disk would provide an estimate of the mass of the putative supermassive black hole (BH) in M84's nucleus. It is plausible that M84 contains a BH, since it is a radio galaxy and the rotation gradient of the ionized gas is spatially unresolved (i.e.,  $> 100 \text{ km s}^{-1} \text{ arcsec}^{-1}$ ) in ground-based observations (Baum et al. 1990, 1992). Previous HST observations using FOS have found gas-dynamical evidence for BHs in other galaxies containing nuclear gas disks, such as M87 and NGC 4261 (Harms et al. 1994; Ferrarese et al. 1996). STIS (through the use of a CCD in a long-slit spectrograph) provides a significant improvement in the HST efficiency for measuring the nuclear dynamics of galaxies. We chose M84 as a target for a demonstration.

### 2. Observations and Data Calibration

Long-slit spectroscopy of M84's nuclear region was obtained with the STIS CCD, which has a pixel scale of  $0''.05/\text{pixel}$  (Baum et al. 1996), aboard HST on 1997 April 14 and 17 with the telescope tracking in fine lock with one FGS probe (nominal jitter  $\approx 0''.007$ ). Since M84's nucleus contains a bright optical point source (Paper I), the nucleus was acquired easily to

---

<sup>1</sup>NOAO/KPNO, P. O. Box 26732, Tucson, AZ 85726

<sup>2</sup>ACC, Inc., NASA/GSFC, Code 681, Greenbelt, MD 20771



## M84

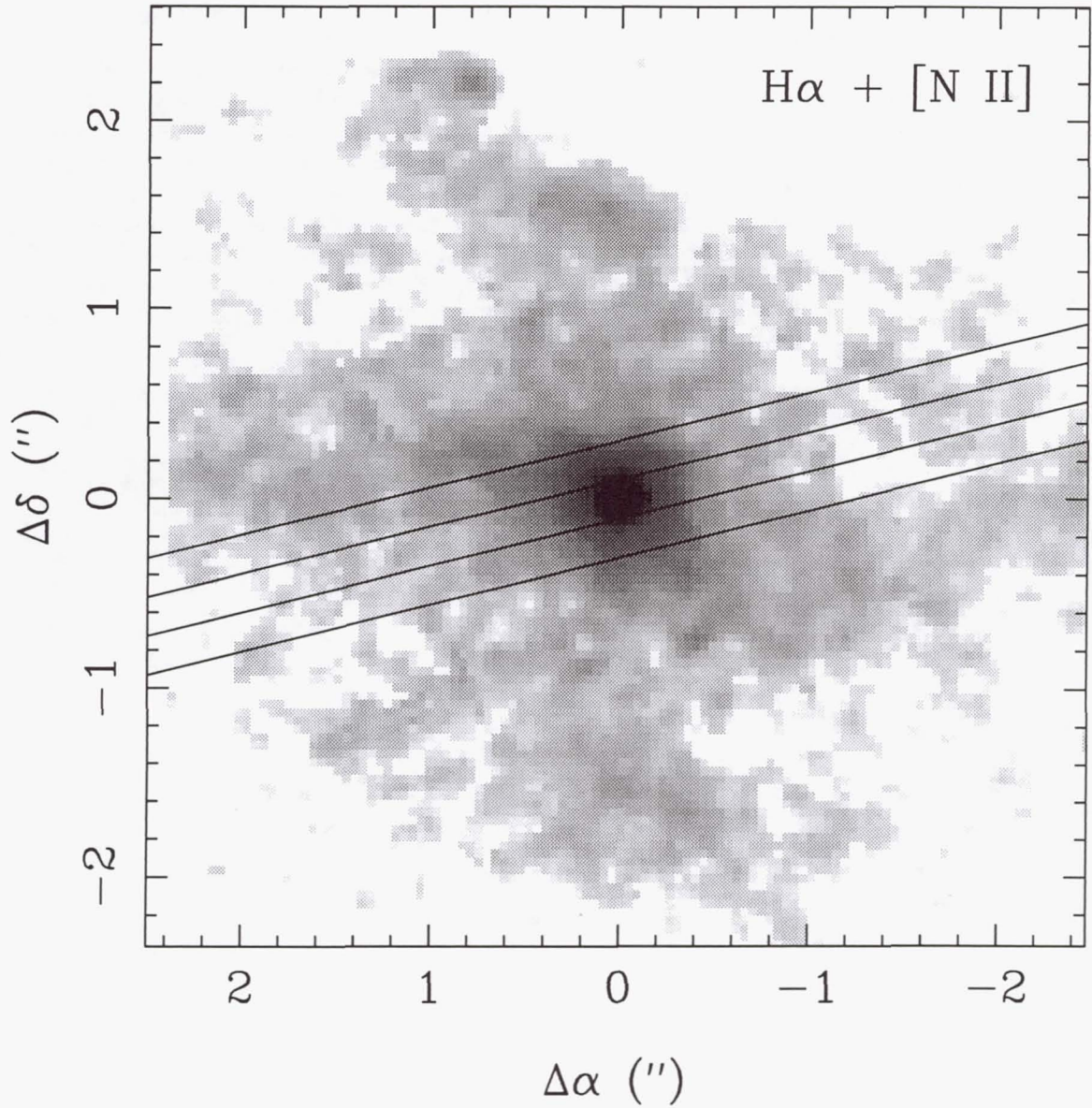


Figure 1. Our STIS slit positions (with the solid lines representing the slit edges) superposed on the Paper I H $\alpha$  + [N II] image, which is displayed here with a logarithmic stretch with a range in intensity covering a factor of 100.



an accuracy of  $0''.05$  by the ACQ mode using two iterations of two 10 sec imaging exposures through the F28X50LP optical long-pass filter. The ACQ/PEAK mode (Baum et al. 1996) was not available during these observations since they were obtained early during Servicing Mission Orbital Verification (SMOV). The  $52'' \times 0''.2$  slit was aligned at a position angle (P.A.) of  $104^\circ$ . This was the closest that the slit could be aligned with the gas disk's major axis (P.A. =  $58^\circ$ ; Paper I) because of HST scheduling constraints during SMOV. To allow for the centering accuracy of only  $0''.05$  and for the offset between the slit P.A. and the gas disk's major axis, we planned to obtain spectra at four different slit positions offset from the nucleus by  $-0''.3$ ,  $-0''.1$ ,  $+0''.1$ , and  $+0''.3$ , where the offsets were perpendicular to the slit and negative spatial offsets moved the slit toward a P.A. of  $14^\circ$  on the sky. However, Bower et al. (1997b; hereafter Paper II) show that the actual offsets were  $-0''.2$ ,  $0''.0$ ,  $+0''.2$ , and  $0''.0$  (see Fig. 1). For the fourth offset position, the discrepancy between the planned and actual positions occurred because this last spectrum was obtained during the second visit of M84, with an erroneously commanded offset. This error was fortuitous because from Paper II's analysis it is apparent that the kinematic signature of the nuclear gas disk is readily detectable only within  $\sim 0''.3$  of the nucleus, beyond which the kinematics of the outer filamentary emission (which do not necessarily provide good leverage on the nuclear gravitational potential) dominates the spectrum.

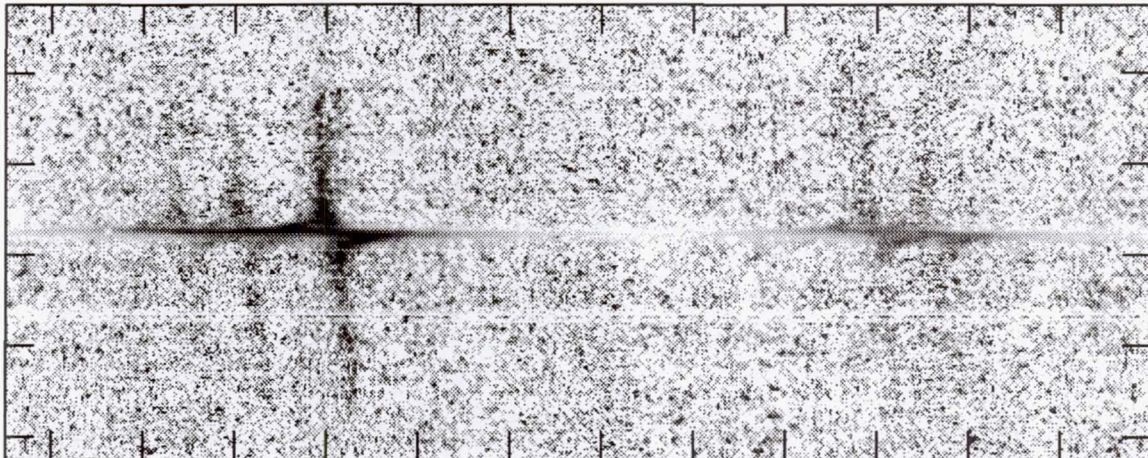


Figure 2. The central region of the last offset =  $0''.0$  spectrum, showing the emission lines (starting from the left) [N II]  $\lambda 6548$ ,  $H\alpha$ , [N II]  $\lambda 6583$ , and [S II]  $\lambda\lambda 6717, 6731$ . To emphasize the velocity gradient, the continuum distribution has been subtracted, and each spectral row has been normalized by its peak intensity of the [N II]  $\lambda 6583$  line. The interval between tick marks is 40 pixels, which corresponds to  $1000 \text{ km s}^{-1}$  along the dispersion axis (horizontal), and  $2''$  along the spatial axis (vertical).

At each slit position, we obtained spectra with the G750M grating, which has a dispersion of  $0.56 \text{ \AA/pixel}$ . This grating was set to cover the wavelength range of  $6295 \text{ \AA}$  to  $6867 \text{ \AA}$ , which includes the emission lines of  $H\alpha$ , [N II]  $\lambda\lambda 6548, 6583$ , and [S II]  $\lambda\lambda 6717, 6731$ . The spectral resolution of our instrumental configuration was  $2.2 \text{ \AA} \approx 100 \text{ km s}^{-1}$  (FWHM), assuming uniform illumination of the slit. However, Paper I shows that at the nucleus, there is a point source in the optical continuum, and the  $H\alpha + [\text{N II}]$  emission is very compact. Thus, our spectral resolution at the nucleus was better than  $100 \text{ km s}^{-1}$ . We integrated for two HST orbits at each slit position, which was equivalent to  $4500 - 5100 \text{ sec}$  per slit position depending on the occurrence of instrumental overheads. Spectra of the internal wavelength calibration source (wavecals) were interspersed among the galaxy spectra to allow for correction of thermal drifts during data reduction.



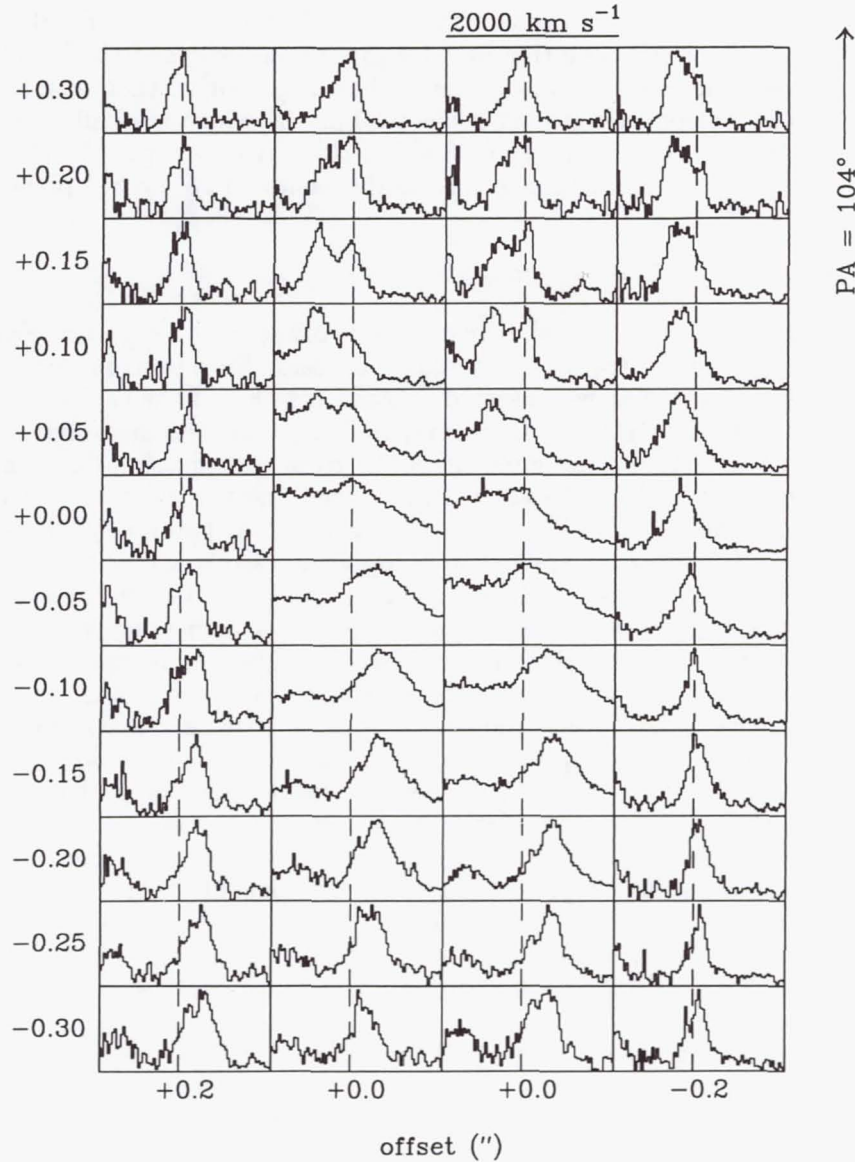


Figure 3. Profiles of the [N II]  $\lambda 6583$  emission line at positions within  $\sim 0''.3$  of M84's nucleus. The spectra have been continuum subtracted and normalized to the peak intensity of [N II]  $\lambda 6583$ . For each of the four slit positions, the offset from the nucleus is given along the bottom, where negative values of the offset move the slit toward P.A. =  $14^\circ$  on the sky. The position along the slit (relative to the nucleus) in arcseconds is shown on the left, where increasing values are toward P.A. =  $104^\circ$ . Each profile covers a heliocentric velocity range of  $200\text{--}2200 \text{ km s}^{-1}$ , and the systemic velocity is indicated by a dashed line. All profiles were taken from a single row in the data, except for the profiles at  $+0''.30$  along the slit which were binned by 4 pixels =  $0''.2$  to improve the S/N.

The data were calibrated using the CALSTIS pipeline to perform the steps of bias subtraction, dark subtraction, applying the flatfield, and combining the two sub-exposures to reject cosmic-ray events. The accuracy of the flatfield calibration was 1%. To reject hot pixels from the data, we employed dark frames obtained immediately before and after the M84 observations. We examined the input data, the flagged hot pixels, and the cleaned output data to ensure that only hot pixels were rejected. The data were wavelength cali-

brated and rectified by tracing the wavecalcs (using the Ne emission lines for the dispersion axis and the shadows of the two occulting bars for the spatial axis) and then applying these solutions for the geometric distortions to the data. The largest offset that we found between the actual and nominal dispersion solutions was 0.30 pixels, which is significant given that the dispersion solutions were accurate to 0.06 pixels ( $0.03 \text{ \AA} = 1 \text{ km s}^{-1}$ ). The data were then rebinned onto a log  $\lambda$  scale with a reciprocal dispersion of  $25 \text{ km s}^{-1} \text{ pixel}^{-1}$ .

### 3. Measurement of the Gas Kinematics

The first iteration at measuring the radial velocities involved cross correlating each spectral row from the four long-slit spectra with a synthetic emission-line spectrum, which included only the five emission lines that we detected in M84 (see Fig. 2) with flux ratios set at values typically found in the data. We then compared the velocities measured by the cross correlation technique with those measured manually from the emission-line peaks. These measurements agree very well for distances  $> 0''.3$  from the nucleus. For rows closer to the nucleus than this, the emission line profiles usually exhibit two kinematic components rather than a single component. These two components are readily seen in the strong [N II]  $\lambda 6583$  profile (as shown in Fig. 3), especially for the two spectra with offset =  $0''.0$ . Since the velocity measured by our cross correlation technique (using our synthetic template spectrum) coincides with the flux-weighted centroid over a given emission-line profile, these measurements will be distorted when more than one kinematic component is present. We determined which of the [N II]  $\lambda 6583$  profiles in Fig. 3 have two kinematic components by fitting model profiles to a few examples. Separate models with one or two Gaussians were fit to the profiles. If the improvement in  $\chi^2$  was significant, then the profile was classified as having two kinematic components. Although these models were not good fits to the observed profiles (which have broader wings than a Gaussian), this procedure was sufficient for objectively determining which profiles have two components. The velocities for the separate components were then measured by finding the centroid of each component peak.

Based on the  $\text{H}\alpha + [\text{N II}]$  image (see Fig. 1), it is not surprising that two kinematic components are seen within  $\sim 0''.3$  of the nucleus in the STIS spectroscopy. Paper I identified three spatial components in the ionized gas, including the nuclear gas disk, the outer filaments, and an ionization cone. Given these spatial components, the line of sight to the nuclear gas disk should also intersect the outer filamentary gas (and perhaps the ionization cone) lying in the foreground. Since the outer filamentary gas rotates about the nucleus at  $\approx \pm 100 \text{ km s}^{-1}$  (Baum et al. 1990, 1992), one expects to see this low-velocity component superposed onto the high-velocity kinematics of the nuclear gas disk. Fig. 4 shows our velocity measurements along the slit for each of the four slits. Our measurements of the low-velocity component agree very well with those of Baum et al. (1990). This measurement of the high-velocity component is the first time that the kinematics of M84's nuclear gas disk have been resolved. Paper II analyzes these data in more detail, leading to the conclusion that a  $\approx 1.5 \times 10^9 M_{\odot}$  dark compact mass (most likely a supermassive black hole) resides in the nucleus of M84.

**Acknowledgments.** We acknowledge useful discussions with Eric Emsellem and Ralf Bender as well as the assistance of Pat Hall and Charles Liu in planning these observations. Support for this work was provided to the STIS Investigation Definition Team by NASA.



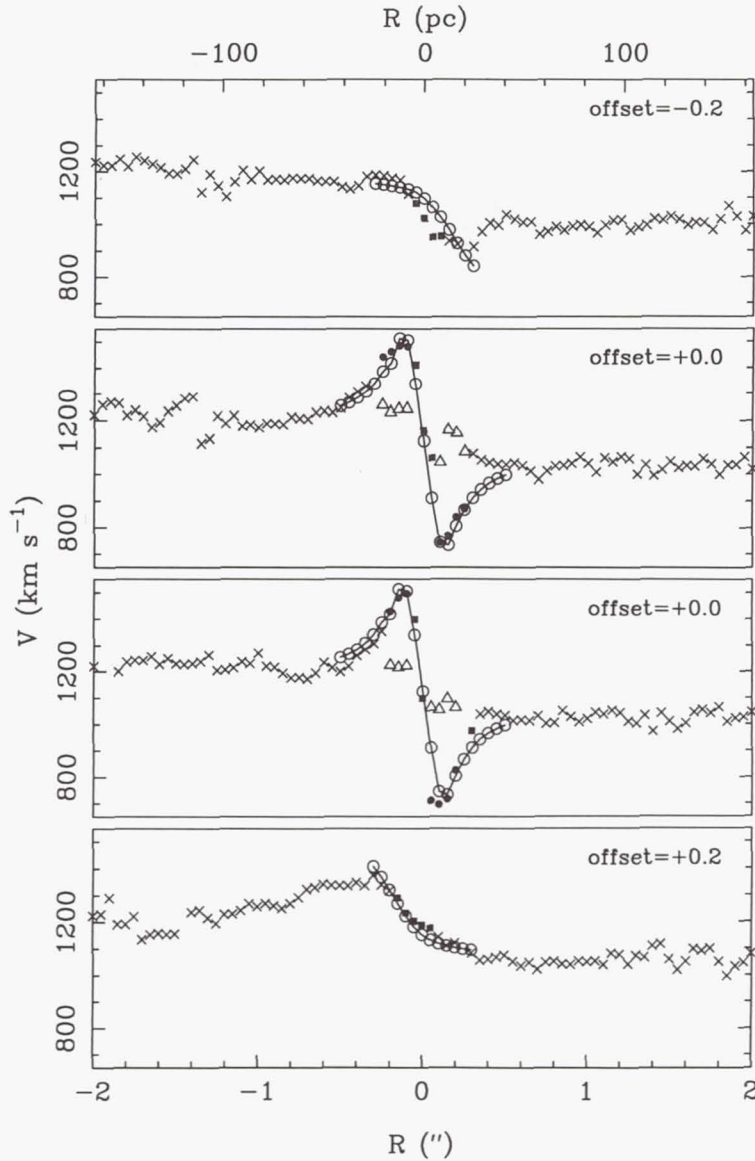


Figure 4. The heliocentric velocity as a function of distance along the slit for each slit position. Crosses indicate velocities measured by the cross correlation technique described in the text. Closer to the nucleus where two kinematic components are present, open triangles represent the low-velocity component, and filled circles or squares represent the high-velocity component. The squares denote positions where the high-velocity and low-velocity components cannot be separated because both are at or near the systemic velocity. The errors in the data points are  $\leq 25 \text{ km s}^{-1}$  (i.e., no larger than the size of the points). The velocities predicted by the best fit thin Keplerian disk model are represented by open circles connected by a solid line.

## References

- Baum, S., et al. 1996, *STIS Instrument Handbook* Version 1.0 (Baltimore: STScI)
- Baum, S. A., et al. 1988, *ApJS*, 68, 643
- Baum, S. A., Heckman, T., & van Breugel, W. 1990, *ApJS*, 74, 389
- Baum, S. A., Heckman, T., & van Breugel, W. 1992, *ApJ*, 389, 208
- Bower, G. A., Heckman, T. M., Wilson, A. S., & Richstone, D. O. 1997a, *ApJ*, 483, L33 (Paper I)
- Bower, G. A., Green, R. F., et al. 1997b, *ApJL*, in press (Paper II)
- Fanaroff, B. L., & Riley, J. M. 1974, *MNRAS*, 167, 31P
- Ferrarese, L., Ford, H. C., & Jaffe, W. 1996, *ApJ*, 470, 444
- Hansen, L., Nørgaard-Nielsen, H. U., & Jørgensen, H. E. 1985, *A&A*, 149, 442
- Harms, R. J., et al. 1994, *ApJ*, 435, L35
- Jones, D. L., Sramek, R. A., & Terzian, Y. 1981, *ApJ*, 246, 28
- Laing, R. A., & Bridle, A. H. 1987, *MNRAS*, 228, 557



## STIS First-Order Low-Resolution Mode Point-Source Sensitivity Curves

Nicholas Collins

*Hughes STX/LASP/GSFC*

Ralph Bohlin

*Space Telescope Science Institute, 3700 San Martin Drive, Baltimore, MD 21218*

**Abstract.** Point source sensitivity curves have been derived for the first order modes G140L ( $\lambda_{\text{central}} = 1425\text{\AA}$ ), G230L (2376 $\text{\AA}$ ), G230LB (2375 $\text{\AA}$ ), G430L (4300 $\text{\AA}$ ), and G750L (7751 $\text{\AA}$ ), spanning a wavelength range from 1140 $\text{\AA}$  to 10320 $\text{\AA}$ . The curves are determined by comparing wide slit ( $52'' \times 2''$ ) observations of the spectrophotometric standard star GD 153 to a pure hydrogen white dwarf model (Bohlin 1996). The calibration is tested by applying the curves to a STIS observation of the spectrophotometric standard star BD+75D325, and comparing these flux calibrated observations to a calibrated FOS spectrum.

### 1. Introduction

A sensitivity curve is used to determine the flux of an observed point-source spectrum by

$$f_{\text{obs}} = C_{\text{obs}}/S \quad (1)$$

where  $f_{\text{obs}}$  is the calibrated spectrum,  $C_{\text{obs}}$  is the observed spectrum in counts  $\cdot \text{pixel}^{-1} \cdot \text{second}^{-1}$ , and  $S$  is the sensitivity as a function of wavelength. The sensitivity is derived by

$$S = C_{\text{std}}/f_{\text{std}} \quad (2)$$

where  $C_{\text{std}}$  is an observation of a spectrophotometric standard star in counts  $\cdot \text{pixel}^{-1} \cdot \text{second}^{-1}$ , and  $f_{\text{std}}$  is a calibrated spectrum of the same standard from some other source, or a model of the standard spectrum.

The " $\text{pixel}^{-1}$ " in the units for  $C$  refers to the cross-dispersion direction, and arises from the extraction of a point source spectrum on a two-dimensional detector using a fixed extraction height.

### 2. The Data Set

Observations of the pure hydrogen white dwarf GD 153 (Bohlin, Colina, & Finley 1995) are used to define the sensitivity curve, since these data are the only set of observations of a fundamental standard in all five low-resolution spectral modes. GD 153 is a preferred calibration standard, because the only lines are from H I and because Bohlin (1996) defined the FOS calibration with a set of four pure hydrogen WD models that includes GD 153. An input spectrum with many lines might produce a confusing sensitivity curve, if the model (or reference) line profiles do not perfectly match those of the observed spectrum.

## 2.1. Observations

All input spectra were obtained using the clear aperture # 38 ( $52'' \times 2''$ ).

Two averaged observations comprise the input spectrum for the far-UV MAMA mode G140L. Only one near-UV (G230L) observation of GD 153 was obtained through aperture # 38. For each of the three CCD modes (G230LB, G430L, and G750L), seven observations were averaged to produce high signal to noise spectra. The component spectra that make up the average spectrum for each mode are listed in Table 1.

Table 1. Observations

Rootname	Observation Date	Target	Optical Element	CRSPLIT	Total ExpTime (sec.)	Slit Number	Slit Size (")
O43J01QAM	09/07/97	GD153	G140L	0	60.0	38	52x2
O3ZX08HHM	13/07/97	GD153	G140L	0	187.0	38	52x2
O3ZX08HLM	13/07/97	GD153	G230L	0	187.1	38	52x2
O3TT42010	21/05/97	GD153	G230LB	2	600.0	38	52x2
O3TT43010	28/05/97	GD153	G230LB	2	600.0	38	52x2
O3TT44010	04/06/97	GD153	G230LB	2	600.0	38	52x2
O3TT45010	10/06/97	GD153	G230LB	2	600.0	38	52x2
O3TT46010	18/06/97	GD153	G230LB	2	600.0	38	52x2
O3TT47010	25/06/97	GD153	G230LB	2	600.0	38	52x2
O3TT48010	01/07/97	GD153	G230LB	2	600.0	38	52x2
O3TT42020	21/05/97	GD153	G430L	2	252.0	38	52x2
O3TT43020	28/05/97	GD153	G430L	2	252.0	38	52x2
O3TT44020	04/06/97	GD153	G430L	2	252.0	38	52x2
O3TT45020	10/06/97	GD153	G430L	2	252.0	38	52x2
O3TT46020	18/06/97	GD153	G430L	2	252.0	38	52x2
O3TT47020	25/06/97	GD153	G430L	2	252.0	38	52x2
O3TT48020	01/07/97	GD153	G430L	2	252.0	38	52x2
O3TT42040	21/05/97	GD153	G750L	2	3240.0	38	52x2
O3TT43040	28/05/97	GD153	G750L	2	3240.0	38	52x2
O3TT44040	04/06/97	GD153	G750L	2	3240.0	38	52x2
O3TT45040	10/06/97	GD153	G750L	2	3240.0	38	52x2
O3TT46040	18/06/97	GD153	G750L	2	2282.0	38	52x2
O3TT47040	25/06/97	GD153	G750L	2	2282.0	38	52x2
O3TT48040	01/07/97	GD153	G750L	2	2282.0	38	52x2

The spectral extraction heights for the component spectra are 11 pixels for G140L and G230L, and 7 pixels for G230LB, G430L, and G750L (Leitherer & Bohlin 1997).

Each of the seven component G750L spectra was fringe-corrected at long wavelengths using a library tungsten lamp flat before averaging them together. For this data set, all tungsten lamp flats used were obtained through slit # 35 ( $52'' \times 0.1''$ ). Briefly, the library flats are generated by (Plait, 1997)

- removing the lamp spectrum from the flat,
- removing scattered light (as determined by profiles obtained along the fiducial bars in the dispersion direction),

Profiles of the data and library flat are cross-correlated to ensure that the fringes in both are in phase. If the fringes are not in phase, the library flat is shifted (typically less than 1 pixel) to match the phase of the fringes in the data. The shifted library flat is then applied to the data image.

## 2.2. Reference Spectrum

The reference spectrum, GD153.MOD.002, is a pure hydrogen white dwarf model normalized to Landolt's visual photometry (Bohlin 1996). The spectrum was obtained from the



Calibration Data Base System (CDBS) at [http://www.stsci.edu/ftp/instrument/news/Observatory/astronomical\\_catalogs.html](http://www.stsci.edu/ftp/instrument/news/Observatory/astronomical_catalogs.html).

### 3. Data Reduction

For each optical mode, the reference spectrum is integrated to match the resolution of each co-added observation, then divided into the observed spectrum, yielding a sensitivity curve in units of

$$\frac{\text{counts} \cdot \text{pixel}^{-1} \cdot \text{second}^{-1}}{\text{ergs} \cdot \text{second}^{-1} \cdot \text{cm}^{-2} \cdot \text{\AA}^{-1}}$$

A spline fit with evenly spaced nodes is performed to each raw curve in order to obtain a smooth sensitivity curve. Each fit is refined by interactively selecting more nodes in regions where a curve varies greatly with small changes in wavelength. Table 2 lists the number of nodes used within the nominal wavelength range for each mode. The wavelength region 1200Å - 1225Å in mode G140L is masked to exclude the strong Ly $\alpha$  feature from the fit. Small residuals at the Balmer lines on G430L and G750L are caused by slight differences in resolution between STIS and the model spectrum.

Some of the sensitivity curve spline fits are extrapolated at either end by at most 20 pixels to account for future planned spectral format, or MSM, shifts. No extrapolation is done past very low signal-to-noise regions. Some curves are cut off in low signal-to-noise regions. Table 2 lists the extrapolated and cropped regions for each mode.

Table 2. Sensitivity Curve Extrapolation Regions

Optical Element	Spline Nodes	Nominal Range(Å)	Short- $\lambda$ Extrap.(Å)	Long- $\lambda$ Extrap.(Å)	Short- $\lambda$ Cutoff (Å)	Full Range (Å)
G140L	26	1118 - 1713	no extrap.	1713 - 1724	1140Å	1140 - 1724
G230L	28	1563 - 3140	no extrap.	3140 - 3171	1600Å	1600 - 3171
G230LB	28	1664 - 3066	1650 - 1664	3066 - 3093	-	1650 - 3093
G430L	40	2885 - 5691	2881 - 2884	5691 - 5746	-	2881 - 5746
G750L	42	5235 - 10229	no extrap.	10229 - 10327	-	5235 - 10327

## 4. Results

The sensitivity curves and their residuals are shown in Figures 1-5. The spline fit and extrapolations described above are represented by the dashed line in each plot. The spline nodes are plotted with diamonds.

### 4.1. Error Analysis

The residuals shown in Figures 1-5 are determined by dividing each curve by its spline fit, and are plotted for the wavelength ranges listed in Table 3. Table 3 lists the percent root-mean-squared residuals averaged over all wavelengths for each mode. Average RMS residuals are listed for three wavelength ranges for mode G750L to show how the scatter increases in the long wavelength region subject to fringing.

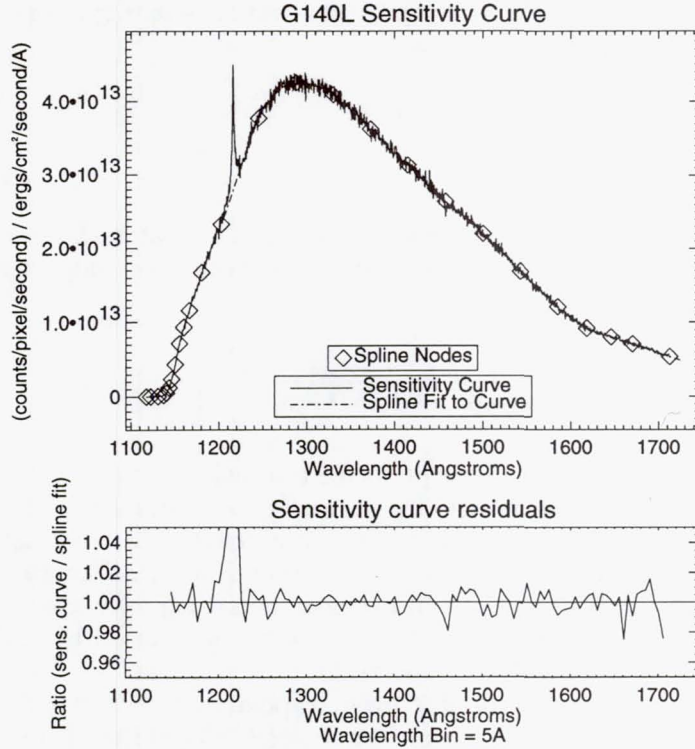


Figure 1. Sensitivity curve for optical element G140L, derived from 2 averaged observations of GD 153.

Table 3. Average Percent RMS Deviation for Each Mode

Optical Element	Wavelength Range(Å)	Avg. $\% \sigma_{rms}$
G140L <sup>a</sup>	1140-1200 and 1225-1713	1.35
G230L	1600 - 3140	1.35
G230LB	1664 - 3066	0.47
G430L	2885 - 5691	0.94
G750L	5235 - 8000	0.57
G750L	8000 - 9000	0.86
G750L	9000 - 10229	1.95

<sup>a</sup>Residuals in the region of the strong Ly $\alpha$  feature (1220-1225Å) are not included in the computation of  $\sigma_{rms}$ .

There is currently no flat field for the G140L mode, which makes the derived sensitivity subject to larger uncertainty at non-standard positions on the detector. For the other modes, the uncertainty in the calibration for continuum fluxes is estimated at  $\sim 3\%$  from a  $\sim 2\%$  uncertainty in the model absolute flux (Bohlin, Colina and Finley 1995) and from the 1-2% photometric repeatability of STIS spectra, as long as the spectra hit the same position on the detector to approximately one pixel. Scattered light from the instrumental PSF fills in the line profile at Lyman-alpha by  $\sim 10\%$  of the continuum level in comparison to the model line profile, as confirmed by FOS observations.

An estimation of the photometric uncertainty in the extrapolated regions is made by computing the average RMS residuals near the extrapolated region and is listed in Table 4. Column (1) lists the optical mode, column (2) lists the wavelength range near the



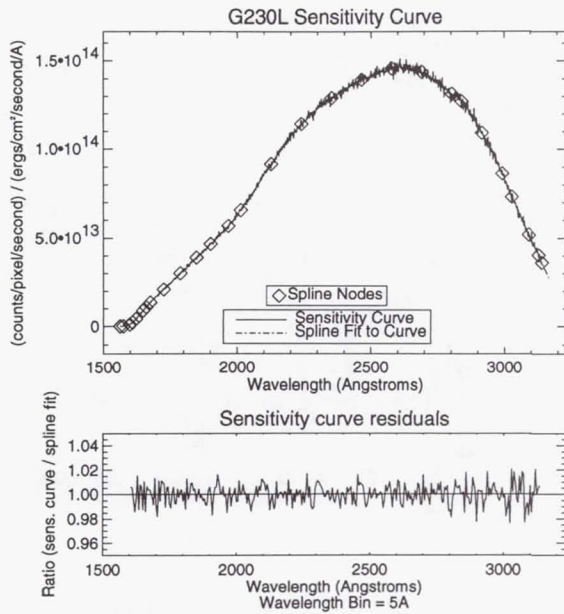


Figure 2. G230L Sensitivity Curve

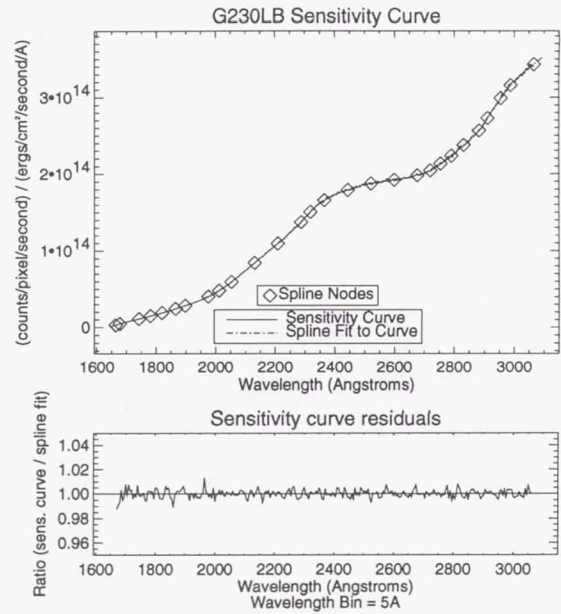


Figure 3. G230LB Sensitivity Curve

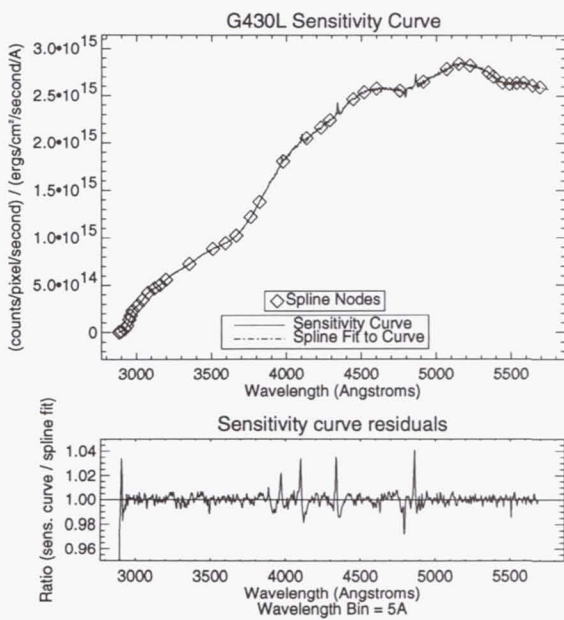


Figure 4. G430L Sensitivity Curve

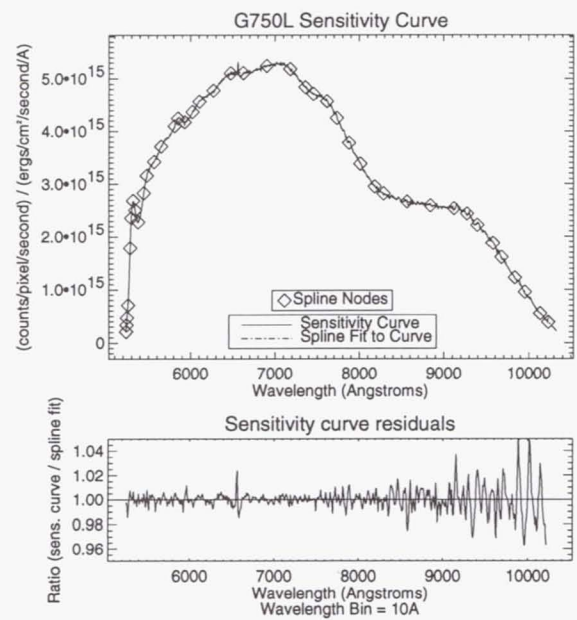


Figure 5. G750L Sensitivity Curve

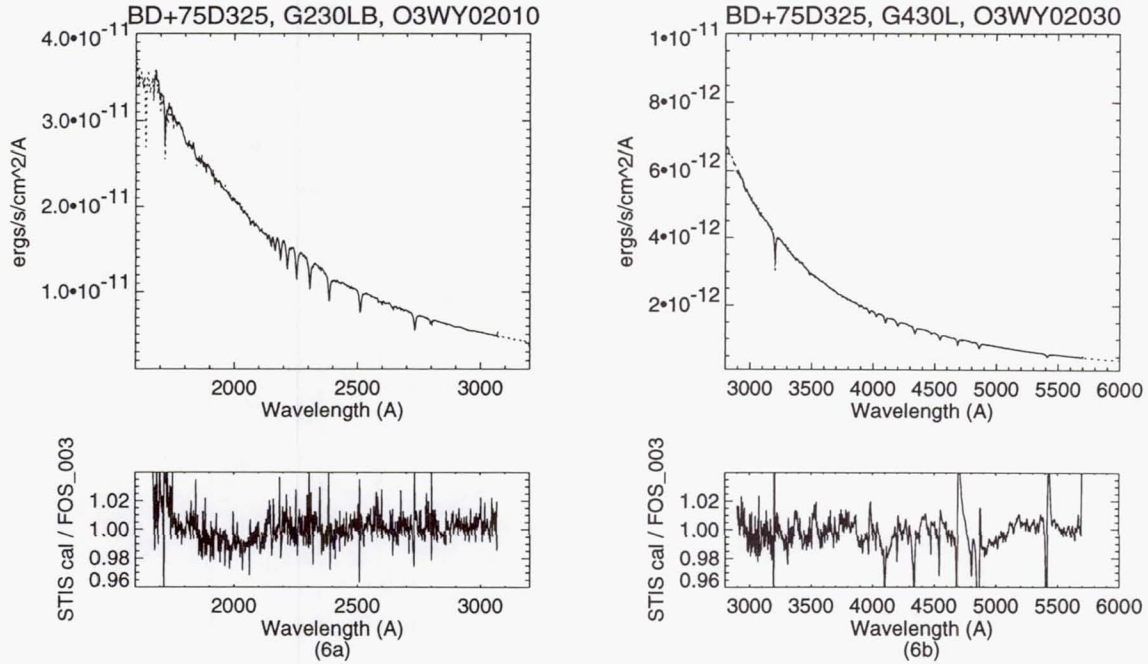


Figure 6. Sensitivity curves for G230LB (left panel) and G430L (right panel) applied to observations of BD+75D325. Top plot: calibrated STIS observation (solid line), and reference spectrum BD\_75D325\_FOS.003 (Bohlin 1996) (dotted line). Bottom plot: ratio of calibrated STIS spectrum to FOS spectrum.

extrapolation for that mode, and column (3) lists the average RMS percent uncertainty in that range.

Table 4. Estimated Average Percent RMS Deviation for Extrapolated Regions

Optical Element	Wavelength Range(Å)	Est. Avg. $\% \sigma_{rms}$
G140L	1700 - 1713	2.30
G230L	3110 - 3140	2.20
G230LB	1664 - 1678	0.85
G230LB	3033 - 3066	0.49
G430L	2884 - 2890	4.30
G430L	5640 - 5690	0.37
G750L	10100 - 10200	1.97

#### 4.2. A Test Case: Application of the Sensitivity Curves to Observations of BD+75D325

The left and right panels of Figure show STIS observations of BD+75D325 calibrated with the sensitivity curves described in this paper and plotted over an FOS spectrum (Bohlin 1996) of the same star. The FOS spectrum, BD+75D325, is obtained from the CDBS at the URL listed in section 2.2. The residuals plotted in the figures are the ratio of the calibrated STIS observation (integrated to the wavelength scale of the FOS spectrum) to the FOS spectrum. Average percent RMS uncertainties are 1.33% and 1.52% for G230LB and G430L, respectively. These values are consistent with the combined uncertainties of



the STIS calibration (see Table 3) and of the photometric accuracy of the FOS spectrum (1-2%) (Bohlin 1996).

**Acknowledgments.** We wish to thank Don Lindler and Phil Plait for essential data reduction advice.

## References

Bohlin, R. C. 1996, AJ, 111, 1743

Bohlin, R. C., Colina, L., & Finley, D. S. 1995, AJ, 110, 1316.

Leitherer, C. & Bohlin, R., 1997, Instrument Science Report STIS 97-13 (Baltimore:STScI)

Plait, P. 1997, this volume

## Simulations of the STIS CCD Clear Imaging Mode PSF

R.H. Cornett

*Hughes STX, Code 681, NASA/GSFC, Greenbelt MD 20771*

A. Gruszczak

*Hughes Danbury Optical Systems, Danbury, CT*

C. Ftacclas

*Michigan Technological Univ., Physics Dept., 1400 Townsend Dr., Houghton, MI 49931-1295*

S.R. Heap and B.E. Woodgate

*Laboratory for Astronomy and Solar Physics, Code 681, NASA/GSFC, Greenbelt MD 20771*

### Abstract.

Detailed understanding of the properties of the point-spread function (PSF) of STIS imaging modes is necessary to separate real effects of geometrically complex astronomical sources, such as protoplanetary disks surrounding bright stars, from instrumental effects, such as scattering and diffraction. In order to investigate STIS imaging properties we have numerically simulated broadband stellar PSFs generated by STIS in CCD clear imaging mode, including the effects of the Lyot stop and the coronagraphic wedges. The input spectrum is a stellar model atmosphere of the appropriate spectral type, convolved with the pre-flight STIS CCD response function. The PSF modeler generates broadband PSFs by co-adding weighted monochromatic PSFs across the waveband.

## 1. Introduction

Several key STIS observation programs depend critically on the details of the STIS PSF. The STIS clear imaging PSF is influenced by the HST input PSF, including its scattering, phase errors, and other effects, as well as novel STIS instrumental features such as the complement of coronagraphic bars and the Lyot stop. We have begun a program to numerically simulate the broadband stellar PSFs generated by STIS in CCD clear imaging mode (3.6), including the effects of the Lyot stop and the coronagraphic wedges.

The purpose of this paper is twofold: a) to describe the characteristics and operation of the STIS coronagraph bars and Lyot stops, which may not be well known or understood; and b) to describe a program of modeling STIS performance using these instrumental features, its results to date, and future plans.

## 2. The STIS Clear CCD Imaging Mode

The clear CCD imaging mode light path leaves the STIS corrector optics to pass through the coronagraphic aperture mask, located at the first STIS focal plane on the slit wheel.



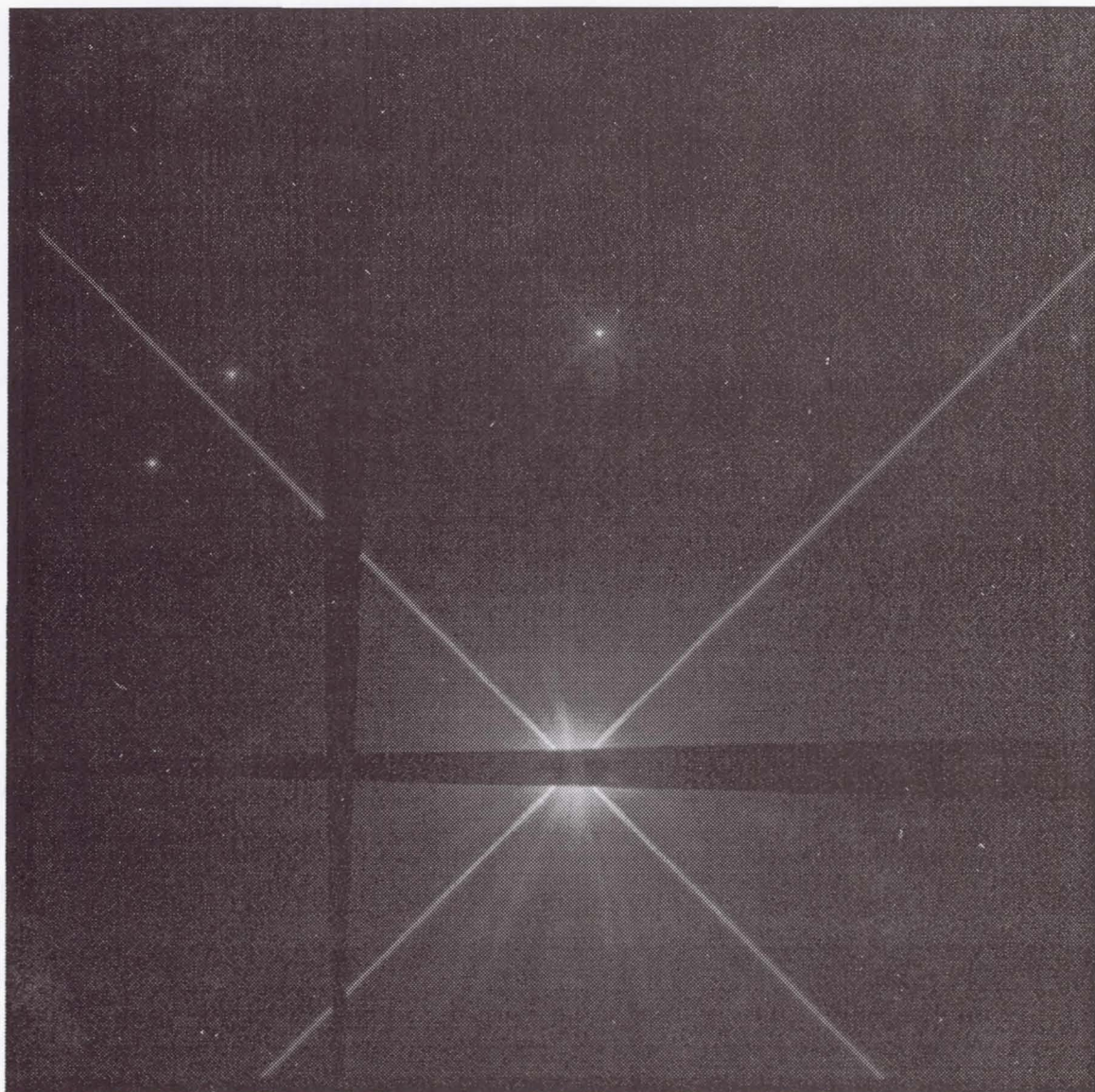


Figure 1. A clear-CCD-mode image of the HST standard star HD60753 positioned to intercept a coronagraph bar, from SMOV program 7088. The square field is 50 arcsec across; the large rectangular bar is 3 arcsec by 10 arcsec; the tapered bars are from 0.5 arcsec to 3 arcsec in width (1.8 arcsec at HD60753's location); and the crooked bar is 0.5 arcsec wide. The exposure duration is 1800 sec.



Subsequently, it encounters the fixed ellipsoidal collimator, a camera flat mirror located on the grating wheel at the second pupil plane, the Lyot stop aperture (which is fixed a few millimeters from the camera flat mirror), a folding flat, the ellipsoidal camera mirror, and the CCD detector. Figure 1 shows the CCD image plane with the coronagraphic aperture mask.

### 3. The STIS PSF Modeler Software (SPM)

The SPM software (Ftaclas *et al.* 1994) simulates PSFs for STIS in the clear CCD camera mode. As currently configured, it can produce broadband PSFs for any stellar input spectrum (represented by model atmospheres), and it can simulate PSFs with varying amounts of focus error due to changes in the Optical Telescope Assembly (OTA) secondary mirror.

SPM uses a diffractive propagator to simulate the propagation of light through the STIS camera. STIS has a focal plane mask which includes the coronagraphic occulting bars at the first focal plane, and a Lyot stop approximately at the second pupil plane. The model can represent a PSF placed at any location in the focal plane, and the Lyot stop may be adjusted in size or removed altogether. The basic logic of the SPM diffractive propagator module is as follows.

SPM first determines overall weights for each wavelength by multiplying the stellar spectrum by the CCD response function. Then, for each wavelength in the PSF being constructed:

- User-specified phase errors are applied to the OTA pupil
- Light is propagated to the first focal plane where the wavelength-appropriate focal plane mask (the coronagraphic wedge set) is applied
- Light is propagated to the second focal plane, where the PSF is computed
- The monochromatic PSF is normalized

Monochromatic PSFs are then co-added to form a broadband PSF, which is output as an image in FITS format.

A comparison of an SPM output PSF and an observed STIS PSF is shown in Figure 2.

### 4. Lyot Stops and Coronagraphic Images

Coronagraphs employ a baffle in a focal plane to block light from a central bright source (*e.g.* a star), to permit study of fainter nearby objects (*e.g.* a protoplanetary disk). "Error" light in the wings of the stellar PSF, caused by diffraction of central-source light from the edges of the telescope aperture or spider, or, in the case of HST, light with phase errors from the sagged edges of the primary mirror, may still dominate in that part of the image. A Lyot stop is a baffle in a pupil plane shaped to block light from the dominant error sources. In the case of STIS, the Lyot stop is not precisely at a pupil, so an approximate shape was chosen—a circular aperture—which eliminates most diffracted light from the aperture edge as well as light having phase errors caused by mirror sag. In the STIS instrument, the Lyot stop (a circular opening in a baffle mounted a few millimeters above the camera flat mirror) is always in place in clear CCD imaging mode. The model will permit "removing" the Lyot stop to test its effects, although we have not yet modeled the relevant situation in which phase errors, simulating primary mirror sag, are input at the OTA pupil.



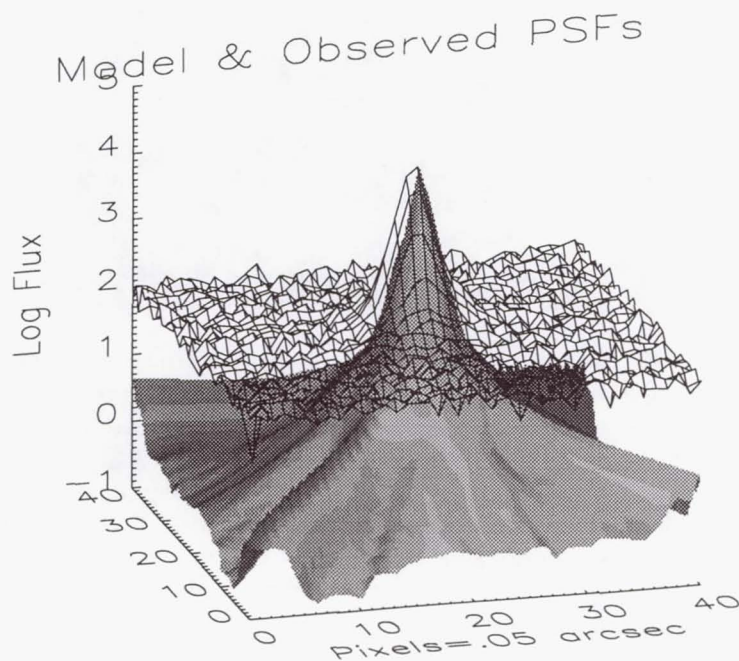


Figure 2. SPM model output (shaded surface) for a star represented by a Kurucz (1992) model atmosphere with  $T_{eff}=10,000$  K located at the center of the STIS image plane, well away from coronagraph bars, superimposed on (wire-grid surface) a subarray of an observed image of the DA1 white dwarf GD153, from SMOV program 7070, for similar conditions. The PSFs have been normalized to the same peak height; the displayed image area is 2.0 arcsec square, the model's current capability. A "floor" of about .3% of the peak height has been added to the observed image to remove negative values. The measured FWHM of the model PSF is 1.26 pixels (.063 arcsec) in both x and y, while for the observed PSF the values are 2.01 pixels (.100 arcsec) and 1.65 pixels (.082 arcsec) in x and y respectively. The difference is due to misalignments, image motion, and scattering from unmodeled sources such as the detector (which depends strongly on wavelength) and background.

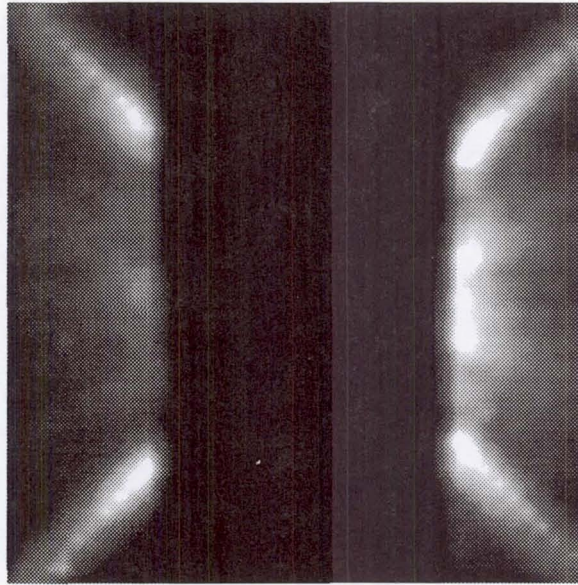


Figure 3. **The Model and Real Coronagraphic Images:** A comparison of a coronagraphic image (above) of the DA1 white dwarf GD153 from SMOV program 7070 with results of a model calculation (Figure 4, below), over the model's current field size of 2 arcsec square. In the model calculation, the star's position has been moved off the center of the bar to give the same net flux asymmetry as the observed image. The two images are normalized to the same total flux and displayed with the same grayscale. The model evidently reproduces major features well, although the effects of scattering and noise sources which are not simulated by the model are manifested in higher peaks and lower background. The model confirms the instrumental origin of several faint radial "rays" which have the potential to be confused with observed objects (*cf* Figure 1). The "beaded" appearance is due to numerical effects of image resampling.

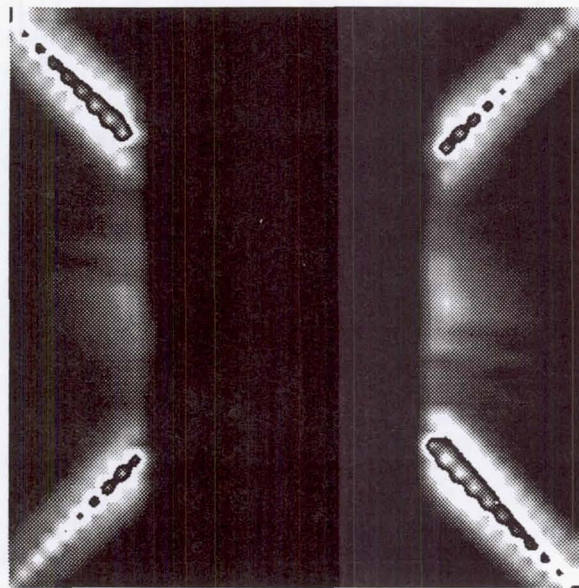


Figure 4.



## 5. Future Work

As described above, the STIS Lyot stop is designed to remove error-dominated light from the sagged outer part of the OTA mirror, as well as light diffracted from the OTA outer boundary. The model permits introducing appropriate phase errors on an OTA phase map; we have acquired the OTA phase map as defined by the WFPC2 team, and will introduce that map as input. These data will permit much more realistic modeling of the Lyot stop performance.

The model is currently limited by the relatively small size (2 arcsec square) of the modeled PSF image, initially held to this size because of computational restrictions. To better simulate observations we will increase the output PSF size to better define "rays" such as those seen in Figure 1, and which must be distinguished from real image features for many scientific programs.

## References

- Ftaclas, C., Nonnenmacher, A. L., Gruszczak, A., Terrile, R. J., & Pravdo, S.H. 1994, Proc. SPIE Vol. 2198, p. 1324-1335, *Instrumentation in Astronomy VIII*, David L. Crawford; Eric R. Craine; Eds.
- Kimble, et al. 1997, ApJ(submitted).
- Kurucz, R.L. 1992, in *The Stellar Populations of Galaxies*, ed. B. Barbuy & A. Renzini (Dordrecht: Kluwer), 225.

## A Test of the STIS CCD Flatfielding Accuracy on Small Scales

H. Ferguson

*Space Telescope Science Institute, 3700 San Martin Drive, Baltimore, MD 21218*

**Abstract.** This is a preliminary report on the reliability of STIS CCD flatfielding on small scales. The STIS CCD flat-field images are constructed from internal calibration lamp observations. As the calibration subsystem does not have the same focal ratio as the input path from the sky, shadows from dust particles on the detector face plate may not be corrected perfectly by the internal calibration. To test the repeatability of stellar photometry in the presence of these flatfield variations, observations of the core of the globular cluster 47 Tuc were made with the telescope offset repeatedly by small amounts between exposures. Preliminary results indicate that photometry is repeatable to better than 1%.

### 1. Introduction

With high throughput, good spatial resolution, and minimal charge-transfer effects, the STIS CCD may find use in many imaging programs. One of the factors that influences the achievable photometric accuracy is the quality of the flat fields, and the ability of calibrations carried out with the internal tungsten lamp to reproduce the detector response to external point sources.

The major small scale features in the STIS CCD flats are shadows of dust particles on the detector face plate (fig. 1). The most pronounced of these "dust motes" shows a 20% change in response from the center to the edge of the feature. Because the focal ratio of the calibration subsystem is different from that of the incoming beam from the telescope, it is unlikely that these features will be removed perfectly by the current pipeline flats.

### 2. Observations and Data Reduction

To test the quality of photometry with the current flats, and to provide data for testing various proposed improvements to the calibration (e.g. sky flats or modeling of the dust motes), observations were made of the center of the globular cluster 47 Tuc. Multiple images were taken with the telescope displaced in successive fine steps (0.02 arcsec in X and Y). The exposure times at each position were 3 seconds, and the exposures were CR-SPLIT to avoid contamination by cosmic rays. The proposal ID was 7641.

The 50CCD (clear aperture) data were calibrated using *calstis*, with the current (prelaunch) pipeline flats and the standard cosmic-ray rejection procedure. An example of a single reduced image is shown in fig. 2. A set of 376 stars brighter than magnitude AB  $\sim$  19 and more than 50 pixels from the edge of the detector were identified using *daofind*, and their magnitudes were measured in a 3 pixel radius aperture in each of 18 individual frames using *daophot.phot*. Centroiding and background subtraction were done separately for each star in each frame.



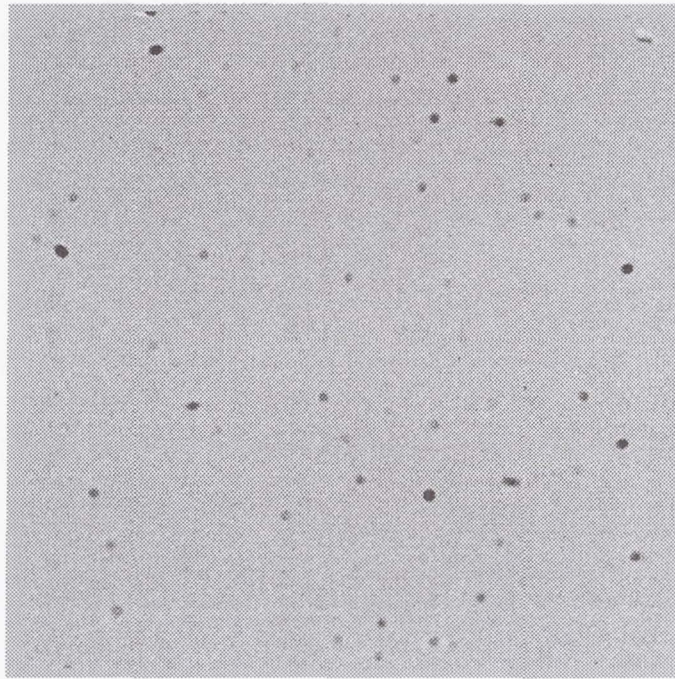


Figure 1. STIS 50CCD pipeline flat. This image was constructed from pre-flight measurements with the internal Tungsten calibration lamp. The circular features (dust motes) are caused by particles on the detector faceplate.

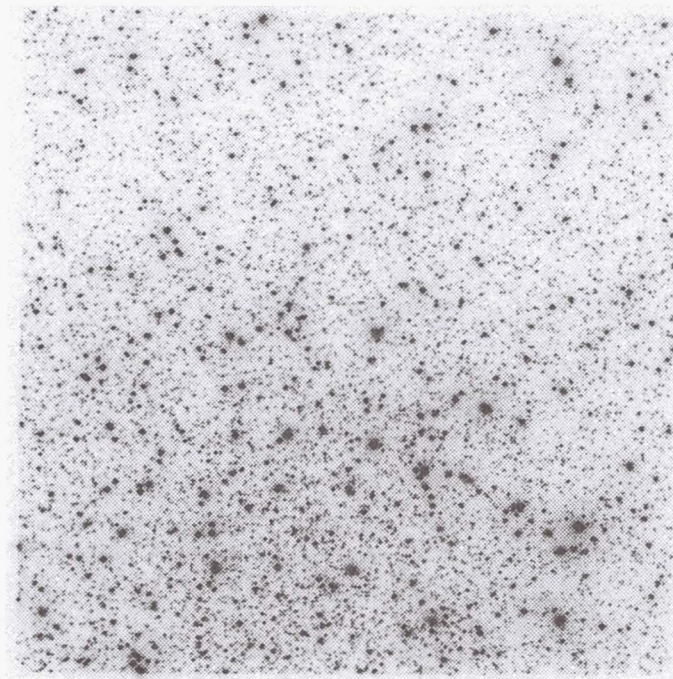


Figure 2. STIS 50CCD 3-second exposure of the center of 47 Tuc.

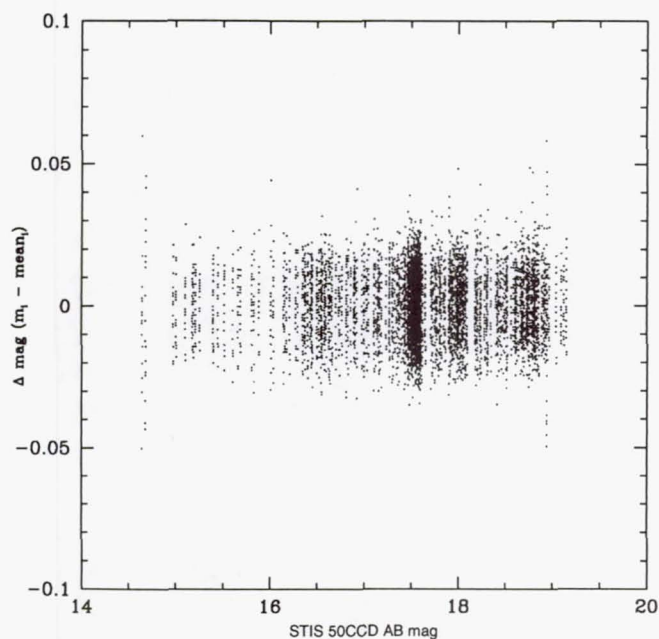


Figure 3. Photometric repeatability. The abscissa is the mean magnitude from the 18 measurements for each star. The ordinate is the difference between the individual measurements and the mean.

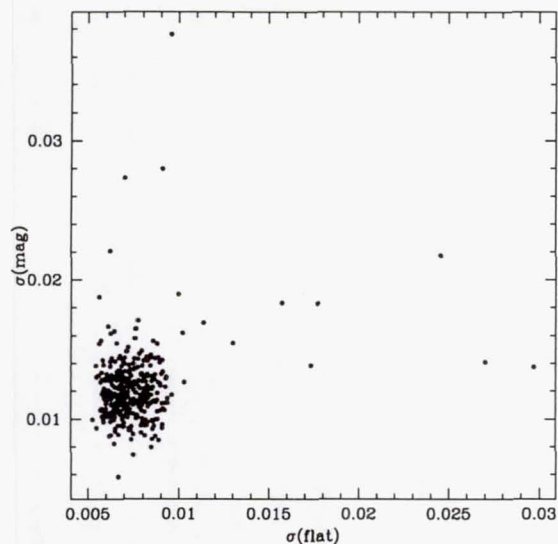


Figure 4. Photometric repeatability vs. stability of the flat. The abscissa shows the standard deviation of the pipeline flat for measurements in 0.2 arcsec radius apertures centered at the 18 positions of each star. The ordinate shows the standard deviation of the stellar magnitude measurements. The lack of a pronounced trend indicates that on average stars crossing pronounced features in the flat have similar photometric errors to those crossing smoother portions of the detector response.



### 3. Analysis

From pure counting statistics, we expect the standard deviation of the measured magnitudes to vary from 0.011 mag at  $AB = 19$  to 0.003 mag at  $AB = 16$ . Figure 3 shows, for each of the  $18 \times 376$  measurements, the difference between the star magnitude in each frame, and the mean magnitude of that star over all 18 frames. The standard deviation is less than 0.009 mag for all the images, and is typically  $\sim 0.007$  mag. Small ( $< 0.02$  mag) systematic shifts in zeropoint are seen in between frames, presumably due to telescope "breathing" which induces slow changes in the PSF with time.

To test whether features in the flat are influencing the photometry, the mean value of the flat in 2-pixel radius apertures was measured for each of the positions of the stars in the various images. For each star, we can then compute the standard deviation of the measured magnitude  $\sigma(mag)$  and the standard deviation of the flat  $\sigma(flat)$  over the range of positions sampled by the star. If uncertainties in the flat are dominating the photometric errors, one might expect to see the largest photometric errors where the flat showed the largest variation. Fig. 4 shows almost no correlation. Nevertheless, inspection of a few of the cases with the largest photometric residuals do show small (1-2 pixel) features in the flat that are the likely culprit. These are not dust motes, but probably something intrinsic to the detector such as charge traps.

### 4. Summary

The accuracy of the current STIS pipeline flats appears to be very good on scales of less than 4 arcsec. Inaccuracies in the flat induce rms photometric errors less (possibly substantially less) than 0.009 mag. Hence for point source photometry, photometric precision is likely to be governed by factors other than the accuracy of the flat, such as (1) changes in telescope and STIS focus with time (2) background subtraction in cases where there is a space or time-dependent background, and (3) corrections for overlapping PSFs in crowded fields.

## The STIS Parallel Survey: Introduction and First Results.

Jonathan P. Gardner<sup>1,7</sup>, Robert S. Hill<sup>1,2</sup>, Stefi A. Baum<sup>3</sup>, Nicholas R. Collins<sup>1,2</sup>, Henry C. Ferguson<sup>3</sup>, Robert A. E. Fosbury<sup>4</sup>, Ronald L. Gilliland<sup>3</sup>, Richard F. Green<sup>5</sup>, Theodore R. Gull<sup>1</sup>, Sara R. Heap<sup>1</sup>, Don J. Lindler<sup>1,6</sup>, Eliot M. Malumuth<sup>1,2</sup>, Alberto Micol<sup>4</sup>, Norbert Pirzkal<sup>4</sup>, Jennifer L. Sandoval<sup>1,6</sup>, Eline Tolstoy<sup>4</sup>, Jeremy R. Walsh<sup>4</sup>, Bruce E. Woodgate<sup>1</sup>

### Abstract.

The installation of the Space Telescope Imaging Spectrograph (STIS) on the Hubble Space Telescope (HST) allows for the first time two-dimensional optical and ultraviolet slitless spectroscopy of faint objects from space. The STIS Parallel Survey (SPS) routinely obtains broad band images and slitless spectra of random fields in parallel with HST observations using other instruments. The SPS is designed to study a wide variety of astrophysical phenomena, including the rate of star formation in galaxies at intermediate to high redshift through the detection of emission-line galaxies. We present the first results of the SPS, which demonstrate the capability of STIS slitless spectroscopy to detect and identify high-redshift galaxies.

### 1. Introduction

The low sky background seen by the Hubble Space Telescope (HST), and the two-dimensional capability of the Space Telescope Imaging Spectrograph (Kimble et al. 1997) enables a survey of faint spectroscopically selected objects for the first time. The STIS Parallel Survey (SPS) uses slitless spectroscopy of random fields to identify and study objects selected by their spectroscopic properties. STIS slitless spectra provide unprecedented sensitivity in the range  $7000 < \lambda < 10000 \text{ \AA}$ , where ground based spectroscopy is difficult due to the variability of the night-sky lines. SPS observations include, as a fiducial for the spectra, unfiltered images of each field, utilizing between 1/6 and 1/4 of the exposure time. The goals of the SPS include studying the evolution of the star formation rate with redshift as measured by emission-line strengths, the evolution of the luminosity function of galaxies, the size and morphological evolution of galaxies with redshift, the study of active galactic nuclei (AGN), weak gravitational lensing, stellar luminosity functions in nearby galaxies, low-mass stars and Kuiper Belt objects. The images will be used to construct magnitude-limited samples and to identify the morphological types of the galaxies in the spectroscopically selected

---

<sup>1</sup>Laboratory for Astronomy and Solar Physics, Code 681, Goddard Space Flight Center, Greenbelt MD 20771

<sup>2</sup>Hughes STX Corp., Lanham MD 20706

<sup>3</sup>Space Telescope Science Institute, 3700 San Martin Drive, Baltimore MD 21218

<sup>4</sup>Space Telescope-European Coordinating Facility, Karl Schwarzschild Str. 2, D-85748, Garching bei München, Germany

<sup>5</sup>National Optical Astronomy Observatories, P.O. Box 26732, Tucson AZ 85726

<sup>6</sup>Advanced Computer Concepts, Inc., 11518 Gainsborough Road, Potomac MD 20854

<sup>7</sup>NOAO Research Associate



samples. SPS data are also a valuable source of calibration information for the STIS CCD detector.

The SPS is being conducted as a service to the astronomical community by the Space Telescope Science Institute (STScI), and the data are made available immediately through the archive. Further information is available on the world wide web at the STIS Investigation Definition Team (IDT) parallel page,

<http://hires.gsfc.nasa.gov/stis/parallels/parallels.html>,

which has links to the STScI parallel page, and the Space Telescope – European Coordinating Facility parallel page. In this paper we describe the survey data, demonstrate the capabilities of random-field slitless spectroscopy with STIS, and show results from some of the first fields to be observed, with an emphasis on star formation at high redshift.

The observational study of galaxy evolution is the study of star formation as a function of lookback time. Determining the star-formation history of the universe, its variation with galaxy morphological type, and its relationship to spectral type and color, places strong constraints on theoretical models. Ground-based imaging and redshift surveys, in combination with the HST Medium Deep Survey key project (MDS; Griffiths et al. 1994), and the Hubble Deep Field (HDF; Williams et al. 1996), have built up a consistent picture of evolution in which the population of early-type galaxies have undergone little star-formation at redshift  $z < 1$  (Lilly et al. 1995), while a population of morphologically complex and active star-forming galaxies were numerous at  $z \sim 0.4$  (Cowie, Songaila & Hu 1991; Glazebrook et al. 1995; Driver, Windhorst & Griffiths 1995), but have disappeared by the present epoch. Star-forming galaxies has recently been discovered at  $z > 3$  (Steidel et al. 1996), but the relatively small number of “UV-dropout” galaxies in the HDF indicates that the bulk of star formation takes place at  $z < 3$  (Madau et al. 1996). Although there is still considerable debate about this picture, it is clear that the poorly studied redshift range  $1 < z < 3$  is of considerable importance. SPS observations are sensitive to  $H\alpha$  emission at  $z < 0.5$ , [O III] emission at  $z < 1.0$ , [O II] emission at  $0.5 < z < 1.5$  and  $Ly\alpha$  emission at  $3.5 < z < 7.0$ .

## 2. The SPS Data

The STIS Parallel Survey began on 1997 June 2. The HST instruments are distributed around the focal plane of the Optical Telescope Assembly (OTA) and a primary instrument aperture is selected by offsetting the pointing of the OTA from the optical axis. The remaining instruments then view a random field in the sky between 5 and 8 arcminutes away from the primary object. Prior to the installation of STIS and the Near Infrared Camera and Multi-Object Spectrometer (NICMOS) during the second servicing mission in 1997 February, parallel observations were only scientifically useful when taken with the Wide Field and Planetary Camera 2 (WFPC2). The MDS, along with the Guaranteed Time Observer’s parallel survey, has used the WFPC2 in parallel to study many aspects of cosmology and stellar populations, obtaining data in about 600 orbits per year. Now, with three cameras capable of making parallel observations, and the greater flexibility provided by the installation of a higher storage capacity Solid State Recorder, the opportunity for random field surveys has increased by a factor of 6 or more.

“Scripted” parallel observations, in which the choice of exposure times, filters and spectroscopic modes depends on the galactic latitude or the available exposure time, will not be implemented for scheduling with STIS until late in 1997. The observations made to date have been in a “non-scripted” mode with two 150s images, and two 600s to 900s spectroscopic exposures per orbit, repeated for multiple orbit pointings. The images are taken in the 50CCD clear camera mode, and are sensitive to  $2200 < \lambda < 11000\text{\AA}$  wavelengths (see Baum et al. 1996). The spectral images use the G750L low resolution grating, with central wavelength  $8975\text{\AA}$ , and have spectra covering about  $4000\text{\AA}$  between  $5500$  and  $11490\text{\AA}$ , depending on the position of the objects on the field. The images are read out in a  $2 \times 2$



binned pixel mode while the spectra are binned by two pixels in the spatial direction only, resulting in  $0.1''$  pixels. SPS images taken after 1997 August, will be unbinned to make the data more suitable for weak lensing measurements, and other scientific programs. The central wavelength of the spectra will be changed to  $7751\text{\AA}$  to take greater advantage of the sensitivity of the CCD, which drops rapidly at wavelengths longer than  $10000\text{\AA}$ . At the time of writing, 7 weeks after the start of observations, 125 fields have been observed, with spectroscopic exposure times up to 16800s.

## 2.1. Data Reduction

The data reduction of SPS data has three main stages: (i) image reduction, including bias and dark subtraction, hot pixel correction and flat fielding; (ii) co-addition of images from multiple and dithered pointings; (iii) object detection and slitless spectrum extraction. We implement these procedures in the Interactive Data Language (IDL), except for the object detection, which is done using the SExtractor package (Bertin & Arnouts 1996).

If the prime observations are dithered, the parallel observations will also be dithered. Visits to the same prime target done at different times can result in offsets between parallel observations of the same field due to change in the roll angle of the spacecraft. The SPS data are put into groups within  $5''$  of each other ( $\sim 10\%$  of the size of the STIS CCD), and subgroups within  $0.025''$  of each other. The images in each subgroup are treated as co-pointed for the purpose of cosmic ray (CR) removal.

Cosmic rays (CRs) are removed using multiple exposures of the same fields. A one-dimensional bias is computed from the overscan portion of the detector and subtracted from the raw image. Two-dimensional bias and dark images are subtracted. Some pixels with high dark rates are not accounted for by the dark frame, since new "hot pixels" are continually generated by the CR flux on orbit, and periodically reduced by annealing. These pixels are tabulated weekly. The hot pixels corrected in the data reduction are the union of the latest list made before the given image and the earliest list made afterward. The correction is done by linear interpolation between neighboring pixels. The images are flat fielded using a median sky flat of the SPS images. Dithered data are co-registered, and the resulting images are co-added by a final step which rejects CRs and hot pixels using all the available data. The processing for slitless spectra is similar to what is described above, except that the dither offsets are computed from those found for the direct images, the spectra are not flat fielded, and a background determined by the median of each column is subtracted. No attempt is made to remove the fringing.

The program SExtractor (Bertin & Arnouts 1996) detects and separates sources on the processed images using a multi-thresholding algorithm. SExtractor subtracts a smoothed 2-dimensional background and convolves the image with a  $0.5'' \times 0.5''$  Gaussian filter before applying the initial detection threshold, which is  $0.7\sigma$  of the empirical sky noise. The program computes location, photometry, and shape parameters for each detected source.

Slitless spectra are extracted as rectangular sub-images, which are resampled using bilinear interpolation to remove geometric distortion. An array of pixel offsets characterizing the distortion is maintained as part of the local calibration database. The first axis of the spectrum image is wavelength, with the zero point and dispersion determined from the object's location in the camera mode image. The second axis is spatial position in the cross-dispersion direction, corrected for the orientation angle of the object. The rectified image is then summed in the cross-dispersion direction. In this paper we used unweighted summation over a simple rectangular extraction slit. However, a scheme for weighted, or "optimal," extraction has recently been implemented (Horne 1986). Optimal extraction increases the signal-to-noise ratio by weighting pixels by their contribution to the total signal, and helps in rejection of bad pixels.

Photometric calibration of the direct images was done independently by three of the authors (EMM, ET and JW) using STIS 50CCD observations of  $\omega$  Centauri and the white



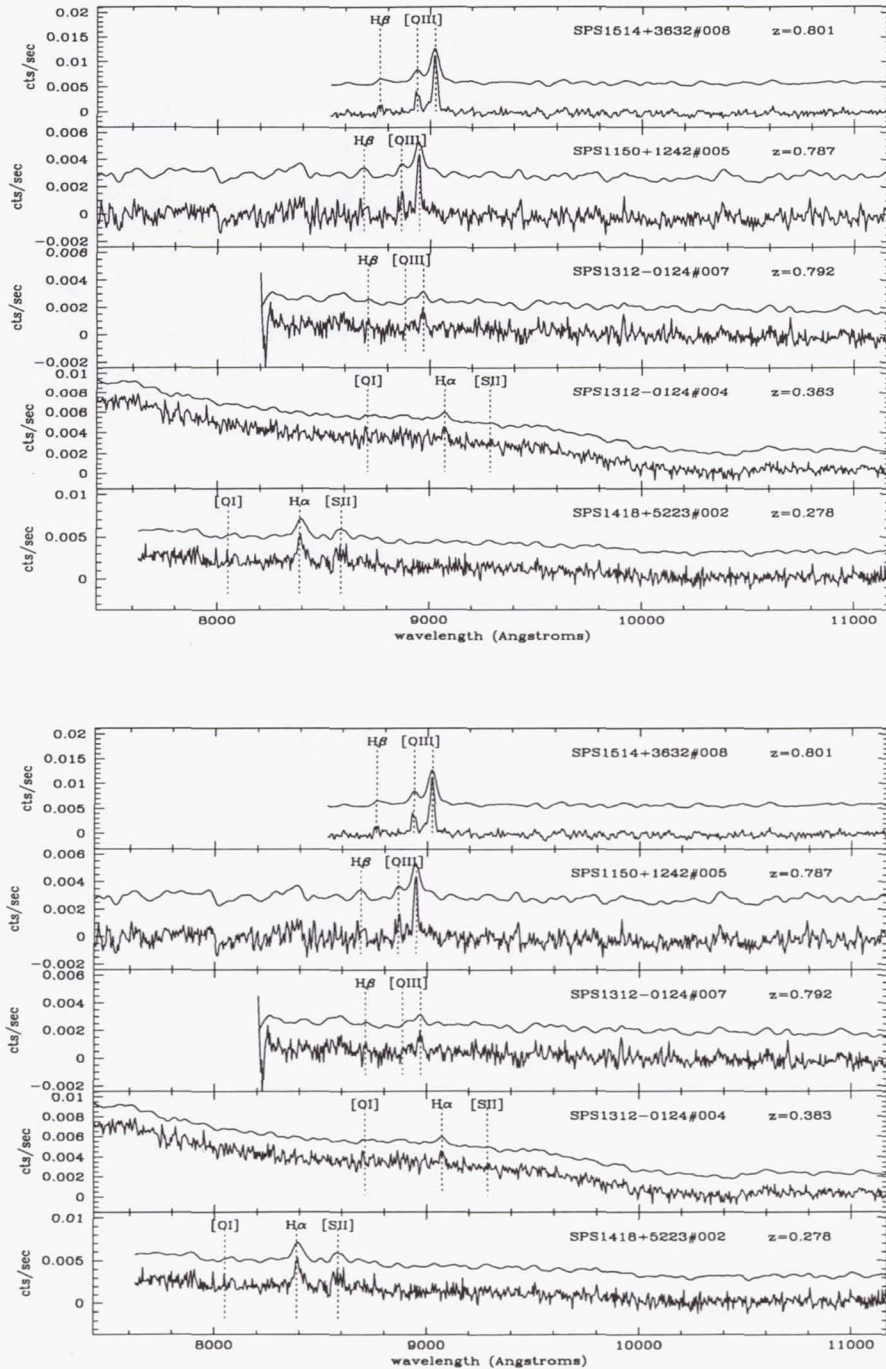


Figure 1. Extracted spectra of emission line objects. In each panel, the sky subtracted spectrum is shown, and a smoothed version of the data is offset and plotted. Lines are marked at their laboratory wavelengths at the redshift of the object.

Object	RA (2000)	Dec	ABmag	z	lines
SPS1418+5223#002	14:18:00.69	52:22:39.3	20.45	0.278	H $\alpha$ , [S II], [O I]
SPS1312-0124#004	13:11:45.60	-02:35:35.1	20.44	0.383	H $\alpha$ , [O I]
SPS1312-0124#007	13:11:46.32	-02:35:33.8	23.58	0.792	[O III], H $\beta$
SPS1150+1242#005	11:49:58.99	12:42:42.8	22.56	0.787	[O III], H $\beta$
SPS1514+3632#008	15:14:22.68	36:31:31.1	22.84	0.801	[O III], H $\beta$
SPS1514+3632#007	15:14:19.72	36:31:25.3	22.75	0.371	[O III], H $\beta$ , [O I]
SPS1550+2122b#004	15:49:35.26	21:21:54.7	22.84	0.486	[O III], H $\beta$ , [O II]
SPS1150+1242#007	11:49:58.41	12:41:55.7	22.75	0.130	H $\alpha$ , [S II], [O I]
SPS1550+2122a#008	15:49:36.15	21:21:45.4	23.61	0.573	[O III], H $\beta$ , [O II], H- $\delta$

Table 1. Emission line galaxies detected by the SPS

dwarf, GRW+70D5824. The field in  $\omega$  Centauri has been observed with WFPC2 by Holtzman et al. (1995) and from the ground by Harris et al. (1993), and the photometry was determined relative to those observations.

### 3. Discussion

A preliminary analysis of the SPS data has discovered 9 emission-line sources, ranging in redshift  $0.12 < z < 0.81$ . Figure 1 shows the spectra, with the strongest lines marked. For each object, the extracted spectrum is shown, and the spectrum smoothed with a Gaussian filter three pixels wide is shown offset upwards for clarity. Table 1 contains additional information about the detected emission line objects. These objects all show two or more emission lines; in addition the data contain several single emission-line objects which will require additional observations to confirm their redshifts. These objects could be at  $1 < z < 1.5$  if the single emission line is [O II] at rest wavelength 3727Å.

SPS1514+3632#008 is our strongest detection, and the spectrum is plotted at the top of Figure 1. The [O III] doublet is clearly seen at 9018Å and 8935Å, indicating a redshift of 0.801. The H $\beta$  line is also seen at the same redshift. As a demonstration of slitless spectroscopy with STIS, we show this field in Figure 2. At the top right is the image, with a total exposure of 2100 seconds, and a limiting detection magnitude ( $5\sigma$  in a 0.5 arcsecond aperture) of AB = 28.0 mag. The bottom of the figure is the slitless spectral image, with a total exposure time of 8400s. At the top left of the figure we show an expanded view of the spectral image in the region around the detected emission lines. The object could be part of an interacting pair, and both members of the pair are visible in the stronger [O III] line at 5007Å.

### 4. Summary

The STIS Parallel Survey is designed to address a wide variety of topics in astronomy, including the detection and study of emission line objects at redshift  $z \approx 1$ . The STIS provides unprecedented sensitivity in the wavelength range  $7000 < \lambda < 10000\text{Å}$  due to the low and constant sky background relative to observations made from the ground. In the first seven weeks of operation, the SPS has obtained images and slitless spectra of 125 fields. We have analyzed nine fields at high Galactic latitude with spectroscopic exposure times of 5400s or more. We find nine emission-line objects with  $0.12 < z < 0.81$ . While it is still too early for a statistical analysis of the data, it is clear that this survey will contribute to our understanding of star formation at one half the Hubble time.

We wish to acknowledge useful discussions with Ray Weymann, Thomas Erben, Mario Nonino, Michael Rosa and Benoit Pirenne, and support and help from the STIS Investi-



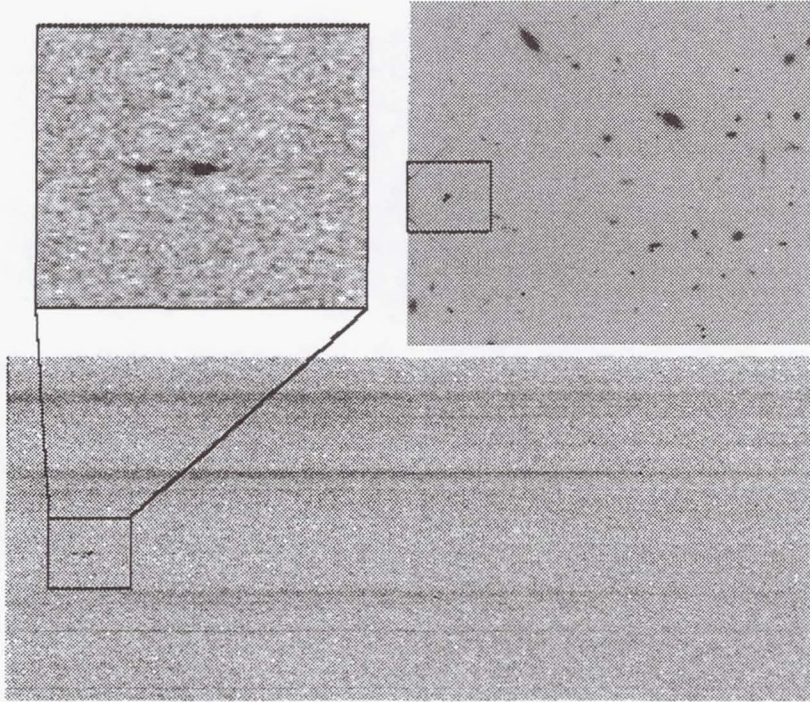


Figure 2. The camera mode image, the spectral mode image and an expanded region containing an emission line galaxy from SPS1514+3632. Two galaxies, possibly an interacting pair, are seen at  $z=0.801$ , and the [O III] doublet is clearly seen for the brighter object.

gation Definition Team. We thank Karl Glazebrook for providing redshift identification software.

## References

- Baum, S. et al. 1996, *STIS Instrument Handbook* Version 1.0, (Baltimore:STScI)  
 Bertin, E., & Arnouts, S. 1996, *A&AS*, 117, 393  
 Cole, S., et al. 1994, *MNRAS*, 271, 781  
 Cowie, L. L., Songaila, A., & Hu, E. M. 1991, *Nature*, 354, 460  
 Driver, S. P., Windhorst, R. A., & Griffiths, R. E. 1995, *ApJ*, 453, 48  
 Glazebrook, K., Ellis, R., Santiago, B., & Griffiths, R. 1995, *MNRAS*, 275, L19  
 Griffiths, R. E., et al. 1994, *ApJ*, 435, L19  
 Harris, H. C., Hunter, D. A., Baum, W. A., & Jones, J. H. 1993, *AJ*, 105, 1196  
 Holtzman, J. A. et al. 1995, *PASP*, 107, 156  
 Horne, K. 1986, *PASP*, 98, 609  
 Kimble, R. A., et al. 1998, *ApJ*, in press  
 Lilly, S. J., Tresse, L., Hammer, F., Crampton, D., & Le Fevre, O. 1995, *ApJ*, 455, 108  
 Madau, P., et al. 1996, *MNRAS*, 283, 1388  
 Steidel, C. C., et al. 1996, *ApJ*, 462, L17  
 Williams, R. E., et al. 1996, *AJ*, 112, 1335

## Fringe Correction for STIS Near-IR Long-Slit Spectra using Contemporaneous Tungsten Flat Fields

Paul Goudfrooij<sup>1</sup> and Stefi A. Baum

*Space Telescope Science Institute, 3700 San Martin Drive, Baltimore, MD 21218*

Jeremy R. Walsh

*Space Telescope – European Coordinating Facility, Karl-Schwarzschild-Strasse 2,  
D-85748 Garching bei München, Germany*

**Abstract.** We report on the accuracy of fringe removal for STIS long-slit near-IR spectra using contemporaneous flats (taken during the course of science data collection). In case of point sources, we use tungsten flats taken through a small slit to mimic illumination by a point source. In case of extended sources, we use long-slit spectra of Jupiter's moon Io as test cases. We find that in case of the G750L grating, fringe residuals can be reduced to below the 1% level, for both point sources and extended objects.

### 1. Introduction: Near-IR Fringing in CCD Spectra

Fringes in CCD observations arise from multiple reflections between the front and back surface of the CCD chip in case the distance between the surfaces is a small integer multiple of the wavelength of the incident monochromatic light from an external source. The small difference in path length gives rise to a series of bright and dark fringes. In effect the surfaces act as an interferometer. In the case of a CCD chip, the front and back surface are never exactly planar or parallel, which results in irregularly shaped fringes.

In the particular case of the STIS SiTE CCD, fringes are only appearing at the longer wavelengths ( $\lambda \geq 7000 \text{ \AA}$ ). If the light incident on any one resolution element is monochromatic (i.e., spectroscopy), the wavelength varies as a function of position along the dispersion direction. Therefore, the fringe pattern for any particular observing mode is a convolution of the contours of constant distance between the front and back surfaces and the wavelength of light incident on that particular part of the CCD. For medium-resolution data (i.e., the G750M grating), the wavelength changes slowly with position ( $\sim 0.5 \text{ \AA/pixel}$ ), so that the shape of the fringes is mostly dictated by the shape of the CCD, while for low-resolution data (G750L grating) the wavelength changes much more rapidly ( $\sim 5 \text{ \AA/pixel}$ ), so that the changing wavelength dictates the shape of the fringes.

Actual flat fields taken in dispersed light show peak-to-peak amplitudes growing to 25% and 32% at 9800  $\text{\AA}$  for the G750L and G750M gratings, respectively. Figs. 1 and 2 depict typical flat fields for the G750L and G750M gratings.

Rectification of the fringing pattern should be a tractable problem, because the behavior is entirely stable with time. However, small shifts in the wavelength mapping onto the detector, caused by grating wheel non-repeatability and thermal drifts on orbit, do cause the fringe pattern to shift from exposure to exposure. Therefore, for accurate fringe removal it is necessary to take contemporaneous spectral flats using the onboard tungsten lamps.

---

<sup>1</sup>Affiliated with the Astrophysics Division, Space Science Department, European Space Agency



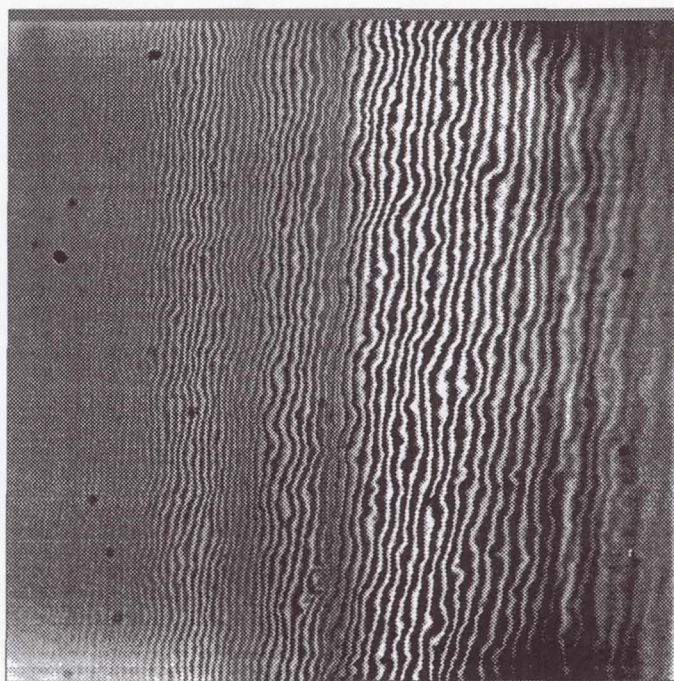


Figure 1. Grey-scale plot of normalized G750L flat field at a central wavelength of 8975 Å. Display cuts are  $\pm 10\%$ .

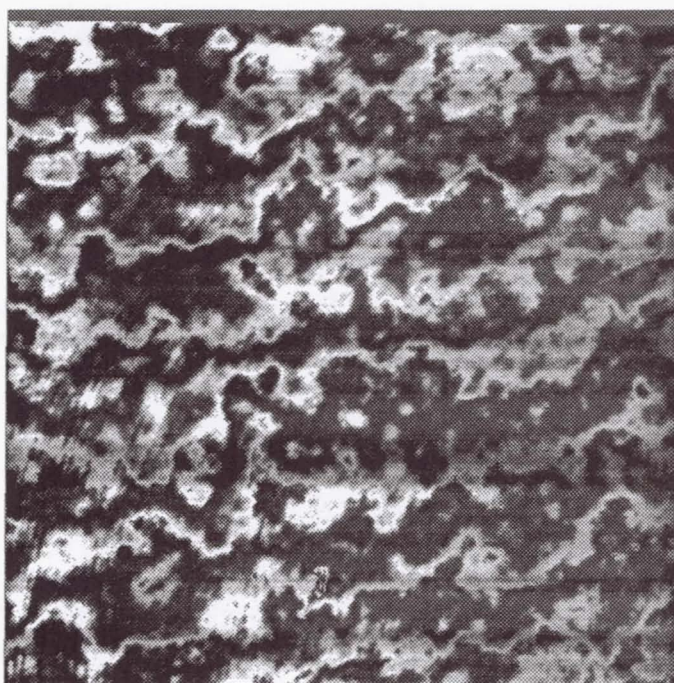


Figure 2. Grey-scale plot of normalized G750M flat field at a central wavelength of 9851 Å. Display cuts are  $\pm 20\%$ .



## 2. Fringe Correction for Extended Sources

To test the fringe correction for extended sources, we obtained long-slit spectra of Io (diameter is 1.15 arcsec) with the 52×0.2 slit and grating G750L (at 7751 Å) along with contemporaneous flats with the same set-up. Io was moved along the slit after each exposure, so that each set of data are corrected by different parts of the flat field. By sampling the intrinsically same region of Io from each individual exposure, any differences among the individual spectra must then be attributable to the flat field correction. We have then averaged the (three) different spectra together, after dividing by (i) no flat at all, (ii) the library (pre-flight) flat (which is used in the STIS pipeline reduction *calstis*), and (iii) the contemporaneous flat. The latter flat was produced by applying *calstis* without flatfield correction, and fitting a cubic spline through each line of the tungsten exposure using the *iraf.twodspec.longslit.response* routine.

Fig. 3 depicts the results of flatfielding the G750L spectra of Io using these three different methods. The residual RMS “noise” in channels 500 – 850 ( $\sim 7630 - 9340$  Å) is 0.9% using the contemporaneous flat, vs. 5.4% for the pre-flight flatfielded data.

## 3. Fringe Correction for Point Sources

Due to scattered light problems, flat field images taken with the standard long slit (52 arcsec long) do not mimic the illumination by a point source adequately without further reduction. One way to accomplish a correction for the influence of scattered light is to assume the amount of scattered light to be equal to the residual light under the fiducial occulting bars of the STIS spectrograph. After this correction for scattered light, long-slit flats are found to be able to reduce fringing to  $\sim 2-3\%$  (cf. Plait & Lindler 1997).

Another method of fringe correction for point sources is to use contemporaneous flats through a short slit which are typically used for echelle spectroscopy (i.e., the 0.2×0.06 or the 0.3×0.09 slit, depending upon which of the two is closer [in the dispersion direction] to the long-slit being used), which should mimic a point source much more accurately. To test the fringe correction for point sources, we used well-exposed spectra of the white dwarf GD 153 using the 52×2 slit and grating G750L (at 7751 Å), which is part of the regular CCD contamination/sensitivity monitor. An ACQ/PEAK peak-up was performed so that the star was very well centered in the slit. A pair of contemporaneous tungsten flats with the 0.3×0.09 slit was taken just before the star observation. Figs. 4 and 5 depict the G750L spectrum of GD 153 reduced with the pipeline (pre-flight) flat and with the contemporaneous flat, respectively. As mentioned above in Section 2, the contemporaneous flat was produced by applying *calstis* without flatfield correction, and fitting a cubic spline through each line of the tungsten exposure using the *response* routine. The residual RMS “noise” in channels 500 – 850 ( $\sim 7630 - 9340$  Å) is 0.95% using the contemporaneous flat, vs. 5.4% for the pre-flight flatfielded data.

## 4. Concluding Remarks

- Fringe removal from G750L spectra can be greatly improved using contemporaneous flat fields. Fringe residuals are approximately 1% in the cases analyzed so far. In the case of G750M spectra (not shown), the improvement is also clear but less dramatic, as expected since the fringing is mostly due to the shape of the CCD chip in that case.
- An STSDAS task for fringe removal using contemporaneous flats for STIS long-slit spectra will be implemented in the near future.
- As of the time of writing, the RPS2 interface for specifying contemporaneous flats is still under development, so they must be inserted by hand into the proposal during



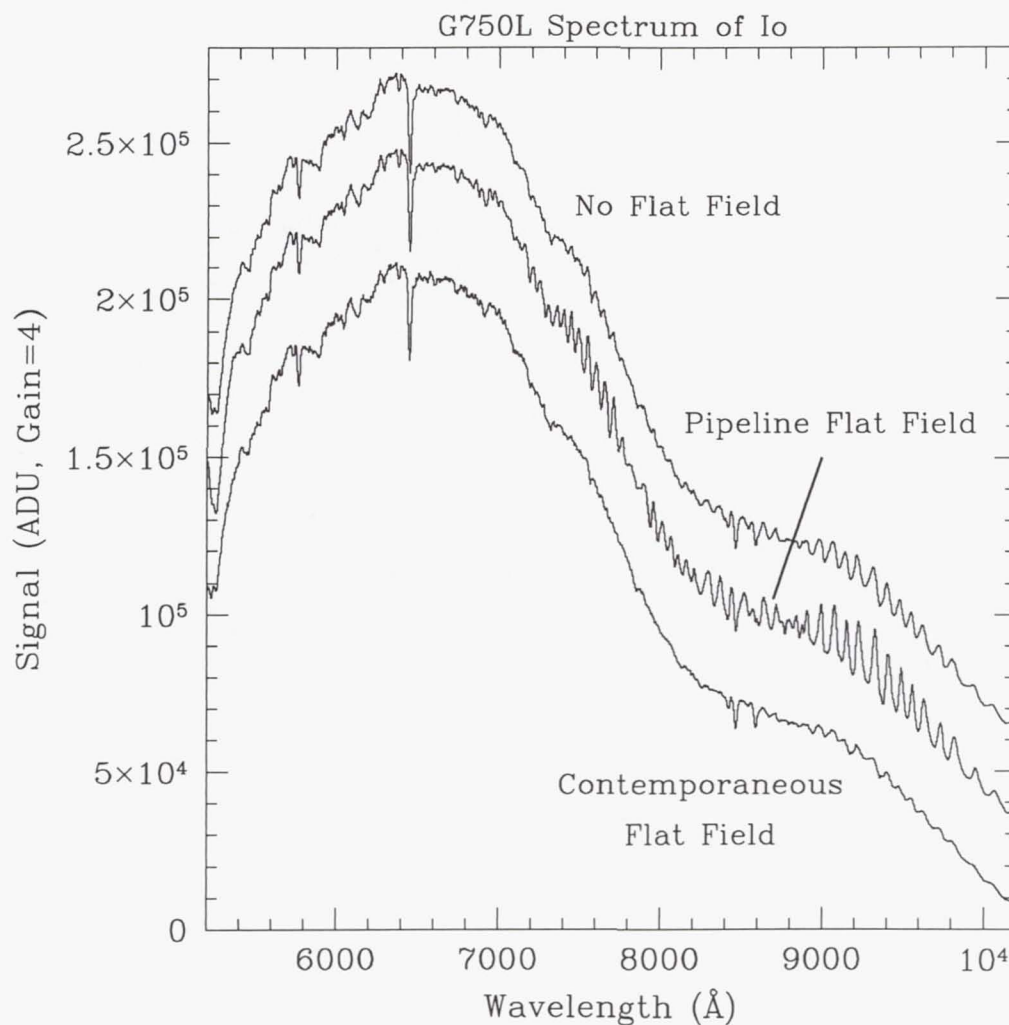


Figure 3. Comparison of G750L spectra of Jupiter's moon Io. The central wavelength is 7751 Å, and the 52×0.2 slit was used. (i, top) reduced without flat fielding, (ii, middle) flatfielded with the standard pipeline (pre-flight) flat, and (iii, bottom) flatfielded with a contemporaneous flat taken during the same orbit as the Io spectra, with the same observational setup. Notice the rather dramatic difference in fringe amplitude.

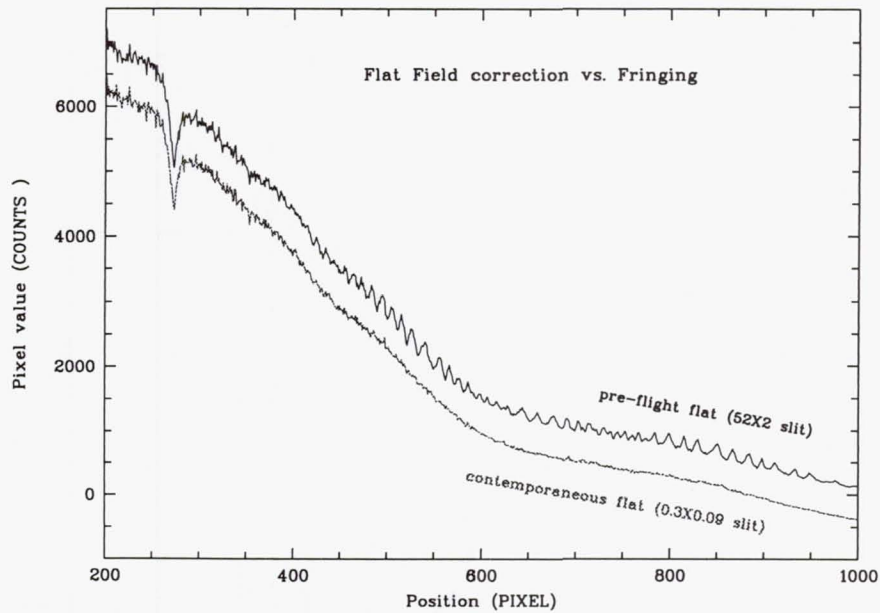


Figure 4. Comparison of two G750L spectra of white dwarf GD 153. The central wavelength was  $7751 \text{ \AA}$ , and the  $52 \times 2$  slit was used. (i, top) flatfielded with the standard pipeline (pre-flight) flat which was taken through the  $52 \times 0.1$  slit, and (ii, bottom) flatfielded with a contemporaneous flat taken during the same orbit as the Io spectra, taken through the  $0.3 \times 0.09$  slit, which is normally used for echelle observations. The latter spectrum has been shifted downward by an arbitrary amount for clarity reasons. Notice the rather dramatic difference in fringe amplitude.

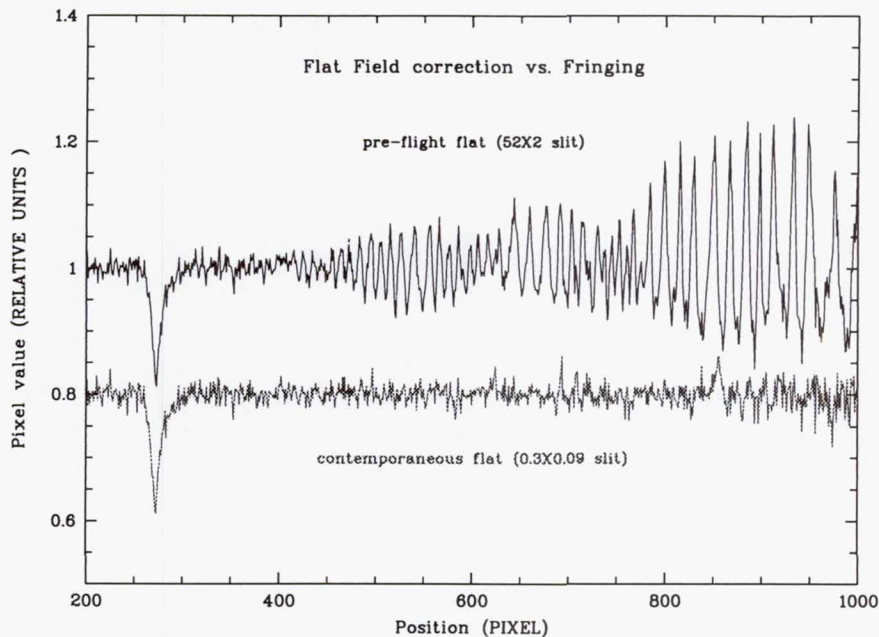


Figure 5. As Fig. 4, but divided by the stellar continuum to show the relative amplitude of the fringes.



phase-B preparation. Observers using G750L or G750M at wavelengths longer than 7000 Å should keep this in mind when finalizing their proposals.

#### **4.1. Possible Future Improvements**

- Fringe correction using a library of in-flight long-slit tungsten flat fields: As time goes by and the number of in-flight tungsten flat fields increases, it will be possible to build a library of long-slit flat field images in the different spectroscopic modes; one can envisage being able to query this library by e.g., the peak of the cross-correlation with a reference flat field for each particular mode, so that one could pick the best library flat for use with any particular long-slit spectrum.
- Fringe correction using White Dwarf Models: comparing observed white dwarf spectra with model atmospheres and building a library of flats from that. These may be quite useful for de-fringing spectra since they are typically of high S/N and no "point-source mimicking" is necessary. Note that in this case, the user will have to apply a shift along the dispersion to the "fringe flat" before de-fringing.

#### **References**

Plait, P., & Lindler, D., 1997, this volume.

## Thermal Motion of the STIS Optical Bench

Theodore R. Gull<sup>1,2</sup>, Mary Jane Taylor<sup>3</sup>, Richard Shaw<sup>4</sup>, Richard Robinson<sup>5,2</sup>, and Robert S. Hill<sup>6,2</sup>

**Abstract.** Various tests have been done of the STIS using internal wavecals to measure thermal motion of the spectral format on the detectors. In most cases, the spectral format moves less than the specification not to exceed 0.2 pixels per hour. Primary causes of the motion are 1) changes to the thermal design dictated by the warmer Aft Shroud environment and 2) on-orbit power cycling of MAMA electronics to minimize the effects of radiation hits on the MAMA detectors. The rear portion of the STIS optical bench is too warm to be held at a constant temperature by internal heaters. Electronics swing in temperature with an orbital and daily frequency. The thermal drift of the optical formats is not negligible, but is well-behaved in most circumstances. The observer is advised to examine the trade-off between the most accurate wavelengths with best spectral/spatial resolutions versus increased overheads that directly affect the observing times. A long term concern is that the Aft Shroud thermal environment is predicted to heat up as much as one Centigrade degree per year. Progressively more of the bench would move out of thermal control. Thus the external cooler for STIS, being considered for the Third Servicing Mission is of major importance to the long term operation of STIS.

### 1. Introduction

The STIS was designed, built and tested over a fourteen year period with the goal that it would provide multiple capabilities of spectroscopy, imaging spectroscopy and imaging over the spectral range from 1175Å to 10000Å. As with all instruments that go into the HST, the STIS was designed to the specifications in the Interface Control Document (ICD). Unfortunately, reality has a way of changing the operating environment when hardware gets close to delivery. STIS has been no exception: In March, 1996, five months before the scheduled delivery of the instrument to NASA, the STIS team was notified that the thermal environment in the Aft Shroud was going to be warmer than specified in the ICD. Moreover, the thermal models predicted, based upon the first six years of HST operations, that the thermal environment would increase as much as one Centigrade degree per year (models incorporating the ACS and COS have not been fully studied at this time). These changes in the thermal environment caused great concern to the STIS development team as the hotter thermal environment and projected warming trend placed the operation of the STIS detectors at great risk. Indeed the thermal environment for the CCD threatened to

---

<sup>1</sup>STIS IDT

<sup>2</sup>LASP, Code 681, Goddard Space Flight Center, Greenbelt, MD 20771

<sup>3</sup>Dept. of Physics and Engineering, Loras College, 1450 Alta Vista, Dubuque, Iowa 52004

<sup>4</sup>Space Telescope Science Institute, 3700 San Martin Drive, Baltimore, MD 21218

<sup>5</sup>Computer Sciences Corporation

<sup>6</sup>Hughes/STX



exceed the operational range of the thermal electric cooler (TEC), leading to the potential of thermal runaway. The MAMA temperatures were projected to be much hotter than the original design specifications. As STIS was less than two months from thermal vacuum testing, changes were quickly done to protect the detectors. Heat pipes were added to the MAMA detectors and insulation was removed from the area surrounding the optical bench to provide better heat conductivity to the external panels.

However increased thermal conductivity is a double edged sword. The STIS optical bench became more vulnerable to thermal changes in the Aft Shroud. STIS was placed in a quadrant on the sunward side. Hence the heat load on STIS changes with solar beta angle, and with spacecraft roll. When the side of HST is directly illuminated ( $\beta=90^\circ$ ), the side panels of STIS receive significant heat input, but the MAMA heat pipes conduct very effectively to the cold surface of the STIS aft bulkhead. Moreover, if HST is rolled with the Sun impinging more directly on the STIS quadrant, the outer panels of STIS receive even more heat input. The maximum roll is about thirty degrees from the nominal Sun line, and, at  $\beta=90^\circ$ , provides the hottest environment for STIS. The coolest environment for STIS occurs when HST is pointed in the antisun direction. The MAMA heat pipes cannot conduct the detector heat away as effectively, but the outer panels of STIS see a significantly colder environment. In one SMOV proposal (7087), we tested the STIS thermal responses in these two conditions by observing an astronomical source in the continuous viewing zone (CVZ) for five orbits, then slewing to a source located in the anti-sun direction and monitoring until STIS achieved a relatively stable cold environment.

We tested the STIS optical bench thermal stability before launch during the thermal vacuum tests at Ball and in ambient air at Goddard. We could not fully duplicate the on-orbit environment, but we did bracket the thermal extremes that were expected to be encountered in the specified five years of on-orbit operations. But the thermal vacuum tests provide insight on how the STIS will operate in equilibrium. The key issue in the optical bench thermal motion is how the bench responds to transients, both external and internal. The thermal design philosophy has been to minimize the thermal changes and to make sure any changes in the optical bench occurred slowly. During the thermal vacuum tests, limited tests were conducted on the optical bench motion by measuring the displacement of spectra in the hot and cold extremes. After delivery of STIS to Goddard, we were limited to testing in ambient air. We could measure the thermal motion of the STIS optical bench as the internal electronics went from ambient to full operation.

On-orbit testing was done for several situations. In addition to the CVZ/ anti-sun thermal conditioning test, we tested the thermal motion of the STIS optical bench in less ideal, but more realistic, on-orbit conditions. The CVZ spacecraft orientation basically conditioned STIS in a hot environment. Then HST was moved to an anti-sun orientation for thirteen orbits. We allowed the STIS to stabilize for the first eight orbits, monitoring the motion of the CCD mode G230MB, then the NUV MAMA mode E230H was interleaved with the CCD. Typical observations with the STIS will not have the benefit of a thermally-stabilized condition. Indeed the thermal environment for the STIS instrument immediately before any STIS observation is most likely to be significantly different. While the scheduling is done to minimize spacecraft maneuvers, the more crucial issue is fitting the observations into the allowable period on the long term schedule. With the long slit of STIS requiring very precise roll angles, and with the full scale application of parallel observations, changes in roll of the spacecraft are highly likely with most observations. We should then expect greater visit-by-visit changes in thermal environment for STIS than occurred for the first generation of instruments. To get a feeling for these variations, several proposals tested for thermal motion measured during single orbit observations (7085,7086) and for thermal motion during about four orbit observations (7143,7144).

On orbit, we found a further complication in the thermal environment for STIS. Early into the SMOV activity, the MAMA electronics were found to be partially reset by radiation events during the SAA passages. Bench testing of engineering units of the MAMA



electronics demonstrated that infrequent partial upset condition could increment the high voltage for the MAMA detectors. If the detector received an overvoltage, survivability of the microchannel plate would be at risk. To protect the detectors, the flight software was changed to cycle the MAMA electronics off during SAA passages. As the MAMA electronics provide a very significant heat input to the rear portion of the STIS optical bench, the MAMA electronics must be powered as much time as possible. Bulkhead six mechanically supports the echelle gratings and various optics, plus the MAMA detectors. Thermal motion of the echelle gratings is likely to be induced by the cycling of the MAMA electronics; indeed we show below that this effect is significant.

## 2. Measurements

Thermal vacuum testing of spectral format motion was limited to measures in the hot and the cold extremes. As the Mode Select Mechanism (MSM) was moved to sample various formats, measures include error in positioning the MSM that is of the order of  $\pm 2$  pixels. The CCD formats tended to move little (spectral direction  $+4$  to  $-2$  pixels; spatial:  $+2$  to  $-2$  pixels). Each CCD mode appeared to correlate closely with the other CCD modes during a given set of measurements at a specific time and temperature. In units of lores pixels, the MAMA detector formats moved differently: in general the low dispersion formats moved less ( $\pm 2$  pixels both spectral and spatial directions); the high dispersion formats moved more (as much as 10 pixels in both spectral and spatial directions). For comparison the bulkhead six temperature changed by as much as fifteen degrees Centigrade during these tests.

Ambient air testing was limited to measuring format motion due to temperature gradients within the instrument. We note that air convection of heat significantly modified the thermal distribution within the instrument. To keep the instrument dry, nitrogen gas was flowed through the instrument at all times. We adopted a procedure to test thermal motion by leaving the instrument off overnight for at least eight hours. Start up of the instrument was done as rapidly as safely possible to begin measurements of the spectral formats starting at ambient. As the day progressed, wavecalcs were repeated for a single mode, not moving any internal mechanical device. For the E230H mode, we measured a drift of five pixels over a temperature change of 3.5 centigrade degrees for bulkhead 5; temperatures of bulkheads 5, 6, and 7 were found to track very closely during all tests. The drift was about three pixels in the spectral direction and four pixels in the spatial direction. Thermal motion with time was determined to be less than 0.3 pixels per hour over an eight hour period. The limited testing for E140H in nitrogen gas indicated a similar motion. Other modes had an amplitude two to three times less.

On-orbit testing was done in three modes: single orbit monitoring of selected modes (proposals 7085 and 7086); four orbit monitoring of selected modes (proposals 7143 and 7144); and one test observing the hot condition, the transition from hot to cold condition and the cold condition (proposal 7087). The desired mode of monitoring the thermal drift of the optical bench is to set all internal mechanisms and then take multiple Pt lamp exposures. Dark frames, CCD biases, and spectra of continuum lamps and external sources can be interspersed as long as the slit mechanism, MSM or filters are not moved. A caution must be interjected here that parallel observations are not guaranteed to prevent mechanism movement. When STIS is in parallel mode and the prime instrument moves HST, the planning software apparently homes the MSM. For the single and four orbit proposals, STIS was in parallel to another instrument. Without detailed review of the observation activity, we cannot guarantee that the MSM was moved between wavecalcs.

The on-orbit hot to cold test (CVZ to anti-sun, proposal 7087) is easiest to understand as the thermal environment for STIS was selected to be initially one of the hottest for visit 1, with an immediate slew to the coldest environment. Between March and August of 1997,



the thermal history of STIS on-orbit indicated that bulkheads 1-4 remained very stable, and Bulkheads 5, 6, and 7 have a daily modulation (see <http://www.sesd.stsci.edu/et/stis/stis.html>). Proposal 7087 was executed beginning on 97.197. During the entire visit 1, temperatures of the outer enclosure panels increase upward, with no plateau. The slew from the hot orientation to the cold orientation causes an immediate downward slope. We note that the CCD housing temperature increased by ten degrees as it dumps heat into radiators on the outer panels. The outer panel temperatures flatten out about ten hours later (during the SAA passages with cycling of the MAMA electronics) and then turn up slightly when the MAMA detectors are turned on continuously for the last five orbits of the visit.

Because of the SAA avoidance for MAMA electronics, we were able to test only the CCD thermal motion for the entire seventeen orbits. Indeed the first four orbits, spent in the hot orientation, and the last five orbits, spent in a stabilized cold orientation, were not pure thermal motion tests as we moved the MSM between the G230MB (CCD) and the E230H (NUV-MAMA). The MSM does not return to original grating positions to sub-pixel accuracy ( $\pm 0.2$  pixel), but rather to a pixel or two accuracy. The measured positions indicated much higher positioning accuracy, likely due to the MSM going between two very well-defined positions repeatedly.

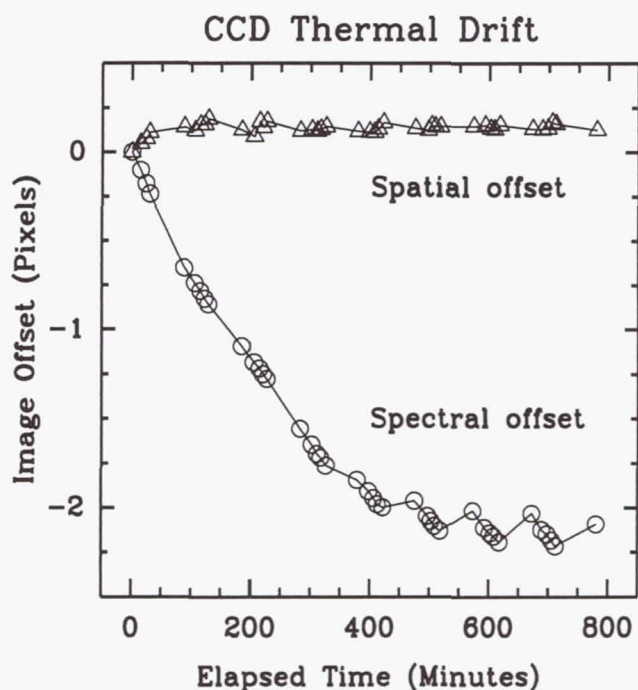


Figure 1. Thermal Motion CCD Mode G230MB for Hot to Cold Transition (Prop 7087)

Moving HST from the hot orientation to the cold orientation yielded a very significant thermal motion for the G230MB format as the enclosure panels cooled down. The CCD format moved at a rate of 0.45 pixels per hour for the first four hours (Figure 1) in the spectral direction (but nearly zero motion in the spatial direction!), then reached a modulated equilibrium by six hours. At that point, the format moves with an amplitude of about 0.5 pixels per orbit. Coincidentally the anti-Sun vector pointed through the SAA on the sunward side of the orbits during the first part of visit 2. The CCD thermal motion has a weak, orbital-period modulation consistent with heating on the back of the spacecraft from the

sun during the SAA passage and cooling during the non-SAA portion of each orbit when the MAMA low voltage electronics is turned on.

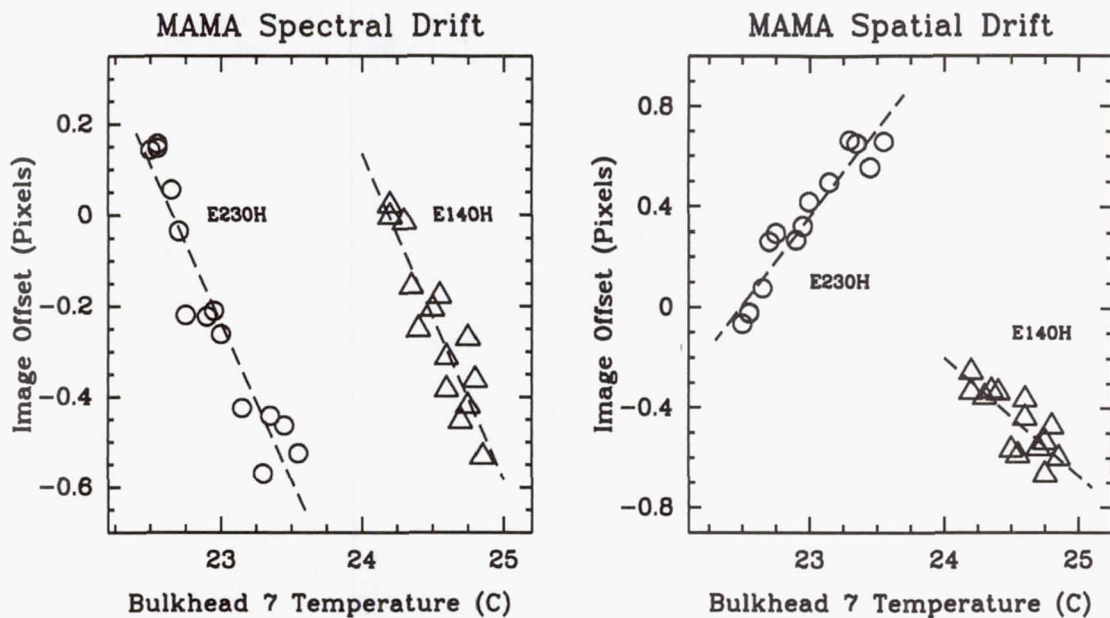


Figure 2. Thermal Motion MAMA Modes E230H and E140H (Prop 7144-5)

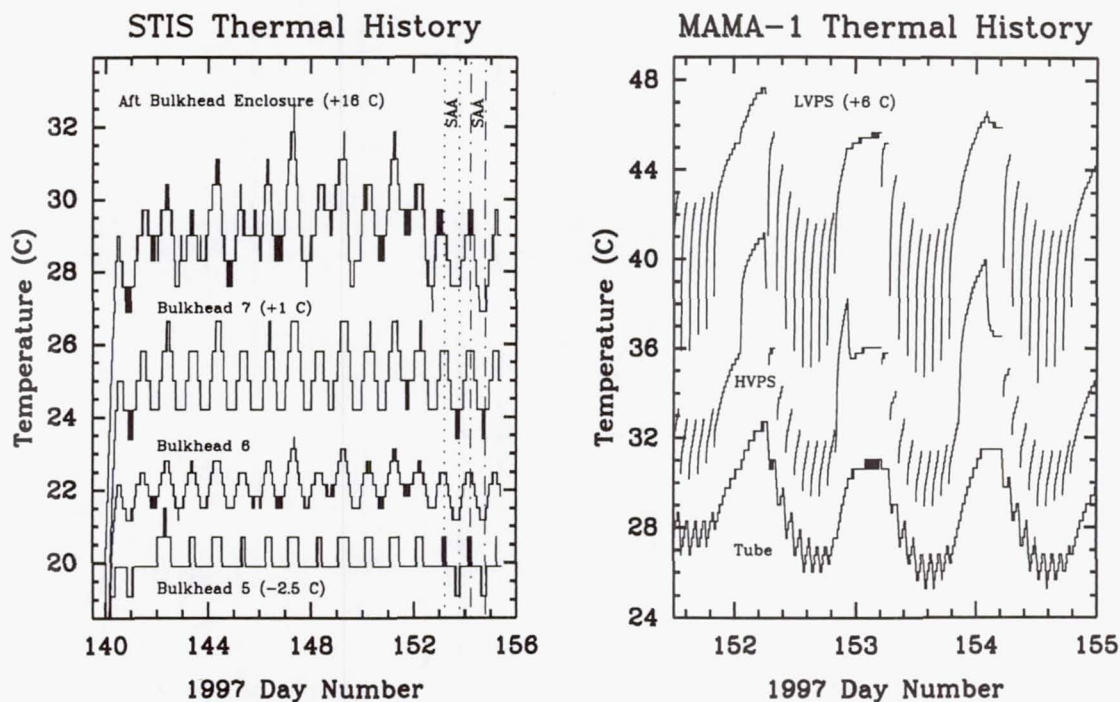


Figure 3. Thermal History of NUV MAMA and Bulkheads

Within each twenty-four hour period, additional thermal cycling influences the optical bench. The temperatures for the low voltage electronics, the high voltage electronics and the tube change as (1 the low voltage electronics are cycled on and off around the SAA passages, (2 the high voltage electronics are cycled on for the period of MAMA usage, and (3 the high voltage is applied to the FUV-MAMA detector (Figure 2). The aft portion of the optical



bench is above the set point of the thermal control electronics, so the heaters designed to keep that portion of the bench in balance are of no use. Instead each bulkhead toward the rear has increasing temperature modulation due to these three effects. Proposals 7143 (CCD) and 7144 (MAMA) were designed to measure the influence of cycling the MAMA electronics on and off. Internal wave calibrations were done for four orbits each with STIS in parallel mode.

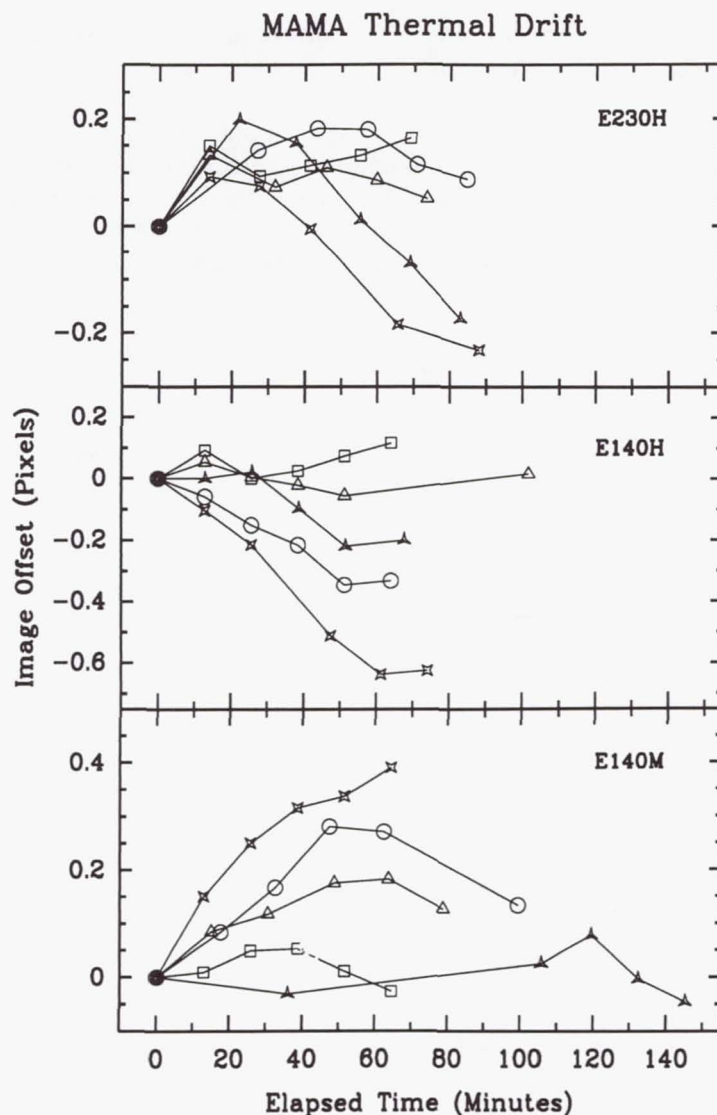


Figure 4. Thermal Drift in Spectral Direction for Echelle Modes (Prop 7086)

Heat input to bulkheads 5-7 warms the deck upon which the echelle and several mirrors are mounted. As the deck heats, the primary change is an "oilcanning" effect where the center of the deck moves axially and the deck warps in a radial tilt. The thermal motions (Figure 3) with temperature measured for modes E230H and E140H are consistent with an oilcanning. The spectral shift is about -0.6 pixels per centigrade degree for both modes, but the spatial shift is about 0.7 pixels per centigrade degree for the E230H and -0.3 pixels per centigrade degree for E140H. For the four orbit tests done under proposal 7144, the

thermal motion with respect to time was about 0.3 lores pixels per hour. The CCD motion was significantly less and appears to be predictable.

The normal application of STIS is likely to be a single orbit, or a few orbits per mode. In proposals 7085 and 7086, measures of spectral motion were taken over single orbit periods. Here the CCD motions appear much more predictable with one qualification: our limited data indicates that the zero-point may move around (MSM positioning inaccuracies). The thermal motion collapses to a common curve that is linearly fitted with a slope of 0.3 to 0.45 per centigrade degree. Shifts are 0.2 pixels per hour or less. The echelle modes were less consistent. Thermal motion in the spectral direction seemed to change from visit to visit, even to the extent of change in slope. The motion does not seem to correlate well with the bulkhead 7 or the aft bulkhead temperatures. However a caution must be added here. These observations were done with STIS in parallel mode, and if the primary instrument was moving the spacecraft, then the HOME command would have been issued, leading to a reset of the MSM position. Since the MAMA camera mirror focal length is longer and the MAMA pixel size is smaller than that of the CCD, then the effect is more pronounced for the MAMA measures. In the spectral direction we measure thermal drifts ranging from 0 to 0.6 pixels per hour (Figure 4 and Figure 5)

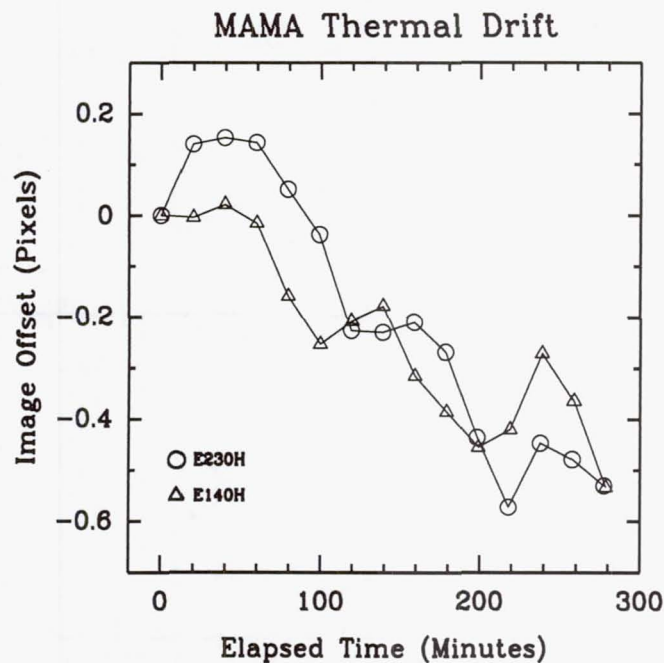


Figure 5. Thermal Drift in Spectral Direction for Echelle Modes: Multiple Orbit Monitoring (Prop 7145)

### 3. Discussion

From the above data, a measurable thermal motion is found for all STIS modes tested to date. Many tests indicate that typically the thermal motion is about 0.2 pixels or less per hour. Under extreme thermal changes, the MAMA echelle modes can move in the spectral direction as much as 0.6 pixels per hour. Substantial changes in beta and roll angles lead



to major changes in solar flux on the STIS quadrant. Most observations are likely to occur with the sun-spacecraft angle at about 90 degrees and as the solar flux changes as the cosine, small beta angle changes from 90 degrees should not affect the thermal condition of STIS. Pointing to the anti-Sun direction however drops the solar flux to zero, and affects the thermal conditioning in a major way. We note that changes in roll angle can induce large thermal change as the average roll angle to STIS is 45 degrees and with changes up to  $\pm 30$  degrees, can provide very significant changes in solar flux.

More frequent wavelength calibrations is an obvious solution, but the observer must carefully examine the tradeoffs between scheduling more wavecal at the expense of observing time as wavecal cannot be buried in earth occultation in the current ground planning software. The impact is much more than just exposure time for wavecal as the overheads of setting up the wavecal, and dumping the buffer memory are significant. A standard of doing at least one wavecal per orbit and bracketing a given mode with wavecal should provide enough information for the observer to establish the reference wavelengths to an accuracy of 0.2 pixels. In the case of the MAMA detectors, if the count rate is less than 30,000 per second, timetag mode is highly recommended. Lindler et al (this volume) have demonstrated that thermal drift and jitter can be corrected for sources with reasonable count rates. Higher count rates with the MAMAs (up to 270,000/sec) must be done in ACCUM mode; if the observer is pushing for the limiting resolutions provided by the hires pixels and the smallest slits, the wavecal should be done more frequently, perhaps as often as once every fifteen to twenty minutes.

## References

Lindler, D. J., Gull, T. R., Kraemer, S. B., & Hulbert, S. J. 1997, this volume

## Correction for the STIS Echelle Blaze Function

Sara R. Heap and Thomas M. Brown<sup>1</sup>

Laboratory for Astronomy & Solar Physics, Code 681, NASA/GSFC, Greenbelt MD 20771

**Abstract.** Using the Early Release Observation of 9 Comae, we demonstrate an iterative method for correcting STIS echelle spectra for the effects of the echelle ripple. This analytic approach allows the actual spectrum of interest to be used in the determination of its calibration. The late F star 9 Comae is not an ideal candidate for this method, due to the many absorption lines present in its E230M spectrum, yet, given this difficulty, the method still works quite well.

### 1. Introduction

Because of the square format of modern imaging detectors, high-dispersion spectrograms are often obtained as echellograms, in which the spectrum is broken up into several orders arranged as horizontal stripes on the detector. This spectral mode provides broad overall wavelength coverage while retaining high spectral resolution. In doing so, it produces a characteristic efficiency along an order known as the echelle blaze function, or more simply, the echelle ripple, because of its characteristic shape. Figure 1 shows a schematic.

The associated calibration problem is to correct each order for the echelle ripple before merging the spectral orders together to form a single, linear spectrum. There are two approaches to ripple correction. The one most often used by spectroscopists at ground-based observatories is an empirical approach. After extraction of an order and subtraction of the inter-order background, the net spectrum of the target is divided by the net spectrum of a spectrophotometric standard observed in the same grating mode. The continuum can be further flattened through polynomial fits to the continuum, if necessary.

Space observatories generally take an analytic approach, in which the shape of the echelle ripple is described by a *sinc* function with appropriate fitting constants. Correction is made by multiplication by the inverse of the ripple function. The fitting constants are derived from observations of spectrophotometric standards, usually stars with a strong, rather flat continuum and weak spectral lines. The analytic approach is both feasible and practical because of the stable response of spectrographs in space and the fixed (usually small) number of grating settings that observers are allowed to use. Operations are more efficient, since calibration observations need be obtained only infrequently as part of the overall calibration program of a spectrograph.

### 2. Description of the Method

In this paper, we demonstrate the application of Barker's (1984) method, one of the analytic methods for correcting the echelle ripple. As a test case, we use the STIS E230M spectrogram of the late F star, 9 Comae (HR 4688, HD 107213) observed by STIS as one of the Early Release Observations (Heap et al. 1997). Figure 2 shows the raw echellogram.

---

<sup>1</sup>NOAO Research Associate



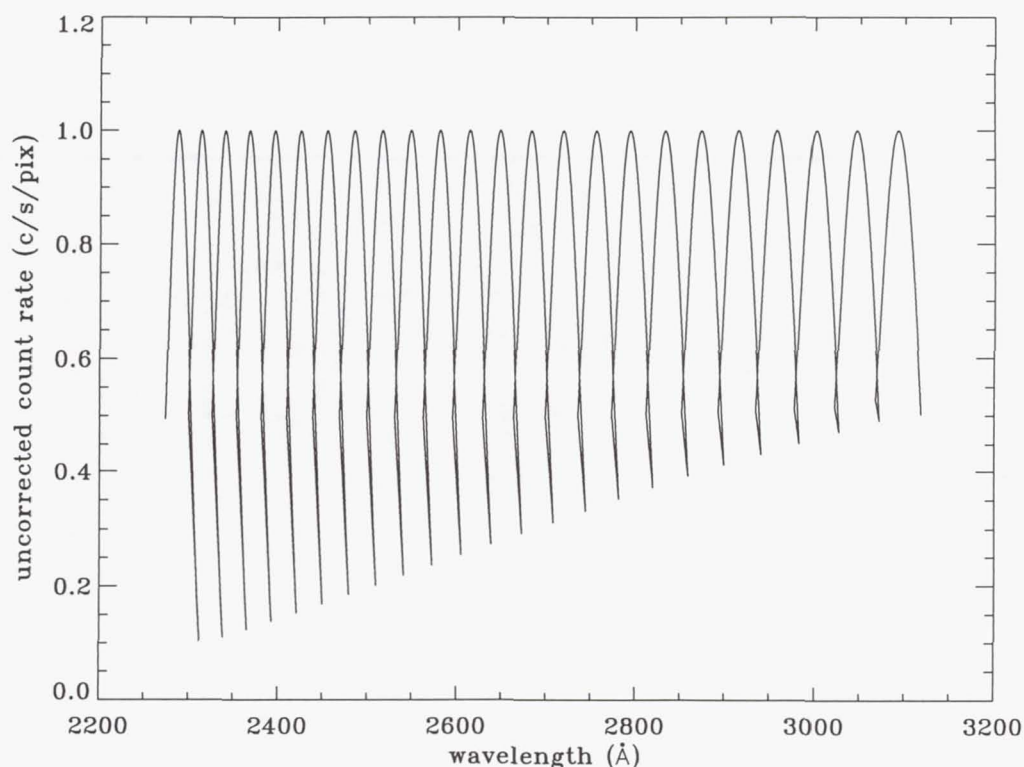


Figure 1. A schematic of the count rate measured from a flat continuum source, after over-plotting the E230M orders without correcting for the echelle ripple.

The spectrum spans the wavelength interval from 2274 Å to 3120 Å at a resolving power  $R=30,000$  ( $10 \text{ km s}^{-1}$ ). Wavelength increases to the right within a spectral order, and from top to bottom (order  $m = 66$  to order  $m = 89$ ). The detector is large enough to accommodate the full length of each order, so the redundant spectral coverage by adjacent spectral orders is easily visible, i.e., a spectral feature at the right (long wavelength) end of order  $m$  is also visible at the left end of order  $m + 1$ .

Since the spectrum of 9 Comae was the first spectrum of an external source obtained by STIS in the E230M mode, the spectrum of the star itself had to be used to derive the echelle ripple function. With its rich absorption line spectrum, 9 Comae is not an ideal calibration source. Nevertheless, it was possible to derive the echelle ripple function by imposing the requirement that where two spectral orders overlap, the two orders must give the same flux. This requirement is the principle behind Barker's (1984) iterative method.

The echelle ripple function,  $R$ , is given by

$$R = \frac{\sin^2(\pi\alpha X)}{(\pi\alpha X)^2}$$

where

$$X \equiv m \frac{1 - \lambda_c}{\lambda}$$

and where the order number  $m$  and the central wavelength of the order,  $\lambda_c$ , are related through the echelle "constant"  $k \equiv m\lambda_c$ . The other grating constant,  $\alpha$ , controls the width of the ripple function. Unlike  $k$ ,  $\alpha$  does not seem to vary with spectral order. For IUE,

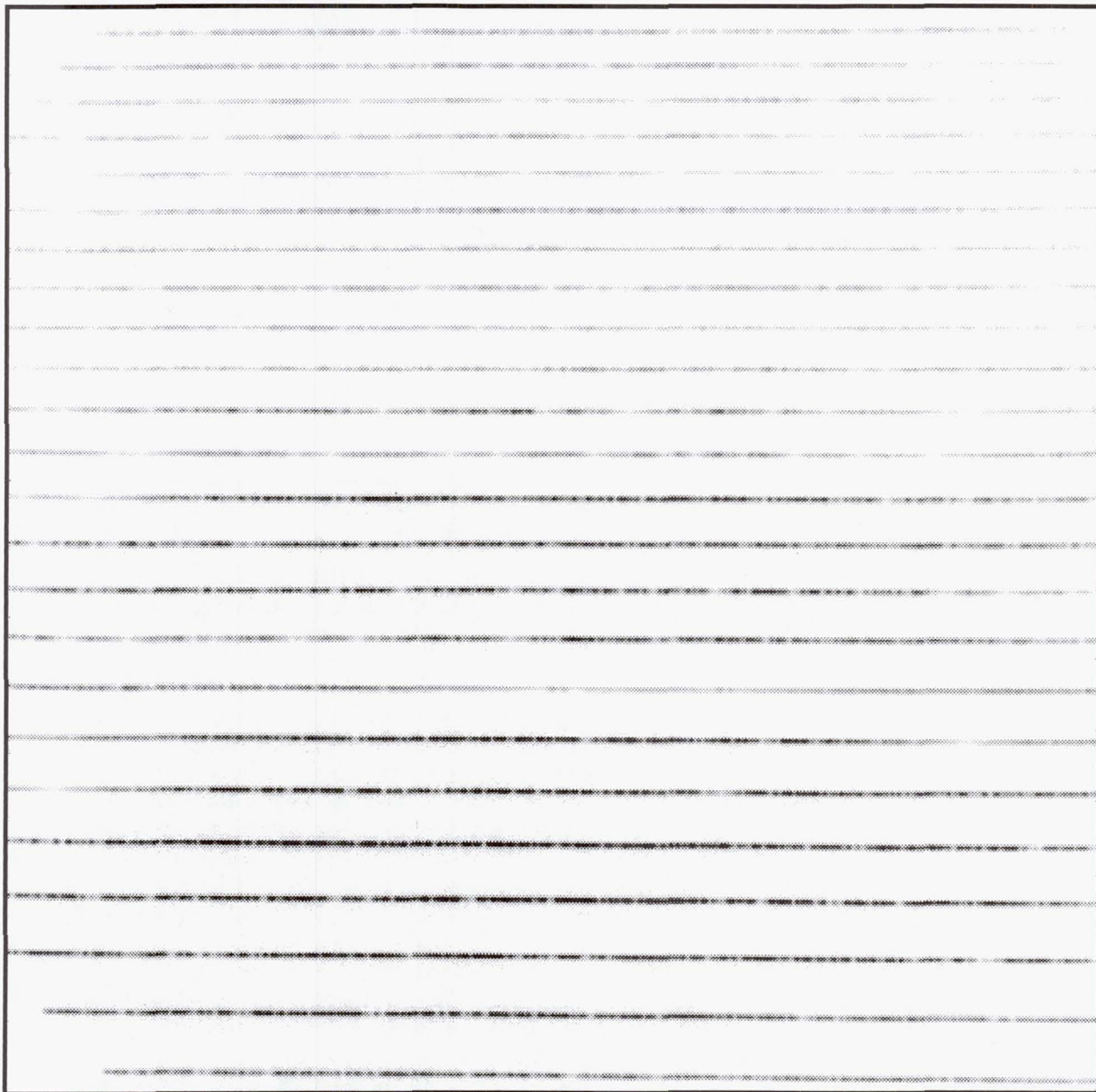


Figure 2. STIS echellogram of 9 Comae. The gray-scale is reversed so that the brightest regions are black. Wavelength increases to the right (within an order) and down (from order to order).



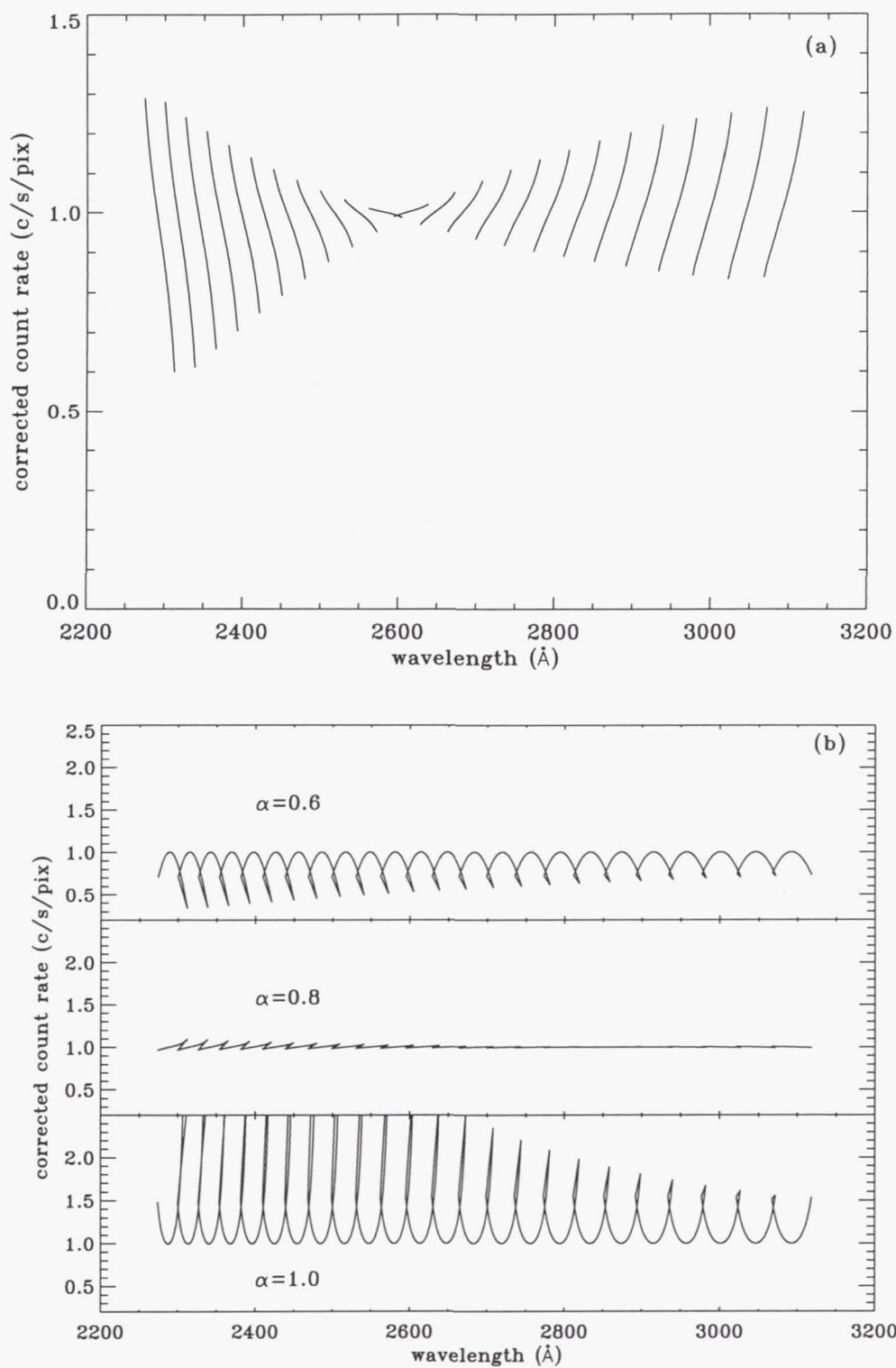


Figure 3. The effect of  $k$  and  $\alpha$  on the correction to the echellogram. The top plot (a) shows the corrected count rate after assuming a constant  $k$  for all orders. The bottom plot (b) shows the effect of varying  $\alpha$  on the corrected count rate.

the KPNO echelle, and the CASPEC spectrograph on the ESO telescope,  $\alpha$  is a constant between 0.75 and 1.0.

In Barker's method, three spectral orders are treated at one time. First, the regions of overlap between the middle order and the two adjacent orders are determined. Then the value of  $k$  is adjusted iteratively until the middle order gives the same flux as the adjacent orders in the two regions of overlap. If  $k$  is incorrect, the spectrum veers up to the right or left. Figure 3a shows the effect of assuming a constant  $k$ . Similarly, the value of the order-width constant,  $\alpha$ , must be adjusted to keep the corrected spectrum from looking scalloped ( $\alpha$  too large) or ripple-shaped ( $\alpha$  too small), as shown in Figure 3b.

The scheme followed for the E230M spectrum of 9 Comae was:

1. Use Barker's iterative method to get  $k_m$  for each order (Figure 4).
2. Make a polynomial fit to  $k_m$  to get  $k(m)$  (Figure 5).
3. Use trial and error to estimate  $\alpha$ .
4. Repeat steps 1–3 with the new value of  $\alpha = 0.80$ .

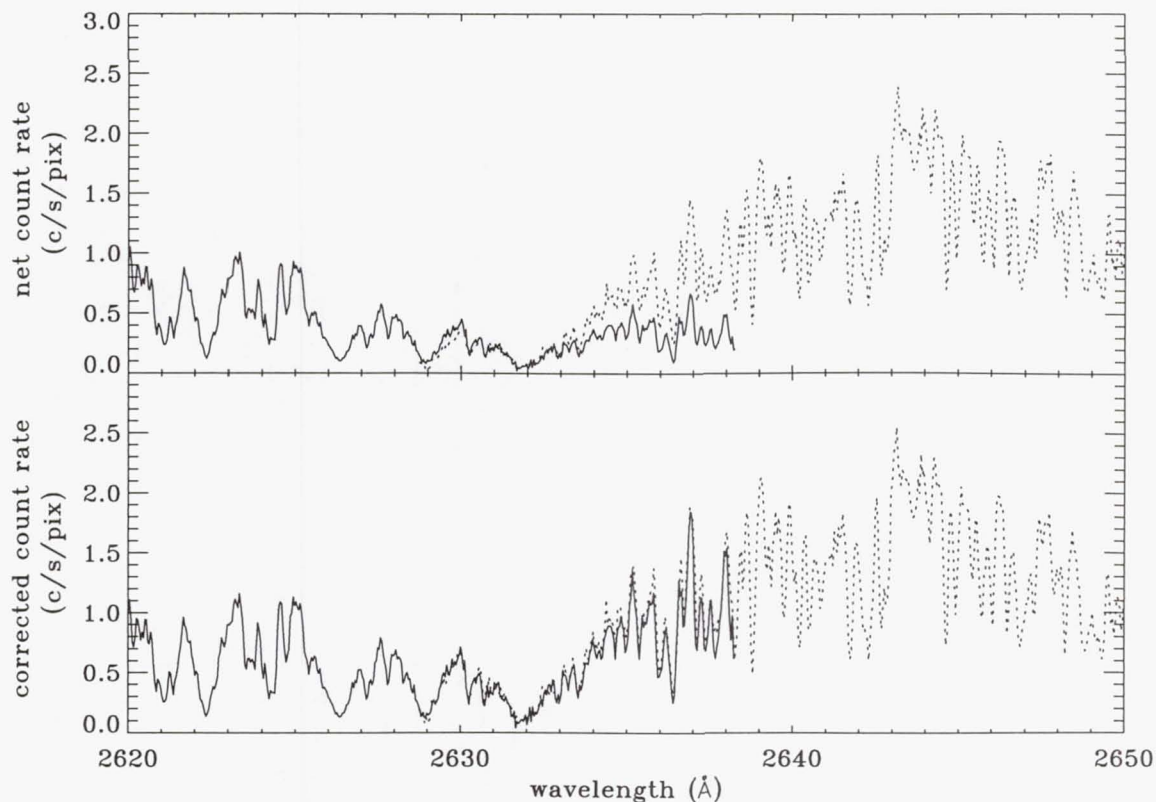


Figure 4. The overlap region for orders 77 (solid) and 78 (dashed), before (top panel) and after (bottom panel) iterating to find  $k_m$ .

### 3. Conclusions & Future Work

This calibration is preliminary, since it does not take into account most of the complexities of real echelle spectra. First, there is the problem of estimating the net fluxes. If there is significant grating scatter or if there are significant wings to the point-spread function (MAMA



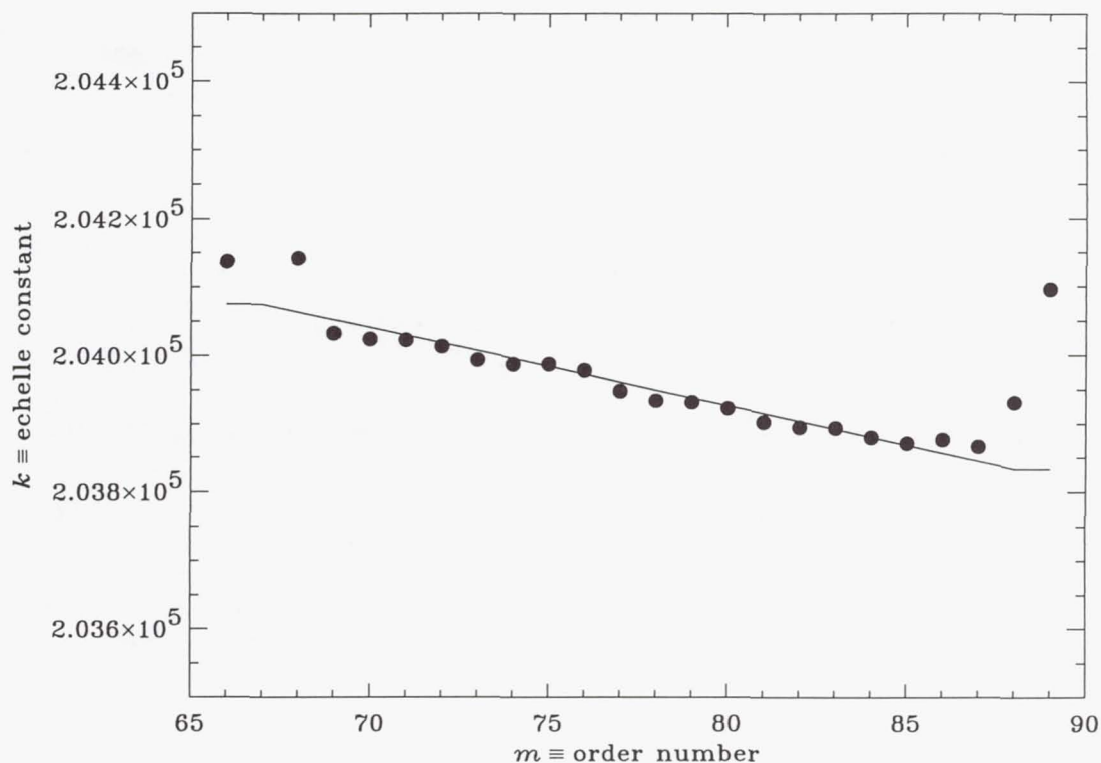


Figure 5. The value of  $k$  for each order (points) and the polynomial fit to these points (curve), as measured for the E230M observation of 9 Comae.

halo) then the background between the orders is not representative of the background under the spectral order itself. Secondly, there is the problem of non-uniformities. Vignetting or regions not fully corrected by flat-fielding will cause deviations from an analytic fit.

Despite the preliminary nature of this calibration, our demonstration shows that calibration by the analytic method is feasible. It is important to maintain a modular approach, e.g., isolate the vignetting from the echelle ripple, in order to understand the workings of the instrument and to identify the cause of possible changes in the future.

## References

- Barker, P. K. 1984, *AJ*, 89, 899  
 Heap, S. R., et al. 1997, *ApJ*, in press

## Cosmic Ray and Hot Pixel Removal from STIS CCD Images

Robert S. Hill and Wayne B. Landsman

*Hughes STX Corp., NASA/GSFC/LASP*

Don Lindler

*Advanced Computer Concepts, NASA/GSFC/LASP*

Richard Shaw

*Space Telescope Science Institute, 3700 San Martin Drive, Baltimore, MD 21218*

**Abstract.** The problem of cosmic ray (CR) removal is a general one plaguing space-borne CCDs, as is the gradual accumulation of single high-dark-rate pixels between CCD annealings. The STIS team at Goddard has developed IDL implementations of standard techniques for dealing with these problems as part of the STIS GTO software. This report summarizes the methods and discusses the pitfalls.

### 1. Why Worry About Cosmic Rays?

Table 1 shows data obtained from long dark images on the rate of accumulation of CR pixels in a given exposure. The typical rate of accumulation is  $\sim 25 - 30$  pixels/s at a detection threshold of  $4\sigma$ . How long does it take to fill the entire detector with CR pixels? The situation is described by exponential decay, because only the first CR to hit a given pixel counts. Thus, the instantaneous probability of another pixel being affected by a CR is proportional to the number of remaining non-CR pixels. The "half-life" of the image in this sense is  $\sim 27,000$  s.

Be that as it may, in a typical STIS CCD exposure of  $\sim 1000$  s,  $\sim 2.5\%$  of the pixels will be affected by CRs. In most cases, omitting the CR correction would interfere with object detection, spectral extraction, and photometry. Nor should the cosmetic problem be discounted, because pattern recognition by the scientist is a necessary part of data analysis.

### 2. Cosmic Ray Removal Methods

There are two main kinds of CR removal technique. One uses the image being cleaned to determine empirically the statistical outlier pixels. Pixels differing from some computed background by a specified threshold are repaired. Although the photons that should have been detected can never be recovered, at least the CR pixels can be flagged and cosmetically improved.

The most rigorous kind of CR removal uses multiple images together with the known, calibrated readout noise and gain of the CCD. Outlier pixel values are defined in relation to the expected distribution of differences between the input images. Usually, the STIS/CCD or WFPC2 observer plans ahead to divide long exposure times into two or more actual exposures (CR-splits) in order to use this method. However, for faint, extended sources, there is a potential trade-off, since with  $N$  exposures, the read noise of the final co-added image increases by a factor of  $N^{0.5}$  over a single exposure of the same duration.



Table 1. Accumulation Rates of Pixels Affected by Cosmic Rays

Date	Number of Pixels	Exp. Time (s)	Rate (pixels s <sup>-1</sup> )	STISLOG Entries
50527.71	228032	5*1800	25.3	716,720,722,724,726
50531.08	221603	5*1800	24.6	737,739,741,745,747
50546.67	296034	6*1800	27.4	792,794,796,827,829,831
50563.83	218052	4*1800	30.3	941,943,945,955
50573.17	235042	5*1800	26.1	1026,1030,1032,1034,1036
50580.09	224395	5*1800	24.9	1104,1106,1108,1110,1120
50587.11	256936	5*1800	28.5	1269,1271,1273,1275,1277
50594.41	270249	5*1800	30.0	1518,1520,1666,1668,1670
50601.22	204008	4*1800	28.3	1973,1975,1977,2006
50605.19	239604	5*1800	26.6	2119,2123,2125,2127,2138
50612.53	178210	5*1350	26.4	2421,2423,2425,2427,2433
50618.08	152793	5*1350	22.6	2701,2707,2709,2711,2713
50618.52	157647	5*1200	26.3	2732,2734,2736,2738,2740
50619.70	191219	5*1200	31.9	2750,2752,2754,2756,2758
50625.10	145831	5*1350	21.6	3035,3037,3039,3041,3043
50631.74	173537	5*1350	25.7	3191,3193,3195,3197,3199
50639.02	131846	4*1350	24.4	3359,3365,3367,3369
50646.49	155334	5*1350	23.0	3691,3693,3695,3697,3701
50653.04	215986	5*1350	32.0	3865,3867,3869,3871,3873
50660.12	214942	5*1350	31.8	4033,4035,4039,4041,4043
50667.10	154941	5*1350	22.9	4168,4170,4172,4174,4176
50674.09	155016	5*1350	23.0	4324 4326 4328 4330 4332
50681.03	148671	5*1350	22.0	4540,4542,4544,4548,4550
50685.13	184481	5*1350	27.3	4613,4615,4617,4619,4621

### 3. What are Hot Pixels?

Hot pixels are individual pixels with a high dark current, that are persistent and occur at fixed positions on the detector. If left alone, they continually increase in number. However, many of them can be repaired physically by turning off the thermoelectric cooler (TEC) and letting the CCD warm from its operating temperature of  $-83^{\circ}\text{C}$  to  $-5^{\circ}\text{C}$ , where it remains for 12 hours. WFPC2 experience indicates that it may be possible to reach a near-steady state in which the net growth rate in the number of hot pixels is  $\sim 8\%$  of the instantaneous growth rate (Kimble 1997).

Another poster in this conference (Beck et al.) discusses hot pixels.

### 4. Hot Pixel Repair Methods

There are two ways to remove hot pixels, analogous to the two ways of removing CRs. One way is to subtract the excess signal from each hot pixel, leaving behind the legitimate astronomical source flux. The other way is to estimate the correct pixel value from surrounding pixels on the same image.

Users of the GTO IDL software often invoke a hybrid method. Many pixels perceived as hot in an image display are actually removed quite well by subtracting a standard weekly dark, which is a high S/N image made by combining five long-duration dark frames. After this step, the software uses a pixel list that is generated from up-to-date darks. The rates given in the list are only used to decide which pixels to correct, and the corrected values are estimated from the surrounding pixels. Thus, two ways of fixing hot pixels are combined. The user must decide at what count rate to put the transition between pure dark subtraction, and dark subtraction followed by interpolation.

### 5. Statistical CR-Removal Programs

A classification of some commonly used CR-removal programs is as follows (Massey 1997, Wells & Bell 1994, and on-line documentation for the various programs):

#### 1. Several images

##### (a) Empirical noise

- i. Iterative: None apparently in common use; such an algorithm was used in processing ground-based STIS/CCD flats
- ii. Non-iterative
  - A. IRAF tasks `combine` and `imcombine` with some options, e.g., `avsigclip`
  - B. Similarly for STSDAS task `gcombine` (works on multi-group GEIS data)

##### (b) Calibrated noise model

- i. Iterative
  - A. IDL program `cr_reject`, as called by `stis_cr` in the GTO IDL system
  - B. STSDAS task `hst_calib.wfpc.crrej`, or `calstis-2` in the STIS pipeline
- ii. Non-iterative
  - A. IRAF tasks `combine` and `imcombine`, with the `crreject` option
  - B. Similarly for STSDAS task `gcombine` (works on multi-group GEIS data)

#### 2. One image: IRAF task `cosmicrays`



## 6. Hot Pixel Removal Programs

A classification of some commonly used hot-pixel repair programs is as follows (Massey 1997, Wells & Bell 1994, as well as on-line documentation for the various programs):

1. History-based
  - (a) Dark frame subtraction
    - i. GTO IDL program `calstis` (`darkfile` option)
    - ii. IRAF task `ccdproc` (`darkcor` option)
    - iii. STSDAS pipeline tasks `calwp2`, `calstis-1` (`darkcorr` option)
  - (b) Hot pixel lists or masks
    - i. GTO IDL program `calstis` (`hrepair` option)
    - ii. IRAF task `ccdmask`, followed by `fixpix`
    - iii. STSDAS tasks `warpix` or `wfixup`
2. Single image
  - (a) GTO IDL program `hotterp`
  - (b) IRAF program `cosmicrays`

## 7. What is the Standard CR Rejection Method for STIS?

The Institute pipeline and the GTO IDL software use very similar programs to remove CRs. Both are based on the STSDAS task `crrej` in the package `hst_calib.wfpc`. The algorithm is iterative, and it uses a calibrated noise model. Typically, the first iteration clips at some high number of  $\sigma$ , such as 6 or 8, then ramps down to 3 or  $4\sigma$ . The STScI routine is called `calstis-2`, and it can be invoked from STSDAS. The GTO IDL program, which is called `cr_reject`, is usually invoked as part of the higher-level routine `stis_cr`.

No one set of parameters for either of these routines can handle all cases. STScI estimates that the `calstis-2` product will be quantitatively usable for  $\sim 50\%$  of the observations (Baum et al. 1996). The STScI pipeline tunes the parameters of `calstis-2` depending on the observation, as shown in Table 2.

## 8. Some Subtleties of the Algorithms

Besides the iterative  $N\sigma$  clip, both programs mentioned above have additional features:

- The CR flags can be propagated in the neighborhood of the initially detected CR pixels, to take into account a failure to detect fainter pixels around the CR edges
- The initial guess at a CR-free image can be either the pixel-by-pixel minimum of the input images, or the pixel-by-pixel median; for only 2 input images, there is really no other good way than starting with the minimum
- The STScI algorithm clears the CR flags between iterations, so that a pixel that has once been flagged can regain its good standing if the average creeps back up toward it; the GTO IDL algorithm by default says, "once a CR, always a CR," but allows re-initialization as an option; this difference probably only affects tight clips, say, 2 iterations at  $2.5$  (N.B.: the GTO IDL default may change)

Table 2. CR Rejection Parameters in STScI STIS Pipeline

Inputs		Outputs <sup>a</sup>	
CR-Split Images	Mean Exp. Time	Initial Guess	Clipping Sigmas
2	3.	minimum	4.0
2	21.	minimum	3.5
2	100.	minimum	3.0
2	3.0E5	minimum	3.0
3	2.	minimum	4.0
3	17.	minimum	3.5
3	82.	minimum	3.0
3	3.0E5	minimum	3.0
4	2.	median	4.0
4	15.	median	3.5
4	71.	median	4,3.0
4	319.	median	5,4,3
4	3.0E5	median	6,5,4,3
5	2.	median	4.0
5	13.	median	3.5
5	63.	median	4,3.0
5	1479.	median	5,4,3
5	3.0E5	median	6,5,4,3
6	2.	median	4.0
6	12.	median	3.5
6	58.	median	4,3.0
6	1479.	median	5,4,3
6	3.0E5	median	6,5,4,3
7	2.	median	4.0
7	11.	median	3.5
7	53.	median	4,3.0
7	3187.	median	5,4,3
7	3.0E5	median	6,5,4,3
8	1.	median	4.0
8	10.	median	3.5
8	50.	median	4,3.0
8	3187.	median	5,4,3
8	3.0E5	median	6,5,4,3

<sup>a</sup>The following outputs are constant: no sky adjustment; no scale noise; CR propagation never done; no input quality flags avoided; mask always produce



- The input images can be sky-adjusted before CR rejection; the GTO IDL program uses a DAOPHOT-like sky computation, whereas `crrej` finds the histogram mode directly
- Scale noise, such that  $\sigma = k \times \text{flux}$ , can be added into the noise model; this is used either for images that are already flat-fielded (not the pipeline default) or in case of a slight PSF mismatch

## 9. What Are the Potential Problems?

- Any sufficiently stringent CR removal program will remove some real data because statistical fluctuations can be mistaken for CR pixels; be cautious, and do not go for better than a 3 or 4  $\sigma$  clip in the final iteration
- PSF mismatches or image shifts, even at the sub-pixel level, cause real flux to be removed
- Some residual CR pixels will be added into the final image, resulting in noise that affects faint source detection; one may need to model this, depending on the goal of the analysis
- Some hot pixels will usually be left over, regardless of the method used, and may need fixing by hand

To assure good results from CR rejection, the user should do the following:

- Check both the co-alignment of the CR-split images and the consistency of the PSFs
- Verify that flux is conserved in the result
- Examine the mask images that most programs produce in order to show which pixels are rejected; if a mask shows the obvious shape of a real source or the contour of a steep flux gradient, then the work probably needs to be redone with new parameters or a new procedure

The user should not take any CR-rejection result on faith. Depending on the situation, even a simple algorithm can sometimes do the job, and with the wrong parameters, even the most sophisticated algorithm can either reject good pixels or retain too many bad ones. Checking the general performance of a program using darks or other test data is not sufficient, as the presence of sources affects the outcome.

## References

- Baum, S., Hsu, J. C., Hodge, P., & Ferguson, H. 1996, Instrument Science Report STIS 96-018 (Baltimore:STSci)
- Beck, T. et al., 1997, this volume
- Kimble, R. et al. 1997, ApJL submitted
- Massey, P., 1997, A User's Guide to CCD Reductions with IRAF (NOAO IRAF Web site)
- Wells, L. A. & Bell, D. J. 1994, Cleaning Images of Bad Pixels and Cosmic Rays using IRAF (NOAO IRAF Web site)

## Laboratory Test Data on the Stability of the STIS MAMAs

Charles L. Joseph

*Rutgers University*

### Overview

STIS has two MAMA detectors systems with distinctly different tube configurations. The first (designated BAND 1) has an opaque CsI photocathode deposited on the microchannel plate (MCP) providing wavelength coverage from 1150Å to 1700Å. The other MAMA (designated BAND 2) has a semitransparent Cs<sub>2</sub>Te photocathode deposited on the faceplate in close proximity to the input of the MCP. It covers the 1650Å to 3100Å bandpass and serves as a backup for the short wavelength detector.

Laboratory test data indicate that both of these detectors have good sensitivity, have good uniformity and provide stable response, making each capable of collecting data with a signal-to-noise ratio in excess of 100 per STIS optical resolution element. See Joseph et al. (1995) for a general description as well as the performance of these subsystems. Over a multiyear development effort, a substantial body of laboratory test data (more than 6 GBytes spanning more than 6 years of collection) has accumulated on more than a dozen fabricated tubes. These tests even included a few destructive evaluations to examine the limitations and operating life. In addition, analyses were conducted regarding impact caused by the specified electronic tolerances and expected changes in the HST thermal environment. This latter analysis is being presented elsewhere (Joseph, Bybee, and Argabright 1997).

Perhaps the simplest test of stability is to collect a sequence of images, each with a uniform illumination, and use these individual "flat fields" to remove the pixel-to-pixel sensitivity in the other flat fields. These sequences typically spanned 3–5 weeks of time. As can be seen in Figure 1, the detectors are very stable, allowing the pixel-to-pixel sensitivity to be removed with good precision. The STIS specification for stability is 1% (sufficient for data with a S/N = 100) over a 1 week period and 2% over 30 days. All Engineering Model Units as well as Flight Detectors tested exceeded this specification.

Other measures of life time as well as bright scene testing have demonstrated the MAMA detectors to be robust and stable beyond all expectation. Figure 2 shows the results of one life test on a Ni-Tec C Plate equivalent to those used in both flight MAMAs. The gain of this MCP is plotted as a function of the total charge extracted from the MCP. There are several curves, each representing the gain produced by a given high voltage across the MCP. MCPs are notorious for their reduction in gain as a function of use. This exponential reduction is the result of contaminants as well as the chemicals responsible for the electrical properties of the MCP being scrubbed out of the MCP and deposited, for example, on the anode structure. Fortunately the gain requirements of the MAMA are about 2 orders of magnitude below that needed by most MCP-based detector systems. The charge amplifiers and discriminators require a minimum gain of approximately  $2.0 \times 10^5 e^-$  for efficient detector operation. This low minimum requirement, shown as a horizontal dashed line in Figure 2, allows the MCPs used in MAMAs be preconditioned to a greater degree than most other MCP-based systems, resulting in a greater stability in the detector performance.



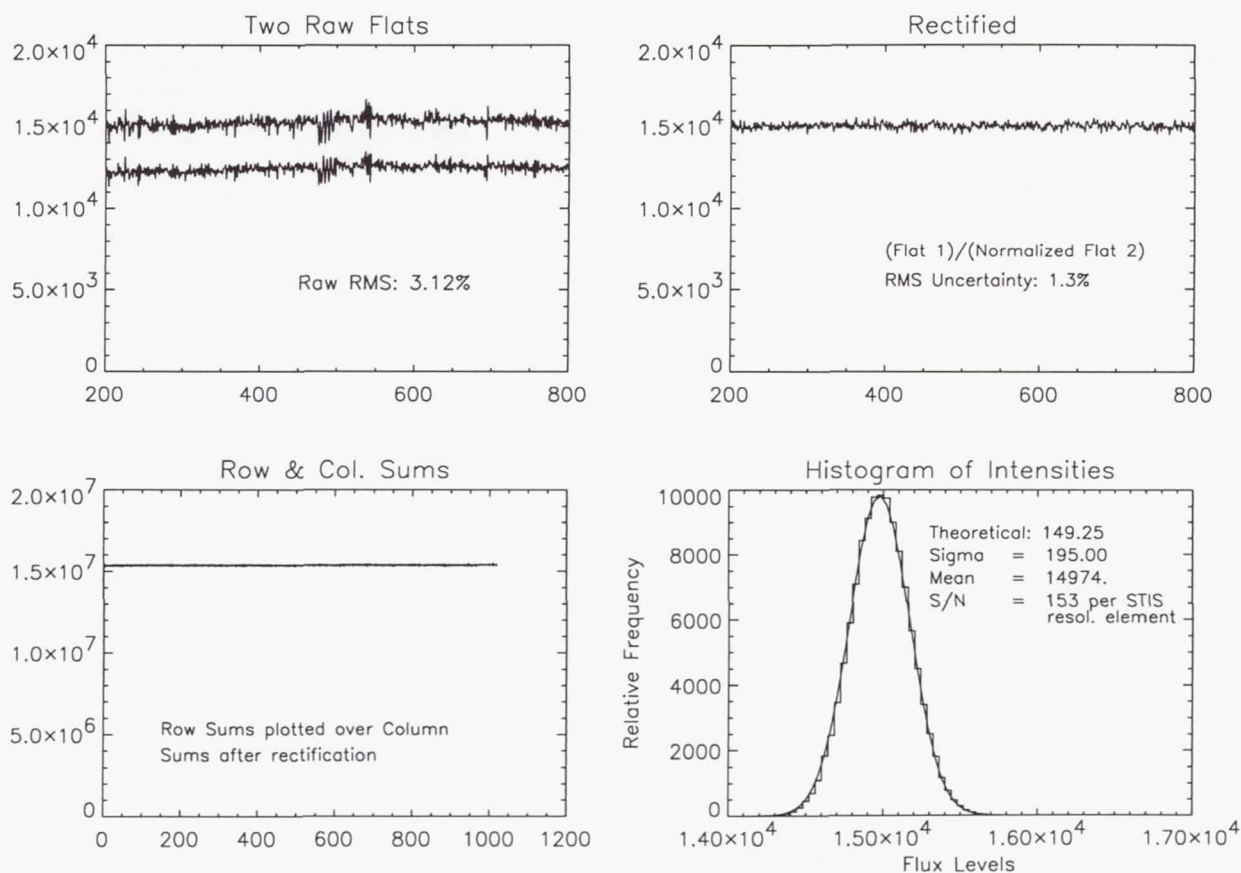


Figure 1. Revealing the stability of the response to a uniform illumination (Flat Field). The top left panel shows the raw pixel-to-pixel variations for a portion of a row, taken on 2 different days. Plotted in the top right panel is the results for same row where the pixel-to-pixel sensitivity from one image is used to remove the detector response of the other. The row and column sums of this corrected image, showing the broad scale stability, are shown at bottom left. A distribution of the intensities of the corrected image is plotted bottom right and is consistent with photon noise-limited data for a signal-to-noise ratio of 153 per STIS resolution element. (A resolution element is taken to be 2x2 pixels.)

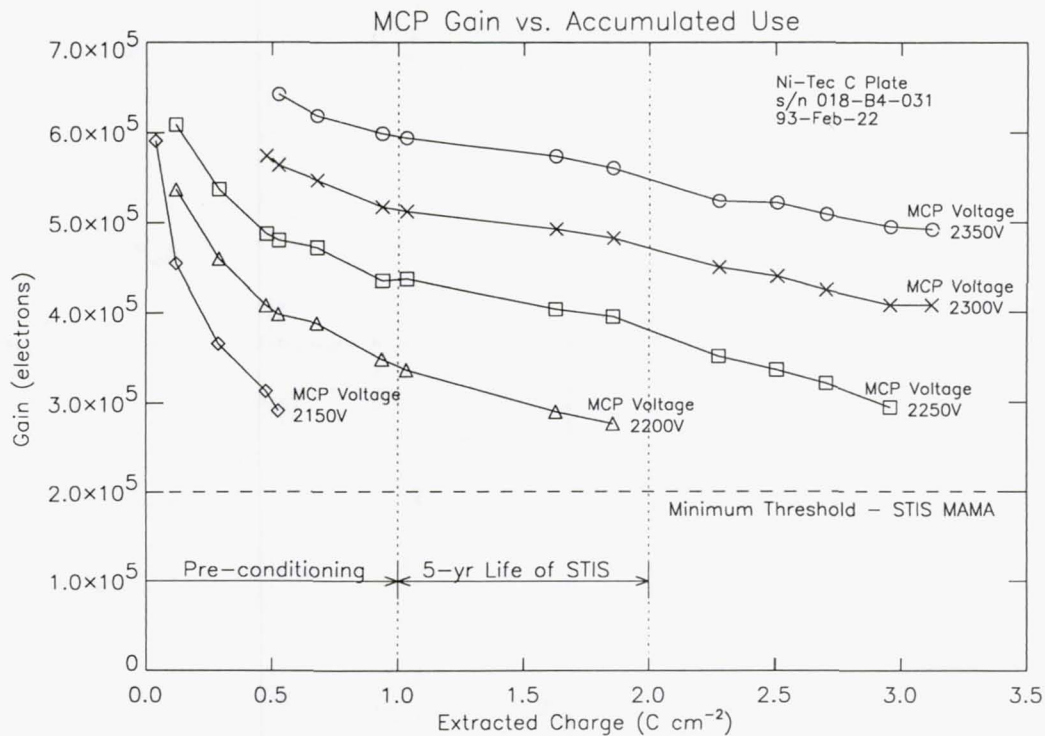


Figure 2. Showing the gain as a function of extracted charge, a measure of the total MCP use. Based on this one parameter alone, the STIS MAMAs should function well for more than 30 years!

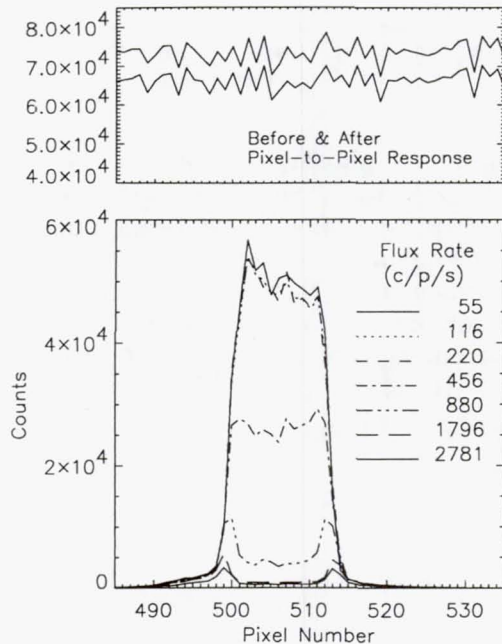


Figure 3. Showing the detector response to an image that is many times brighter than the local dynamic range. Localized gain sag within the MCP at the location of the image causes a temporary loss in counting efficiency leaving the rest of the detector unaffected. This test also demonstrates the safety and robustness of the MAMA detector to bright localized sources for brief periods of time.



Figures 3 and 4 show the response of the MAMA detector to very bright localized illuminations. For flux levels up to approximately  $1000 \text{ counts second}^{-1}$ , a factor of  $20\times$  over specification, the detector responds gracefully by becoming self-limiting and there is no permanent change in the pixel-to-pixel response. For prolonged exposure to extreme flux levels (i.e., above  $6,000 \text{ counts second}^{-1}$  sustained for 2500 seconds), preferential aging of the MCP does occur. Once the bright source is removed, however, the pixel-to-pixel response is once again highly stable.

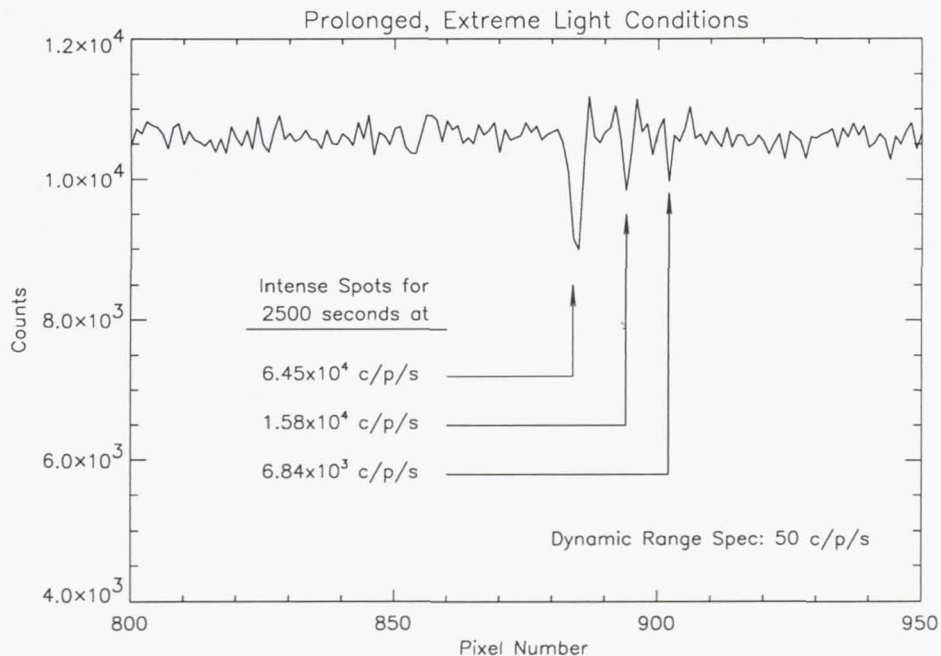


Figure 4. Showing the permanent change in the pixel-to-pixel response due to very bright, localized illumination over extended periods of time. Three spots with the various count rates indicated were imaged onto three locations on the detector. A uniform illumination image (flat field) was used to remove the pixel-to-pixel response from a similar image taken after the exposure to the three bright spots. The dips indicate the relative losses in sensitivity due to preferential aging. Subsequent testing reveal this new pixel-to-pixel response to be very stable.

Finally, there is interest in pushing the detector beyond its inherent limitations and sampling the data at  $1/2$  pixel (hi-res) intervals. The motivation is to obtain the highest resolution data possible even at the cost of some photometric stability. Laboratory testing indicate reasonable stability (sufficient for  $S/N > 20$  per hi-res sample) is maintained over periods of days or weeks, but that changes do occur abruptly and a new "fixed pattern" is established for another unspecified period. The nature of the instability is such that the sensitivity gained/lost in one half of the full pixel appears in the other half, so that the sensitivity sampled at the full pixel size remains constant. In addition, nonlinearities are more severe when the data are sampled in the hi-res mode. These nonlinearities might be confused by some investigators as instabilities. Figure 5 shows raw images of a  $2.5 \text{ mm}$  diameter spot taken at various flux rates. The images are uncorrected for pixel-to-

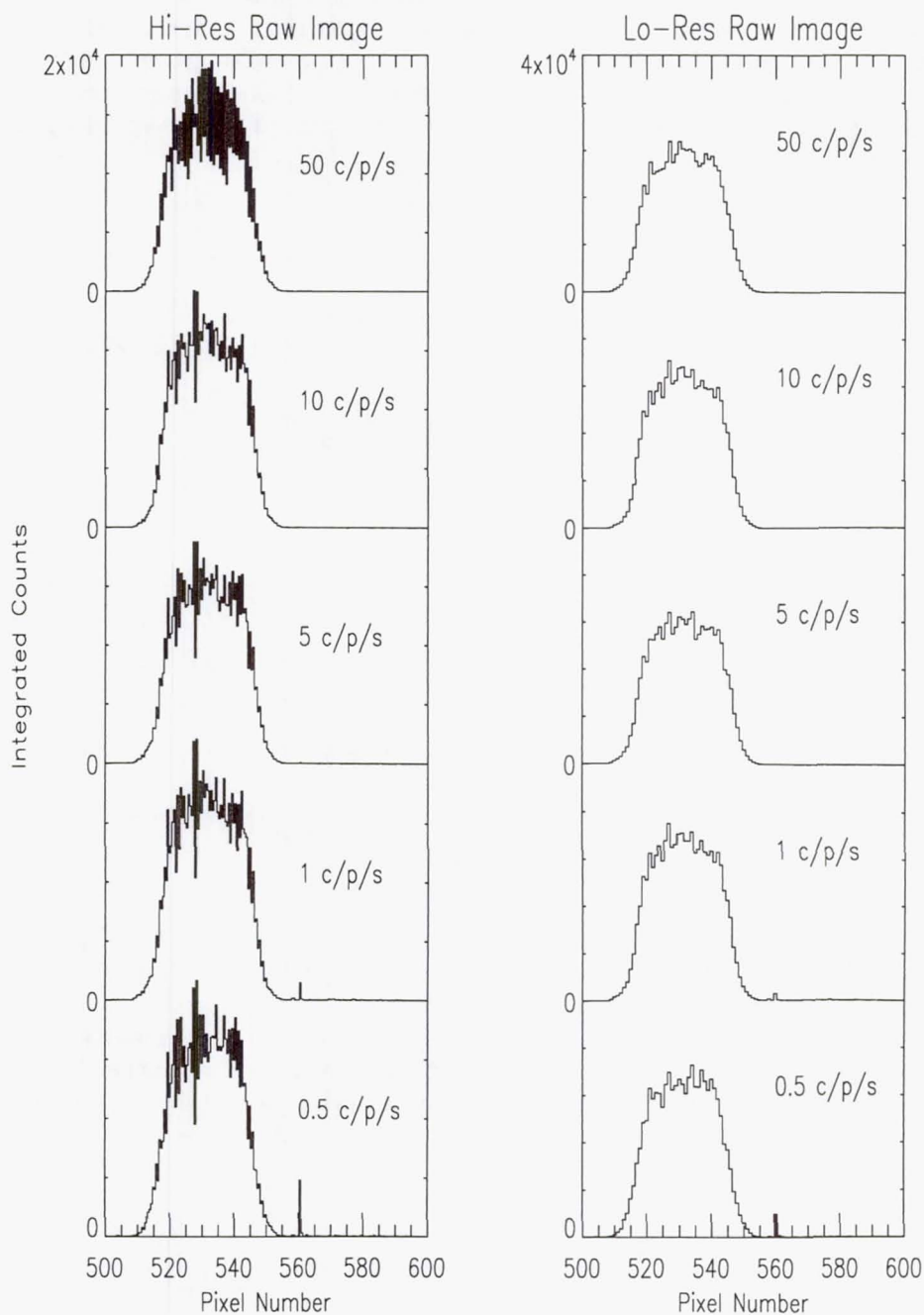


Figure 5. Showing the pixel-to-pixel response to a 100-pixel diameter spot imaged onto the detector as a function of various count rates. Nonlinearities in the individual pores of the MCP caused a change in the pixel-to-pixel response of the sub-pixel sampling (hi-res) case at the higher flux rates. This is not an instability, although some investigators may mistake it as such. As can be seen at the right, the images formed on standard MAMA pixel sampling (lo-res) are more robust, maintaining the pixel-to-pixel sensitivity much better.



pixel sensitivities variations. As can be seen, the pixel-to-pixel sensitivity in the 50 counts second<sup>-1</sup> case is significantly altered in the hi-res but not the lo-res mode.

### Acknowledgement

This work was supported in part by NASA grant NAG5-3158 to Rutgers University. Many individuals at Goddard Space Flight Center and Ball Aerospace Systems Group have made numerous contributions to the development and successful fabrications of the MAMA detectors.

### References

- Joseph, C.L., Argabright, V., Abraham, J., Dieball, D., Franka, S., Styonovich, M., Van Houten, C., Danks, T., & Woodgate, B., 1995, *Proc. SPIE*, 2551, 248
- Joseph, C.L., Bybee, R., & Argabright, V., 1997, in preparation

## Scattered Light in the STIS Echelle Modes

W. Landsman

*Hughes STX, NASA/GSFC, Greenbelt, MD 20771*

C. Bowers

*NASA/GSFC, Greenbelt, Maryland 20771*

### 1. Introduction

The STIS echelle spectra obtained during the Early Release Observations (Heap et al. 1997, Walborn et al. 1997, Jenkins et al. 1997) have non-zero residuals in the cores of saturated interstellar lines, indicating the need for a scattered light correction. A rough measure of the magnitude of the needed correction is given in Figures 1 and 2, which show the ratio of the interorder to the in-order flux in different echelle modes in both pre-launch calibration images of a continuum lamp source (Figure 1), and in post-launch images of stellar continuum sources (Figure 2). The interorder and in-order fluxes are computed by averaging the central 200 pixels in the dispersion direction. The amount of scattered light in the interorder region rises toward shorter wavelengths for two reasons: (1) the order separation decreases toward shorter wavelengths, and (2) the amount of echelle scattering is expected to have an inverse dependence on wavelength (e.g., Cardelli, Ebbets & Savage 1990). At the shortest wavelengths the fraction of light scattered into the interorder region can be 10% for the NUV-MAMA and 15% for the FUV-MAMA.

### 2. Sources of Scattered Light

The strong narrow emission lines of deep platinum line lamp WAVECAL images can be used to isolate the scattering sources in the echelle modes. Figure 3 shows a very deep NUV-MAMA line lamp image taken during the pre-launch calibration, while Figure 4 shows the deepest line lamp image thus far obtained during flight. Both images were obtained with the 0".1 by 0".09 slit. These images do not show extended wings perpendicular to the orders, indicating that the contribution of cross-disperser grating scattered light is negligible. Instead, the two main sources of scattered light are the following:

1. A detector halo surrounds the strong emission lines. This halo is never larger than about 16 pixels in radius. This value should be compared with the interorder spacing, which is about 15 pixels at the shortest wavelengths of both MAMA detectors, and about 40–50 pixels at the longest wavelengths. The size of the detector halo is larger in the NUV-MAMA and has a radius increasing with increasing wavelength.
2. Scattering from the echelle gratings causes a continuum which connects the appearance of an emission line in different orders. Note that this source of scattered light is very "non-local".

Two minor sources of scattered light can also be seen in Figures 3 and 4. First, reflections in the optical path cause a secondary image of the emission lines, as seen at about "five o'clock" off the edge of the haloes of the strong lines. Second, the emission lines near the bottom edge of the NUV-MAMA detector show vertical spikes, whose origin is presently uncertain.



Figure 1. Ratio of interorder to in-order flux for ground calibration data. Each plot includes data from at least two images (marked with different symbols).

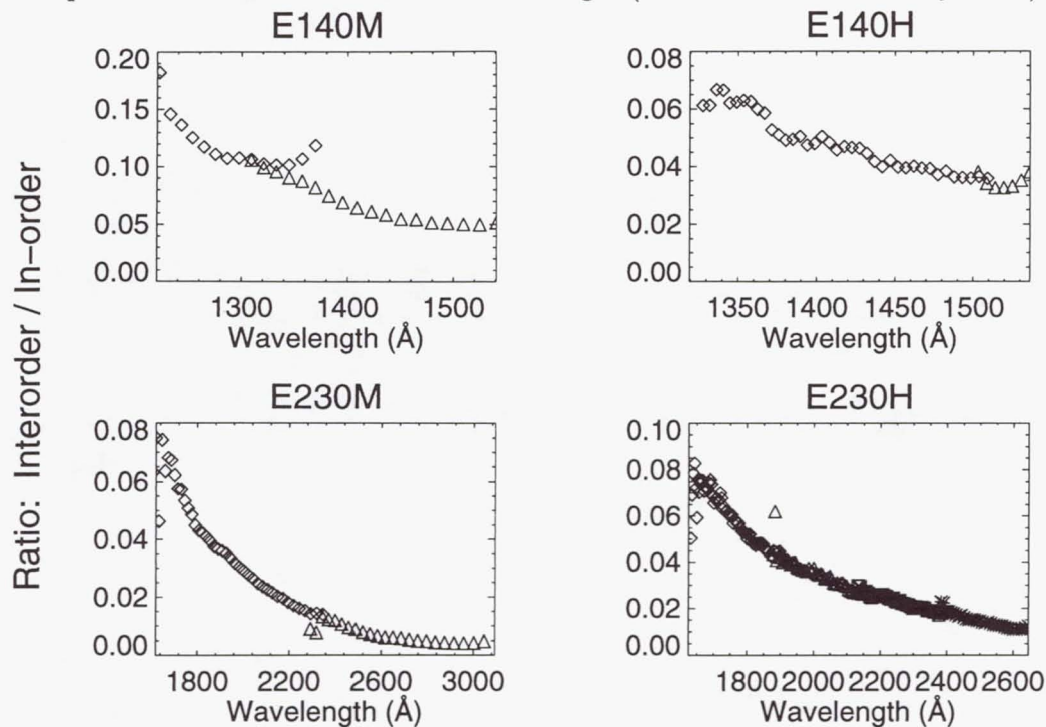


Figure 2. Ratio of interorder to in-order flux for flight data.

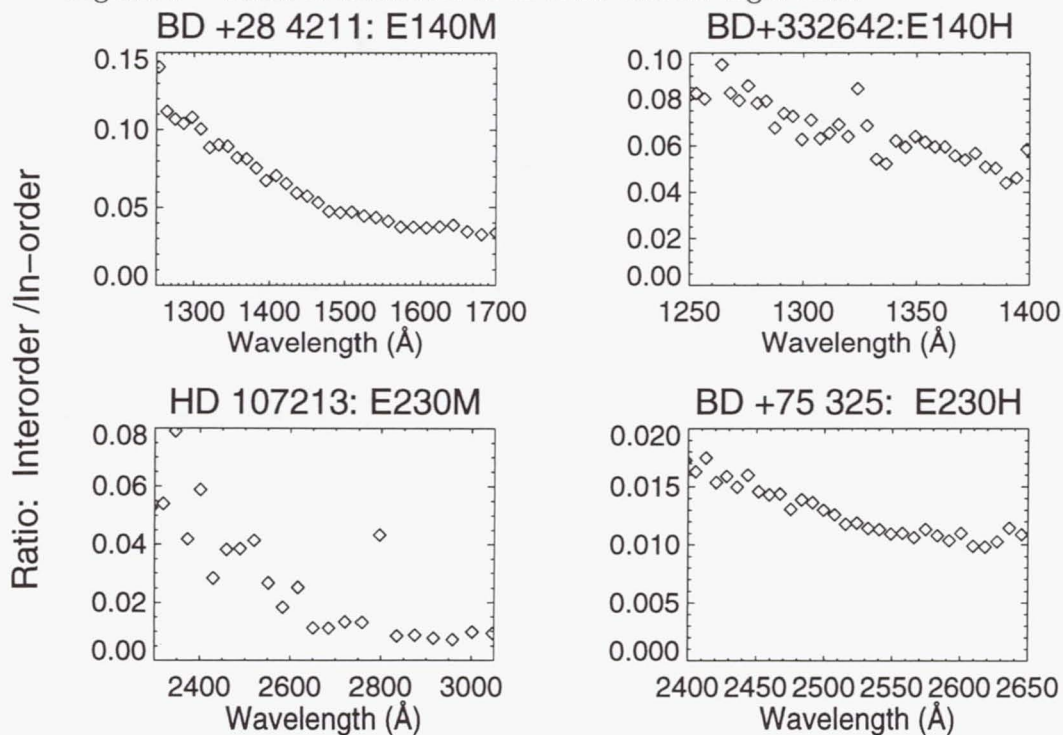


Figure 3. A deep pre-launch calibration E230H line lamp spectrum with a central wavelength of 2762 Å.

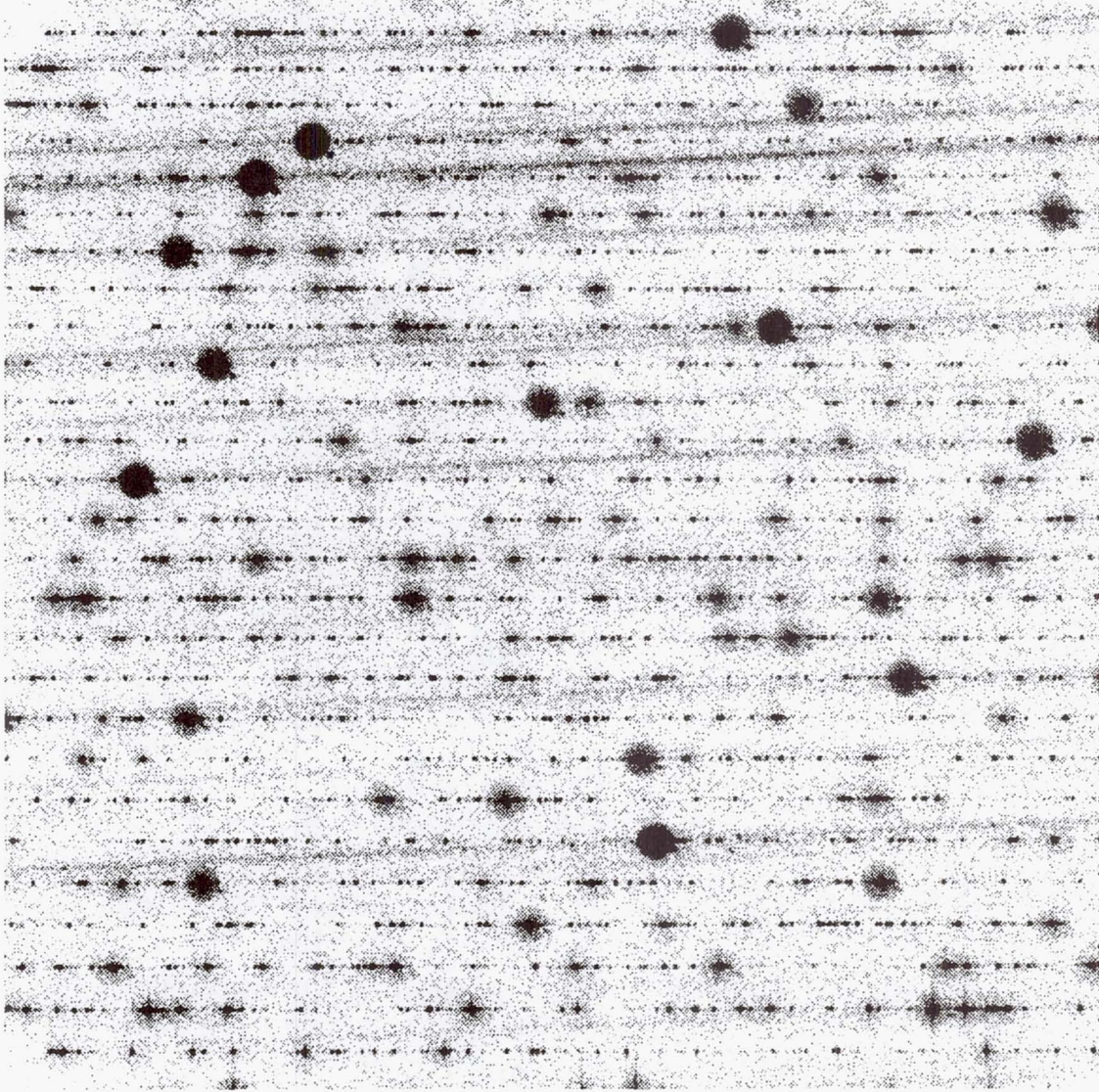




Figure 4. A post-launch E230H line lamp spectrum (O42704KGM) with a central wavelength of 2513 Å.

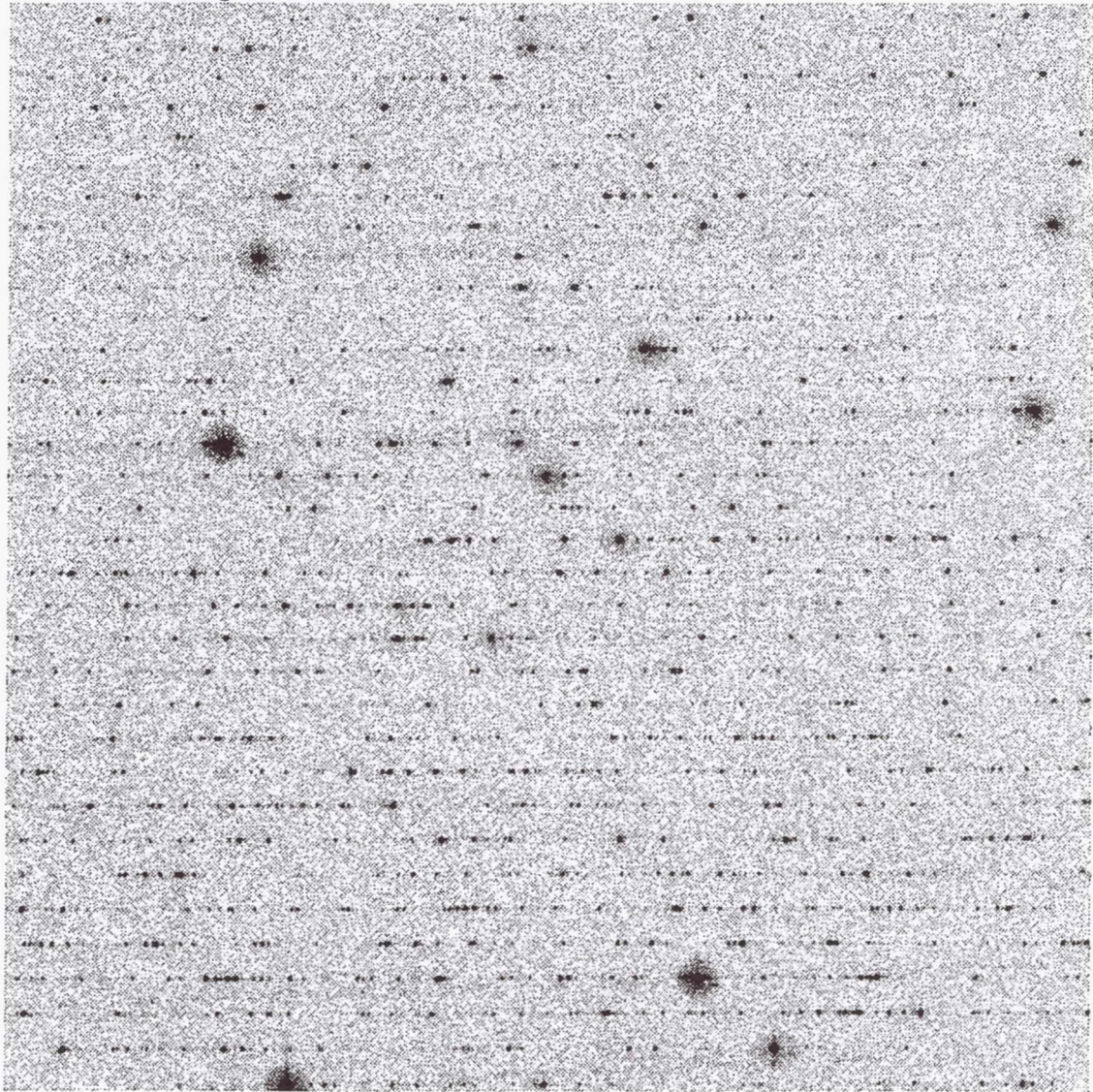
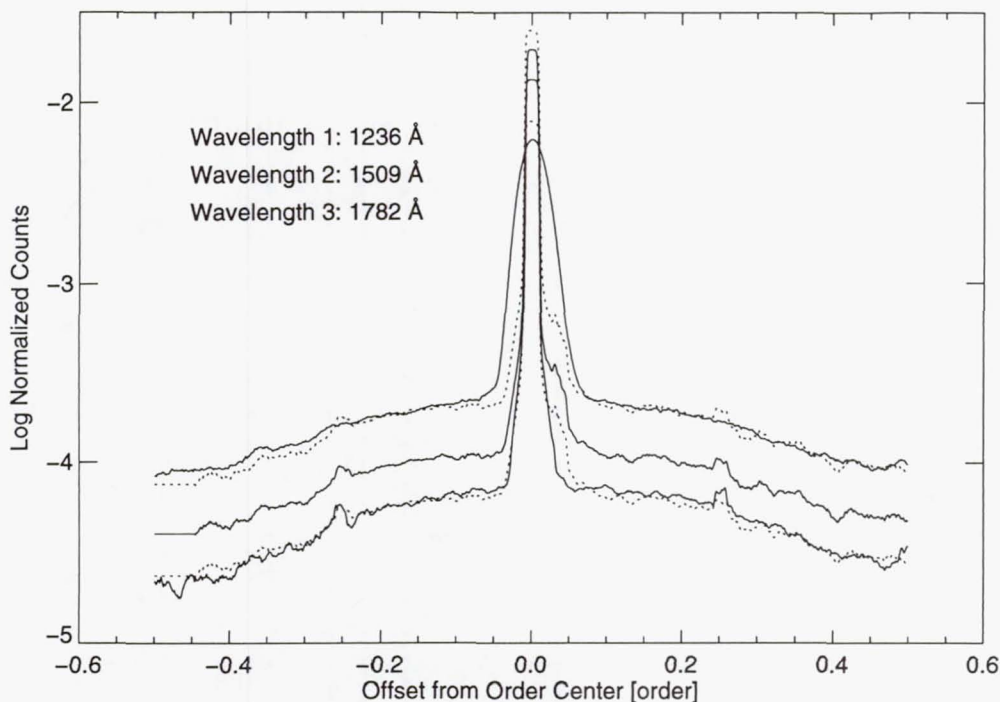




Figure 5. Laboratory measurement of the scattering profile of the E140M grating at three different wavelengths. The dotted lines show the predicted scattering profiles at 1230 Å and 1780 Å computed by scaling the 1509 Å scattering profile by  $\lambda^{-3.2}$ .



### 3. Laboratory Measurements of Echelle Scatter

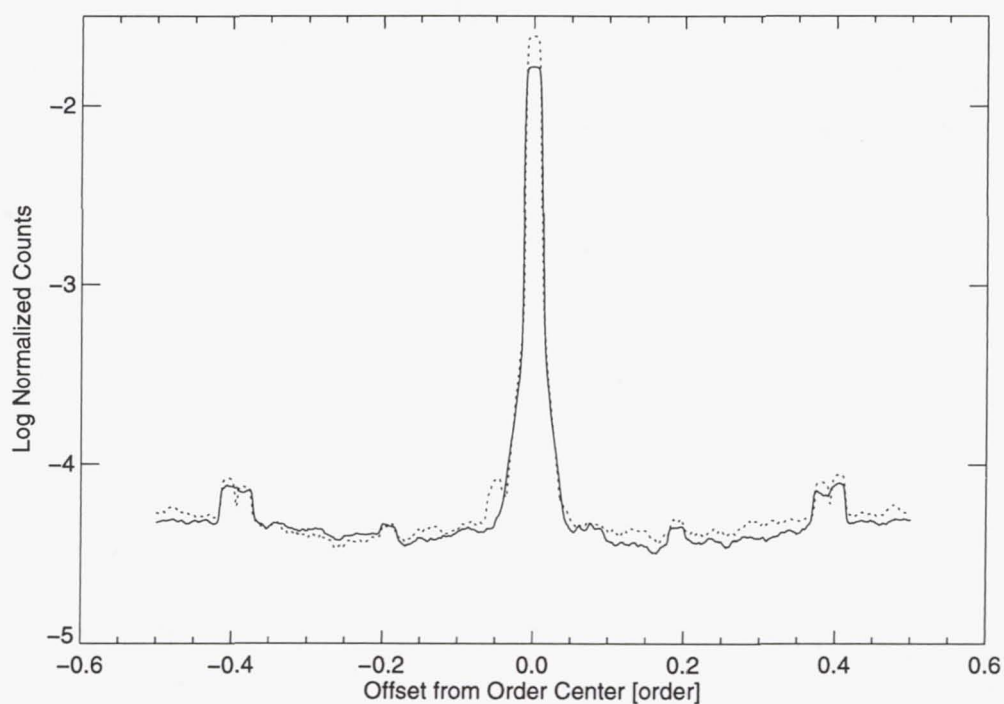
The scattering properties of the STIS echelle gratings were studied prior to their integration into the instrument. Figure 5 shows the scattering function of the E140M grating at 1230 Å, 1509 Å, and 1780 Å. The amount of scattered light is found to be a strong function of wavelength, with a  $\lambda^{-3.2}$  dependence. On the other hand, the amount of scattering in the E140H grating shows little dependence on wavelength (Figure 6), at least for the two wavelengths measured. The scattering profile of the E140H grating is also flatter than that of the E140M grating, and shows more pronounced order ghosts.

### 4. Status

Unlike IUE or GHRS, the scattering in the STIS high-resolution modes appears to be dominated by scattering from the echelle grating, rather than from the cross-disperser. The non-local nature of echelle grating scatter makes a correction algorithm more difficult to implement. The most complete correction algorithm will likely be an iterative scheme, in which an initial spectrum is first extracted without any correction for scattered light, and then convolved with the echelle scattering function and detector response function. The amount of scattered light is then computed and used to correct the initial spectrum. A simpler local correction algorithm (e.g., Bianchi & Bohlin 1984) should still be useful where there are no strong variations in the continuum, or where the order overlap due to the detector halo is significant.



Figure 6. Laboratory measurement of the scattering profile of the E140H grating at 1509 Å (solid line) and 1782 Å (dotted line).



### References

- Bianchi, L., & Bohlin, R.C., 1984, *A&A*134, 31  
Cardelli, J.A., Ebbetts, D.C., & Savage, B.D., 1990, *ApJ*365, 789  
Heap, S., et al., 1997, *ApJ*, submitted  
Jenkins, E., et al., 1997, *ApJ*, submitted  
Walborn, N., et al., 1997, *ApJ*, submitted

## Analysis of STIS Time-Tag Data

Don J. Lindler

*Advanced Computer Concepts, Inc.*

Theodore R. Gull

*NASA/Goddard Space Flight Center*

Steven B. Kraemer

*Dept. of Physics, Catholic University*

Stephen J. Hulbert

*Space Telescope Science Institute*

**Abstract.** Very high time resolution data can be obtained from the STIS MAMA detectors using the time-tag observing mode. In this mode, the photon events are not accumulated onboard the spacecraft. Instead, each event is recorded internally and transmitted to the ground as an  $X$  and  $Y$  location with an event time. Event times are recorded in units of 125 microseconds. Analysis of STIS Crab Pulsar data demonstrates that a time resolution of approaching 125 microseconds can be achieved. Furthermore, the time-tag observing mode has been demonstrated to be a very powerful diagnostic tool and can be used to increase the resolution of both imaging and spectral data.

### 1. Introduction

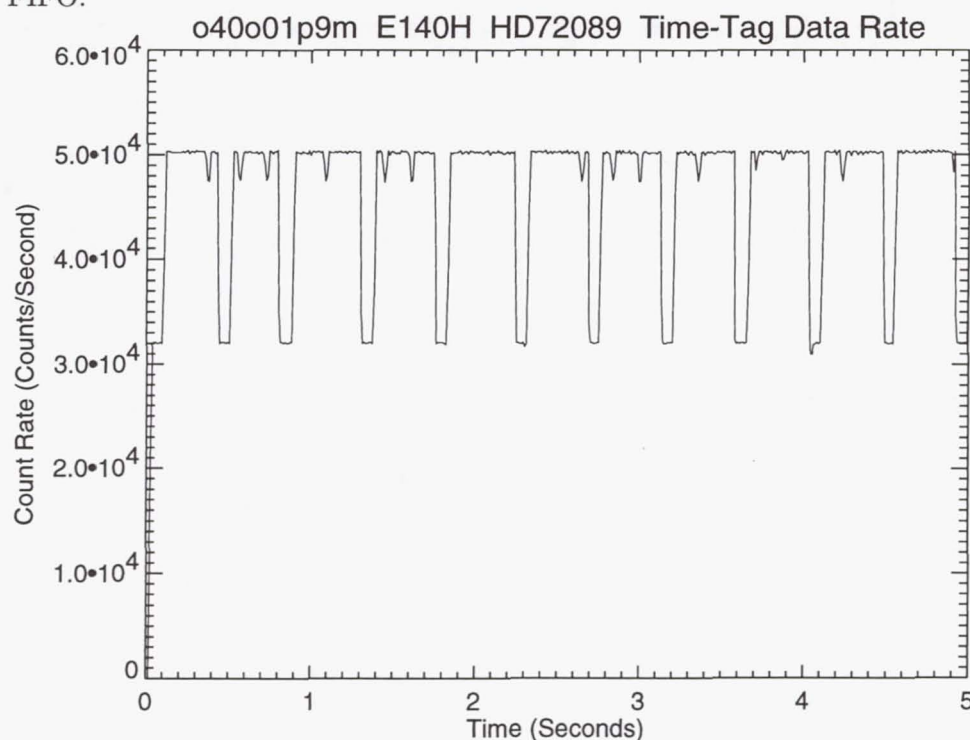
As the MAMA detects events, the  $X$  and  $Y$  locations of the events are placed on a FIFO (First-In-First-Out) data stack which can hold 4096 events. In the MIE (MAMA Interface Electronics) routine that processes time-tag, the FSW (flight software) checks the status of the data FIFO. If the FIFO is half full the MIE will pull off the first 2K events and attach the current fine time to them. This is called "fast" processing, and can run at up to 50,000 events per second. Note, however, that the time-stamping won't be accurate, since it will take much more than one fine time interval (125 microseconds) to process this many events.

If the FIFO is not half full, the MIE will continuously poll the FIFO and pull off each event separately. This process has more overhead and can only process up to approximately 32,000 events/second. The time-stamping is more accurate in this mode and has a 125 microsecond granulation (one fine time interval). In this "slow" mode up to 4 events can be processed in each fine time interval. If there are bursts at higher rates, events after the first 4 will be given later fine time stamps.

Since the trigger between these two processes is the FIFO being half full, there can be discontinuities in the processing. Figure 1 shows the recorded event rate for an observation with an input count rate of approximately 47,000 counts/second. The FSW starts by recording events in the "slow" mode at 32,000 counts/second. Within approximately a tenth of a second, the FIFO becomes more than half-full and the FSW switches to the fast mode and counts at a rate of approximately 50,000 counts/second. Since the input count



Figure 1. The plot shows the recorded event rate for a time-tag observation with an input count rate of approximately 47,000 counts/second. The FSW starts by recording events in the "slow" mode at 32,000 counts/second. Within approximately a tenth of a second, the FIFO becomes more than half-full and the FSW switches to the fast mode and counts at a rate of approximately 50,000 counts/second. Since the input count rate is less than 50,000 counts/second, the FSW alternates between the fast and slow modes depending on the state of the FIFO.



rate is less than 50,000 counts/second, the FSW alternates between the fast and slow modes depending on the state of the FIFO.

## 2. Telemetry Data

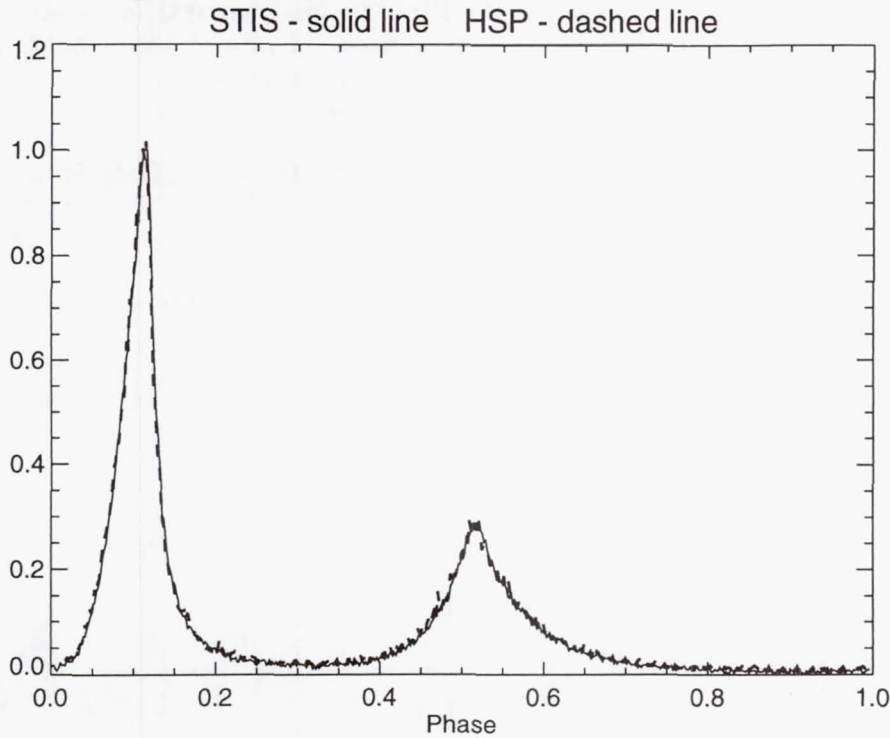
The telemetry data in time-tag mode consist of a series of 32 bit coarse time words and 32 bit fine time words. Coarse time words have a one in the first bit followed by a 31 bit integer giving the time in units of 32 milliseconds (256 fine time intervals). Fine time words contain a zero in the sign bit followed by: an unused bit; an 8 bit fine time (in units of 125 microseconds); and 11 bit *X* and 11 bit *Y* location. The time for any event can be computed by combining the most recent coarse time and the fine time of the event.

## 3. Crab Pulsar Observations

The Crab Pulsar was observed using the grating G230L in time-tag mode on August 7, 1997 (observations o45701c0m and o45701c2m). Two 2400 second exposures in sequential orbits were taken. The processing algorithm is:

1. Read the raw time-tag events (time, *X*, and *Y*).

Figure 2. The plot shows the pulse profile constructed from the G230L Crab Pulsar time-tag data (solid line) compared to HSP observations (dashed line) in the same wavelength band (Percival et al. 1993)

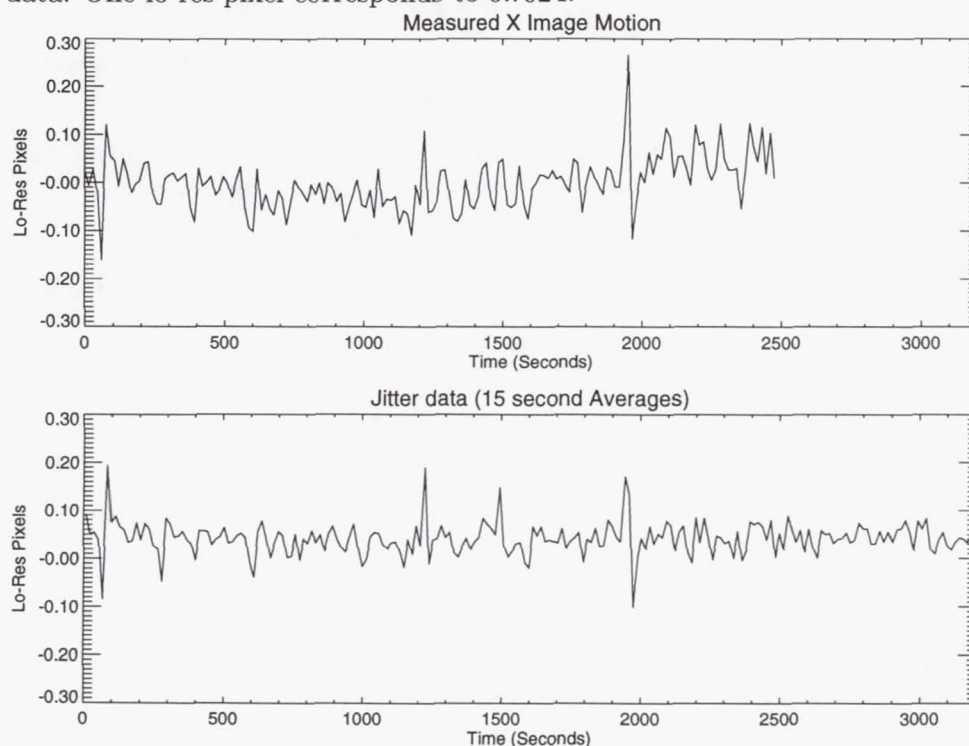


2. Construct an ACCUM mode image by computing the total events at each  $X$  and  $Y$ . This image is used to locate the spectrum to allow selection of time-tag events based on location.
3. Correct the arrival times of the events for the HST position w.r.t. the center of the Earth and the position of the Earth w.r.t. to the solar system barycenter.
4. Select pulsar events with  $X$  and  $Y$  positions within 5 pixels in the cross-dispersion (spatial) direction of the center of the spectrum found in the ACCUM image.
5. Select nebular events with  $X$  and  $Y$  positions within the range of 25 to 35 pixels from the center of the spectrum, both above and below the spectrum. These regions are within the  $2'' \times 2''$  aperture used to observe the pulsar.
6. Compute the period of the pulsar using the events selected in step 4 by maximizing the sum of the squares of the values in a pulse profile divided into 512 time bins (result = 33.473313 milliseconds).
7. Compute the pulse profile of the pulsar by subtracting the pulse profile of the nebular region (normalized to the same area as the pulsar region of the image) from the pulse profile of the pulsar region.

Figure 2 shows that the resulting pulse profile agrees with the HSP observations (Percival et al. 1993) in the same wavelength band.



Figure 3. The plot shows image motion for a FUV-MAMA camera mode image (observation o40q01a5m) of a star field. Positions (centroids) of the brightest stars were determined from images constructed from time-tag data integrated in 15 second periods. The average motion of the stars in the STIS dispersion axis direction are plotted versus time along with a corresponding plot of the FGS jitter data. One lo-res pixel corresponds to  $0.''024$ .



#### 4. Resolution Enhancement Using TIME-TAG Mode

STIS time-tag data can be used to increase the resolution of both spectral and imaging mode data by correcting for the motion of the spectral or imaging format on the detector. Sources of the motion include: Doppler motion due to HST's motion around the Earth; motion caused by changes in the thermal environment; and movement of the target(s) within the aperture due to spacecraft jitter and drift. On-board processing of the data during ACCUM mode will only correct for the Doppler motion. The other sources of motion can result in a loss of resolution.

Two techniques have been successfully used to model and correct for thermal motion. The first uses the time-tag data to estimate the motion. The time tag data are divided into small time intervals (typically a few minutes) and an image is constructed for each time interval. Cross-correlation of spectral or imaging features between the different time intervals can then be used to determine the motion. A low order polynomial (e.g., a linear fit) can be used to model the thermal motion. A second technique is to use wavelength calibration observations taken before and after the science exposure to estimate an average rate of motion during science exposure.

Techniques to use the FGS jitter data to improve resolution are currently being investigated. Figure 3 demonstrates the correlation of image motion at the detector and the spacecraft jitter, as determined by the Fine Guidance Sensors, for a FUV-MAMA camera mode image (observation o40q01a5m) of a star field. Centroids of the brightest stars were

determined from the time-tag data in 15 second intervals. The average motion of the stars in both axes are plotted versus time along with corresponding plots of the FGS jitter data. The significant correlation between the observed motion and the jitter data indicates that correcting for jitter using the FGS data can be used to increase resolution.

## 5. TIME-TAG Observing as a Diagnostic Tool

In addition to analysis of high time resolution science data and correction for image motion, time-tag mode can be a valuable diagnostic tool. Examples of past uses include:

1. Characterization of the output of the internal lamps versus time after turn-on including the wavelength calibration lamp turn on spikes.
2. Monitoring the count rates during the detector's high voltage turn on.
3. Characterization of the "micro-bursts" seen in the NUV-MAMA dark/ phosphorescence data.
4. Measurement of short term image motion.
5. Investigation of anomalous count rate changes in stellar spectra taken for measurement of image motion by correlation of the rapid count rate changes with FGS jitter data.
6. Investigation of short term changes in the camera mode point spread functions.

## 6. Why Not Use TIME-TAG All of the Time?

Considering all of the benefits of time-tag mode over ACCUM mode, it is logical to ask, "Why not use time-tag for all MAMA observations?" There are two primary reasons:

1. Data Volume: Consider an exposure that would generate an ACCUM mode image with an average of 100 counts/pixel. In ACCUM mode, the telemetry volume would be approximately 2 megabytes as opposed to over 400 megabytes generated in the time-tag mode.
2. Observing Efficiency: In ACCUM mode, events can be counted up to approximately 270,000 events/second as compared to 50,000 events/second in time-tag. In ACCUM mode, the observing efficiency could be over a factor of five times higher. Even with input count rates less than 50,000 counts/second, observing efficiency can be decreased in time-tag mode. The STIS FSW maintains a buffer that must be dumped once it is filled. During the dump, additional time-tagged events are not recorded. This is illustrated in a 1420 second time-tag exposure of HD72089 (observation o40o01p9m) where the input count rate is approximately 47,000 counts/second. The observed count rate/time shows periods during data dumping where the count rate drops to zero. For this observation, only 47% of the counts that would have been collected in the ACCUM mode were recorded. By contrast the Crab Pulsar data were collected with 100% efficiency.

## 7. TIME-TAG Data Anomalies Currently under Investigation

1. Analysis of the Crab Pulsar data shows a shift in the event times. The time recorded for each event corresponds to the  $x$  and  $y$  values recorded for the following event. This appears to be a feature of the STIS electronics and can easily be corrected by properly shifting all event times by one event with respect to the  $x$  and  $y$  values as received.



2. Occasional telemetry words, with the sign bit indicating a coarse time word, are found which do not contain valid coarse times. This typically occurs a few times per observation.
3. The fine time word cycles back from 255 to 0 before a coarse time update is received. This occurs in approximately one out of every 16,000 events.
4. The fine time decrements by one between events. This was seen in approximately one out of every 300,000 events.
5. A few fine time words have been seen where the unused bit was set to one. In these cases, the fine time appeared invalid.
6. In one case, the fine time incremented from 82 to 200 and then back to 101 indicating that the word with the 200 fine time is not valid.
7. The period determined for the Crab Pulsar from the STIS time-tag data differed by 0.025 microseconds from the period from an ephemeris.

## References

- Percival, J. W., Biggs, J. D., Dolan, J. F., Robinson, E. L., Taylor, M. J., Bless, R. C., Elliot, J. L., Nelson, M. J., Ramseyer, T. F., van Citters, G. W., & Zhang, E., 1993, *ApJ*, 407, 276

## Determination of Geometric Distortion in STIS Images

Eliot M. Malumuth<sup>1</sup>

*Hughes STX/LASP*

Charles W. Bowers<sup>1</sup>

*NASA/LASP*

**Abstract.** This is a report on the characterization of the geometric distortion of the STIS CCD and the STIS FUV-MAMA detectors when used in imaging mode. We find that the amount of the distortion is fairly small over most of the field. The maximum displacement is 1.66 pixels for the CCD and 2.71 pixels for the FUV-MAMA. This data also allows us to determine the plate scale for both cameras. For the CCD the scale is  $0''.05071 \pm 0''.00007 \text{ pixel}^{-1}$ . For the FUV-MAMA the scale is  $0''.02447 \pm 0''.00001 \text{ pixel}^{-1}$  in  $x$  and  $0''.02467 \pm 0''.00002 \text{ pixel}^{-1}$  in  $y$ .

### 1. Introduction

In order to combine HST images taken of the same field with different pointings or orientations the images must be free of spatial distortions caused by the optical path and/or detector irregularities. This is especially true if one wishes to take advantage of dithering the field at sub pixel spacings to increase the spatial resolution using techniques such as drizzle (Hook & Fruchter 1997). Thus, it is important to be able to predict or measure the distortions so that the images can be rectified in the combining process.

To measure the geometric distortion in the STIS CCD and FUV-MAMA cameras we followed a procedure similar to that used to measure the geometric distortion in the WFPC2 (Holtzman et al. 1995). For the CCD we observed the same field in the outer region of the globular cluster  $\omega$  Cen observed by Holtzman et al. (1995). The central region of the cluster NGC6681 was observed for the FUV-MAMA.

### 2. Strategy

In principle the geometric distortion can be determined by observing a field of stars with known location and solving the following set of equations:

$$\begin{aligned} x_t &= C_0 + C_1x + C_2y + C_3x^2 + C_4xy + C_5y^2 + C_6x^3 + C_7yx^2 + C_8xy^2 + C_9y^3 \\ y_t &= D_0 + D_1x + D_2y + D_3x^2 + D_4xy + D_5y^2 + D_6x^3 + D_7yx^2 + D_8xy^2 + D_9y^3 \end{aligned} \quad (1)$$

where  $x_t$  and  $y_t$  are the true  $x$  and  $y$  positions of the stars, in pixel coordinates measured from the center of the image, and  $x$  and  $y$  are the observed positions of the stars also in pixels measured from the center of the image.

---

<sup>1</sup>Goddard Space Flight Center, Code 681, Greenbelt MD, 20771



In practice, we do not know the true location of stars in a dense enough field to map the geometry of the whole detector at once. However, moving the telescope by a known amount will put the same star in a different location on a second image. The true offsets are determined by the telescope slew and are accurate to  $\sim 0''.02$ . Subtracting equation 1 for a star on image 2 from equation 1 for the same star on image 1 we get:

$$\begin{aligned} (x_{t1} - x_{t2}) &= C_0 + C_1(x_1 - x_2) + C_2(y_1 - y_2) + C_3(x_1^2 - x_2^2) + C_4(x_1y_1 - x_2y_2) + C_5(y_1^2 - y_2^2) \\ &\quad + C_6(x_1^3 - x_2^3) + C_7(y_1x_1^2 - y_2x_2^2) + C_8(x_1y_1^2 - x_2y_2^2) + C_9(y_1^3 - y_2^3) \\ (y_{t1} - y_{t2}) &= D_0 + D_1(x_1 - x_2) + D_2(y_1 - y_2) + D_3(x_1^2 - x_2^2) + D_4(x_1y_1 - x_2y_2) + D_5(y_1^2 - y_2^2) \\ &\quad + D_6(x_1^3 - x_2^3) + D_7(y_1x_1^2 - y_2x_2^2) + D_8(x_1y_1^2 - x_2y_2^2) + D_9(y_1^3 - y_2^3) \end{aligned} \quad (2)$$

where  $(x_1, y_1)$  and  $(x_2, y_2)$  are the  $x$  and  $y$  location of the star on images 1 and 2, and the quantities  $(x_{t1} - x_{t2})$  and  $(y_{t1} - y_{t2})$  are the known offsets between images 1 and 2 in units of pixels.

The CCD field has a large number of bright stars which fairly uniformly cover the whole field but which are not very crowded. The field was observed in a  $5 \times 5$  pattern with a step size of  $15''$  ( $\sim 296$  STIS CCD pixels). Figure 1 shows the center image of the pattern.

The FUV-MAMA field has a large number (over 40) of stars which are bright in the far UV and are spread out fairly uniformly over the whole  $25'' \times 25''$  field of the FUV-MAMA. The field was observed in a  $5 \times 5$  "plus" pattern (i.e., 9 images) with a step size of  $5''$  ( $\sim 204$  STIS low-res MAMA pixels). Figure 2 shows the center image of the pattern.

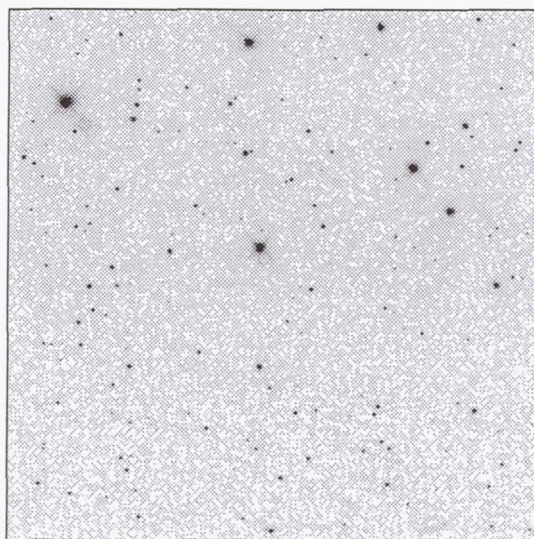


Figure 1. STIS CCD image of  $\omega$  Cen (outer region). This image was the image in the center of the  $5 \times 5$  pattern.

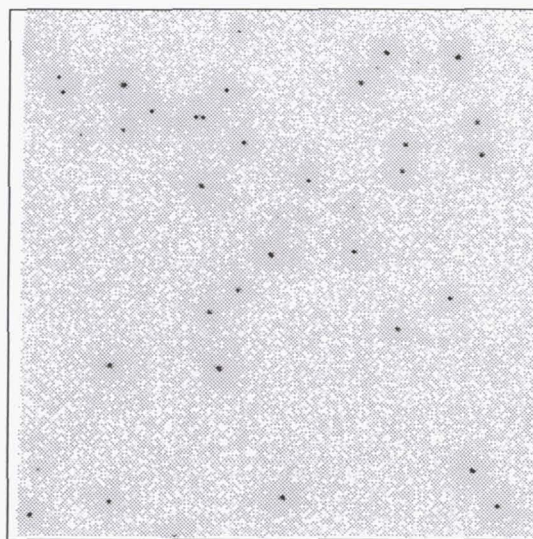


Figure 2. STIS FUV-MAMA image of NGC 6681. This image was the image in the center of the  $5 \times 5$  "plus" pattern.

The special parameter POS TARG was used to move the telescope purely in the  $x$  direction, then purely in the  $y$  direction. In practice the STIS to FGS alignment isn't exactly known, therefore there was a small movement in the other coordinate as well.

### 3. Reductions

Each image was run through the IDL program CALSTIS to perform the standard image reduction steps and to put the data into units of counts second<sup>-1</sup>. The luminosity-weighted centroid  $(x, y)$  of each star on the first image of each data set was determined using an IDL program. Next, the location and centroid of each star found on image 1 was found on the second image by using the image 1 centroids and the known offsets in  $x$  and  $y$ . Then the first program was used to find and centroid all of the stars on image 2 which were not located on image 1. This procedure was continued until each star on each image was found and its luminosity weighted centroid measured. Finally, a program which cross compared all of the star lists was run. The search was done in such a way that only succeeding images were examined so that each pair was identified only once. The resulting table listed the  $(x_1, y_1)$  and  $(x_2, y_2)$  positions of each pair (note that a star on one image could be paired with the same star on several other images—for example, CCD star #2 is on 11 images, so there are 55 pairs). In this way we found 11,338 pairs of stars for the CCD data and 834 pairs of stars for the FUV-MAMA data.

The most critical step was to determine the “true” offset between each image. We decided to use the measured star positions to determine the offsets, because the STIS to FGS alignment isn’t exactly known and the pixel size isn’t exactly known. The shifts between more distant images were found by summing the shifts of the images in between. No measurement of more than one step was used since the overlap region becomes small and far from the center. This procedure showed that there were some unexpected systematic effects. The telescope slews were intended to be purely in one direction or the other, however, as Figure 3 illustrates, there were small shifts in the other direction as well. Figure 3 shows the  $y$  offset of stars in the first CCD image from those in the second image (plus signs), the third image (filled circles) and the fourth image (diamonds) plotted as a function of the  $y$  position of the star. The offset is not only non-zero but a function of the  $y$  position: the higher up the chip the the larger the shift in  $y$ .

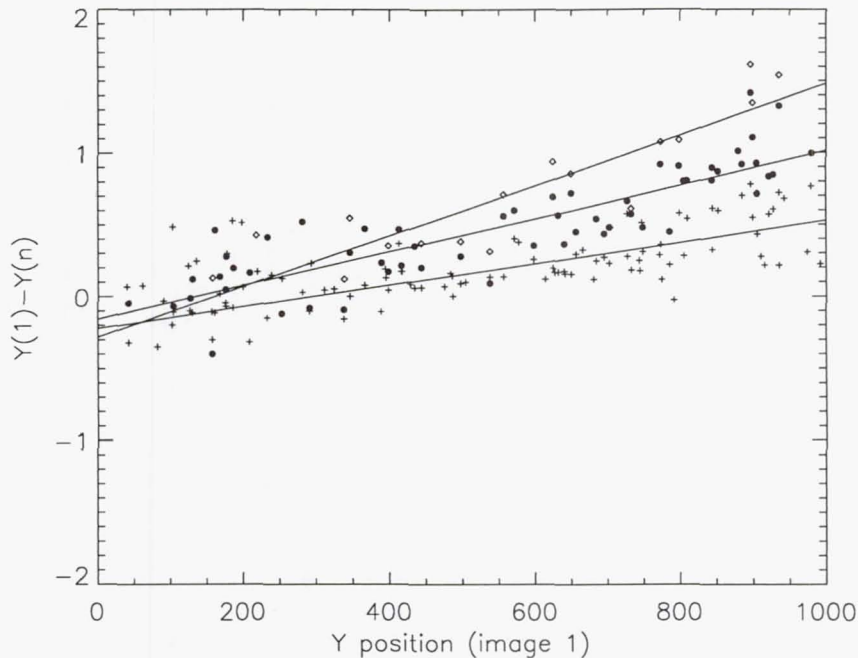


Figure 3. The difference in the  $y$  position of the same stars are shown for CCD image 1–image 2 (plus sign), image 1–image 3 (dots), and image 1–image 4 (diamonds), as a function of the  $y$  position. Notice that there is a systematic shift in the  $y$  position as a function of  $y$ .



Once the average shifts are determined, they can be subtracted from the  $x_1 - x_2$  and  $y_1 - y_2$  pairs to give us a measure of the extent of the distortion. If there were no distortions, all of the differences would be zero. Figure 4 shows histograms of the  $x$  and  $y$  residuals for the CCD, while Figure 5 shows the histograms for the FUV-MAMA. The RMS deviation in  $x$  was 0.410 pixels and in  $y$  was 0.375 pixels for the CCD. For the FUV-MAMA the RMS deviation in  $x$  was 0.591 pixels and in  $y$  was 0.377 pixels.

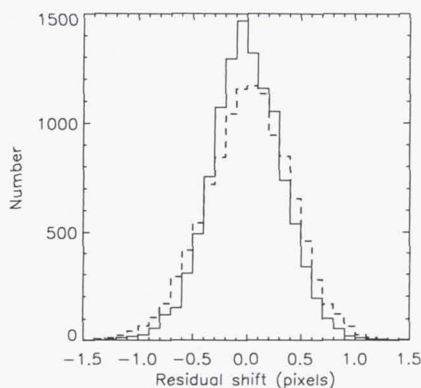


Figure 4. Histogram of the  $x$  (solid line) and  $y$  (dashed line) residuals after the average shift was subtracted from each pair for the CCD.

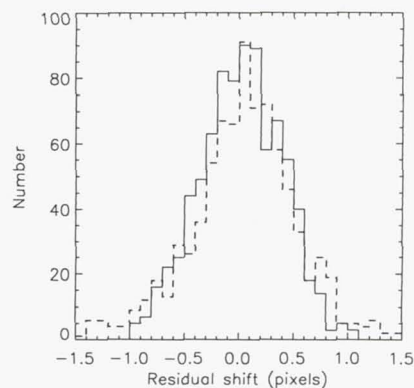


Figure 5. Histogram of the  $x$  (solid line) and  $y$  (dashed line) residuals after the average shift was subtracted from each pair for the FUV-MAMA.

An added benefit of this approach is that we can determine the scale of a pixel at the center of the image from the slews in arcseconds. For the CCD the scale is  $0''.05071 \pm 0''.00007 \text{ pixel}^{-1}$ , with no significant difference between  $x$  and  $y$  directions. For the FUV-MAMA the scale is  $0''.02447 \pm 0''.00001 \text{ pixel}^{-1}$  in the  $x$  direction and  $0''.02467 \pm 0''.00002 \text{ pixel}^{-1}$  in the  $y$  direction. This difference between the  $x$  and  $y$  scales is due to, and consistent with, the  $7.6^\circ$  tilt between the FUV-MAMA camera focal plane and the detector.

A least squares matrix inversion program was used to solve the  $N$  equations (represented in Equation 2) for the 10 coefficients  $C_i$  and the 10 coefficients  $D_i$ . Note that the solution was based on a coordinate system where the central pixel was defined as  $x = 0$  and  $y = 0$ . Thus,  $x = \text{measured } x - 512.0$  and  $y = \text{measured } y - 512.0$ . The constant terms  $C_0$  and  $D_0$  are defined so that the central pixel will be  $(0, 0)$  in both the corrected and uncorrected images. Table 1 shows the determined coefficients for the CCD and the FUV-MAMA images respectively.

Table 1. Geometric Distortion Coefficients

i	CCD		FUV-MAMA	
	$C_i$	$D_i$	$C_i$	$D_i$
0	0.0000000	0.0000000	0.0000000	0.0000000
1	1.0011324	$-5.6351965 \times 10^{-05}$	0.9990498	$-0.0001417$
2	$-1.2427886 \times 10^{-04}$	1.0006398	$-0.0005722$	1.0005972
3	$-3.9052366 \times 10^{-07}$	$1.4414957 \times 10^{-07}$	$2.1279013 \times 10^{-07}$	$6.5272699 \times 10^{-07}$
4	$-2.3388352 \times 10^{-07}$	$2.1911561 \times 10^{-06}$	$6.1468474 \times 10^{-06}$	$4.7377267 \times 10^{-07}$
5	$-2.7747067 \times 10^{-06}$	$-1.5699432 \times 10^{-07}$	$2.3167273 \times 10^{-06}$	$-2.6421370 \times 10^{-06}$
6	$-5.8339901 \times 10^{-09}$	$2.2058683 \times 10^{-10}$	$4.6704462 \times 10^{-09}$	$5.5607193 \times 10^{-10}$
7	$1.4677396 \times 10^{-09}$	$-3.0218644 \times 10^{-09}$	$1.2221236 \times 10^{-09}$	$-8.2054558 \times 10^{-10}$
8	$-3.4363894 \times 10^{-09}$	$8.2253175 \times 10^{-10}$	$-4.5285643 \times 10^{-09}$	$7.4727479 \times 10^{-10}$
9	$6.8542388 \times 10^{-10}$	$-3.1486902 \times 10^{-09}$	$1.5149124 \times 10^{-09}$	$-1.5672843 \times 10^{-09}$

The histograms of the residual differences between positions corrected using equation 1 are displayed in figures 6 and 7. The RMS residuals have been reduced to about one quarter of a pixel (CCD:  $x = 0.245$  pixels,  $y = 0.267$  pixels, FUV-MAMA:  $x = 0.228$  pixels,  $y = 0.264$  pixels).

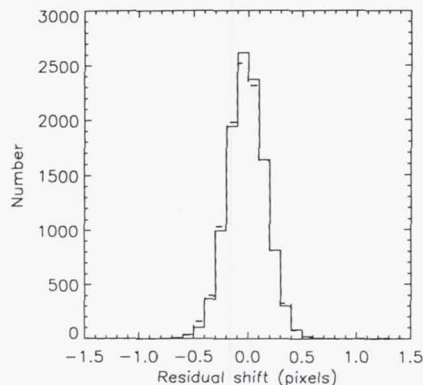


Figure 6. The same as Figure 4 except after a correction to the location of each star using Equation 1 and Table 1 was applied.

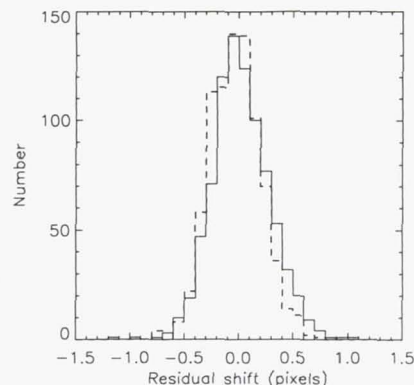


Figure 7. The same as Figure 5 except after a correction to the location of each star using Equation 1 and Table 1 was applied.

Finally, it is instructive to examine exaggerated maps of the distortion. Figures 8 (CCD) and 9 (FUV-MAMA) show the distortion pattern magnified by a factor of 50. The diamonds mark the positions where each star would be if there were no geometric distortion. The lines show the direction to where they were actually detected, the length of the line is 50 times as long as the actual displacement. The largest displacement is just over one and a half pixels (1.66 pixels) in the CCD image, while it is a little over two and a half pixels in the FUV-MAMA (2.71 pixels).

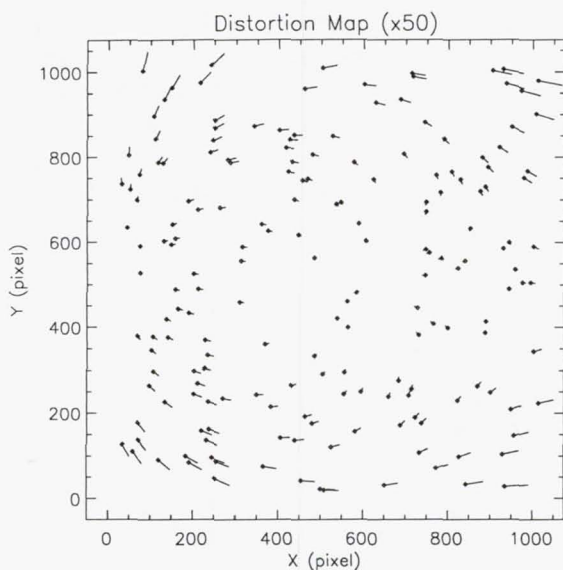


Figure 8. Map of the CCD geometric distortion magnified by a factor of 50.

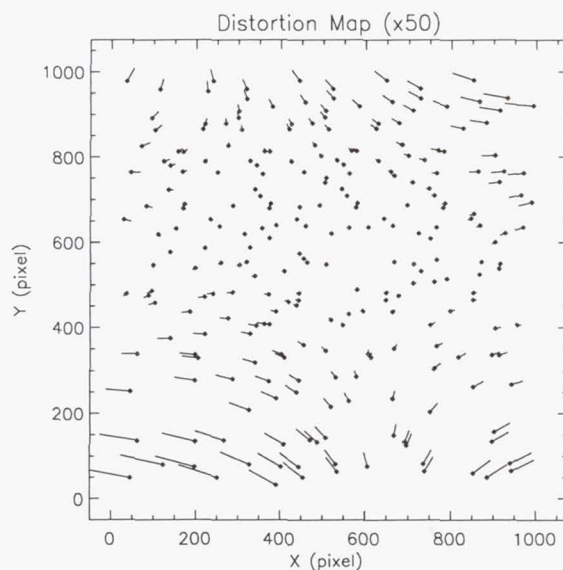


Figure 9. Map of the FUV-MAMA geometric distortion magnified by a factor of 50.



#### 4. Applying the solution

To apply the solution we need to solve for the value of  $x$  given the true value  $x_t$ . However, what we have is the equation that gives  $x_t$  as a function of  $x$  (equation 1). The IDL program CALSTIS\_UNRECTIFY written by Lindler (1997) was used to invert  $X$  and  $Y$  maps made from Equation 1 and Table 1. First,  $X$  and  $Y$  maps are made where the value in each  $(x, y)$  pixel in the  $X$  map is the value of  $x_t$  for that pixel, and the value in each  $(x, y)$  pixel in the  $Y$  map is the value of  $y_t$  for that pixel. CALSTIS\_UNRECTIFY is then used to interpolate within the  $X$  and  $Y$  maps to get the  $X_U$ ,  $Y_U$  maps where each pixel is the value of  $x$  and  $y$  that go to the pixel value of  $x_t$  and  $y_t$ . These maps can be used to interpolate in a STIS image and produce a geometrically corrected image.

An alternative method of applying the solution is to invert the equation and determine the value of the measured position as a function of the true positions. All of the measured positions of all of the stars on all of the images and coefficients  $C$  and  $D$  from above were used to determine the true positions  $(x_t, y_t)$  for all of the stars. We then used Equation 1 (with  $x_t$  substituted for  $x$  and  $y_t$  substituted for  $y$ , etc.) to solve for the coefficients  $C_t$  and  $D_t$  which will give the value of  $x$  and  $y$  as functions of  $x_t$  and  $y_t$ . These coefficients are given in Table 2.

Table 2. Correction Coefficients

i	CCD		FUV-MAMA	
	$C_{t_i}$	$D_{t_i}$	$C_{t_i}$	$D_{t_i}$
0	0.0000000	0.0000000	0.0000000	0.0000000
1	0.9988664	$5.6727465 \times 10^{-05}$	1.0009502	0.0001418
2	0.0001248	0.9993592	0.0005731	0.9994030
3	$3.9591137 \times 10^{-07}$	$-1.4366138 \times 10^{-07}$	$-2.0869856 \times 10^{-07}$	$-6.5273543 \times 10^{-07}$
4	$2.3331625 \times 10^{-07}$	$-2.1919157 \times 10^{-06}$	$-6.1460401 \times 10^{-06}$	$-4.7437861 \times 10^{-07}$
5	$2.7776938 \times 10^{-06}$	$1.5749193 \times 10^{-07}$	$-2.3189523 \times 10^{-06}$	$2.6408455 \times 10^{-06}$
6	$5.8428546 \times 10^{-09}$	$-2.2236194 \times 10^{-10}$	$-4.6635149 \times 10^{-09}$	$-5.5504118 \times 10^{-10}$
7	$-1.4750553 \times 10^{-09}$	$3.0328006 \times 10^{-09}$	$-1.2247637 \times 10^{-09}$	$8.2536032 \times 10^{-10}$
8	$3.4351917 \times 10^{-09}$	$-8.2897208 \times 10^{-10}$	$4.5476076 \times 10^{-09}$	$-7.4670016 \times 10^{-10}$
9	$-6.8621846 \times 10^{-10}$	$3.1482116 \times 10^{-09}$	$-1.5125294 \times 10^{-09}$	$1.5814600 \times 10^{-09}$

#### References

- Holtzman, J., et al., 1995, PASP, 107, 156
- Hook, R. N. & Fruchter, A. S., 1997, in *Astronomical Data Analysis Software and Systems VI*, A.S.P. Conf. Ser., Vol. 125, eds. G. Hunt and H. E. Payne (San Francisco: ASP), 147
- Lindler, D., 1997, private communication

## Fringe Science: Creating a STIS CCD Fringe Flat Field

Philip Plait<sup>1</sup>

*Advanced Computer Concepts, Code 681 Bldg 21 Rm G69A, NASA/Goddard Space Flight Center, Greenbelt, MD 20771; e-mail plait@abba.gsfc.nasa.gov*

Ralph Bohlin

*Space Telescope Science Institute, 3700 San Martin Dr., Baltimore, MD 21218; e-mail bohlin@stsci.edu*

**Abstract.** Internal interference in the STIS CCD in mode G750L causes large amplitude fringing in spectra at wavelengths longer than 7000Å. Flat fields taken contemporaneously with a spectral observation will usually reduce the effect of fringing, but there may be occasions when previously observed flat fields will be more useful. We present a method for modifying long slit (52x0.1 arcsec) internal tungsten lamp flat observations for this use. We find that in many cases, the effect of fringing can be reduced by more than a factor of four.

### 1. Introduction

Fringing is a well-known problem in thinned CCDs such as the one used in STIS. Briefly, light entering the CCD will undergo a series of internal reflections which produces an interference pattern in the spectrum. This fringing pattern is a complicated function of wavelength, CCD face non-planarity and source spectrum, making modeling extremely difficult (Figure 1). The fringing becomes apparent at approximately 7000Å, where the chip becomes semi-transparent to incoming light. The amplitude is variable with wavelength, but has a maximum of  $\sim \pm 20\%$  near 9000Å. This means that any observations using the low resolution G750L grating will be affected by fringing (the medium resolution grating G750M is not affected nearly as much by fringing because of the much smaller bandpass). For point source targets, the best solution in general is to take an observation of the STIS internal tungsten lamp with a short slit as close in time as possible to the primary observation. This method is discussed in detail by Goudfrooij & Baum (1997). However, there are times when this approach is not feasible. For example, a spectral observation of a Seyfert galaxy core may have several knots of emission located along the slit. In this case, the flat field must be sampled at different spatial positions. An extended source will also need a spatially well sampled flat field, and the flat field may need to include scattered light as well. A short short slit flat field will not sample scattered light well, and won't be the best choice for such an observation.

In those cases, or when a short slit flat field simply cannot be done (for example, due to overhead time constraints), a previously observed long slit flat may be the only solution. Many long slit flat fields have already been observed since launch and are public data. Processed properly, these may be useful as substitute flat fields. In this paper we discuss how to process a tungsten lamp observation so that it may be used as a flat field and to reduce fringing. We also discuss the pros and cons of this method.

We'll note here that this method is *not* a panacea for fringing; it does not completely erase the fringing, it may not be applicable in all cases, and worst of all, if not done properly



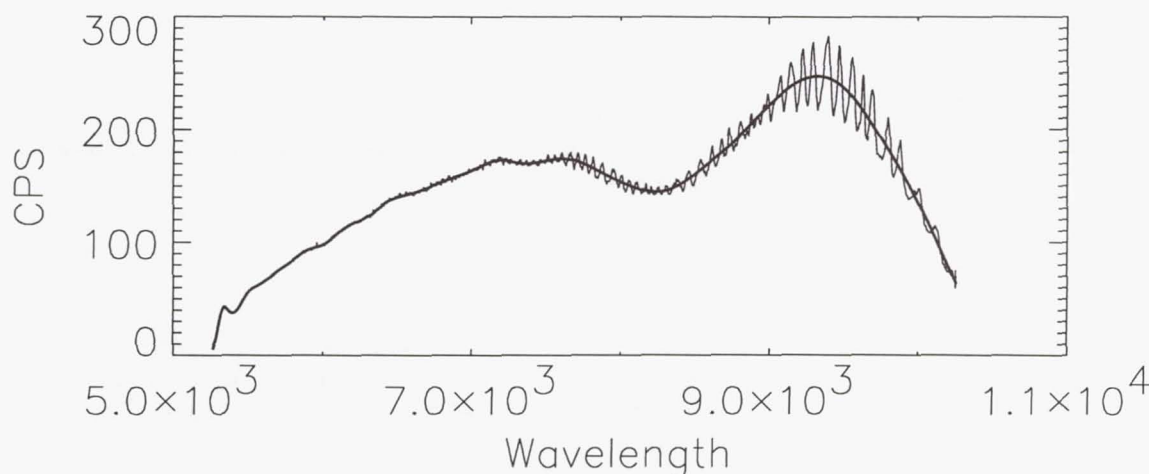


Figure 1. A single row of an unprocessed tungsten lamp observation (thin line) and the result of the spline fit (thick line, see section 2.2).

it can actually increase the amount of fringing. If possible, we always recommend taking a contemporaneous flat field with your observations.

## 2. Making the Flat Field

Assuming you have no flat field observation taken with your data, where should you start? Numerous long slit flat fields have been taken that are public data; a search of the Hubble Data Archive will find them (excellent software such as STARVIEW is available for searching the archive—use proposal ID 7642, 7063 or 7095 to find some of the tungsten lamp observations). A good example is observation O3TT42030, taken on May 21, 1997. This is a well-exposed tungsten lamp observation using the 52x0.1 arcsecond slit, and is what we use below as our example.

However, take care! Not all flats are the same. Unfortunately, two observations with even slightly different central wavelengths will have fringe patterns that do not shift identically. Grabbing any old tungsten lamp observation to make a flat field will not necessarily work, and *may make the situation worse*. The fringes *must* line up well with your observation, or else you might wind up dividing by fringes that are off by half a phase, making your problem twice as bad. Luckily, there is a relatively straightforward, if tedious, solution: download as many long slit tungsten lamp observations as you can find in the archive (at the time of this writing there are perhaps twenty), and cross correlate the fringes in each one with the fringes in your observation. You want the minimum shift, of course, but you must still be careful: a shift of more than 3 pixels means the tungsten lamp flat will not do a good job removing the fringing, even if the flat is shifted to compensate. Due to the limited number of tungsten lamp observations, however, you may not have a choice. If at all possible, you should take a contemporaneous tungsten lamp observation, and should also use a slit that is concentric with the slit used for your target observation. This ensures the central wavelength will not shift by very much.

Once a long slit lamp observation is obtained, some processing must be done to prepare it. Besides the usual processing, the lamp observation must be normalized to remove

instrumental effects, which includes fitting the lamp function and removing scattered light, if necessary. When finished, the final flat field should contain the fringing pattern and the pixel-to-pixel variations, but not any of the broader STIS response patterns. It should also be normalized to unity.

### 2.1. Initial Processing

We recommend doing the initial processing of the tungsten lamp observation in the usual way; removing the cosmic rays and the dark and bias frames in your favorite manner. Some tungsten lamp observations have multiple readouts making cosmic ray removal easier. Divide the image by the clear aperture camera mode flat field to remove blemishes and other CCD related variations in the image; we do not want to fit these features. After the image has the lamp function removed, the camera flat will be multiplied back in. Hot pixels are a different issue from cosmic rays; the CALSTIS pipeline will remove known hot pixels, but the effects of "cooler" pixels may not be removed, and they can adversely affect the removal of the lamp function. For display purposes, we find that dividing the image by the boxcar smoothed image makes the remaining hot pixels stand out well. For our processing we replaced these pixels with the median value of a small box centered on the pixel in question.

### 2.2. Lamp Function

The lamp function is the response of STIS to the lamp versus wavelength, and removing it is the most difficult and tedious step of this processing. The lamp function can be seen in Figure 1 as the broad-ahumped shape of the plot. To remove it, we made a low-frequency spline fit to each row of the observation, which was then divided into the observation; in a sense flattening the observation. Care must be taken to fit all the broad features of the observation (including the large amplitude bump at the extreme blue end caused by the order blocker), but not the fringes or the pixel-to-pixel variations, which of course must remain for the image to be useful as a flat field. That is why the cooler hot pixels must be carefully removed—the spline fit will produce large amplitude ringing around any hot pixels remaining in the image. The sensitivity curves for STIS (Collins & Bohlin 1997) have the STIS response built into them, and will take care of the broader features.

We were able to produce excellent fits using a second order spline with about 50 nodes. The large number of nodes is needed to accurately sample the relatively rapid variations in the lamp function at the blue end of the observation. At the red end, nodes were placed much farther apart, so that the broad features, and not the fringes themselves, were fitted. Figure 2 shows the results of this processing along one of the rows. Note that the slit-occulting bars will not be fitted well, but these areas of the image will not normally be used in the processing of spectra anyway, so the poor fit is not important. When this processing step is done, multiply the image by the clear aperture camera mode flat field, to put the blemishes and other detector features back into the image.

### 2.3. Scattered Light

A point source spectrum will not usually have scattered light in it, but the long slit tungsten lamp observation will. The CCD has a substantial halo towards the red end, and light from one row of the chip will "leak" into adjacent rows. This adds a pedestal to the lamp observation which must be removed to model a point source flat field. For an extended target, it may be beneficial to leave this scatter in the flat field, but be warned that the scattering is wavelength dependent, and the tungsten lamp is not likely to have the same flux distribution as the source.

The lamp observation (normalized to unity by the removal of the lamp function) is a combination of wavelength-dependent features (i.e., the fringing) and wavelength-independent features (i.e., the pixel-to-pixel variations). The wavelength-independent fea-



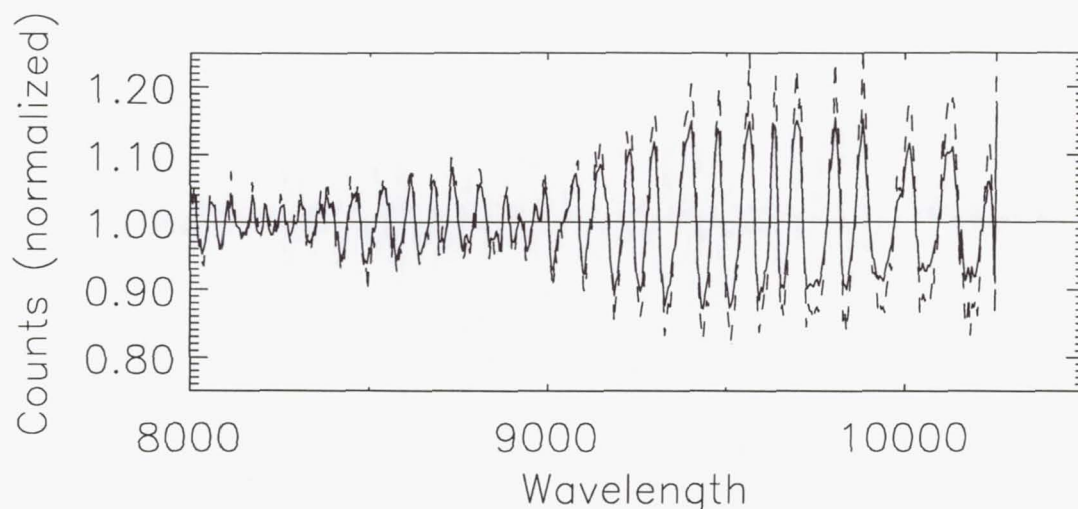


Figure 2. A single row of a processed tungsten lamp observation (solid line) and the same row with scattered light removed (dashed line, see Section 2.3).

tures may be more properly called “wavelength-averaged features” since the camera mode image will average the tungsten lamp spectrum over the detector’s spectral range. The observation can then be represented mathematically as

$$F_{obs} = SL \times F_{cam} + (1 - SL) \times F_{\lambda} \quad (1)$$

where  $F_{obs}$  is the observed tungsten lamp image,  $SL$  is the scattered light profile,  $F_{cam}$  is an image containing the wavelength independent features (that is, the clear aperture camera mode flat field, also available from the Data Archive), and  $F_{\lambda}$ —the final flat field and the goal of this whole process—is the image with the wavelength dependent features. The scattered light profile can be determined roughly by taking a cut across the lamp observation behind the slit’s two occulting bars, normalized to cuts taken just above and below the occulting bars. We found that the scattered light profile was very similar in both bars, so we recommend simply averaging them to increase the signal-to-noise. As a test, we used different multiplicative constants on the scattered light function to check if we were under- or overestimating the profile, but found that simply taking a cut across the bars worked quite well.

The results of this operation can be seen in Figure 2, where a row from processed flat field is compared to the same row after scattered light removal. Note that after removing the scattered light, the amplitude of the fringes *increases*. This is because the pedestal has been removed, so the ratio of the amplitude goes up (a 10 count amplitude, for example, is negligible compared to a spectrum with 10000 counts per pixel, but is large if the spectrum has only 100 counts).

The final flat field,  $F_{\lambda}$ , should now contain only the fringing, pixel-to-pixel variations and blemish maps. Congratulations! You are ready to flat field your observation.

### 3. Applying Your New Flat, With An Example

To flat field the image, simply apply the flat as you normally would any flat field. The fringes in the flat may not line up perfectly with the fringes in the target observation, so it

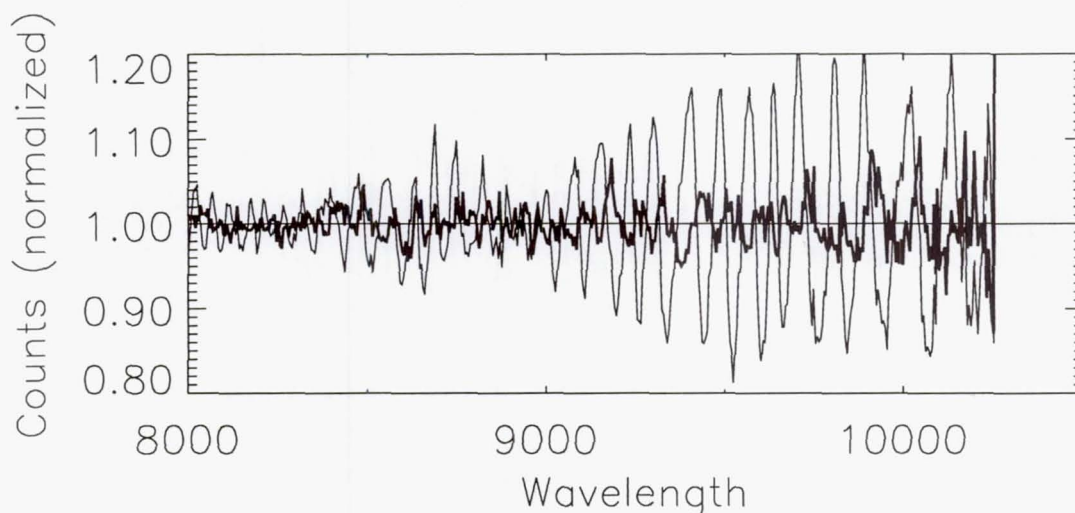


Figure 3. The un-flattened calibrated spectrum of GD153 (thin line) and the corresponding flattened spectrum (thick line).

is helpful to process the target observation with and without the flat field applied, to see just how well the fringes were removed.

You may find that you need to shift the flat field a bit to get the fringes to line up. A cross correlation of the fringes between your target and the processed flat field should yield an accurate shift (remember to keep it to 3 pixels or less). However, shifting the fringes also shifts any blemishes in the camera mode flat as well. Before shifting, divide by the camera mode flat, shift, then multiply the camera mode flat back in to keep the blemishes in the same place.

Using the method outlined above, we processed the flat field O3TT42030 to produce a fringe flat and applied it to the observation O3TT48040, a G750L spectrum of the photometric standard star GD153 (the same star used by Collins & Bohlin 1997 to determine the STIS sensitivity). Figure 3 shows the normalized spectrum of the star with and without the processed fringe flat field applied. The fringe amplitude dropped from an rms of 8% (from 7000 to 9000 Å) to  $\sim 1.5\%$  after flat fielding.

Note that the fringe removal is not complete, and adds some systematic noise to the spectrum. By comparing the spectrum calibrated without the flat field to the spectrum that did use the flat field, it is not hard to see what features arise from misaligned fringes. We strongly recommend making this comparison as a check on this.

#### 4. Conclusions

A long slit tungsten lamp observation can be converted into a flat field that reduces the rms fringing in a STIS G750L observation from 8% to  $\sim 1.5\%$ . There are several pros and cons to this method:



**PROS:**

- Many tungsten lamp observations are available for processing.
- Multiple targets can be flat fielded simultaneously.
- Scattered light can be removed adequately for point source targets.
- This method is a reasonable substitute if no contemporaneous flat field was taken (although again we stress that a contemporaneous flat field should be taken if at all possible).

**CONS:**

- There may not be a tungsten lamp observation that matches your target observation fringe pattern.
- A shifting mismatch will make the fringing worse.
- Even a good match will leave some residuals that look like spectral features. A comparison between using the flat and using no flat is **strongly** recommended to identify such features.
- The processing needs to be meticulous and can be very time-consuming.

**Acknowledgments.** We acknowledge the generous help and advice of Don Lindler, Eliot Malumuth and Nicholas Collins.

**References**

- Goudfrooij, P., & Baum, S. A., 1997, this volume  
Collins, N., & Bohlin, R., 1997, this volume

## Extraction of Point Source Spectra from STIS Long Slit Data

J. R. Walsh

*Spect Telescope European Coordinating Facility, European Southern Observatory,  
Karl-Schwarzschild Strasse 2, D-85748 Garching, Germany*

**Abstract.** STIS provides a unique opportunity to obtain spectra of point sources from very crowded fields and complex scenes, such as galactic nuclei, utilising high spatial resolution. A small suite of programs is described for simple and optimal extraction of point source spectra, targeted specifically at STIS data. A multi-channel (spatial) restoration is also under development using the method employed by Lucy and Hook for imaging data. The algorithms are briefly described and applications to STIS SMOV data illustrates the potential.

### 1. Introduction

STIS long slit spectra can be obtained both with the MAMA and CCD detectors with slit lengths of  $24''.6$  and  $51''.2$  respectively. The Line Spread Function (LSF) of the spectrometer in the spectral direction is excellent (2.0 pixels FWHM for the CCD and about 3.0 for the MAMAs); the Point Spread Function (PSF) of the telescope and instrument is 4.3 pixels ( $0''.10$ ) for the FUV-MAMA at  $1430\text{\AA}$  and 3.2 pixels ( $0''.08$ ) for the NUV-MAMA at  $2400\text{\AA}$ ; at  $7750\text{\AA}$  the FWHM is 2.3 pixels for the CCD ( $0''.12$ ). The MAMA detectors suffer from a halo of radius about 20 pixels (worse for the NUV MAMA—Fig. 7.3 in Baum et al. 1996) and the CCD shows a halo at wavelengths beyond  $7000\text{\AA}$  increasing in strength to longer wavelengths; these haloes add a pedestal to the otherwise narrow PSF. In comparison with ground-based long slit spectrographs, STIS offers a very stable PSF—one which is suited to well defined extraction methods and also to image restoration.

With excellent spatial resolution and a stable PSF, STIS is thus ideally suited to obtaining spectra of point sources in crowded fields—such as stellar spectra of stars in globular clusters, spectra of single stars in nearby galaxies (e.g., supergiants, supernovae), resolution of the spectra of close visual binaries and faint companions in multiple star systems, compact emission line knots in nearby nebulae (e.g., Herbig-Haro objects), the spectrum and hence velocity dispersion in stellar cusps in galaxy cores and the emission from AGN resolved from the surrounding narrow line region or circumnuclear starburst. Indeed many of the STIS GO and GTO programmes reflect these advantages and this is one of the areas in which STIS will have the greatest scientific impact, since FOS already offered large continuous wavelength coverage and GHRS a high spectral resolution UV capability.

There are excellent tools available for the extraction of spectra from long-slit data such as in the IRAF TWODSPEC.APEXTRACT package. Whilst they are not designed for STIS data, the STIS pipeline data can be easily adapted to their use. However, the fixed PSF of STIS suggests that the extraction of point source spectra from complex scenes could be optimized for this instrument. In response to these differences a package of routines is in preparation, to be run under IRAF, to specifically handle STIS long slit data. This contribution provides a brief description of the elements of the package so far built and the plans for implementing (spatial) restoration tools aimed at exploiting to the full the 2-D spectral data from STIS.



## 2. Software Package

The baseline was to provide a tool for optimal extraction of point source spectra from STIS long slit spectra. This can be done with the IRAF interactive task APALL. However, since pipeline calibrated STIS data come with carefully produced data quality and propagated statistical error images in the association, these should be fully incorporated in the extraction software. The usual implementations of the optimal extraction algorithm, such as that due to Horne (1986) and Robertson (1986), and later improvements such as for distorted spectra by Marsh (1989) and for cross dispersed spectra by Mukai (1990), determine the spatial PSF from the data itself, fitting it in the spectral direction to form the extraction weights ( $W_{x\lambda}$ , see Horne 1986). However, given the fixed PSF for STIS, the extraction weights could be a priori assigned using a model PSF. The TIM (<http://www.stsci.edu/ftp/software/tim/>) and TinyTim (<http://scivax.stsci.edu/~krist/tinytim.html>) packages allow PSFs to be constructed for HST instruments, such as WFPC2 and NICMOS for example; as yet no implementation in TinyTim for STIS is available, although one is planned (Hook, private communication) and would be very useful for enhancement of both imaging and long slit spectral data.

A number of routines have been written in FORTRAN 77, using F77VOS for the data I/O, for spectral PSF image manufacture, simple extraction, profile fitting and optimal extraction. Under development are a 2-channel restoration tool and enhancements for multiple object spectral extraction. The input data are the reduced STIS associations (bias corrected, flat fielded, hot pixel cleaned, cosmic ray rejected and wavelength and flux calibrated) and the output point source spectrum is written as an STSDAS table with columns of wavelength, flux, propagated statistical error and data quality.

### Spectral PSF image

A number of images of model PSFs at different wavelengths are read and a long slit "PSF spectrum" is formed. The pixel size and slit width can be adjusted and the slit can be offset from the centre of the source in the wavelength direction. The integrated spatial profile of the PSF at the different wavelengths are formed and interpolated onto the wavelength grid of the data frame to be analysed. This is used for subsequent processing.

### Simple extraction

Simple extraction of the spectrum is achieved by fitting the background column-by-column (where the slit length is in the column direction and the dispersion in the row direction) and summing the point source over some selected extent (e.g., to 1% of the peak). Various forms of fit to the background are possible such as low order polynomial (for isolated point sources) or interpolation (e.g., cubic spline). Fitting the PSF image to the data can also be performed and the point source flux can be summed over the PSF rather than the data—this allows imperfections and cosmic rays to be distinguished and rejected from the spectrum. The extracted spectrum is output as a table and the background image, without the point source, can be saved.

### Optimal extraction

Optimal extraction is performed using the Horne (1986) algorithm and a polynomial is fitted to the wavelength variation of the PSF with iterative rejection of points a selected distance from the fit. The background is subtracted from the image prior to optimal extraction and the errors are fully propagated. The point source spectrum is again an STSDAS table. Instead of using the input spectrum to produce the weights, another spectrum such as that produced from model PSFs or from an archival, high signal-to-noise, isolated point source spectrum (with the same slit, grating and central wavelength) can be applied. This would be advantageous when the signal-to-noise ratio is very low, when there are regions of the spectrum without data (such as saturated absorption lines) or for emission line spectra.



Numerical experiments are required to determine the advantages to be had for extracting very low signal-to-noise spectra with a prior PSF. Optimal extraction cannot be readily applied to blended spectra without first decomposing the two point source profiles through fitting.

### Two-channel restoration

The constancy of the PSF implies that restoration techniques (in the spatial dimension) should be applicable. The two-channel restoration algorithm (Lucy 1994, Hook & Lucy 1994) could be used here. The position of the point source is given and the (smooth) background is fitted by the second channel using the Richardson-Lucy technique. Initial experiments have shown that this technique may be promising. However, the current implementation of the code (`plucy` in the STSDAS.CONTRIB package) only allows the point sources to be specified by integer pixel values—a refined code is under development by Lucy and Hook whereby the point sources are specified by non-integral pixel coordinates. Each spatial column is then separately restored with the 2-channel restoration and the point source flux written to the output table and background to a separate file. There could be some smoothing applied before restoration, such as summing several columns (although this will degrade the spectral resolution). Since the position of the point source may shift slightly with wavelength, the position of the point source for input to the 2-channel restoration may have to be redetermined across the spectrum. The advantage of this method is that a number of point source spectra can be extracted simultaneously, whereas for the optimal extraction the background fitting and point source extraction are independent.

### 3. Initial Results

Currently there are no public STIS data on which to comprehensively test these routines. Tests of the point source extraction software were performed using STIS CCD (grating G750L) spectra (e.g., for standard stars GD153 and Feige 110). However, to simulate point sources on an extended background, simulated data was produced by adding existing STIS point source spectra to model images. In addition, no model PSFs at different wavelengths were available, so 2-D Gaussians were used.

Figure 1 shows an extracted spectrum (not flux calibrated) of the spectrophotometric standard star GD 153 (DA white dwarf) taken from a G705L spectrum (data set O3TT20040). Here the data were fitted by the PSF spectrum and the flux of the best fitting PSF at each wavelength increment was output to the extraction table. Bad pixels have been excluded and the error bars have been propagated from the pipeline calibrated data and are plotted in Fig. 1. The wavelength scale was produced from the image header.

Figure 2 shows the cross-section, in the spatial direction, through a simulated image of a point source on an extended background. The dotted line shows the restored background resulting from a two-channel restoration (using the code `plucy`). The “ringing” around the restored point source is due to the position of the point source being specified only to the nearest pixel. The upper line shows the estimated errors on the two-channel restoration. The errors were computed by restoring 25 separate spectra each with the statistical errors given by the spectrum counts together with the STIS read-out noise ( $4 e^-$ ). The computed error was added to each spectrum using a different random number seed. The mean error from the 25 trials is plotted. These errors were found to be about half of the statistical errors on the data (an entropy term was applied to the background which forces it to be smooth).



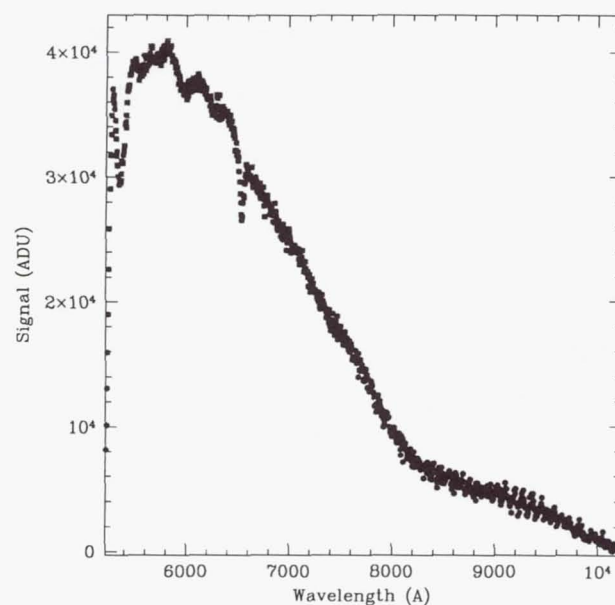


Figure 1. Unweighted extracted spectrum of GD 153 taken from a STIS G750L CCD longslit image.

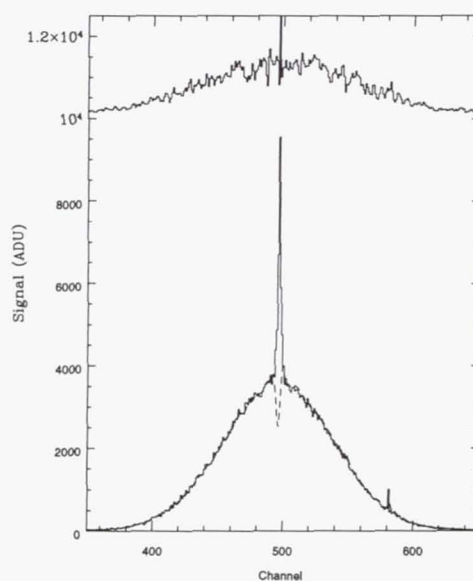


Figure 2. Spatial cross section through a model STIS longslit spectrum showing a point source on an extended background. The dotted line shows the resulting background from a two-channel restoration. The upper line shows the mean error ( $\times 20$ ) on the restoration from Monte Carlo trials.

#### 4. Conclusions

A package of programs to extract point source spectra from longslit data, tailored to STIS MAMA and CCD data, is under development. Extensive testing of the package of programs on realistic data will take place when the GTO data are released in October 1997. The package, including the two-channel restoration code, will be made public.

**Acknowledgments.** I thank Richard Hook for unfailingly providing computer code and help when (often) requested.

#### References

- Baum, S., et al., 1996, *STIS Instrument Handbook*, Version 1.0, Baltimore, STScI
- Hook, R. A., Lucy, L. B., 1994, in *The Restoration of HST Images and Spectra II*, eds. Hanisch, R. J. & White, R. L., STScI, p. 86
- Horne, K., 1986, PASP, 98, 609
- Lucy, L. B., 1994, in *The Restoration of HST Images and Spectra II*, eds. Hanisch, R. J. & White, R. L., STScI, p. 79
- Marsh, T. R., 1989, PASP, 101, 1032
- Mukai, K., 1990, PASP, 102, 183
- Robertson, J. G., 1986, PASP, 98, 1220



## Part 2. NICMOS





## NICMOS Status and Plans

Rodger I. Thompson

*Steward Observatory, University of Arizona, Tucson, AZ 85721*

**Abstract.** NICMOS has been in orbit for about 8 months. This is a report on its current status and future plans. Also included are some comments on particular aspects of data analysis concerning dark subtraction, shading, and removal of cosmic rays.

### 1. Introduction

Since the beginning of NICMOS operation in February of 1997 there have been several thousands of images taken. Most of these have been related to the Servicing Mission Observatory Verification (SMOV) program and calibration observations, however, recently many GO science programs have executed. The following is a summary of the current status of NICMOS and some future plans. This paper does not extensively cover the coronagraphic and polarimetric aspects as there are other presentations in this conference on those issues. Some aspects of data reduction are covered to help the users of NICMOS obtain the best scientific benefit from their observations.

### 2. Current Status

At present NICMOS provides excellent images of high scientific content. Most of the observations utilize Cameras 1 and 2 which are in excellent focus. Camera 3 is not yet within the range of the focus adjustment mechanism, but its current images are still quite excellent. In the following we will present the status of various aspects of the NICMOS instrument.

#### 2.1. Photometric Status

All three of the NICMOS cameras are operational and capable of delivering excellent photometric images. The photometric characteristics of the cameras are well within the original design specifications and are close to the expected performance maximums predicted before launch. The primary photometric characteristics are shown in Table 1 below:

Table 1. Photometric Characteristics

Camera	Noise <sup>a</sup>	Dark Current <sup>b</sup>	Gains <sup>c</sup>
1	22	0.16	5.4
2	29	0.15	5.4
3	30	0.15	6.5

---

<sup>a</sup>Value in electrons

<sup>b</sup>Value in electrons per second

<sup>c</sup>Value in electrons per ADU

*Background Flux* The NICMOS background fluxes are dominated by the natural zodiacal light background at wavelengths shorter than 2 microns and by the thermal emission from the HST mirrors at longer wavelengths. The overall background is about two thirds of the flux expected from Instrument Design Team's (IDT) calculations and significantly less than the early handbook listings. This is partially due to a lower operating temperature of the main HST optics than assumed in the calculations. The zodiacal background estimates were also on the conservative side.

## 2.2. Photometric Calibration

During SMOV there were observations of two photometric standard stars in a few selected filters. These results are shown in Table 2. The Camera 3 data were taken with the Field Offset Mirror (FOM) in a position that created vignetting in Camera 3. The vignetting created a high thermal background so no background numbers are quoted for Camera 3.

Table 2. Photometric Response

Camera	Filter	e/sec per Jy	background	Flux for S/N = 1 <sup>a</sup>
1	F090M	$3.72 \times 10^5$	0.10	$1.83 \times 10^{-7}$
1	F110M	$7.10 \times 10^5$	0.11	$9.51 \times 10^{-8}$
1	F145M	$9.25 \times 10^5$	0.13	$7.00 \times 10^{-8}$
1	F165M	$1.12 \times 10^6$	0.20	$5.93 \times 10^{-8}$
2	F110W	$2.37 \times 10^6$	0.30	$3.62 \times 10^{-8}$
2	F165M	$1.16 \times 10^6$	0.26	$7.39 \times 10^{-8}$
2	F207M	$8.49 \times 10^5$	0.59	$2.29 \times 10^{-7}$
2	F222M	$8.93 \times 10^5$	9.00	$3.91 \times 10^{-7}$
2	F237M	$1.12 \times 10^6$	39.0	$6.26 \times 10^{-7}$
3	F110W	$2.12 \times 10^6$		$3.33 \times 10^{-8}$
3	F160W	$2.17 \times 10^6$		$3.64 \times 10^{-8}$
3	F166N	$9.76 \times 10^4$		$5.45 \times 10^{-7}$
3	F222M	$9.00 \times 10^5$		$7.76 \times 10^{-7}$
3	F240M	$1.47 \times 10^6$		$1.41 \times 10^{-6}$

<sup>a</sup>Signal in Jy for 1000 second integration

## 2.3. Optical Status

NICMOS Cameras 1 and 2 have excellent images that meet all of the Point Spread Function (PSF) and encircled energy specifications. Sharply defined Airy rings are evident in all images. The depth of focus range for these cameras overlap and there is a common focus position specified for these cameras.

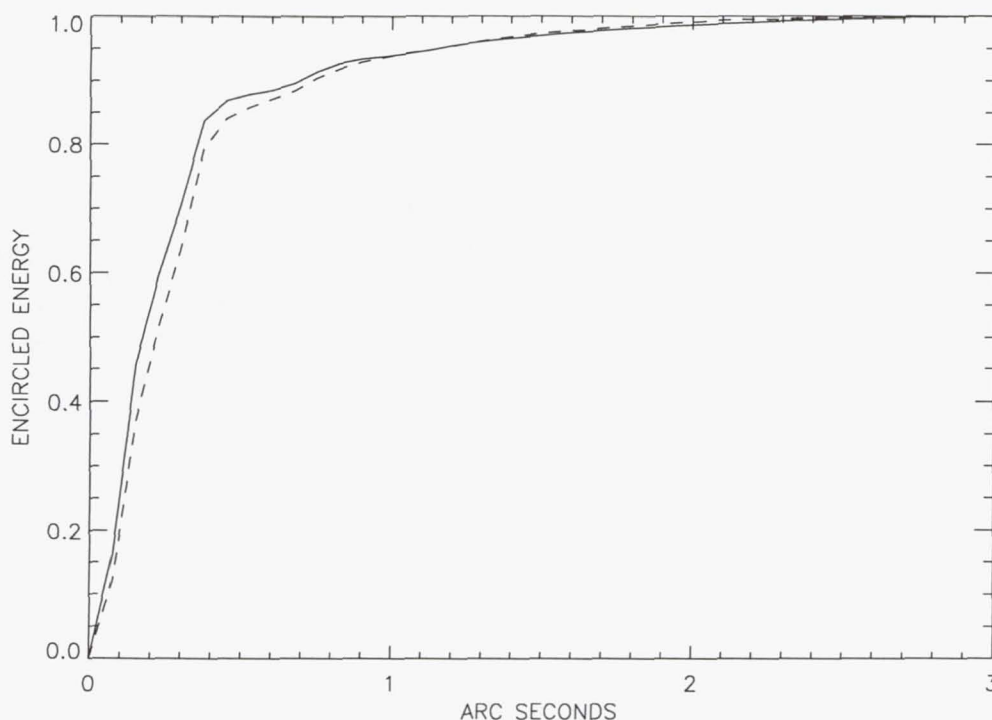
Camera 3 has a focus position that is currently beyond the range of the focus adjustment mechanism, however, the current images are of high quality and quite sufficient for many investigations. This is a great improvement over the image data taken early in the mission.

*Camera 1 and 2 Image Quality* Our most utilized camera has been Camera 2 followed by Camera 1. Figure 1 has a comparison of the encircled energy of an actual Camera 2 image with a synthetic image from the TinyTim PSF synthesis package. The solid line is the theoretical image and the dashed line is the measured encircled energy. The measurement is for an isolated star in the F160W filter.

*Camera 3 Image Quality* At the present time the energy contained in the central pixel of a Camera 3 PSF is about 65 percent of the theoretical maximum. This is an excellent image quality for many programs and represents a significant improvement over the image quality near the beginning of the mission. The rate of focus return has declined in the last



Figure 1. The solid line is the theoretical, the dashed line is the measured encircled energy distribution



few months but continues to be in the desired direction. We expect further improvement during the course of the mission but quantitative predictions are not warranted.

Observations with the current FOM setting for Camera 3 yield a vignetted image. Recent FOM offset observations indicated that the vignetting is eliminated for an offset FOM setting. A new default Camera 3 FOM setting is under development at STScI.

*Plate Scales and Apertures* At the present time the following are the best representations of the plate scales and apertures for the three NICMOS cameras. As the focus moves further back the numbers for Camera 3 may need alteration. The plate scales are in arc seconds per pixel and the aperture reference angle is in degrees from the +V3 axis in the SIAF frame. The image plane of NICMOS is slightly tilted at the detector arrays. This tilt creates the difference between the X and Y plate scales.

Table 3. The NICMOS Plate Scales

Camera	X-scale	Y-scale	X-FOV	Y-FOV	V3 Angle
1	0.043328	0.043231	11.09190	11.04154	315.3270
2	0.076216	0.075502	19.52282	19.32851	314.5190
3	0.204538	0.203916	52.36173	52.20250	314.8610

NICMOS currently supports two standard aperture positions in addition to the special apertures associated with coronagraphic images. The NICMOS FIX apertures are at the center of the detector array at the intersection of row and column 127 (0 is the first row or column). The straight NICMOS apertures are given below.

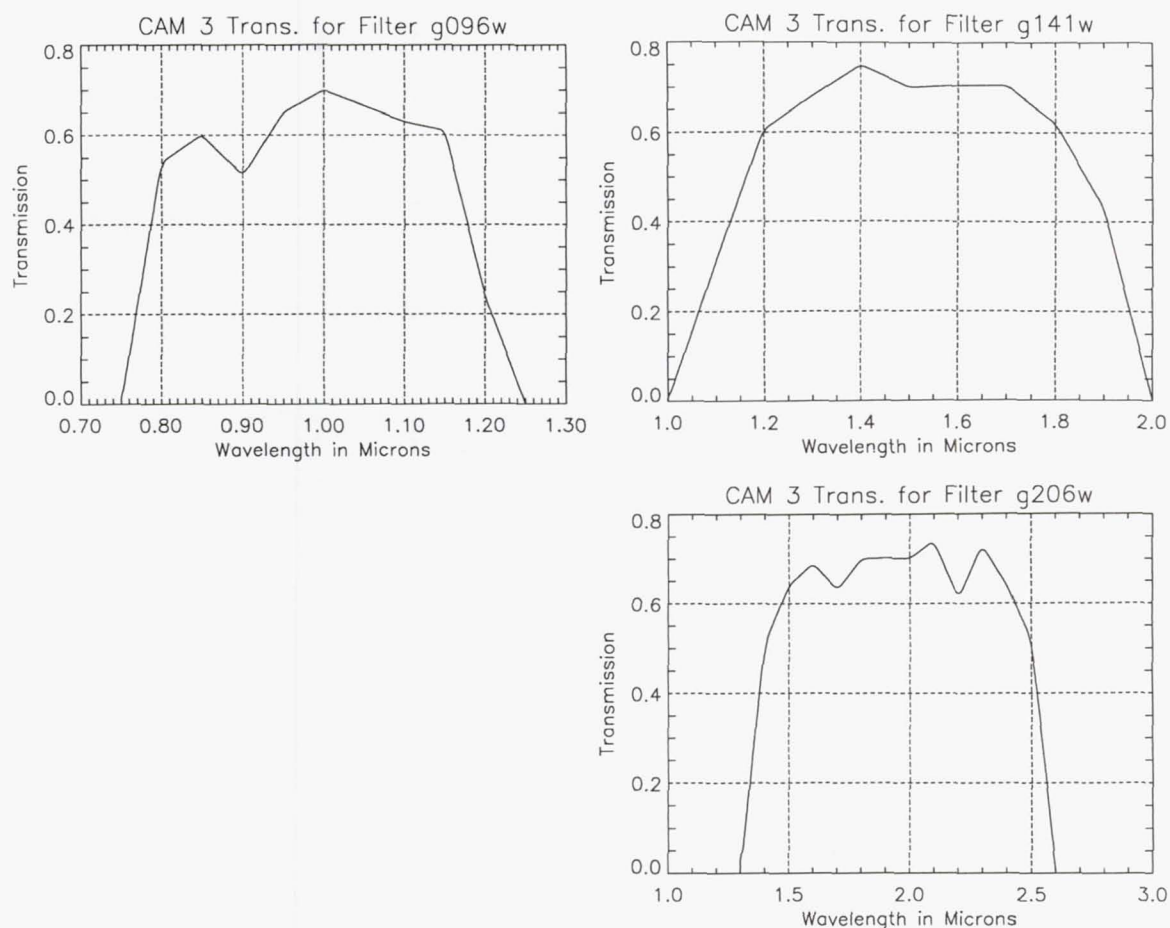
Table 4. NICMOS Aperture Locations

Camera	X-pixel	Y-pixel
1	162	100
2	149	160
3	140	135

## 2.4. Spectroscopic Status

NICMOS contains three gratings in Camera 3, G096, G141, and G206 with resolutions of  $R=200$  per pixel or  $R=100$  for Nyquist sampling. These gratings cover the full wavelength range of NICMOS. G096 and G141 have wavelength ranges with minimal background contamination. G206, however, receives substantial thermal background radiation from the HST optics. At this point we do not have a wavelength calibration for the gratings. Inspection of the parallel grating observations indicates that the gratings appear to be operating as designed. Figure 2 indicates the grating efficiency functions.

Figure 2. These are the efficiency curves for the gratings measured during ground testing of the grating optics only.





## 2.5. Polarization and Coronagraphic Status

These areas are covered in other articles in this volume so only summary remarks will occur here. Polarization studies have been carried out with the NICMOS polarizers. Their lower than expected polarization efficiency and non-symmetrical angles require a different computational algorithm than appears in the NICMOS Instrument Handbook (MacKenty et al., 1997). Refer to the article in this volume on polarization (Hines, Schmidt & Lytle 1997). With the modified computational procedures polarizations on the order of a few percent can be measured. The NICMOS polarizers are intended for highly polarized objects such as star formation regions.

Coronagraphic tests were performed during the SMOV and calibration observations. These tests showed that coronagraphic observations at two different roll angles reduce the scattered light by about a factor of 30 over non-coronagraphic imaging. Refer to the article on NICMOS coronagraphic observations (Schneider). At spacings greater than the radius of the occulting spot ( $0''.3$ ) coronagraphic imaging is very effective in detecting faint objects or structure near bright objects.

It should also be noted that NICMOS has a very low-scattering optical train. This, coupled with very low cross talk and no charge transfer makes the detection of faint structures in the presence of bright objects reasonably easy even without the coronagraph. The combination of these characteristics with the coronagraph makes NICMOS a very powerful tool for planet or brown dwarf detection as well as the study of structure around bright quasars.

## 3. Future Plans

The Space Telescope Science Institute has committed itself to utilizing NICMOS efficiently until the end of its cryogenic lifetime. The Call for a delta round of proposals was part of that commitment. STScI is also committed to at least two Camera 3 imaging campaigns which put the camera in focus by a small adjustment of the HST secondary. The first campaign is scheduled for late this year and the second will occur next year unless the camera returns to proper focus on its own.

The same motion that produced the focus anomaly also produced the thermal contact that is limiting the lifetime of the instrument. It is not known if this thermal contact will release in the future. If it does not the cryogen will last until approximately February of 1999. If the thermal contact does release the lifetime will depend upon the time of release. Goddard Space Flight Center is studying the possibility of installing an auxiliary cryogenic cooler for NICMOS during the 1999 HST Maintenance Mission. If this mechanism is successful the lifetime of NICMOS could be extended indefinitely.

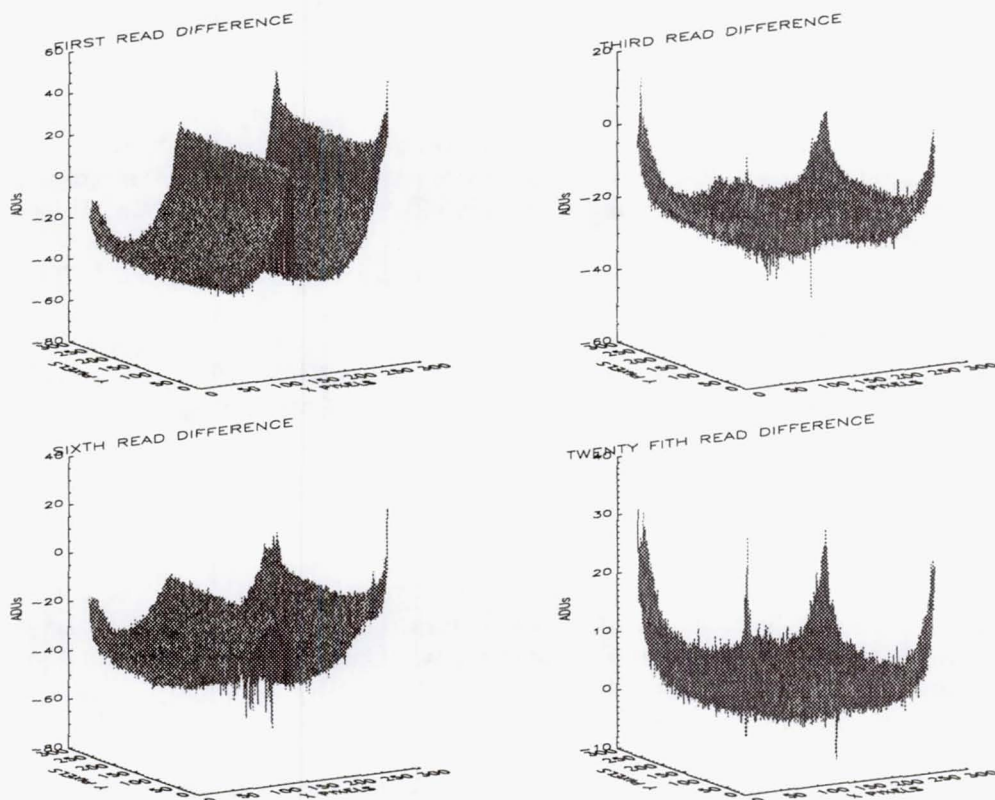
## 4. Some Aspects of Data Analysis

The NICMOS IDT has pursued some aspects of data analysis and reduction in parallel to the efforts of STScI and the pipeline analysis procedures. One of these alternative procedures follows the flow listed here.

1. Start with the raw fits data
2. Form the first differences (Read1 - Read0, Read2 - Read1, etc)
3. Subtract the cosmic ray cleaned darks of the same sampling sequence. Make sure the proper history has been kept on the dark frames.
4. Perform the linearity correction

5. Perform the cosmic ray elimination.
6. Perform the flat field correction

Figure 3. Dark first differences showing shading



#### 4.1. Comments on Data Analysis

In this last section are some comments on a few aspects of the data analysis procedure shown above that may help some observers.

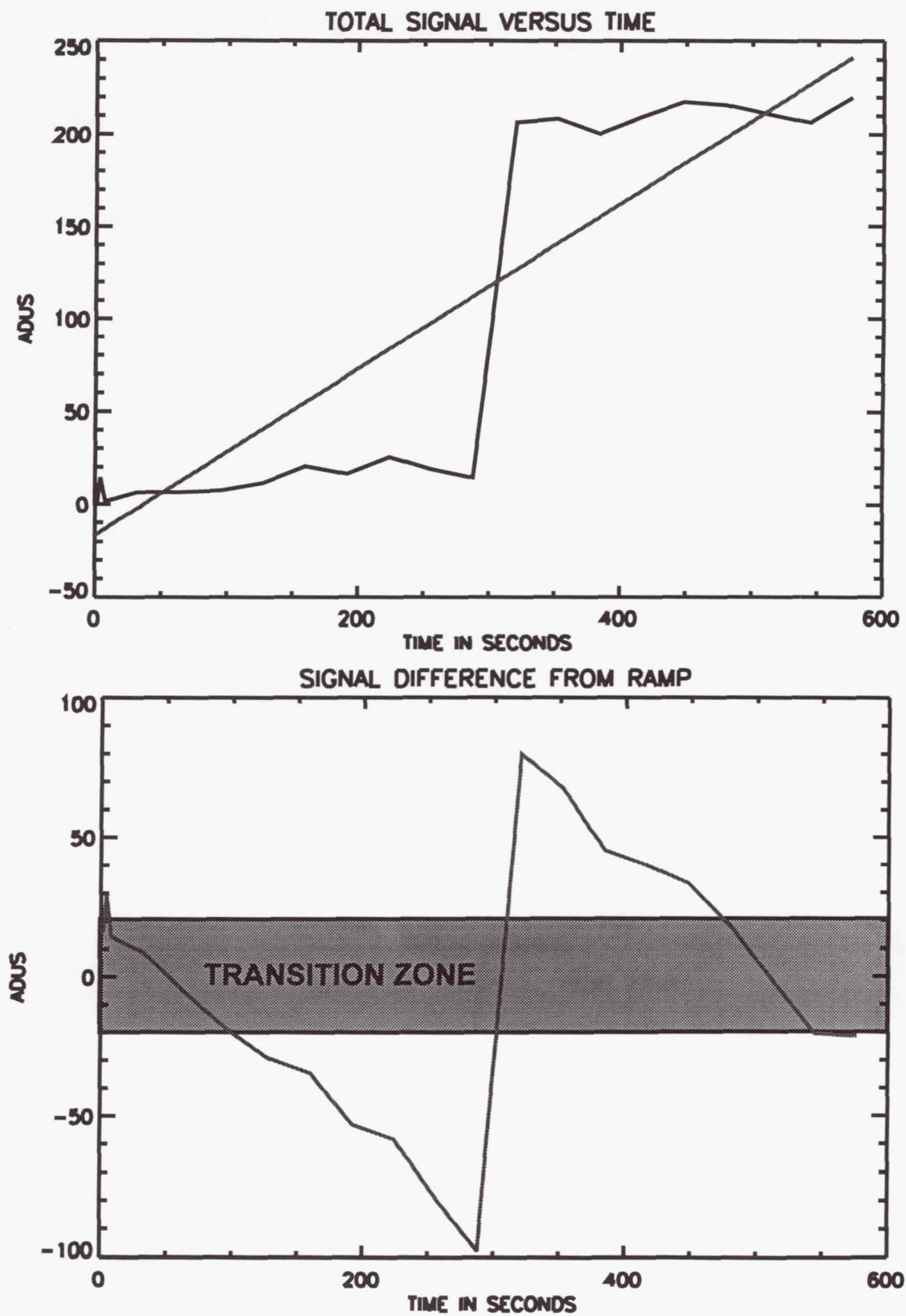
*First Differences* This analysis uses the first differences as the fundamental data unit. Each of the first differences in a multi-accum integration contains independent signal data. This is very useful in a statistical evaluation of the signal. Also, first differences that are contaminated in any way can be discarded and not affect the flow of the data analysis.

*Dark Subtraction* In subtracting the dark frames it is important to know the history of the dark frames and the image frames. Darks and images are frequently taken in substantial blocks with no pause between them. The initial observations with NICMOS showed what is now termed the pedestal effect. The first and second multi-accum observations differed from later ones by having an excess flux levels on the order of a few tens of ADUs per pixel for the whole integration and an altered shading structure. This was most apparent in the 127 column of Cameras 2 and 3 and the 127 row of Camera 1.

Particular care should be taken to subtract the first dark integration of a sequence from the first image of a sequence and the second dark from the second image. After two images



Figure 4. Relevant signals for cosmic ray elimination.



a median dark of the remaining darks in the sequence can be subtracted from the remaining images. If the images are part of a dither pattern the small delay may partially reset the effect and an appropriate combination of first and second darks may be more appropriate.

Figure 3 shows the shading characteristics of a darkframe for the first third sixth and last first difference in Camera 2. Note the very sharp discontinuity at column 127 in the first of the first differences and again for the sixth. It is slight changes in the depth of this discontinuity that causes a stripe in column 127 if there has not been proper history kept in the dark frames.

There has been a flight software change in an attempt to eliminate the pedestal effect. The NICMOS detectors are in a state of constant readout when they are not in use. The flight software now maintains the detector output amplifiers in an ON state during this time. It is hoped that this will stabilize the amplifiers during integration. The effectiveness of these changes is under evaluation.

*Cosmic Ray Elimination* The non-destructive readout mode of the NICMOS detectors offers a very efficient mechanism for detecting and eliminating cosmic ray hits. The mechanism also allows collection of useful information after the cosmic ray hit as long as the pixel is not saturated.

The various multi-accum sample sequences record the signal levels at several times during the integration. This provides a history of the signal in any pixel as a function of time. Cosmic ray hits produce an instantaneous step in the signal level. Cosmic rays are detected by searching for this signature.

One of the cosmic ray elimination packages developed by the team fits the signal versus time function with a linear function. The fit is very poor at the step function caused by the cosmic ray. The difference between the fit and the actual signal shows a very sharp negative to positive transition at the cosmic ray event.

The program looks for this signature in both the difference function and the ratio of the difference to the actual signal. It also utilizes the variance of the fit as another indicator of a true hit. Once a cosmic ray has been identified the bad first difference is removed and a new fit performed. The value predicted by the new fit replaces the bad first difference. In this way all signals other than the bad read are utilized. The linearity correction performed earlier in the process identifies and flags saturated cosmic ray hits.

**Acknowledgments.** The NICMOS team wishes to thank the dedicated personnel at Ball Aerospace, Rockwell International, NASA Goddard Space Flight Center, NASA Headquarters, and the Space Telescope Science Institute who have worked over the last 13 years to make this mission possible. We also greatly thank the crew of STS 82 who installed NICMOS into HST along with STIS and greatly improved the overall performance of the telescope. NICMOS was built under NASA contract NASA 5-31289 and this work is supported in part by NASA grant NAG 5-3042. This article is based in part on observations with the NASA/ESA Hubble Space Telescope, obtained at the Space Telescope Science Institute, which is operated by the Association of Universities for Research in Astronomy under NASA contract NAS5-26555.

## References

Mackenty, J. W., et al., 1997, *NICMOS Instrument Handbook*, Version 2.0 (Baltimore: STScI).



## Characteristics of the NICMOS Detectors

C. J. Skinner<sup>1</sup>, L. E. Bergeron & D. Daou

*Space Telescope Science Institute, 3700 San Martin Drive, Baltimore, MD 21218*

**Abstract.** We present an overview of the properties of the NICMOS flight detectors as measured on-orbit, including the flat-field response, the dark current, the linearity, and the read-noise. We show for the first time all the dependencies of the various components of a NICMOS dark exposure, and show how to generate "synthetic" dark current calibration files. An unexpected time-varying bias known as the "pedestal", is described, along with some efforts to remedy it. We describe the effects on the detectors of exposure to very bright sources, and finally, we briefly describe the sensitivity of NICMOS to cosmic rays.

### 1. Introduction

NICMOS underwent its System Level Thermal Vacuum (SLTV) testing at Ball Aerospace during August and September of 1996, and was launched in February 1997. Prior to SLTV, STScI had no data using the NICMOS flight detectors, which are substantially different both physically and in their properties and performance to the NICMOS3 detectors widely used at ground-based telescopes. Thus all of our experience with these detectors has accrued during the last 12 months, and most of it in the last 5 months. During this time our understanding of the detectors has improved at a rapid pace, and the instrumental calibration has been evolving at a similar rate. We describe in the following sections the more important detector properties, as we understand them in September 1997.

### 2. Detector Properties

#### 2.1. Flat-field Response

We show in Figure 1 the flat-field response for the three NICMOS detectors, measured for the F160W filters. These measurements were made during SLTV. On-orbit measurements of the flat-field response have been made for most of the Camera 1 and 2 filters by now, but many have not yet been reduced and converted into reference files. A detailed analysis of the flight-spare NICMOS detector was presented by Skinner et al., (1995a,b), and the amplitude of the flight detector flat-field response variations, both pixel-to-pixel and on longer scale-lengths, is basically consistent with that presented by Skinner et al. The conclusions of Skinner et al., regarding the effects of the flat-field response on photometric fidelity as a function of wavelength are valid for these detectors.

#### 2.2. Darks

The "dark current" of an array detector is generally thought of as any signal which is accumulated during an exposure with no external illumination. In CCD cameras the only such signal is, in general, electrons generated in the silicon detector at a constant rate and

---

<sup>1</sup>deceased

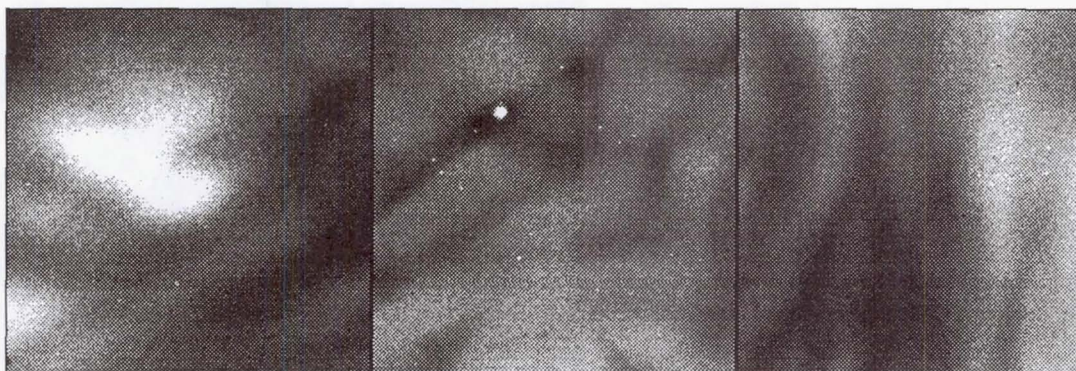


Figure 1. Flat-field responses for Cameras 1 (left) through 3 (right), on a uniform greyscale.

trapped in the potential wells. This is a continuous feed of electrons into the pixels, unprompted by photons, and the total charge accumulated in an exposure is linearly dependent on exposure time. This signal is not subject to modulation by the detector non-linearity or flat-field response. Thus in a calibration of an image from a CCD, the dark subtraction must be among the first steps. In the case of NICMOS detectors, the darks are considerably more complicated, with contributions from a number of sources. Additionally, it is possible to read the detectors non-destructively, and so it is possible to see the signal accumulating in each pixel during the course of an observation. However, the act of reading the detector in fact has a small effect on the signal. As a result of these complications, a significant "folklore" has been established among ground-based users of NICMOS detectors. One of the elements of this tradition is the belief that to calibrate a NICMOS exposure, it is essential to obtain a "dark" (i.e. unilluminated) exposure matched exactly in number of readouts and timing of all the readouts. We will show here that this is not, in fact, necessary.

The three components of the signal in a NICMOS dark exposure are "amplifier glow", "shading", and the real, linear dark current.

A NICMOS detector is a continuous single slab of HgCdTe, pixelated such that each pixel is individually bump-bonded to a single pixel of a CCD which is used as a readout. However, there are four separate readout amplifiers, each of which addresses one quadrant of the detector. Each time the detector is read out, the readout amplifiers, which are situated near the corners of the detector, are turned on. These amplifiers emit IR radiation that is detected by the pixels in the detector - similar to having a small "light bulb" in each corner. This produces a pattern of light that is highest in the corners and decreases towards the center of the detector. This is known as "amp glow". A typical single readout produces about 20–30 ADUs of amp-glow per pixel in the corners of the detector, and 2–3 DN near the center. Since the readout time of the detector is the same each time (it takes 0.203 seconds to read the whole image), the on-time for the amplifiers is always the same for each readout, and thus the light pattern seen by the array is repeatable. So in a given readout, the amount of signal due to amp-glow in each pixel scales directly with the number of readouts since the last reset:

$$A(i, j) = a(i, j) * n_r \quad (1)$$

where  $A(i, j)$  is the observed signal due to amp-glow in a given readout for pixel  $i, j$ ,  $a(i, j)$  is the amp-glow signal per readout (different for each pixel), and  $n_r$  is the total number of readouts of the array since the last reset. So in the corners of a full 26-readout MULTI-ACCUM there will be of order 500–800 ADUs due to amp-glow, along with the expected Poisson noise from this signal. It can immediately be seen from the size of this signal that



making excessive numbers of readouts during a MULTIACCUM exposure is harmful to the results, because although the amp-glow signal is highly reproducible and can be subtracted very effectively, the Poisson noise added by it can significantly degrade the S/N of the resulting image, even close to the center of the detector where the amp-glow signal is at its minimum. Amp-glow images for each detector are shown in Figure 2.

The bias level, or "DC offset", in a given pixel in a NICMOS array, is time-dependent. This is the so-called "shading", which visually in an uncorrected image looks like a ripple and gradual signal gradient across a given quadrant. The pixels in a given quadrant of a NICMOS detector are read out sequentially. It takes a little over a  $\mu\text{sec}$  to read a single pixel, and so with four readout amplifiers reading in parallel it takes just over 0.2 sec to read the entire 256x256 pixel detector. Considering a quadrant as an array of  $i \times j$  pixels, the readout sequence consists of reading sequentially along a detector row  $i$ , clocking  $j$  from 1 to 128, then moving to row  $i+1$  and clocking  $j$  from 1 to 128, and so on. Since the amplifier bias changes pseudo-exponentially with time over the course of the readout, the observed signal, in the absence of any external illumination, varies rather slowly along the rows ( $i$ ), but rather rapidly along the columns ( $j$ ). This signal is not accumulated in the pixels each readout, but rather is superimposed on the actual signal at the time of each detector readout. The shading signal is not the same for each readout. Its amplitude, and to some extent its shape, are a function of the time since a pixel was last read out (*not* reset). So readouts with the same DELTATIM (this is the keyword used in NICMOS data to denote the time since the previous readout) will have the same bias signal, for a given pixel. The dependence of this bias on DELTATIM is nearly logarithmic and quite repeatable. It is possible to find a numerical fit to the shading function in DELTATIM for each pixel of each detector. Thus it is (in principle) possible to predict what the bias signal is in any given pixel for any possible readout sequence. Another way to attack the problem is to make an average image of the bias for each of the DELTATIMs in the predefined MULTIACCUM sequences. Then to build a synthetic dark, the bias component can be had by using the bias image for each appropriate DELTATIM in the sequence:

$$B(i, j) = S(i, j, \text{DELTATIM}) \quad (2)$$

where  $S(i, j)$  is the bias signal in a given pixel as a function of DELTATIM. It is the latter operation which is currently used in generating our synthetic darks.

The linear dark current component is the traditional observed detector dark current when no outside signal is present. This component scales with exposure time only:

$$D(i, j) = T * d(i, j) \quad (3)$$

where  $D(i, j)$  is the observed dark current signal in pixel  $i, j$  for a given readout,  $T$  is the time since the last detector reset, and  $d$  is the dark current (in  $e^-/\text{sec}$ ). The NICMOS dark current is extremely small and is very difficult to measure. It is approximately  $0.05 e^-/\text{sec}$  for Camera 2, and no larger than about half this value for Cameras 1 and 3 (we have only upper limits for these two).

The challenge in calibrating these dark components for NICMOS detectors is disentangling the three components so that each can be measured independently of the other. Fortunately each component has entirely different sets of dependencies, and this can be used, along with the flexible way the NICMOS detectors can be operated, to achieve our goal. First we note that the amp-glow is dependent only on the number of readouts since the last detector reset. This means that to calibrate the amplifier glow, we need to find images with identical shading components but different number of readouts. Because of the dependence of shading, this turns out to be easy: if we look at any of the STEPxxx MULTIACCUM readout sequences, we find that after a set of logarithmically increasing DELTATIMs, they settle to a constant DELTATIM. For example, in the case of the STEP256 sequence, after an exposure time of 256 sec, readouts occur every 256 sec, and thus the shading is identical



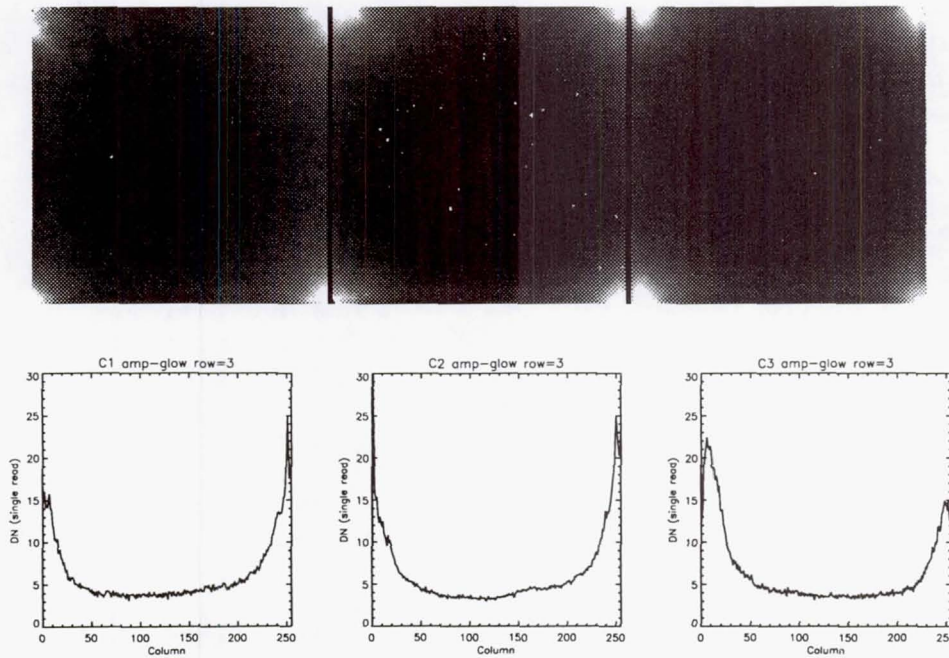


Figure 2. Amplifier glow for Cameras 1 (left) through 3 (right), on a uniform greyscale, and below a plot of row 3 (near the bottom) of each camera.

for each of these linearly spaced readouts. In this linear regime, the difference between the  $n$ th and the  $(n+1)$ th readouts is simply the signal added by 1 readout's worth of amp-glow (ignoring the dark current). Taking a full set of  $m$  linearly spaced readouts yields  $m$  lots of amp-glow, and thus obtains the highest S/N for the resulting amp-glow image. Finally, to correct the amp-glow images for the small effects of the linear dark current, we can compare the amp-glow images generated as above using many different STEPxxx readout sequences, and use the difference in DELTATIMs to measure the linear dark current. The resulting amp-glow images for all three cameras are shown in Figure 2.

In order to measure the shading, first we correct each read of a MULTIACCUM exposure for amp-glow, using the amp-glow calibration images obtained above. Having removed this component, shading is now the dominant remaining component. If we plot the amplitude of the shading signal against DELTATIM, we find the two are very strongly correlated. In fact, the shading amplitude is dependent only on DELTATIM, and has no dependence on time since last reset whatsoever. This is illustrated by the fact that if we find any read in the STEP16 pattern whose DELTATIM is 16 seconds, for example, the shading amplitude for the same pixel of the same detector will be identical, for example, the shading amplitude for the same pixel of the same detector will be identical for a read from the STEP256 pattern for which DELTATIM is 16 seconds - regardless of how many reads have occurred previously in either observation. In Figure 3 we plot the shading amplitude against DELTATIM for a pixel near the center of a quadrant, using observations made using many different MULTIACCUM sequences. Figure 4 shows the shading image as a function of DELTATIM for all three cameras. The detectors are mounted in the cameras such that the readout directions are rotated by multiples of 90 degrees with respect to one another, and so the shading patterns in Cameras 2 and 3 run parallel to one another, while that for Camera 1 is in the orthogonal direction. In Camera 1 the shading generates a bright band along the first row to be read out of each quadrant, parallel to the time axis in Figure 4. In Camera 3 a similar bright band is generated, but now the band runs orthogonal to the time axis of Figure 4. Note that the shading generates a large negative signal. The gradient of the



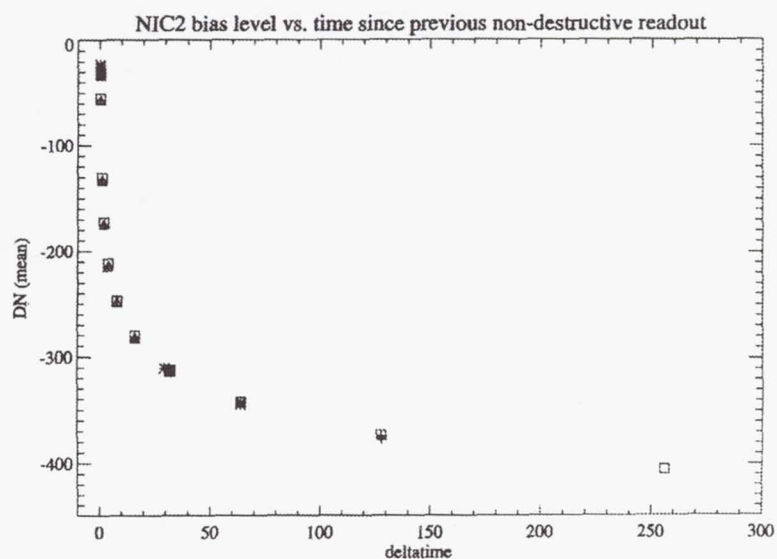


Figure 3. Shading amplitude for a single pixel as a function of DELTATIM. Different symbols represent measurements from different MULTIACCUM sequences: equal DELTATIMs from different sequences coincide, showing that shading is a function *only* of DELTATIM.

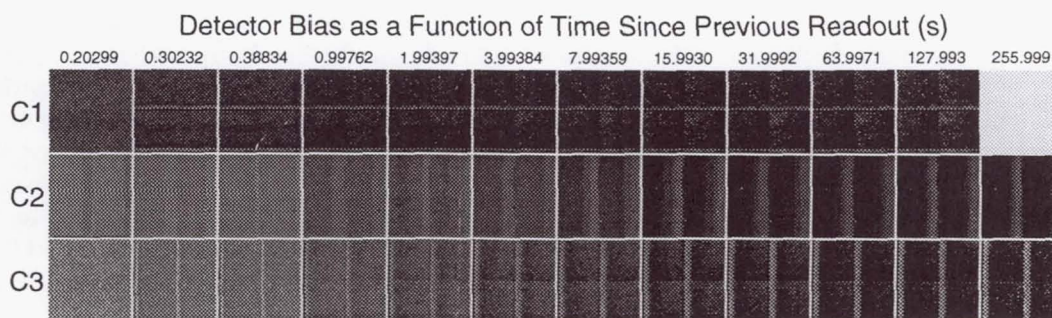


Figure 4. Shading images for each camera plotted as a function of DELTATIM (shown in seconds at the top).

shading function is seen to be quite steep in the direction orthogonal to the bright bands seen in Cameras 1 and 3: this direction is the "slow clocking direction", as the time between pixel readouts in this direction is 128 times a single pixel readout time. In the orthogonal direction, the "fast clocking direction", it is more difficult to see the gradient in the shading — but it can be seen in Camera 3 by virtue of the quadrant boundaries.

The linear dark current can be measured a number of ways. The technique which has been used so far has been to derive, for a number of MULTIACCUM sequences for which high quality on-orbit darks have been obtained, synthetic dark current images using the amplifier glow and shading contributions as determined above. These are then subtracted from the observations. The residual is seen for Camera 2 to be a very low amplitude signal increasing roughly linearly with time. This is the linear dark current. For Cameras 1 and 3 no residual could be seen above the uncertainties, indicating that the dark current is very small for these two cameras.

The total "dark" signal in any given pixel of any given NICMOS MULTIACCUM readout is just the sum of the 3 components described above:

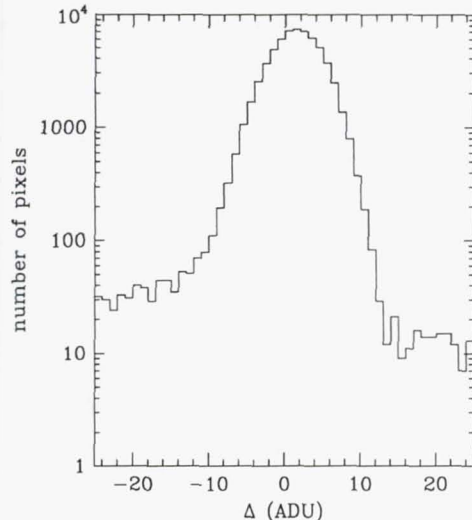


Figure 5. Histogram of the pixel values in the difference image between an observed and a synthetic STEP8 dark (see text)

$$DARK(i, j) = D(i, j) + A(i, j) + B(i, j) \quad (4)$$

An IDL routine has been developed to make synthetic darks. This routine uses the amplifier glow image displayed in Figure 2, and simply multiplies it by the accumulated number of reads in order to generate  $A(i, j)$  for each readout. The shading as a function of DELTATIM has been populated by the technique described above, yielding an array of shading images some of which are displayed in Figure 4. An appropriate image is picked out of this array in order to generate  $B(i, j)$  for each readout. Finally, the linear dark current as described above is calculated from the elapsed time per readout. The routine now sums the three contributions for each readout. The calibration database has been populated with MULTIACCUM darks for all sequences which have not yet been observed on-orbit, or for which other effects, such as the pedestal, have contaminated the early on-orbit dark observations. There are plans to tune up the synthetic dark algorithm somewhat (see next section) and eventually release it as an STSDAS tool in the NICMOS package.

Comparisons of on-orbit to synthetic darks show that the differences are relatively small — usually of the order of a few ADUs, with the largest differences in the corners of the detectors. Most of this can be alleviated by better characterizing the amp-glow from on-orbit data. In particular, we are observing some low-level non-linearity in the behavior of the amp-glow — that is, the amplifier glow contribution in observed darks is seen to differ a little from being an exact linear multiple of a single read's worth of amp-glow. Further investigation of this is required, but we note that the effects are small, and will rarely be significant. As an example, we show here the difference between a synthetic STEP8 dark calibration reference file, and a STEP8 reference file generated as the mean of a set of 8 22-readout STEP8 dark observations obtained as part of the 7116 ERO observation. The observed dark contains a few hundred Cosmic Rays which were not successfully median filtered out when the individual exposures were combined. (Overall we would expect to have received about 2000 Cosmic Ray hits in the set of darks; most of these have been successfully removed by the combination algorithm, with about 10–20% of them remaining, mostly because their amplitude was too low to be detected.) There is no residual shading pattern in the difference image, and very little residual amp-glow (there is about a couple of ADUs in the corners). There is a small gradient across the image from right to left, with an amplitude of about 1 ADU. However, the residual signal is very small. The histogram



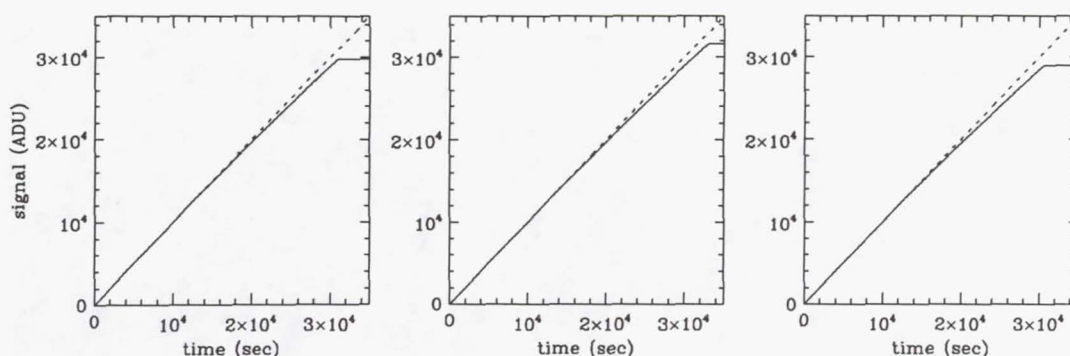


Figure 6. Response of pixel 100,100 of Cameras 1 (left) through 3 (right) to a uniform signal, illustrating the linearity behaviour. The dashed line is the theoretical pixel response (if the behaviour were linear), while the solid line is the observed response, plotted only up to the signal level at which the pixel is deemed to be saturated and uncorrectable.

of pixel values in the difference image, which is shown as Figure 5, shows that the modal difference is about 1 ADU between the observed and synthetic dark.

### 2.3. Linearity

Measurements of NICMOS3 detectors, and their successor the HAWAII detectors, by Rockwell (e.g. Poksheva et al 1993; Kozlowski et al 1994) show non-linearity at both very small and very large total charge accumulations. Measurements of the flight detector non-linearity during SLTV suggested that in fact the detectors were quite linear up to charge accumulations of order 5000 ADUs, and that non-linearity was evident from there up to their saturation level of around 30000 ADUs. A typical linearity curve for a single pixel for each camera, derived from SLTV data, is shown in Figure 6. The linearity curve is somewhat different for different pixels, and the saturation levels show a fairly wide dispersion. From on-orbit measurements we now have indications that at least some pixels may now be saturating at somewhat lower charge accumulations than were determined from SLTV. Whether this is attributable to a problem in the SLTV measurements, to problems in their analysis, or to a real change in the linearity properties since launch, is not currently clear. A new set of measurements of the linearity are planned to take place during October 1997.

### 2.4. Read Noise

The read noise for the pixels in the NICMOS detectors is highly variable from pixel to pixel, in a basically random fashion. It was measured during SLTV by the usual means, plotting for each pixel the mean detected signal versus its standard deviation. The result is a curve whose gradient yields the gain in  $e^-/\text{ADU}$  and whose intersection with the signal axis (at zero detected signal) yields the read noise. Images of the read noise for each detector are shown in Figure 7.

## 3. The Pedestal

This effect was first observed in SLTV data, but not understood. It has been observed on-orbit since launch, and we are now finally beginning to understand it. When a detector is to be unused for some period (e.g. during Earth occultations or filter wheel movements), it enters a mode known as "autoflush", in which it is reset several times per second to

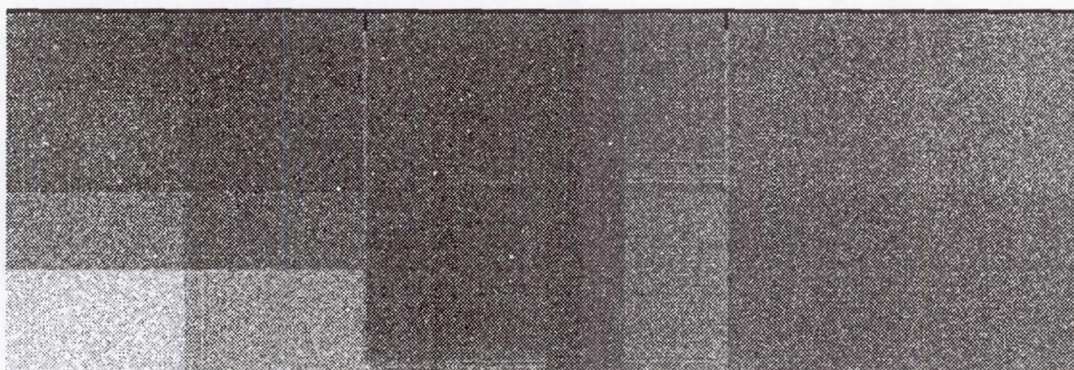


Figure 7. Images of the read noise for Camera 1 (left) through Camera 3 (right), scaled from 15 electrons (black) to 55 electrons (white).

prevent saturation. When the detector is used after a period in autoflush, its output is observed to be somewhat unstable. It is as though an excess bias is present on emergence from autoflush, which decays on a timescale of many minutes. This excess bias has become known as the “pedestal”. Its amplitude seems to be roughly uniform across a quadrant, but to vary somewhat from quadrant to quadrant. The largest amplitude seen for the pedestal so far is about 20–30ADUs. It seems that the amplitude is usually greater after long periods of autoflush (e.g. Earth occultations), and much smaller after short periods of autoflush (e.g. a spacecraft dither), and the timescale for decay from a large amplitude pedestal can be as long as 30 minutes. An example of the pedestal in a series of STEP8 darks is shown in Figure 8, while in Figure 9 the modes of the reads in another sequence of darks, this time with Camera 1, are shown.

We currently believe that the pedestal may be driven by small changes in the detector temperature. The readout amplifiers are known to be a source of heat. At launch, during autoflush the amplifiers were switched off. During an exposure, the amplifiers must be switched on for readouts, and this led the detector temperatures to rise during exposures. The zero level for the detector output is highly temperature-sensitive, and so the temperature drift causes a zero-level drift which appears as a bias drift, or excess dark signal. Recently the flight software has been changed such that the amplifiers are left switched on during autoflush, and only switched off between readouts during exposures, in an attempt to reduce temperature fluctuations of the detectors. As might be expected, the temperature changes of the detectors are now in the opposite direction, and the pedestal also appears to have reversed its sign. Its amplitude appears to have been reduced, although it has not disappeared. Further work is underway to categorize the new pedestal properties.

#### 4. Persistence

The observed persistence properties are described by Daou & Skinner (1997a,b). Saturation of the NICMOS detectors can cause after-images, or “persistence”, which can linger for up to 30 minutes after the saturated exposure was completed and read out. The count-rates in these persistent images can be significant, and the mechanism and behaviour are not understood. Recent tests have suggested that following a saturated exposure, a few short ACCUM images (minimum exposure time) with many initial and final reads can almost completely eradicate persistence. About 20 to 30 initial and final reads appears to be sufficient.



NIC2 STEP8 Darks With Pedestal

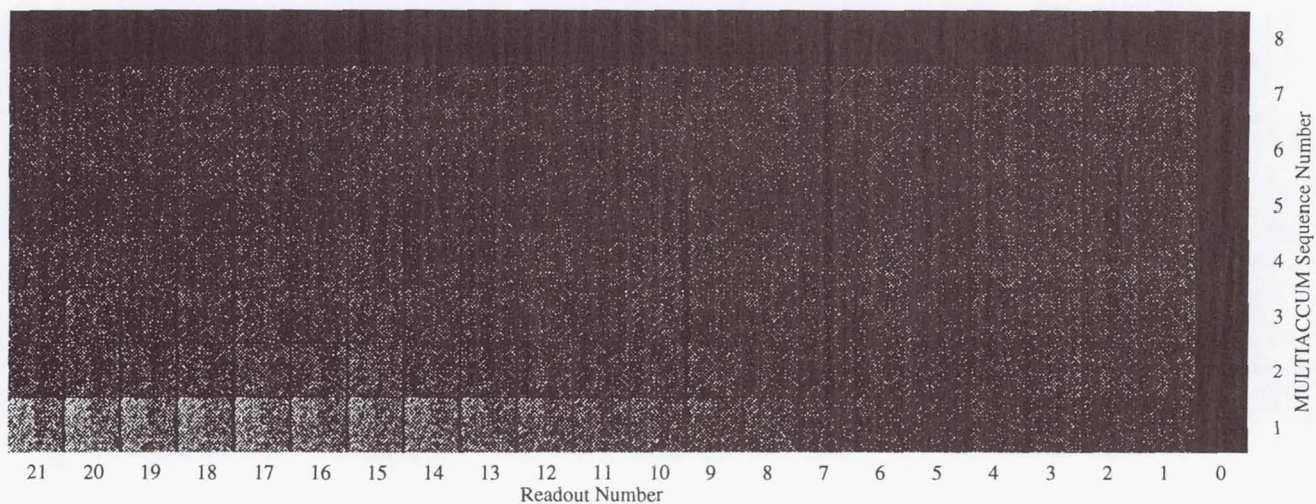


Figure 8. Images of the pedestal effect in Camera 2. Every readout of this series of eight STEP8 darks is shown sequentially along the x direction, with the first exposure at bottom, and last at top; the last has been subtracted from every one, to show the effect of the decaying pedestal signal.

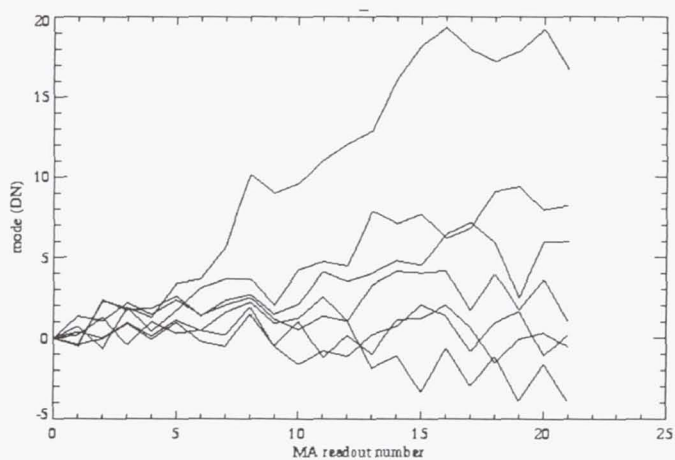


Figure 9. Modes of a series of darks in Camera 1, differenced exactly as shown in Figure 8, shown as a function of readout number for each exposure in the series. The first exposure shows a strong pedestal, rising to an excess bias of 20 ADUs by the end, and subsequent exposures show decreasing effects.



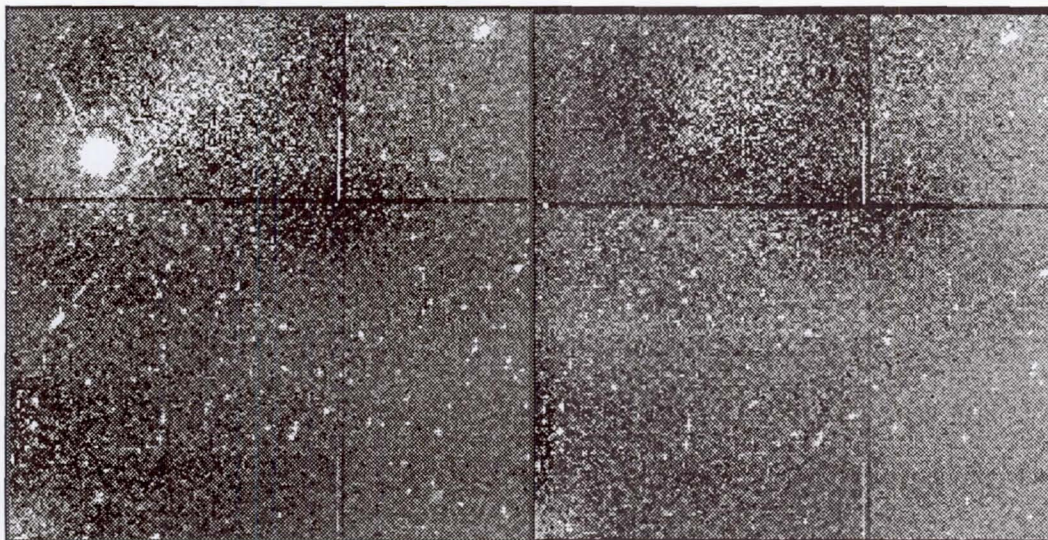


Figure 10. Part of a Camera 1 image showing a massive CR hit: the readout immediately after the hit is on left, and the previous readout at right.

## 5. Cosmic Rays

NICMOS detectors are quite sensitive to CRs. For the WFPC2 CCDs, the energy spectrum of detected CRs shows a distinct peak. For NICMOS we observe no such peak; instead the detectors appear to be sensitive to CRs down to energies as low as the read noise (Calzetti, 1997). It is therefore quite possible that a non-negligible fraction of the noise in on-orbit NICMOS images is due to low-energy CR hits. Typically, about 2 CR hits are experienced per second on each detector, if we count hits only down to energies four times the read noise or larger, but the rate is rather variable. Occasionally enormous CR hits are experienced, in which a radius of up to 10 pixels can be instantaneously saturated, with a surrounding ring of what may be secondary emission. An example of such an image is shown in Figure 10. These hits can be distinguished from real sources by the fact that they appear instantaneously between reads, that the entire hit region is saturated without surrounding regions of lower counts, and that there is no spider pattern to the image. We are currently seeing a few of these hits per month. These hits can leave persistent after-images in subsequent NICMOS exposures up to at least half an hour later.

## References

- Calzetti, D., 1997, Instrument Science Report NICMOS-97-022 (Baltimore: STScI).
- Daou, D. & Skinner, C. J., 1997, Instrument Science Report NICMOS-97-023 (Baltimore: STScI).
- Daou, D. & Skinner, C. J., 1997, Instrument Science Report NICMOS-97-024 (Baltimore: STScI).
- Kozlowski, L. J., Vural, K., Cabelli, S. C., Chen, C. Y., Cooper, D. E., Bostrup, G. L., Stephenson, D. M., McClevige, W. L., Bailey, R. B., Hodapp, K., Hall, D., Kleinhans, W. E., 1994, SPIE Vol. 2268, 353.
- Poksheva, J. G., Tocci, L. R., Farris, M. C., Tallarico, S. I., 1993, SPIE Vol. 1946, 161.
- Skinner, C. J., 1995, Instrument Science Report NICMOS-006 (Baltimore: STScI).



Skinner, C. J., Mentzell, E., Schneider, G., 1995, Instrument Science Report NICMOS-005  
(Baltimore: STScI).

## The Photometric Performance of NICMOS

L. Colina<sup>1</sup>

*Space Telescope Science Institute, 3700 San Martin Drive, MD 21218*

M.J. Rieke

*University of Arizona, Steward Observatory, Tucson, AZ 85721*

**Abstract.** This contribution reviews our current understanding of NICMOS photometric characteristics paying special attention to the absolute calibration of NICMOS detectors and the sources of systematic uncertainty when performing the calibration. Preliminary results based on SMOV and Cycle 7 calibration programs are presented.

### 1. Introduction

The near-infrared wavelength range was opened to HST with the installation of the Near-Infrared Camera and Multi-Object Spectrometer (NICMOS) last February, during the second HST servicing mission. Unaffected by atmospheric absorption and emission, NICMOS covers the entire 0.8  $\mu\text{m}$  to 2.5  $\mu\text{m}$  wavelength range. Similarly, NICMOS, being above the atmosphere, is not forced to adopt filter bandpasses like those used at ground-based observatories matching the near-infrared atmospheric windows. In practice NICMOS does not have a set of filters matching any of the standard ground-based photometric bands and this poses a challenge when trying to achieve precise absolute photometry. On the other hand, NICMOS absolute calibration requires a set of faint spectrophotometric standards covering the entire 0.8–2.5  $\mu\text{m}$  wavelength range. Such a set of standards didn't exist before and the selection and generation of NICMOS standards represented additional challenges.

This paper reviews the several steps taken to ensure accurate absolute calibration of the NICMOS detectors. Details on NICMOS absolute spectrophotometric standards are given in Section 2. Section 3 discusses some of the sources of uncertainties when performing absolute calibration with NICMOS. The results of the first on-orbit absolute calibration of NICMOS are given in Section 4 while Section 5 mentions the transformation of the HST photometric system into JHK ground-based systems. Section 6 describes future plans towards the characterization of NIC3 photometric performance. This paper does not mention the performance of the NIC3 GRISMs as they will be the topic of a separate contribution (Freudling 1997).

### 2. Absolute Spectrophotometric Standards for NICMOS

The absolute calibration of the ultraviolet and optical instruments onboard HST is based on the existence of absolutely calibrated spectra of a few pure hydrogen white dwarfs (WD) and hot stars, the so-called HST set of absolute spectrophotometric standards (Colina & Bohlin 1994; Bohlin, Colina & Finley 1995; Bohlin 1996). The absolute calibration of the set of HST absolute standards in the UV and optical, is based on a detailed model of

---

<sup>1</sup>Affiliated with the Astrophysics Division, Space Science Department, ESA



the primary standard G191-B2B, a hot pure hydrogen white dwarf, after normalization to accurate Landolt visual photometry (Bohlin et al., 1995; Bohlin 1996). This model covers the entire NICMOS wavelength range and therefore G191-B2B has been selected as the primary NICMOS WD standard.

An alternative method for calibrating NICMOS uses solar analogs (Campins et al., 1985). Three faint solar analogs were selected by the NICMOS Investigation Definition Team (IDT), and observed repeatedly on the ground at JHK (E. Green and E. Persson, private communication). Spectra of these three solar analogs were taken with the HST Faint Object Spectrograph (FOS) in the 0.2–0.8 $\mu$ m wavelength range to study how accurately their spectral energy distribution matched that of the Sun (Colina & Bohlin 1997). The absolute flux distribution of these three solar analogs covering the ultraviolet to near-infrared range was obtained by combining a scaled version of an absolutely calibrated solar reference spectrum (Colina, Bohlin & Castelli 1996) with the FOS spectra (Colina & Bohlin 1997). In the near-infrared, the solar reference spectrum was generated by computing the energy output of a solar photospheric model using the most recent version of Kurucz ATLAS code (see Colina et al., 1996 for details). Of the three solar analogs, P330E was selected as the primary NICMOS solar analog standard.

### 3. NICMOS Absolute Photometry: Sources of Uncertainty

#### 3.1. Absolute Spectrophotometric Standards

One white dwarf (G191-B2B) and one solar analog (P330E) have been selected as NICMOS primary spectrophotometric standards. To assess the accuracy of the G191-B2B model in the near-infrared, two state-of-the-art atmosphere flux distributions for exactly the same physical parameters were computed independently by two different experts in this field. The largest differences in the continuum fluxes of the two independent models were 3.5% in the near-infrared at 2.5 $\mu$ m (Bohlin 1996).

The spectral energy distribution of P330E in the 0.4–0.8 $\mu$ m range is the same as the solar reference spectrum, within the uncertainties of the FOS measurements (Colina & Bohlin 1997). The near-infrared spectrum of P330E, created by rescaling the reference spectrum of the Sun (see Colina & Bohlin 1997 for details), agrees to within 2–3% with ground-based near-infrared photometry.

In summary, the accuracy of the absolute spectral energy distribution of NICMOS primary standards introduces a systematic uncertainty of about 2–3% in the absolute calibration of the different filters.

#### 3.2. Differential Photometry Across Detectors

The photometric values provided in the headers are obtained from measurements of standard stars in the central regions of the detectors. Both high frequency (i.e. pixel-to-pixel) and low frequency (i.e. large scale structures) sensitivity variations will be corrected using on-orbit flats. The results of the SMOV differential photometry characterization of NICMOS cameras indicate that relative photometry to better than 2% should be attained across the NIC1 and NIC2 detectors when on-orbit flats become available. A Cycle 7 calibration program has been designed to measure, for each camera, and with a fine grid, the photometric deviations as a function of position. A correction image might be generated as a product of this program, if measurable deviations are found.

#### 3.3. Intra-pixel Sensitivity Variations

As with many other array detectors, the sensitivity of the NICMOS detectors is lower near the edge of the pixels than in their centers. It is as though there were small regions of reduced sensitivity along the intra-pixel boundaries. In practical terms this means that for



a source whose flux changes rapidly on a size comparable with or smaller than the pixel size, the measured countrate, and therefore flux, will depend on where the center of the source lies with respect to the center of the pixel. Since this is not known a priori, this effect will introduce some uncertainty in the flux calibration for a point source. This uncertainty will be largest (no more than few percent, we expect) for NIC3 at short wavelengths, for which the PSF is undersampled. For high precision photometry and to compute the amount of photometric uncertainty in a particular camera and filter combination due to this effect, subpixel dithering is recommended.

### 3.4. PSF Variations

The point spread function (PSF) of the telescope changes with time, and this can affect photometry using very small apertures ( $\sim 3$ – $5$  pixels in NIC1 & NIC2). Changes in focus are observed on an orbital timescale due mainly to thermal breathing of the telescope. In addition to this short term PSF variation there is an additional long term NICMOS component, as the cryogen evaporates and the dewar relaxes. As a result of the stress produced by the solid nitrogen on the cameras, NICMOS detectors have been moving, and are still moving, along the focus direction. The motion of the cameras is monitored twice a month and NICMOS focus updates can be periodically implemented, if required. In addition, PSF changes as a function of position in the detector. Tiny Tim simulations are recommended if high precision is required (for details see Krist 1997).

### 3.5. Aperture Corrections

The absolute photometry keywords (PHOTFNU, PHOTFLAM) provided in the header of NICMOS images are currently obtained using an aperture of 25 pixels for NIC1 and of 15 pixels for NIC2 and NIC3. It is often difficult to measure the total flux of a point source using such large apertures where the flux contribution from the extended wings of the PSF, diffraction spikes, and scattered light is also included. This is in particular true in crowded fields where the extended wings of well resolved sources could overlap with each other. If no aperture correction is done, the absolute photometry will be in error, the exact amount depending on the specific aperture radius, filter and camera combination. To take into account aperture correction effects it is advisable to use Tiny Tim PSFs to measure the encircled energy curve of growth as explained in the HST Data Handbook (Voit 1997).

### 3.6. Red Leaks

Many very red targets will be observed with NICMOS at short wavelengths (i.e.  $\sim 1\mu\text{m}$ ). For these sources the flux at  $\sim 2.2$ – $2.5\mu\text{m}$  could be orders of magnitude larger than at  $\sim 1.0\mu\text{m}$  and therefore exceptionally good out-of-band blocking would be required. Pre-launch simulations indicated that for very red sources (temperature  $\sim 700$  K), the photometric errors induced by red leaks might be as large as an order of magnitude in a few filters. The filters for which red leaks might be a problem are: F090M, F095N, F097N, F108N, F110M, F110W, and F113N. Strategies involving observations in multiple filters to model the source spectral energy distribution are required in these cases. Observations of a very red star (Oph S1) have recently been obtained as part of the Cycle 7 calibration plan, the analysis is underway and the results will be posted on the NICMOS Web page.

### 3.7. Non-Zero Zeroth Read Correction

The zeroth read in a MULTIACCUM image happens 0.203 seconds after the reset of the detector. In case a bright source is being observed, this implies that a non-negligible amount of charge will be already accumulated on the detector by the time the zeroth read is performed. The consequences for the absolute calibration of bright sources (i.e. sources for which the measured countrate per pixel is in the range of about 14000 to about 25000 counts



per second) are obvious. Since the zeroth read subtraction from all subsequent reads in a MULTIACCUM exposure is the first step of the calibration processing, the handling of the detector nonlinear response by the current version of the calibration pipeline will be inaccurate. At the time of this writing (September 1997) a modification of the calibration pipeline software is under testing and MULTIACCUM images processed after the new software is installed in the pipeline should be free of the non-zero zeroth read problem. The software fix requires that the observations of bright sources be performed using the MULTIACCUM read mode where all individual readouts are returned from the spacecraft thus permitting an extrapolation of the counts back to the reset time to recover the true charge level.

### 3.8. Color Dependence of Flatfields

The strong wavelength dependence of the NICMOS flatfields limits the photometric accuracy of sources with extreme colors observed in broad-band filters. Simulations with a very red source ( $J-K = 5$  equivalent to a 700K black-body) indicates that these photometric errors are small, around 3% or less (see Chapter 7 of NICMOS Instrument Handbook for details; MacKenty et al. 1997).

### 3.9. Velocity shifts and Photometry with Narrow-band Filters

The photometric conversion factors PHOTFLAM and PHOTFNU for all NICMOS filters are obtained from observations of continuum, emission line free, standards. The integrated flux in  $\text{erg sec}^{-1} \text{cm}^{-2}$  can be obtained as a function of the full width half maximum of the filter and the PHOTFLAM parameter as explained in the HST Data Handbook (Voit 1997). However, if the target has velocity shifts like the system velocity in galaxies or high velocity flows in galactic sources, and the emission line is not at the central wavelength of the filter, the line flux will be in error (in general few to several percent, depending on the filter and velocity shift) and a correction to account for the filter transmission curve is required (see details in Voit 1997).

## 4. NICMOS Absolute Photometry: Preliminary Results

### 4.1. The SMOV Absolute Photometry Tests: First On-orbit Calibration

Images of two solar analogs (P330E and P177D) and a red star (Oph S1) were taken as part of the NICMOS SMOV absolute photometry test in April (proposal ID 7049) and May (proposal ID 7152) of 1997. The two solar analogs were observed with each of the three NICMOS cameras at four (NIC1) or five (NIC2 & NIC3) different wavelengths spanning the NICMOS wavelength range. The red star Oph S1 was observed only with NIC1 and NIC2.

The NICMOS synthetic system consists of a set of response curves which give the transmission/reflectance of all the components which determine the response of the three cameras. Measurements of the detectors' DQE, filter transmissions and NICMOS mirror reflectivities were done in the laboratory. Estimates of the HST Optical Telescope Assembly (OTA) and obscuration by the secondary mirror and NICMOS cold mask have also been included. All these response curves are combined and used with the HST Synthetic Photometry package (*synphot*) to compute the predicted countrates for the observed standards, as a function of camera and filter. The predicted countrates are obtained for a specific set of gain values (5.4 e/ADU for NIC1 and NIC2 and 6.5 e/ADU for NIC3) and the results are compared with the observed countrates, that are flat-field dependent.

The results of the SMOV absolute photometry tests, i.e., the observed/predicted countrate ratios, for the three cameras are shown in Figures 1 to 3. The main results of these tests can be summarized in three major points:

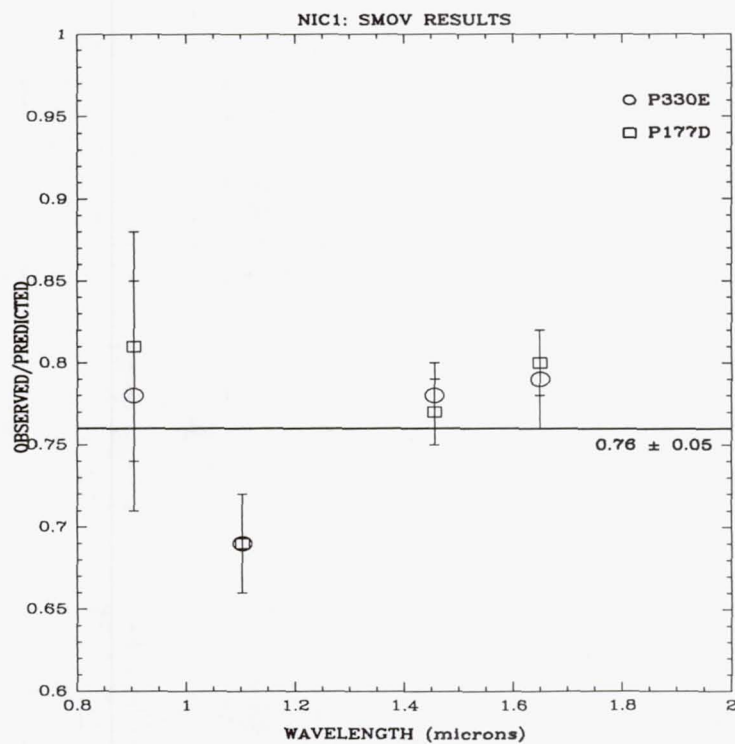


Figure 1. Results of the SMOV absolute photometry tests for NIC1

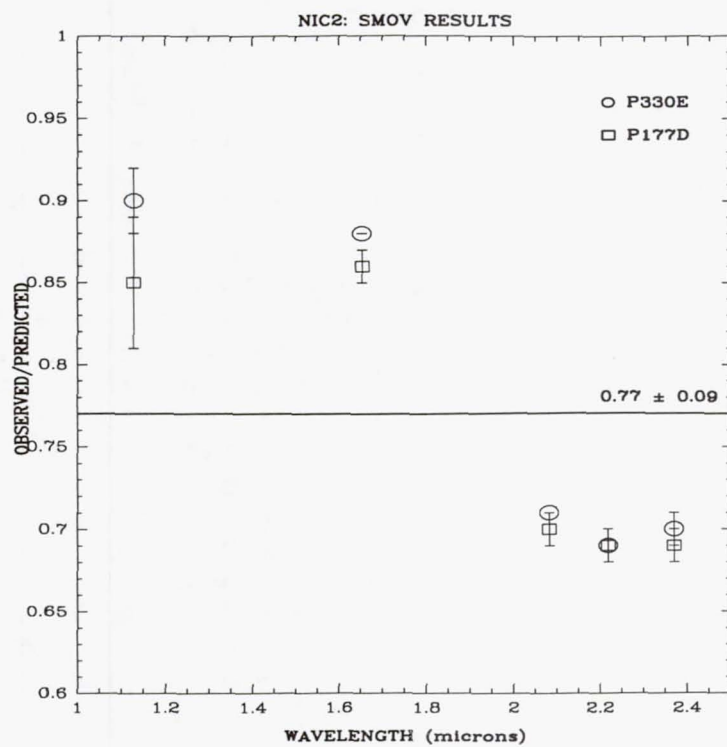


Figure 2. Results of the SMOV absolute photometry tests for NIC2



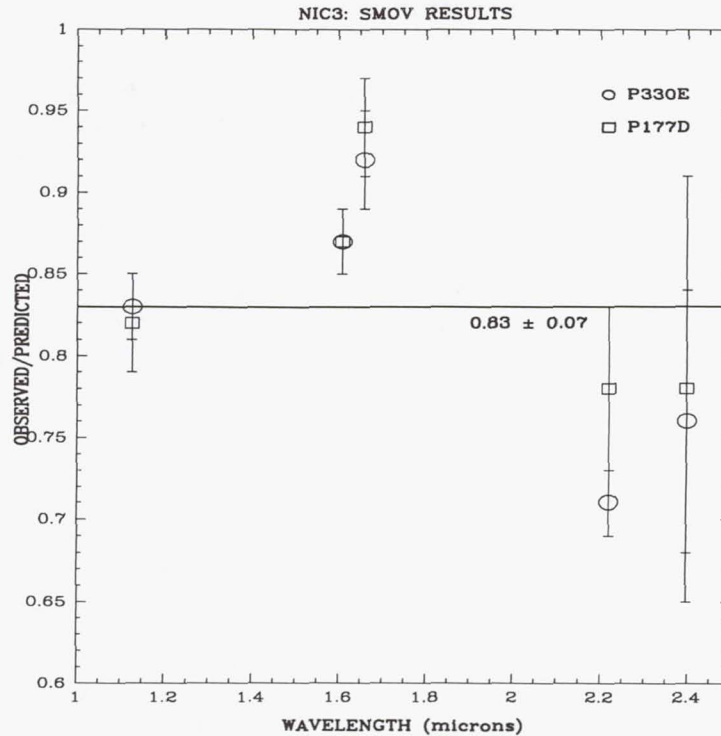


Figure 3. Results of the SMOV absolute photometry tests for NIC3

1. The observed/predicted countrates for the two standard stars agree to within the uncertainties of the measurements which were in general less than 5%. The independent measurements of the observed/predicted ratios show larger uncertainties in some filters like F090M in NIC1, and F222M and F240M in NIC3 (uncertainties at the 7% to 16% level).
2. The observed countrates are lower than the predicted values by about 10% to 30%.
3. The average ratios and uncertainties are very similar for all three cameras:  $0.76 \pm 0.05$  for NIC1,  $0.77 \pm 0.09$  for NIC2, and  $0.83 \pm 0.07$  for NIC3.
4. There exists a smooth wavelength dependence in the ratio of observed/predicted countrates. NIC2 and NIC3 have a ratio that decreases with increasing wavelengths while the opposite seems to be true for NIC1.

In view of these results, preliminary adjustments to the prelaunch countrate predictions to match the observed countrates were implemented in July 1997. The prelaunch NICMOS throughputs were multiplied by wavelength independent factors 0.76, 0.77 and 0.83 for cameras NIC1, NIC2 and NIC3, respectively. This adjustment affected the photometric parameters delivered by the calibration pipeline and an updated photometric table (with new PHOTFLAM and PHOTFNU values) was subsequently created and delivered in July 1997. As a result of these adjustments, the current NICMOS photometric calibration (September 1997) should be correct to 10–15% for all three cameras and across the entire wavelength range covered by NICMOS, if no large normalization errors exist in the transmission curves of filters not used during SMOV.

#### 4.2. Towards an Accurate Calibration: The Cycle 7 Photometric Program

High signal-to-noise images of the primary NICMOS white dwarf (G191-B2B) and solar analog (P330E) standards were taken through all the NIC1 and NIC2 narrow, medium, and broad-band filters as part of the Cycle 7 NICMOS photometric zeropoint program (proposal ID 7691). Additional images of the red star Oph S1 ( $J-K \sim 3$ ) were obtained for a subset of filters, mostly filters at the short wavelength range, to detect any possible red leaks and quantify their contribution when very red sources are observed. No data for NIC3 were taken as part of this program (see plans for this camera in Section 6).

These data have already been calibrated with the most up-to-date version of the calibration pipeline but are still using the vacuum ground-based flats. A recalibration of the data will be done when the on-orbit flats for the different filters become available. A detailed analysis of all the data is underway but a few basic preliminary results can already be mentioned:

1. We confirm the results of the SMOV tests in the sense that there is a smooth wavelength dependence in the ratio of observed/predicted countrates with NIC1 and NIC2 going in opposite directions. This trend is observed in narrow, medium, and broad-band filters.
2. There exists an almost universal systematic difference between the observed/predicted countrate ratios obtained for the solar analog and for the white dwarf. However, the amount and trend of these differences changes from NIC1 to NIC2 and it is unlikely to be due to uncertainties in the spectral energy distribution of the standards. More analysis needs to be done before drawing any firm conclusions.
3. The observed/predicted countrate ratio for most of the filters lies within the expected 10–15% uncertainty, after the adjustment done in July 1997. However, a few filters seem to have normalization errors, the exact amount has not yet been quantified.

#### 4.3. Differential Photometry Accross NICMOS Detectors

Images of a standard star (P330E) in a grid of 25 positions were taken for each of the cameras during SMOV (proposal ID 7050). The images were taken with filter F165M (NIC1 & NIC2) and F160W (NIC3). Countrates were measured for each of the 25 positions across the detectors. NIC1 and NIC3 data were calibrated with vacuum ground-based flats while NIC2 data were calibrated with both vacuum and on-orbit flats available at the time of the observations. The photometric differences normalized to the countrate measured in the central position are shown in Figures 4 and 5 for NIC1 and NIC2, respectively. The main results of these tests are:

1. NIC1 shows photometric differences at the 7% to 9% level but the photometric deviations are only 3% from the average value. It is likely that these photometric differences and deviations will be reduced when on-orbit flats become available.
2. NIC2 shows very good behaviour in terms of differential photometry. The largest photometric differences are at the  $\sim 2\%$  level while the deviations from the average are at the 1% level, or smaller.
3. NIC3 was heavily vignetted at the time the data were taken and the vacuum flats used in the calibration didn't give an accurate representation of the on-orbit pixel-to-pixel and large scale response of this detector.



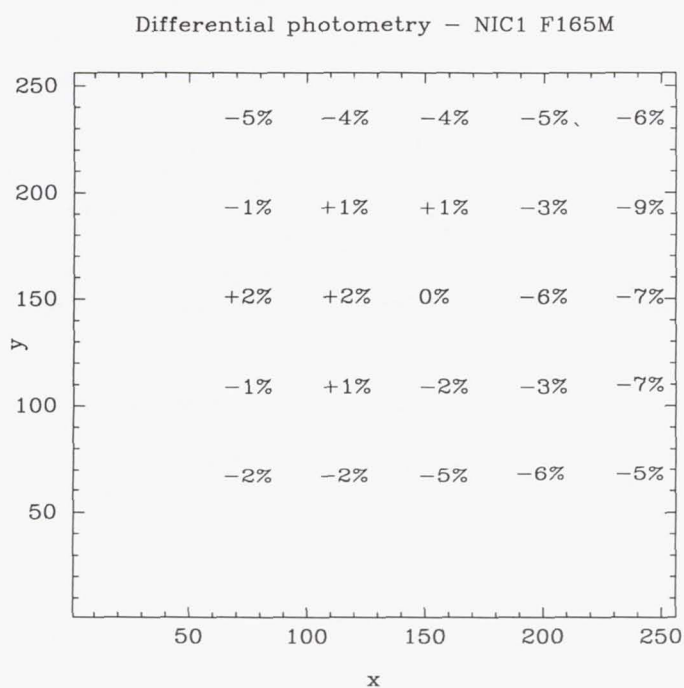


Figure 4. Results of the SMOV differential photometry test for NIC1. Values give the photometric differences with respect to the central value in percentage.

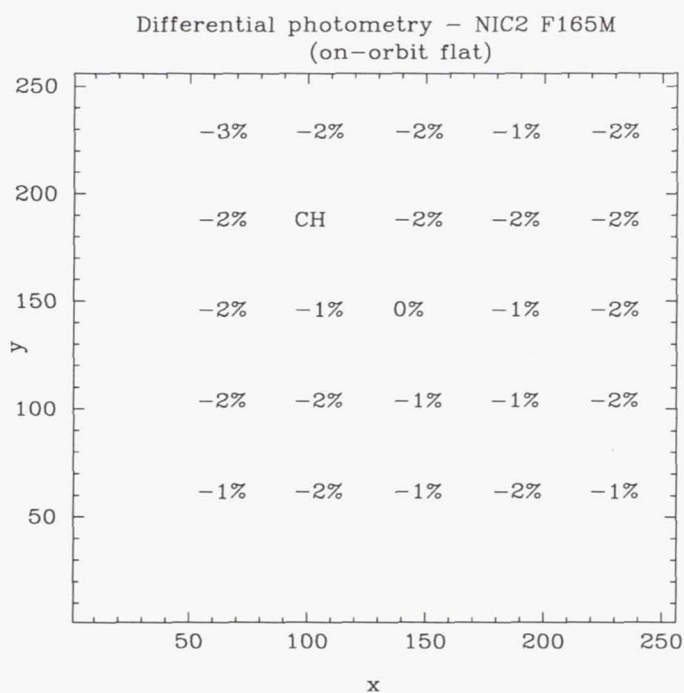


Figure 5. Results of the SMOV differential photometry test for NIC2. Values give the photometric differences with respect to the central value in percentage.

#### 4.4. Photometric Stability of NICMOS Detectors

The photometric stability of NICMOS cameras is being monitored once every four weeks by taking images of one solar analog (P330E) in a subset of filters covering the NICMOS wavelength range (proposal ID 7607). These data are supplemented with additional data from SMOV proposals (7049, 7050, and 7152) to cover the first months of NICMOS after the Servicing Mission and to therefore create a longer temporal baseline.

Analysis of the data is currently underway but independent preliminary measurements by the NICMOS IDT and the NICMOS STScI groups show that the photometric stability of all three cameras during the April–August 1997 period is better than 5%, at least at  $1.6\mu\text{m}$ . The photometric stability as a function of wavelength is also under investigation.

### 5. NICMOS Versus Ground-Based Magnitude Systems

The standard HST JHK system is formed by the F110W, F160W and F222M filters. NICMOS images are calibrated in units of Janskys or Janskys  $\text{arcsec}^{-2}$  and currently there are no plans to compute color corrections and to provide transformations to convert HST F110W, F160W and F222M magnitudes onto ground-based magnitude systems. However, as part of the Cycle 7 absolute photometry program, a few blue stars (white dwarfs), intermediate color stars (solar analogs), and very red stars covering a large range in color ( $-0.2 \leq J-K \leq 3.0$ ) will be observed. Images for a white dwarf (G191B2B), a solar analog (P330E), and a red star (Oph S1) have recently been obtained. Additional standards are being considered and data for these stars could be taken in the future.

Table 1. List of Stars for Photometric Transformations

Name	Type	H	J-H	H-K	Status
G191-B2B	white dwarf	12.6	-0.10	-0.14	data taken
GD71	white dwarf	13.8	-0.08	-0.13	pending approval
P330E	solar analog	11.6	+0.28	+0.07	data taken
P177D	solar analog	12.0	+0.28	+0.06	partially taken
OPH-S1	red standard	7.3	+1.53	+0.94	data taken
CSKE-12	red standard	9.5	+2.08	+0.89	pending approval
BRI0021	red standard	11.1	+0.75	+0.52	pending approval

### 6. The NIC3 Campaign and Related Calibration Plans

As a consequence of the NIC3 defocus, the Cycle 7 calibration plan has been focussed on getting an accurate calibration for NIC1 and NIC2 and on executing a limited calibration program for NIC3. In particular, the Cycle 7 absolute photometry program (proposal 7691) only obtained data to accurately calibrate NIC1 and NIC2 and no data were taken for NIC3. The photometric monitoring program (proposal ID 7607) includes observations with NIC3 in only two filters, F110W and F160W, to monitor the photometric stability of the camera and follow its behaviour. An accurate photometric calibration of the NIC3 camera will be obtained during the NIC3 campaign. This calibration includes observations at the beginning of the campaign of at least three standards (one white dwarf, one solar analog, and one red standard) using all NIC3 filters. Towards the end of the campaign, images for one standard will be taken in several filters to monitor the photometric stability of NIC3 during the campaign.



**Acknowledgments.** E. Bergeron, S. Holfeltz and C. Ritchie have contributed in several aspects to this project but in particular recalibrating SMOV and Cycle 7 data and performing most of the actual measurements reported here. Dr. E. Persson provided ground-based measurements of the solar analogs and red stars. Dr. A. Alonso analysed the data taken for the SMOV differential photometry tests. The authors thank Dr. R. Bohlin for his many contributions in defining and generating the set of NICMOS spectrophotometric standards. The authors want also to thank Dr. C. Skinner for many enlightening conversations regarding the performance and characteristics of NICMOS detectors.

## References

- Bohlin, R.C., 1996, *AJ*, 111, 1743.  
Bohlin, R.C., Colina, L., & Finley, D.S., 1995, *AJ*, 110, 1316.  
Campins, H., Rieke, G.H., & Lebofsky, M.J., 1985, *AJ*, 90, 896.  
Colina, L., & Bohlin, R.C., 1994, *AJ*, 108, 1931.  
Colina, L., & Bohlin, R.C., & Castelli, F., 1996, *AJ*, 112, 307.  
Colina, L., & Bohlin, R.C., 1997, *AJ*, 113, 1138.  
MacKenty, J.W. et al., 1997, *NICMOS Instrument Handbook*, Version 2.0 (Baltimore: STScI).  
Voit, M., 1997, *HST Data Handbook*, Version 3.0 (Baltimore: STScI).

## NICMOS PSF Variations and Tiny Tim Simulations

John E. Krist

*Space Telescope Science Institute, 3700 San Martin Drive, Baltimore, MD 21218, USA*

Richard N. Hook

*Space Telescope – European Coordinating Facility, European Southern Observatory, Karl Schwarzschild Str. 2, D-85748, Garching, Germany*

**Abstract.** Analysis of NICMOS images indicates that the instrument's optics provide high quality imaging over the wavelength range and field of view of the cameras (assuming that NICMOS 3 can be placed in-focus during campaign modes). Optical misalignments and low-level field- and focus-dependent aberrations have slight effects on the imaging performance. Variations of the point-spread functions (PSFs) with wavelength may be important when comparing images through different filters, especially in NICMOS 1 due to its high resolution.

The NICMOS 1 and 2 camera cold masks are shifted with respect to the telescope obscurations, causing elliptical diffraction rings and alteration of the diffraction spike patterns. The mask shift varies with time, altering the diffraction structure mostly in the wings and spiders. It is not currently known whether the NICMOS 3 mask is similarly shifted.

The effects of these alignment and optical surface errors can be studied using the Tiny Tim PSF modeling software. The NICMOS field and focus dependent aberrations and obscuration misalignments derived from the image measurements are included in the simulated PSFs, along with variations due to the filter passbands. The model PSFs match the observed ones well.

### 1. Introduction

When dealing with images from the Hubble Space Telescope (HST) it is necessary to be aware of the characteristics of the point spread function (PSF). The PSF often defines the resolution and sensitivity limits of an observation, rather than the sizes or efficiencies of the detector pixels. Unfortunately, the PSF can vary with time, wavelength, position, and camera. Because of the wavelengths at which it operates, NICMOS has PSFs which differ markedly from those in the other HST cameras (WFPC2, FOC).

NICMOS PSFs vary from well sampled (NICMOS 1 at long wavelengths) to significantly undersampled (NICMOS 3 at shorter wavelengths). One must deal with the large size of the diffraction structure at long wavelengths, which effectively limits the object resolution in some cases. In NICMOS 2, shifting obscurations cause spider patterns and diffraction rings in the wings to vary with time. These changes may be larger than those caused by breathing or object color effects.

These effects can be well modeled by Tiny Tim, a program which can generate simulated PSFs for any wavelength or filter. Tiny Tim PSFs are good matches to the observed ones, making them useful for photometry, deconvolution, and image modeling.

*Note:* In the following discussions, we assume that NICMOS 3 is in-focus, as it will be during observing campaigns with the HST secondary mirror adjusted.



## 2. Wavelength Variations

PSF diffraction structures (Airy rings, spiders) grow larger with increasing wavelength. At longer wavelengths the detector pixels better sample the PSF. This has consequences with regards to sensitivity and contrast.

For instance, as shown in Table 1, in NICMOS 1 ( $f/80$ ,  $0.043''$  pixels) at  $2.2\mu\text{m}$  the peak pixel contains only 3% of the total flux, and the PSF core has a FWHM of over four pixels. The first Airy ring is about 15 pixels ( $0.65''$ ) in diameter. In this case a significant amount of light is distributed over a number of pixels. At  $1.1\mu\text{m}$  the FWHM is 2.3 pixels ( $0.1''$ ) with 10% of the total flux in the central pixel. In NICMOS 2 ( $f/45$ ,  $0.076''$  pixels) the situation is less drastic, since that camera undersamples the PSF at wavelengths less than  $1.8\mu\text{m}$ . The large pixels of NICMOS 3 ( $f/17.2$ ,  $0.2''$  pixels) result in the FWHM remaining constant in that camera, as it undersamples over the entire NICMOS wavelength range.

Table 1. PSF Widths and Peak Pixel Fluxes

	1.1 $\mu\text{m}$	1.1 $\mu\text{m}$	2.2 $\mu\text{m}$	2.2 $\mu\text{m}$
	FWHM (pixels)	Flux in Peak	FWHM (pixels)	Flux in Peak
NICMOS 1	2.3 ( $0.1''$ )	10%	4.5 ( $0.2''$ )	3%
NICMOS 2	1.3 ( $0.1''$ )	25%	2.5 ( $0.2''$ )	8%
NICMOS 3	1.3 ( $0.3''$ )	52%	1.3 ( $0.3''$ )	39%

One must be cautious when comparing images at different wavelengths taken in NICMOS 1, and to a lesser degree in NICMOS 2. Objects with sharp features may show color differences between PSFs rather than actual spatial color gradients. Also, the measures of object widths are limited to the PSF width at a given wavelength (jet widths or nebula tendrils, for instance). It is especially important to convolve data models with a PSF before comparing with observed images. An example of this is shown in Figure 1.

Because little light is in the peak pixel at long wavelengths in NICMOS 1 and 2, deconvolution may provide improvements in sharpness. As discussed later, Tiny Tim model PSFs match the observed ones well and have the advantage that they are noiseless. However, as Figure 1 demonstrates, deconvolution may introduce image artifacts which can negate its advantages.

Narrow-band filter images will show very sharp diffraction structures, since the PSF does not vary significantly over the filter bandpass. A PSF in a wide-band filter is smoother, since the expansion of the diffraction structure over the filter's wavelength range blurs the rings. Figure 2 shows observed and model NICMOS 2 PSFs in different filters.

The PSFs in wide-band (and to a lesser degree, medium-band) filters are somewhat dependent on the spectrum of the object being observed. Within the same filter, the PSF of a very red object will be slightly different from that of a blue one. In most cases, the differences will actually be insignificant (except, for example, if one is comparing well-exposed PSFs of M versus O type stars). See the discussion on PSF subtraction by Krist (1997) in these proceedings.

Another aspect of increasing wavelength is that the PSF becomes less sensitive to aberrations in the system, as the path length differences caused by optical surface errors become smaller relative to the wavelength of the light. One-quarter of a wave of an aberration at  $\lambda = 0.5\mu\text{m}$  is only  $1/16$  wave at  $\lambda = 2\mu\text{m}$ .

## 3. Field and Focus Dependent Aberrations

As with any real-world optical system, NICMOS has low level aberrations which cause observed PSFs to differ slightly from theoretically perfect ones. The dominant aberrations

Figure 1. A simulation of Io on NICMOS 1 ( $0.043''/\text{pixel}$ ), assuming that Io appears constant with wavelength. All images are at the same angular scale, which is indicated in the upper right image. The mapping of the image onto NICMOS 1 detector pixels is shown at the top, without the PSF. In the lower left frame, the image has been convolved with a  $1\mu\text{m}$  PSF, and by a  $2\mu\text{m}$  PSF to its right. Note that the differences in light distribution between the two. The  $2\mu\text{m}$  deconvolved image reveals artifacts of the restoration process, notably brightening of the left limb.

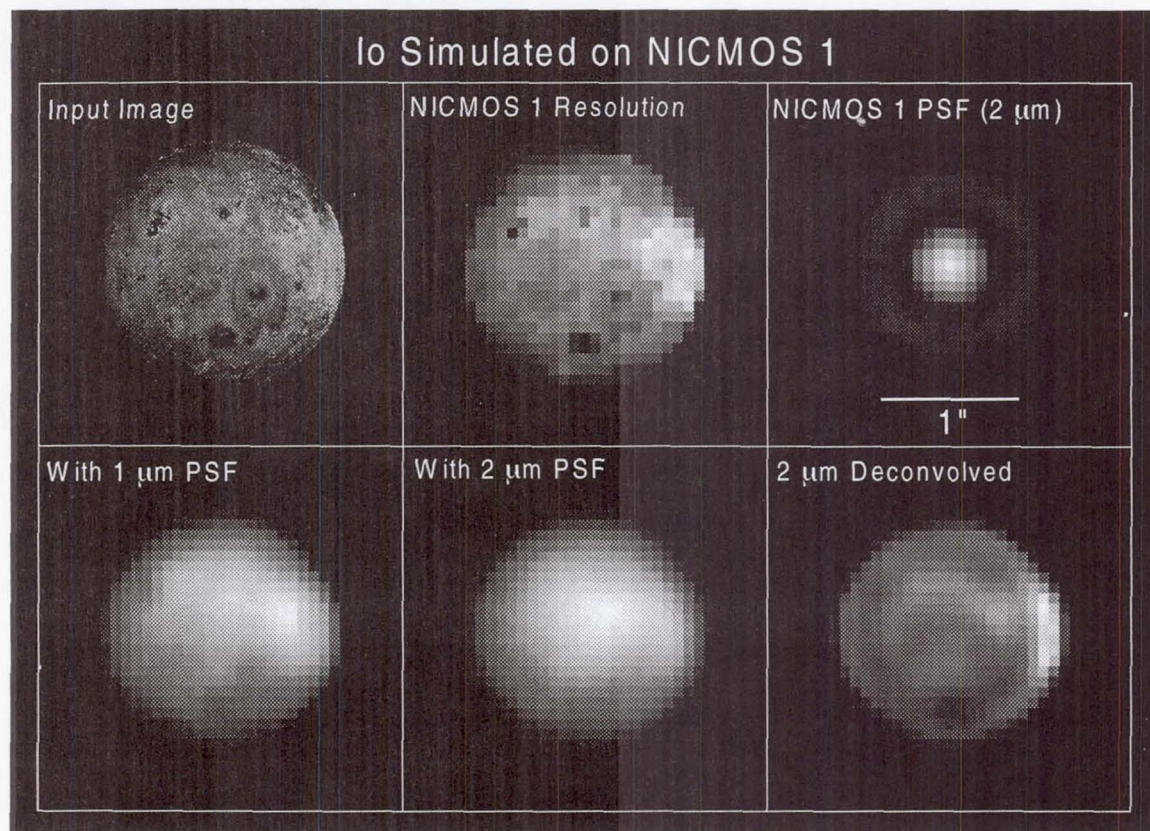
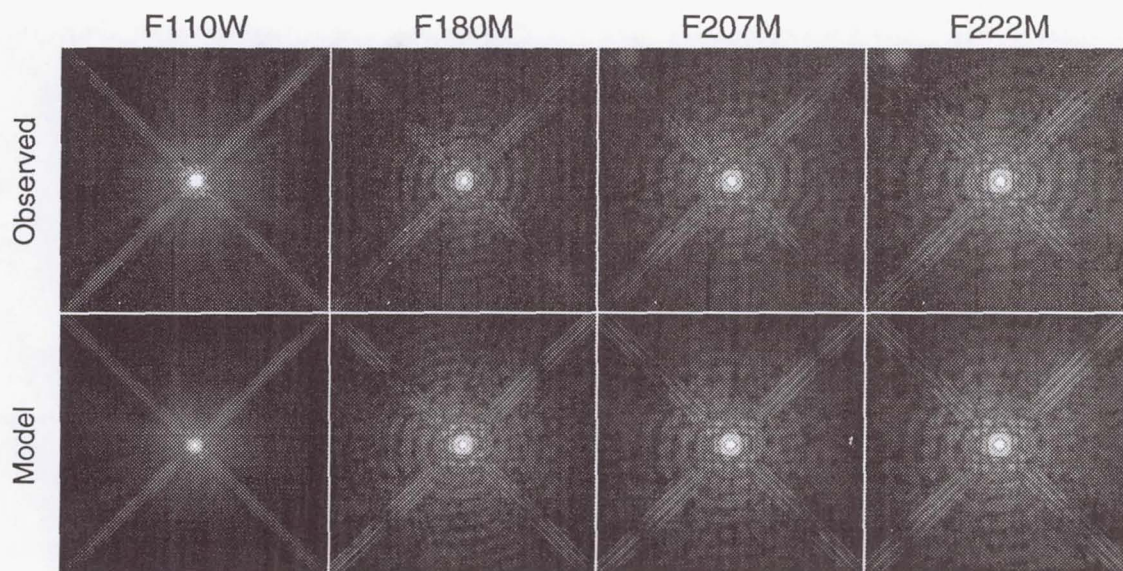




Figure 2. Variations of the NICMOS 2 PSF with wavelength and filter bandwidth. The corresponding Tiny Tim model PSFs are also shown. The images are 10" on a side.



(excluding focus) are coma, astigmatism, and residual spherical aberration. An extensive analysis of NICMOS star images was done using phase retrieval methods (Krist and Burrows 1995) to measure these aberrations and determine their dependence on field position and focus. This used focus monitoring images of a star cluster in which the focus was varied by moving the Pupil Alignment Mechanism (PAM) (phase retrieval is more accurate when defocused PSFs are used).

There is roughly 1/15 of a wave (@ 630 nm) of astigmatism, 1/15 wave of coma, and 1/30 wave of spherical in NICMOS, with the values varying slightly among the three cameras. Some of the astigmatism is due to the imperfect HST optics rather than the camera. The sign and amount of spherical aberration is consistent with that measured in the other corrected HST cameras (WFPC2 & COSTAR/FOC), indicating that the officially designated amount of HST primary mirror spherical aberration is probably in error by a small amount (see Krist & Burrows 1995). In any case these aberrations are small and are similar to those measured in other HST instruments.

Focus, astigmatism, and coma vary slightly with field position, as they do in most optical systems, including WFPC2. The largest variations are in NICMOS 3, due to its larger field of view. The focus in NICMOS 1 and 2 changes linearly with field position, and in NICMOS 3 it varies quadratically with the best focus near the center of the detector. Analysis by Eddie Bergeron (STScI) of the horizontal and vertical plate scales indicates that the detectors are not significantly tilted, so the focus position dependence is due to optical errors or misalignment. Bergeron has also confirmed the focus variations (at least in NICMOS 2) by measuring changes in encircled energy curves. Anatoly Suchkov (STScI) has verified these variations using the same phase retrieval software on later focus monitoring data.

When NICMOS 3 is placed in focus during the upcoming campaigns by moving the telescope's secondary mirror, it will be necessary to adjust the Field Offset Mechanism (FOM) to avoid vignetting. This will introduce changes in the aberrations (mostly astigmatism). The FOM can also be moved during observations with the other cameras to select adjacent fields. The PSFs in those cases will change as well due to increased astigmatism.



Because NICMOS operates at longer wavelengths than the other HST instruments it is less sensitive to aberrations, and they cause little variation on the PSF structure or light distribution. For example, PSFs were simulated using Tiny Tim at  $1.6\mu\text{m}$  at opposite corners of the field of view, with field dependent aberrations included. The variations in flux within small apertures centered on the PSFs were then computed, as shown in Table 2. Because NICMOS 3 undersamples the PSF, it is largely insensitive to small aberration changes.

Table 2. Flux variations between extreme NICMOS field positions

	Aperture Radius (pixels)		
	1	3	5
NICMOS 1	2.2%	1.9%	1.5%
NICMOS 2	3.6%	1.9%	0.7%
NICMOS 3	2.4%	0.0%	0.0%

Coma, astigmatism, and spherical aberration also vary with large changes in focus. However, since the focus of each camera remains essentially constant, the effects on PSFs are negligible. Variations at the level of breathing are not measureable.

#### 4. Cold Mask Misalignment

At the entrance of the dewar containing the NICMOS detectors is a mask intended to block infrared emission from the telescope spiders and primary mirror edge. The mask itself is cooled, hence it is called a cold mask. Each camera has a mask, and those for NICMOS 2 and 3 contain additional tabs to cover the support pads on the HST primary mirror. In NICMOS 2 the mask also serves to reduce scattered light from the telescope obscurations as part of the coronagraph.

The masks and the telescope's obscurations are supposed to be aligned, but recent analysis of NICMOS 2 SNAP images (see Krist (1997) in these proceedings) indicate that camera's mask is shifted with respect to the HST obscurations. The visible results of this shift are elliptical diffraction rings and changes in the banding patterns in the spiders. There are more bands in one spider diagonal than the other, which suggests that the HST and cold mask spiders appear separated along one direction.

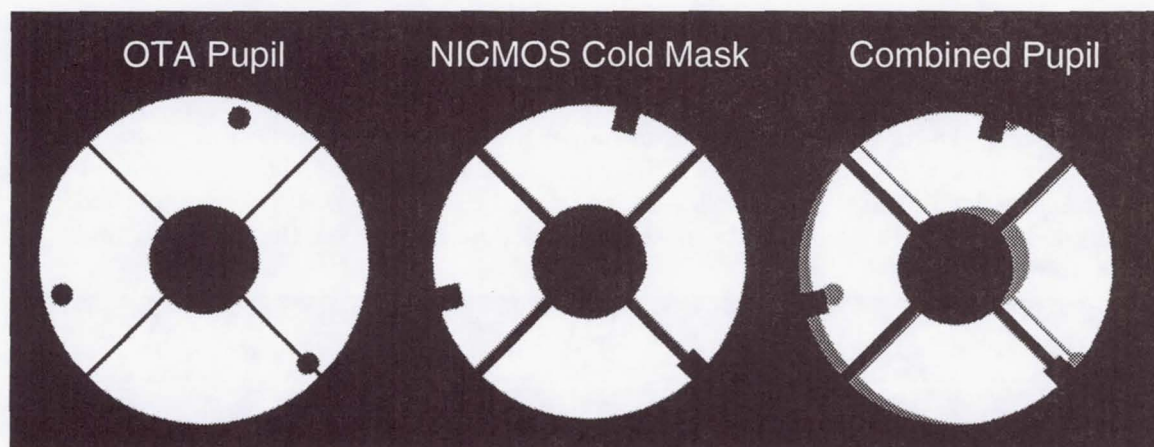
Experiments with shifting the NICMOS 2 cold mask in Tiny Tim reproduced these effects well. The mask is shifted by about 11% of the pupil radius (defined by the edge of the telescope primary), with the HST and mask spiders well separated along one direction, as shown in Figure 3. Figure 4 illustrates the difference between PSFs with aligned and shifted masks and the ability of Tiny Tim models to reproduce the effects.

The match between model and observed PSFs is somewhat indirect evidence of the mask shift, but there is more direct proof. Gerchberg-Saxton (GS) phase retrieval can be used to obtain pupil and wavefront information by iteratively solving for the complex-valued optical transfer function (Krist & Burrows 1995). An initial guess for the wavefront and obscuration pattern is provided to the algorithm, and constraints on the pupil function can be enforced at each iteration (such as zero transmission outside of the pupil).

GS algorithms require high signal-to-noise data over a large number of pixels to define the high frequency structure in the pupil function. This typically means that highly defocused PSFs are used, since they have a large number of pixels with similar intensities. In-focus PSFs are usually well exposed in the core but have faint wings, where most of the optical information lies. However, because the SNAP program PSFs are so highly exposed, there is enough signal in the wings to use GS phase retrieval methods.



Figure 3. Simulated obscuration patterns for HST and NICMOS. On the left is the telescope pattern with secondary mirror obscuration, spiders, and mirror support pads. The middle image shows the NICMOS 2 cold mask, which would optimally be aligned with the telescope obscurations. On the right is the predicted NICMOS 2 obscuration pattern with the cold mask shifted. The telescope obscurations are color coded grey.



A SNAP PSF was selected which was well exposed and had no companions. The core was saturated, so those pixels were replaced by ones from an unsaturated PSF with a similar registration. GS phase retrieval was applied with only a clear aperture as the initial pupil function. At each iteration the pupil function was constrained to have zero flux outside of it, but no constraints were placed inside.

As shown in Figure 5, at the first iteration the algorithm produced an elliptical central obscuration. In later iterations, as higher frequency structure was fitted, the spider obscurations became more pronounced. Because the telescope pupil is generally symmetrical, there is some ambiguity as to which side the mask is shifted - either way would produce most of the same effects in the PSF. Because of this, the GS routine has essentially created two pupils, with the mask shifted to either side of the center. Each pattern contributes half of the throughput of the pupil function. This creates spiders on each side of the thinner telescope spiders along one diagonal, as well as two alternative central obscurations. The offset of the darker (cold mask) spiders from the thinner (telescope) spiders is the same as that derived from the Tiny Tim model experiments.

The shifted mask causes a 10% decrease in throughput relative to an aligned one and reduces the peak pixel by 10% with respect to the total PSF flux. It also likely reduces the efficacy of the coronagraph, since the HST obscurations are not covered. One unsolved problem is how the unmasked portions of the relatively warm HST optics (especially the region outside the primary mirror) contribute to the dark count rate in NICMOS 2. The off-primary region comprises 3% of the clear aperture. There have been no indications of an abnormally high rate, which one would expect with the observed mask shift.

The NICMOS 2 mask appears to shift slightly (0.5% of the pupil radius) and randomly with time (on order of an orbit) about the general offset position. The bands in the spiders change location, with bands along one diagonal moving outwards while those on the other diagonal move inwards. This can only be explained by obscuration shifting, as color or focus variations would cause the bands to move together, and such variations are too small to account for the amount of band motion. There are also small changes in the flux distribution among the rings and core. For example, at  $\lambda = 1.6\mu\text{m}$ , a 0.5% mask shift will change the peak pixel value by 1.1%. In comparison,  $3\mu\text{m}$  of breathing will change the pixel by 0.6%



Figure 4. Examples of the effects of cold mask shift on NICMOS 2 PSFs at  $2.2\mu\text{m}$ . An observed PSF from the NICMOS SNAP program is shown in the upper left. To its right is a Tiny Tim model PSF with the measured aberrations but no mask shift, and a model PSF with mask shift on the right. Notice the circular rings in the aligned mask case, compared to the observed PSF and shifted mask model. Also, the bands in the spiders match between the observed and shifted mask model.

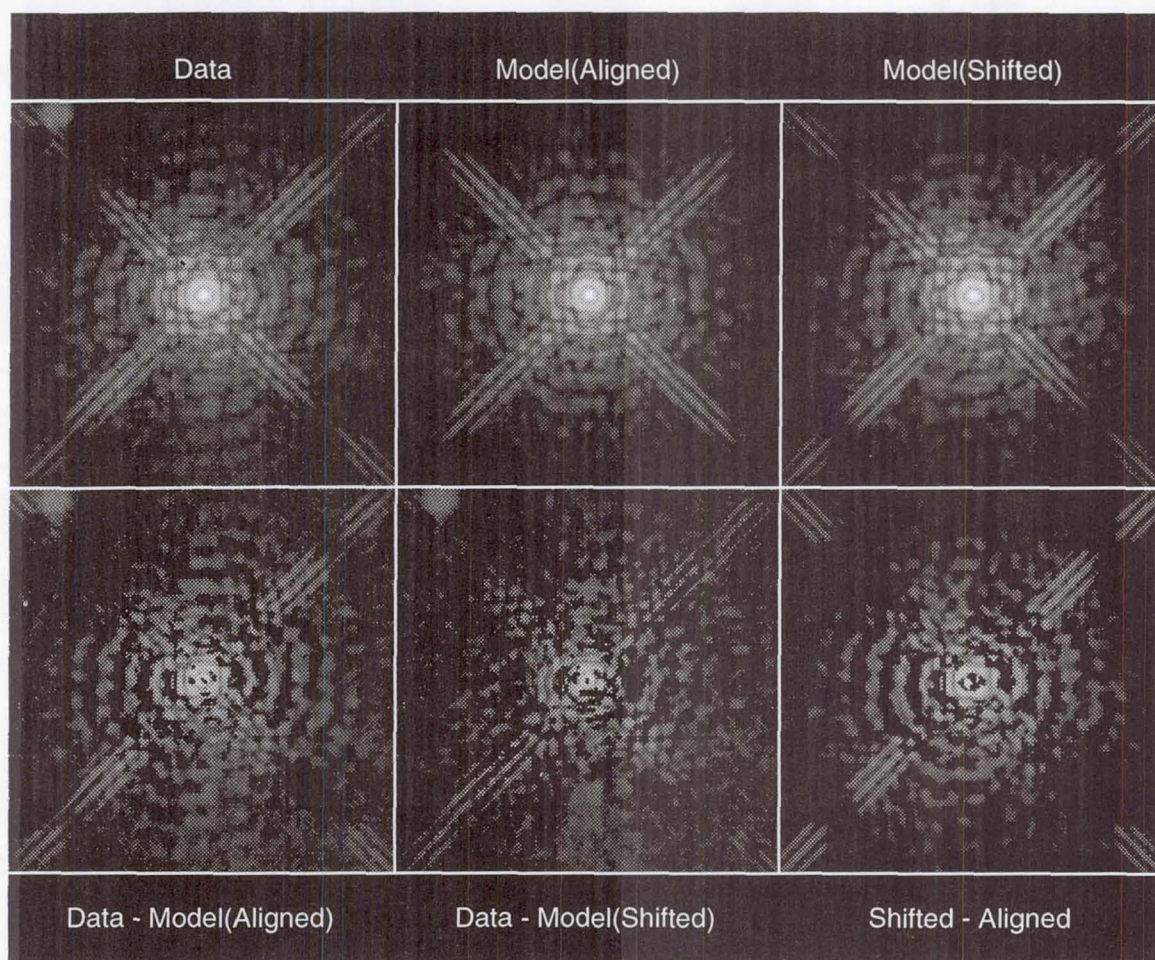




Figure 5. Results of Gerchberg-Saxton phase retrieval on a F222M NICMOS 2 PSF from the SNAP program. On the left is the observed PSF. The retrieved pupil amplitude after one iteration of the algorithm is shown in the middle. Note the elliptical central obscuration. After twenty iterations, the spiders are better defined.

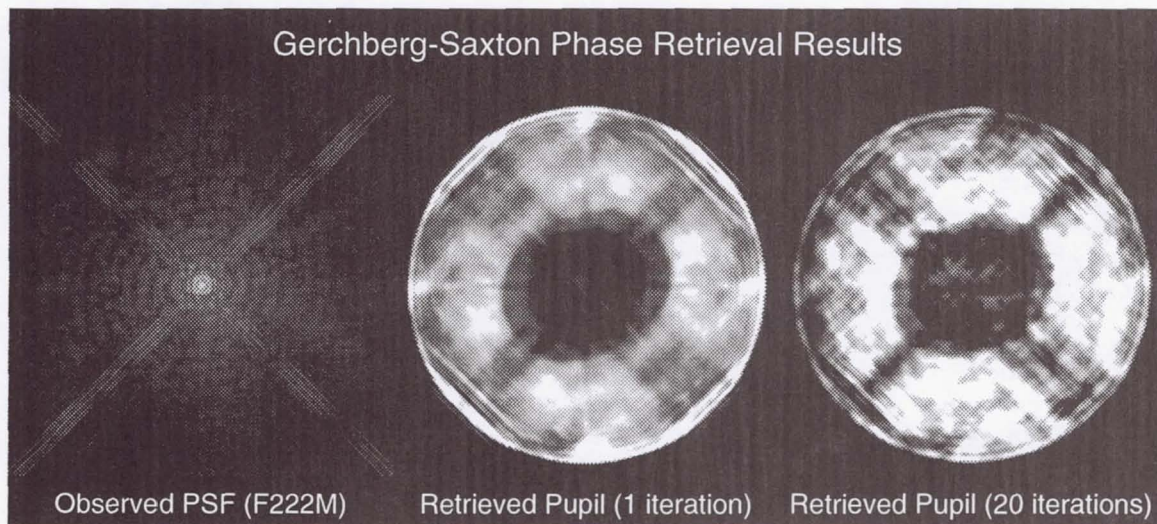
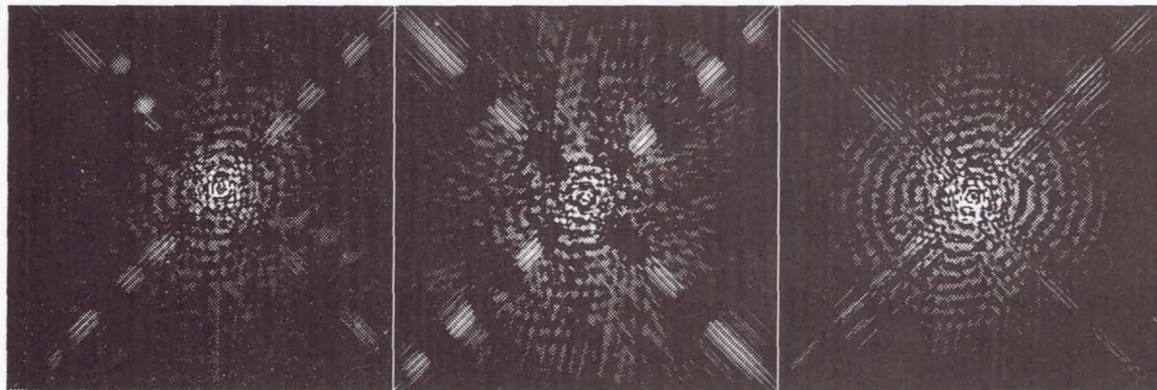


Figure 6. Examples of the effects of time-dependent shifting versus focus changes. The image on the left is the subtraction of one observed NICMOS 2 SNAP PSF from another. The middle panel shows the subtraction of two Tiny Tim model PSFs generated different cold mask shifts. On the right is the difference of two model PSFs, one in-focus and the other with  $7\mu\text{m}$  of breathing. Note the differences in the diffraction spike residuals between the mask shifted and the focus-modified PSFs.





and  $7\mu\text{m}$  by 1.4%. Thus, mask shift in NICMOS 2 is as important as breathing for core photometry, and is more important for PSF subtraction in the wings. The mask shifting affects throughput by less than 0.3%.

Figure 6 shows subtractions using observed PSFs and models with the mask shifted by a small amount (in addition to the large scale shift). The similarity between the two images prove that the residuals seen in the SNAP program subtractions discussed by Krist (1997) are due to time-dependent cold mask shifting.

The diffraction spikes in NICMOS 2 PSFs are 0.5 degrees from being perpendicular, indicating that there is some rotation of the cold mask with respect to the HST obscurations. Because of the added complexity of determining both mask shift and rotation, this effect is not currently included in the Tiny Tim models. It is only obvious in the wings of the PSF (beyond about  $4''$ ).

NICMOS 1 PSFs show evidence for a similarly shifted mask. NICMOS 3 may also have a shifted mask, but there is currently no known data sufficient to show it.

## 5. Tiny Tim

Tiny Tim has been used since 1991 to create synthetic HST PSFs for deconvolution, algorithm testing, proposal planning, and optical analysis. It is written in standard C and has been used on a wide variety of computers running VMS, UNIX, and Windows. The software can generate a PSF for a given wavelength or filter passband, and subsampling and jitter are options. Zonal errors in the HST mirrors are included. The PSFs are written out as FITS or GEIS (STSDAS) image files.

Support for NICMOS was added in version 4.2 by Hook with the addition of the cold mask to the pupil pattern and a new option for user-defined spectra/filter throughput tables. Krist added field and focus dependent aberrations to version 4.3 and cold mask misalignment to version 4.4.

The software consists of two programs: `tiny1` and `tiny2`. `tiny1` asks the user a series of basic questions about the PSF and then generates a parameter file. The second program, `tiny2`, reads the parameter file and computes the PSF model.

The user is asked for the position of the PSF on the detector, the position of the PAM mirror during the observation (provided by the NPFOCUS keyword in the calibrated data header), and the PAM position for best focus (available on the World Wide Web). The amount of defocus at the center of the field is computed from the difference between PAM positions and then added to the focus value given in the parameter file (which is zero by default but can be changed by the user to investigate breathing effects, etc.). Coma, spherical, and astigmatism are adjusted for focus. Then, the specified PSF position is used to compute the changes to coma, astigmatism, and focus.

Cold mask misalignment is included for NICMOS 1 and 2, while the mask in NICMOS remains aligned. The user can adjust the mask shift by changing values in the parameter file.

Before the addition of NICMOS, the user was allowed to generate either a purely monochromatic PSF or a polychromatic one through a given filter using one of seven object colors. The polychromatic PSF is formed by adding monochromatic PSFs generated at wavelengths sampling the filter's bandpass, with appropriate weighting for filter response and object spectrum. This filter scheme would not have worked as well for NICMOS, given the spectral energy distributions (SEDs) of the objects observed in the infrared. Instead of having to select a combination of a filter and an object color, the user can now provide a list of wavelengths and weights to use for generating a polychromatic PSF. Files containing wavelengths and respective throughputs for NICMOS filters were provided by Glenn Schneider (NICMOS IDT) which a user can multiply by an SED of their choice to provide input to Tiny Tim. This option is available for all cameras, not just NICMOS.



Tiny Tim generates PSFs by computing the Fourier transform of the optical transfer function of a system, which is comprised of the obscuration pattern and wavefront error function. All obscurations are assumed to be in the same plane (thus the coronagraphic mode cannot be modeled using the current code). At each wavelength a critically sampled PSF is generated which is then integrated over detector sized pixels, which may be subsampled if the user wishes.

The NICMOS PSF models produced by Tiny Tim are excellent matches to the observed ones, typically better than those for the other HST cameras. This is due to a number of factors. In the infrared the PSF is less sensitive to aberrations, so mismatches between assumed and actual optical errors are less important than in instruments which observe at shorter wavelengths. Also, because focus runs were obtained on a star cluster, the field and focus- dependent aberrations could be measured for each of the three cameras and incorporated into the models. Unlike WF/PC-1 and WFPC2, the NICMOS obscurations (the cold masks) do not shift with respect to the telescope's depending on position, so the PSF is more stable across the field.

Since a significant portion of the total flux in a NICMOS PSF may be in the diffraction rings or off-center portions of the core (especially in NICMOS 1), there will be some inherent blurring of an object relative to the resolution of the detector. As mentioned previously, such images are candidates for deconvolution, which could improve contrast. Because they are noiseless and easy to obtain, Tiny Tim PSFs are good alternatives to using observed ones.

**Acknowledgments.** Much of the work described here used NICMOS 2 star images from SNAP program 7420, which are presented with permission of David Golimowski (JHU), Principal Investigator.

## References

- Krist, J.E., 1997, this volume.
- Krist, J.E. & Burrows, C. J., 1995, *Appl.Optics*, 34, 4951.
- Krist, J.E. & Hook, R.N., 1997, *The Tiny Tim User's Manual v4.4* (Baltimore: STScI).

## Narrow-Band Emission Line Imaging with NICMOS: Lessons Learned from the Data Reduction of OMC-1

Susan R. Stolovy

Steward Observatory, University of Arizona, Tucson, AZ, 85721

**Abstract.** Narrow-band emission-line imaging with NICMOS is discussed, with an emphasis on what has been learned from the data reduction of the molecular hydrogen imaging of OMC-1 with Camera 2. Issues discussed here include: continuum subtraction, photometry, electronic ghosts, and mosaicking images with different sky orientations.

### 1. Continuum Subtraction

Accurate continuum subtraction is clearly a crucial step to obtaining a pure line image. For this reason, pairs of narrow-band filters have been provided in NICMOS to image such astrophysically interesting lines as: HeI (F108N/F113N), [FeII] (F164N/F166N), Pa  $\alpha$  (F187N/F190N), [SiV] (F196N/F200N), H<sub>2</sub> (F212N/F215N), and Br  $\gamma$  (F216N/F215N). The discussion here is based on the Early Release Observations (ERO) of the Orion Molecular Cloud (OMC-1) in H<sub>2</sub> taken on April 12-13, 1997. (Stolovy et al. 1997).

#### 1.1. Relative Photometry

Table 1 shows a comparison of five different methods of determining the *relative* flux calibration for the two narrow-band filters F212N and F215N for Camera 2. None of these assumes any prior (ground-based) knowledge of the absolute flux of the astronomical object. These methods were remarkably consistent. A multiplicative factor of 1.10 was adopted to normalize the F215N filter to the F212N transmission.

Table 1. Relative Photometry of Filters <sup>a</sup>

Method	F212N	F215N	Ratio (215/212)
Absolute Flux (P330E)	$4.07 \times 10^{-5}$ Jy/ADU/s	$4.48 \times 10^{-5}$ Jy/ADU/s	1.10
Flat Field Avg. Count Rate	29.8 ADU/s	26.6 ADU/s	1.12
Photometry Header Keyword PHOTFNU	$4.97 \times 10^{-5}$ Jy/ADU/s	$5.49 \times 10^{-5}$ Jy/ADU/s	1.10
Median in 'blank' part of OMC-1 <sup>b</sup>	0.517 ADU/s	0.475 ADU/s	1.07
Exposure Time Calculator (S/N) <sup>c</sup>			1.08

<sup>a</sup>All values rounded to 3 significant figures

<sup>b</sup>Median over 400 pixels in area with minimal H<sub>2</sub> emission; Typical 1- $\sigma$  for ratio is 0.05

<sup>c</sup>Ratio based on signal/noise estimates for fluxes ranging from 1mJy to 1 Jy, exposure times chosen to give S/N  $\geq$  100

#### 1.2. Absolute Photometry

The absolute photometry was based on observations of the standard star and solar analog, P330E. This star was observed in many NICMOS filters, although not in F212N and F215N.



The spectrum of P330E is sufficiently well-known that, in conjunction with known filter response curves and flat fields, the error in characterizing the standard star spectrum (and translating that to photometry in the NICMOS filters) is estimated to be accurate to better than 5% (M. Rieke, private communication). However, the absolute photometry derived from observations of P330E have been updated several times since the Orion observations in April. The header keyword values (e.g. PHOTFNU, PHOTFLAM) have changed quite drastically since these very early observations in April, and we caution observers to employ independent methods of absolute flux calibration if possible. There is some evidence of time-dependent photometric behavior in NICMOS, which has yet to be fully understood. The current estimate of absolute photometry accuracy is 10–15% (Colina & Rieke 1997).

We have also done a rough comparison of the adopted absolute photometry with both ground-based continuum (K-band at  $2.2\ \mu\text{m}$ ) and  $\text{H}_2$  (with  $1.5''$  resolution). Both were consistent to within the rather large errors of the ground-based measurements ( $\pm 15\%$ ). In a field full of bright, extended emission as well as crowding from stars, one must first degrade the NICMOS image to the equivalent beam size of ground-based images to truly compare the photometry. This has yet to be done in detail; at this point, the absolute photometry of highly saturated sources in NICMOS images (such as BN in the OMC-1 image) is suspect, but all other objects should be valid to an estimated 15%.

## 2. Linearity and Persistence

At the time of observation, it was clear that the “calnica” reduction software was not properly correcting non-linear responses of some pixels, which appeared as low values near the centers of moderately bright stars and in the first Airy ring for highly saturated stars. We interpreted this as a failure of the linearity reference file to flag non-linear pixels early enough during the onset of saturation, when the count rate displays a marked decrease. To correct this, the linearity reference file was modified by multiplying by 0.95 to lower the threshold for saturation flagging. This appeared to work to first order, but the preferred algorithm for linearity correction is still work in progress, including the effects of high count rates in the “zeroth” read.

Persistence must be present in those pixels that are saturated or near saturation. However, since no dithers were done during an orbit (although a change in filter was made), there is no way to observe latent images directly from the OMC-1 data. There was no clear signature of persistence between the last observation of the bright star BN (which saturated in 3 seconds) and the first observation of the new target, about 1 hour later. We hope to model persistence characterized by other observations (with dithers) in order to estimate the effects on photometry of bright objects. Latent images in such a dither pattern have recently been observed in darks taken after observing saturated sources even 30 minutes after exposure.

## 3. Seeing Ghosts

It is now well-known that “electronic ghosts” appear one quadrant (128 pixels) away from saturated pixels due to electrical crosstalk between detector quadrants. For especially bright sources, a “stripe” spanning two adjacent quadrants is seen along the readout direction where the bright source is located as well as 128 pixels away in the other 2 quadrants. This is often a very subtle effect (with signal levels for the “ghost” typically  $\geq 1000$  times fainter than the bright object), but an important one in assessing the validity of faint sources in a field such as OMC-1. For instance, a faint source located near the suspected outflow source ‘I’ thought to power the molecular outflow in OMC-1 was observed in two overlapping frames (see Stolovy et al. 1997). In one pointing, a bright star was located exactly 128 pixels away, but no such star was present in the other pointing, where the faint source was

weaker in flux. Therefore, this object of intrinsic scientific interest is part real and part electronic ghost!

It has yet to be determined if optical ghosts (caused by reflections) exist in NICMOS images. Latent images can mimic in-focus optical ghosts as seen in the FOM test (proposal 7156) where a bright star is moved around on the detector.

#### 4. Orientation Considerations

For these ERO observations, no ORIENT constraint was given between visits. Each visit was an orbit, and the SAME ORIENT in RPS2 should have been used to force the different visits to have the same sky orientation. This complicates the analysis and mosaicking of NICMOS images in several ways, as discussed below. These are listed as a caveat to others who might either inadvertently or purposefully (for instance, in the case of roll angle changes for coronagraphic observations) obtain spatially overlapping NICMOS data with different sky orientations. The maximum change in orientation between the 5 orbits of the OMC-1 data was  $\sim 4.5$  degrees.

- Each image must be rotated according to orientation in header before mosaicking. Note that header parameter ORIENTAT is the angle required to rotate the image by to get north up; e.g., if ORIENTAT =  $-120$ , rotate the image clockwise 120 degrees. The IRAF routine `rotate` with cubic spline interpolation was used, which inevitably smooths the data slightly.
- The spatial coverage was not as complete as it would have been with a constant orientation.
- Diffraction patterns are fixed relative to detector coordinates, so patterns will not match up if overlapping frames have different orientations. Note that diffraction patterns from nearby bright stars are not attenuated when star is off detector. (BN's diffraction spikes can be seen more than  $20''$  from the star's centroid!)
- If deconvolution is used, each image must be deconvolved with *unrotated* images so that the diffraction pattern of the PSF matches the data. If each image is part of a mosaic with large overlaps between frames of different orientations, the S/N will be compromised, as the mosaic cannot be deconvolved.

#### 5. Construction of F212N, F215N and H<sub>2</sub> Mosaics

A mosaic routine written in IDL was used to assemble the OMC-1 images. It accepts a list of offsets determined by centroids on stars common to both images or one can "blink" images by eye to align and produce the offset list (this is especially useful for diffuse features). The mosaic procedure keeps track of statistical weights for each pixel and replaces bad with good pixels if there is overlap. Each image was corrected for the aspect ratio of the plate scale and was then rotated so that north was up and east to the left before mosaicking. The plate scale, determined on April 17 (a few days after the observations), was  $0.076320''/\text{pix}$  in x and  $0.075655''/\text{pix}$  in y. The  $256 \times 256$  pixel images were rebinned to  $516 \times 511$  images to correct the non-square aspect ratio and to allow for a more accurate registration of spatially overlapping images. The F212N and F215 mosaics were produced with identical rotations and offsets. The resulting alignment accuracy is better than  $0.02''$  (half of the small pixel size). The mosaics were then rebinned by a factor of two to approximate the size of original detector pixels, producing square pixels with a plate scale of  $0.07577''/\text{pix}$ . The effects on point-spread functions due to rotation and rebinning caused a minimal amount



of broadening (less than 3% FWHM). Each mosaic was then converted to Jy/pixel using the absolute conversion factors listed above derived from the P330-E model.

In order to produce a pure H<sub>2</sub> line image, the flux-calibrated F215N image needs to be subtracted from the F212N image. It became apparent that there was a shift in the centroids of stars in the two mosaics. A shift of  $\approx 0.2$  pixels was necessary in order to align the mosaics, which was done with the IRAF routine `imshift`. This rather large shift (twice the rms jitter of 7 mas) may have been partly explained by ill-defined apertures during the ERO phase; the targets were not in the center of the array, which could have introduced a small tracking error. Whether such shifts are caused by pointing shifts or filter optics, they will likely be present at small levels for narrow-band imaging. A shift as small as 0.02 pixels (Camera 2) is evident in comparing subtracted images.

As a sanity check on the correct subtraction of F215N from F212N, the relatively "blank" areas of the OMC-1 mosaic do indeed have a median value near zero (the median is of order  $1.3 \times 10^{-6}$  Jy/pix or  $\sim 2\sigma$  in the subtracted image). Some of the stars in the H<sub>2</sub> image also have a median (or mean) integrated value near zero, but others, including BN, are distinctly negative. Since H<sub>2</sub> is essentially never optically thick (i.e. it's never seen in absorption), we interpret these "negative" stars as being so red that they are intrinsically brighter at F215N than F212N. In the case of BN, it is measured to be 17% brighter at F215N. However, the effects of persistent images accumulating in the F215N filter (taken after the F212N in the same orbit) need to be explored more carefully.

**Acknowledgments.** I would like to acknowledge Marcia Rieke for her insightful discussions and careful assessment of NICMOS performance.

## References

- Colina, L. & Rieke, M., 1997, this volume.  
Stolovy, S. R., Burton, M. G., Erickson, E.F., Kaufman, M.J., Chrysostomou, A., Young, E.T., Colgan, S.W.J., Axon, D.J., Thompson, R.I., Rieke M.J., and Schneider, G. 1997 ApJ Letters (in press).



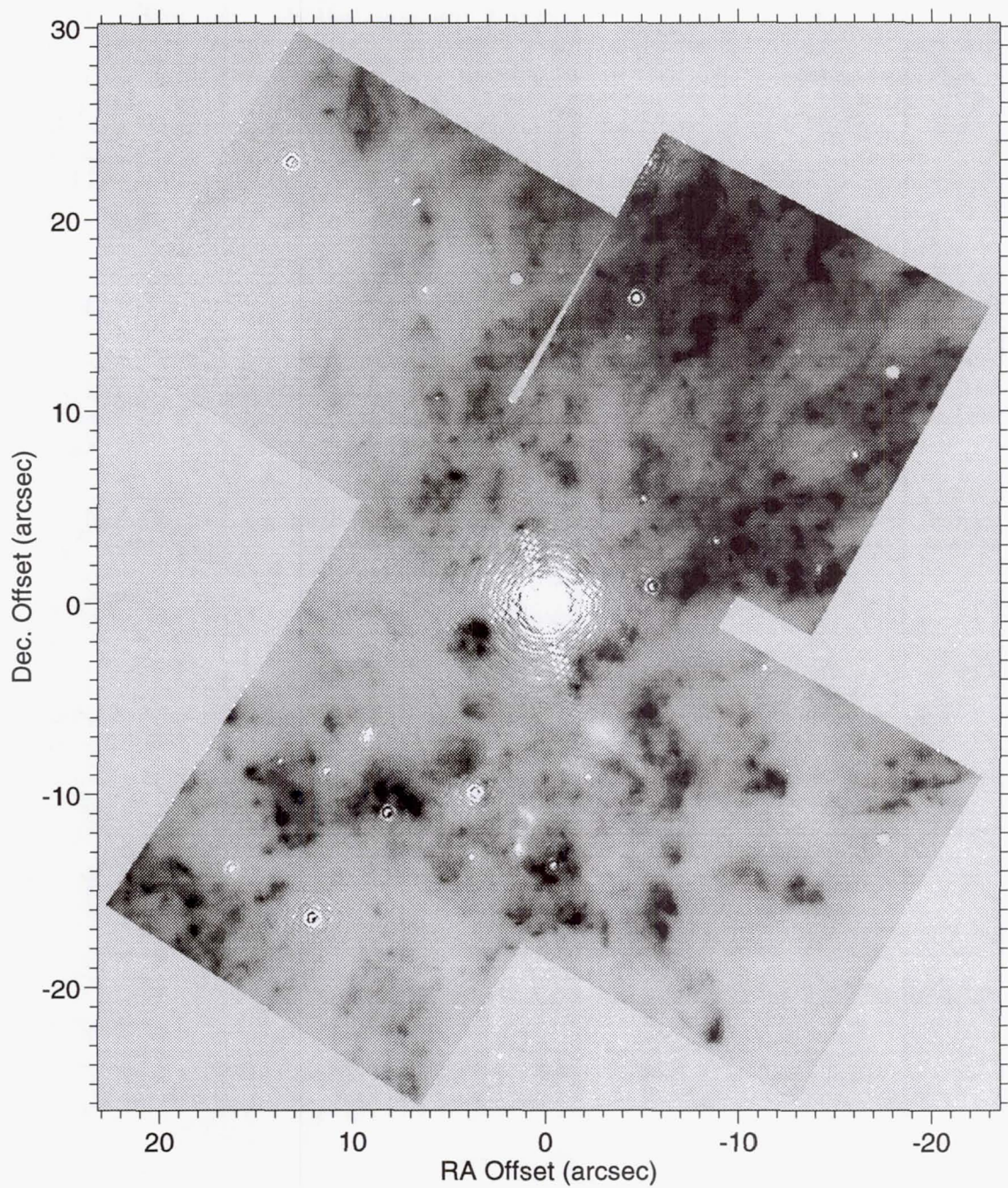


Figure 1. Molecular hydrogen mosaic of the core of OMC-1 in the  $2.12\mu\text{m}$  line, adapted from Stolovy et al. (1997). The gray scale is linear, increasing from white to black.



## The NICMOS Grism Mode

Wolfram Freudling

*Space Telescope - European Coordinating Facility (ST-ECF), Garching, Germany*

### Abstract.

In addition to broad band, medium band and wide band filter sets, the NICMOS Camera 3 (NIC3) filter wheel contains three grisms. These grisms provide low-resolution slitless spectroscopic capabilities. SMOV data verified basic properties of the grisms. Two weeks of grism data with the best possible focusing for NIC3 have been collected in late July and early August 1997. Spectra have been extracted from all visible sources in that data set using software developed at the Space Telescope - European Coordinating Facility. No emission lines or absorption lines are found in any of the objects.

## 1. Introduction

The NIC3 provides the largest field of view of the three NICMOS cameras. In addition to four wide-band, two medium band and ten narrow band filters, the filter wheel for NIC3 also contains 3 grisms for slitless spectroscopy, which cover the entire NICMOS wavelength range of 0.8–2.5 microns with a spectral resolving power of about 200 per pixel. Characteristics of the grisms are given in Table 1. Since there are no slits, an image of the same field through a matching wide-band filter is needed to obtain a zero point for wavelength calibration. For that purpose, a matching filter with similar throughput as the grism should be used for each of the grisms. The recommended matching filters are also listed in Table 1. A standard procedure for the grism observations is to spend a small fraction of the total integration time to obtain the image.

The current optimum focus position for NIC3 is beyond the reach of the PAM focusing mechanism, i.e., at this time NIC3 can only be perfectly focused by moving the secondary mirror of HST. Since such a move prevents other HST instruments from being focused, it will be carried out only during special NIC3 campaigns, the first one of which is planned for January 1998. The optimum position of the focus has moved over the last few months to a more favorable location (Suchkov et al. 1997). Recent NIC3 images taken by moving the PAM to its optimum position without changing the focus of HST itself are closer to being in focus than older images. The SMOV data discussed in Section 2 were taken while the focus position was still in an unfavorable focus position. Therefore, those images are less well focused than the parallel data discussed in Section 3.

## 2. SMOV data

A first set of grism calibration data was taken in April 1997. The spectra were used to measure the location of the spectra relative to the position of the object on the direct image taken with the same pointing. The resulting offset of the spectrum relative to the direct image and the orientation of the spectrum relative to a row of the image are listed in Table 1. There is no significant position dependence of these values. These values are consistent with pre-flight measurements.

Owing to the location of the focus at that time, the effective wavelength resolution of the spectra was very low. No lines have been detected in any of the spectra, and therefore the best available wavelength calibration at that time were still the pre-flight measurements. The in-orbit wavelength calibration will be carried out on two bright emission line sources in October 1997.

In order to calibrate extracted spectra, the wavelength dependent response of each pixel has to be known (see Section 4). For that purpose, flatfields of the narrow band filters will be used. Since the flatfields depend on the position of the field offset mirror (FOM), its optimum setting has to be found first. Flatfields for most filters will be found before or during the NIC3 campaign in early 1998 (see Colina & Storrs 1997).

Table 1. Grisms Characteristics

Grism	Central Wavelength ( $\mu$ )	Wedge Angle (degrees)	Bandpass ( $\mu$ )	Matching filter	Lines per mm	Offset spectrum (pixels)	Orientation of spectrum (degrees)
G096	0.96	5.21	0.8 - 1.2	F110W	45.0	-4.4	-3.0
G141	1.40	5.58	1.1 - 1.9	F150W	30.8	-6.7	-1.3
G206	2.06	5.69	1.4 - 2.5	F175W / F240W	21.1	-2.2	-1.7

### 3. Parallel Program

Public pure-parallel observations with NICMOS started on June 2, 1997. These observations become public as they are included in the archive. Currently, parallels are implemented with simple single orbit exposure sets. For longer pointings, identical pre-defined sequences are simply replicated. As the scheduling software is developed further, more sophisticated scheduling algorithms will be used to implement strategies adapted to specific scientific goals.

To date, most parallel data have been taken with a focus position appropriate for NIC1 and NIC2. However, for a two week period between July 21, 1997 to August 4, 1997, the PAM was moved to its best possible position to focus NIC3. In that period, a total of 19 fields were imaged with grism G141, for 13 of them at least 2 exposures were taken. For each of the fields, matching images with the F160W filter were taken. The fields contain a total of 98 objects with a high enough signal-to-noise ratio to extract spectra. A typical grism image is shown in Figure 1. The raw images were reduced using *calnica*, selecting appropriate dark and flat fields from the calibration database. The individual images of the parallel program are not taken as an association, i.e. there are no association tables which identify overlapping images which should be co-added. Such association tables are needed to co-add images with *calnicb*. Therefore, an IRAF *cl* script was written which produced appropriate association tables and images of the same fields were co-added using *calnicb*. Spectra for all objects were extracted using *NICMOSlook* and *calnicc* (see Section 5). Figure 1 also shows two typical spectra. None of the extracted spectra contained obvious emission or absorption lines.

### 4. Analysis of Grism Data

A set of grism observations consists typically of one or several images taken with one of the three grisms, and a shorter exposure taken with the matching filter for that grism. The direct image can be calibrated using standard procedures, e.g. the pipeline programs *calnica* and *calnicb* (see Bushouse 1997). For grism images, the same processing steps except the flatfielding should be applied. This is the default for the processing of grism images



Figure 1. Example of an grism image taken in the parallel program. The two objects are galaxies which can be recognized on the matching direct image. The image was fully processed but is not flatfielded, which is the default for grism images. This can be recognized as structure in the background. At the bottom, the two spectra extracted with NICMOSlook are seen.

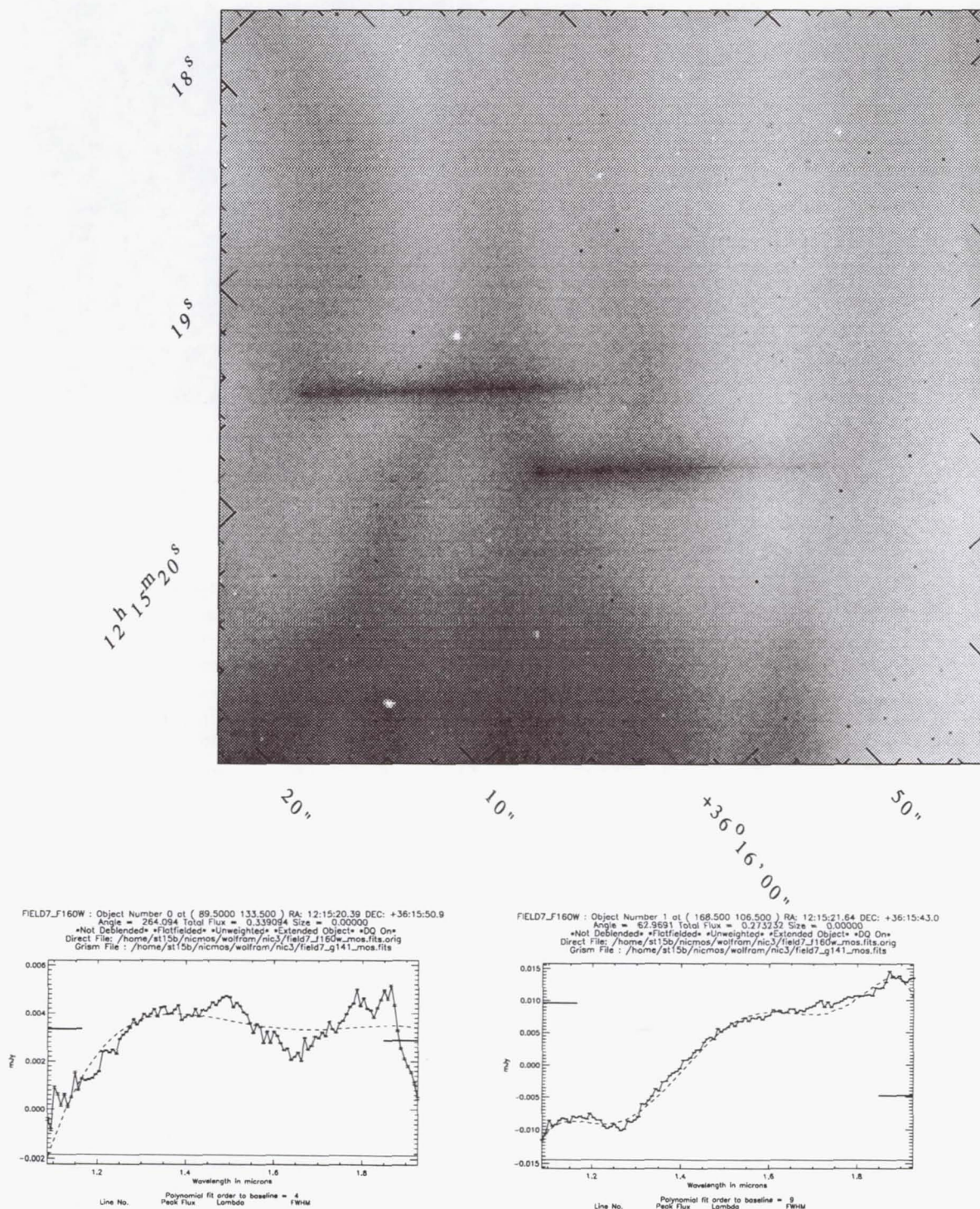
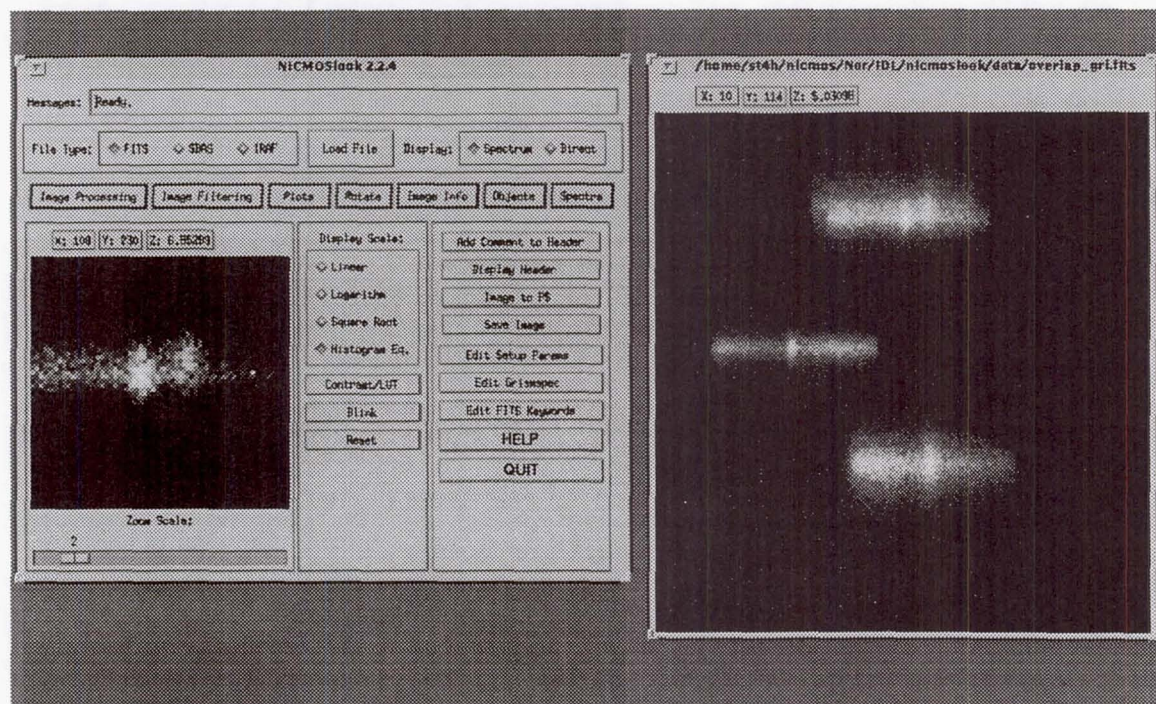




Figure 2. The NICMOSlook spectrum extraction tool main widget.



with *calnica*. Since the flatfields strongly depend on the wavelength, and the relevant wavelength for a given pixel depends on the spectrum to which this pixel belongs, no single flatfield can be applied to grism images. Rather, appropriate correction for wavelength dependent pixel response should be applied after the spectrum has been extracted.

After the calibration of the direct and grism images, the direct images can be used to measure the position of objects, and these coordinates can in turn be used to extract spectra from the matching grism images. Convenient software tools to accomplish this within a single program have been developed at the ST-ECF. Using those, observers are able to extract spectra of individual objects from the images. The tools include limited capabilities to correct spectra of contamination by spectra from neighboring images. These tools are described in detail in Section 5.

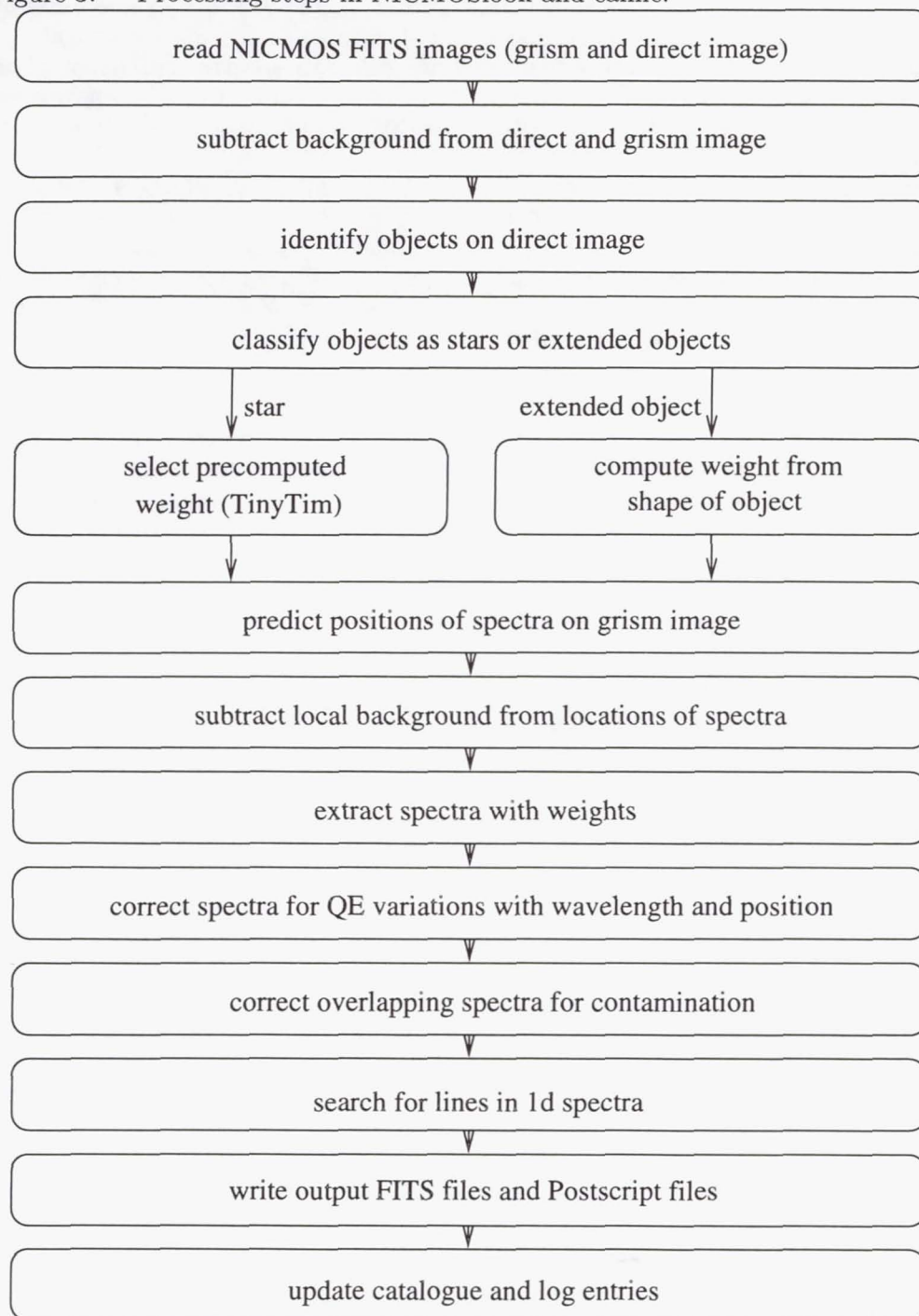
For large extended objects and in crowded fields, slitless spectroscopy does not lead to satisfactory spectra. In such circumstances, it is recommended to obtain grism images at more than one spacecraft roll angle (preferably 3 or more). Such data sets can be deconvolved to recover a full wavelength-position cube. One approach to achieve this is briefly described in Section 6.

## 5. Software Tools to Extract Spectra: *calnicc* and NICMOSlook

Software to extract spectra from calibrated grism images has been developed at the Space Telescope - European Coordinating Facility (ST-ECF). The programs are written in IDL, and a valid IDL license is necessary to run these programs. The software is available at <http://ecf.hq.eso.org/nicmos/nicmos.html>. There are two versions of the grism extraction software, the interactive version NICMOSlook and the pipeline program *calnicc*. Detailed documentation of the programs and employed algorithms are available at the above WWW page contact.



Figure 3. Processing steps in NICMOSlook and calnic.



The programs run both under IDL 4.x and IDL 5.0, and have been tested under SunOS 4.1, Solaris and Linux. *Calnicc* uses a C-program (*SExtractor*, Bertin & Arnouts, 1996) to detect objects, therefore a C-compiler is required to install the program.

*NICMOSlook* provides a fully interactive environment for locating objects on a direct image and extracting spectra from a matching grism images. All interaction is driven by IDL widgets. The main widget is shown in Figure 2. *NICMOSlook* also has some limited capabilities to manipulate and analyze extracted spectra in an interactive widget. On the other hand, the purpose of *calnicc* is to extract and calibrate spectra of all detected objects in pairs of direct and grism images with minimal human intervention. Both programs use the same code to extract spectra, but the source detection and parameters can be interactively adjusted in *NICMOSlook*.

The programs share a calibration database, which contains parameters for the extraction of the spectra. This database can conveniently be updated with the interactive tools in *NICMOSlook*, and later be used to process grism images in a batch mode using *calnicc*.

The steps performed by both programs are listed in Figure 3. An overview over the employed algorithms is given in the remainder of this section. For more details, refer to the manuals (Freudling et al., 1997a and 1997b).

### 5.1. Input Images

*NICMOSlook* and *calnicc* take full advantage of the NICMOS image FITS format, which includes error estimates and flags. They also need some specific information from the image headers. Therefore, they will perform best when used on *calnica* / *calnicb* reduced images. However, the programs can be fully customized, and will assume reasonable defaults for information not available.

### 5.2. Object Detection & Classification on Direct Images

One of the major differences between *calnicc* and *NICMOSlook* is the object detection. Within *NICMOSlook*, the user has the choice of selecting objects with the cursor, or using FOCAS with adjustable threshold and sharpness criteria. In addition, the size of objects can be marked interactively or found automatically. The user also decides, which objects are to be considered as point sources, which is relevant for the weights used to extract the spectra (see Section 5.5)

On the other hand, *calnicc* uses the *SExtractor* program, which is a major object finding package which also classifies objects as extended or point sources. This program is thoroughly documented in the *SExtractor 1.0 User's Guide* (Bertin & Arnout, 1996). An IDL interface has been written so that this program can be used by *calnicc*.

### 5.3. Background Subtraction

The quantum efficiency varies strongly with position on the NICMOS detectors. This leads to significant structure in an image of the blank sky (see Figure 1). Therefore, before spectra can be extracted from grism images, it is necessary to subtract the local background. This is done by estimating the local background from a region around each spectrum, excluding regions which are occupied by other spectra. This background estimate is then used to scale a background image to the same background as the grism observation.

### 5.4. Extraction of Spectra

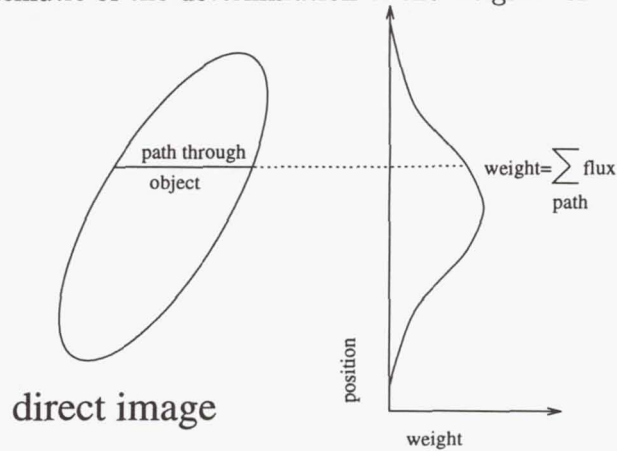
*Wavelength calibration and distortions* Spectra are extracted from the background subtracted grism image by summing the flux

$$F_l = \sum w_{i,l} \cdot g_{i,l} \quad (1)$$

where the sum is over all pixels with flux  $g_{i,l}$  and weight  $w_{i,l}$  for a given wavelength  $l$ .



Figure 4. Schematic of the determination of the weights for extended objects.



For the errors, the error estimate for each pixel is taken from the array 'err' of the input grism image. The error estimate for each wavelength is then the quadratic sum over the same region,

$$\epsilon_l = \sqrt{\sum (w_{i,l} \cdot \epsilon_{i,l})^2}. \quad (2)$$

The pixels included in the sums are determined by the position of the object on the direct image, and the location of the spectra relative to the direct image. This relative location is parameterized as third order polynomial and a rotation of the spectrum relative to the rows of the images. In NICMOSlook these parameters can be found interactively, whereas calnirc uses predefined locations.

Similarly, the dispersion relation of the gratings are parameterized as third order polynomials. Currently, only pre-flight determinations of the parameters are available.

### 5.5. Weights

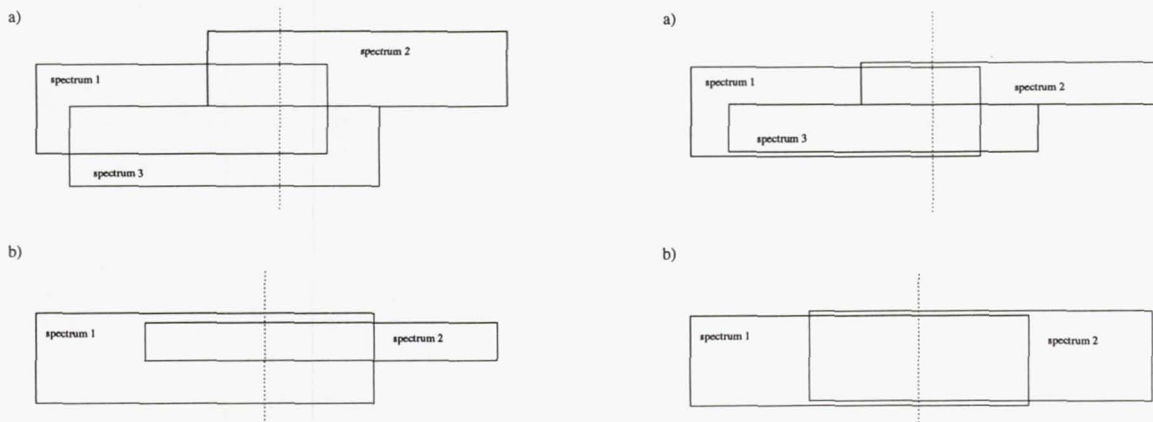
The weights used to compute the spectra and errors depend on the size of the objects. There are two scenarios and they are handled differently. One is for point source objects and the other for extended objects. For the former, the dependence of the PSF on the wavelength is taken into account. For the later, it is assumed that the size of the objects do not change as a function of wavelengths. When those assumptions are valid, the used weights result in an optimal extraction of the spectra.

*Weights for Point Sources* The programs use pre-computed weights for the extraction of spectra of point sources. These weights were computed from monochromatic PSFs simulated with the PSF generation software TinyTim for each wavelength (Krist & Hook, this workshop, see also <http://ecf.hq.eso.org/~rhook/nicmos-tinytim.html>).

*Weights for Extended Objects* Extended objects are treated differently from point sources since the proper weighting of the spectra is not known a priori. The proper weights are determined with the help of the direct image.

The weights of extended objects are computed by summing the pixel values in a given row of the direct image that fall within the ellipse defined by the size and orientation of the object (see Figure 4). Since the orientation of the object is not necessarily along the columns of the image, lines of constant wavelength are not necessarily perpendicular to the dispersion direction. This is later taken into account for the extraction of spectra of extended objects.

Figure 5. Examples of situations which can be solved by the deblending algorithm at the wavelength of the dashed line (left) and those which cannot be solved by it (right)



### 5.6. Flatfielding of Spectra

When spectra are extracted, the fluxes have to be corrected for the variations of the quantum efficiency of the detector. These variations depend both on the wavelength and on the position of the object on the detector. The correction factors are derived through interpolation from monochromatic flatfields. Currently, only pre-flight flatfield are used to derive the monochromatic flatfields, but in-orbit flatfields will be incorporated as they become available.

### 5.7. Deblending Overlapping Objects

On grism images where many objects are detected, it is likely that the spectrum of some objects overlap with those of other objects. In these cases, attempts can be made to "deblend" the spectra, i.e. subtract the estimated contribution from neighboring spectra. This is accomplished in using the assumption that the shape of each object is identical at all wavelengths and can be determined from the direct image. In that case, the contribution of adjacent objects to each others spectrum could be computed if the "true" spectrum were known. The situation can easily be solved by solving a set of equations through matrix inversion.

Deblending spectra in such a manner is not always possible. A possible scenario is that two or more spectra are almost aligned and separating them is quite impossible. There could be other cases (such as for two or more extended objects which are almost aligned) in which weights along the y-axis happen to add up in such a way that the algorithm to separate the spectra fails. Note that in this situation, there is no information in the image which could be used to decide to which spectrum a particular feature belongs. Two such situation are illustrated in Figure 5.

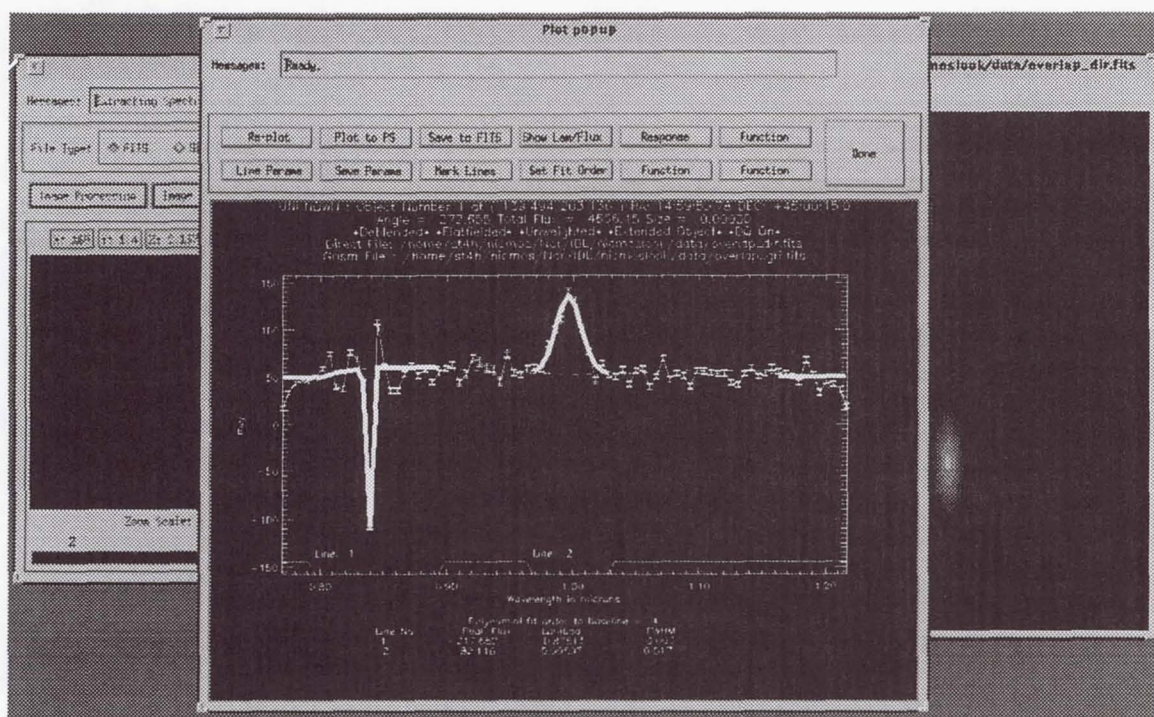
### 5.8. Characterization of Extracted Spectra

The purpose of the grism tools is to provide the user with a robust extraction of spectra from the grism images. The extracted spectra can be analyzed with other available tools. However, both NICMOSlook and calnicc have some limited capabilities to analyze the spectra.

In NICMOSlook, the extracted spectra pop up in a special spectrum analyzer tool (see Figure 6). This tool allows to interactively select lines, fit polynomials to the continuum



Figure 6. The NICMOSlook spectrum analysis pop-up.



and Gaussians to selected lines, divide the spectrum by user defined functions, and query for wavelength and flux at cursor positions. Spectra can be saved as PostScript plots or FITS files.

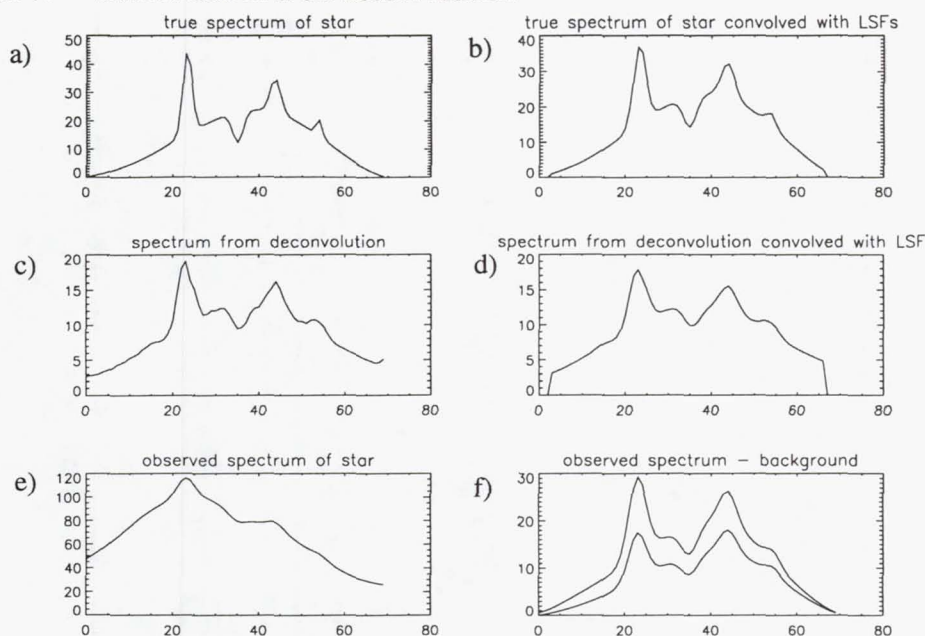
*calnicc* tries to automatically detect lines, fit polynomials to the continuum (see Figure 1) and Gaussians to detected lines. By default, PostScript plots are created for each spectrum. All spectra from a given grism image are saved in a single FITS file. In addition, a catalog of spectra with relevant information is created.

## 6. Grism 3d Deconvolution

For a single objective grism image of an extended source, the spectral information for a given spatial position is not unique since there is a degeneracy between the flux at a given wavelength from one position and the flux at a different wavelength at another position. This leads to extracted spectra of very low spectral resolution and/or contamination. In some cases, this might make slitless spectroscopy useless for obtaining spectra with a single exposure. However, this degeneracy can be removed if several grism images of the same field are obtained which differ in the direction of the dispersion, e.g. with different roll angle of the telescope.

Other constraints can be obtained with direct images of the same field without the grism. If it is possible to reconstruct the position-wavelength data cube from such a data set, using a general Lucy-Richardson algorithm (Richardson 1972, Lucy 1974). Such a program has been implemented in IDL and is available from the author. An illustration of the deconvolution on a simulated images of a star superimposed on a bright background galaxy is shown in Figure 7. Observations of the object at 10 different roll angles were simulated and the fed to the deconvolution program. The "true" spectrum of the star is shown in Panel a, Panel b shows the same spectrum reduced to the resolution of the grism.

Figure 7. Simulation of a 3d deconvolution



The deconvolution reconstructs the full wavelength-position cube. Panels c and d show the spectrum of one pixel centered on the star, once at full resolution and once convolved with the resolution of the grism. These spectra should be compared to a direct extractions of the spectrum from a single grism image with one specific roll angle (Panels e and f, the later with two different attempts to subtract the local background). It can be seen that the spectrum is more faithfully extracted using the deconvolution algorithm. Note for example the line at a pixel position of about 55, which is not recovered as a local maximum in the single image extraction attempts.

**Acknowledgments.** The NICMOSlook widget is based on a similar widget STISlook, which was kindly made available before its release by Terry Beck. The following people contributed in various stages to the development of programs discussed in this paper: Rudolf Albrecht, Hans-Martin Adorf, Markus Dolensky, Norbert Pirzkal, Robert Thomas and Lin Yan. Jeremy Walsh kindly proof read an early version of this manuscript.

## References

- Colina, L., & Storrs, A., 1997, this volume.  
 Bertin, E., & Arnoult, S., 1996, *A&AS*, 308, 601.  
 Bushouse, H., 1997, this volume.  
 Freudling, W., Pirzkal, N., Thomas, R., Yan, L., 1997a, NICMOSlook manual, Version 1.5 (Garching: ST-ECF).  
 Freudling, W., Pirzkal, N., Thomas, R., 1997b, *calnicc* Manual, Version 1.5 (Garching: ST-ECF).  
 Krist, J.E., & Hook, R.N., 1997, this volume.  
 Lucy, L.B., 1974, *AJ*, 79, 745.  
 Richardson, W.H. 1972, *J. Opt. Soc. Am.*, 62, 55.  
 Suchkov, A.A., Bergeron, L., Galas, G.G., 1997, this volume.



## The Polarimetric Capabilities of NICMOS

D. C. Hines<sup>1</sup>, G. D. Schmidt & Dyer Lytle<sup>1</sup>

*Steward Observatory, The University of Arizona, Tucson, AZ 85721*

**Abstract.** The polarimetric capabilities of NICMOS are demonstrated from data obtained during the Early Release Observations of IRC +10216 and CRL 2688 (the Egg Nebula). Preflight Thermal Vacuum tests revealed that each polarizer has a unique polarizing efficiency, and that the position angle offsets differ from the nominal positions of 0°, 120° & 240°. Therefore an algorithm different from that of an ideal polarizer is required for proper reduction of astronomical polarimetry data. We discuss this new algorithm and the results of its application to NICMOS data.

We also present preliminary estimates of the Instrumental Polarization, the sensitivity of the grisms to polarized light, and the accuracy of NICMOS imaging polarimetry for faint and low polarization objects. Finally, we suggest strategies for maximizing the success of NICMOS polarimetry observations.

### 1. Introduction

Studies of polarized light have effected profound changes in our understanding of astronomical objects, especially within the last two decades with the advent of sensitive, large format imaging arrays such as optical CCDs and the NICMOS3 infrared detectors. Imaging of linearly polarized light from young stellar objects, bipolar nebulae, radio galaxies and hyperluminous infrared galaxies has shown that disks of dusty gas play a key role in the birth and death of stars, and can strongly influence the appearance of quasars and QSOs.

The Near Infrared Camera and Multi-Object Spectrometer (NICMOS) contains optical elements which enable high spatial resolution, high sensitivity observations of linearly polarized light from 0.8–2.1  $\mu\text{m}$ . The filter wheels for Camera 1 (NIC1) and Camera 2 (NIC2) each contain three polarizing elements sandwiched with a band-pass filter. The design specifies that the position angle of the primary axis of each polarizer projected onto the detector be offset by 120° from its neighbor, and that the polarizers have identical efficiencies. While this clean concept was not strictly achieved, the reduction techniques described below permit accurate polarimetry to be carried out with both the short- and long-wavelength cameras over their full fields of view.

### 2. Thermal Vacuum Tests

The preflight thermal vacuum test program for NICMOS included an extensive characterization of the polarimetry optics and the overall sensitivity of the non-polarimetry optics to polarized light. Uniform illumination of the entire camera field with light of known polarization and position angle was provided by a calibration polarizer attached to the CIRCE standard light source.

---

<sup>1</sup>NICMOS Project, The University of Arizona

Images were obtained as a function of the calibration polarizer position angle with and without the NICMOS polarizers in place to determine the polarizing efficiencies,<sup>1</sup> the absolute position angles of the NICMOS polarizers with respect to the NICMOS entrance aperture, and to evaluate the polarization signature imparted by the mirrors which comprise the NICMOS imaging system. Images were also obtained with the grisms of Camera 3 to characterize their sensitivity to polarized light.

The Thermal Vacuum tests showed that:

- Each polarizer has a unique polarizing efficiency, with the POL120S having a very low efficiency of only 48%.
- The offsets between the position angles of the polarizers within each filter wheel differ from their nominal values of 120°.
- The polarization induced by the mirrors in the NICMOS optical train appears to be small ( $\lesssim 1\%$ ).
- The grisms are slightly sensitive to the orientation of incoming polarized light, with G206 showing the largest variation in intensity ( $\sim 5\%$ ) for completely polarized light. This effect scales with percentage polarization and will be negligible for the majority of astronomical situations.

### 3. The HSL Algorithm for Reducing NICMOS Polarimetry Observations

The “standard theory” algorithm for polarimetry data reduction as outlined in the original NICMOS Manual (Axon et al., 1996) assumes that the polarizers have uniform and perfect (100%) polarizing efficiencies, and that the projected position angles of the primary axis of the polarizers are offset by exactly 120°. The thermal vacuum tests showed that the NICMOS polarizers are not ideal, so a more complex technique is required. The new algorithm developed by Hines, Schmidt & Lytle (hereafter HSL) is presented below.

The observed signal from a polarized source of total intensity  $I$  and linear Stokes parameters  $Q$  and  $U$  measured through the  $k^{th}$  polarizer oriented with a position angle<sup>2</sup>  $\phi_k$  is

$$S_k = A_k I + \epsilon_k (B_k Q + C_k U), \quad (1)$$

where

$$A_k = \frac{1}{2} t_k (1 + l_k), \quad B_k = A_k \cos 2\phi_k, \quad C_k = A_k \sin 2\phi_k,$$

and  $\epsilon_k$  is the polarizing efficiency,  $t_k$  is the fraction of light transmitted for a 100% polarized input aligned with the polarizer's axis, and  $l_k$  is the fraction transmitted (exclusive of that involved in  $t_k$ ) when the incoming light is perpendicular to the axis of the polarizer (see Table 1). After solving this system of equations to derive the Stokes parameters at each pixel ( $I, Q, U$ ), the percentage polarization ( $p$ ) and position angle ( $\theta$ ) at that pixel are calculated in the standard way:

$$p = 100\% \times \frac{\sqrt{Q^2 + U^2}}{I}, \quad \text{PA} = \frac{1}{2} \tan^{-1} \left( \frac{U}{Q} \right).$$

<sup>1</sup>Polarizer efficiency is defined as  $\epsilon = (S_{\text{par}} - S_{\text{perp}})/(S_{\text{par}} + S_{\text{perp}})$ , where  $S_{\text{par}}$  and  $S_{\text{perp}}$  are the respective measured signals for a polarizer oriented parallel and perpendicular to the axis of a fully polarized beam.

<sup>2</sup>Polarizer position angle as measured from the NICMOS Aperture Offset Angle of 224.52°, about the aperture center toward the +U3 axis.



[Note that the arc-tangent function is implemented differently on different systems and programming environments, so care must be taken to ensure that the derived angles place the electric vector in the correct quadrant.]

Table 1 presents the properties of the individual polarizers, and Table 2 lists the coefficients derived from these parameters for use in solving Equation 1.

Table 1. Characteristics of Polarizers:

Filter	$\phi_k^a$	$\epsilon_k$	$t_k$	$l_k$	Comments
POL0S	1.42	0.9717	0.7760	0.0144	...
POL120S	116.30	0.4771	0.7760	0.3540	Possible "ghost" images
POL240S	258.72	0.7682	0.7760	0.1311	...
POL0L	8.84	0.7313	0.9667	0.1552	...
POL120L	131.42	0.6288	0.9667	0.2279	...
POL240L	248.18	0.8738	0.9667	0.0673	...

<sup>a</sup>As measured from the NICMOS aperture 224.52° about the +U3 axis.

Table 2. Coefficients for Simultaneous Solution of Equation 1:

Filter	$A_k$	$\epsilon_k * B_k$	$\epsilon_k * C_k$
POL0S	+0.3936	+0.3820	+0.0189
POL120S	+0.5253	-0.1522	-0.1991
POL240S	+0.4389	-0.3113	+0.1293
POL0L	+0.5584	+0.3890	+0.1240
POL120L	+0.5935	-0.0465	-0.3703
POL240L	+0.5159	-0.3262	+0.3111

#### 4. On-Orbit Results

Polarimetry data were obtained for IRC +10216 and CRL 2688 in NIC1 and NIC2 respectively as part of the Early Release Observations program. The descriptions of the observations can be obtained on the STScI website via the Cycle 7 proposal number or PI name (ERO 7120: Skinner; ERO 7115: Hines). Overall, the NICMOS and ground-based polarimetry agree remarkably well, once the NICMOS polarimetric images are binned to match the spatial resolution of the ground-based images.

##### 4.1. NIC1 — IRC +10216

Figure 1 presents the NICMOS polarimetry results for IRC +10216 (Skinner et al. 1997) compared with the available ground-based data from Kastner & Weintraub (1994). The polarization map derived by processing the NICMOS data with the new HSL algorithm (center panel) agree well with the ground based data. In contrast, polarization images derived by using the "standard theory" underestimate the polarization and lead to incorrectly oriented electric vector position angles.

Variations of the percentage polarization in relatively uniform regions of the HSL-reduced IRC +10216 data suggest uncertainties  $\sigma_{p, meas} \sim 3-5\%$  (in percentage polarization per pixel), and comparison with the ground-based data suggests an uncertainty in the position angles  $\sim 2^\circ$  in a  $5 \times 5$  pixel bins (Figure 1).

## J-Band Imaging Polarimetry of IRC +10216

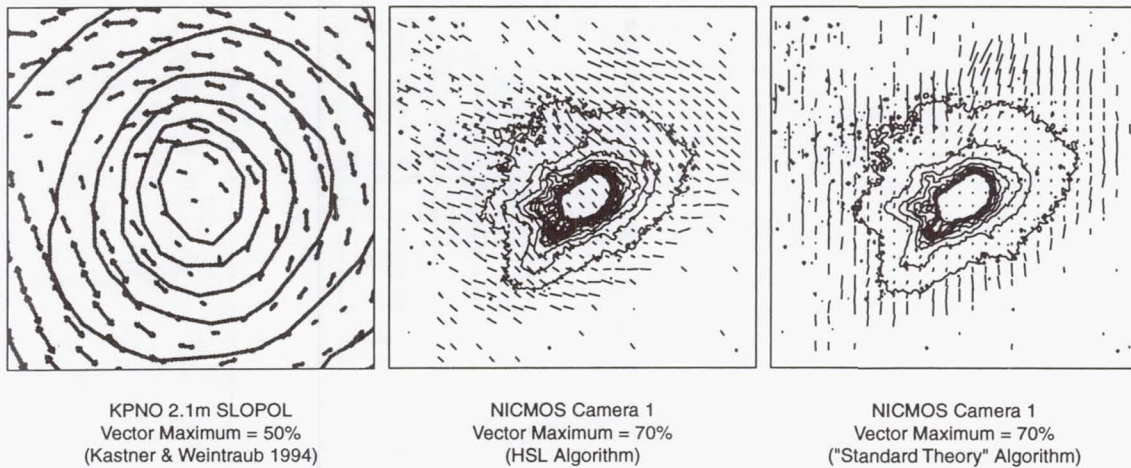


Figure 1. J-Band Imaging Polarimetry of IRC +10216 observed from the ground (Kastner & Weintraub 1994), compared with data obtained using NICMOS Camera 1 and reduced with the HSL and “standard theory” algorithms. The data reduced with the HSL algorithm agree well with the ground based data. For clarity, the NICMOS polarization vectors are plotted for  $5 \times 5$  pixel bins, and the faintest and brightest intensity contours have been omitted.

#### 4.2. NIC2 — CRL 2688

Figure 2 presents the NICMOS polarimetry results for CRL 2688 compared with observations obtained from the ground (Sahai et al. 1997). In this case the ground-based data are of exceptional quality and allow a more detailed comparison than for IRC +10216. Overall, the NICMOS and ground-based data agree quite well and show centrosymmetric patterns of position angle within the polar lobes.

Other, more subtle, features of the polarization morphology that are seen in the ground-based polarization map are reproduced precisely in the NICMOS map, confirming that the NICMOS polarimetry is well calibrated. However, the superior resolution of the NICMOS data reveals polarization features that are not apparent in the ground-based polarization map. In particular we note the very high polarizations ( $\sim 70$ – $85\%$ ) in the arcs and filamentary structure — features that are washed out (beam averaged) in the ground-based images resulting in lower observed polarization.

As for IRC +10216, uncertainties in the spacecraft data are estimated to be  $\sim 3$ – $5\%$  in percentage polarization, and  $\sim 2^\circ$  in the position angles.

### 5. Recommended Strategies

As illustrated by the EROs discussed above, the NICMOS system is capable of producing accurate polarimetry for highly polarized objects.

**Limiting Polarization:** Because the errors for percentage polarization follow a Rice distribution, precise polarimetry requires measurements such that  $p/\sigma_{p,\text{meas}} > 4$  (Simmons & Stewart 1985). Therefore, the preliminary uncertainty estimates discussed above  $\sigma_{p,\text{meas}} \approx 3$ – $5\%$  (per pixel) imply that objects should have polarizations of at least 12–20%



## CRL 2688 — The Egg Nebula

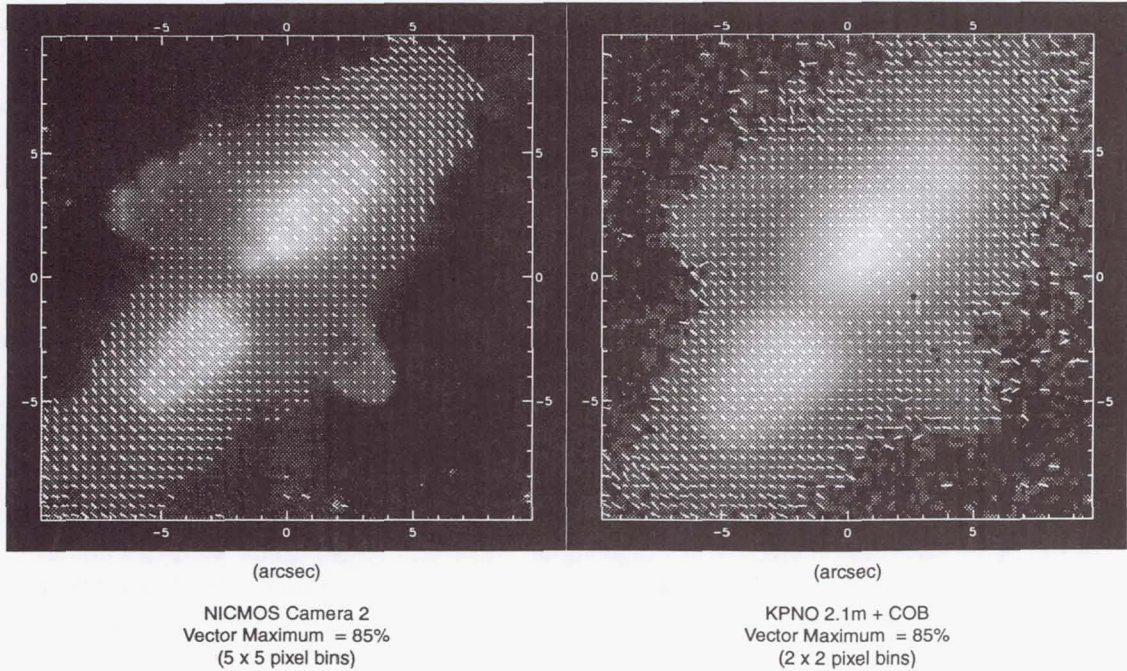


Figure 2. K-band Imaging Polarimetry of CRL 2688 (The Egg Nebula) using NICMOS Camera 2, and the Cryogenic Optical Bench (COB) attached to the 2.1m at Kitt Peak. For clarity, the vectors in the NICMOS and COB data are binned by  $5 \times 5$  and  $4 \times 4$  pixels respectively.

per pixel. Our experiments show that binning the Stokes parameters before forming the percentage polarization ( $p$ ) and the position angles reduces the uncertainties by  $\sim 1/\sqrt{N}$ , where  $N$  is the number of pixels in the bin (see Limiting Brightness discussion below). In principle, uncertainties as low as 1% should be achievable with bright objects.

In addition, the instrumental polarization (IP) is still unknown. The thermal vacuum tests suggest that it will be about 1%, but preliminary results from the Cycle 7 calibration program indicate that this may be an underestimate. Until *both* the magnitude and position angle of the IP are well established, the IP should be treated as an unknown quantity.

**Limiting Brightness of the Target:** In a perfect photon-counting system,  $\sigma_{p,\text{phot}} \approx \sqrt{2/E}$ , where  $E$  is the total number of photons counted. For CRL 2688, the signal strength even in regions of low intensity (e.g. the  $\text{H}_2$ -emitting torus) should have produced  $\sigma_{p,\text{phot}} \approx 1\%$ , but we measure  $\sigma_{p,\text{meas}} \approx 3\text{--}5\%$ , which suggests that the uncertainties are dominated by noise other than that from the source itself. Conservatively, integration times should be set such that the  $\sigma_{p,\text{phot}} < 4\sigma_{p,\text{meas}}$ .

**Position Angle of Incoming Polarization Relative to NICMOS Orientation:** Because of the non-optimum polarizer orientations and efficiencies, the uncertainty in polarization is also a function of the position angle of the electric vector of the incoming light. For observations with low signal-to-noise ratios (per polarizer image), and targets with lower polarizations, the difference between the signals in the images from the three polarizers becomes dominated by photon noise rather than analyzed polarization signal. Therefore, observations that place important incoming electric vectors at  $\approx 45^\circ$  and  $\approx 135^\circ$

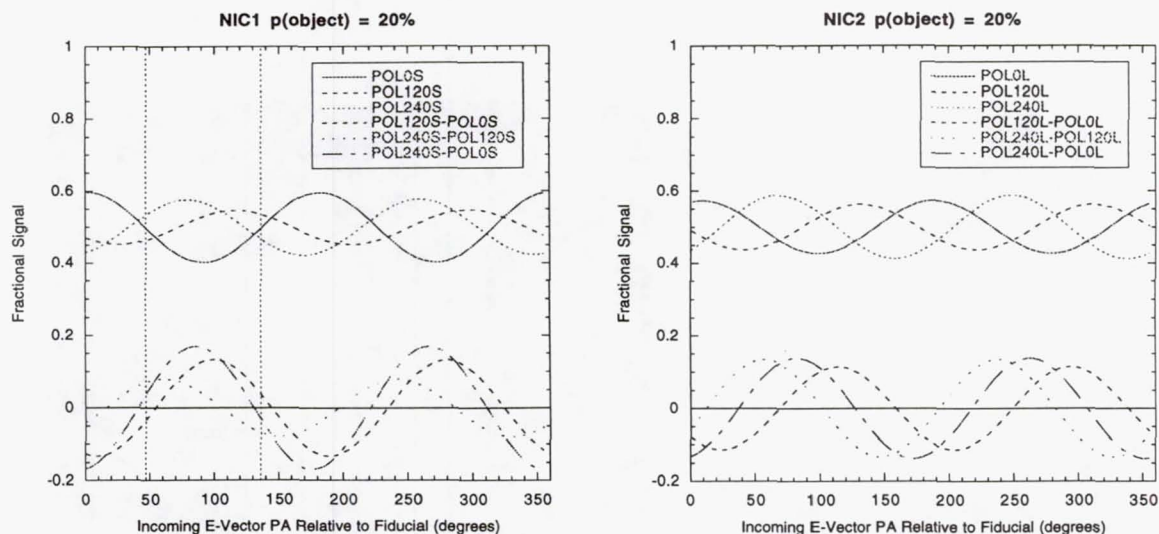


Figure 3. Fractional signal measured in each NICMOS polarizer as a function of incident electric vector position angle (PA) for 20% polarized light. The lower curves are the differences in fractional signal between images taken with successive polarizers. The vertical dashed lines in the left panel (NIC1) represent the position angles where these differences are all small.

in the NICMOS aperture reference frame should be avoided in NIC1. No such restriction is necessary for NIC2.

## 6. Future Directions

The Cycle 7 calibration program will observe several polarized and unpolarized targets in both cameras to measure the instrumental polarization and verify the absolute position angle calibration. These observations will be repeated later in the season when the spacecraft is oriented  $90^\circ$  with respect to the initial observations, thus allowing a unique determination of the instrumental polarization. In addition, the redundant data sets will allow a more detailed characterization of the polarization uncertainties.

**Acknowledgments.** It is a pleasure to thank B. Stobie, L. Bergeron and A. Evans for assistance with the (non-polarimetric) data calibration. We also thank Joel Kastner for the use of his COB observations of CRL 2688 in advance of publication, and Chris Skinner for making the IRC +10216 data available. DCH acknowledges support from the NICMOS project under NASA grant NAG 5-3042.

## References

- Axon, D., et al., 1996, *NICMOS Instrument Handbook*, Version 1.0 (Baltimore: STScI).
- Kastner, J. & Weintraub, D. 1994, *ApJ*, 434, 719.
- Sahai, R., Hines, D. C., Kastner, J. H., Weintraub, D. A., Trauger, J. T., Rieke, M. J., Thompson, R. I. & Schneider, G., 1997, *ApJ*, in press.
- Skinner, C.J., et al., 1997, in prep.
- Simmons, J.F.L. & Stewart, B.G, 1985, *A&A*, 142, 100.



## The NICMOS CALNICA and CALNICB Pipelines

Howard Bushouse

*Space Telescope Science Institute, 3700 San Martin Drive, Baltimore, MD 21218*

**Abstract.** This paper describes the STScI NICMOS calibration pipeline tasks CALNICA and CALNICB. Section 1 describes the input and output files for each task. Sections 2 and 3 describe features that are common to both tasks, and how to run them. Sections 4 and 5 describe in detail the processing steps applied by CALNICA and CALNICB, respectively. Section 6 gives information on the version histories of both tasks.

### 1. Introduction

The STScI NICMOS calibration pipeline is composed of two major tasks, CALNICA and CALNICB. CALNICA applies instrumental calibration to all images and includes basic corrections such as dark current subtraction, detector non-linearity correction, and flat-fielding. CALNICA operates on one image at a time. It takes as input the raw science data files (designated by the “\_raw” filename suffix) produced by the Generic Conversion process in the STScI OPUS environment. Its outputs are calibrated files (“\_cal” filename suffix) and, for MULTIACCUM observations only, an intermediate calibrated file (“\_ima” filename suffix). CALNICA also adds processing history information to the OPUS trailer files (“\_trl” filename suffix).

CALNICB is only applied to associated NICMOS observations and is executed after all images in an association have first been calibrated with CALNICA. CALNICB combines images into mosaics and also removes background signal from the images. Its inputs are an association table (“\_asn” filename suffix), the cal files produced by CALNICA, and the science support data files (“\_spt” filename suffix) accompanying each cal file. Its outputs are an updated version of the association table (“\_asc” filename suffix), mosaic images (“\_mos” filename suffix), and an spt file to accompany each mos file. CALNICB also adds processing history information to the trl files in the association.

### 2. CALNICA/CALNICB Common Features

Both CALNICA and CALNICB are built as host-level tasks and can therefore be executed directly from the host (e.g. Unix or VMS) system level, or they can be executed from within the IRAF environment in the STSDAS `hst_calib.nicmos` package. The tasks are completely data driven in that they derive all information that is necessary to guide the processing from values of the input image header keywords and, in the case of CALNICB, the asn table. The run-time file format for all data I/O is FITS files with IMAGE and BINTABLE extensions. All input data, as well as calibration reference data, is held in memory during processing. Each image set (or “imset”), which is comprised of the five science (SCI), error (ERR), data quality (DQ), samples (SAMP), and exposure time (TIME) arrays associated with each detector readout, occupies ~1 Mbyte of memory. Thus a full 26-readout MULTIACCUM observation will require on the order of 30 Mbytes of memory for the science and reference data. CALNICB will require ~1 Mbyte of memory per input image.

All input and output files conform to the same file structure, which allows output files to be reused as input if desired. All steps involving reference data (e.g. dark and flat-field images) propagate statistical uncertainties from the ERR arrays and data quality flags from the DQ arrays of the reference data into the science data being processed. Furthermore, all steps involving image combination propagate the number of samples (SAMP) and their total exposure time (TIME) used to compute each resulting science (SCI) image value.

### 3. Running the Tasks

The current version of CALNICA two command-line arguments, namely the input and output file names of the data to be processed. The output file name is optional and, if not specified by the user, will default to the root name of the input file. Both the input and output file names can be given as either just root names or full names including the suffixes (e.g. “\_raw” and “\_cal”) and extension (e.g. “.fits”). File names using suffixes or extensions other than these defaults may be used, but in this case the entire file name must be specified by the user. The following examples are all valid ways of running CALNICA:

- `cl> calnica n45m04c8m ""`
- `cl> calnica n45m04c8m_raw.fits ""`
- `cl> calnica n45m04c8m_raw.fits n45m04c8m_cal.fits`
- `cl> calnica n45m04c8m_cal.fits n45m04c8m_special`

CALNICB takes one command-line argument, the name of the input association table. The association table file name can be specified using either only the root name or the full file name. For example:

- `cl> calnicb n3v701060`
- `cl> calnicb n3v701060_asn.fits`

Before running either task, the user may want to modify some of the input image header keywords containing reference file names or calibration “switches”. It is very important to remember that all such keywords are contained in the *primary* header of NICMOS data files, therefore it is the primary header (extension number zero) that must be edited. For example, the IRAF `hedit` or STSDAS `chcalpar` tasks must be used as follows:

- `cl> hedit myfile_raw.fits[0] <keyword> <value>`
- `cl> chcalpar myfile_raw.fits[0]`

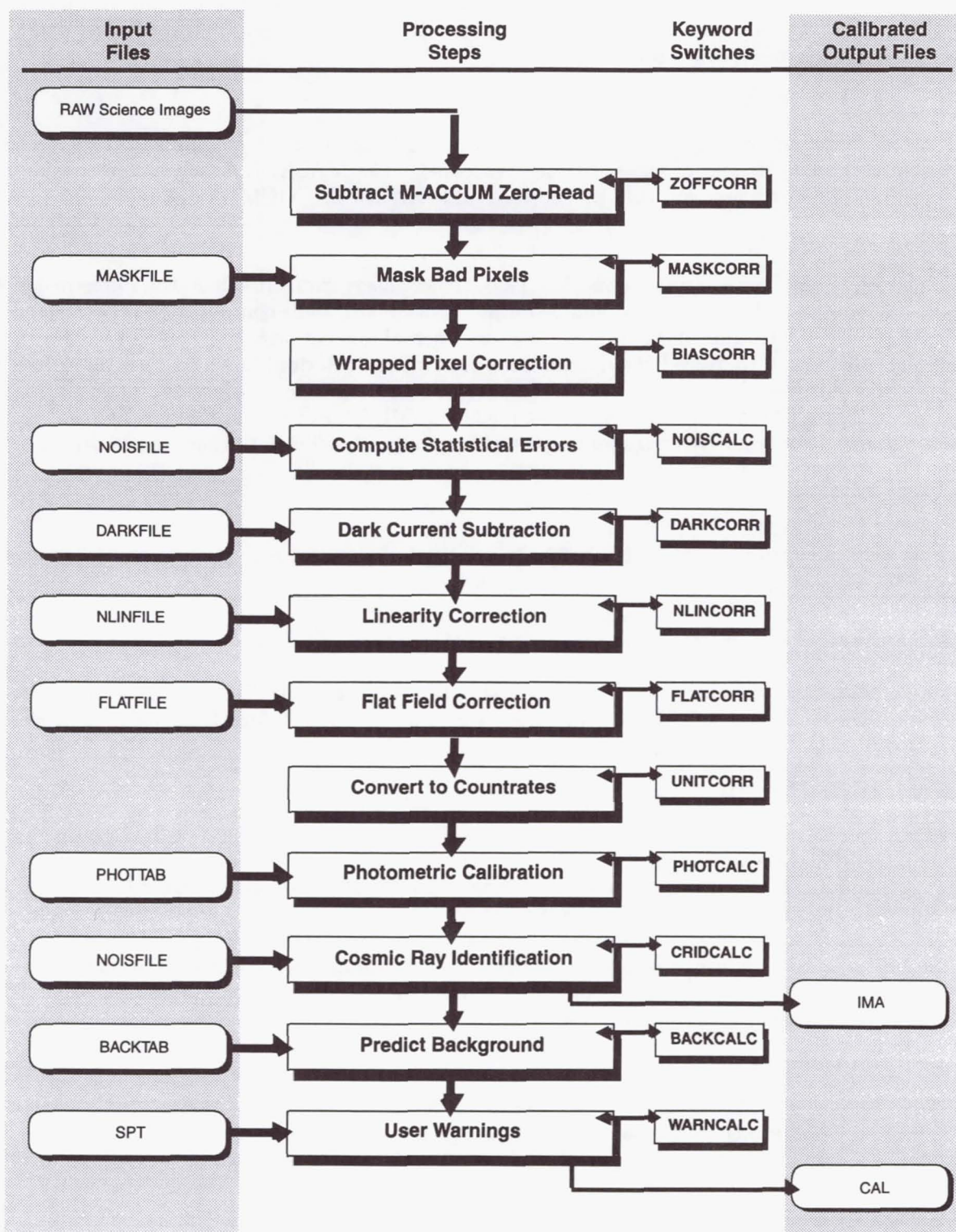
where the “[0]” appended to the file name indicates that it is the primary header which is to be modified.

### 4. CALNICA Processing

The overall flow of CALNICA processing is shown in Figure 1. Included in this figure are the names of the image header keywords that are read by CALNICA to determine the names of reference files (left column) and the “switches” used to turn each step on or off. The details of each step are described below.



Figure 1. CALNICA Processing Flow.



#### 4.1. ZOFFCORR

This step is only executed for MULTIACCUM observations and simply subtracts the SCI image of the zeroth readout from the SCI images of all other readouts. The zeroth-read SCI image is also subtracted from itself, so the zeroth-read SCI image in the output ima file will have a constant zero value. The zeroth-read DQ image is also logically "or-ed" with the DQ images of all other readouts.

#### 4.2. MASKCORR

This step propagates (logical "or" operation) the DQ image from the MASKFILE reference file into the DQ images of the file being processed. The MASKFILE DQ image contains flags for the known hot and cold pixels (flag value=32) in the NICMOS detectors.

#### 4.3. BIASCORR

This step is only necessary for non-MULTIACCUM observations in which the difference of the final and initial detector readouts is computed on-board. This computation is performed in 16-bit arithmetic and therefore it is possible, when observing bright targets, for the result of the subtraction to exceed the dynamic range of the calculation, in which case the values for pixels with very large signal will "wrap around" the maximum available value of +32767 to negative values in the range -23500 to -32768 DN. This step searches the SCI images for values in this negative range and, upon finding any, adds 65536 to them to restore them to their proper values.

#### 4.4. NOISCALC

This step initializes the ERR images by summing (in quadrature) the detector readnoise and the Poisson noise in the recorded signal for each pixel, i.e.

$$ERR = \sqrt{readnoise^2 + SCI * adcgain / adcgain}, \quad (1)$$

where *adcgain* is the electron-to-DN conversion factor. The NOISFILE contains the pixel-by-pixel readnoise, in units of electrons, in its SCI image. The NOISFILE DQ image data is also propagated into the DQ images being processed.

#### 4.5. DARKCORR

This step subtracts the detector dark current signal from the science data. It is necessary to use a DARKFILE containing dark images with exposure times matching those of the science data readouts so that the correct levels of dark current, amplifier glow, and "shading" are removed from the data. CALNICA selects a DARKFILE imset that has a matching exposure time for each science imset exposure time and subtracts the DARKFILE SCI image from the SCI images being processed. The DARKFILE ERR images are summed (in quadrature) with the science file ERR images, and the DARKFILE DQ image data are also propagated into the DQ images of the data being processed.

#### 4.6. NLINCORR

This step corrects for the non-linear response of the detectors. The response can be conveniently divided into three regimes. In the low signal regime, the detector response is linear, hence no correction is applied. In the mid-level regime, the response deviates from true linearity in a way that is correctable using a first-order polynomial of the form

$$SCI(corrected) = (c_1 + c_2 * SCI) * SCI \quad (2)$$

$$ERR(corrected) = \sqrt{ERR^2 + e_1 + e_2 * SCI^2} \quad (3)$$



where  $c_1$  and  $c_2$  are the polynomial coefficients and  $e_1$  and  $e_2$  are the uncertainties in the coefficients. These quantities are stored, on a pixel-by-pixel basis, in the "coef" and "err" images in the NLINFILE. In the high signal regime, where pixels begin to saturate, no correction is applied to the data, but a saturation flag value is set in the DQ image. The DN levels defining the boundaries between the regimes are also stored on a pixel-by-pixel basis in two "node" images in the NLINFILE.

#### 4.7. FLATCORR

This step corrects for pixel-to-pixel gain variations by multiplying the SCI images by the inverse flat field image contained in the FLATFILE SCI image. The FLATFILE ERR and DQ image data are propagated into the science data ERR and DQ images. The ERR data are updated using

$$ERR = \sqrt{(SCI * ERR_{FLATFILE})^2 + (ERR * SCI_{FLATFILE})^2} \quad (4)$$

#### 4.8. UNITCORR

The step converts the data from units of counts to countrates (DN per second) by dividing both the SCI and ERR image data by the value of the SAMPTIME keyword for each imset.

#### 4.9. PHOTCALC

This step does not alter the data, but simply sets the values of certain photometry-related header keywords. The values of the PHOTFLAM and PHOTFNU keywords can be used to convert data to an absolute flux scale using

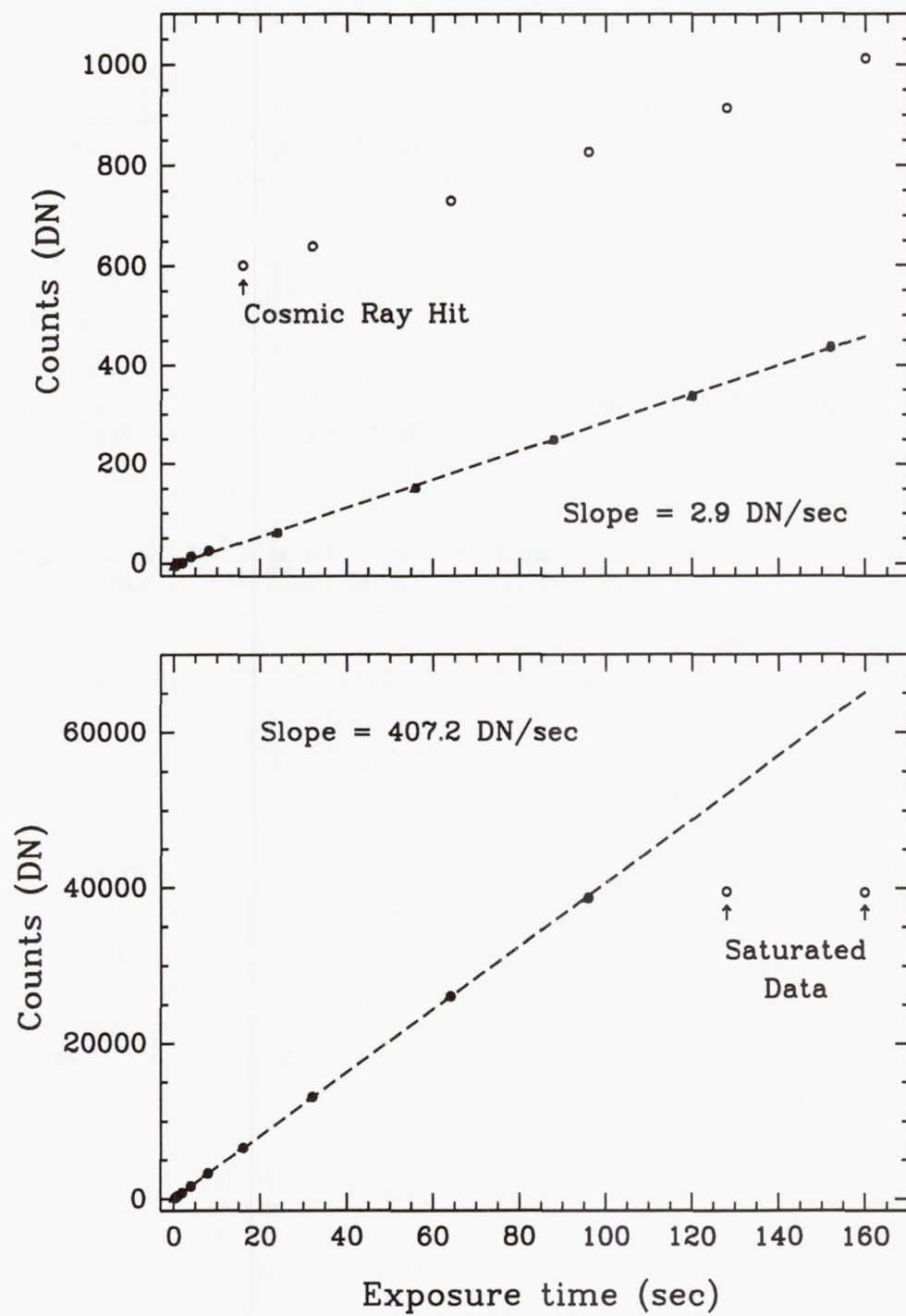
$$f_{\lambda}(\text{ergs/sec/cm}^2/\text{\AA}) = SCI(\text{DN/sec}) * PHOTFLAM \quad (5)$$

$$f_{\nu}(\text{Jy}) = SCI(\text{DN/sec}) * PHOTFNU \quad (6)$$

#### 4.10. CRIDCALC

For MULTIACCUM observations, this step combines the calibrated data from all readouts into a single image and, in the process, rejects bad data due to, for example, cosmic ray hits and saturation. The rejection of data and computation of the final image are accomplished in two steps. First, accumulated signals from one readout to the next are differenced so that the signal that arrived between individual readouts can be examined. The error-weighted mean of the difference signals is computed, not including data samples already flagged with a non-zero DQ value. Outliers are identified as those samples lying more than 5 times their error away from the mean. This process is iterated by rejecting the largest outlier and recomputing the mean until no new outliers are found. When all outliers have been rejected, the accumulated signal as a function of time is recomputed using only the non-rejected samples. These data are then fit with a first-order polynomial using standard linear regression. The slope of the polynomial is used as the final countrate (SCI) for each output ("cal" file) pixel and the uncertainty in the slope is assigned to the output ERR value. The number of non-rejected data samples and their total exposure time are recorded in the output SAMP and TIME images, respectively. If at least one good sample was found for a pixel, its output DQ value is set to zero. The ima file SCI, ERR, SAMP, and TIME image data are not modified by this step. The ima file DQ images will have cosmic ray flag values set for those pixels where samples were rejected. Examples of the fits produced for pixels having a cosmic ray hit and saturated samples are shown in Figure 2.

Figure 2. CRIDCALC Examples.





#### 4.11. BACKCALC

This step does not alter the data. It computes an estimate of the sky plus telescope background signal for an observation, based on its position in the sky relative to the sun and zodiacal plane. The BACKTAB file contains a table of background model parameters. This step has not yet been implemented in the current version of CALNICA.

#### 4.12. WARNCALC

This step also does not alter the data. It examines engineering data contained in the `_spt` file and issues warnings to the user if certain parameters, such as temperatures or voltages, had suspect values during the observation. This step has not yet been implemented.

### 5. CALNICB Processing

The overall flow of CALNICB processing is shown in Figure 3. Each step is described in the following sections.

#### 5.1. Read ASN Table

The association (`asn`) file is a FITS file with a BINTABLE extension containing the list of (root) file names to be processed, as well as the (root) file names of all output mosaic (`mos`) image files to be produced. CALNICB determines which names in the list are input file and which are output files based on the MEMTYPE column in the ASN table. Input files have a MEMTYPE prefix of "EXP" (exposure), while output files have a prefix of "PROD" (products). Furthermore, association members that are observations of the target of interest have a MEMTYPE suffix of "TARG" (target), while observations of sky background locations (which are only produced by using chop patterns) have a suffix of "BCKn", where `n` is the background region number in the pattern (see Table 1). One `mos` image will always be produced for the target, and chop patterns will result in one `mos` image being produced for each background region observed.

#### 5.2. Read CAL Images

This step simply reads the input `cal` images into memory.

#### 5.3. Determine Processing Parameters

This step reads the values of various keywords from the input image headers to determine what processing needs to be performed. Certain keywords, such as PATTERN, NUMPOS, and NUMITER should have the same value in all images and are therefore only read from the first image in the association. Others are image specific, such as PATT\_POS and World Coordinate System (WCS) keywords, have unique values in each image and are therefore read from each image. From this information CALNICB determines what type of pattern was used, how many positions are in the pattern, how many images there are at each pattern position, the relative positions of each image in the pattern, and which input images go into which output mosaic.

#### 5.4. Combine NUMITER Images

If there is more than one image at each pattern position, this step will combine the images at a given position into a single image. The offsets between each image at a given position are computed from their WCS information, using the first image at each pattern position as a reference. These offsets are then refined using a cross-correlation technique. The images are then aligned with their reference image, using bilinear interpolation, and are then combined. The combining process computes the ERR-weighted mean for each SCI

Figure 3. CALNICB Processing Flow.

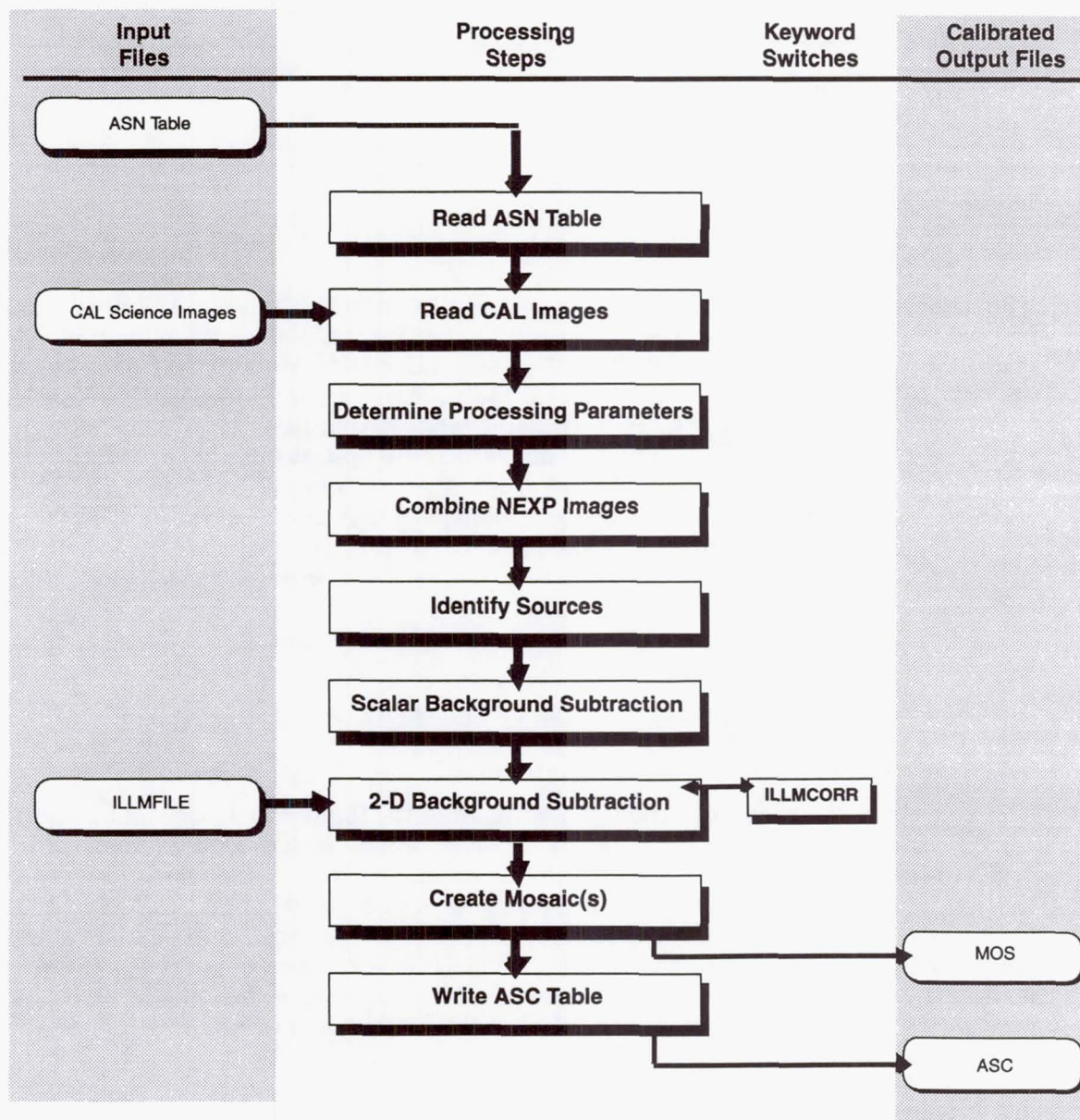




image value, with rejection of bad (non-zero DQ) pixels and iterative sigma clipping. The number of non-rejected samples, and their total exposure time, are saved in the SAMP and TIME images.

### 5.5. Identify Sources

This step flags (in the DQ images) pixels suspected of containing flux from a source. This is accomplished using a 3-stage process. First, pixels that are greater than 5 sigma above the mean signal level in each image are identified as candidate source pixels. Second, in order to filter out spurious identifications, only those candidates having 2 or more neighboring pixels also identified as containing a source are retained. Finally, the surviving pixels have their source DQ flags "grown" to their 4-immediate neighbors.

### 5.6. Scalar Background Subtraction

This step computes and subtracts a scalar (or "DC") background signal from all images in the association. This is accomplished as follows. First, the mean signal level in each BCK image in the association is computed. The computation excludes bad and source-flagged pixels and uses iterative sigma clipping to avoid any possible contamination. If there are not any BCK images in the association (e.g. the observations are from a pure dither pattern), the same computation is performed on the target images. In this case the computed background level is compared with the CALNICA estimate that was stored in the BACKESTn keywords and if the computed results differ substantially from the CALNICA estimates, it is assumed that the computed result is biased by the presence of the target and it is replaced with the CALNICA estimate. The resulting background levels for each image are then averaged to compute the overall mean background level for the whole association. This overall mean is then subtracted from all images. The mean background level is recorded in the MEAN\_BKG keyword in the output association (asc) table.

### 5.7. 2-D Background Subtraction

This step subtracts the ILLMFILE image from the association images. It is intended to remove any spatial variations in the telescope background illumination pattern, but to date, little if any such spatial variations have been seen. Thus the ILLMFILES currently contain dummy data (constant zero values). CALNICB recognizes that the files are dummy and skips the subtraction.

### 5.8. Create Mosaics

This step performs the final combination of images to produce the output mosaics. The process is very similar to the step that combines the NUMITER images at each pattern position. The relative offsets for each image in a given mosaic are first computed from their WCS information, using the first image in each mosaic as a reference. The offsets are refined using cross-correlation, and then the images are aligned using bilinear interpolation and combined. The combining process computes the ERR-weighted mean of overlapping pixels, rejecting those with non-zero DQ values and applying an iterative sigma clipping. The number of non-rejected samples and their total exposure time are saved in the output SAMP and TIME images of the mos files.

### 5.9. Write ASC Table

This step creates the output association (asc) table. The asc table is a copy of the input asn table, with four new columns of information appended. An example of an asc table is shown in Table 1. The new columns are BCKIMAGE, MEANBCK, XOFFSET, and YOFFSET. The BCKIMAGE column indicates whether or not a given image was used in the scalar background computation. The example shown in Table 1 is for a TWO-CHOP

pattern, with NUMITER=2, and NUMPOS=5. So there are two images at each of the 5 pattern positions and two of the positions are background (BCK) regions. Thus, in this example, only the images at the BCK positions were used to compute the scalar background level. The MEANBCK column records the background signal computed for each individual image. The XOFFSET and YOFFSET columns record the computed offsets for each image relative to its reference image.

Table 1. Output Association (ASC) Table.

MEMNAME	MEMTYPE	MEMPRSNT	BCKIMAGE	MEANBCK (DN/sec)	XOFFSET (pixels)	YOFFSET (pixels)
n3uw01a1r	EXP-TARG	yes	no	INDEF	0.00	0.00
n3uw01a2r	EXP-TARG	yes	no	INDEF	-0.15	0.00
n3uw01a3r	EXP-BCK1	yes	yes	0.28	0.00	0.00
n3uw01a4r	EXP-BCK1	yes	no	INDEF	0.00	0.20
n3uw01a5r	EXP-TARG	yes	no	INDEF	0.32	0.00
n3uw01a6r	EXP-TARG	yes	no	INDEF	0.00	0.00
n3uw01a7r	EXP-BCK2	yes	yes	0.26	0.00	0.00
n3uw01a8r	EXP-BCK2	yes	no	INDEF	0.00	0.00
n3uw01a9r	EXP-TARG	yes	no	INDEF	0.00	0.00
n3uw01a0r	EXP-TARG	yes	no	INDEF	0.00	-0.15
n3uw01010	PROD-TARG	yes	no	INDEF	INDEF	INDEF
n3uw01011	PROD-BCK1	yes	no	INDEF	INDEF	INDEF
n3uw01012	PROD-BCK2	yes	no	INDEF	INDEF	INDEF

## 6. Version Histories

### 6.1. CALNICA

- Version 2.1: Version in use in OPUS at the time NICMOS was launched.
- Version 2.2: Installed 19 May 1997, this version corrected minor arithmetic bugs.
- Version 2.3: Installed 19 June 1997, this version contained a major rewrite of the CRIDCALC step, and also populates the CAL\_VER keyword in the output file headers to record which version of CALNICA was used to process the data.
- Version 3.0: This version is currently in testing. It includes a modification to the WRAPCORR threshold, fixes some bugs in the CRIDCALC routine, corrects for signal from bright sources in the zeroth-read of MULTIACCUM observations, and allows the user to set the cosmic ray rejection threshold level for the CRIDCALC step.

### 6.2. CALNICB

- Version 1.4: Version in use in OPUS at the time NICMOS was launched.
- Version 1.5: Installed 11 April 1997, this version fixed minor bugs.
- Version 1.6: Installed 19 May 1997, this version correctly updated the FILENAME and EXTNAME keywords in all output files.
- Version 2.1.1: Installed 14 July 1997, this version was a major rewrite of the entire task and introduced the use of cross-correlation for refining image offsets, the flagging of sources, and the rejection of source-flagged pixels from the scalar background computation.
- Version 2.1.2: Installed 23 July 1997, this version fixed a sporadic arithmetic bug in the cross-correlation routine.



## Improving on the NICMOS Calibration Pipeline Products

C. J. Skinner<sup>1</sup>

*Space Telescope Science Institute, 3700 San Martin Drive, Baltimore, MD 21218*

**Abstract.** We describe a variety of operations which can be carried out using IRAF software to improve upon the quality of the calibrated data when a variety of problems are present in it. The problems covered include such diverse topics as the pedestal, problems with Cosmic Ray rejection, problems with saturated or non-linear pixels, and multiple coronagraphic holes appearing in images.

### 1. Introduction

We have now had almost a year of experience of processing NICMOS images. The first 6 months consisted only of processing images obtained during SLTV at Ball Aerospace, but even these data contained a number of the problems encountered on-orbit (the "pedestal", Cosmic Rays), and so gave us early indications of the areas that would later prove the most difficult to deal with in an automated calibration pipeline. For the past 6 months we have been taking data on-orbit, at an ever-increasing rate, and our experience in recognising, and in some cases finding ways to cope with, these difficulties is increasing accordingly. There are some problems for which there is no cure, and for which the major battle is recognising that the problem exists in a given dataset. Other problems can be cured by some extra processing. We describe in this paper our experience with such problems. The list here is by no means exhaustive, and we expect that by the time of the next Calibration Workshop, there will be both a lengthier list and for already known problems better solutions.

### 2. Pedestal Cures

The pedestal basically acts like a time-dependent extra bias which has been added to the signal. Therefore, in order to fix it, all that is needed in principle is a measurement of the extra bias that has been added. In practise, determining this bias can of course be exceedingly difficult, and in some cases impossible.

The simplest situation is where more than one exposure has been taken back-to-back, at the same pointing. In this case, we should be able to difference the two exposures to obtain a first order estimate of how the pedestal was decaying between the exposures. An example of this is plotted here, where we had two back to back exposures. Figure 1 shows the first exposure, which was badly affected by the pedestal: the pedestal is easily diagnosed by the large inverse flat-field pattern which is stamped on the calibrated image. To estimate its amplitude, we first subtracted the zeroth read from all reads of the first and second exposures, and then differenced the results. This told us how much the signal had changed between the two exposures. However, there is no guarantee that the pedestal had decayed to zero by the beginning of the second exposure. We subtracted this pedestal measurement from the first exposure, and then recalibrated it with CALNICA. The result still yielded an inverse flat-field pattern, but with an amplitude roughly half that present

---

<sup>1</sup>deceased



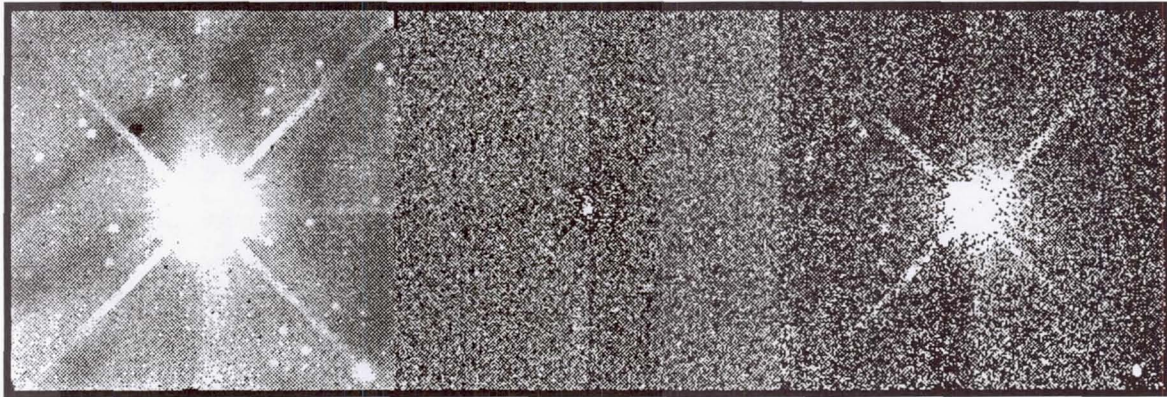


Figure 1. Left: image in Camera 2 badly affected by the pedestal. Centre: pedestal image, determined by subtracting from the image at left an identical exposure taken immediately afterwards. Right: the same image, with the pedestal image subtracted and then recalibrated using CALNICA – almost all the inverse flat-field signature of the pedestal has been removed, but the S/N is worse.

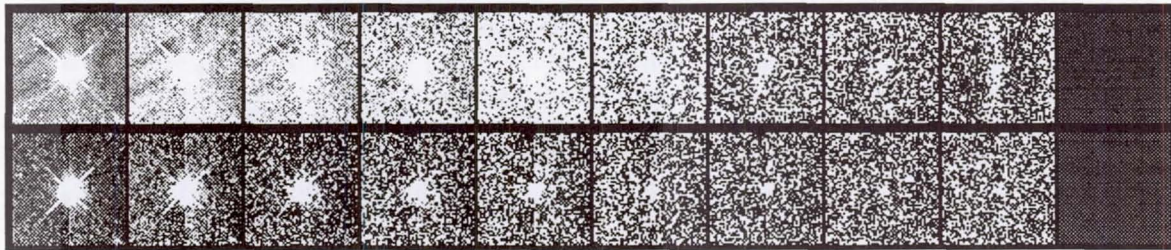


Figure 2. Top row: the exposure whose last read is displayed in Figure 1, with all 10 reads shown, the zeroth on the right and the final on the left. Bottom row: the pedestal corrected exposure (as described in the text) plotted as for the top row. The removal of the inverse flat-field pedestal signature is dramatic, although the S/N is worse.

in the original calibrated image, confirming that indeed there was still pedestal present in the second exposure. We therefore doubled our pedestal signal measurement, subtracted this from the original raw data, and recalibrated a second time. The result is plotted in Figure 1, and almost all the pedestal signal has now been removed. In Figure 2 we show the whole sequence of 10 reads with the original calibration and the recalibration after pedestal removal. Figure 3 shows the amplitude of the pedestal as a function of time since reset for the duration of the first of the pair of exposures.

The major problem with the above technique is that we are making a pedestal amplitude estimate for each pixel, but the data are intrinsically noisy, and by combining the raw image with our pedestal estimate, we are roughly doubling the noise in the image. We have plotted the pedestal image for the final read in Figure 1, and it appears to be fairly uniform (this is typical for the pedestal, although it does sometimes have more of a quadrant dependence than we found here). Therefore we could obtain a less noisy result by determining an average signal for each quadrant, and subtracting that instead. The type of average to determine is clear: a mean would work very poorly because of the very bright star present in this field, but the mode will work rather well. Determining the quadrant-based modes is a more involved effort, and less amenable to inclusion in an IRAF script, but can be done.



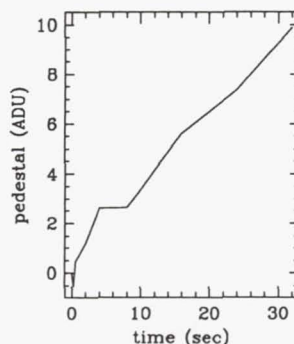


Figure 3. Amplitude of the pedestal signal seen in Figure 2, as a function of time since reset in the first exposure.

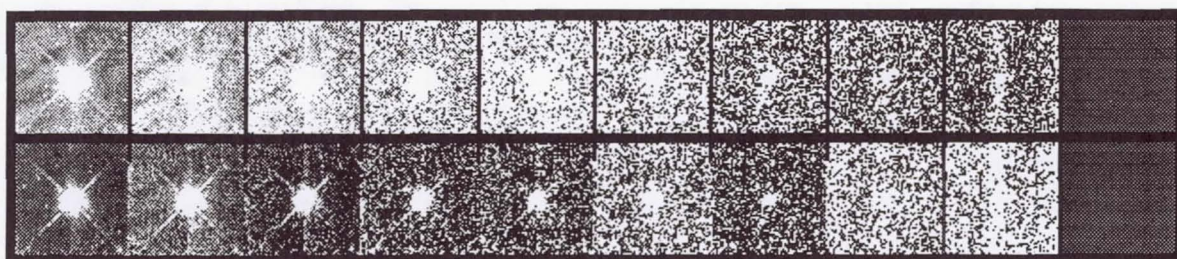


Figure 4. Same as Figure 2, but this time instead of subtracting the measured pedestal on a per pixel basis, we have subtracted the mode of the pedestal image for each readout: this yields better S/N.

Using the mode in this manner also works when there are repeated observations, but they have been dithered, so that sources appearing at different locations in the multiple images would spoil the pedestal image calculated as described in the previous paragraph. We show the result of subtracting the mode of the entire pedestal image for each readout in Figure 4, and the result is seen to be very much less noisy for the final few reads. A few of the reads in this image show significant residual pedestal, indicating that the mode is still not estimating the pedestal amplitude perfectly, but the results are clearly better than the previous pixel-by-pixel subtraction. A small further improvement would result from a quadrant based subtraction rather than an entire image subtraction, although in this particular case we find that the amplitude does not vary much from quadrant to quadrant (Figure 1).

The situation becomes much more difficult when there is only one exposure in a given filter. In this situation, the best we can do is to measure the modes for each quadrant, assume that most of this value is due to inverse flat-fielded pedestal signal, and remove this modal value from each quadrant, recalibrate through CALNICA, and then repeat the process iteratively until the modal value has been minimized. An automated procedure of this sort is under development at STScI currently, and may be ready for general release in a few months. However, this use of the mode as an indicator of pedestal will only work provided the field is relatively sparse and Cosmic Rays have been rejected. In a field which is dominated by "real" signal, the mode will not yield a useful estimator of any pedestal, and in this situation there is probably very little that can be done. Anecdotally there has been some suggestion that the "photometrically challenged column" (see Skinner, Bergeron & Daou 1997) may provide a useful barometer of the pedestal, but this has yet to be demonstrated.



### 3. Multiple Coronagraphic Holes

One of the most frequently received questions at STScI in the NICMOS group regarding data calibration is "Why does my calibrated Camera 2 data contain what looks like three coronagraphic holes?". If we examine the 300Gb of NICMOS images in the archive, we will find coronagraphic holes at positions which cover a significant fraction of the upper left quadrant of Camera 2. The root cause of the problem is that as the NICMOS dewar has variously expanded or contracted through the course of its 1.5 year life since it was filled with cryogen in 1996, the detectors have been moving in a direction which, while predictable in a gross sense, has many unfathomable fine details. As the Camera 2 detector has moved, the image of the Coronagraphic hole in the FOM has moved across the face of the detector. As a result, exactly where the hole appears in any Camera 2 calibration reference file depends on when the relevant observations were made.

In the case of the flat-field response reference files, some observations were made during SLTV in 1996, some were made during SMOV in the first half of 1997, and some have been made during Cycle 7. Currently, for some filters we have observations made at only one epoch, while for others we have as many as three. Where there are multiple observations, we have been able to remove the hole from the reference file by populating each pixel only with data obtained at a time when that pixel was not looking at the hole. Since some variations in flat-field response between the different epochs have been observed, the results do often yield a visible "patch" at one location or another. If data are available from only one epoch, then it is likely that a hole will be present in the reference file at a location which does not correspond to the current hole location. A hole in the reference file will be flagged in its Data Quality extension, and CALNICA will then flag these pixels.

The hole does not appear in the read noise or the dark current calibration reference files. It does appear in the linearity reference file, however, and in this case, at the time of writing the only suitable calibration data are from SLTV. A new linearity calibration is planned to take place during October, and following this it should be possible to remove the hole from the reference file.

### 4. Cosmic Ray Problems

A multitude of problems have been experienced with various versions of CALNICA in dealing with CRs, and they are still sometimes problematic. The basic technique adopted in CALNICA since launch has been to calculate a count-rate for each read by determining the total counts received *since the previous read*, and dividing this by the time between the two reads. The count rates for all the reads are then compared, and outliers beyond some limiting threshold are flagged as CR hits. There are, however, a multitude of pitfalls in this process, and we have slowly been discovering some of them and refining the technique.

First, the technique can only ever work on bright sources if the linearity correction is good. On a pixel in which 20,000 ADUs have been accumulated, the S/N is likely to be estimated as 100 or more by CALNICA. If the linearity correction is significantly in error, the countrates may be seen to differ by CALNICA by more than its built-in threshold ( $5\sigma$ ), and a CR hit will be flagged. If the saturation value in the linearity calibration reference file is incorrect for the pixel, and the pixel does in fact saturate during the exposure but the saturation is not noticed by CALNICA because of the error in the reference file, then CALNICA may flag some or even all of the reads as CR hits, because all of them may deviate from the mean count-rate it determines. Both of the above problems have occurred frequently. We have reduced the saturation values in the linearity reference files by 10% from the values measured in SLTV, and this appears to have almost completely cured the frequent failures to detect saturation. Incorrect CR identification due to what appear to be incorrect



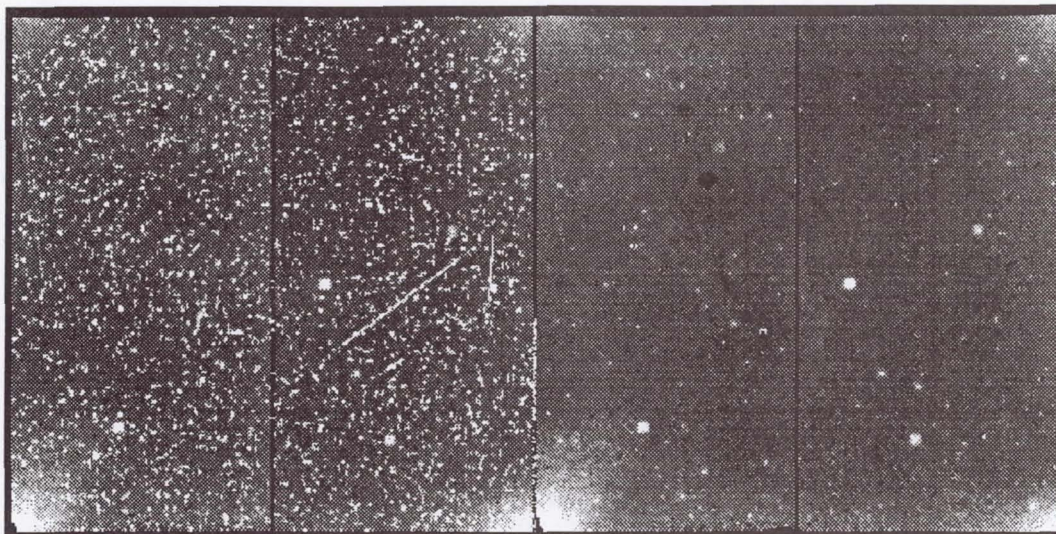


Figure 5. Left: 2500 second image in Camera 2 badly beset by Cosmic Rays. Right: the final, CR rejected output product from CALNICA: almost every CR was successfully removed, despite rather indifferent dark subtraction and significant pedestal amplitude.

linearity corrections do still sometimes occur. We should soon be obtaining on-orbit linearity calibration measurements, and hopefully this will remedy the problem.

Second, good dark correction is necessary in order for the CR identification algorithm to succeed. The dark current amplitude is quite large for these detectors, as well as highly time variable (see Skinner et al. 1997). Therefore, if it is not correctly subtracted, CALNICA will see a varying count-rate, especially for pixels with only faint (or no) illumination, and again will incorrectly flag CR hits. Situations where this has occurred with NICMOS observations so far include observations badly affected by the pedestal, and observations for which no good dark reference file was available (early in SMOV this included all observations, because no dark calibrations were available at all then; more recently the dark calibration reference files again became rather poor after the Flight Software change on August 22 1997 – see Skinner et al. 1997). Under these circumstances almost all the pixels are sometimes flagged as CR hit, especially early in an exposure when the accumulated source counts are often small and the dark current is changing rapidly.

Given the kinds of calibration problems mentioned in this section so far, effective CR correction will be impossible, and it is advisable to switch off the CR-Identification step in CALNICA (see Bushouse 1997). A new version of CALNICA which is currently under development will contain the ability for the user to set the CR detection threshold manually. Currently the threshold is hardwired in the code.

So long as there are no problems with the reference files, and there is no large instrumental anomaly (such as the pedestal) present, CALNICA usually successfully identifies the great majority of CRs in a MULTIACCUM observation. A good example of CALNICA performing well in this regard in the face of adversity is shown in Figure 5. Here we see the final read of a 2500 second exposure in which the dark current was rather poorly corrected; nonetheless, almost all of the CRs seen in the calibrated exposure on the left were successfully removed in the final product on the right. Incidentally, this exposure also shows the presence of three coronagraphic holes, as well as a significant amplitude pedestal and a very prominent “photometrically challenged column”.



## 5. Calibration Reference File Problems

It is not uncommon for data to be obtained and calibrated at a time when ideal calibration reference files are not available. A good example currently is the lack of any dark calibrations since the August Flight Software change. All data obtained since then have been calibrated in the pipeline using old darks which only partially correct the data. Whenever you receive calibrated data (either as a GO or as an archival researcher), you should check the names of the reference files which were used to calibrate the observations: these can be found by reading the paper products which were sent to you if these were GO data, or can be generated yourself using the paper products software available in IRAF, or you can find the names by reading the latter part of the primary header of the data files (raw or calibrated). The NICMOS pages on the STScI WWW site contain a page listing all the available calibration reference files for NICMOS. Included in this listing is a usage date, which indicates the observing periods during which each reference file is believed to be appropriate. If the file that was used to calibrate your data appears to have been superseded by a more recent file, you should obtain it and recalibrate the data. If you are not sure whether the reference files used were appropriate, contact your Instrument Scientist or the STScI Help Desk.

## 6. Zero Read Problems

NICMOS has no shutter. In order to make an exposure, the detector is first reset, and then a "zeroth" read made. All subsequent reads have this zeroth read subtracted in order to define the counts per unit time. Unfortunately, the zeroth read occurs 0.203 seconds *after* the reset. For any pixel exposed to a bright source, this means that the total charge accumulated in the potential well will *not* correspond with the counts recorded after zeroth read subtraction, and therefore the subsequent linearity correction and saturation detection steps will not be successful, leading in turn to major CR detection problems.

In the earlier versions of CALNICA, we were not aware of this problem, and bright sources regularly caused major problems in calibration. A new version to be released shortly attempts to correct this problem by using the first few reads to estimate the count-rate for each pixel, and then extrapolating backwards to estimate how many counts should have been recorded in the 0.203 seconds before the zeroth read. If this turns out to be a statistically significant number, it is added onto the signals in all the subsequent steps, after the zeroth read correction. It may seem odd to be subtracting a zeroth read, and then adding back in all the counts that were subtracted! Unfortunately, the zero level for the ADC in these detectors is not stable. From one exposure to the next there is some drift in the zero level, which can approach one thousand ADUs, and is randomly variable from one quadrant to another. It is necessary to subtract the zeroth read in order to correct for this instability. The backwards extrapolation technique outlined above usually works quite well, but in pathological cases the pixel may saturate at the first read, but not be saturated in the zeroth read. To allow for these cases, we have given CALNICA the ability to read a "super zeroth-read" image, which is the average zeroth read level determined from a large number of zeroth read observations. This image can be subtracted from the zeroth read to yield the counts in this read for the pixels which saturated by the later reads. We have found this technique often works quite well, but sometimes still is unable to cope with very bright sources. In such cases it is necessary to individually examine the pixels concerned in the various reads in order to make a determination of the "real" counts: usually there are not very many such pixels in an image, and so the task is not overwhelming.



## 7. Conclusions

The CALNICA and CALNICB software is in general performing rather well, and most of the problems which need to be corrected before subsequent reprocessing of the data relate to instrumental anomalies (e.g. the pedestal, linearity changes) or changes in instrument operation (e.g. the August 1997 Flight Software change). A few suggestions for how to approach such refinement of the pipeline processing have been suggested here. We expect that over the course of the next year or so our understanding of the best ways to process NICMOS data will continue to improve.

## References

- Bushouse, H., 1997, this volume.  
Skinner, C.J., Bergeron, L.E. & Daou, D., 1997, this volume.

## Understanding the NICMOS Darks

L. E. Bergeron, C. J. Skinner<sup>1</sup>

*Space Telescope Science Institute, 3700 San Martin Drive, Baltimore, MD 21218*

**Abstract.** This paper describes the characteristics of the “dark current” for the NICMOS flight detectors, namely the instrumental signal present in exposures made in the absence of any external illumination. We show how this comprises three distinct components — the shading, amplifier glow, and the true dark current. We then describe a recipe for generating “synthetic” dark current calibration reference files, which could in principle be used to generate darks for any arbitrary sequence of MULTIACCUM reads.

### 1. Introduction

Each readout of a NICMOS detector includes not only the desired detected signal, but also the signatures of the detector itself and the readout electronics, which would be present in the signal recorded during any exposure, even in the absence of any external illumination. These parts of the output signal must be removed to get the true detected signal.

### 2. Components of a NICMOS dark

#### 2.1. Amplifier Glow

Each time the detector is read out, the readout amplifiers, which are situated near the corners of the detector, are turned on. These amplifiers emit IR radiation that is detected by the pixels in the detector — similar to having a small “light bulb” in each corner. This produces a pattern of light that is highest in the corners and decreases towards the center of the detector. This is known as “amp glow”.

A typical single readout produces about 20–30 ADUs of amp-glow in the corners of the detector, and 2–3 DN near the center (Figure 1). Since the readout time of the detector is the same each time (it takes 0.203 seconds to read the whole image), the on-time for the amplifiers is always the same for each readout, and thus the light pattern seen by the array is repeatable. So in a given readout, the amount of signal due to amp-glow in each pixel scales directly with the number of readouts since the last reset:

$$A(i, j) = a(i, j) * n_r \quad (1)$$

where  $A(i, j)$  is the observed signal due to amp-glow in a given readout for pixel  $i, j$ ,  $a(i, j)$  is the amp-glow signal per readout (different for each pixel), and  $n_r$  is the total number of readouts of the array since the last reset. So in the corners of a full 26-readout MULTIACCUM there will be of order 500–800 ADUs due to amp-glow, along with the expected Poisson noise from this signal.

---

<sup>1</sup>deceased



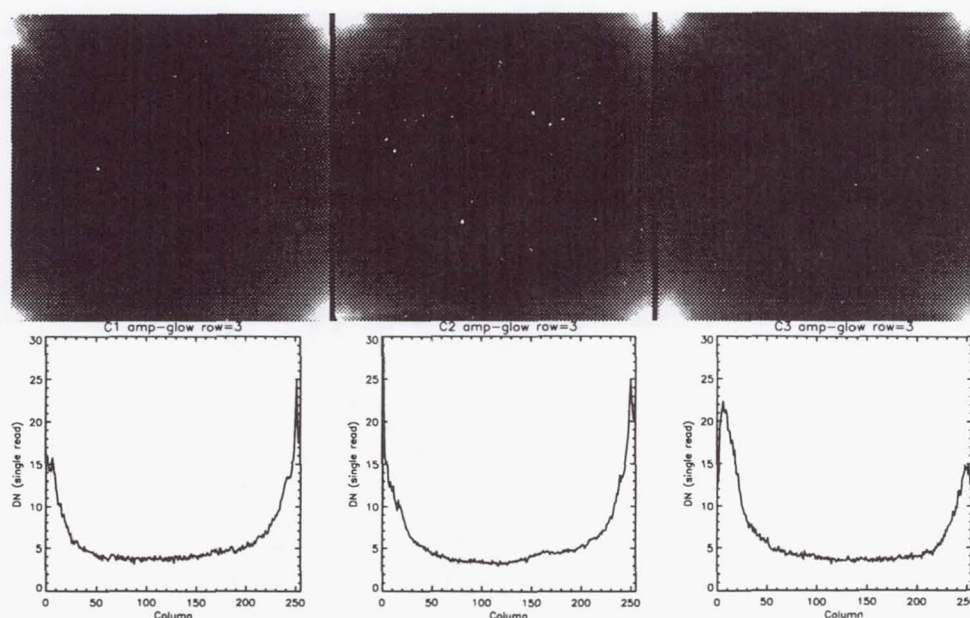


Figure 1. Amplifier glow for Cameras 1 (left) through 3 (right), on a uniform greyscale, and below a plot of row 3 (near the bottom) of each camera.

## 2.2. Shading

The bias level, or “DC offset”, in a given pixel in a NICMOS array is time-dependent. This is the so-called “shading”, which visually in an uncorrected image looks like a ripple and gradual signal gradient across a given quadrant. The pixels in a given quadrant of a NICMOS detector are read out sequentially. It takes a little over a msec to read a single pixel, and so with four readout amplifiers reading in parallel it takes just over 0.2 sec to read the entire  $256 \times 256$  pixel detector. Considering a quadrant as an array of  $i \times j$  pixels, the readout sequence consists of reading sequentially along a detector row  $i$ , clocking  $j$  from 1 to 128, then moving to row  $i+1$  and clocking  $j$  from 1 to 128, and so on. Since the amplifier bias changes pseudo-exponentially with time over the course of the readout, the observed signal, in the absence of any external illumination, varies rather slowly along the rows ( $i$ ), but rather rapidly along the columns ( $j$ ). This signal is not accumulated in the pixels each readout, but rather is superimposed on the actual signal at the time of each detector readout.

The shading signal is not the same for each readout. Its amplitude and to some extent its shape (Figure 2) are a function of the time since a pixel was last read out (not reset). So readouts with the same DELTATIM (this is the keyword used in NICMOS data to denote the time since the previous readout) will have the same bias signal, for a given pixel. The dependence of this bias on DELTATIM is nearly logarithmic and quite repeatable (Figure 3), although there are some circumstances when this is not the case (namely in the MIF sequences it has been seen in on-orbit data that when changing from a very long DELTATIM to a very short one, the shading is not quite what is expected).

It should be possible to find a numerical fit to the shading function in DELTATIM for each pixel of each detector. Then it would be possible to predict what the bias signal is in any given pixel for any possible readout sequence. Another way to attack the problem is to make an average image of the bias for each of the DELTATIMs in the predefined MULTIACCUM sequences (Figure 4). Then to build a synthetic dark, the bias component can be had by using the bias image for each appropriate DELTATIM in the sequence:

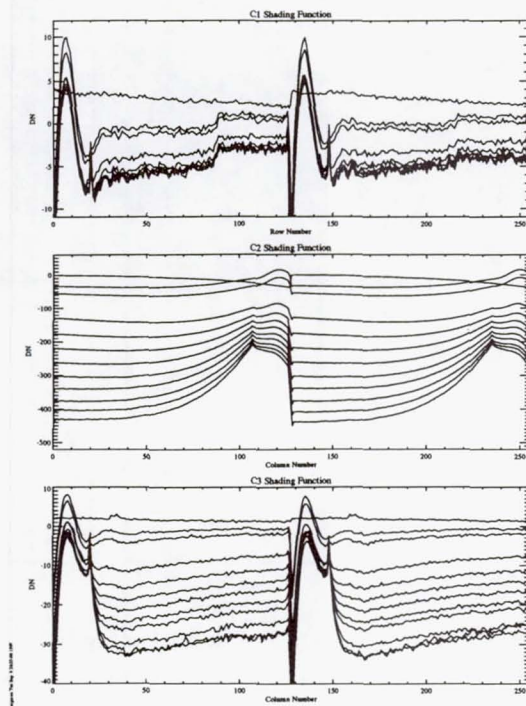


Figure 2. Representative shading functions in the slow clocking direction for each of the three detectors. These have been generated by taking medians along the fast clocking direction in order to improve S/N while filtering out bad pixels.

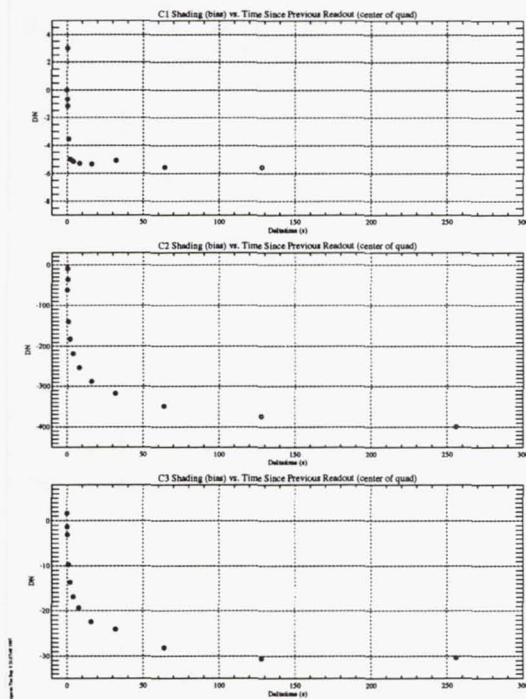


Figure 3. Amplitude of the shading signal vs. DELTATIM for a single representative pixel at the center of a quadrant for each of the three detectors.



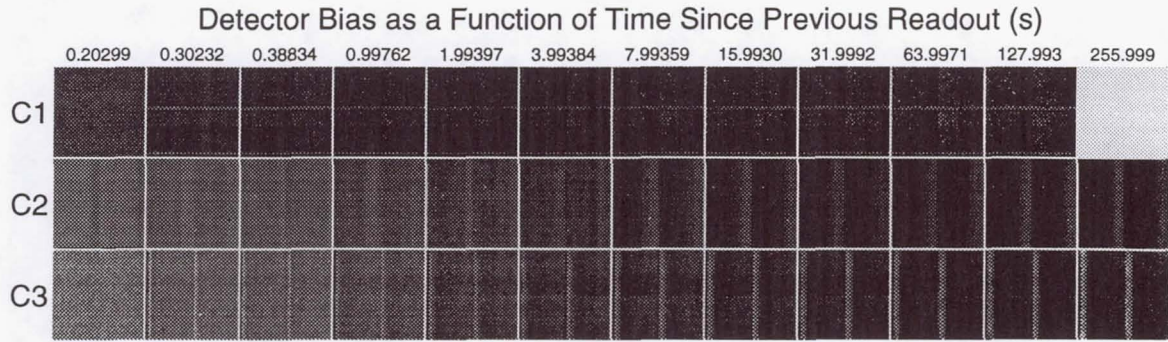


Figure 4. Images of the shading for each of the three cameras as a function of DELTATIM (indicated at the top in seconds).

$$B(i, j) = S(i, j, DELTATIM) \quad (2)$$

Where  $S$  is the bias signal in a given pixel as a function of DELTATIM.

### 2.3. Linear Dark Current

The linear dark current component is the traditional observed detector dark current when no outside signal is present. This component scales with exposure time only:

$$D(i, j) = T * d(i, j) \quad (3)$$

Where  $D(i, j)$  is the observed dark current signal in pixel  $i, j$  for a given readout,  $T$  is the time since the last detector reset, and  $d$  is the dark current (in  $e^-/\text{sec}$ ). The NICMOS dark current is extremely small and is very difficult to measure. It is approximately  $0.05 e^-/\text{s}$  for Camera 2, and no larger than about half this value for Cameras 1 and 3 (we have only upper limits for these two).

## 3. Making a Synthetic Dark

The total "dark" signal in any given pixel of any given NICMOS MULTIACCUM readout is just the sum of the 3 components described above:

$$DARK(i, j) = D(i, j) + A(i, j) + B(i, j) \quad (4)$$

Figure 5 shows this graphically. An IDL routine has been developed to make synthetic darks. This routine uses the amplifier glow image displayed in Figures 1 and 2, and simply multiplies it by the accumulated number of reads in order to generate  $A(i, j)$  for each readout. The shading as a function of DELTATIM has been populated by the technique described above, yielding an array of shading images some of which are displayed in Figure 5. An appropriate image is picked out of this array in order to generate  $B(i, j)$  for each readout. Finally, it has not been possible to measure the linear dark current for each pixel. Using the on-orbit data available so far, we have been able only to generate a mean linear dark current over the whole array for Camera 2, while for Cameras 1 and 3 we have not yet obtained high enough S/N to achieve even this: therefore for the latter two cameras, the linear dark current is left as zero currently. Finally, the routine now sums the three contributions for each readout.

The calibration database has been populated with MULTIACCUM darks for all sequences which have not yet been observed on-orbit, or for which other effects, such as the

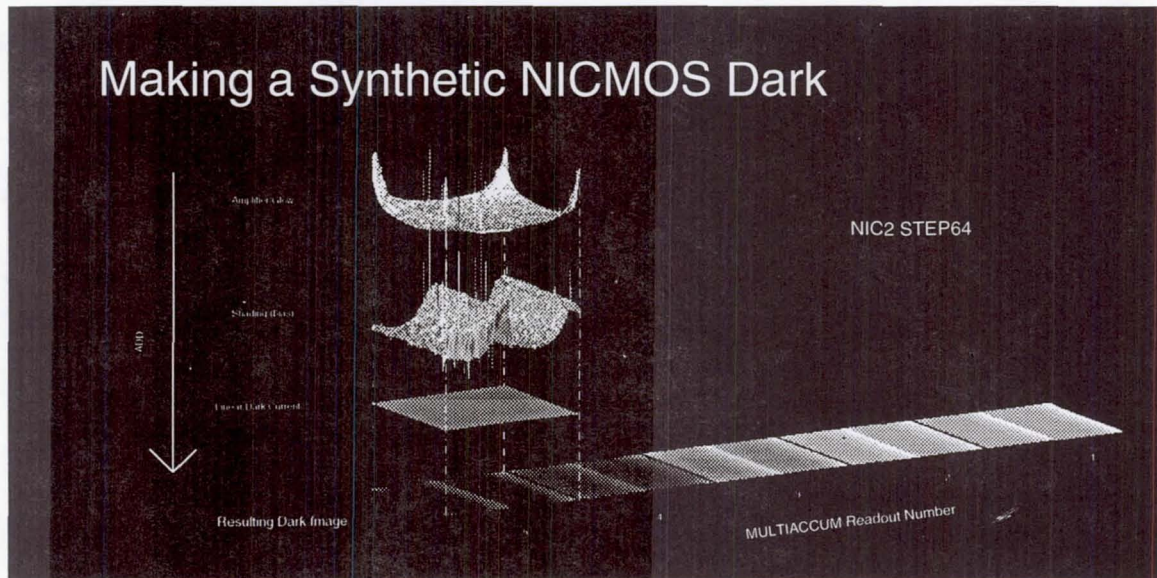


Figure 5. A graphical representation of the addition of the 3 components of a NICMOS dark to build a dark reference file for the NIC2 STEP64 sequence. The three components are shown in shaded relief to show their amplitude and spatial extent. The "spikes" are bad pixels on the array.

pedestal, have contaminated the early on-orbit dark observations. There are plans to tune up the synthetic dark algorithm somewhat (see next section) and eventually release it as an STSDAS tool in the NICMOS package.

Comparisons of on-orbit to synthetic darks show that the differences are relatively small — usually of the order of a few ADUs, with the largest differences in the corners of the detectors. Most of this can be alleviated by better characterizing the amp-glow from on-orbit data.

#### 4. Finding More Information About NICMOS Darks

All of the information presented in this poster is available in more detail in a new NICMOS Instrument Science Report:

- NICMOS-97-026 *Characteristics of NICMOS Detector Dark Observations*

This document and others like it may be found on the NICMOS web page in the documentation section. All of the past and present dark reference files used in the calibration pipeline are available for download from one of our web pages as well, in a point-and-click tabular form. Here are the URLs:

*Main NICMOS Page:*

- [http://www.stsci.edu/ftp/instrument\\_news/NICMOS/topnicmos.html](http://www.stsci.edu/ftp/instrument_news/NICMOS/topnicmos.html)

*NICMOS Instrument Science Reports:*

- [http://www.stsci.edu/ftp/instrument\\_news/NICMOS/nicmos\\_doc\\_isr.html](http://www.stsci.edu/ftp/instrument_news/NICMOS/nicmos_doc_isr.html)

*NICMOS Reference Files:*

- [http://www.stsci.edu/ftp/instrument\\_news/NICMOS/nicmos\\_doc\\_cal\\_list.html](http://www.stsci.edu/ftp/instrument_news/NICMOS/nicmos_doc_cal_list.html)



## NICMOS Data Processing Software in STSDAS

Ivo C. Busko

*Space Telescope Science Institute, Baltimore*

### 1. Motivation

Until now the standard form of accessing observational data from the Hubble Space Telescope was through GEIS (or STF) files. The GEIS format was designed to allow storage of multiple "images" in a single file. The files however must store the same kind of information, e.g. science pixels, data quality flags, etc. If a given instrument generates, e.g., both science and data quality arrays, they must be stored in separate files.

The new HST instruments STIS and NICMOS generate several "pixel" arrays from each exposure. Besides the usual science and data quality arrays, there is an *error* array, and NICMOS includes additional *exposure time* and *number of samples* arrays. It would be impractical to store all this associated information in separate files. In order to keep all information pertaining to a single exposure packed together in a single file, the standard data format adopted for STIS and NICMOS data files is FITS with multiple extensions.

Each associated "chunk" of information is named an IMSET, and a single file can store multiple IMSETs, each one identified by a number stored in the EXTVER keyword in each FITS extension header.

The existing IRAF and STSDAS tasks can operate upon individual FITS extensions as individual images with no problems, but in this way it becomes extremely cumbersome to properly propagate the error, data quality and other information from the input IMSETs into the result. Thus the need for brand-new tasks that could perform basic image processing and at the same time automatically propagate the associated information.

### 2. The mstools package

Most of the processing tasks that can handle IMSETs as a whole are included in the *mstools* package in STSDAS. There are also tasks to deconstruct and reassemble multi-IMSET FITS files into isolated IMSETs, and tasks that perform a variety of operations on individual FITS extensions in multi-IMSET files. All tasks support NICMOS and STIS files. The tasks included in STSDAS v.2 are:

<code>ecdel</code>	Deletes an entire class of FITS extensions from a FITS file.
<code>ecextract</code>	Selects all extensions of one selected type from a FITS file.
<code>extdel</code>	Deletes single extensions from a FITS file.
<code>msarith</code>	Image arithmetic with NICMOS and STIS files.
<code>mscombine</code>	Combines NICMOS or STIS files using <code>gcombine</code> .
<code>msdel</code>	Removes one IMSET from a FITS file.
<code>mssort</code>	Sorts a FITS file to get all extensions of like number together.
<code>msjoin</code>	Joins files containing single IMSETs into one file.
<code>mssplit</code>	Splits NICMOS or STIS IMSETs out into separate files.
<code>msstatistics</code>	Extended <code>gstatistics</code> for OIF, GEIS, NICMOS and STIS files.

The package also includes *psets* that help in selecting/masking specific data quality bits. These are used by tasks such as `mscombine` and `msstatistics`.

### 3. The `nicmos` package

This package includes NICMOS-specific tasks such as the calibration pipelines and some specialized display tasks. It also includes tasks that are used solely for the purpose of generating calibration reference files. Some of these tasks support other instruments in addition to NICMOS, and are actually installed in the `ctools` package (the entries here are links). The tasks included in STSDAS v.2 are:

<code>calnica</code>	Pipeline calibration for single NICMOS images.
<code>calnicb</code>	Pipeline calibration for NICMOS associations.
<code>markdq</code>	Marks DQ flags on a displayed image.
<code>msbadpix</code>	Detects bad pixels in STIS and NICMOS images.
<code>msreadnoise</code>	Measures readout noise in STIS and NICMOS images.
<code>msstreakflat</code>	Processing of Earth streaked images for WFPC and NICMOS.
<code>ndark</code>	Builds NICMOS DARKFILE calibration reference file.
<code>ndisplay</code>	Displays a science image with DQ flags superimposed.
<code>nlincorr</code>	Builds NICMOS NLINFILE calibration reference file.
<code>pstack</code>	Plots a stack of pixel values from a MULTIACCUM image.

As with the `mstools` package, the `nicmos` package includes *psets* that help in selecting/masking specific data quality bits.

### 4. Basic image processing

For generic image processing of NICMOS images with full propagation of the extra arrays into the output, two tasks are available in STSDAS v.2:

#### 4.1. `msarith`

This task works *only* with NICMOS and STIS files, it does not replace the standard `imarith` task in the IRAF `images` package. The task was designed to look and perform in a similar way as `imarith` but with added features to take into account the peculiarities found in NICMOS and STIS data:

- It fully propagates all extra arrays into the output. The rules for propagation are described in Table1.
- It can operate on all IMSETs in the input files or just a subset of them.
- In NICMOS images each pixel has its own associated exposure time, which can differ from pixel to pixel. The task takes this factor into account when performing operations in which the factor can be of significance, e.g., when adding two calibrated images (whose pixels store count rate instead of raw counts).

#### 4.2. `mscombine`

This task can be used to combine NICMOS or STIS exposures using either an average or median. A variety of clipping/cleaning algorithms are provided, including discarding pixels based on any data quality flag combination. In STSDAS v.2 the task is actually an IRAF CL script that invokes the `gcombine` task to operate upon the input files' IMSETs. Thus most of the features and capabilities of `gcombine` are available to `mscombine`.



```

operand1 = "file1.fits"    >File template/list or constant + error
  op = "+"                 >Operator
operand2 = "file1.fits"    >File template/list or constant + error
  result = "result"        >Resultant file name/list or directory path
  (list1 = "1,2,21,10")    >IMSETs in operand1
  (list2 = "3")            >IMSETs in operand2
  (crate = no)             >Count rate ? (NICMOS only)
  (divzero = 0.)           >Replacement value for division by zero
  (verbose = 1)            >Verbosity level
  (version = "23May97")    >Date of installation
  (mode = "al")

```

Figure 1. `msarith` task parameters. Any combination of input file lists/IMSETs can be supplied to the task. It chooses automatically the appropriate mode (raw counts vs. count rate) based on information retrieved from the file header. If that information is not present or is contradictory, the "count rate" switch forces the task to work in the designated mode.

Table 1. Rules for operations performed by `msarith`.

Operation/ 2nd operand	EXTNAME				
	SCI	ERR	DQ	TIME	SAMP
add / image	add <sup>1</sup>	comb. <sup>1,3</sup>	OR	add	add
sub / image	sub	comb	OR	copy <sup>4</sup>	copy
mult / image	mult	comb	OR	copy	copy
div / image	div	comb	OR	copy	copy
add / const.	add	comb.	—	—	—
sub / const.	sub	comb.	—	—	—
mult / const.	mult	comb.	—	mult <sup>2</sup>	—
div / const.	div	comb.	—	div <sup>2</sup>	—
(1) if pixels are in raw counts	- add raw counts. - translate count rate to counts in both input images; add counts and integration times; translate result back to count rate.				
if pixels are in count rate					
(2) if pixels are in raw counts	- multiply/divide time array by constant. - copy time from input image.				
if pixels are in count rate					
(3) errors are combined in quadrature					
(4) copy from first operator into result					

input = "@list1.lst"	>List of file names to combine
output = "result"	>Output file name
(dqbits = "")	>DQ bits to reject input pixels (pset)
(nsmod_e = no)	>Use noise model for computing errors ?
(reject = "ccdcrrrej")	>Type of rejection
(combine = "average")	>Type of combine operation
(weight = "none")	>Type of weighting scheme
(nsmod_w = no)	>Use noise model for weighting ?
(blank = 0.)	>Output value when zero pixels survive
(scale = "median")	>Image scaling
(zero = "none")	>Image zero level offset
(statsec = "")	>Image section for computing statistics
(expname = "SAMPTIME")	>Image header exposure time keyword
(lthreshold = INDEF)	>Lower threshold
(hthreshold = INDEF)	>Upper threshold
(nlow = 1)	>minmax: Number of low pixels to reject
(nhigh = 1)	>minmax: Number of high pixels to reject
(nkeep = 1)	>Min. to keep (pos) or max. to reject (neg)
(mclip = yes)	>Use median in clipping algorithms ?
(lsigma = 3.)	>Lower sigma clipping factor
(hsigma = 3.)	>Upper sigma clipping factor
(rdnoise = "30")	>Readout noise (electrons)
(gain = "5")	>Gain (electrons/DN)
(snoise = "0.")	>Sensitivity noise (fraction)
(tempdir = "tmp\$")	>Directory for temporary files
(version = "07May97")	>Date of installation
(mode = "al")	

Figure 2. `mscombine` task parameters. The parameters are basically the same as the `gcombine` parameters but with no provisions for input/output of error maps or masks, since these are already stored internally to the input/output IMSETs. An important new parameter is the data quality flags pset, which enables `mscombine` to discard pixels based solely on their DQ value.

## 5. Image statistics

Task `msstatistics` is an extension of `gstatistics`, in the sense that it supports not only all file formats already supported by `gstatistics` (OIF and GEIS) but can process the new NICMOS and STIS formats as well. Its parameter list resembles `gstatistics` with some additional parameters used to handle the extra complexities of the new FITS files. Two notable additions in relation to `gstatistics` are:

- Two new statistics were added to the list supported by `gstatistics`: weighted mean and weighted variance of the pixel distribution. These are possible for NICMOS and STIS exposures since they always have an associated error map.
- Pixels can be rejected out from the statistical computations based on specific bits set in their data quality flags.



```

input = "f.fit,g.hhh"    >Images template/list
(masks = "")             >Masks template/list
(dqf = "")               >Data Quality File template/list (OIF/GEIS only)
(groups = "*")           >Groups/IMSETs to be processed
(stats = "npix,mean,stddev") >Statistics to be computed
(lower = INDEF)          >Lower cutoff
(upper = INDEF)          >Upper cutoff
(gaccum = no)            >Accumulate across groups ?
(egstp = "")             >Statistics results of last image (pset)
(namecol = 25)           >columns used by file name in output printout
(dqon = yes)             >Turn on pixel masking by Data Quality bits ?
(dqbits = "")            >Generic Data Quality bits (pset)
(nsstatpar = "")         >NICMOS and STIS parameters (pset)
(wfdqpar = "")           >WFPC parameters (pset)
(version = "16Apr97")    >Date of installation
(mode = "al")

```

Figure 3. `msstatistics` task parameters. The parameters are basically the same as the `gstatistics` parameters but with additional ones that take care of specific aspects of the NICMOS and STIS file structure.

# image	npix	mean	stddev
#			
u2a31504t.c0h[1]	640000.	299.373	108.757
u2a31504t.c0h[2]	640000.	1396.86	426.502
u2a31504t.c0h[3]	640000.	1438.88	455.329
u2a31504t.c0h[4]	640000.	1432.47	486.197
n3ug06cyr_ima.fits[SCI,1]	13764.	0.271452	0.114495
n3ug06cyr_ima.fits[ERR,1]	13764.	0.0158293	0.00723336
n3ug06cyr_ima.fits[TIME,1]	13764.	575.952	0.
n3ug06cyr_ima.fits[SAMP,1]	13764.	26.	0.
n3ug06cyr_ima.fits[SCI,2]	14182.	0.272135	0.117022
n3ug06cyr_ima.fits[ERR,2]	14182.	0.0165362	0.00757553
n3ug06cyr_ima.fits[TIME,2]	14182.	543.953	0.
n3ug06cyr_ima.fits[SAMP,2]	14182.	25.	0.
n3ug06cyr_ima.fits[SCI,3]	14617.	0.273101	0.120651
n3ug06cyr_ima.fits[ERR,3]	14617.	0.0173648	0.00796676
n3ug06cyr_ima.fits[TIME,3]	14617.	511.953	0.
n3ug06cyr_ima.fits[SAMP,3]	14617.	24.	0.

Figure 4. Example output from `msstatistics`. File types can be mixed at will in the input list. There are parameters for selecting which IMSETs and which extensions within each IMSET must be operated upon.

## NICMOS Sensitivity to Cosmic Rays

Daniela Calzetti

*Space Telescope Science Institute, 3700 San Martin Drive, Baltimore, MD 21218*

**Abstract.** NICMOS dark frames obtained during Servicing Mission Observatory Verification (SMOV) were used to derive the sensitivity of the detectors to cosmic ray hits. The number of cosmic ray events ( $5\sigma$  detections) is about 1.2–1.6 events/camera/sec, comparable to the WFPC2 detection rate for the same detector area. The mean size of the  $5\sigma$  cosmic ray hits is 1.65 to 2 pixels, similar to the value measured during the NICMOS System Level Thermal Vacuum (SLTV) experiments. The number of pixels affected by cosmic ray hits is between 2 and 3 pix/camera/sec. This value depends on the position of the telescope relative to the South Atlantic Anomaly (SAA), and variations up to 60% in the rate of affected pixels have been observed between different dark frames during the same orbit. Information in the affected pixels can be partially recovered with the use of the MULTIACCUM readout mode. However, seldomly (once–twice per month), cosmic ray hits have been observed to persist between frames during an orbit.

### 1. Introduction

The impact of cosmic rays (CRs) on the detectors of an instrument strongly affects the observing strategies which can be adopted, and NICMOS is no exception to this. Here, images (dark frames) obtained during SMOV are used to characterize the sensitivity of the NICMOS detectors to CR hits. As we will see in the next sections, NICMOS detection of CRs is comparable to WFPC2. However, the multiple non-destructive reads of the MULTIACCUM readout mode allow observers to partially recover the information in the affected pixels. Recommendations for observing strategies are given in the Discussion section.

### 2. The Data

Sets of darks were obtained during the SMOV program 7051 for each of the 3 NICMOS detectors and during the ERO program 7119 for NIC2 and NIC3. For each camera, sets of 5 to 9 MULTIACCUM frames were obtained, with exposure times between 250 and 2,000 sec.

Each camera was analyzed independently to control systematics. Data from the two different programs were compared in the case of NIC2 to check for variations in the number of CR-affected pixels due to variations in the observing conditions. A total of 18,432 seconds of dark exposure are available for each camera from program 7051, and additional 1,280 seconds are available for NIC2 (2,560 seconds for NIC3) from program 7119. Because of the presence of the “pedestal” effect, the first frame of each set shows more average counts (between 35 and 55 DN) per pixel than the others. The analysis was pursued both discarding and including the first image of each set of darks. The results do not show dependence on the inclusion/exclusion of the first image, and should be considered robust against this characteristic of the dark frames.



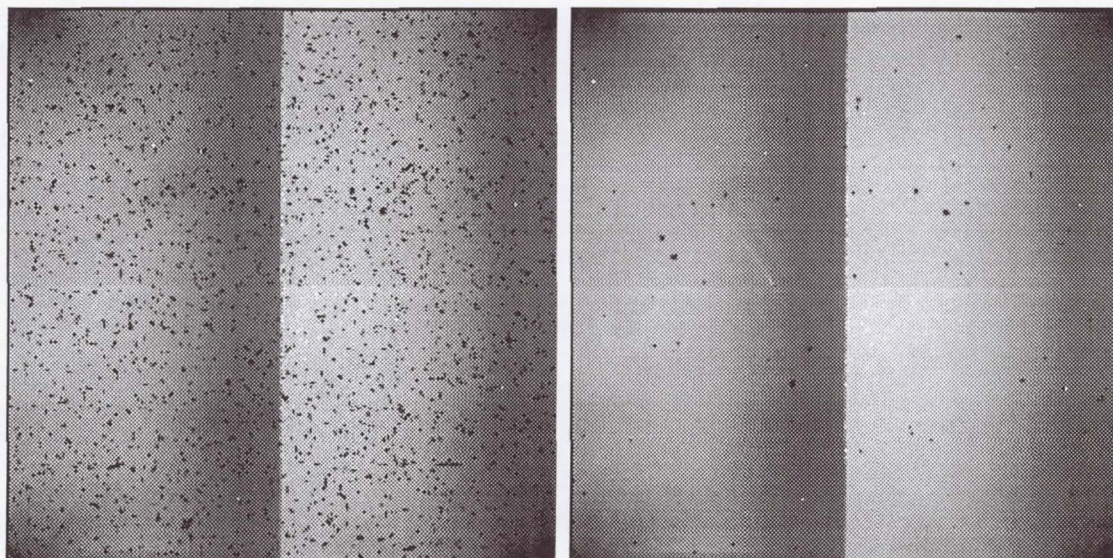


Figure 1. A NIC2 dark frame exposed for 2,048 sec is shown, before (left) and after (right) CR-removal. There are about 4,000 CR-affected pixels ( $T_{CR}=5\sigma$  and  $T_S=5\sigma$ ) in the left panel. In the combined dark (right panel) the remaining dark spots are bad pixels.

### 3. The Analysis

The detection of CR events was performed using both the `crrej` routine in the STSDAS package and the generic `imcombine` routine in IRAF. The products of `crrej` are a “CR-free” image and one image of the rejected pixels for each input image. The latter are used to count CR-affected pixels. A rejection threshold  $T_{CR}=5\sigma$  was used to identify “CR-hits”; the radius of the region around a CR-hit subject to further scrutiny was set to 1.5 pixels, and the rejection threshold for this area was set to two different values:  $T_S=5\sigma$  (see Figure 1) and  $T_S=3\sigma$ . The case  $T_{CR}=3\sigma$  and  $T_S=3\sigma$  was also considered. The central  $236 \times 236$   $\text{pix}^2$  were analyzed in each frame, to avoid edge effects and the biases in the statistics introduced by the amplifier glow. The standard deviation calculated by CRREJ combines the readout noise with the statistical noise on the counts. The detector’s parameters were set to  $\text{gain}=5.5 \text{ e}^-$  for NIC1 and NIC2 and  $\text{gain}=6.5 \text{ e}^-$  for NIC3, and readout noise of  $30 \text{ e}^-$ . The latter is the dominant term for the rejection threshold, since the dark current is comparatively small (about  $0.05 \text{ e}^-/\text{sec}$  for the darks of program 7051). The dark frames were also processed with `imcombine`, adopting median scaling and the `crreject` option, to compare the “CR-free” image so produced with the output from `crrej`. No differences were found between the combined frames produced by the two tasks.

### 4. Results

The number of CR-affected pixels from program 7051, given in units of /camera/second, are reported in Table 1, for each camera and for the three combinations of  $T_{CR}$  and  $T_S$  considered. Although only the central portion of each frame was analyzed, the numbers reported are normalized to the entire area of the camera. The typical number of pixels above the  $3\sigma$  threshold in each 2048 sec dark is about 5,400 versus an expected number of 177 pixels/camera due to chance events; above the  $5\sigma$  threshold there are typically 4,100 pixels versus an expected number of  $<1$  pixels/camera due to chance. The number of CR events has been counted for the  $T_{CR}=5\sigma$  case (column 4 of Table 1), giving about



1.2 events/camera/sec. For comparison, the number of CR-hits experienced on-orbit by WFPC2 is 1.24 events/s/cm<sup>2</sup>, very close to the number observed for NICMOS (each NICMOS detector has an area of 1.049 cm<sup>2</sup>). The size of the CRs in the  $T_{CR}=5\sigma$  frames is between 1.55 and 1.70 pixels (mean value about 1.65 pixels), similar to the value reported from the SLTV data.

Table 1. Cosmic Ray Event Statistics

Camera	Threshold	Affected Pixels (#/camera/sec)	Number Events (#/camera/sec)
NIC1	$T_{CR}=5\sigma, T_S=5\sigma$	2.11	1.28
NIC1	$T_{CR}=5\sigma, T_S=3\sigma$	2.50	
NIC1	$T_{CR}=3\sigma, T_S=3\sigma$	2.74	
NIC2	$T_{CR}=5\sigma, T_S=5\sigma$	1.99	1.21
NIC2	$T_{CR}=5\sigma, T_S=3\sigma$	2.28	
NIC2	$T_{CR}=3\sigma, T_S=3\sigma$	2.43	
NIC3	$T_{CR}=5\sigma, T_S=5\sigma$	1.90	1.15
NIC3	$T_{CR}=5\sigma, T_S=3\sigma$	2.53	
NIC3	$T_{CR}=3\sigma, T_S=3\sigma$	2.79	

The comparison between the CR-hit characteristics in programs 7119 and 7051 is reported in Table 2 for NIC2. In 7119 the rate of CR-affected pixels is about 60% higher than in the case of 7051. The size of the typical CR is also larger: 2.00 pixels versus 1.65 pixels. However, the larger size does not compensate entirely for the increased rate of affected pixels, and the rate of CR-hits increases slightly, to 1.6 events/sec/camera. The 7119 darks show a decreasing trend in the number of affected pixels from one frame to the next both in NIC2 and NIC3, going, for NIC3, from 3.35 pix/sec/camera to 1.50 pix/sec/camera over a period of 42 minutes (half orbit). The largest counts were observed while the telescope was close to the SAA, while the minimum was observed when the telescope was the farthest from the SAA. Between the two programs (7119 and 7051) the main difference in term of observing conditions is the distance of the telescope from SAA impacted orbits.

Table 2. Cosmic Ray Events in NIC2 (7119 versus 7051)

Program ID	Threshold	Affected Pixels (#/camera/sec)	Number Events (#/camera/sec)
7119	$T_{CR}=5\sigma, T_S=5\sigma$	3.21	1.61
7119	$T_{CR}=3\sigma, T_S=3\sigma$	3.96	
7051	$T_{CR}=5\sigma, T_S=5\sigma$	1.99	1.21
7051	$T_{CR}=3\sigma, T_S=3\sigma$	2.43	

*In general, the average number of about 2-3 pix/sec/camera lost to CR hits ( $5\sigma$  level) implies that about 10% of the detector area will be affected by CRs after about 2,000 to 3,300 seconds. These figures are a factor between 2.2 and 3.5 shorter than the average time necessary to reach the same coverage in WFPC2 (about 7200 sec).*

## 5. Discussion

The CR-affected pixels have a frequency distribution which decreases for increasing energy (DN) values (Figure 2), and individual pixels typically do not saturate after a single CR event. This characteristic, together with the non-destructive readout capability available in NICMOS, can be used to partially recover the signal in CR-affected pixels. Let's make the case of an exposure obtained using a series of  $N-1$  non-destructive reads, before the final (destructive) read is taken (total of  $N$  readouts); if a CR hits a pixel between any two of



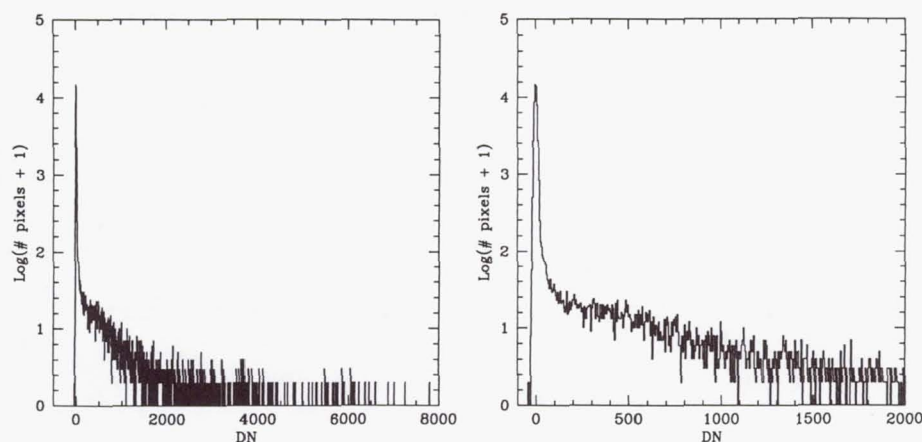


Figure 2. The pixel distribution of one of the NIC2 residual images, obtained from the subtraction of the combined dark from one of the original 2,048 sec dark frames. The distribution is shown for two magnification scales, with the abscissa expressed in DN. The measured  $5\sigma$  is 33.0 DN, slightly above the theoretical expectation (30.5 DN). The energy distribution of the CR-affected pixels is thus given by the positive tail above 33 DN. The saturation is reached at about 32,700 DN. Most of the pixels are characterized by low energy values.

the  $N$  reads, the remaining, unaffected  $N-1$  readouts can be recovered in most cases. If the CR has deposited enough energy onto the pixel to saturate it, then only the reads before the CR-hit can be recovered. Indeed, the NICMOS calibration pipeline is designed to deal with these cases when non-destructive readouts (MULTIACCUM sequences) are present.

Theoretically, one could think that with this technique very long exposure times could be employed, the only limitation being the probability that any given pixel is hit twice by CRs or that the exposure becomes background limited. However, observers interested in long exposures (faint targets) may select one of the MULTIACCUM MIF sequences, if on-orbit experience prove the multiple initial and final reads advantageous for the reduction of the readout noise. For pixels hit by CRs this advantage will be lost, since the intermediate, non-destructive reads used for the information-recovery are obtained with single readouts. In addition, although quite seldomly (once/twice per month), CR-hits have been observed to persist from one frame to the next during the course of an entire orbit. All this sets a practical limit to the longest exposure that observers interested in faint, non-extended sources may want to use. Depending on the details of the observation, the maximum exposure time advisable will be in the neighborhood of 1,000–2,000 sec. One added problem is the difficulty of discriminating between noise and low-energy CR-affected pixels (Figure 2). The shape of the distribution of Figure 2 is such that low-energy CR-affected pixels will be undetected by the calibration pipeline software, since they'll look like noise. The basic effect will be an small increase in the general noise level of the images.

## 6. Summary

The in-flight rate of CR-hits is about 1.2 to 1.6 events/sec/camera for the NICMOS detectors, consistent with the rate observed by WFPC2 on the same area. The size of each CR is between 1.6 and 2 pixels. The CRs affect on average between 2 and 3 pix/s/camera, depending on the orbital position of the telescope relative to the SAA, with an observed peak in the counts of 3.35 pix/s/camera in NIC3 and 3.60 pix/s/camera in NIC2 for the

dark frame closest to the SAA. The percentage of detector's area lost to CR-hits has a rate between 2 and 3.5 times bigger than WFPC2, owing to the bigger size of the NICMOS pixels ( $40\mu\text{m}^2$  versus  $15\mu\text{m}^2$ ). However, the use of the non-destructive readout capability of NICMOS can partially compensate for the CR-sensitivity. This solution, although it greatly improves the NICMOS performance, is not perfect, since CR-affected pixels cannot take advantage of the reduction in readout noise potentially provided by the multiple initial and final reads. In addition, CR have been infrequently observed to leave persistence on the detectors. Therefore, for studies of faint targets a limit to the length of the usable exposure time is probably about 1,000–2,000 seconds. To avoid the potential problems induced by the infrequent, but possible, CR-persistence, dithering between exposures within the same orbit is advisable.



## The NICMOS Data Handbook

Daniela Calzetti and Howard Bushouse

*Space Telescope Science Institute, 3700 San Martin Drive, Baltimore, MD 21218*

**Abstract.** The Data Handbook contains important information on the HST data GOs and GTOs receive, including explanations on the data format, on the data reduction steps performed by the automatic pipelines, on sources of uncertainties in the data, and on available tools for data analysis. The NICMOS sections of the Data Handbook will soon be available, and a draft can be already retrieved from the NICMOS WWW Documentation Page. In this Poster we present the organization of the NICMOS sections of the Data Handbook, and the relevant topics there covered.

### 1. Introduction

The new version of the HST Data Handbook is due to be released around mid-November 1997. This version contains for the first time the sections on the NICMOS data calibration and analysis. This Poster contains a brief description of the organization and content of the NICMOS sections.

Due to the accelerated schedule of the NICMOS observations, a large number of GOs and GTOs are receiving data *prior* to the release of the new version of the Data Handbook. For these observers, the mid-November official release date may represent a cumbersome "waiting period". In order to help NICMOS GOs and GTOs with their data analysis, a preliminary version of the NICMOS sections of the HST Data Handbook has been pre-released, and is available on the NICMOS WWW page, under Documentation, or at the direct address:

[http://www.stsci.edu/ftp/instrument\\_news/NICMOS/nicmos\\_doc.html](http://www.stsci.edu/ftp/instrument_news/NICMOS/nicmos_doc.html)

It is stressed again that prior to mid-November, the WWW address contains a *preliminary* version of those sections; changes and improvements may be introduced in the final version of the Data Handbook. Observers are invited to switch to the final version of the Handbook as soon as it becomes available.

### 2. Organization of the NICMOS Data Handbook

The NICMOS part of the Data Handbook is divided into five chapters:

1. **Instrument Overview:** a summary of the capabilities of the NICMOS instrument on-board HST.
2. **Data Structure:** the description of the structure of the FITS files produced by NICMOS observations and by the pipeline calibration.
3. **Calibration and Recalibration:** the description of the calibration software for NICMOS observations, available both in the STScI pipeline and standalone.

4. **Error Sources:** a summary of the most common sources of uncertainty that will affect the NICMOS calibrated data, as known as of September 1997.
5. **Data Analysis:** the presentation of IRAF/STSDAS tools developed for the analysis of NICMOS data and the discussion of general topics, such as photometric calibration (see Colina & Rieke 1997), Point Spread Function subtraction, and polarimetric analysis.

### 3. Data Structure

A NICMOS observation produces a number of FITS files, which are delivered to the observer. The files can be both raw data and pipeline-calibrated data. A subset of these files (*\*\_raw.fits*, *\*\_cal.fits*, *\*\_ima.fits*, *\*\_mos.fits*) contain the science data proper.

An individual NICMOS science image consists of five arrays, each stored as a separate image extension in the FITS file. The five data arrays represent: 1) the science image (SCI) from the detector; 2) the error array (ERR) containing statistical uncertainties of the science data in  $1\sigma$  units; 3) an array of bit-encoded data quality (DQ) flags representing known status or problem conditions of the science data; 4) an array containing the number of data samples (SAMP) that were used to compute each science image pixel value; 5) an array containing the effective integration time (TIME) for each science image pixel.

A grouping of the 5 data arrays for one science image is known as an *image set* or IMSET. A science data file can contain one or more IMSETs, depending on the readout mode used. The raw (*\*\_raw.fits*) and calibrated (*\*\_cal.fits*) science images produced by the readout modes ACCUM, BRIGHTOBJ, and RAMP contain one IMSET. The raw (*\*\_raw.fits*) and intermediate-calibrated (*\*\_ima.fits*) MULTIACCUM science images contain  $N+1$  IMSETs, for  $N$  readouts plus the zeroth readout. The calibrated (*\*\_cal.fits*) MULTIACCUM science images contain one IMSET. The science images resulting from mosaics (*\*\_mos.fits*, see next section) contain one IMSET.

### 4. Calibration and Recalibration

#### 4.1. The Calibration Pipeline

The science data the observer receives are calibrated in the pipeline by at least one, and possibly two, calibration routines, *calnica* and *calnicb*. The two routines perform different operations:

1. *calnica*: performs the basic task of removing the instrumental signature from the science data. It is the first calibration step and is applied to **all** NICMOS datasets individually. The science data file input to *calnica* are the *\*\_raw.fits* files, and the outputs are the *\*\_cal.fits* and *\*\_ima.fits* files (the latter for the MULTIACCUM readout mode only).
2. *calnicb*: operates on associations of datasets. An association is created when the observer specifies a dither and/or chop pattern, and/or multiple iterations of the same exposure in the Phase 2 proposal. *Calnicb* co-adds datasets obtained from multiple iterations of the exposure; mosaics images obtained from dither patterns; background-subtracts images obtained from chop patterns. The input science data files required by *calnicb* are the calibrated files, i.e. the *\*\_cal.fits* outputs from *calnica*; the outputs are called *\*\_mos.fits*.

#### 4.2. Calibration of Grism Observations

A separate software task, *calnicc*, has been developed in IDL by the ST-ECF to reduce NICMOS Grism observations (see Freudling 1997). The *calnicc* routines perform a series



of steps devoted to identifying and extracting the spectra from the 2D images. The software currently is **not** part of the NICMOS automatic pipeline processing, and must be applied by individual users to their grism images. The spectra extraction processing can be started using **NICMOSlook**, the interactive and quick-look counterpart to **calnicc**, also written in IDL.

The user manuals, the software, and the installation instruction for **calnicc** and **NICMOSlook**, respectively, can be found at the WWW addresses:

<http://ecf.hq.eso.org/nicmos/calnicc/calnicc.html>

<http://ecf.hq.eso.org/nicmos/nicmoslook>

#### 4.3. Recalibration

For users who wish to recalibrate their NICMOS data, **calnica** and **calnicb** are also available in STSDAS as standalone software in the **hst\_calib.nicmos** package. Recalibration may be necessary in those cases when updated calibration reference files and/or software become available after the data have been processed by the pipeline. This is especially true for data obtained during the early phases of NICMOS observations, as our understanding of the on-orbit performance of the instrument increases.

#### 5. Error Sources

In many circumstances, calibration uncertainties will contribute to determine the quality of the final science data. For NICMOS data, calibration uncertainties may be grouped under the following categories:

- **Flatfield Uncertainties:** NICMOS flatfields are known to show significant large-scale non-uniformity, in addition to pixel-to-pixel fluctuations. The non-uniformity is also a strong function of the wavelength; at  $0.8\mu\text{m}$  there is a variation of a factor  $\sim 5$  in the relative response across the array, which declines to a factor  $\sim 3$  at  $2.2\mu\text{m}$ , while at  $2.5\mu\text{m}$  the array is almost flat. The mean uncertainties of the flatfield response are around 4% (as of August 1997).
- **Dark Current Subtraction Errors:** the dark current proper, the dark current "pedestal", the amplifier glow, and the shading (the latter a *noiseless*, but pixel-dependent signal gradient) all contribute to affect the accuracy of the dark current subtraction from the science data. Three of the four components have been modelled and used to build synthetic darks as calibration reference files (see Bergeron & Skinner 1997). The effects of the fourth component, the "pedestal", still need full characterization before inclusion in the synthetic darks. As of August 1997, random uncertainties introduced by the synthetic darks are of the order of 1–5 DN, but systematic uncertainties appear to be larger, in the range 0–15 DN, with observed excursions to 30–40 DN.
- **Instrument Artifacts:** vignetting, effects of overexposure, intra-pixel sensitivity variations, and hot/cold pixels can affect the data analysis (e.g., photometry).
- **Cosmic Rays.**

#### 6. Data Analysis

A number of software tools have been developed within STSDAS which can help the analysis of NICMOS data, since they have been designed to handle the multiple extensions of the

NICMOS data files, and propagate the error and data quality arrays, thus fully exploiting the information contained in the data. The tools with the most general applications are (see Busko 1997 for a more complete description of the tools):

- **msarith**: an extension of the IRAF task **imarith**, with the capability of propagating into the output file error information from both arrays and constants;
- **msstatistics**: an extension of the STSDAS task **gstatistics**, which includes error and data quality information in the computation of the statistical quantities;
- **mscombine**: a CL script which allows one to run the STSDAS task **gcombine** on NICMOS files to combine images.
- **markdq** and **ndisplay**: the first task reads the DQ array of a NICMOS image and marks the DQ flags on top of the displayed image, using different colors for different flags. **Ndisplay** combines the capabilities of the IRAF task **display** with **markdq**; it displays a NICMOS image and overlays the DQ flags according to the user-specified color code; both **markdq** and **ndisplay** are useful for locating the position of specific DQ flags, e.g. the cosmic rays rejected by **calnica** in a **MULTIACCUM** image.

## References

- Bergeron, L.E. & Skinner, C.J., 1997, this volume.  
Busko, I.C., 1997, this volume.  
Colina, L. & Rieke, M.J., 1997, this volume.  
Freudling, W., 1997, this volume.



## NICMOS Cycle7 Calibration Plan and Beyond

Luis Colina<sup>1</sup> and Alex Storrs

*Space Telescope Science Institute, 3700 San Martin Drive, Baltimore*

**Abstract.** This document summarizes the various calibration programs that form the basis of the NICMOS Cycle 7 calibration plan. Specific calibration plans to support the NIC3 campaign are also described.

### 1. Introduction

The calibrations available during Cycle 7 and Cycle7-NICMOS are based on three distinct calibration activities. First, NICMOS has been extensively tested on the ground. These tests included a limited amount of calibration, particularly during the System Level Thermal Vacuum (SLTV) testing. Second, a period following the installation of NICMOS into HST for testing and initial calibration has been completed. This activity is known as the Servicing Mission Observatory Verification (SMOV). Finally, the routine Cycle 7 calibration program is now underway.

It is important to distinguish between the various goals of these calibration activities. SLTV was intended to demonstrate the proper functioning of NICMOS and to obtain an initial calibration of a subset of its capabilities. SMOV was intended to demonstrate that the instrument is functioning as expected, based on the SLTV experience, to characterize those parameters not measurable during SLTV (e.g. the thermal background generated by the HST optics), to establish necessary operation parameters (e.g. plate scale), and to begin the calibration of NICMOS. In many cases the complete calibration will be conducted during Cycle 7 with SMOV being used to demonstrate that the planned calibrations are in fact feasible. This document summarizes the content of the Cycle 7 calibration plan for NICMOS and also describes the calibration plans to support a NIC3 campaign.

### 2. Cycle 7 Calibration Plan

As a consequence of the NIC3 defocus, the Cycle 7 calibration plan that went into operation in June 1997 focuses only on the calibration of NIC1 and NIC2 cameras and executes a limited calibration programs for NIC3. A summary of the calibration programs included in the Cycle 7 calibration plan is found in Table 1.

The Cycle 7 calibration plan consists of routine monitoring and special calibration programs as well as of contingency calibration programs that will be executed only in the event the cameras show large physical displacements. NIC3 specific calibration programs were part of the calibration plan but are now included in the NIC3 campaign calibration plan.

A revision of this calibration plan will be undertaken by the end of 1997, after we gain experience during the first 5–6 months of Cycle 7 and after the evolution of NICMOS is better known. A postscript version of the Report fully describing NICMOS calibra-

---

<sup>1</sup>Affiliated with the Astrophysics Division, Space Science Department, ESA

tion activities for Cycle 7 (NICMOS ISR-021) is available on the NICMOS WEB page: [http://www.stsci.edu/ftp/instrument\\_news/NICMOS/nicmos\\_doc.html](http://www.stsci.edu/ftp/instrument_news/NICMOS/nicmos_doc.html)

The calibration programs may each be examined by using the ID number and the HST Program and Schedule Information Page:

<http://presto.stsci.edu/public/propinfo.html>

Information about all the reference calibration files and tables created as a result of the various calibration programs is available on the NICMOS documentation page: [http://www.stsci.edu/ftp/instrument\\_news/NICMOS/nicmos\\_doc\\_cal\\_list.html](http://www.stsci.edu/ftp/instrument_news/NICMOS/nicmos_doc_cal_list.html)

Table 1. NICMOS Cycle 7 Calibration Plan

ID	Proposal Title	Frequency	Execution	Accuracy	Comments
<i>Routine Monitoring Program</i>					
many	MULTIACCUM Darks	1	Jun. 97	10 DN	Data in all cameras
7596	Darks Monitoring	monthly		10 DN	Data in all cameras
7689	Earth Flats	continuous		2%	NIC1&2; reduced NIC3
7690	Internal Lamp Flats	monthly		1%	NIC1&NIC2
7607	Photometric Monitoring	monthly		2%	NIC1&2; reduced NIC3
7608	Focus Monitoring	bi-weekly		1 mm	Data in all cameras
<i>Special Calibration Programs</i>					
7688	ACCUM Darks	1	Sept. 97	10 DN	Data in all cameras
7691	Photometric Zero Point	1	Aug. 97	5-10%	NIC1&NIC2
7692	Polarizers	1	Sept. 97	1%	NIC1&NIC2
7693	Pupil Transfer Function	1	Sept. 97	1%	NIC1&NIC2
7611	Thermal Background	continuous	Jun/Jul. 97	n/a	Data in NIC2&NIC3
<i>Contingency Calibration Programs</i>					
7609	NICMOS to FGS Astrometry	TBD	TBD	0.1	On hold
7610	Plate Scale	TBD	TBD	0.2%	On hold
7694	Coronagraph Stability	TBD	TBD	n/a	On hold

## 2.1. Detector Performance

All three detectors are being characterized to the same extent. High quality darks were obtained for all requested MULTIACCUM sequences during June and early July 1997 (proposals ID 7703 to 7710). Changes in the detectors' performance are being monitored with a monthly periodicity (proposal ID 7596). Darks are also being obtained for a limited subset of ACCUM exposure times (proposal ID 7688). Other ACCUM exposure times will require an interpolated dark current subtraction that may be less satisfactory.

## 2.2. Flat Fields

High quality internal lamp flat-fields for all NIC1 and NIC2 polarizers, broad- and medium-band filters have been obtained during July and August 1997 (proposal ID 7690). The temporal evolution of the pixel-to-pixel response as a function of camera and wavelength is being monitored once a month using a subset of NIC1 and NIC2 filters. Earth flat-fields are been obtained for the complete set of NIC1 and NIC2 narrow-band filters as well as for a few NIC3 filters (proposal ID 7689). Data in a few medium-band filters are also being obtained to characterize the OTA illumination patterns. Additional measurements aimed at the detection and modelling of any spurious large scale structure in the flat-fields will be obtained (proposal ID 7693). Since flat-fields are generated illuminating the detectors with a bright diffuse source (i.e. internal lamps or Earth), these spurious structures could be introduced by the possible leaks of NICMOS cold mask when illuminated by these diffuse sources.

## 2.3. Photometry

Photometric observations of two standard stars have been obtained for NIC1 and NIC2 filters (proposal ID 7691). In addition, images of a bright red star (OPH-S1) were also



taken to measure possible red-leaks in the filters, in particular the narrow filters at the short wavelength range of NICMOS. The photometric stability of NIC1 and NIC2 cameras as a function of time and wavelength is being monitored once a month with observations of a standard star in a subset of filters (proposal ID 7607). In addition, the photometric stability of NIC3 camera is being monitored with observations in the filters F110W and F160W.

## **2.4. Thermal Background**

The absolute level and stability of the thermal background as seen by the NICMOS cameras has already been measured as part of the SMOV program. The Cycle 7 calibration program extends the SMOV program with images obtained in the F237M (NIC2) and F222M (NIC3) filters (proposal ID 7611). Images were taken during June and July 1997 as pointed parallel observations to map possible changes in the thermal background as a result of temperature changes in HST optics.

## **2.5. Polarizers**

The instrumental polarization and zero position angle of NIC1 and NIC2 polarizers will be measured by taking images of two bright near-infrared polarized standards: HDE283812 and CHA-DC-F7. Changes in the polarization as a function of position within the detectors will also be measured by moving one of the polarized targets in a spiral pattern across the detector. Additional images of the HST unpolarized standards HD64299 and BD+32d3739 will also be taken.

## **2.6. Focus Monitoring**

The focus of all three cameras is being monitored throughout the entire Cycle 7 (prop ID 7608). During the first few months, focus measurements will be obtained every other week with the three cameras. The frequency of the monitoring will most likely be decreased to once a month, after the first few months. Information regarding the results of the focus monitoring program are posted on the NICMOS focus Web page:

[http://www.stsci.edu/ftp/instrument\\_news/NICMOS/nicmos\\_doc\\_focus.html](http://www.stsci.edu/ftp/instrument_news/NICMOS/nicmos_doc_focus.html)

## **2.7. Point Spread Function**

No calibration program specifically designed to measure the point spread function of the three cameras as a function of wavelength and location was included in the Cycle 7 calibration plan. Observers requiring PSFs in specific filters and/or locations within the field of view are advised to include these in their own program. NICMOS PSFs can also be modeled using Tiny Tim V4.3. Tiny Tim software can be retrieved from the Web at:

<http://scivax.stsci.edu/~krist/tinytim.html>

## **2.8. Coronagraph**

The ability to position a star behind the coronagraphic mask has been enabled during SMOV. The PSF within the coronagraph has also been characterized during SMOV. A contingency program designed to measure the stability of the coronagraph performance will be executed as part of the Cycle 7 calibration plan if large physical motions in the NIC2 camera are detected (proposal ID 7694). This program focus on measuring the possible change in the scattering and diffracted energy rejection patterns as a function of target decentration in the mask. The latest information on the status of the coronagraph can be found on the NICMOS updates page:

[http://www.stsci.edu/ftp/instrument\\_news/NICMOS/NICMOS\\_updates/](http://www.stsci.edu/ftp/instrument_news/NICMOS/NICMOS_updates/)

### 3. Calibrations Supporting the NIC3 Campaign

In support of the NIC3 campaign, the original Cycle 7 calibration plan is being expanded to include NIC3-specific programs. These new programs will provide an accurate calibration of the NIC3 detector and its different modes of operation: imaging and spectrophotometry. A preliminary list of programs is indicated in the accompanying table.

MULTIACCUM darks are being obtained as part of the regular Cycle 7 calibration plan and no additional data are required to support the campaign. Flats will be obtained before the campaign once the validation of the Field Offset Mirror (FOM) is completed. A revalidation of the grisms' wavelength calibration is also needed before the campaign since the results of the corresponding SMOV test have not been conclusive.

The rest of the NIC3 calibration programs will be executed during the campaign. These include the photometric calibration of the filters, the accurate calibration of the grisms and additional programs aimed at measuring the plate scale of the detector during the campaign and at characterizing any residual large scale effects due to NICMOS cold mask.

Table 2. Preliminary NIC3 Campaign Calibration Plan

ID	Proposal Title	Frequency	Execution	Accuracy	Comments
<i>Before the Campaign</i>					
many	MULTIACCUM Darks	1	Jun/Oct. 97	10 DN	Data for all MULTIACCUMs
new	Earth Flats	continuous	Nov/Dec. 97	2%	details to be defined
new	Internal Lamp Flats	1	Nov/Dec. 97	1%	medium- & broad-band filters
7806	GRISM Revalidation	1	Oct. 97	n/a	wavelength cal: G096, G141
<i>During the Campaign</i>					
new	Photometric Zero Point	1	Jan. 98	5-10%	all filters
new	Photometric Monitoring	2	Jan. 98	2%	subset of filters
7610	Plate Scale	1	Jan. 98	0.2%	
new	Pupil Transfer Function	1	Jan. 98	1%	two/three filters
7695	GRISM Wavelength Calib.	1	Jan. 98	0.01 $\mu$ m	
7696	GRISM Absolute Calib.	1	Jan. 98	20-30%	

**Acknowledgments.** The implementation and analysis of all the calibration programs summarized in this document is the result of the work and dedication of all our colleagues in the NICMOS group, of members of the IDT, G. Schneider and M. Rieke, and of many people in PRESTO, in particular G. Chapman, M. Reinhard, D. Taylor and G. Sleiman.



## Persistence in NICMOS: Results from On-Orbit data

Doris Daou and C. J. Skinner<sup>1</sup>

*Space Telescope Science Institute, 3700 San Martin Drive, Baltimore, MD 21218*

### Abstract.

We present the results of the analysis of NICMOS persistence data taken as part of the Servicing Mission Observatory Verification (SMOV). This test is a sequel to the System Level Thermal Vacuum (SLTV) persistence tests performed with NICMOS. The goal is to reassess the conclusions previously reached with SLTV data and determine the level of persistence and operational limitations required for programs dealing with previous overexposures to bright objects. The results and analysis of the SMOV test show persistence to be present in data taken after a bright illumination for at least 60–120 seconds followed by a decay. The S/N of the data is not high enough to accurately fit a function to the persistence observations. After analysis, it is discovered that the type of sequence used in obtaining the SMOV data is not the most revealing for persistence study.

### 1. Introduction

The persistence is the excess dark current observed immediately after the detectors have been saturated with bright light. The results and analysis of the persistence data taken with NICMOS during the System Level Thermal Vacuum (SLTV) tests showed that persistence was fairly high in the first 30 to 60 seconds of the exposures. The level of persistence seemed to decay following a power law (Daou & Skinner 1997a).

The data that are presented are of rather low S/N, as too few exposures were made in the proposal to obtain reasonable accumulated counts on the persistent images. Therefore only very crude characterisation can be made of the behavior of the persistence or its amplitude.

### 2. Data

- 1 long exposure of 512 seconds where the selected star, Oph S1, is observed with the F160W filter filter and an over-exposure level of 300 to 500 times linear full well are expected.
- 1 DARK exposure of 512 seconds.
- 1 long exposure of 512 seconds of Oph S with F160W.
- 6 sets of DARKS (6x512seconds).

For each camera, the data is taken using the MULTIACCUM readout mode, the MIF512 sequence and a total exposure time of 512 seconds with the NSAMP keyword set to 25.

---

<sup>1</sup>deceased

### 3. Analysis

- To eliminate counts resulting from other detector-amplifier phenomena, subtract background darks from the dark exposures. The background darks are synthetic darks.
- To isolate the counts accumulated exclusively by each readout, subtract from each readout the previous one.
- To determine the level of persistence in the illuminated area, calculate the delta-count in a box 40x50 pixels. Concentrating on this area diminishes the uncertainty introduced by other factors such as amplifier glow and pedestal effect.

### 4. Results

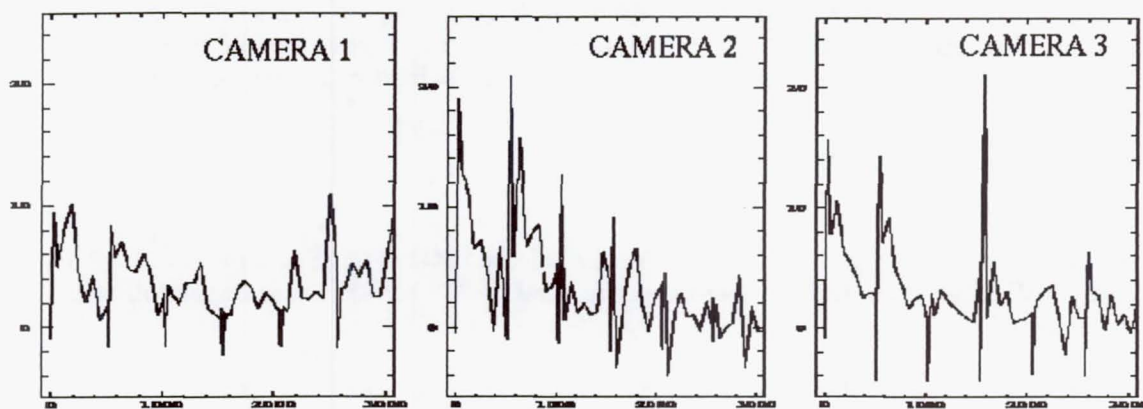


Figure 1. 6 MULTIACCUM Exposures for each Camera. From Left to Right consecutively: Camera 1, Camera 2 and Camera 3. The Y-axis is the average delta count (ADU) and the X-axis is the SAMPTIME (sec). The results show the darks to have a relatively high level of counts in the area of overexposure. This symptom persists for  $\sim 120$  seconds. It also shows a slow decrease as a characteristic of the persistence. But although the persistence is decaying, it is still visible in all five dark exposures at a lower level of about 0.05–0.1 ADU/sec, and the persistent stellar image is still visible after 3000 seconds.



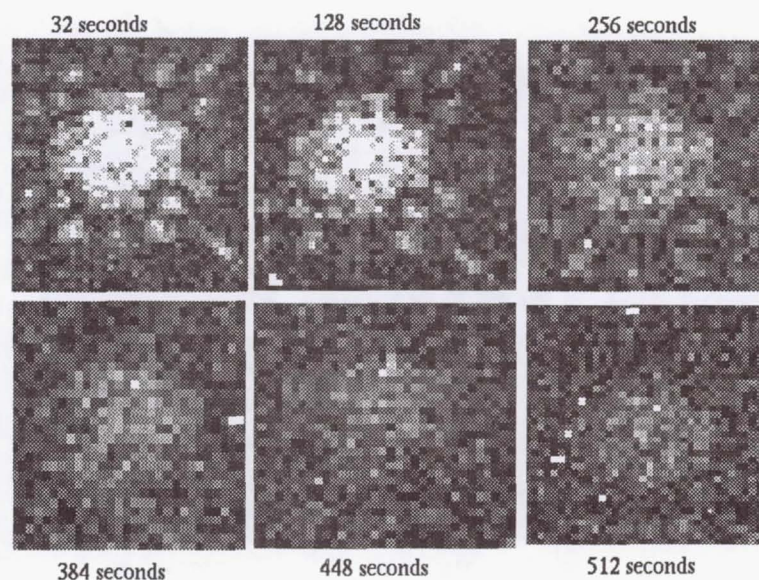


Figure 2. Example of the persistent stellar image in CAMERA 1 in the first DARK exposure after a 512 seconds exposure of a bright target. These images represent different readouts from one DARK exposure at different times. From Left to right, Top to Bottom the SAMPTIMES are: 32 seconds, 128 seconds, 256 seconds, 384 seconds, 448 seconds and 512 seconds.

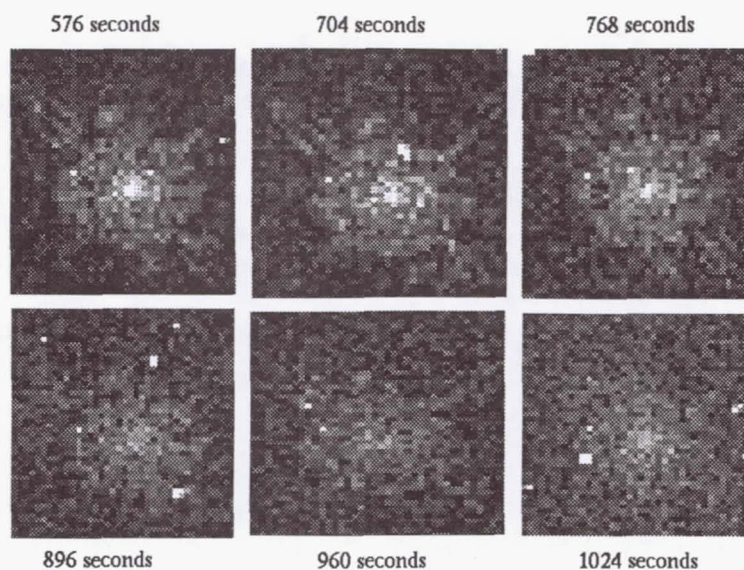


Figure 3. Persistent stellar image is still present in the second DARK exposure in Camera 2. We can easily observe a fairly pronounced decay in the persistence signal over the first 1024 seconds. These images represent different readouts of DARK exposures at different times. From Left to right, Top to Bottom the SAMPTIMES are: 576 seconds, 704 seconds, 768 seconds, 896 seconds, 960 seconds, and 1024 seconds.



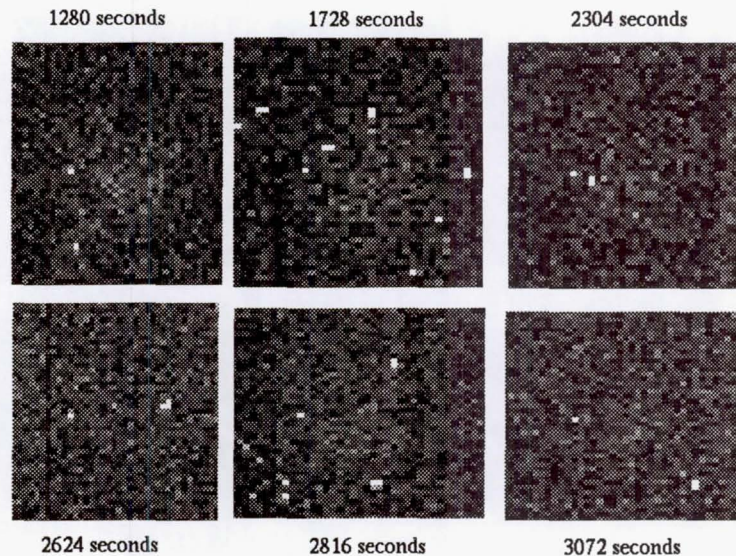


Figure 4. The residual persistent stellar images throughout the 5 following DARKS exposures in Camera 2. As shown in the plot, the persistent signal follows a slow decay to zero. But is not totally null. These images represent different readouts of DARK exposures at different times. From Left to right, Top to Bottom the SAMPTIMES are: 1280 seconds, 1728 seconds, 2304 seconds, 2624 seconds, 2816 seconds, and 3072 seconds.

## 5. Conclusions

We have demonstrated that persistence is fairly high in the first 60–120 seconds of an exposure. The persistent images are visible as long as 3000 seconds after the initial saturation on a bright source, confirming that persistence is likely to leave image artefacts during programs of observations of bright sources.

Although the total counts in an exposure decreases with time since the last autoflush, the count-rate during the first read of an exposure is usually higher than that in the last read of the previous exposure, indicating that the persistence is not as simple as a steadily changing bias with time since autoflush.

However, the S/N in the images obtained here is too low to accurately characterize the behavior of the persistent signal.

## 6. Recommendations

After the analysis of the persistence in NICMOS, the Instrument Definition Team suggests that an ACCUM exposure with multiple reads after a bright object exposure, could be the solution to eliminate any persistent post-illumination light. This theory is in the process of being tested.

## References

- Daou. D. and Skinner C., 1997a, Instrument Science Report NICMOS 97-023 (Baltimore: STScI).



## NICMOS Pointed Thermal Background: Results from On-Orbit data

Doris Daou, C. J. Skinner<sup>1</sup> and David Axon<sup>2</sup>

*Space Telescope Science Institute, 3700 San Martin Drive, Baltimore, MD 21218*

### Abstract.

We present the results of the analysis of NICMOS pointed thermal background data taken as part of the Servicing Mission Observatory Verification (SMOV). Observations in NICMOS Camera 3 are taken at different pointings and analysis of the data determines HST thermal emission to be stable. Furthermore, data obtained with multiple filters show no differences from the background calculated with the NICMOS Exposure Time Calculator.

## 1. Introduction

During observations with NICMOS, thermal emission from the HST OTA reaches the instrument's focal plane. To measure and characterize the HST thermal background effects on NICMOS, a test was performed as a part of the Servicing Mission Observatory Verification (SMOV) plan. The data were obtained with NICMOS Camera 3 by observing at a variety of pointings. The observations are used to: 1) determine at which wavelength the HST thermal emission exceeds the zodiacal background; 2) measure the stability of the thermal emission from the telescope, by estimating dependencies of the intensity and structure of the thermal background on large slews and observation time.

## 2. Data

Table 1. Characteristics of Observations.

OBSERVATIONS*	FILTER	EXPTIME (sec)	NSAMP	SAMP SEQUENCE
ORBIT-POLE	F222M	63.964	10	STEP32
ANTI-SUN**	F222M	63.964	10	STEP32
LOW-BCK	F110W	191.959	12	STEP64
LOW-BCK	F160W	191.959	12	STEP64
LOW-BCK	F175W	63.964	10	STEP32
LOW-BCK	F222M	63.964	10	STEP32
LOW-BCK	F250M	31.965	9	STEP32

\*16 exposures for each observation.

\*\*6 sets of observations.

<sup>1</sup>deceased

<sup>2</sup>on assignment from the Space Sciences Division of the European Space Agency

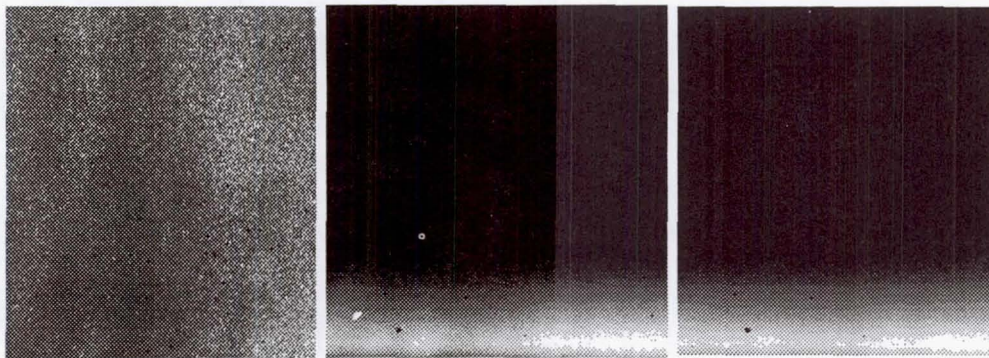


Figure 1. Example of Thermal Background observations where the bottom row shows the dramatic effects of the thermal emission from the obstructions which cause the vignetting. The images from left to right represent 3 different filters: F110W, F175W and F240M consecutively.

### 3. Results

Table 2. Results from Pointed Observations of 3 different targets as average count-rate.

Target	(ADU/sec)	( $e^-$ /pix/sec)
ORBIT-POLE	9.068	58.08
ANTI-SUN	9.004	54.02
ZODIACAL BACKGROUND	8.882	53.29

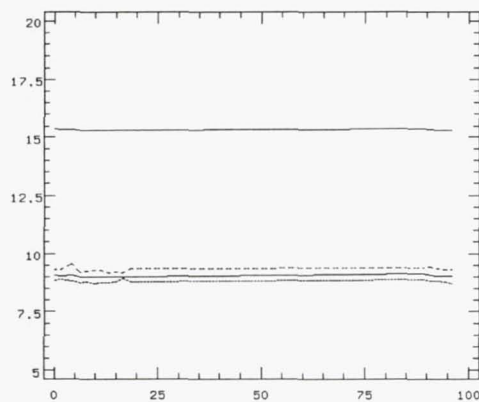


Figure 2. Thermal Background measurement from one Observation set. The Y-axis is the average count-rate (ADU/sec) and the X-axis is the observation time (min). The average count-rate is stable from the first dither pattern exposure to the last. This is true for all data sets of each of the three pointings. Also the average is within the same count-rate of 9 ADU/sec as shown by the first three curves (3 areas on the chip excluding the vignettted parts). The fourth curve is computed over the entire chip including the vignettted area. Each observation set has 16 exposures. Each exposure has an exposure time of 64 seconds. The first 10 exposures of the dither patterns are consecutive and the last 6 begin after 60 minutes.



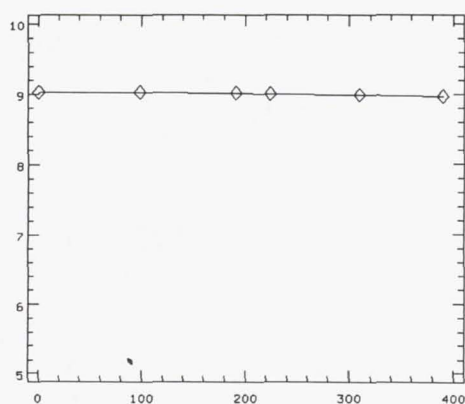


Figure 3. Thermal Background Measurement from the ANTI-SUN. The Y-axis is the average count-rate (ADU/sec) and the X-axis is the observation time (min). These 6 sets of ANTI-SUN observations were taken consecutively with the F222M filter. Each point represents the combined average count-rate of 16 dither patterns. Again the measurements show no variability over a longer period of observation time.

Table 3. Results from Pointed Observations of Zodiacal Background as average count-rate.

FILTER	Observed Background (ADU/sec)	Observed Background ( $e^-$ /pix/sec)	ETC Background $e^-$ /pix/sec
F110W	0.1288	0.77	0.71
F160W	0.1246	0.75	0.65
F175W	11.35	68.10	79.58
F222M	8.882	53.29	58.28
F240M	57.69	346.14	362.79

Table 4. Comparison with COSTAR Deployment Observations.

Filter	Before COSTAR (ADU/sec)	After COSTAR (ADU/sec)	Pointed Thermal Bckgrd (ADU/sec)
F110W	0.16	0.16	0.1288
F175W	11.92	12.15	11.35
F240M	61.45	62.57	57.69

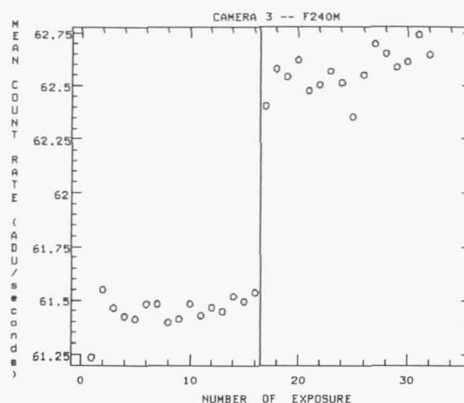


Figure 4. The thermal background measured after the COSTAR arm deployment is marginally higher than that before deployment. However, the difference is small enough that it could easily be due to a change in the Sun angle of the telescope rather than being a result of COSTAR.

The background count-rates observed after COSTAR deployment are very close (within a few percent) to those calculated with the NICMOS Exposure Time Calculator (ETC). They imply, when compared with the pointed thermal background observations, that the background count-rate can change by at least 10% over multiple orbit timescales. However, the data presented here do not give an indication of the length of this variation timescale. The pointed background observations suggest that so long as the pointing remains fixed the thermal background is remarkably stable on the timescales of a few orbits. The ETC appears to give a good estimate of the maximum thermal background likely to be observed, and the minimum appears to be only about 10% lower.

#### 4. Conclusions and Recommendations

We have demonstrated that the HST thermal background seems to be independent of large slews, and regardless of the pointing it is estimated to be about 9ADU/sec (58.53  $e^-$ /pic/sec) in the F222M filter in Camera 3.

Also the observed thermal background agrees well the background determined from the Exposure Time Calculator.

However, until an analysis of a much larger set of parallel thermal background observations has been completed, we still recommend that observers obtain a background measurement at least once per orbit, as we do not yet know the timescale or causes of background changes which can be as large as 10%.



## Subtraction of Well-Exposed NICMOS 2 PSFs

John E. Krist

*Space Telescope Science Institute, Baltimore, MD*

### 1. Introduction

A SNAP program (7420) proposed by David Golimowski (JHU) and Todd Henry (CfA) is underway to search for companions to nearby stars using NICMOS 2 ( $f/45$ ,  $0''.076/\text{pix}$ ). Well- to over-exposed star images are obtained at the center of the detector in four filters: F110W, F180M, F207M, and F222M. The stars are typically saturated to allow for the detection of faint companions. The point spread function (PSF) often fills the entire field of view, with diffraction rings visible out to a radius of  $10''$ .

The program was designed with the expectation that a large number of the stars would not have any companions or material around them, making them suitable for use as reference PSFs to subtract from other star images. The reference PSF would be shifted and intensity scaled to provide the best subtraction.

In addition to the possible discoveries of companions, the high signal-to-noise structures in the wings of these PSFs have provided new, unexpected information on the optical characteristics of the NICMOS 2 camera which cannot be obtained from the current PSF monitoring program.

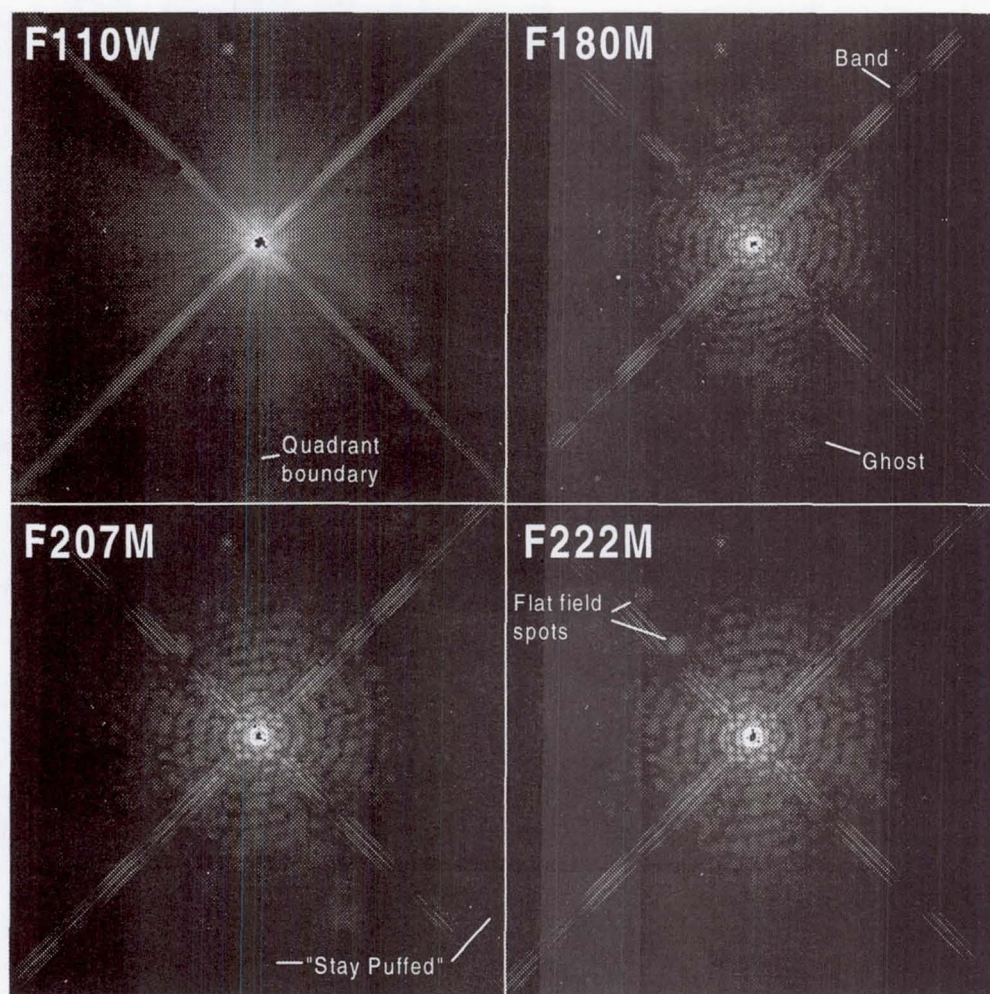
### 2. Observations

Figure 1 shows a star from our program in each of the four filters. These are standard pipeline-processed images obtained from the HST archive. A stellar companion is  $7''.7$  away. The wings in the F110W image appear relatively smooth because the PSF structure expands with increasing wavelength, blurring the diffraction rings over the range of the wide-band filter. The PSF does not change as much over the wavelength range of the medium-band filters, so the diffraction rings are plainly visible in those images.

There are some optical and calibration artifacts in the data. A ghost is visible in the lower half of the image, most notably in the first three filters, and its position varies with the location of the star and the filter used. Two spots in the upper left portion of the images (best seen in F222M) are caused by flat field errors. The flat fields were generated by combining pre-launch and on-orbit data. At those times, the coronagraphic occulting spot was at a different position in the field, so there are two "ghost" masks in the flats. The leftmost spot is the current location. The dark spot located on the upper left spider (most visible in the F110W image) is the mask location in the linearity file.

The dark, vertical line at the center of the image is the boundary between quadrants on the detector. The diffuse, vertical band, most visible in F222M, is the "Stay Puffed" anomaly, which also causes the brighter columns on the right sides of the images, especially in F110W. A horizontal trail of unknown origin can be seen to the right of the PSF center, especially in the F180M image. Individual bright points may be dark pixels not corrected by the pipeline. The cores of the stars appear black because they are saturated.

Figure 1. An example SNAP program target in four filters, with optical and calibration artifacts marked.





### 3. Initial PSF Subtraction Method

At the onset of the program, the quality of the PSF subtractions was expected to be dependent mostly on the focus stability of the telescope/camera. The differences among star images with various spectral energy distributions (SEDs) were expected to be negligible, since neither the PSFs nor the SEDs varied much over the filter bandpasses, especially in the medium-band filters.

The initial procedure was to subtract a star with each of the previously observed PSFs in each filter and choose the one which provided the best subtraction. An IDL program was developed to allow experimentation with the PSF shifts, background levels, and normalizations.

The program first computes the median values within two boxes on the extreme right and left sides of the star image and takes the minimum of the two as the initial background estimate, which is subtracted from the image. The same is done for the reference PSF.

Normalizing the reference PSF is complicated by the fact that most of the star images in our program are saturated in the core, so direct determinations of total stellar flux are not possible. Instead, the medians are computed in two boxes to the left and right of the core of the image and then averaged. The same is done for the reference PSF, which is then multiplied by the ratio of the intensity values to normalize it to the star.

The final step is image registration by shifting the PSF at the subpixel level using interpolation. Cubic convolution interpolation is performed using the `interpolate` function in IDL, which offers better results with the narrow diffraction rings than bilinear interpolation. Cubic convolution approximates sinc interpolation, which is appropriate since NICMOS 2 is nearly critically sampled at longer wavelengths.

The PSF shift is adjusted manually until the residuals in the subtraction appear symmetric. This method is sensitive to shifts of less than 0.05 pixels (4 mas). The image and PSF backgrounds, as well as the PSF normalization factor, can be adjusted interactively along with the shifts.

The quality of a subtraction is subjective, based on a visual examination of the residuals. The goal is to produce a result that provides the best chance for detecting a faint companion, which is not necessarily provided by a minimum chi-squared subtraction due to differences between the PSF structures (diffraction rings, spider patterns, etc).

### 4. Initial Subtraction Results

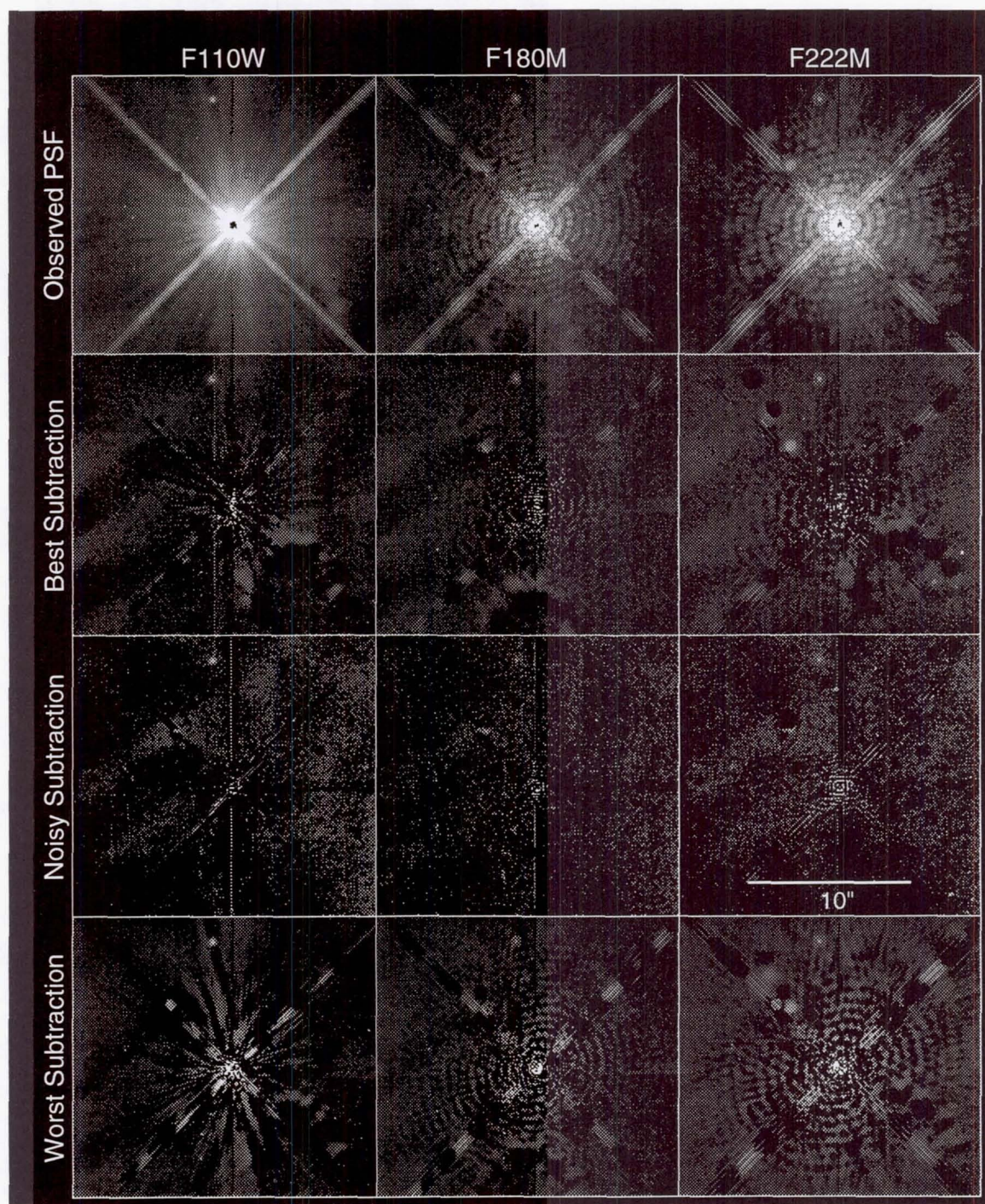
Using the procedure described above, subtractions were performed on most of the targets available at the time (about 20). These included a variety of star brightnesses and colors, from spectral type F to M. In some cases up to three targets were observed on the same day, which provided important information on the time variability of the NICMOS PSF. The PSFs were all located near the center of the field.

The subtractions ranged from very good to very poor. As expected, the largest residuals were near the core, where interpolation errors and PSF mismatches combined with the high data values. In most cases the diffraction spikes did not subtract out well, and there were large variations in how well they did from image to image. The subtraction of the diffraction rings in the wings also varied greatly. Figure 2 shows examples of both good and poor subtractions.

When the registered, normalized PSFs were blinked against each other, it was apparent that something was causing the diffraction structure to vary in unexpected ways. The largest changes were evident in the banding patterns in the diffraction spikes. Bands along one diagonal spike would move towards the PSF core while those along the other diagonal would move away. At the same time, the diffraction rings would move slightly in various



Figure 2. NICMOS 2 PSF Subtractions. The noisy subtractions used PSFs that were about eight times fainter than the star but with a similar band ratio. The poor subtractions used PSFs with similar exposure levels which were not good band ratio matches.





directions. In some cases the bands and rings would not move between two PSFs, and these cases provided the best subtractions.

## 5. NICMOS 2 PSF Variations with Time

The opposite motions of the spike bands could not be explained by focus or wavelength effects, as experiments with Tiny Tim models proved. Focus changes, such as those caused by breathing or dewar shrinkage, barely alter the position of the bands, even with large focus offsets. And as with wavelength-induced alterations, the bands would move together, either towards or away from the core. Variations like those seen can only be caused by changes in the obscuration pattern of the optical system — namely, changes in the positions of the spiders which generate the diffraction spikes.

Additional evidence pointed towards a change in the obscuration pattern. Close examination of the diffraction rings showed that they are actually elliptical. While astigmatism in the optics might be the easy explanation as the cause, the aberrations in NICMOS 2 have been well measured using phase retrieval, and are included in Tiny Tim PSF models. With the measured amount of astigmatism, those models had visually circular rings, and no amount of astigmatism could be added to make them elliptical without significantly distorting the PSF.

In addition, the banding in the diffraction spikes was not symmetric — one spike had more bands, and at different places, than the other. This indicated that the spiders in the obscuration pattern are not symmetrical and probably misaligned.

As described by Krist and Hook (1997), each NICMOS camera has a mask at the entrance of the dewar which is intended to block thermal emission from the telescope obscurations (spiders, primary mirror edge, secondary mirror baffle); hence it is called a cold mask. Optimally, the mask and telescope obscurations would be aligned, producing a PSF with essentially circular diffraction rings and symmetrical spike banding patterns.

However, by shifting the cold mask with respect to the telescope obscurations in Tiny Tim, the observed PSF anomalies could be reproduced. The diffraction rings and the positions of the spike bands were matched.

The elliptical diffraction rings are caused by an elliptical central obscuration, a result of the offset of the NICMOS central mask relative to the telescope's secondary mirror obscuration. The asymmetry in the spike bands are caused by the offsets of the mask spiders relative to the telescope's. Along one direction the spiders are barely separated, while along the other they are offset by about 10% of the pupil radius (which is defined by the outer edge of the mask or telescope primary). The widely separated spiders cause the greater frequency of banding along one spike diagonal. Other implications of the mask shift are described in Krist & Hook (1997).

A mask offset can also explain the variations seen among the observed PSFs, if the mask moved with time. This was verified with Tiny Tim. If the mask was moved so that the separation of the spiders along one direction increased while the separation along the other direction decreased, the in-and-out changes in the spike bands could be reproduced well. Subtracting model PSFs generated with two slightly different mask shifts also reproduced the sort of residuals seen in the observed PSF subtractions. Further experiments showed that the mask moves randomly around the general offset amount by up to 0.5% of the pupil radius. Differences between PSFs taken on the same day indicate that the mask shift varies on orbital timescales.

## 6. Revised PSF Subtraction Method

Since obscuration shift is the largest contributor to PSF errors in our program, a method of determining the closest matches was devised. For each target, the distances from the

core to the second bands in the upper right and lower right spikes in the F222M image are measured. The ratio of these two values, the *band ratio*, provides a measure of the banding asymmetry. The same ratio is assumed for the PSFs in the other filters.

PSFs with the closest ratios tend to be better matches to each other and provide better subtractions. Using this method, only the closest three or four PSFs need be subtracted before finding the best result. This is important in a program with 120 targets (and even more if the Cycle 7.5 program is accepted).

## 7. Other Subtraction Considerations

In one case, a companion star was located in the brightest portion of the ghost mentioned earlier. Rather than choosing the PSF that provided the best overall subtraction, one was selected which was at the same position. This placed the ghost at the same location, which subtracted out well.

Except for the ghosts, the PSFs do not show any significant field dependence. The cold mask shift does not vary with position, since the mask is in a plane conjugate to the entrance pupil.

Some of the target stars are considerably fainter than the others. These make poor reference PSFs, since the noise in the images will be multiplied by the normalization factor. Examples are shown in Figure 2.

Good subtractions can be obtained using different spectral types, at least in the filter used in this program. A G8 star subtracts well from a M1V, though residuals are high when using F-types.

With plenty of observed PSFs available, Tiny Tim models are not useful for subtractions. Considerable work would be required to fine-tune the obscuration shifts for each PSF, and even then high-order aberrations and distortion would introduce significant residuals in the wings. They are, of course, useful for diagnosing optical problems.

Experiments with Tiny Tim models demonstrate that changes in the PSF wings caused by focus variations (breathing) are less than from mask shifting.

**Acknowledgments.** This work was supported by the HST GO Grant for SNAP program 7420. Investigators in this program are David Golimowski (Principal Investigator, JHU), Chris Burrows (STScI/ESA), Holland Ford (JHU), Todd Henry (CfA-Harvard), John Krist (STScI), Don McCarthy (U. Arizona), and Daniel Schroeder (Beloit). Thanks to Ed-die Bergeron (STScI) for discussions on NICMOS image artifacts.

## References

Krist, J. E. & Hook, R.N., 1997, this volume.



## NICMOS File Formats

D. Lytle, E. Stobie, A. Ferro, I. Barg

*Steward Observatory NICMOS Project, University of Arizona, Tucson, AZ*

### 1. Introduction

This is a quick overview of some key points about the NICMOS data formats to help the user understand and manage his or her data.

### 2. FITS extensions, IMSETs, etc.

NICMOS adopted the FITS image extension format for storing data instead of GEIS format (ippssoot.c0h, ippssoot.cod) used by previous HST instruments. The primary advantages are:

1. The files are machine-independent
2. Images of different data types may be stored in the same file

NICMOS observations are composed of multiple nondestructive reads of the detectors. In the case of ACCUM mode, processing is done onboard the spacecraft so that only one read is recorded<sup>1</sup> while target acquisitions record two reads and up to 26 reads are recorded for MULTIACCUM mode. Each of these reads, regardless of the OBSMODE used, require five image extensions to fully describe the data. A single group of these five associated image extensions is referred to as an IMSET. The components of an IMSET are as follows:

- |    |      |   |
|----|------|---|
| 1. | SCI  | science image, int*2 in raw, real*4 in calibrated   |
| 2. | ERR  | statistical uncertainties, null image in raw <sup>2</sup> , real*4 in calibrated  |
| 3. | DQ   | data quality image, int*2, if no telemetry dropouts or reed-solomon errors in raw data then null image <sup>2</sup> in raw file |
| 4. | SAMP | number of samples image, constant (null image <sup>2</sup> ) in raw, int*2 in calibrated  |
| 5. | TIME | exposure time image, constant (null image <sup>2</sup> ) in raw, real*4 in calibrated   |

---

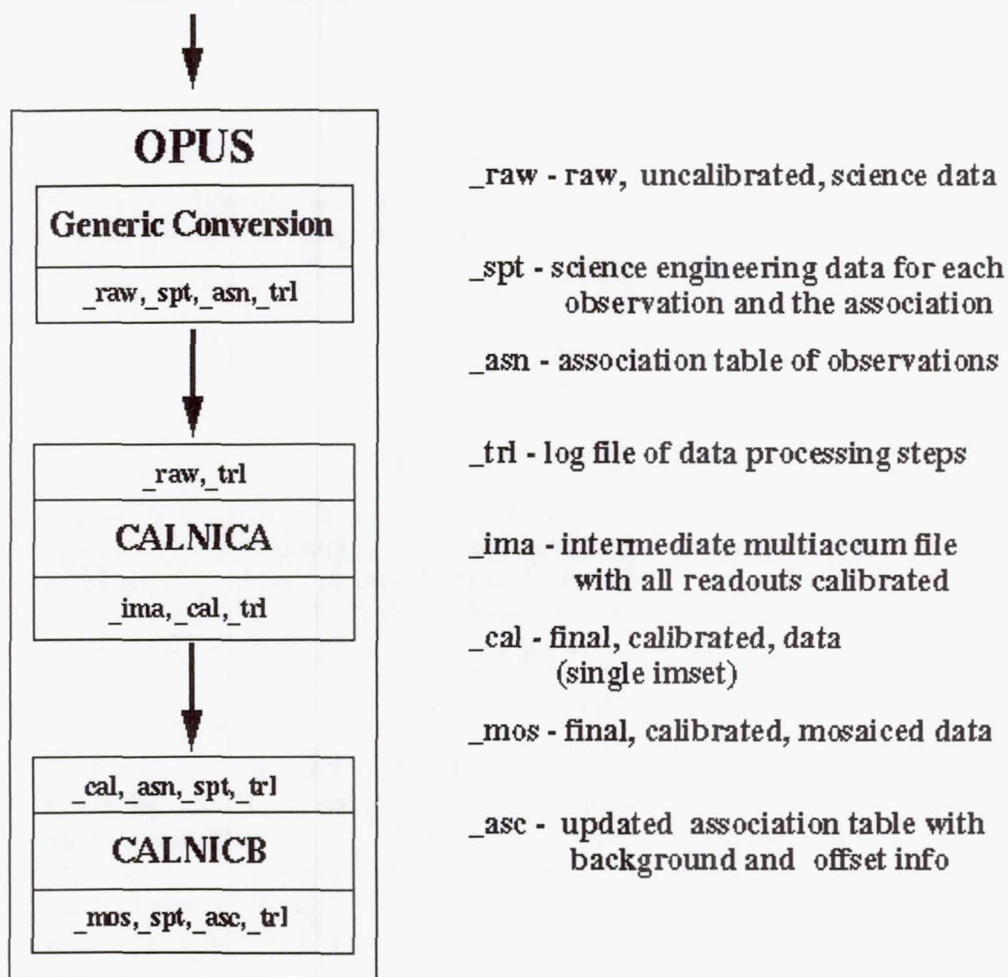
<sup>1</sup>In ACCUM mode, multiple initial and multiple final reads are averaged and differenced by the flight software to return a single image to the ground.

<sup>2</sup>In order to make files space efficient, no image is written with the image extension header if that image is a constant value. Instead, the image is described by three (3) keywords in the extension header, NPIX1, NPIX2, and PIXVALUE.

### 3. Calibration data flow

The following figure shows the flow of NICMOS data from the science packets received from HST to the final archived data products. Each FITS file name has the following format `ipppssoot.ext.fits` where the "ext" part varies from file to file and describes the type of file. The different "underbar-label"s for the different file types are described in the figure.

science packets from HST

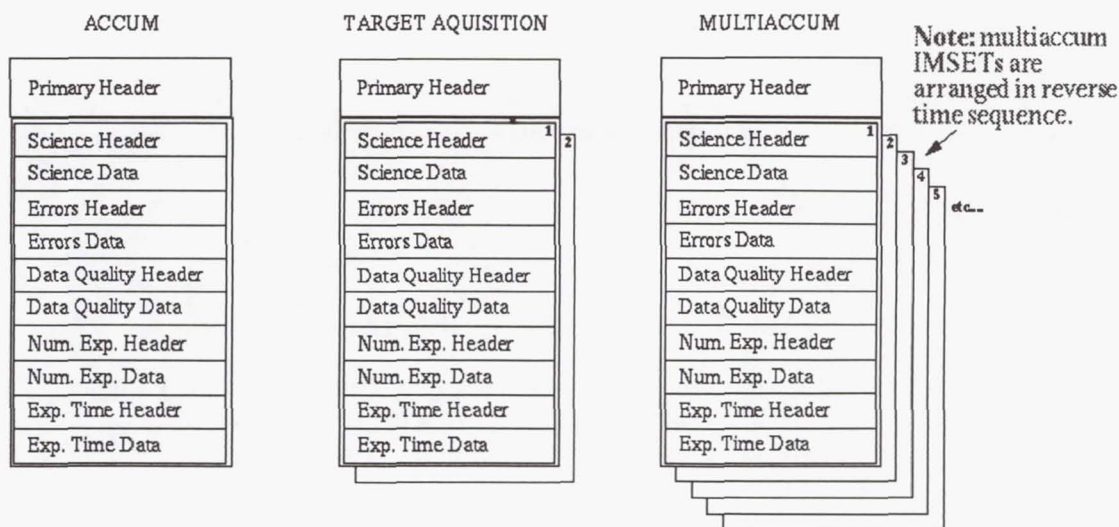


An "association" is a grouping of several observations taken by a single command, e.g., multiple observations at a single pointing (NUMITER greater than 1) or dither patterns. These observations are bound together through the calibration process by an association table (`_asn`).



#### 4. Raw File Formats

The raw files are the output of OPUS and are available to the PI from the STScI database. There are three raw formats, ACCUM, Target Acquisition, and MULTIACCUM. The structure of these three formats is shown in the following figure:



#### 5. Effects of Calibration

In the raw files described above, most of the extensions in each IMSET contain constant data arrays which are stored compressed. After calibration, the IMSETs will contain only uncompressed images. This difference between raw and calibrated data is illustrated in the figure below:

##### RAW Data File

Science Extension (exname = SCI) (data type = 16 bit integer)	Header	
	Data	DATA
Errors Extension (exname = ERR) (data type = Real)	Header	
	Data	CONSTANT
Data Quality Extension (exname = DQ) (data type = 16 bit integer)	Header	
	Data	Very Likely CONSTANT
Number of Samples Extension (exname=SAMP) (data type = 16 bit integer)	Header	
	Data	CONSTANT
Exposure Time Extension (exname = TIME) (data type = Real)	Header	
	Data	CONSTANT

##### Calibrated Data

Science Extension (exname = SCI) (data type = Real)	Header	
	Data	DATA
Errors Extension (exname = ERR) (data type = Real)	Header	
	Data	DATA
Data Quality Extension (exname = DQ) (data type = 16 bit integer)	Header	
	Data	DATA
Number of Samples Extension (exname=SAMP) (data type = 16 bit integer)	Header	
	Data	DATA
Exposure Time Extension (exname = TIME) (data type = Real)	Header	
	Data	DATA

## 6. Data volume

Approximate disk file sizes of NICMOS data products.

Primary Header	0.34 Mbytes
Raw Imset	0.15 Mbytes
Calibrated Imset	0.66 Mbytes
26 read _raw file	4.24 Mbytes
26 read _ima file	17.5 Mbytes
_cal file	1.1 Mbytes
_mos file	depends on dither, could be large

## 7. Important Header Keywords

### 7.1. Primary Header

1. Target info (TARGNAME, RA\_TARG, DEC\_TARG)
2. Proposal info (PROPOSID, etc.)
3. Instrumental configuration info (CAMERA, APERTURE, OBSMODE, etc.)
4. CALNICA calibration reference files (DARKFILE, FLATFILE, etc.)
5. CALNICA calibration switches (DARKCORR, FLATCORR, etc.)
6. CALNICB calibration info (ILLMCORR, ILLMFILE, etc.)
7. Association keywords (ASN\_ID, ASN\_TAB)

### 7.2. Image Extension Header

1. World coordinate system (CRPIX1, CRPIX2, CRVAL1, CRVAL2, etc.)
2. Readout parameters (SAMPNUM, SAMPTIME, DELTATIM)

## 8. Association Tables

Below is an example of the contents of two types of association tables.

row	MEMNAME	MEMTYPE	MEMPRSNT	BKGIMAGE	MEANBKG	XOFFSET	YOFFSET
					DN	pixels	pixels
1	n3up04d2r	EXP-TARG	yes	yes	0.91	0.00	0.00
2	n3up04d3r	EXP-TARG	yes	no	INDEF	0.00	0.00
3	n3up04d5r	EXP-TARG	yes	no	INDEF	0.00	0.00
4	n3up04d7r	EXP-TARG	yes	no	INDEF	0.00	0.00
5	n3up04dar	EXP-TARG	yes	no	INDEF	0.00	0.00
6	n3up04dcr	EXP-TARG	yes	no	INDEF	0.00	0.00
7	n3up04der	EXP-TARG	yes	no	INDEF	0.00	0.00
8	n3up04020	PROD-TARG	yes	no	INDEF	INDEF	INDEF

The small rectangle encloses the columns found in an association table before CALNICB calibration, the larger rectangle encloses the columns found in an association table after CALNICB calibration



## NICRED: Reduction of NICMOS MULTIACCUM Data with IRAF

Brian A. McLeod

Harvard-Smithsonian Center for Astrophysics, 60 Garden St., Cambridge, MA  
02138

**Abstract.** I describe a set of algorithms and associated IRAF package, NICRED, for reducing NICMOS MULTIACCUM data. In particular, this package addresses the problems of cosmic ray rejection, and the bias problems seen in early NICMOS data.

### 1. Introduction

NICMOS MULTIACCUM mode is a powerful data-taking technique that can substantially increase the dynamic range of an image, and can provide substantial cosmic-ray rejection capability without significant loss of data. The down-side is that the data are somewhat more difficult to reduce than previous HST data. The NICRED package was developed to allow reduction of the data from within the IRAF environment and independently of the STScI pipeline software, CALNIC, described elsewhere in this volume. NICRED requires the IRAF FITS kernel, which is built into IRAFv2.11, but is easily installed into version 2.10. All of the tasks operate directly on multiextension FITS files.

### 2. Dark Subtraction

Dark subtraction, done with `darksub`, is a straightforward procedure consisting of subtracting from each readout the corresponding readout from a dark file with the same sample sequence. Example raw and dark-subtracted images are shown in Figures 1 and 2.

Dark current and the sky background may also be subtracted together by constructing a sky frame from dithered observations, much like the traditional ground based approach. For those users who have enough dither positions to construct such a frame, the task `multicomb` will be of use to construct the sky frame. It combines each of the readouts from several dither positions, producing as output another multi-readout file that can be used for sky-subtraction.

### 3. MULTIACCUM Fitting and Cosmic Ray Rejection

The non-destructive readout mode of NICMOS allows for rejecting cosmic rays from exposures with a minimum loss of information. In the absence of cosmic-rays, the count-rate would be determined by doing a linear least-squares fit to the signal as a function of time. The slope of the fit is the count-rate. In the presence of cosmic rays, we also fit a slope, but we allow for a jump in the intercept where the cosmic ray occurs. The program `fullfitbam` performs this function, assuming that there is only one or zero cosmic-ray hits per pixel in a given image. This is a reasonably good assumption for all but the longest exposures. Since we do not know *a priori* whether there is a cosmic ray hit in a pixel, or when it occurred, we must make this determination. For each pixel with  $N$  readouts, we consider the  $N$  possible times that a cosmic ray could have hit, and fit a slope and two intercepts,  $a$  and  $b$ . Then



Figure 1. A raw image.

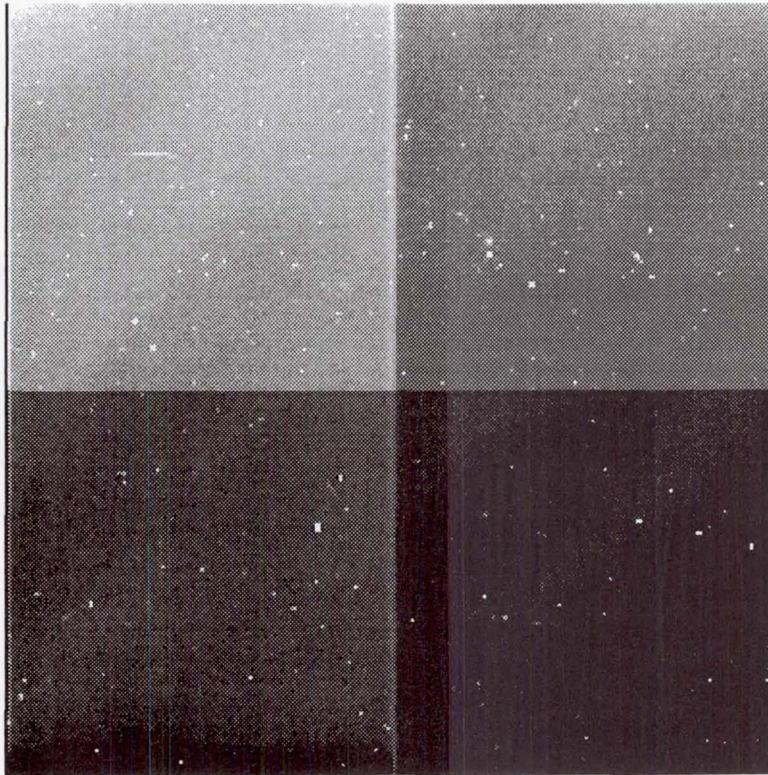


Figure 2. A dark-subtracted image.

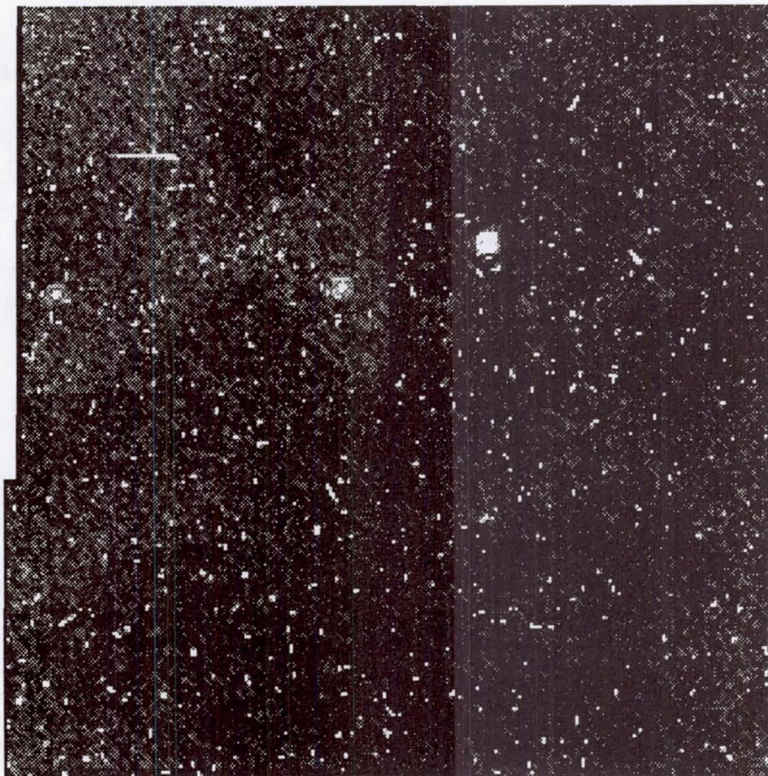
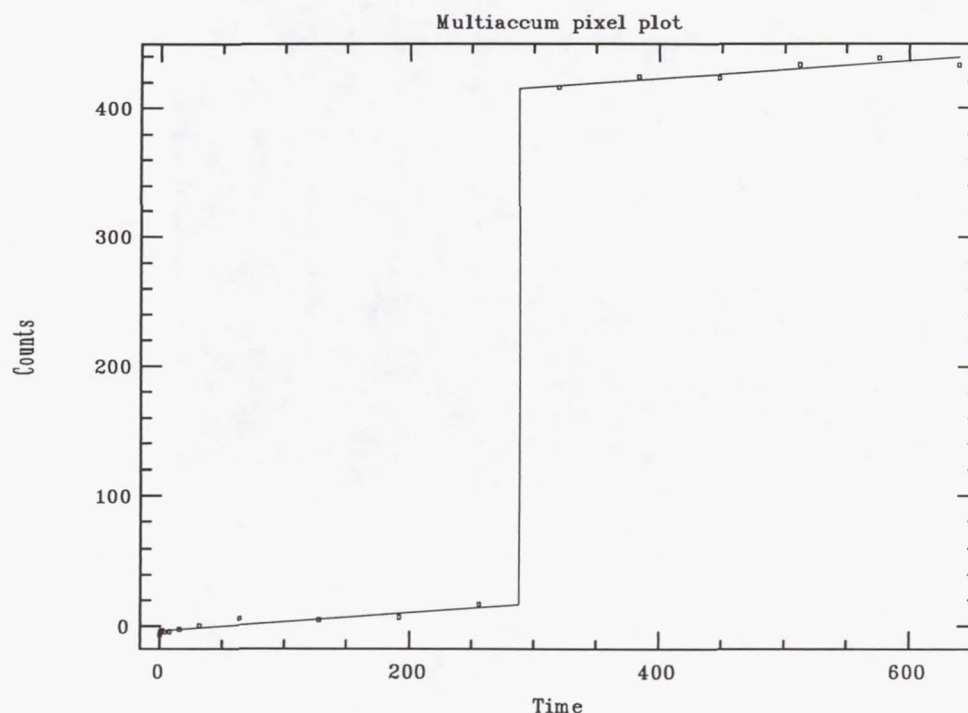




Figure 3. A cosmic ray hit and the fit to the data



we compute the residuals of the fit and compare with the difference in the two intercepts. If  $a - b$  is large compared with the uncertainty in  $a - b$ , as determined from the residuals, it is likely that a cosmic ray hit occurred between the readouts. Note that even in the event of a cosmic ray hit *all data readouts are used* unless the pixel is saturated!

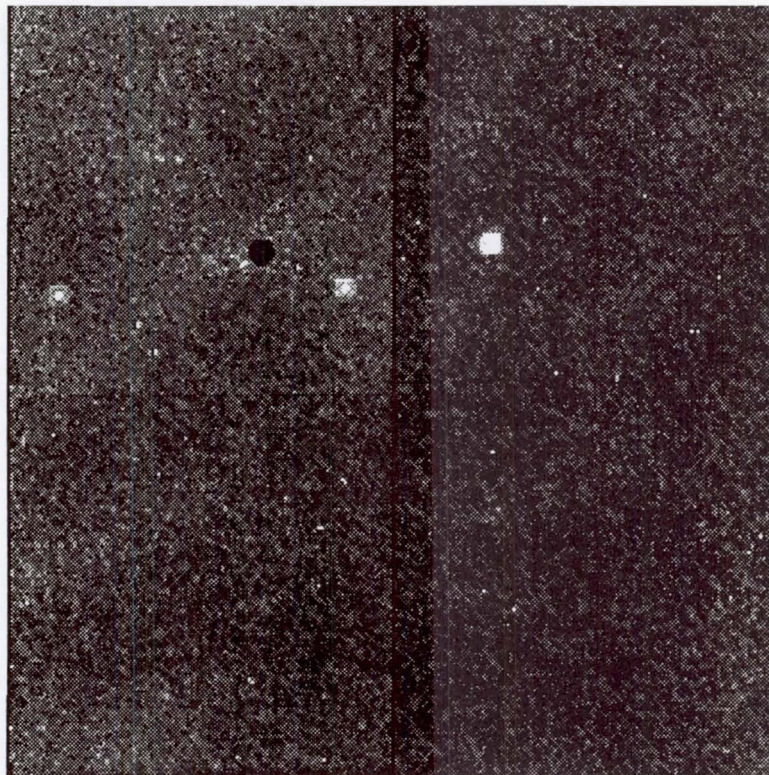
Lets make this process more explicit. For a trial cosmic ray hit occurring between readout times,  $t_j$  and  $t_{j+1}$ , we fit the constants  $m$ ,  $a$ , and  $b$ , in the expression,

$$y = \begin{cases} mt + a & t < t_j, \\ mt + b & t > t_j \end{cases}.$$

Then, define the merit function,  $M = (a - b)/\sigma_{a-b} \approx (a - b)/\sqrt{\sigma_a^2/j + \sigma_b^2/(n - j)}$ , where  $\sigma_a$  and  $\sigma_b$ , are the residuals over the points with  $t < t_j$  and  $t > t_j$ , respectively. We compute the merit function over each possible  $j$ , and choose the largest value. This is where the cosmic ray occurred. If the largest value of  $M$  doesn't exceed a user-defined threshold, no cosmic ray is flagged and we do a standard fit with one intercept. The program also enforces the condition that  $\sigma_a, \sigma_b \geq \text{readnoise}$ . When  $N$  is small, this prevents statistical flukes of fits with unusually small sigmas from being flagged as cosmic ray hits. I have typically been using a threshold of  $M = 3-5$ , and  $\text{readnoise} = 10\text{ADU}$ .

To assist in tuning up the parameters for the fit, there is a utility program, `multiplot`, which plots the data values vs. time, and shows the fit. The pixel to plot is selected with the image cursor. Figure 3 shows a pixel with a cosmic ray hit and the associated fit. Figure 4 shows a slope-fitted, cosmic-ray rejected image.

Figure 4. Result of fitting cosmic rays



#### 4. Bias Problems

Early observations with NICMOS have suffered from a drifting bias level, also known as the "pedestal effect" (NICMOS STScI Analysis News #4, August 1997). The result is that each readout contains the true signal plus an additional value constant over the array, but varying with readout number. This problem is propagated by the fitting process so that the final image also suffers from an additional constant. After applying the flat, the constant component is "unflattened" so that the resulting image shows the flat-field image in reverse (see Figure 5).

Another effect of the wandering bias is to make the MULTIACCUM data ramps non-linear. Since it is constant over the array, the slopes are affected equally, but the cosmic ray rejection algorithm gets confused because it detects false excursions from the expected linear ramp. This can result in a speckled-looking image when some pixels have false cosmic rays detected in the presence of the non-linear ramp. NICRED solves both of these problems.

The output of `fullfitbam` can be flattened using `nicflatten`. First, the user specifies threshold values, between which it is assumed the image contains blank sky. If the image is extremely crowded, this program may not work. It is assumed that the spatial variations of the blank sky on the detector are identical to that of the flat. The program then minimizes the quantity  $\sum_i (S_i - aF_i - b)^2$ , where  $a$  and  $b$  are the fitted constants, and  $S_i$  and  $F_i$  are the pixels in the slope image and the flat. The fit is only done over those image pixels meeting the threshold requirements. In other words, the flat and an additive constant are fitted to the sky regions of the image. The residual of the fit is the sky-subtracted, bias-corrected image. This procedure is done independently for each of the four quadrants of the image, with the result shown in Figure 6.



Figure 5. Un-bias corrected, flattened image. Residuals from the flat are apparent.

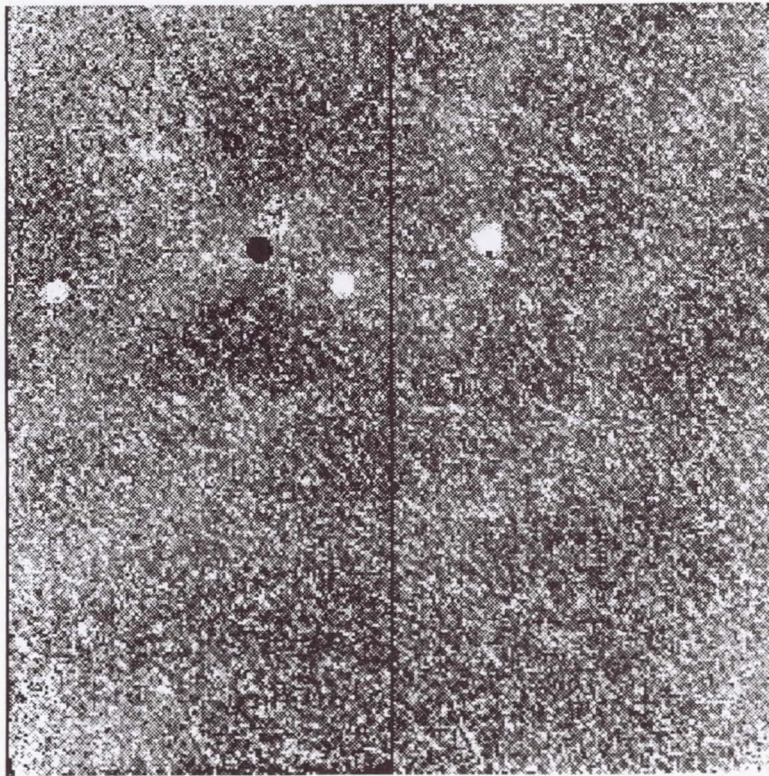
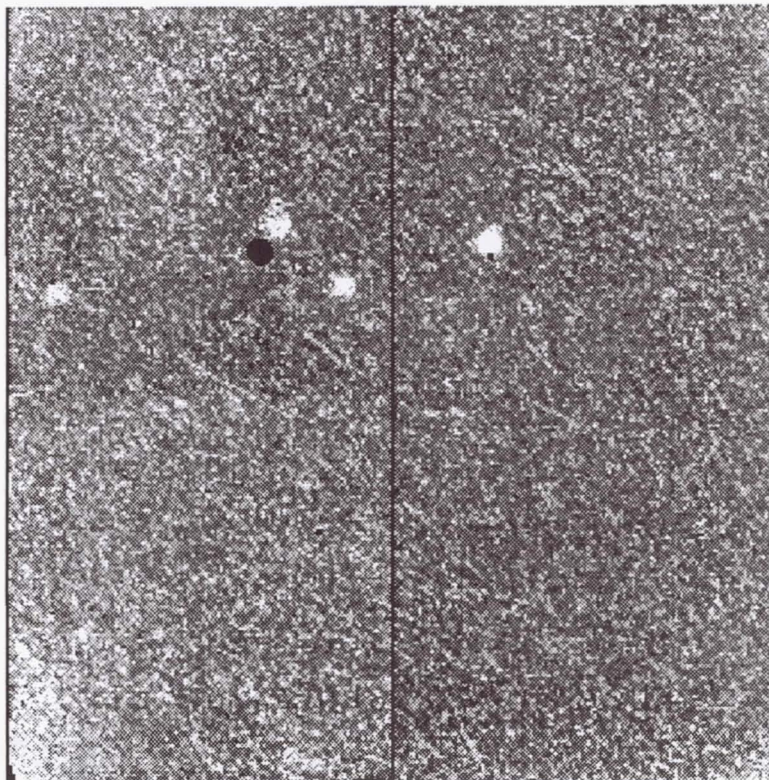


Figure 6. Sky-subtracted, bias-corrected, flattened image.



Given this initial estimate of the cumulative bias drift, we can eliminate the bias drift in the individual readouts. The bias error for frame  $j$  is  $E_j = \text{Median}_i(I_{ji} - t_j(S_i - b))$ , where  $t_j$  is the sample time for frame  $j$ ,  $I_{ji}$  is the  $i$ th pixel in the  $j$ th frame, and as before  $S_i$  is the fitted slope (counts/sec) for pixel  $i$ . The bias is removed from the slope image with `biasfix`, and the individual biases are removed with the IRAF script `nicbias`. Once the individual bias errors are removed, `fullfitbam` is run again to refit the slopes and cosmic rays, and `nicflatten` is rerun to flatten and sky subtract.

## 5. Summary of the Processing Steps

- `darksub` – Subtract the dark current from each frame.
- `fullfitbam` – Linearize, check for saturations, fit the slopes, and remove the cosmic rays.
- `biasfix` – Remove bias error from initial slope image.
- `nicbias` – Remove bias errors from MULTIACCUM frames.
- `fullfitbam` – Recompute slopes and remove cosmic rays.
- `nicflatten` – Compute flattened, sky-subtracted image.

## 6. Obtaining NICRED

The NICRED package is available on the World Wide Web at <http://cfa-www.harvard.edu/~bmcleod/Nicred>, or by contacting the author at [bmcleod@cfa.harvard.edu](mailto:bmcleod@cfa.harvard.edu).

**Acknowledgments.** I would like to thank Marcia Rieke for providing her MULTIACCUM fitting program `fullfit`, which mutated into the program described here. My collaborators Emilio Falco and Joseph Lehar tested the programs and found various bugs. John Roll provided the FITS library `fitsy`.



## NICMOS Data Quality Control and Paper Products

C. Ritchie, H. Bushouse, L. Colina, D. Calzetti, C. Skinner<sup>1</sup>, A. Storrs

*Space Telescope Science Institute, Baltimore, MD 21218*

### Abstract.

The HST pipeline routinely creates hardcopy products, or paper products, for all data. These products are used both to provide hardcopy output for the GOs and also by the Contact Scientists for data quality evaluation. The products must therefore be general enough to support both sets of users. This poster provides an introduction to the NICMOS paper products.

A set of paper products summarizes a set of exposures, typically a single visit in a proposal. The pages are separated into visit-level and exposure-level pages. The visit-level pages include the cover page, explanatory notes, and tables summarizing the details of the observations. These are followed by the exposure-level pages which include a picture of each calibrated (cal) exposure followed by a data quality summary and a calibration reference file summary for that exposure. For associated data, there is first a picture of the mosaicked (mos) image. For associations with a pattern, this is followed by a cartoon of the observing pattern and on-target and background individual images. All associated exposures also have stamp-sized pictures of each of the calibrated images in that association.

Sample images with possible data quality concerns are shown at the end.

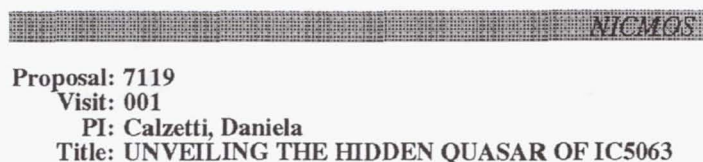


Figure 1. The Cover Page contains the proposal ID, visit numbers, PI's name, and proposal title. The second page consists of Explanatory Notes which explain the contents of the paper products. If you have questions about your data please send e-mail to your Contact Scientist.

---

<sup>1</sup>Deceased

VMS-001

Proposed Title: NICMOS

Target List

Target Name	R.A. (J2000)	Dec. (J2000)	Description
IC5063	20:52:02.33	-57:04:07.0	GALAXY SEYFERT QUASAR INTERACTING G

Observation List

Visit/Exp#	Run Name	Target Name	Camera Used/Prime	Operating Mode	Spectral Element	Observing Pattern	Exposure Time per Integration (sec)	Number of Exposures	Quality Flags: Obs Pass Fail
1.0.0	NUV01030	IC5063	2/2	MULTIACCUM	F222M	ONE-CHOP	127.942	1	○ ○ ●
Quality Flags: ○ = OK    ● = Not OK    Blank = Unknown or file missing									

Observation List-Optional Parameters

Visit/Exp#	Run Name	Target Name	Camera Used	Operating Mode	Optional Parameters
1.0.0	NUV01030	IC5063	2	MULTIACCUM	SAMP-SEQ=STEP256 NSAMP=10 OFFSET=JAM-NO-OVERO

Spitzer Telescope Science Office, WFO 15-0000 17-Aug-97, Pg. 1

Figure 2. The Target List contains the name, predicted coordinates, and text description of each target. The Observation List has exposure information - camera, filter, mode, exposure time - as well as the status of the spacecraft and ground-system performance during execution of the observation. The Observation List-Optional Parameters lists the optional parameters, other than pattern related parameters, specified in the proposal.

VMS-001									
Proposed Title: NICMOS									
Observing Pattern Strategy									
Visit/Exp#	Run Name	Target Name	Camera Used	Operating Mode	Pattern Name	Pattern Orient (degrees)	Number of Positions	Dither Size (")	Chop Size (")
1.0.0	NUV01030	IC5063	2	MULTIACCUM	ONE-CHOP	0.00	12	0.00	119.00

Spitzer Telescope Science Office, WFO 15-0000 17-Aug-97, Pg. 2

Figure 3. The Observing Pattern Strategy lists the optional parameters used to specify the dithering/chopping pattern for each exposure. These include the pattern name, pattern orient, number of positions, dither and chop sizes.



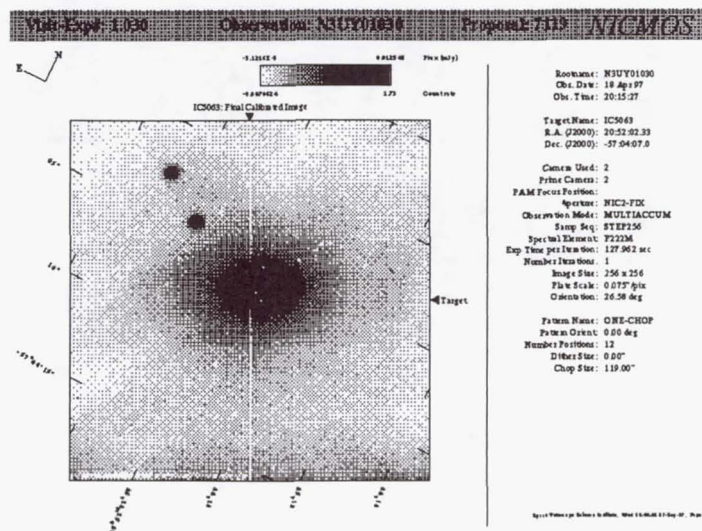


Figure 4. An image of each final calibrated exposure is included in the paper products. In this case the exposure is an association and the picture is of the final mosaicked (mos) image. Exposure information from the observation header are provided at the right. The PAM focus keyword, NPFOCUSP, was added to the headers 6 May 1997.

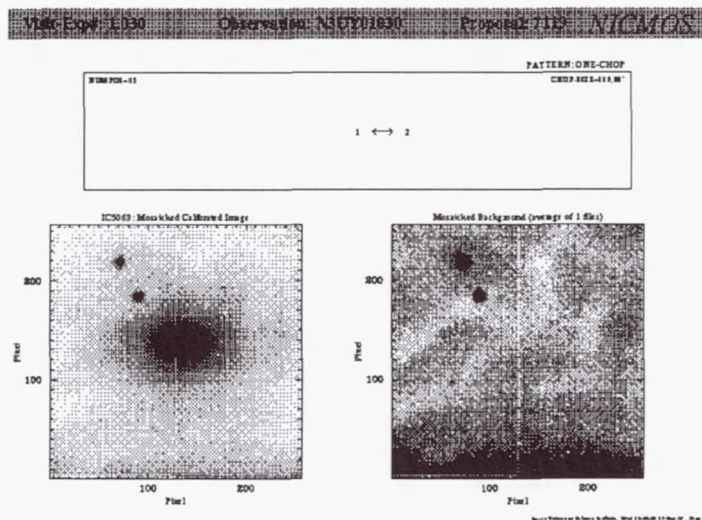


Figure 5. A cartoon of the pattern, in this case a ONE-CHOP, is shown at the top. On the left is the mosaicked calibrated image, the same as in the preceding figure. At the right is a representation of the background created by averaging the individual output background mosaics from calnicb. Note that this averaged background image is not an output product of calnicb.





Calibration Status Summary						
Switches and Flags			Reference Files and Tables			
Keyword	Value	Calibration Step	Keyword	File Name	Pedigree	
BIASCORR	PERFORMED	Wavelength correction	N/A			
ZOFFCORR	PERFORMED	Subtract MULTIACCUM zero read	N/A			
MASKCORR	PERFORMED	Mask bad pixels	MASKFILE	nmdb14599a_mask.fits	GROUND 15/01/1997	
NOISYCORR	PERFORMED	Compute statistical noise	NOISYFILE	nmdb146218a_noisy.fits	GROUND 27/01/1997	
DARKCORR	PERFORMED	Dark subtraction	DARKFILE	nmdb15280a_dark.fits	MODEL 01/07/1997	
LINECORR	PERFORMED	Linearity correction	LINEFILE	nmdb161654a_line.fits	GROUND	
FLATCORR	PERFORMED	Flatfield correction	FLATFILE	nmdb161397a_flat.fits	GROUND 15/01/1997	
UNITCORR	PERFORMED	Convert to counts/s	N/A			
PHOTCALC	PERFORMED	Photometric calibration	PHOTTAB	nmdb160826a_phot.tbl	GROUND 17/01/1996	
CRIDCALC	PERFORMED	Identify cosmic rays	N/A			
BACKCALC		Predict background	BACKTAB			
WARNCALC		Generate warnings	N/A			
ILLMCORR	SKIPPED	Subtract background illumination	ILLMFILE	nmdb141324a_illm.fits	DUMMY 04/02/1997	

Figure 8: Reference Files and Tables, Used 15/01/1997, Page 1

Figure 8. The Calibration Status Summary gives detailed information about the calibration of the observation. Calibration switch keywords are listed along with completion status and definition of the calibration step. Reference file name keywords are provided with the name and pedigree (DUMMY, GROUND, IN-FLIGHT, or MODEL) of the reference file used. Older data processed with DUMMY reference files are good candidates for recalibration. The exception are DUMMY ILLMFILES used by the calnibc step, as no real data are yet available.

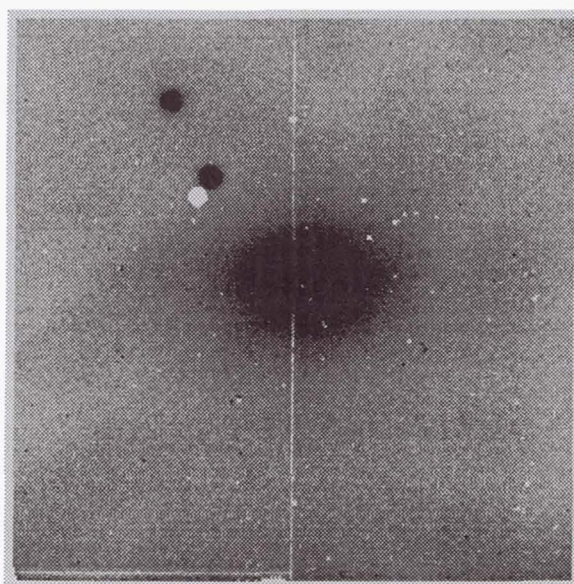


Figure 9. An example of the moving coronagraphic spot. The dark hole at the top was the current position of the coronagraphic spot when the image was taken. The white hole comes from the linearity file [dq] array. The dark hole above the white hole comes from the flatfield and shows the position of the coronagraphic spot when the flat was created. Newer reference files have employed patching to remove the spot.

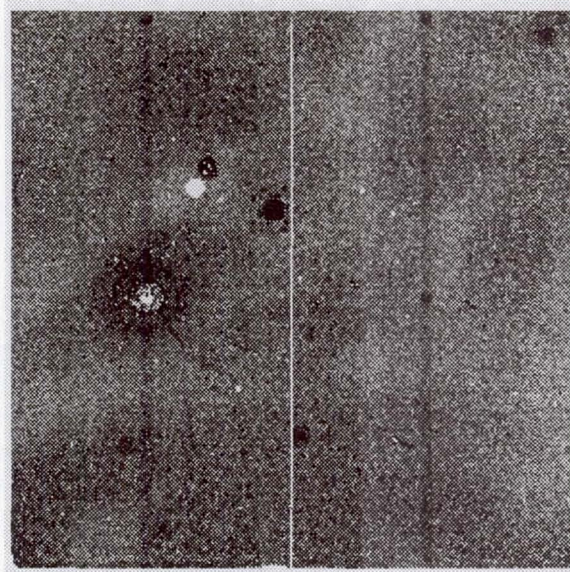


Figure 10. An example of "Mr. Staypuft", electrical ghosts. A bright pixel, in this case a large cosmic ray hit, at pixel 62,124 in the lower left quadrant has a faint "echo" at the same pixel location in the other 3 quadrants. In addition there are faint bands running through the ghosts along columns.

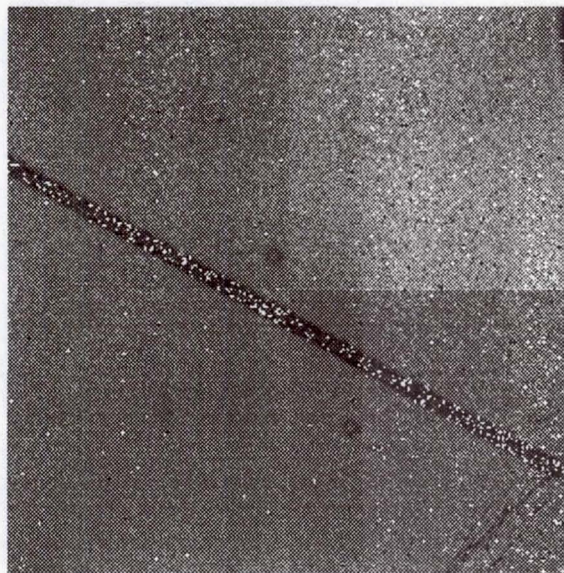


Figure 11. An image with a trail from space junk.



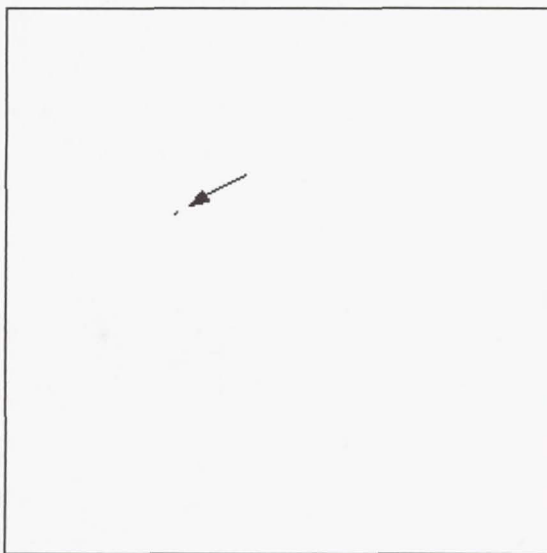


Figure 12. An image with a bad pixel set at E8. This occasionally happened with images processed before calnica3.0 due to a math roundoff error when attempting to perform a fit to only 1 good sample. Fixed in data with calnica3.0 and for paper products display purposes by PaperProducts2.9 which uses a different method of greyscale determination.

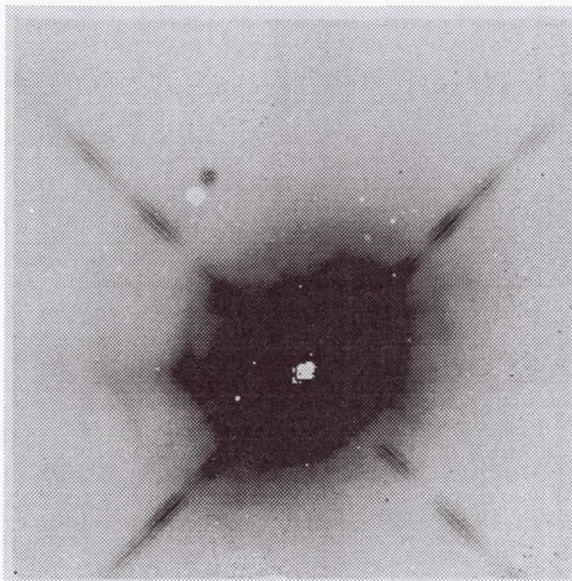


Figure 13. An image with saturated central pixels that aren't getting flagged properly. The use of calnica3.0 which makes a correction for non-zero signal in the zeroth read of a MULTIACCUM image along with new linearity files with the [ZSCI] and [ZERR] extensions will fix most pixels.

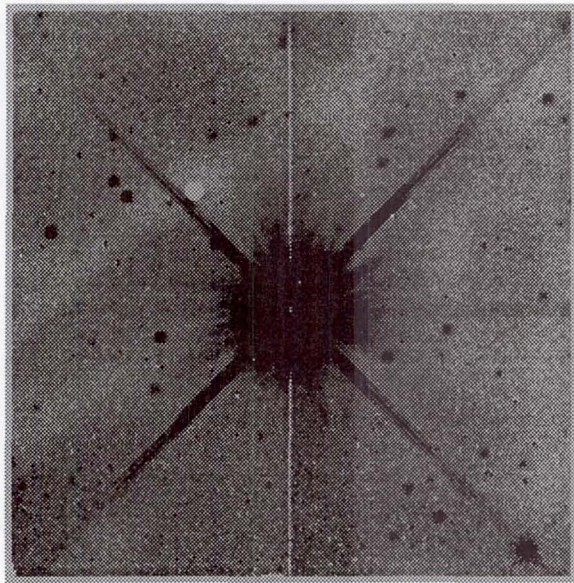


Figure 14. A NIC2 image showing dark current pedestal. This is a random, quadrant-dependent additive signal that appears whenever the detector's amplifiers are switched on. The pedestal is a uniform offset without any flatfield variations, and so the FLATCORR step in calnica will impose an inverted flatfield response in the final calibrated image.

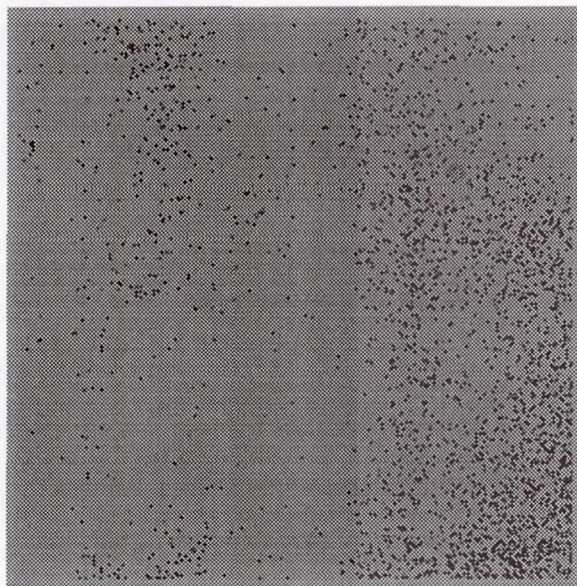


Figure 15. A NIC3 image from the public parallel program. Problems mostly due to the calnica CRIDCALC cosmic ray rejection algorithm. Readouts with good data are sometimes thrown out leaving only the first few reads with low, slightly negative signal. A new algorithm is being tested.



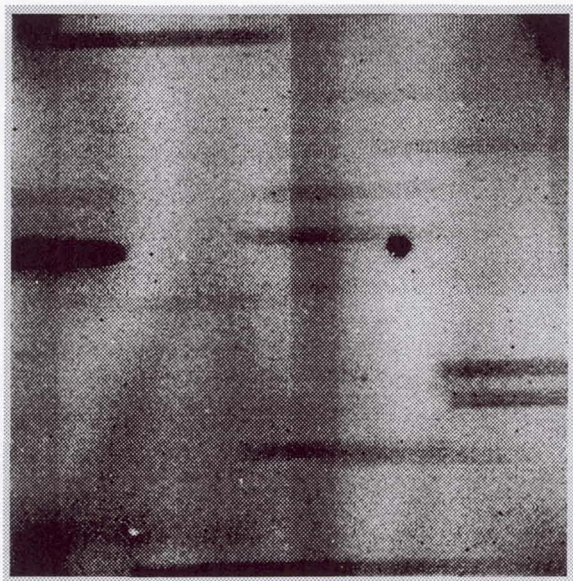


Figure 16. An example of a grism image. Nothing wrong with the horizontal bars, this is how it should look! At the time this image was processed only DUMMY darks were available, and the dark vertical bands (shading) and dark corners (amplifier glow) can be removed by recalibrating with the appropriate epoch INFLIGHT or MODEL dark. Grism data are not flatfielded and the NIC3 flatfield pattern can also be seen.

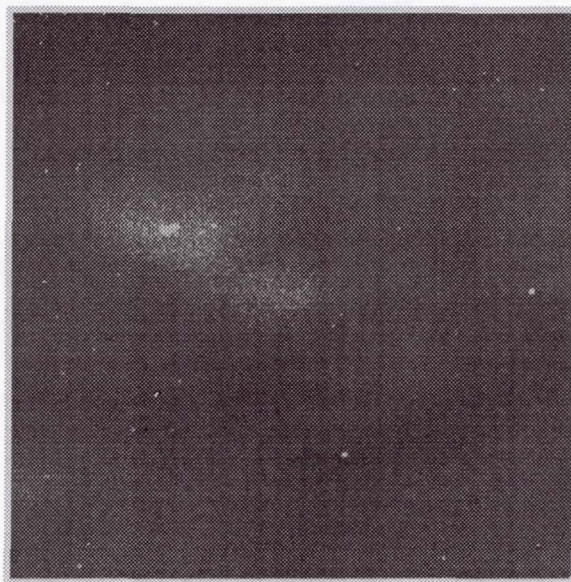


Figure 17. A NIC1 flatfield image showing "grot" and bad pixels. In addition to bad pixels which were already known from ground-based testing, more pixels have shown low measured quantum efficiency in orbit. These pixels are possibly affected by debris lying on top of the detectors. Paint flakes from the optical baffles are one possible source. The bad pixels are often clustered in groups and appear as spots in flatfield frames.

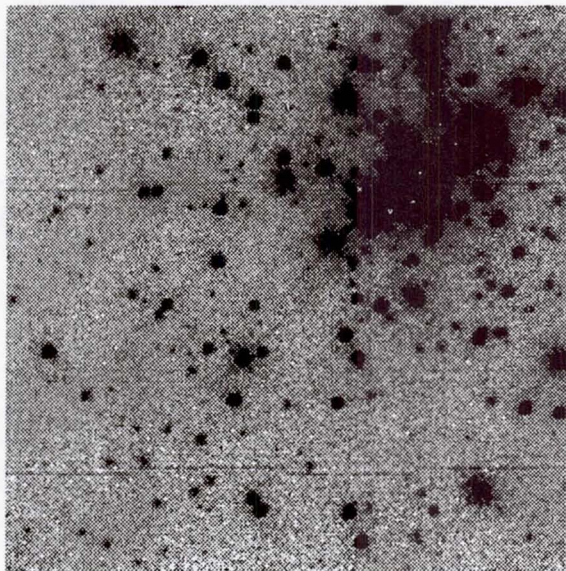


Figure 18. Bars in a NIC2 focus image. Cause unknown but may be related to onboard timing patterns.



## Software Tools for NICMOS

E. Stobie, D. Lytle, A. Ferro, I. Barg

*Steward Observatory NICMOS Project, University of Arizona, Tucson, AZ 85721*

### 1. Introduction

The NICMOS Software Group (NSG) at the University of Arizona has built a number of software tools in IDL<sup>1</sup> for processing NICMOS data. These tools are described below according to their category.

### 2. Planning

#### 2.1. HSTField

HSTField is based on a program originally written at Goddard by Eliot Malumuth and heavily modified to our purposes at the University of Arizona. The program displays an image of the sky, often a digitized sky survey image, then overlays the Space Telescope apertures allowing the user to pick a prime aperture, orient the telescope, mark guide stars, get coordinates in RA and DEC as well as Ecliptic and Galactic coordinates, and determine the positions of other Space Telescope instruments. This program is designed for planning observations both single and parallel. The HSTField display is shown in Figure 1.

#### 2.2. Simimage

Simimage is an IDL widget layered on top of the STSDAS task `simimg`. The STSDAS task computes a simulated image for the HST instruments FOC, NICMOS, and WFPC2 given the observing configuration and table of objects. Simimage allows a convenient mechanism for determining the necessary parameters plus the additional features of displaying the final result both as an image and shaded surface plot, computing statistics on the result, and generating a group of dithered images across the object field.

### 3. Editing

#### 3.1. Cal\_Edit

Cal\_Edit is used to edit FITS header keywords in preparation for re-calibrating NICMOS data with CALNICA. The display consists of a set of action buttons at the top of the screen. The various calibration flags can be set using the radio buttons next to each flag. The calibration reference files can be changed by typing directly into the appropriate text fields or the Pick button can be pressed to bring up a file selection widget.

#### 3.2. FHE

FHE is an IDL program for editing headers of groups of FITS files. It is particularly well suited to editing FITS files with multiple image extensions. One of its primary uses is to

---

<sup>1</sup>IDL (Interactive Data Language) is an interactive analysis and visualization program written by Research Systems, Inc..



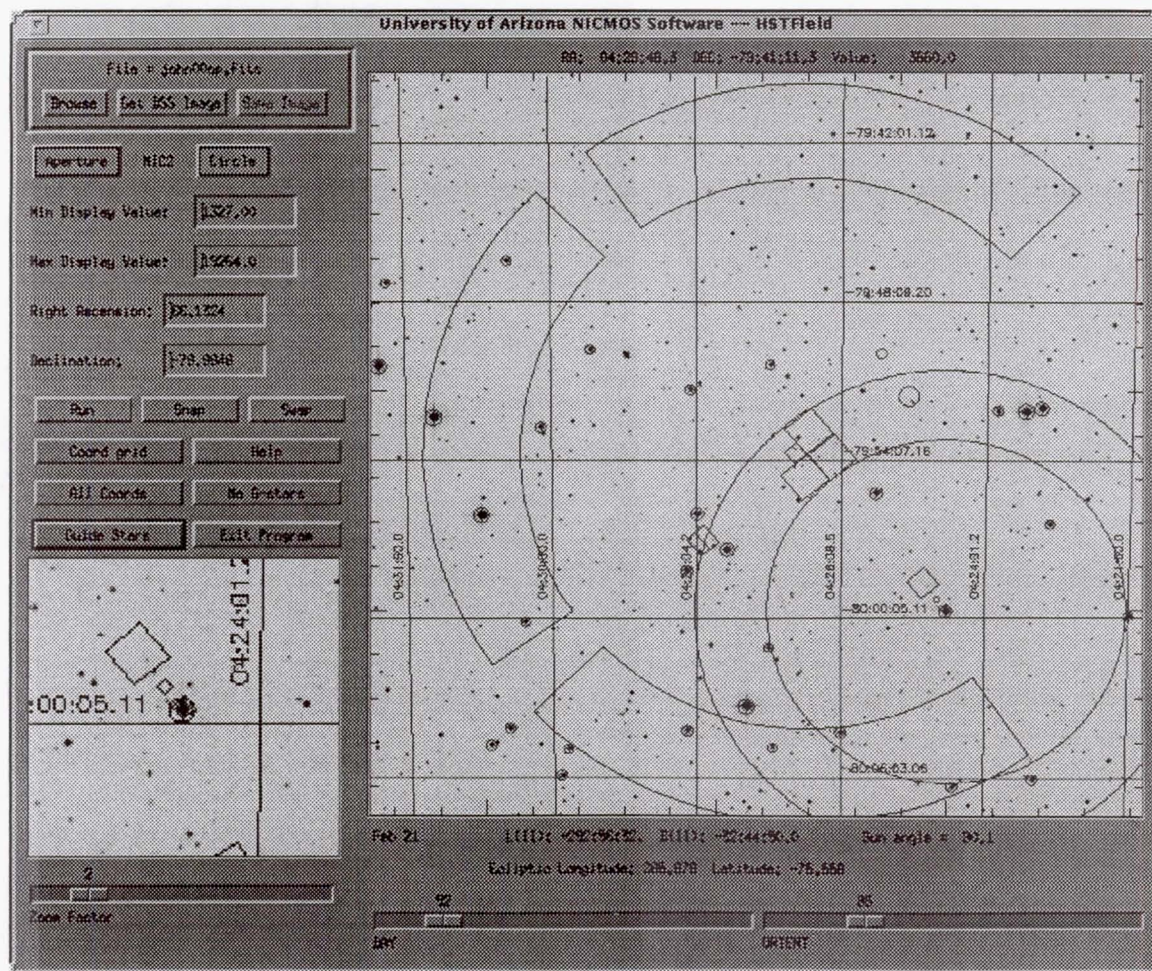


Figure 1. Example of HSTField display with HST apertures and guide stars marked.

edit the calibration switches and reference file keywords in the headers of the NICMOS raw data files. Any keyword in the primary header or any extension header (excluding reserved FITS keywords) may be edited. Keywords may be modified, added, or deleted.

### 3.3. Maskedit

Maskedit is used to edit bad pixel masks. The inputs are the FITS data image and the FITS mask image. There are various keywords that can be used on input to scale the image and to set the "good pixel" value for the mask. The program displays the data image and marks the "bad" pixels based on values in the mask image (bad pixels are circled). The user may then set or unset masked pixels using the mouse buttons. Finally, the new, edited, mask can be saved to a file.

## 4. Calibration

### 4.1. Buildref

Buildref is an IDL program for building reference files from single FITS images. Buildref stitches together single-image FITS files into multi-extension FITS files. The user provides a command file that specifies the input images to be combined, the method of combination,



and any keyword additions or changes that should be made to the standard NICMOS header template files that are used. The outputs of this program are NICMOS standard multi-extension FITS files. Buildref also includes support for nonlinearity reference files.

#### 4.2. CALNICA

CALNICA is an IDL replication of the `calnica` task in IRAF/STSDAS. Its single argument is the list of files to process. The outputs are a calibrated image with associated extensions and, in the case of MULTIACCUM data, an intermediate file with each readout fully calibrated excluding cosmic ray rejection.

### 5. Data Analysis

#### 5.1. FITS List Calculator

FITS List Calculator (FLC) is a program to process large groups of FITS files together by creating data lists. The program parser supports a simple command syntax including the ability to process pre-defined scripts, do-loops, and if-then-else constructs as well as arithmetic operators, native IDL commands, and UNIX system commands. The program has an image scanner feature to view a list of images in a movie-like format, a more detailed graphics display which includes the image header, full image, single quadrant or zoomed region of the image, and the image histogram. There are also windows for editing pixels in an image and for building lists. The program supports four data types: lists, images, arrays, and scalars. The user may customize the number of each data type by editing the user definitions file. Several mathematical functions for lists are pre-defined for convenience including the computation of image statistics, pixel statistics, medians, means, and first differences.

#### 5.2. Lucy

Lucy is a program that generates a deconvolved image from an input image and point spread function (PSF) using the algorithm developed independently by Richardson (1972) and Lucy (1974). The widget is based on the original and accelerated algorithms with optional damping developed by Rick White at STScI. The IDL program displays the original data as well as the result at the end of each iteration.

#### 5.3. NICLook

NICLook is a quick look analysis tool for NICMOS data. The widget contains three display windows: full window, zoom window, and graphics window. Statistics may be computed for the full or zoom window. World coordinates may be overlaid on the full window and coordinates may be printed for any pixel in either the full or zoom window. Image arithmetic may be done on any of the five loaded images using arithmetic operators or IDL functions. Two images may be blinked. All commands are logged in a journal file.

#### 5.4. NICMosaic

NICMosaic is a tool for mosaicing NICMOS images. The inputs are a list of images to mosaic and, optionally, a table of position data previously output from NICMosaic. If no table is given, the program attempts to line up the input images as best it can based on the world coordinate information in the image headers. Image rotation and fractional pixel shifts are used to accomplish this alignment. Once the data are loaded, the user may select two of the images (called the primary and the secondary images) and blink these two images. The user may then shift and rotate the selected primary image to improve the alignment using the buttons and value fields provided. On exiting, a table of positions is written that can

be used by the program NICMerge to create a final, mosaic, image. The NICMosaic display is shown in Figure 2.

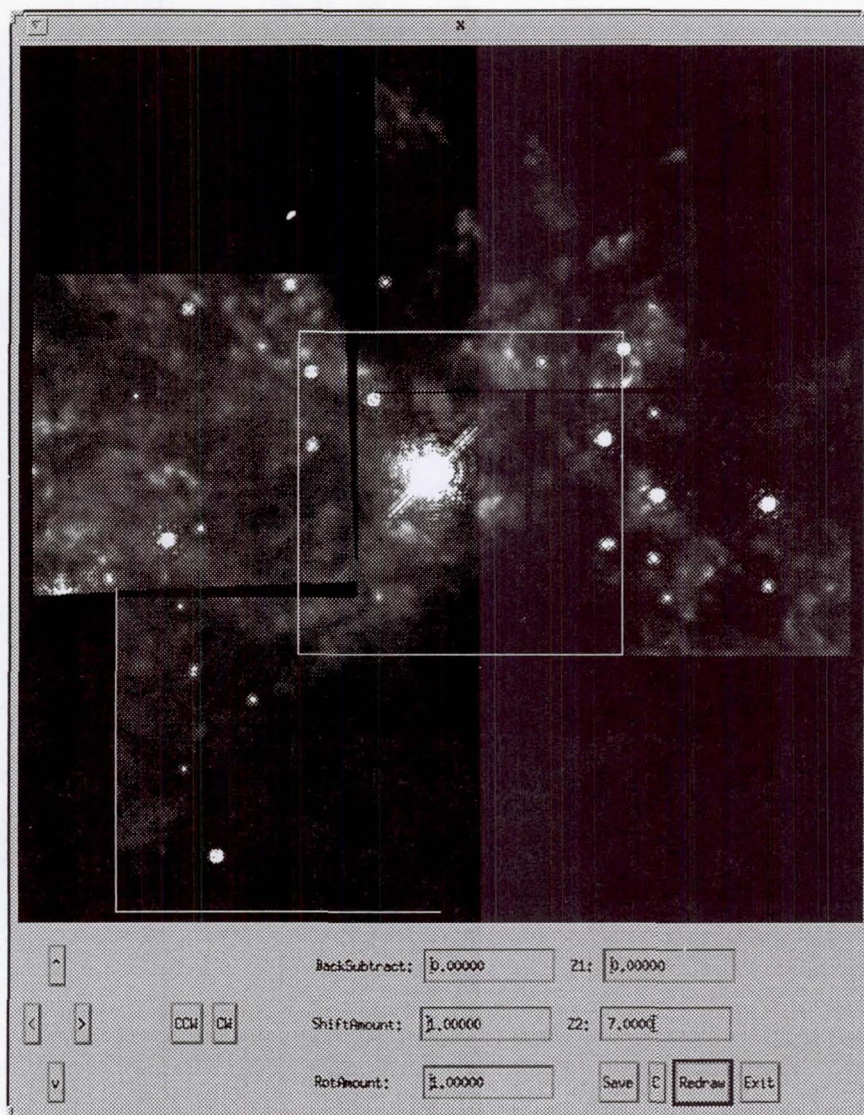


Figure 2. Example of NICMosaic display with sample data.

### 5.5. Polar and Polarplot

Polar and Polarplot are two programs that have been written for the analysis of NICMOS polarization data. Polar is a program that takes three images (one from each polarizer) as input, solves the linear equations, and produces as output the "I", "Q", "U", "P", and "Theta" images. Polarplot, shown in Figure 3, allows the user to overlay the polarization vectors on the intensity image. This program has many user adjustable parameters to customize the plot such as intensity image color table manipulation, axis, contour map, and polarization vector color manipulation, contour overlay, and thresholds for polarization intensity.



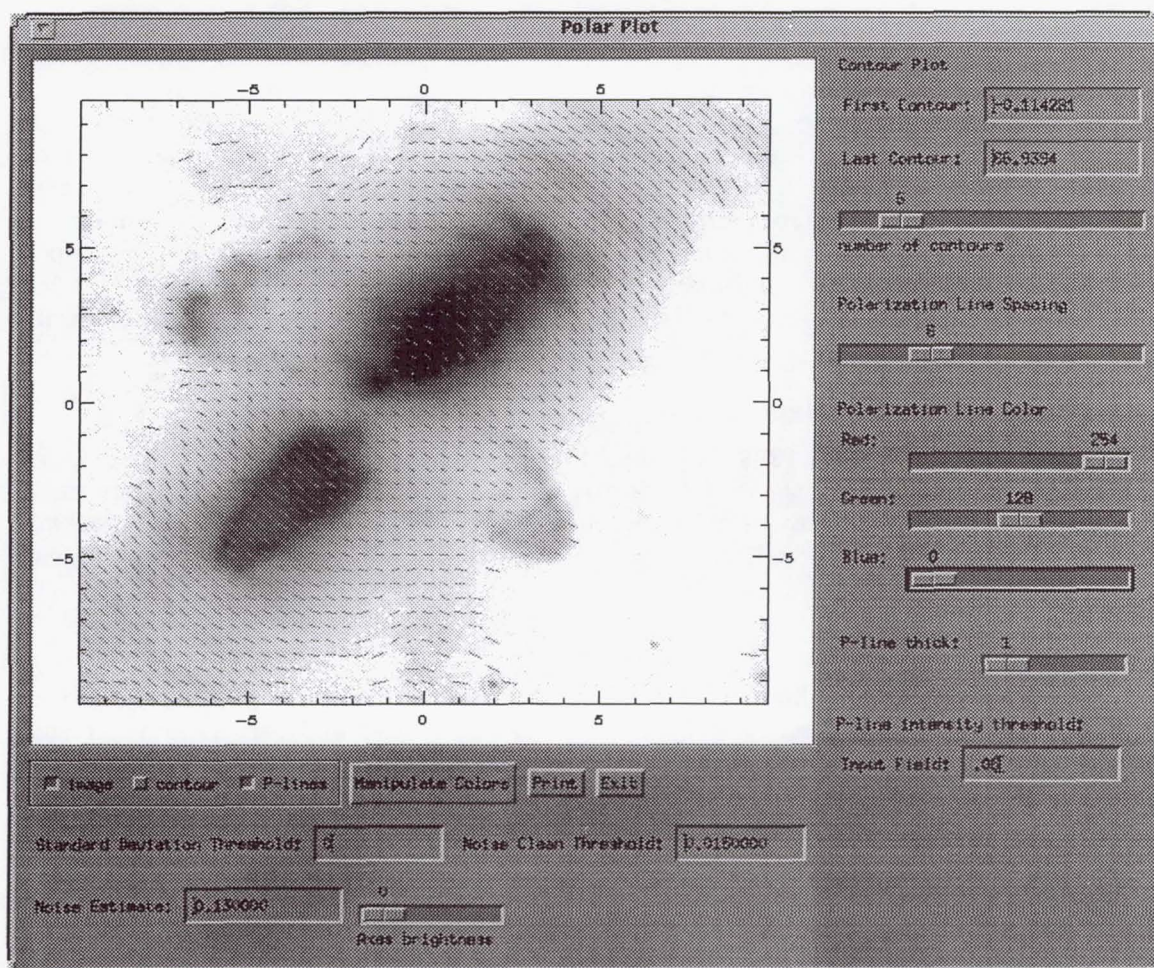


Figure 3. Example of Polarplot display: an intensity image is shown overlotted with polarization vectors.

## 6. Display

### 6.1. FITSTOOL

FITSTOOL is used to examine multiextension FITS files and allows the user to edit the primary and extension headers. The display consists of a file structure window down the left side, a header display window in the upper right, a full image display window in the lower center, and a zoom window in the lower right. There are three header editing buttons above the header display window that are used for adding, deleting, or editing header keywords. Certain header keywords are protected and can't be edited; the keyword "SIMPLE" is an example of a protected keyword. Clicking on any displayed extension in the file structure window will load that extension, image and header, into the appropriate windows. Clicking the left mouse button in the full image display window loads a subsection of the image centered on the cursor into the zoom window. Successive clicks without moving the cursor will increase the zoom factor. The File pull down menu at the top of the widget allows the user to load FITS files and save edited files.



## 6.2. MultiM

MultiM is an IDL widget for displaying many images simultaneously. The maximum number of images displayed is 144 by compressing from 256x256 pixels to 64x64 pixels, by either averaging or subsampling. Statistics for each image and each quadrant in the image are generated as data are loaded. Plots may be generated of a row or column in a single image, or of a single pixel across all images. A mean and a standard deviation image can be computed over all images and a median background may be calculated over a group of dithered images. This background may be subtracted and images then registered by world coordinates and averaged together. Bad pixels may be located according to the specific thresholds across all images with a sorted table as the output.

## 6.3. Super Display Widget

The Super Display Widget (SDW) is designed to be a general purpose FITS image viewer. It is very much a program in that is evolving day by day as time allows. In its current state, it allows general image display of multi-extension FITS files, zooming, bad pixel masking, log scaling, rudimentary pixel editing, min/max scaling, general IDL colormap adjustment, and cursor readback.

## 6.4. Trucolor

Trucolor is a program for displaying and printing true color images by loading the three display color tables, red, green, and blue with separate images and overlaying the result. Each color table can be scaled individually to obtain the desired "look". The images may also be log scaled to bring up background detail. This program works on systems with 8-bit or 24-bit color display and produces appropriate output postscript files when the print button is pressed.

## 7. Utilities

### 7.1. Delread

Delread is a batch program to delete one or more readouts (imsets) from a raw or ima MULTIACCUM file.

### 7.2. Kwlist

Kwlist is a batch program to print a table of keyword values for the specified list of files. The desired keywords are defined in a string array and the files to be read are defined in an ascii text file. The information is printed to the user's screen and to the specified output file.

### 7.3. Unstitch

Unstitch is a batch process to separate the readouts (imsets) of MULTIACCUM files into different files. Output files are named by replacing the last character of the IPPSSOOT designation with the readout number. Readouts count from one to a maximum of 26 in forward time order (normal NICMOS files are in reverse time order). The inputs are an ascii text file of filenames and an optional path parameter.

## References

- Richardson, W. H., 1972, J. Opt. Soc. Am. 62, 55  
Lucy, L. B., 1974, AJ 79, 745



## Making Maps and Mosaics

Alex Storrs

*Space Telescope Science Institute, 3700 San Martin Dr., Baltimore, MD 21218*

**Abstract.** This document attempts to clarify some of the ways in which maps and mosaics can be made with NICMOS. Some of the tradeoffs inherent in these are discussed.

### 1. Introduction

Observers frequently want to obtain near-IR images of larger parts of the sky than a single camera's format allows. If the desired area is not elongated, a simple SPIRAL-DITH pattern may fill the bill (Figure 1). If the target is a jet or a galaxy, however, there are a bewildering number of ways to map it, and some fairly obscure considerations as well. This paper attempts to address these concerns, under the assumption that the observer has read the NICMOS Instrument Handbook and the HST Phase II Proposal Instructions.

The basic idea is to make an image, move the telescope, and make another image, repeating the process until the total area to be mapped is covered. Unfortunately HST is not set up to make a series of images at a given pointing (in e.g. different filters) and then move on to the next mapping position automatically. We recommend that a series of monochromatic maps be made, and then compared.

### 2. Orientation

One major complication of mapping with HST is that the telescope doesn't maintain the same orientation on the sky like ground based (equatorially-mounted) telescopes do. The position angle of the columns of the NICMOS cameras varies with time for any given target. Thus the overlap of an array of adjacent images will depend on when the observations are scheduled. To ease the observer's work, the PATTERN-ORIENT optional parameter was developed. This parameter controls how the different pointings are arranged on the sky, irrespective of how the spacecraft is oriented. To avoid gaps in such maps, the spacing between successive grid points should be less than  $\sqrt{2}/2$  times the camera size. Figure 2 shows an example of this type of map. If more than two rows of images are needed, an XSTRIP-DITH pattern may be used with offsets between rows controlled by either the POS TARG exposure-level special requirement or by defining a different target for each row.

This mapping technique will result in considerable overlap between adjacent images. If less overlap is desired, the spacecraft orientation must be controlled. This is done through the visit-level special requirement ORIENT, whose argument is the north position angle of the U3 axis seen on the sky, which is 225 degrees greater than the +Y direction of NICMOS. Once the orientation is fixed, a standard mapping sequence (with the default PATTERN-ORIENT=DETector), or the POS TARG requirement, can be used to map the target. Note that the former moves the telescope against the sky, while the latter moves the sky seen in telescope: care must be taken to move in the correct direction! Figure 3 shows an example of this type of map—less overlap, but potentially impossible to schedule.

Figure 1. Map which covers region of interest regardless of orientation

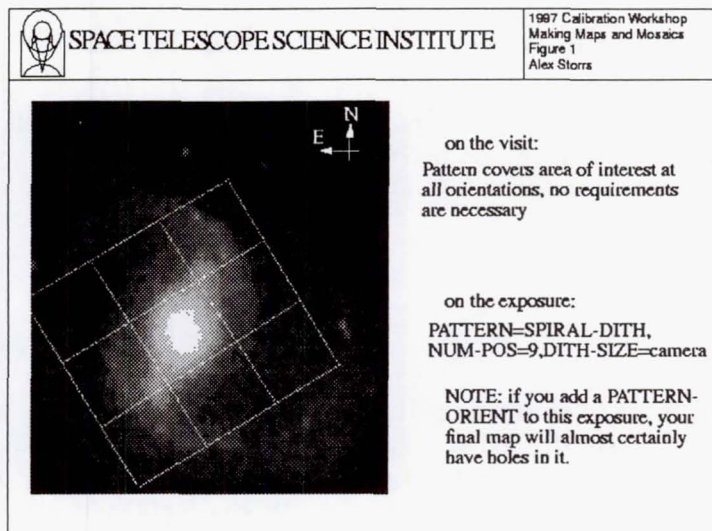


Figure 2. Map which more than covers region of interest, regardless of orientation

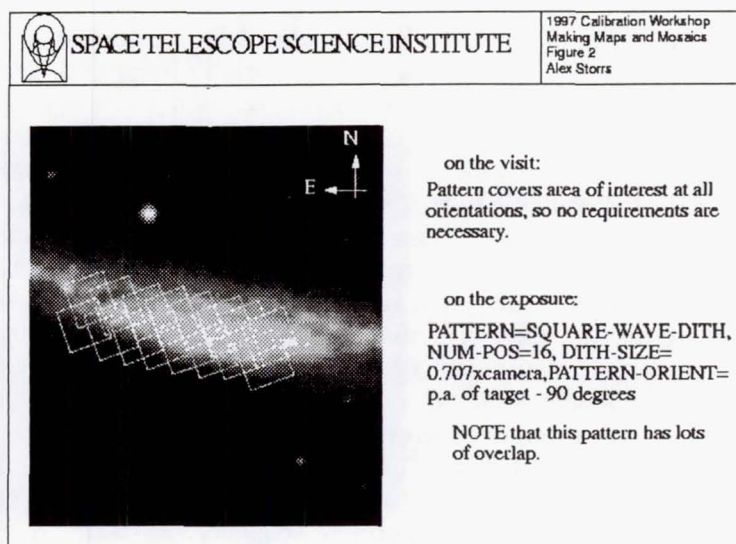
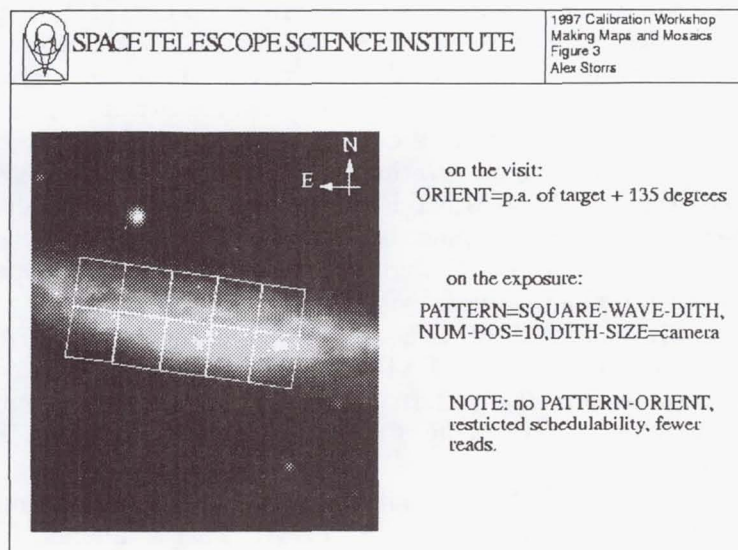




Figure 3. Map which covers region of interest but has orientation constraint



### 3. Scheduling

Another complication of observing with HST is scheduling the observations. Again, unlike most ground-based telescopes, the observer has little or no control over when their observations will be made. While it is possible to restrict the timeframe for an observation (e.g., by the visit-level special requirement `BETWEEN`) such a restriction will restrict when other observations can be scheduled, and so its use must be carefully justified.

Use of the `ORIENT` parameter will restrict when an observation can be made. RPS2 will calculate these constraints and display them. Observers should check this display to make sure there are at least eight weeks of "schedulability" for a given visit. If there are less than eight weeks, the orientation of HST's orbit with respect to the target may not allow for as long a visibility period as RPS2 uses by default. If there are less than eight weeks of "schedulability" the observer is well advised to use the visit-level special requirement `SCHED` to shorten the visibility period, thereby increasing the opportunities for the observations to be done. If orientations 90 or 180 degrees away from that specified are o.k., please add a comment to this effect. We have not yet implemented the automatic intersection of `ORIENT` requirements.

### 4. Details

There is much confusion about the use and interaction of the `ORIENT` visit-level special requirement, the `PATTERN-ORIENT` exposure-level optional parameter, and the `POSITION TARGET` exposure-level special requirement.

One source of confusion is due to the different philosophies used in defining the `PATTERN` and `POS TARG` requirements. The former moves the field of view (FOV) of the camera on the sky, while the latter moves the sky in the field of view of the camera. Thus a pattern move of the FOV in +X and +Y direction is equivalent to a `POSITION TARGET` in the -X, -Y direction. Pattern motions are demonstrated on pages 154-157 of the NICMOS instrument handbook. Observers using a combination of these parameters should double-check to make sure they are getting what they want. It is best to describe what is wanted in a comment as well.

The interaction between ORIENT and PATTERN-ORIENT is not always clear. The default for PATTERN-ORIENT is DETECTOR, so that the dithering and/or chopping patterns are done in the row/column frame of the camera. If no ORIENT is specified as well, the positions of the second and subsequent positions on the sky are arbitrary, and depend on when the observations are scheduled (called the "nominal roll" at a given time). Specifying an ORIENT (but not a PATTERN-ORIENT) will constrain where the offset fields are on the sky, as well as the directions of the rows and columns of the detectors on the sky, but will also constrain the time the observations can be scheduled. Thus use of ORIENT is strongly discouraged. PATTERN-ORIENT is the recommended flexible alternative if the position of the offset fields on the sky must be defined. While it constrains the position of the offset observations, it does not constrain the orientation of the telescope and hence the direction of the camera rows and columns with respect to the sky.

Note that PATTERN-ORIENT=0 is not the same as the default (PATTERN-ORIENT=DETECTOR)! Non-default values of PATTERN-ORIENT can lead to odd amounts of overlap among adjacent fields in the pattern. The detector rows and columns may not be parallel or perpendicular to the pattern offset motions if a non-default PATTERN-ORIENT is used.

To clarify, the PATTERN-ORIENT requirement specifies the orientation, North through East on the sky, of the +Y direction of the PATTERN. This is different from the +Y direction of the camera if PATTERN-ORIENT is not the default. For example, using the XSTRIP-DITH pattern with PATTERN-ORIENT=0 will move the FOV from East to West on the sky, while PATTERN-ORIENT=45 will move the FOV from Southeast to Northwest, regardless of which way the detector Y (column) axis is pointing. YSTRIP-DITH with PATTERN-ORIENT=0 will track from South to North.

Thus if you just want to map an unconnected series of fields (e.g. for background measurements) you probably only need to specify PATTERN-ORIENT and that only if you're worried about objects contaminating your backgrounds. If you are mapping a series of contiguous fields, however, and want to minimize overlap between adjacent images, you may have to use the ORIENT requirement. You can improve the schedulability of the observations by using PATTERN-ORIENT instead, and CHOP- and DITH- SIZE chosen so that the distance between adjacent field centers is  $\sqrt{2}/2$  times the camera dimension. This will cover the whole area at least once, and much of it twice. Note that the SPIRAL-DITH pattern is symmetric and should rarely require an ORIENT, and should only need a PATTERN-ORIENT if you are using a SPIRAL-DITH-CHOP pattern.

## 5. Checking

Observers should note that the RPS2 description generator has an "FOV Tool" which can be of use in interpreting what the system will do with your observations. The tool draws a scaled picture with a coordinate system indicated, for each exposure which uses a PATTERN. The numbers indicate the center of the fields of view in a pattern, as well as their order in the sequence of the pattern. These are circumscribed either by a square (if the orientation of the camera is known in the given coordinate system) or a circle (which shows the union of the possible orientations of the camera in use, if it is not constrained). Note that current POS TARGs are not reflected in this tool, although this change is in the works.

## 6. Special Cases

If you want to minimize telescope motion by taking a series of exposures at one pointing (not recommended because of residual image considerations) before moving to the next, you will have to use POS TARGs to define the pattern. Set up the first sequence of exposures



at the first pointing, then replicate the series with the desired POS TARG on each repeat exposure. You may want to put POS TARGs on the first series as well, to offset the first pattern point if the pattern is not symmetrical. There is no automatic way to check this method; the observer should thoroughly document what is desired.

One not uncommon situation is when NICMOS observations are made in parallel with WFPC, and the observer wants to subsequently image the region covered by NIC3 with WF3. To do this the same pattern on the same target should be repeated with the WFPC, but with the exposure level special requirement POS TARG 370,-30 (assuming the WFALL "aperture" is used). Note that this also assumes the FOM is offset 18 arcsec to minimize the vignetting in NIC3—this should become automatic in the fall of 1997.

Another situation is the desire to chop between NIC1 and NIC2. The two detectors are offset in the detector Y direction, and the simple ONE- and TWO-CHOP patterns move in the detector X direction. The solution to mimic a ONE-CHOP is to use two exposures with a POS TARG 0,-32.6 if NIC2 is prime, or POS TARG 0,32.6 if NIC1 is prime. For a TWO-CHOP, do a three position YSTRIP-DITH with DITH-SIZE=32.6 and POS TARG 0,32.6 followed by a single exposure on the target, with no PATTERN or POS TARG. This will give the equivalent of a TWO-CHOP pattern in Y, but starting with the prime detector off target, then on, then off, then on, rather than the reverse. Note that CALNICB will not reduce this pattern automatically for you, since the last observation is unassociated with the first three. Note also that the POS TARG and the PATTERN appear to be going in the same direction— but in fact, since the former moves the sky and the latter the telescope, they oppose each other. Finally, remember that NIC1 and NIC2 are not confocal— images in the parallel camera are going to be out of focus.

## 7. Conclusion

Whatever you are doing, you are strongly urged to document it with a comment.

## Long-Term and Short-Term Variations of NICMOS Foci

A. A. Suchkov, L. Bergeron, & G. G. Galas<sup>1</sup>

*Space Telescope Science Institute, 3700 San Martin Dr., Baltimore, MD 21218*

**Abstract.** We present the results of the NICMOS focus monitoring program and discuss long-term focus variations due to ongoing deformation processes within NICMOS, short-term variations due to HST "breathing" effects, and focus spatial variations across NICMOS fields of view.

### 1. Introduction

The NICMOS cameras were designed to share a common focus whose position can be adjusted using the Pupil Alignment Mechanism, or PAM. PAM's main part is an adjustable mirror which can be moved within  $\pm 10$  mm about its zero position, thus allowing fine tuning of the actual location of the focus. It was hoped that, whatever changes to the HST optical path may happen, the focus could always be brought back to the position of the detectors. Unfortunately, the unforeseen deformation of the NICMOS dewar has caused large mechanical distortions within NICMOS, which resulted in loss of a common focus for the three cameras. Worst of all, the camera 3 detector was pushed way out of the range within which the PAM can adjust the focus position. Soon after the Servicing Mission, this detector required a PAM position of about  $-17$  mm to be in focus, which was far beyond the reach of the PAM (see Burrows 1997 for more extensive discussion of the issue).

The ongoing deformation processes in NICMOS keep changing the location of the detectors with respect to the PAM zero position. This necessitates checking the NICMOS camera foci on a regular basis so as to ensure timely adjustments of PAM nominal settings if required. To this end a special focus monitoring program observes biweekly a stellar field of the open cluster NGC 3603, and the data are analyzed to retrieve the current focus position.

### 2. Long-term Focus Variations

The results of long-term focus monitoring as of September 8 are presented in Figure 1. The abscissa is the day of observation (day number starting January 1, 1997). The ordinate gives the position that the PAM should have to get the focus at the location of the detector (implied PAM position, often referred to as focus position in the PAM space). It is obtained using three different techniques based on phase retrieval, encircled energy, and plate scale measurements, respectively. Phase retrieval provides absolute value for the focus position. The method was developed by Krist & Burrows (1995) and expanded lately by Krist & Hook (1997b) to incorporate the NICMOS cameras. Encircled energy and plate scale provide independent focus measurements, which allows double-checking phase retrieval results.

Inspection of Figure 1 suggests that the detector positions have been pretty stable over the last three months except perhaps for the point at day 224, August 12. A slight difference between phase retrieval and encircled energy results, especially noticeable for NIC2, is

---

<sup>1</sup>Greater Homewood Community Corp, Inc., Baltimore, MD 21218



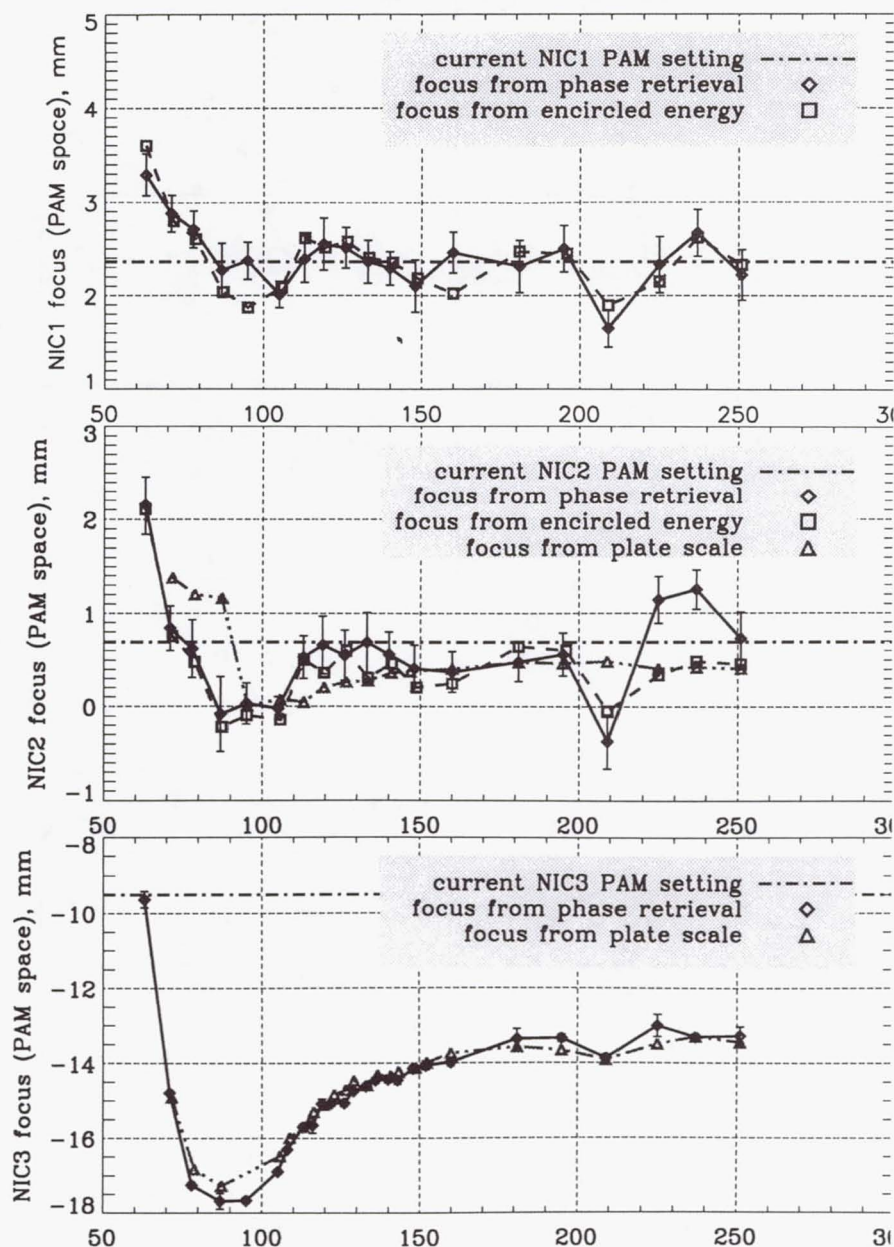


Figure 1. NICMOS focus history (as of September 8, 1997)

mainly due to the fact that the former were corrected for focus spatial variations across the camera field of view (see below) whereas the phase retrieval results were not.

### 3. Focus Variations on an Orbital Time Scale

Alongside with long-term focus variations displayed in Figure 1 there are short-term variations which potentially may impact photometry. They occur on the HST orbital time scale and are caused by changing HST thermal conditions as the spacecraft moves from night to

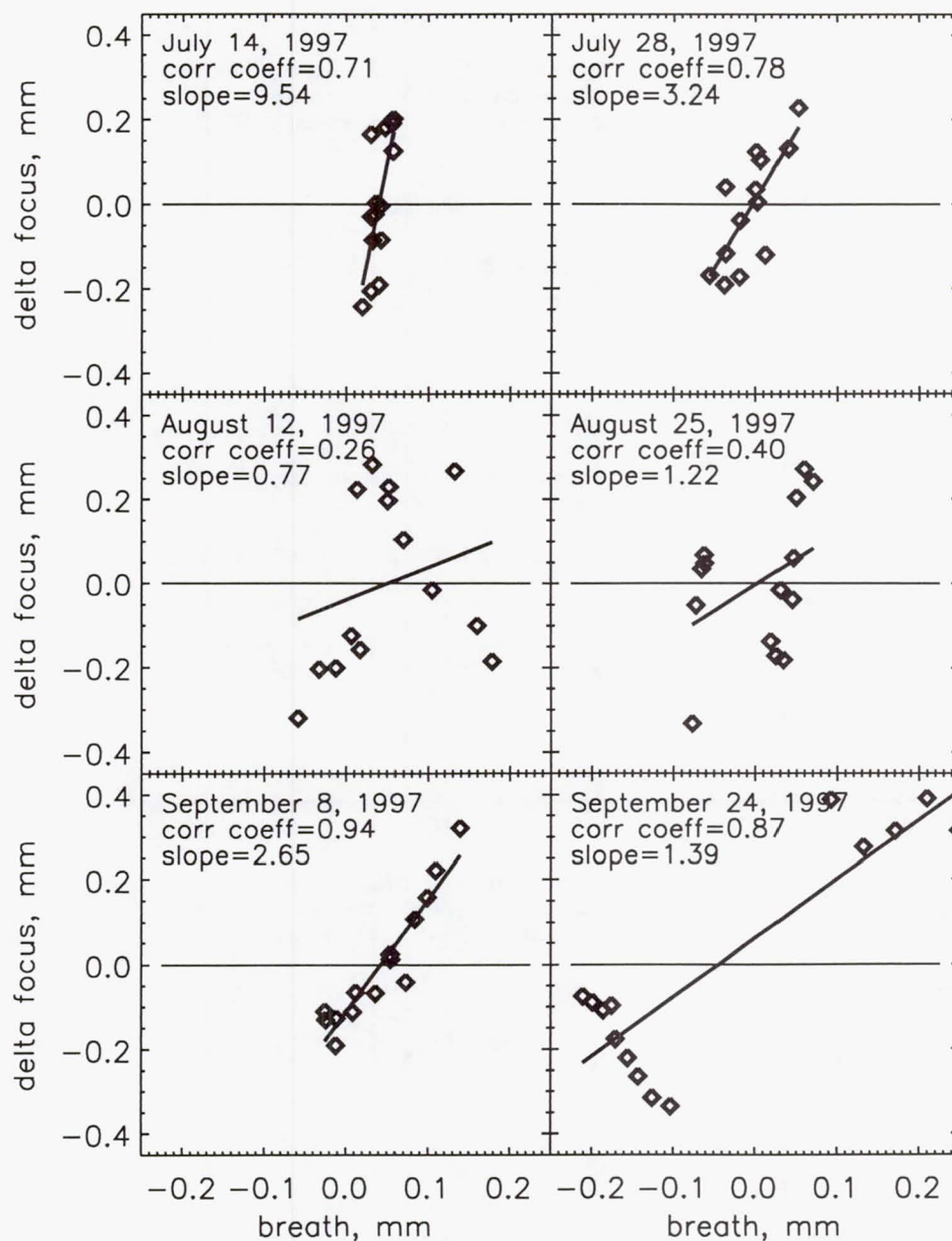


Figure 2. Correlation between focus position and breathing for NICMOS 1 data from six different data sets. The focus is measured relative to the mean value determined by each of the data sets. Both focus and the breathing parameter are given in mm in PAM space. The Figure illustrates that although in some cases focus follows the telescope temperature variations pretty much as expected from the current breathing model, the cases with low correlation coefficient and the correlation slope different from 1 indicate that the model is far from being ideal.

day and back to night. The resulting effect is known as “breathing” (see Suchkov & Casertano 1997 for the details of this effect and its impact on photometry). The NICMOS focus monitoring data provide a unique data set to quantify focus breathing and assess its impact on photometry. In Figure 2 we display the correlation between the measured focus position for camera 1 and a “breathing” parameter derived from telescope temperature data. There is no doubt that in some cases focus follows the telescope temperature variations.



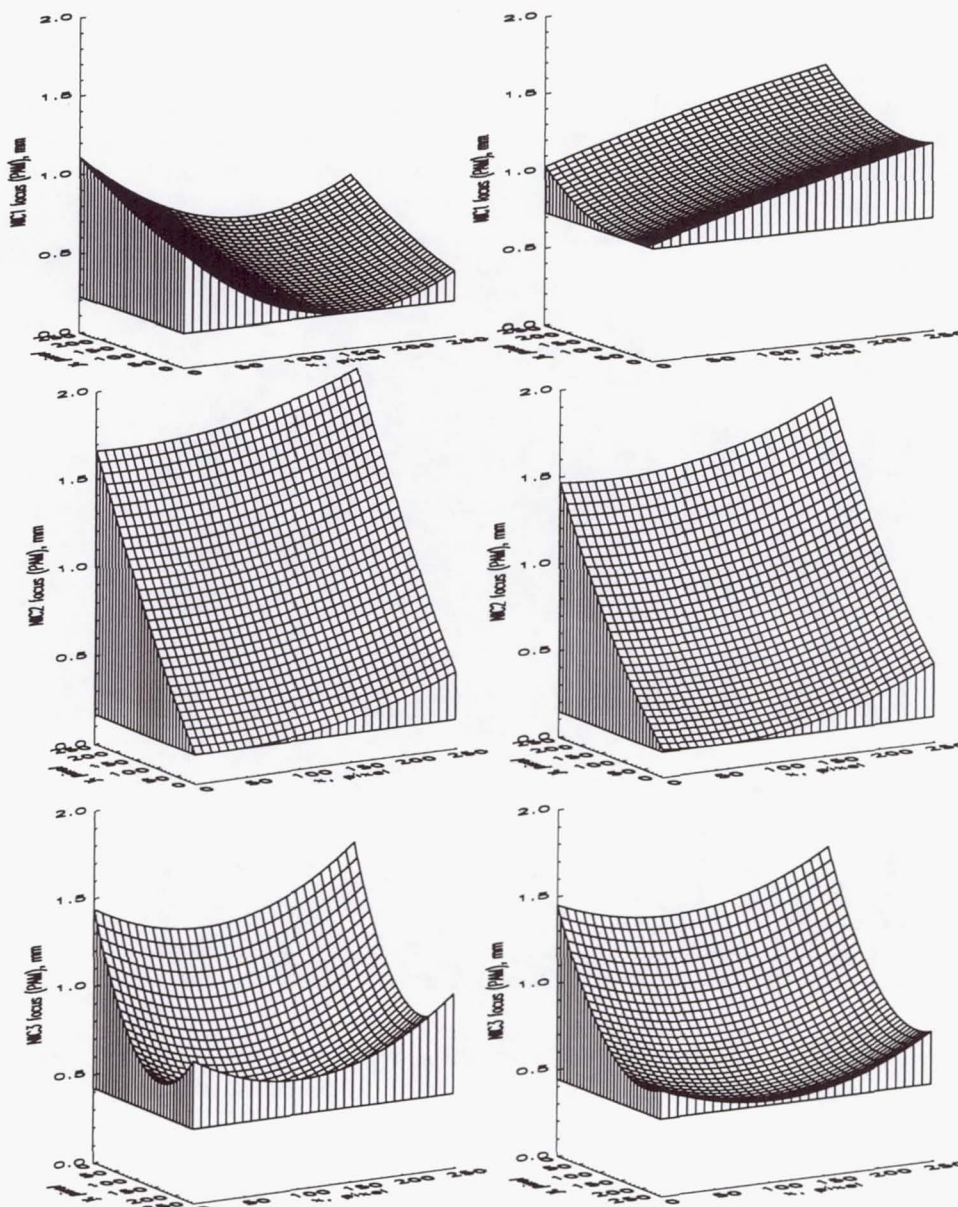


Figure 3. Focus variations across the field of view of NIC1 (top), NIC2 (middle), and NIC3 (bottom) from two different data sets taken at the same epoch for each of the cameras. The two sets are given to illustrate the level of statistical significance for geometrical pattern of focus variations. The differences between the patterns from paired data sets are within statistical errors.

However, in other cases the correlation coefficient is low and the slope of the correlation is far from being 1, suggesting that the breathing model which converts temperature variations to focus change is not ideal. This makes the application of breathing corrections to focus data a tricky task. Fortunately, the magnitude of breathing is typically smaller than  $\pm 0.2$  mm and actual focus variations are smaller than  $\pm 0.5$  mm (in PAM space) over the orbital period. Thus breathing may probably be important only for high-precision, small-aperture photometry, especially in cases when the detector is out of the best focus position.



#### 4. Focus Variations Across the Detectors' Field of View

Along with temporal variations, the NICMOS foci have been found to vary spatially across the detectors' field of view. The effect is not so large as to be of prime concern for photometry. However, observers doing high-precision photometry may want to keep it in mind to better assess the accuracy of their photometry and to be able to correct for this effect if necessary.

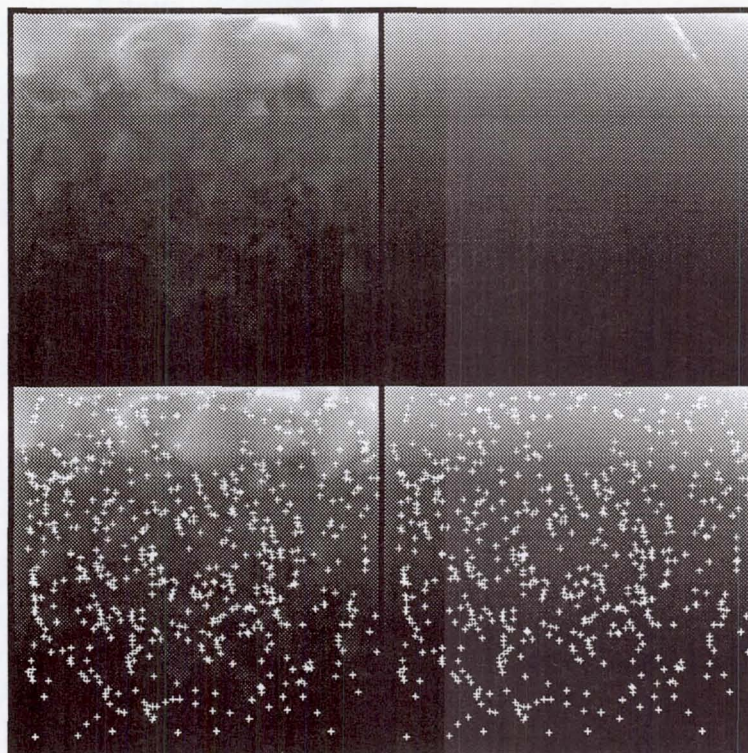


Figure 4. Grey scale presentation of the tilt in NIC2 obtained from encircled energy measurements. Upper left is triangle interpolation between all 630 encircled energy points in NIC2 through day 251, all normalized to 0 PAM at the center and included in the fit. The upper right is a smooth surface fit to the interpolated data. The lower 2 images are the same as above, but with the 630 measurement points overplotted as crosses.

To quantify focus positional dependence in all three cameras, we used focus measurements from phase retrieval for all suitable stars in a set of different frames. Thus we were able to restore the two-dimensional geometry of focus variations from different sets of independent data. In each case the focus values were fitted using multiple quadratic regression in  $x$  and  $y$ . The result of the fit for two different data sets is shown in Figure 3. In all panels, the fitting surface has been plotted in the same scale to allow straightforward comparison of the amount of focus deviations from the focal plane for all detectors. The focus position is measured in millimeters of the PAM space, with an arbitrary zero chosen so as to ensure better viewing.

The results for camera 2 show the largest range of focus variation, about 1.5 mm. Consistent results from different frames have been shown also by camera 3, with a more complicated focus aberration pattern and a smaller range of peak-to-peak focus variations. Camera 1 has the smallest field of view and thus provides us with smaller number of stars to derive the focus. As a consequence, statistical uncertainties as obtained for individual



frames are in that case larger, with any systematics in focus variations being not much different from statistical errors. These results are consistent with earlier results obtained by John Krist from different data sets (unpublished).

The results from phase retrieval have been found to be consistent with independent focus measurements from encircled energy. Figure 4 gives a grey scale representation of the focus variation across the NIC2 field of view which has been obtained from encircled energy measurements for 630 stellar images in the focus monitoring data. One can see that both Figure 3 and Figure 4 are suggestive of the same top-to-bottom geometry of focus variation across the NIC2 detector field of view, with peak-to-peak focus difference of about 1.5 mm (in PAM space).

In an independent study, Krist & Hook (1997a) have estimated the impact of spatial focus variations on aperture photometry for all three cameras. They have incorporated the focus positional dependence into the *Tiny Tim* software, so the observers can now use *Tiny Tim* to simulate the corresponding NICMOS PSFs variations across the detectors' field of view.

## References

- Burrows, C. J., 1997, this volume
- Krist, J. E. & Burrows, C. J., 1995, *Appl. Opt.*, 34, 4951
- Krist, J. E. & Hook, R., 1997a, this volume
- Krist, J. E. & Hook, R. 1997b, *The Tiny Tim User's Guide, v4.4*
- Suchkov, A. A. & Casertano, S., 1997, Instrument Science Report WFPC2 97-01 (Baltimore: STScI)





### Part 3. WFPC2





## WFPC2 Status and Overview

B. C. Whitmore

*Space Telescope Science Institute, 3700 San Martin Dr., Baltimore, MD, 21218*

### Abstract.

The current status of the Wide Field and Planetary Camera 2 is reviewed, with special emphasis on the 2.5 years since the last HST Calibration Workshop. The WFPC2 continues to take excellent images (e.g., the "Eagle" Nebula, the Hubble Deep Field) that are making fundamental contributions to astronomy. The calibration and understanding of the WFPC2 continues to improve, as does the available documentation and access to WWW tools. Photometric accuracies of a couple percent are now routinely possible for the common observing modes. There are ongoing efforts to more fully characterize the less commonly used modes such as polarization and linear ramp filter observations. The WFPC2 came through the 1997 servicing mission with essentially no changes to its characteristics. Finally, new observing techniques (e.g., subpixel dithering) are allowing observers to push the instrument to the limits of its capabilities.

### 1. Highlights Over the Past Two Years

The Wide Field and Planetary Camera 2 (WFPC2) has continued to work flawlessly during the 2.5 years since the previous HST Calibration Workshop (see MacKenty 1995 for a status report on the first 1.5 years of operation). Spectacular images such as the "Eagle" Nebula and the Hubble Deep Field have captured the public's imagination, perhaps like no astronomical image since the picture of the crescent Earth rising over the lunar surface. The astronomical community owes a great debt of gratitude to John Trauger and the Investigation Definition Team that designed and built the WFPC2.

In December of 1995, the WFPC2 was used to obtain the deepest astronomical image ever taken: a 10-day exposure of a piece of "blank" space called the Hubble Deep Field (HDF; Williams et al. 1996). This had two important spinoffs for the WFPC2. The first was the development of higher quality flats, superbias, and superdarks required to keep the observations from being noise-limited. These higher quality calibration reference files went into the pipeline in December 1995. Similar high quality flats for all filters redward of 3000 Å went into the pipeline during the subsequent year.

The second spinoff from the HDF was the development of the DRIZZLE task for reducing subpixel dithered images (Fruchter & Hooks 1997; also see Fruchter 1997 and Mutchler & Fruchter 1997 in this volume). Taking a series of exposures which have been offset from each other (i.e., "dithered") by a non-integer number of pixels allows observers to improve the spatial resolution of the WFPC2 images, since the pixels on the cameras are too large to properly sample the point spread function. Dithering also flattens the background and hence allows observations of fainter objects. The dithering technique is now used for roughly 25 % of WFPC2 science exposures, and DRIZZLE is used to reduce the vast majority of these images.

The second servicing mission to HST occurred in February 1997. While the installation of STIS and NICMOS were the main activities, the WFPC2 group was intent on two goals: 1) making sure the WFPC2 did not become contaminated, 2) determining whether

there where any changes to the WFPC2 characteristics. An extensive set of calibration observations showed that the servicing mission caused essentially no change to: photometric calibration, baseline far-UV response, focus, PSF, flat fields, read noise, A-to-D gain, and dark current. The only discernible effect was a small and temporary increase in the contamination rate during March and April of 1997. See Instrument Science Report (ISR) WFPC2 97-03, *Summary of WFPC2 SM97 Plans*, by Biretta, McMaster, Baggett, and Gonzaga, and ISR WFPC2 97-09, *Results of the WFPC2 post-Servicing-Mission-2 Calibration Program*, by Biretta and the WFPC2 group for details. All ISRs are available from the WFPC2 site on the WWW (see Section 4).

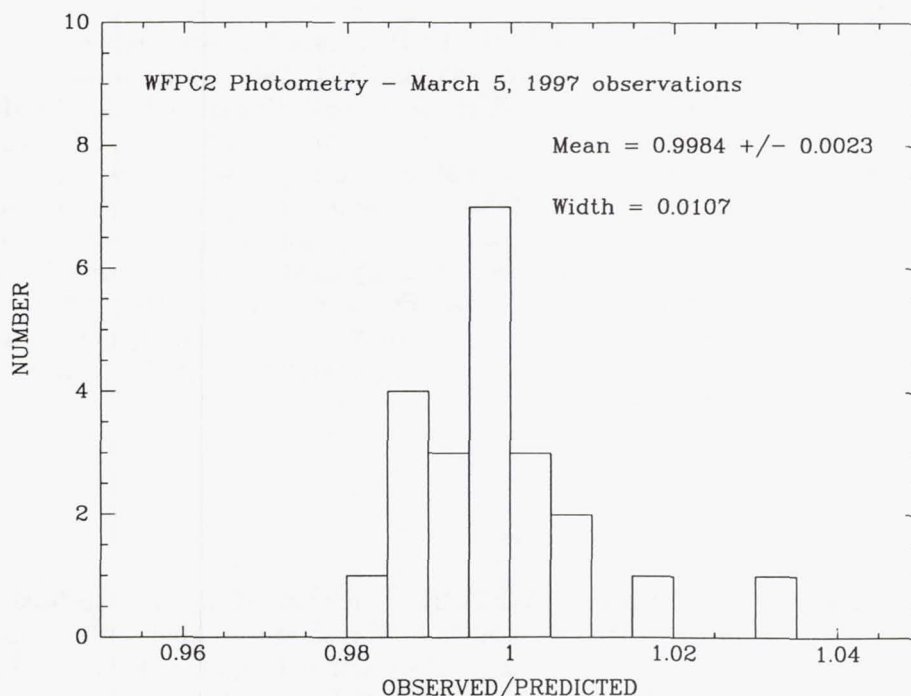


Figure 1. The distribution of observed/predicted values for observations of our photometric standard star using 9 filters and all 4 chips, where “observed” is immediately after the 1997 servicing mission and “predicted” is based on the baseline measurements from the previous 2 years. The data show that the throughput was not affected by the servicing mission. See ISR WFPC2 97-09 for details.

## 2. Operational History

A major date in the history of WFPC2 was April 23, 1994, when the temperature was reduced from  $-77^{\circ}\text{C}$  to  $-88^{\circ}\text{C}$ , in order to minimize the charge transfer efficiency (CTE) problem and reduce the number of hot pixels. A side effect of this temperature change is that the contamination rates are higher, as determined by the UV throughput of a standard star (see Section 2.3).



## 2.1. Filter Usage

Coincidentally, WFPC2 has now been operating for nearly the same length of time that WF/PC-1 was onboard HST, 3.7 years. However, it has taken nearly three times as many exposures as the WF/PC-1, with over 35,000 external observations. The WFPC2 continues to work flawlessly, with essentially no mechanical, electrical, or systems problems. Table 1 shows the 25 most frequently used WFPC2 filters. As expected, the broad-band UBVR<sub>I</sub> equivalents are the most popular, along with the wide-band analogs of these filters.

Table 1. Approximate WFPC2 Filter Usage as of August, 1997

Filter				Number <sup>1</sup>
F814W	"I"			7680
F555W	"V"			5506
F606W		wide "V"		3033
F702W		wide "R"		1755
F675W	"R"			1516
F300W		wide "U"		1381
F439W	"B"			1254
F336W	"U"			1225
F170W		uv		1129
F547M			Stromg.	806
F160BW		uv		755
F850LP				698
F656N			narrow-band	684
F450W		wide "B"		680
F953N			narrow-band	549
POLQ			polariz	519
F673N			narrow-band	518
F1042M				500
F255W		uv		487
F218W		uv		469
F502N			narrow-band	451
F410M			Stromg.	382
FQCH4P15				361
F658N			narrow-band	300
FR680			LRF	261

<sup>1</sup> External exposures only.

## 2.2. Focus History

Periodic adjustments have been made to the focus every 6–8 months in order to correct for shrinkage of the optical telescope assembly due to desorption of water. The goal has been to keep the focus within about 3 microns of optimal, which approximately matches the typical excursions due to "breathing", which occur on orbital time scales. The focus position during the period October 30, 1996, through March 18, 1997, was slightly positive (see Figure 2) apparently due to a slowing of the desorption rate which caused an overestimate of the required focus move on October 30, 1996. Relatively little WFPC2 data were actually taken during this period since most of the HST observations employed the FOS or GHRS prior to their removal. The focus move on March 18, 1997, corrected the problem and appears to have returned the WFPC2 to its optimal focus position.

ISR WFPC2 97-01, *Impact of Focus Drift on Aperture Photometry*, by Suchkov and Casertano shows that aperture photometry with a 1 pixel radius may vary by about 10 %,

but with a 3–5 pixel radius, variations of only a couple percent are seen for typical changes in the focus (e.g., due to breathing).

#### Focus with relative breathing correction

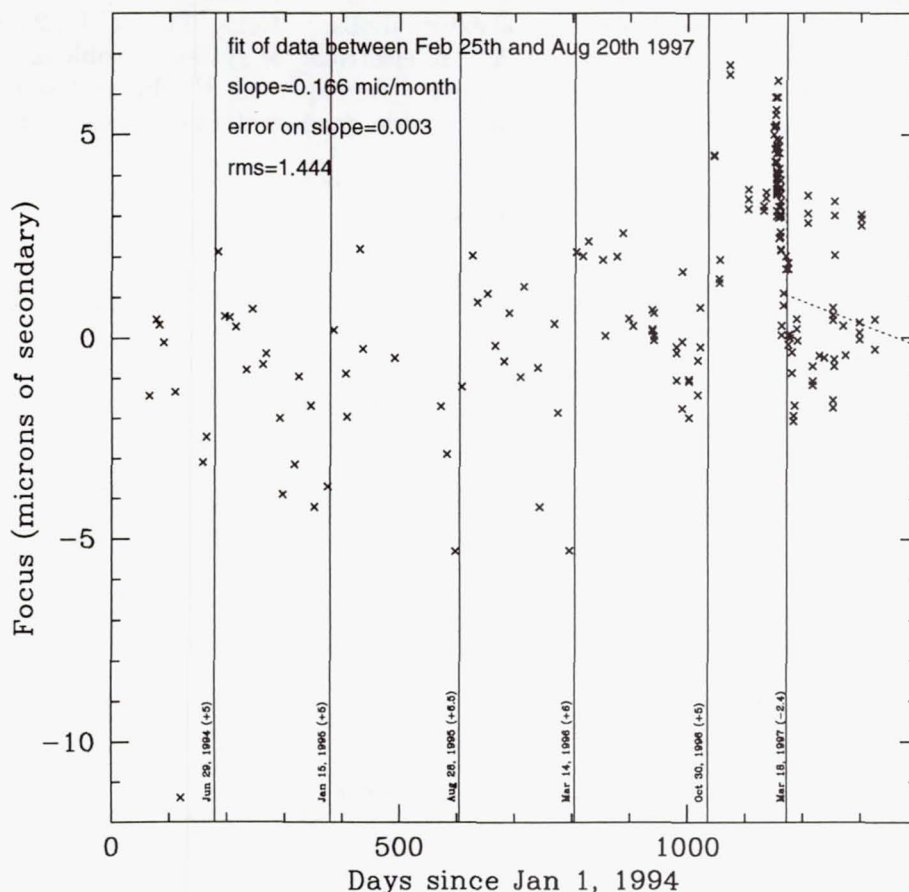


Figure 2. The focus position since Jan. 1, 1994, where 0.0 microns is the optimal focus. Note that the focus was slightly positive from October 30, 1996, until March 18, 1997. The large number of points near day 1150 are immediately following the 1997 servicing mission. The vertical lines show the dates when focus changes were made.

### 2.3. Photometric Monitoring

A bright star is observed before and after each decontamination procedure (i.e., the camera is warmed to evaporate the contaminants responsible for the decrease in the UV sensitivity) for the purpose of monitoring the photometric throughput. Figure 3 shows the resulting data. A continually updated version of this plot, and the corresponding data, are available from our WWW site.

The bimodal appearance of the data for the far UV filters is due to the decontamination procedure, with the high points taken just after the decontamination and the low points just before. The contamination rates can be easily characterized by a simple linear decline. The original throughput is recovered after each decontamination (see the WFPC2 Instrument Handbook or ISR WFPC2 96-04, *Effects of Contamination on WFPC2 Photometry*, by Whitmore, Heyer, and Baggett for values of the contamination rates for commonly used filters, and for other details concerning the effects of contamination).



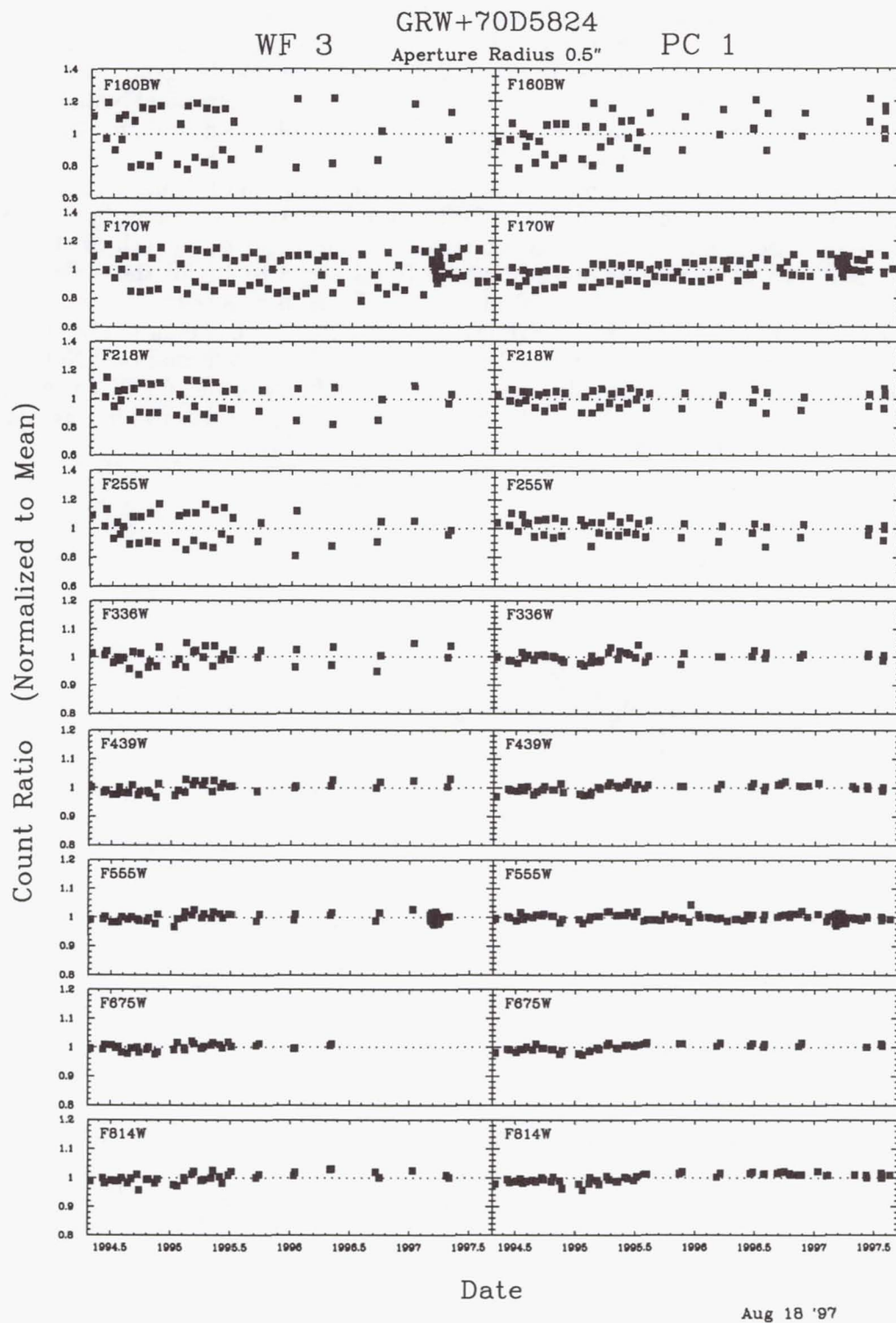


Figure 3. The photometric monitoring data on GRW+70D5824 since the cooldown on April 23, 1994. See text for details.

The photometric monitoring observations from Figure 3 show that the throughputs in nearly all filters have been stable to better than a couple percent over the full lifetime of the WFPC2. The main exception to this stability has been the throughput for the F170W and F160BW filters which have actually increased on the PC, presumably due to the slow outgassing of some contaminants within the PC. This can be seen in Figure 3, but is more clearly seen in Figure 4 of ISR WFPC2 96-4.

A close look at Figure 3 shows a 1–2 % discontinuity around February, 1995, for several filters. Figure 4 shows this more clearly for the WF3 observations using the F555W filter. This small discontinuity is apparently due to an increase in the length of the exposure times used for the monitoring observations (a factor of 1.4 to 4.0 for the different filters), and may be related to the CTE problem, since CTE loss is reduced when the background is higher and when the target is brighter. A more complete examination of this effect is currently underway; consult our WWW page for the latest information. Note that the presence of this small discontinuity means that the stability of the WFPC2 is even better than previously believed. For example, if we use only the observations after Feb. 13 1995, the F555W observations have an rms scatter of less than 1 %.

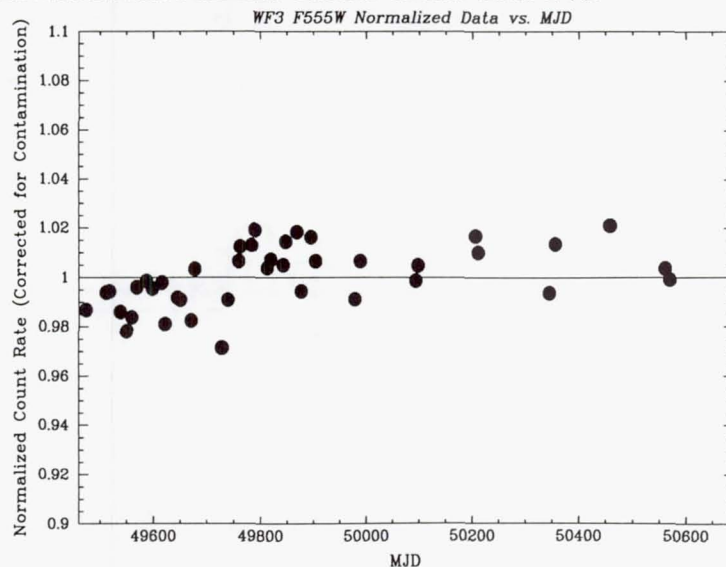


Figure 4. A blowup from Figure 3 of the F555W observations on the WF3. The small discontinuity around MJD 49750 (February 1995) is apparently due to an increase in the exposure time used for the observations. See text for details.

The photometric keywords provided in the headers of WFPC2 images were updated on May 16, 1997, as part of an update to SYNPHOT. With a few exceptions, changes to non-UV filters were relatively minor, generally 1–2 % or less. The UV filters required somewhat larger changes ranging from 2–10 %, or even more in the case of the rarely used F375N filter. See Casertano (1997) in this volume for details.

The small 1–2 % discontinuity mentioned in the previous paragraph has very little effect on the SYNPHOT update. However, it does highlight the fact that zeropoint determinations are most appropriate for observations which are similar to those used in the calibration observations (i.e., short exposures of bright, hot standards against a faint background). A variety of effects (e.g., CTE, long-vs-short, redleaks, different spectral types) can require corrections for observations under different conditions. While these are generally only a few percent, they can cause effects of 10–20 % in certain circumstance (e.g., very faint stars with very faint background). These non-linearities are discussed in more detail in Trauger (1997) and Casertano (1997) in this volume.



## 2.4. Pipeline Changes

While there have been roughly a dozen changes to the pipeline during the past 2.5 years, most of these have not changed the data, only the header information. Some of the main changes have been:

Table 2. Major WFPC2 Pipeline Changes During the Past 2.5 Years

Jul 1995	SYNPHOT tables updated. Changes made to the photometric keywords in the header.
Dec 1995	New flats to support the Hubble Deep Field observations (F300W, F450W, F555W, F606W, and F 814W).
Jun, Jul, Oct, 1996	New flats delivered for filters redward of F300W.
Aug 1996	Small change to the way darks are generated.
Aug 1996	Automatic bias jump detection begins, with messages put into the trailer file.
Jan 1997	Fixed problem with processing images when fewer than all 4 chips are read out (mainly calibration observations; assumed single read-outs were always the PC). The problem originated in December 1994.
May 1997	SYNPHOT tables updated. Changes made to the photometric keywords in the header.

## 2.5. History File

A wide variety of information on the operational history of WFPC2 is listed in the *WFPC2 History File*, which can be found under the documentation section of the WFPC2 WWW site. Included is information on: decontamination dates and descriptions, darks and super-darks, focus changes, temperature changes, pipeline changes, safings, plate scale changes, miscellaneous, and a chronological history in table format.

## 3. Calibration and Characterization

The WFPC2 calibration plans for Cycles 5 and 6 can be found in version 4.0 of the WFPC2 Instrument Handbook. The Cycle 7 calibration plan is in ISR WFPC2 97-06 by Casertano. All calibration observations are non-proprietary. We encourage observers to make use of this resource and to let us know when they find something other people might find useful. For example, an extensive set of observations is scheduled for the Fall of 1997 to study the long vs. short and CTE effects (proposal 7630; see ISR WFPC2 97-06 for details). These observations may be of interest to a variety of people.

### 3.1. Point Spread Function

A detailed knowledge of the point spread function is required for a variety of projects, ranging from PSF subtraction (e.g., to search for planets around stars) to aperture corrections for photometric measurements. The fact that the focus varies with position on the chip makes this more difficult.

There are two basic approaches observers can use. The first is to use observed PSFs from the archives. The new PSF Library available on the WWW (Wiggs et al. 1997) makes this relatively easy. The second approach is to use the TINY TIM simulations developed by John Krist, with a WWW page at: <http://scivax.stsci.edu/~krist/tinytim.html> Surdej et al. (1997) and Remy et al. (1997) provide examples of how TINY TIM can be used for PSF subtraction and to estimate the position of the focus.

### 3.2. Polarization

The measurement of polarization with WFPC2 is somewhat problematic, for a variety of reasons. For example, the pickoff mirror introduces instrumental polarization, transmission of the perpendicular component is a function of wavelength hence the effective range is roughly 2000–7500 Å, and vignetting reduces the effective field of view. In addition, a complete set of polarization calibration observations would be prohibitive (i.e., observations using all polarization angles, all filters, and all filter rotations would require over 1000 orbits). Our approach has instead been to build a model and spot check it with observations using commonly used observing modes.

To support this effort, a model has been developed using Mueller matrices that can predict observed counts with roughly 2% accuracy. An ISR on *WFPC2 Polarization Calibration* by Biretta and McMaster describing the model is nearing completion. Two WWW tools have been developed to support polarization observations. The first is a simulator while the second is a calibration tool based on the Mueller matrix model.

### 3.3. Linear Ramp Filters

Linear ramp filters (LRFs) provide narrowband photometry over a continuous range from 3710–9762 Å, but within a field of view of roughly 13". Again, a full set of calibration observations for the LRFs would be very expensive in terms of telescope time, hence our approach has been to take a few typical observations to spot check the model. In this case the model uses SYNPHOT. Preliminary photometric calibration indicates that an accuracy of ~ 3% can be obtained with the LRFs. See ISR WFPC2 96-05, *Wavelength/Aperture Calibration of the WFPC2 Linear Ramp Filters*, by Biretta, Ritchie, and MacKenty, and ISR WFPC2 96-06, *Photometric Calibration of WFPC2 Linear Ramp Filter Data in SYNPHOT*, by Biretta, Baggett, and Noll for details. An ISR on the calibration observations should be out later this year.

### 3.4. Image Anomalies

The vast majority of WFPC2 observations are successfully obtained (e.g., do not experience guide star problems) and contain no anomalies. However, a few percent of the observations suffer some form of image anomaly, hence it is useful to know what kinds of things to look out for. During the past two years the WFPC2 group at STScI has examined all science images and informed observers when important anomalies are found. See ISR WFPC2 95-06, *A Field Guide to WFPC2 Image Anomalies*, by Biretta, Ritchie, and Rudloff for examples and detailed descriptions of the various anomalies. Some of the more interesting examples are the following.

- Residual Images: Very bright objects can leave a residual charge in subsequent images, with an e-folding decay time of about 15 minutes. Residuals from strongly saturated images can require several hours to completely clear.
- Ghost Images: Internal reflections in the CCD field-flattener lenses or in filters can result in doughnut- or fan-shaped artifacts near bright stars.
- PC1 Stray Light: Stray light from a bright star which is within the "missing" L-shaped region around the PC can find its way onto the PC, producing one or more broad arc-like patterns.
- Scattered Earth Light: Observations taken near the Earth limb (e.g., observations in the CVZ, the Continuous Viewing Zone) can suffer from reflected Earth light off the baffles and spiders of the optical telescope assembly. Dark diagonal bars can appear due to shadowing by the WFPC2 camera relay spiders. See Figure 5.



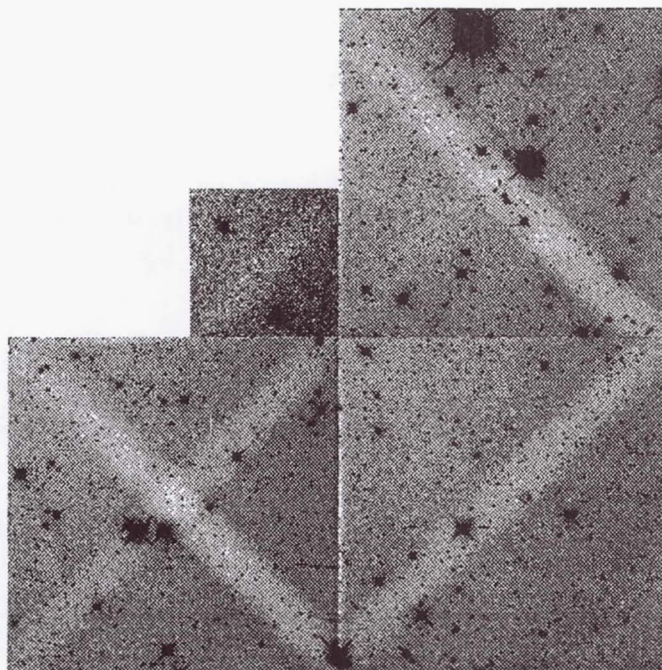


Figure 5. An example of a pattern produced by scattered Earth light. The diagonal lines are the result of shadowing by the WFPC2 camera relay spiders. See ISR WFPC2 95-06 for details.

#### 4. Sources of Information

The WFPC2 has now been in orbit for almost four years, and an extensive set of documentation has been developed. In addition, several hundred articles describing WFPC2 observations have been written. The primary sources of WFPC2 information are the following.

- WFPC2 Instrument Handbook—Version 4, June 1996 (Biretta et al. 1996). Updates include new sections on comparisons with FOC, STIS and NICMOS, observation strategies, and calibration plans for Cycles 5 and 6.
- HST Data Handbook—Version 3.0, October 1997 (Voit et al. 1997; WFPC2 section by Casertano et al.). Updates include modifications to the astrometry, polarimetry, and photometry sections (including improved zeropoints).
- Journal Articles: In particular, the two Holtzman et al. articles (1995a, 1995b). The WFPC2 Clearinghouse, available via our WWW site, provides easy reference to other journal articles.
- WFPC2 STAN—Space Telescope Analysis Newsletter. The electronic newsletter sent every month or two with the latest WFPC2 information. Old issues are available via the WFPC2 WWW site.
- WFPC2 World Wide Web Site: The top level includes sections on advisories, documentation, software tools, user support, and frequently asked questions. Of particular note are the software tools, which now include:

- Exposure Time Calculator

- PSF Library Search and Retrieval
- Polarization Calibration Tool
- Linear Ramp Filter Calculator
- WFPC2 Clearinghouse

The WFPC2 Clearinghouse is the most recently developed tool, providing easy access to both STScI documentation and the rapidly expanding literature on WFPC2 observations.

## 5. Summary

The WFPC2 continues to work extremely well, with essentially no operational problems. Over the past 3.7 years the WFPC2 has been used for the lion's share of HST observations, with roughly 40 % of the observing time. Observers are pushing the instrument to the limits of its capabilities with observations like the Hubble Deep Field, and by using techniques such as subpixel dithering. The photometric stability of the instrument has been excellent. The photometric calibration of the WFPC2 continues to improve, although there are still important questions about the effects of CTE and other non-linearities. In general, the commonly used modes are well calibrated and characterized. Work continues on the more infrequently and more complicated modes such as polarization and LRF observations. An extensive set of documentation and analysis tools have been developed and can be accessed through the WFPC2 WWW homepage at:

[http://www.stsci.edu/ftp/instrument\\_news/WFPC2/wfpc2\\_top.html](http://www.stsci.edu/ftp/instrument_news/WFPC2/wfpc2_top.html)

**Acknowledgments.** Most of the material summarized in this report was developed by the WFPC2 group at STScI. A special thanks to Matt Lallo for some of the focus monitoring analysis and figures. Also, thanks to John Trauger and the IDT for designing and building the WFPC2, and John Holtzman and Chris Burrows for their extensive work calibrating, characterizing, and documenting the WFPC2 during the first year of operation.

## References

- Biretta, J., et al., 1996, *WFPC2 Instrument Handbook*, Version 4.0 (Baltimore: STScI)
- Casertano, S., 1997, this volume
- Fruchter, A., 1997, this volume
- Fruchter, A. & Hooks, R., 1997, Proc. SPIE, 3164, ed. A. Tescher (also available from the LAN preprint server as astro-ph/9708242)
- Holtzman J., et al., 1995a, PASP, 107, 156
- Holtzman J., et al., 1995b, PASP, 107, 1065
- MacKenty, J. W., 1995, *Calibrating HST: Post Servicing Mission*, ed. Koratkar & Leitherer (Baltimore, STScI)
- Mutchler, M., & Fruchter, A., 1997, this volume
- Remy, M., Surdej, J., Baggett, & Wiggs, M., 1997, this volume
- Surdej, J., Baggett, S., Remy, M., & Wiggs, M., 1997, this volume
- Trauger, J., 1997, this volume
- Voit, M., et al., 1997, *HST Data Handbook*, Version 3.0 (Baltimore: STScI)
- Williams, R., et al., 1996, AJ, 112, 1335
- Wiggs, M., Baggett, S., Surdej, J., & Tullos, C., 1997, this volume
- Wiggs, M., Whitmore, B. C., & Heyer, I., 1997, this volume



## WFPC2 Photometric Calibration

Stefano Casertano<sup>1</sup>

*Space Telescope Science Institute*

### Abstract.

The updated absolute photometric calibration for WFPC2 yields typical uncertainties for bright sources below 2% for the photometric filter set and of about 3% for other filters between 400 and 800 nm. We present a quantitative characterization of some well-known WFPC2 non-linearities, the CTE error and the long vs. short anomaly, which allows a better estimate of their possible impact under a variety of observing conditions.

### 1. Absolute Photometry with WFPC2

Over its nearly four years of operations, the WFPC2 has proven to be an extremely stable and repeatable instrument. Apart from the well-characterized contamination in the UV, which can be predicted to better than 1% under almost all circumstances, the signal detected from our main standard star, GRW+70d5824, has remained stable to better than 1% over the years (see Whitmore 1997). For example, comparison of the camera sensitivity before and after the Second Servicing Mission indicates that the sensitivity has remained the same to within 0.7% rms (Biretta et al. 1997, Whitmore 1997).

Despite the *stability* of WFPC2, its precise photometric calibration, both relative and absolute, has been somewhat elusive. The camera is known to have some weak non-linearities, discussed in Section 2 below. These non-linearities affect the comparison of observations taken under different conditions (background, exposure time, pointing, crowding), and thus the relative photometric accuracy of WFPC2. In addition, relative photometry must take into account PSF variations vs. time, wavelength and position in the field of view, as well as difficulties with the background measurement due to the fact that WFPC2 gain levels undersample the read noise.

Because of these various effects, any *absolute* photometric calibration of WFPC2 refers of necessity to observations taken under a well-defined set of circumstances. In the following, we will refer primarily to the absolute photometric calibration of well-exposed, isolated stars with very low sky background.

Another difficulty in determining the absolute calibration of WFPC2 is in the fact that its filters differ substantially from any of the "standard" filter sets used in ground-based observations, resulting in some confusion as to the meaning of any photometric calibration. This problem was addressed cleverly by Holtzman et al. (1995b), who compared ground-based and space-based photometry with the WFPC2 filter set to ground-based photometry with standard Johnson-Cousins UBVRI filters, and determined a photometric calibration which included transformation to the UBVRI system. Holtzman et al. (1995b) used the WFPC2 "photometric set", consisting of F336W, F439W, F555W, F675W, and F814W, as an approximate match to Johnson-Cousins UBVRI, respectively, and determined zero

---

<sup>1</sup>On assignment from the Space Sciences Division of the European Space Agency

points and color terms appropriate to bright stars in  $\omega$  Cen and NGC 6752. Their results still stand as probably the best way to relate WFPC2 measurements to UBVR photometry.

The approach taken here is somewhat different, and it deals exclusively with determining the *absolute* flux scale of WFPC2, as opposed to a conversion from WFPC2 to standard filters. The data consist of observations of the spectrophotometric standard GRW+70d5824, a hydrogen white dwarf, taken in all UV filters and other selected broad- and intermediate-band WFPC2 filters between 1994 and 1997. A synopsis of the observations used, with the measured count rates and the number of independent measurements for each filter/chip combination, is given in Table 1. The camera sensitivity is characterized by throughput curves for the telescope and the instrument, which are held fixed, a Detector Quantum Efficiency (DQE) curve, and individual scalings for each filter. The throughput and DQE curves are function of wavelength, and the latter is determined independently for each detector. The wavelength dependence of each filter's throughput is considered fixed as measured in the laboratory before launch, but an overall scaling factor is allowed for each filter. Synthetic photometry and least-squares minimization is used to determine these free parameters.

Table 1. Count rates for GRW+70D5824, corrected for contamination, used to characterize the WFPC2 photometric throughput

Filter	PC		WF2		WF3		WF4	
	Nexp	Count rate	Nexp	Count rate	Nexp	Count rate	Nexp	Count rate
F122M	1	27.49	1	34.87	1	26.47	1	30.12
F160W	27	84.22	2	79.16	23	69.21	5	72.80
F170W	63	164.24	12	192.37	61	160.30	13	169.84
F185W	2	98.22	1	103.94	1	87.42	1	96.74
F218W	27	140.16	1	141.67	24	135.97	1	143.75
F255W	27	160.74	2	169.13	6	165.95	3	167.40
F300W	1	986.28	1	1014.85	1	1031.81	1	1056.82
F336W	27	773.33	2	789.06	24	800.19	5	786.98
F343N	1	4.84	1	5.04	1	4.96	1	4.94
F375N	1	10.92	1	11.30	1	10.80	1	11.21
F380W	1	1132.40	1	1175.98	1	1151.33	1	1153.45
F390N	1	43.93	1	43.37	1	42.78	1	43.57
F439W	36	894.33	2	905.09	23	893.60	5	892.54
F555W	61	3744.80	2	3811.86	24	3818.50	5	3829.37
F675W	27	2103.52	1	2153.77	18	2087.88	1	2122.27
F814W	43	1359.80	2	1393.16	24	1359.79	5	1379.88

While filter scalings and DQE curves cannot be measured fully independently, the method we adopted, described in detail in Baggett et al. (1997), results in smoothly varying DQE curves and in relatively modest filter scalings, with the exception of two narrow-band UV filters (F343N and F375N) which had not been revisited since launch. The derived DQE curves for each detector are given in Figure 1. On the basis of these curves, we have determined the new photometric throughput and zero points given in Table 2.

### 1.1. Aperture corrections

Any photometric calibration refers to the flux enclosed in a predefined area of the image. The standard photometry of Holtzman et al. (1995b), for example, refers to an aperture with radius  $0''.5$ . This aperture is a convenient compromise: large enough to be pretty much independent of changes of the PSF core with focus and position in the chip, and to include most of the flux, yet not so large that the errors are dominated by the background—for most well-exposed objects. Smaller apertures may be desirable in some cases, especially for crowded fields or very faint stars, but it is almost always possible to find a bright,



isolated star to determine an aperture correction for the specific observation. Lacking that, the results of Suchkov and Casertano (1997a, b) can be used to determine an aperture correction for a given observation.

Table 2. New values of PHOTFLAM and of photometric zero points, as of May 1997 (Baggett et al. 1997)

Filter	PHOTFLAM ( $\text{erg cm}^{-2} \text{s}^{-1} \text{\AA}^{-1}/\text{count}$ )					VEGAMAG zero point			
	PC	WF2	WF3	WF4	new/old (WF3)	PC	WF2	WF3	WF4
F122M	8.088e-15	7.381e-15	8.204e-15	8.003e-15	1.046	13.768	13.868	13.752	13.778
F160BW	5.212e-15	4.563e-15	5.418e-15	5.133e-15	1.168	14.985	15.126	14.946	15.002
F170W	1.551e-15	1.398e-15	1.578e-15	1.531e-15	1.072	16.335	16.454	16.313	16.350
F185W	2.063e-15	1.872e-15	2.083e-15	2.036e-15	1.095	16.025	16.132	16.014	16.040
F218W	1.071e-15	9.887e-16	1.069e-15	1.059e-15	1.058	16.557	16.646	16.558	16.570
F255W	5.736e-16	5.414e-16	5.640e-16	5.681e-16	1.063	17.019	17.082	17.037	17.029
F300W	6.137e-17	5.891e-17	5.985e-17	6.097e-17	1.019	19.406	19.451	19.433	19.413
F336W	5.613e-17	5.445e-17	5.451e-17	5.590e-17	0.961	19.429	19.462	19.460	19.433
F343N	8.285e-15	8.052e-15	8.040e-15	8.255e-15	2.090	13.990	14.021	14.023	13.994
F375N	2.860e-15	2.796e-15	2.772e-15	2.855e-15	0.865	15.204	15.229	15.238	15.206
F380W	2.558e-17	2.508e-17	2.481e-17	2.558e-17	0.987	20.939	20.959	20.972	20.938
F390N	6.764e-16	6.630e-16	6.553e-16	6.759e-16	1.012	17.503	17.524	17.537	17.504
F410M	1.031e-16	1.013e-16	9.990e-17	1.031e-16	0.977	19.635	19.654	19.669	19.634
F437N	7.400e-16	7.276e-16	7.188e-16	7.416e-16	0.978	17.266	17.284	17.297	17.263
F439W	2.945e-17	2.895e-17	2.860e-17	2.951e-17	0.965	20.884	20.903	20.916	20.882
F450W	9.022e-18	8.856e-18	8.797e-18	9.053e-18	0.992	21.987	22.007	22.016	21.984
F467M	5.763e-17	5.660e-17	5.621e-17	5.786e-17	0.981	19.985	20.004	20.012	19.980
F469N	5.340e-16	5.244e-16	5.211e-16	5.362e-16	0.982	17.547	17.566	17.573	17.542
F487N	3.945e-16	3.871e-16	3.858e-16	3.964e-16	0.984	17.356	17.377	17.380	17.351
F502N	3.005e-16	2.947e-16	2.944e-16	3.022e-16	0.985	17.965	17.987	17.988	17.959
F547M	7.691e-18	7.502e-18	7.595e-18	7.747e-18	0.993	21.662	21.689	21.676	21.654
F555W	3.483e-18	3.396e-18	3.439e-18	3.507e-18	0.995	22.545	22.571	22.561	22.538
F569W	4.150e-18	4.040e-18	4.108e-18	4.181e-18	0.995	22.241	22.269	22.253	22.233
F588N	6.125e-17	5.949e-17	6.083e-17	6.175e-17	0.998	19.172	19.204	19.179	19.163
F606W	1.900e-18	1.842e-18	1.888e-18	1.914e-18	1.013	22.887	22.919	22.896	22.880
F622W	2.789e-18	2.700e-18	2.778e-18	2.811e-18	1.000	22.363	22.397	22.368	22.354
F631N	9.148e-17	8.848e-17	9.129e-17	9.223e-17	1.002	18.514	18.550	18.516	18.505
F656N	1.461e-16	1.410e-16	1.461e-16	1.473e-16	1.003	17.564	17.603	17.564	17.556
F658N	1.036e-16	9.992e-17	1.036e-16	1.044e-16	1.003	18.115	18.154	18.115	18.107
F673N	5.999e-17	5.785e-17	6.003e-17	6.043e-17	1.002	18.753	18.793	18.753	18.745
F675W	2.899e-18	2.797e-18	2.898e-18	2.919e-18	1.007	22.042	22.080	22.042	22.034
F702W	1.872e-18	1.809e-18	1.867e-18	1.883e-18	1.008	22.428	22.466	22.431	22.422
F785LP	4.727e-18	4.737e-18	4.492e-18	4.666e-18	0.948	20.688	20.692	20.738	20.701
F791W	2.960e-18	2.883e-18	2.913e-18	2.956e-18	1.003	21.498	21.529	21.512	21.498
F814W	2.508e-18	2.458e-18	2.449e-18	2.498e-18	0.988	21.639	21.665	21.659	21.641
F850LP	8.357e-18	8.533e-18	7.771e-18	8.194e-18	0.932	19.943	19.924	20.018	19.964
F953N	2.333e-16	2.448e-16	2.107e-16	2.268e-16	0.827	16.076	16.024	16.186	16.107
F1042M	1.985e-16	2.228e-16	1.683e-16	1.897e-16	0.868	16.148	16.024	16.326	16.197
FQUVN	1.344e-15	8.251e-16	1.084e-15	1.403e-15	0.955	16.319	17.369	17.042	16.624
FQUVN33	—	1.325e-15	—	—	—	—	16.334	—	—
FQCH4N	—	2.719e-16	3.366e-16	1.651e-16	0.883	—	17.812	16.076	17.387
FQCH4N15	1.800e-16	—	—	—	—	17.829	—	—	—
FQCH4P15	3.518e-16	—	—	—	—	16.028	—	—	—
FQCH4N33	—	1.758e-16	—	—	—	—	17.855	—	—

On the other hand, the photometric calibration defined by STScI and returned by STSDAS programs traditionally refers to an *infinite* aperture, allowing a better conversion between point sources and extended sources. Very large apertures (5'' or more) can be used for photometric standards, which are bright, isolated sources, but are impractical for the analysis of most science observations. Besides, the aperture corrections to very large apertures are rather poorly known (Holtzman et al. 1995a, Suchkov and Casertano 1997b), due to the difficulty of measuring the background with sufficient precision. For these reasons, we adopt the compromise solution of *defining* the aperture correction from 0''.5 to "infinity" as  $-0.10$  mag. This amounts to adopting a *nominal* infinite aperture which is defined as containing  $1.096 (= 10^{0.1/2.5})$  times the flux enclosed in a 0''.5 radius. The number 0.10 is close to the values listed in Holtzman et al. (1995a), and is consistent with Whitmore (1995), thereby maintaining continuity in our definitions. A more accurate measurement

of the aperture correction is only needed when dealing with extended sources larger than about  $1''$  (Suchkov and Casertano 1997b).

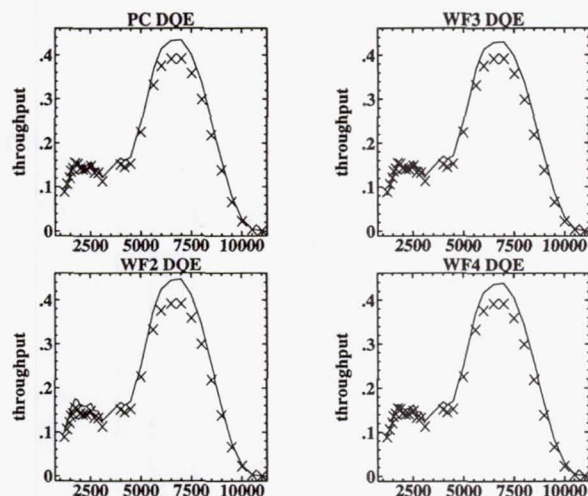


Figure 1. The new DOE curves (solid lines), compared with the previous values (crosses). The previous values were identical for all four chips.

## 1.2. Photometric Systems and Zero Points

The photometric systems used in the definitions presented here are closely tied to an absolute flux scale. Three different, but related, definitions are used: the sensitivity parameter PHOTFLAM, reported in the image header, and the zero points in the STMAG and VEGAMAG systems.

The quantity PHOTFLAM, also reported in each image as a group parameter, is defined as the spectral flux density per unit wavelength that would generate 1 count/second (within the nominal infinite aperture defined above) for the observing mode used. Thus, PHOTFLAM can be used to convert directly count rates to average flux density. The units of PHOTFLAM are  $\text{erg cm}^{-2} \text{s}^{-1} \text{\AA}^{-1}$ .

The zero point in the STMAG system is directly related to the flux density, and is defined by setting the magnitude of a source that has a flux density of  $1 \text{ erg cm}^{-2} \text{s}^{-1} \text{\AA}^{-1}$  as  $-21.10 \text{ mag}$ . Equivalently, a source with magnitude 0.00 (in the STMAG system) has flux density  $3.63 \cdot 10^{-9} \text{ erg cm}^{-2} \text{s}^{-1} \text{\AA}^{-1}$ . This value is chosen so that Vega has approximately magnitude 0 in V (and in F555W). However, since Vega does not have constant flux per unit wavelength, it will not have magnitude  $\sim 0$  in other filters, thus the STMAG system deviates from conventional magnitude systems at other wavelengths.

The VEGAMAG system, although also related to the absolute flux scale, is designed to resemble more closely the standard Johnson-Cousins system. In this system, the zero of the magnitude scale is defined so that a star with the spectral flux density measured for Vega has magnitude exactly zero in all filters. This differs from the standard Johnson-Cousins definition by a few hundreds of magnitude throughout the visible and near-UV.

For more details on the definition of these photometric systems, please consult Simon (1997) and Voit et al. (1997).

## 1.3. Verification of the New Throughput Curves

The new photometric calibration of WFPC2 has been verified with a number of observations of different standard stars, including another white dwarf, HZ-44, and the three solar analogs P041-C, P177-D, and P330-E, used as primary standards for NICMOS. The spectrophotometry of the solar analogs is based on FOS spectra covering most of the WFPC2



sensitivity range, taken by Colina & Bohlin (1997). The inclusion of solar analogs provides a sanity check of the validity of our calibration for a spectral energy distribution different from that of our primary standard.

The result of the comparison is shown in Table 3. The predictions for the photometric filter set are typically within 1–2% of the observations, with a slightly higher error for F555W; these discrepancies are consistent with the uncertainty in the absolute flux scale from the FOS measurements, and thus represent an upper limit to the photometry errors. The predictions for other filters are typically in error by 3%. This might reflect the need for a more detailed modeling of the DQE curve, especially since large deviations are seen in the region around 5000 Å, where the DQE curve is steep. These measurements will be incorporated in a future SYNPHOT update in 1998.

Table 3. Ratio of SYNPHOT-predicted over observed count rates for four standards not used in determining the WFPC2 sensitivity. Observations are in WF3.

Filter	Predicted/observed counts			
	HZ-44	P041-C	P177-D	P330-E
<i>Photometric filter set</i>				
F336W	0.997	1.009	1.022	0.983
F439W	0.992	1.007	1.006	0.989
F555W	0.994	1.031	1.030	1.017
F675W	0.993	1.006	1.005	1.006
F814W	—	1.019	1.018	1.012
<i>Other filters</i>				
F380W	1.000	1.042	1.045	1.024
F410M	1.018	0.996	1.003	0.986
F450W	1.008	1.027	1.022	1.014
F467M	0.992	1.032	1.034	1.023
F547M	0.987	1.049	1.045	1.061
F606W	0.973	1.032	1.026	1.011
F622W	—	1.030	—	—
F702W	1.005	1.022	1.008	1.004
F785L	—	1.044	1.031	1.011

#### 1.4. Caveats

A few points are worth keeping in mind when assessing the accuracy with which any WFPC2 observation can be calibrated.

- Weak non-linearities cause each calibration to be applicable mostly over a limited range of observing conditions, defined by total counts, background level, and image crowding. The calibration described so far, and performed by SYNPHOT, has been derived from well-exposed, isolated stars on negligible background, with an aperture of radius 0".5 in the center of each detector, and assuming a 2% CTE loss with respect to a star at the bottom of the chip. Other observational conditions may require various additional corrections because of the non-linearities of WFPC2, some of which are addressed in the next Section.
- The WFPC2 PSF varies slightly as a function of time (because of focus), wavelength, and position in the field of view; since WFPC2 pixels undersample the PSF, its variations are difficult to measure directly, yet they can affect photometric results at the level of a few percent (see Suchkov and Casertano 1997a, b).

- The WFPC2 gain levels (7 or 14  $e^-$ /DN) undersample the read noise (5 or 7  $e^-$ /pixel, respectively), which can lead to poor determination of the background (see Ferguson 1996 for background determination strategies).

## 2. Non-linearities in WFPC2

### 2.1. Characterization of the CTE Error

Early WFPC2 observations indicated a difference in the signal detected for the same star as a function of its position on the chip, and especially the row number  $y$ , in the sense that a weaker signal was detected at high row numbers than at low row numbers (Holtzman et al. 1995a). The effect appeared to be approximately linear with  $y$ , with a total amplitude of 10% top-to-bottom for well-exposed stars, and was attributed to a charge transfer efficiency (CTE) error. Partly to limit this effect, the camera's operating temperature was brought down from the original  $-77$  C to  $-88$  C, and as a consequence, the amplitude of the effect decreased to about 4% (Holtzman et al. 1995a). However, until recently there was no detailed characterization of the CTE error as a function of position, luminosity, and background.

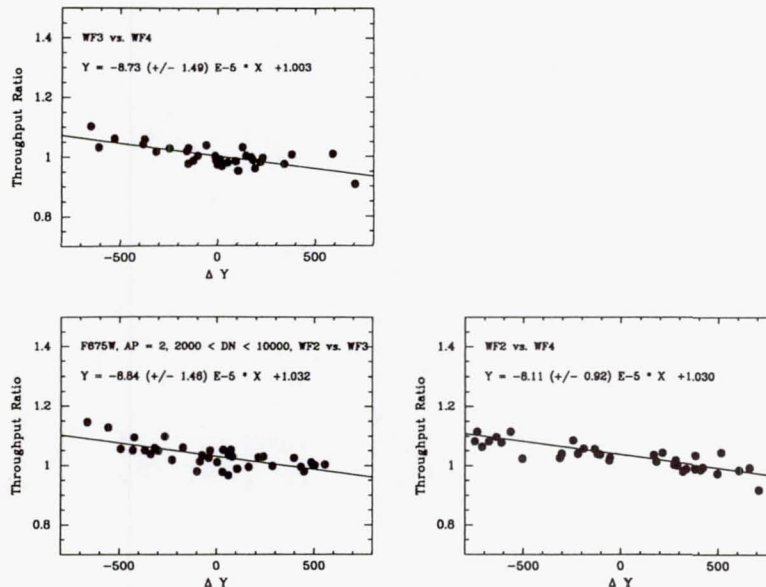


Figure 2. The ratio of the difference in the brightness of the same star (i.e., the throughput ratio) as a function of the difference in  $y$  position for stars with counts in the range 2000 to 10000 DN. The three panels show comparisons between the three WF chips. From Whitmore and Heyer (1997).

A recent campaign of WFPC2 observations of a dense stellar field centered in different chips has provided a perfect data set for the investigation of the CTE error (see Figure 2). The results, reported in Whitmore and Heyer (1997), can be summarized as follows:

1. The CTE error can be well fit by a linear dependence on row number  $y$  under all circumstances.
2. There is a similar, but weaker effect as a function of *column* number  $x$ , possibly due to CTE in the shift-register.
3. The amplitude of the CTE effect can be estimated on the basis of the total counts in the source and of either background level, or total counts on the chip.



4. The overall top-to-bottom effect is indeed  $\sim 4\%$  for bright sources on high background, but increases substantially for fainter sources on dim backgrounds; CTE effect of up to 15% top-to-bottom has been seen.
5. There is no obvious wavelength dependence, except for that induced by the background difference.

After correcting for the best-fit CTE error and for an overall chip-to-chip normalization constant, Whitmore and Heyer (1997) find that the residual discrepancies between photometry obtained at different positions in the WFPC2 field of view are less than 2% rms, consistent with a combination of measurement errors and flat-field variations.

## 2.2. Count rates and exposure times, or the long vs. short anomaly

Another WFPC2 anomaly, long thought to be connected with the CTE error, was discovered by Stetson (1995) and initially reported by Kelson et al. (1996) and Saha et al. (1996). The characteristic of this non-linearity is that count rates measured for the same object through the same filter are a function of exposure length, with count rates systematically larger in longer exposures.

Table 4. List of  $\omega$  Cen and NGC 2419 observations used to characterize the long vs. short anomaly

Target	Filter	Rootname	Date	Time	Exposure time
$\omega$ Cen	F814W	u27rgf01t	7 May 1994	03:07	140
$\omega$ Cen	F814W	u27rgf02t	7 May 1994	03:11	140
$\omega$ Cen	F814W	u27rcj01t	7 May 1994	03:57	1200
$\omega$ Cen	F814W	u27rcj02t	7 May 1994	04:20	1200
$\omega$ Cen	F814W	u27rc701t	7 May 1994	05:34	1000
$\omega$ Cen	F814W	u27rc702t	7 May 1994	05:53	1000
$\omega$ Cen	F814W	u27rag01t	7 May 1994	07:10	900
$\omega$ Cen	F814W	u27rag02t	7 May 1994	07:28	900
$\omega$ Cen	F814W	u27rdt01t	7 May 1994	07:51	300
$\omega$ Cen	F814W	u27rdt02t	7 May 1994	08:00	300
$\omega$ Cen	F814W	u27r9u01t	7 May 1994	08:47	700
$\omega$ Cen	F814W	u27r9u02t	7 May 1994	09:01	700
$\omega$ Cen	F814W	u27rfh01t	7 May 1994	09:20	400
$\omega$ Cen	F814W	u27rfh02t	7 May 1994	09:30	400
$\omega$ Cen	F814W	u27r8501t	7 May 1994	10:23	600
$\omega$ Cen	F814W	u27r8502t	7 May 1994	10:37	600
NGC 2419	F555W	u2dj0c01t	21 May 1994	2:33	60
NGC 2419	F555W	u2dj0c02t	21 May 1994	2:39	60
NGC 2419	F555W	u2dj0c03t	21 May 1994	2:45	60
NGC 2419	F555W	u2dj0c04t	21 May 1994	2:52	60
NGC 2419	F555W	u2dj0c05t	21 May 1994	2:58	60
NGC 2419	F555W	u2dj0c06t	21 May 1994	3:04	60
NGC 2419	F555W	u2dj0a01p	21 May 1994	18:51	1400
NGC 2419	F555W	u2dj0a02p	21 May 1994	20:09	1400
NGC 2419	F555W	u2dj0a03p	21 May 1994	12:45	1400
NGC 2419	F555W	u2dj0a04p	21 May 1994	11:22	1400
NGC 2419	F555W	u2dj0a05t	22 May 1994	0:58	1400
NGC 2419	F555W	u2dj0a06t	22 May 1994	2:35	1400
NGC 2419	F555W	u2dj0a07t	22 May 1994	4:11	1400
NGC 2419	F555W	u2dj0a08p	22 May 1994	5:48	1400
NGC 2419	F555W	u3ip0101t	21 Dec 1996	17:37	60
NGC 2419	F555W	u3ip0102t	21 Dec 1996	17:43	60
NGC 2419	F555W	u3ip0103t	21 Dec 1996	17:54	60
NGC 2419	F555W	u3ip0104t	21 Dec 1996	18:00	60
NGC 2419	F555W	u3ip0105t	21 Dec 1996	18:11	60
NGC 2419	F555W	u3ip0106t	21 Dec 1996	19:07	60
NGC 2419	F555W	u3ip0107t	21 Dec 1996	19:13	60
NGC 2419	F555W	u3ip0108t	21 Dec 1996	19:24	1400

The effect was initially reported as a zero point difference of 0.05 mag between "long" ( $\sim 1000$  second) and "short" exposures (tens of seconds), hence its commonly used moniker

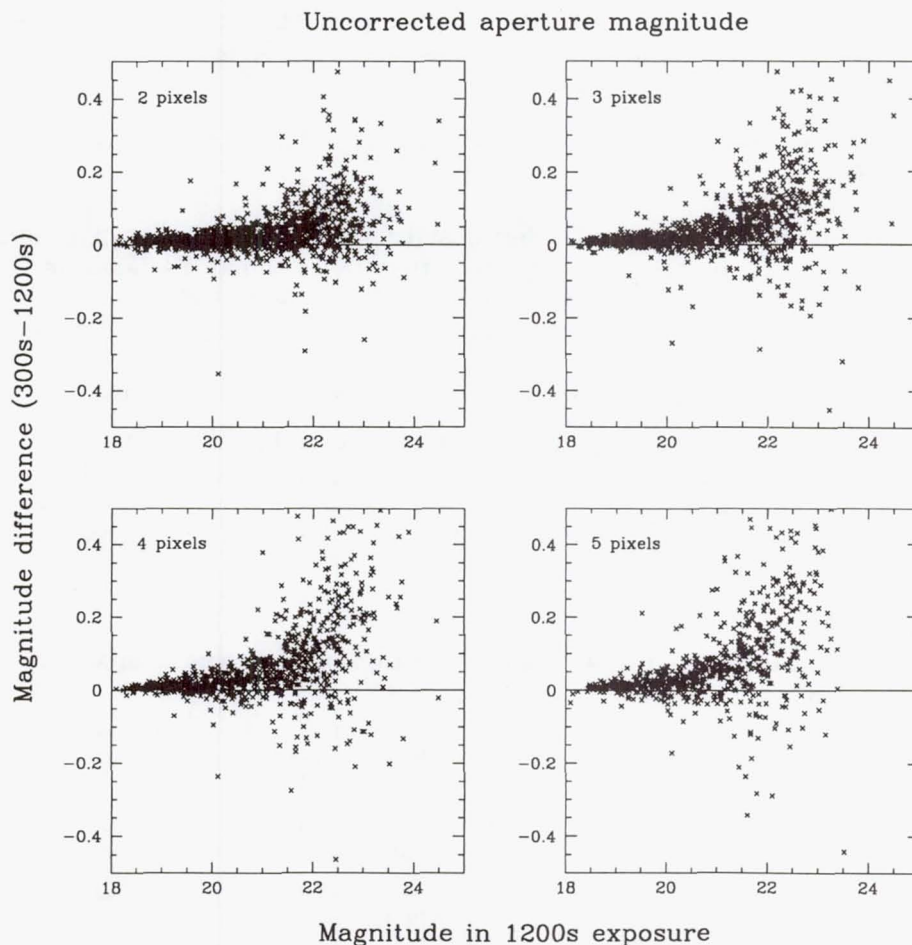


Figure 3. Comparison of 300 and 1200s exposures within different aperture radii.

of “long vs. short” anomaly. The existence of the effect has been independently confirmed in a number of studies; for a list of papers that address this point, see the WFPC2 clearinghouse (Wiggs et al. 1997) at URL

[http://www.stsci.edu/ftp/instrument\\_news/WFPC2/Wfpc2\\_clear/wfpc2\\_clrhs.html](http://www.stsci.edu/ftp/instrument_news/WFPC2/Wfpc2_clear/wfpc2_clrhs.html))

A more detailed characterization of the “long vs. short” anomaly was obtained by Stiavelli (1995) and Casertano (1995). Stiavelli (1995) used 60 and 1400s exposures of the distant globular cluster NGC 2419, one of two originally used by Stetson (1995) to detect the anomaly. Casertano (1995) used exposures in a dense field in  $\omega$  Cen (much closer to the cluster core than the standard photometric fields) with multiple exposure times ranging from 140s through 1200s; many intermediate exposure times were available, so that the effects of total signal and exposure time could be separated cleanly. The observations used are listed in Table 4.

The results obtained in this analysis are illustrated in Figure 3, which shows how the measured magnitude difference varies with total counts and aperture radius used, for an exposure time ratio of 4 (300s and 1200s).

The main conclusion is that the long vs. short non-linearity can produce a range of magnitude discrepancies, from essentially zero for well-exposed stars ( $> 2,000$  DN in short exposure) to more than 0.10 mag for faint sources ( $\sim 100$  DN), and that the magnitude discrepancy is determined primarily by the total signal in the short exposure. Thus, in



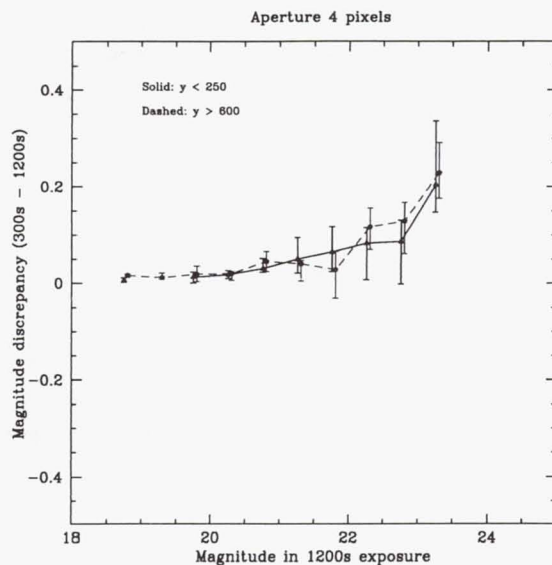


Figure 4. Comparison of 300 and 1200s exposures in a 4 pixel radius for both low and high row number  $y$ . Median and quartiles are shown for each magnitude bin. No dependence with row number is seen, unlike the CTE error—the magnitude difference is quantitatively the same in the two cases.

a sense the name “long vs. short” is a misnomer, in that the non-linearity (and thus the difference in count rates and measured magnitudes) is really driven by the total amount of signal, rather than by the actual length of the exposure. The difference of 0.05 mag found by Stetson (1995) is applicable to a well-defined set of circumstances, which include the typical objects used in the  $H_0$  project, but is not applicable in general.

Another relevant result is that the magnitude discrepancy increases with increasing disparity of exposure times, and also increases with the aperture size, roughly quadratically for apertures up to 5 pixels. (Uncertainties increased with larger apertures for these crowded fields).

*Dependence on Position on the Chip* On the other hand, the “long vs. short” discrepancy appears to be completely independent of position in the chip, especially row number (see Figure 4). This was somewhat surprising at first, because of the superficial similarity between this non-linearity and the CTE error, which depends strongly on the  $y$  coordinate. More recent data confirm that the long vs. short non-linearity differs in other major respects from the CTE error, mainly in that it is not affected by the background level (see Section 2.2), indicating that the two phenomena are caused by different physical mechanisms.

*A Phenomenological Approximation: The  $2.5e^-$  Law* The basic nature of the long vs. short non-linearity is that shorter exposures, with less total signal, yield lower count rates than long exposures, with more total signal. A natural interpretation is that a greater fraction of the signal is somehow lost when less signal is available. If this signal loss could be modeled, then the effect can be quantified and even corrected for.

An extremely simple law that produces very good results is the “ $2.5e^-$  law”: which postulates that every pixel in the aperture loses a fixed amount of charge,  $2.5e^-$ . The “true” signal can then be recovered by adding back  $2.5e^-$  times the number of pixels in the aperture. Indeed, when this operation is carried out, the magnitude discrepancy disappears almost entirely (Figure 5).

This law, as stated, is non-physical: for it to apply, somehow the pixels used in the sky determination must not be affected by the charge loss, else there would be no net effect. However, this law does seem to match the long vs. short effect in all data sets where it has been tried, with the "optimal" amount of charge loss per pixel ranging somewhere between  $2.0$  and  $3.0e^-$  per pixel, for apertures up to 5 pixels in radius.

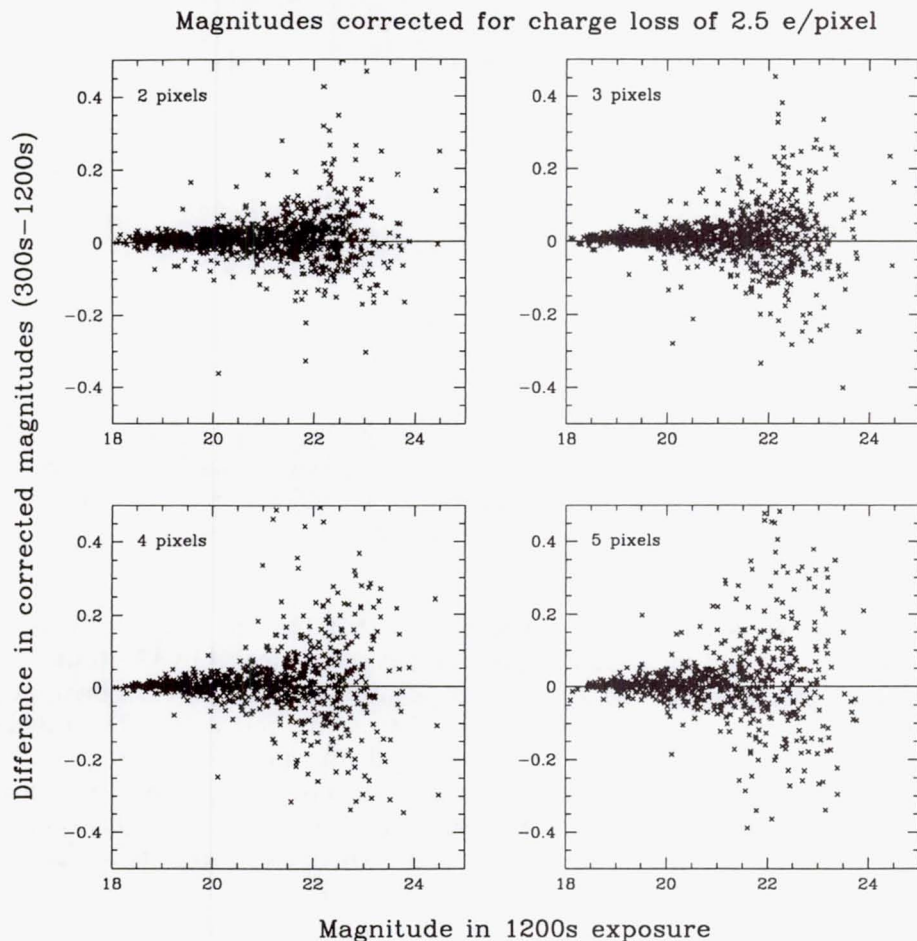


Figure 5. Comparison of 300 and 1200s exposures within multiple apertures with charge-loss correction of  $2.5 e^-/\text{pixel}$

We have tried more physically plausible descriptions of this effect, such as a charge loss per pixel that depends non-linearly on the total signal in the pixel, thus possibly generating a larger charge loss above a certain threshold (for source pixels) and a smaller charge loss below (for sky pixels). None of these laws has managed to achieve nearly as good, or as general, a match as the simple  $2.5e^-$  law.

Despite the apparent success of the  $2.5e^-$  law, we do not yet recommend using it, or any other rule, to correct actual data, because of its lack of physical plausibility and of the small number of cases in which it has been tested so far. However, this law can be used as a "rule of thumb" in order to estimate the potential loss of signal, and thus the absolute photometric error, caused in actual data by the long vs. short non-linearity.

*The Effect of the Background—Preliminary Results* New observations have been carried out recently to improve the characterization of the long vs. short anomaly, and especially to determine whether it is reduced in the presence of a strong background, as the CTE error



is. A preliminary analysis of a limited data set, with background artificially produced by preflashing the exposure by up to  $250e^-/\text{pixel}$ , indicates that the background has very little effect on the long vs. short anomaly.

A more complete data set, including several filters, a wider range of exposure time ratios, and larger background levels, will be acquired in late 1997 as a part of proposal CAL 7630, and should lead to a more complete characterization of the long vs. short anomaly.

**Acknowledgments.** Most of the work described here is the result of a group effort over the last three years, including contributions from Brad Whitmore, Sylvia Baggett, John Biretta, Harry Ferguson, Shireen Gonzaga, Inge Heyer, Max Mutchler, Christine Ritchie, and Massimo Stiavelli. The original, high-quality photometric calibration of WFPC2 is due to the Investigation Definition Team, and especially to Jon Holtzman, Chris Burrows, Jeff Hester, and John Trauger, who have been very generous with their time and advice over these years.

## References

- Baggett, S., Casertano, S., Gonzaga, S., & Ritchie, C., 1997, Instrument Science Report WFPC2 97-10
- Biretta, J., et al., 1997 Instrument Science Report WFPC2 97-09
- Casertano, S., 1995, at URL [http://www.stsci.edu/ftp/instrument\\_news/WFPC2/Wfpc2\\_cte/shortnlong.html](http://www.stsci.edu/ftp/instrument_news/WFPC2/Wfpc2_cte/shortnlong.html)
- Colina, L., & Bohlin, R., 1997, AJ 113, 1138
- Ferguson, H., 1996, Instrument Science Report WFPC2 96-03
- Holtzman J., et al., 1995a, PASP, 107, 156
- Holtzman J., et al., 1995b, PASP, 107, 1065
- Kelson, D. D., et al., 1996, ApJ 463, 26
- Saha, A., Sandage, A., Labhardt, L., Tammann, G. A., Macchetto, F. D., & Panagia, N., 1996, ApJ 466, 55
- Simon, B., 1997, *SYNPHOT User's Guide* (Baltimore: STScI)
- Stetson, P., 1995, unpublished (referenced in Kelson et al. 1996 and Saha et al. 1996)
- Stiavelli, M., 1995, unpublished
- Suchkov, A. A. & Casertano, S., 1997a, Instrument Science Report WFPC2 97-01 (Baltimore: STScI)
- Suchkov, A. A. & Casertano, S., 1997b, this volume
- Voit, M., et al., 1997, *HST Data Handbook*, Version 3.0 (Baltimore: STScI)
- Whitmore, B., 1995, in *Calibrating Hubble Space Telescope: Post Servicing Mission*, eds. A. Koratkar and C. Leitherer (Baltimore: STScI), 269
- Whitmore, B. C., 1997, this volume
- Whitmore, B., & Heyer, I., 1997, Instrument Science Report WFPC2 97-08
- Wiggs, M., Whitmore, B. C., & Heyer, I., 1997, this volume

## WFPC2 Calibration for Emission Line Images

G. Dudziak

*European Southern Observatory, Karl-Schwarzschild Strasse 2, D85748 Garching bei München, Germany.*

J. R. Walsh

*Space Telescope European Co-ordinating Facility, European Southern Observatory, Karl-Schwarzschild Strasse 2, D85748 Garching bei München, Germany.*

**Abstract.** Formulae for the flux calibration of WFPC2 emission lines are presented. The photometric information given in the header is not adequate, and does not consider the contamination due to neighbouring emission lines in the filter pass-band or by the continuum. The formulae were originally calibrated using ground-based images of the Orion Nebula. The photometric accuracy of the flux calibration process is assessed by comparing WFPC2 fluxes with ground-based absolute fluxes and aperture photometry of four bright planetary nebulae. A 5 % absolute accuracy for the H $\alpha$  emission line is achievable using this method.

### 1. Introduction

The flux calibration of HST images is a well studied problem in reference to wide band filters. The accuracy of these calibrations is claimed to be  $\sim 5\%$  (Holtzmann et al. 1995). The header of the HST images provides the values of the parameter PHOTFLAM for each of the individual images, which allows, in principle, a direct conversion from data numbers (DNs) into physical flux in units of  $\text{erg cm}^{-2} \text{s}^{-1}$ . As PHOTFLAM actually represents the mean flux density (i.e., the flux density of a source with a spectrum which is flat in  $f_\lambda$  across the bandpass of the filter), this calibration method is not applicable to sources whose spectra differ significantly from flat (strong slope or emission lines for example).

The WFPC2 narrow band filters are mostly used for the observation of emission line objects and their flux calibration should therefore not be made using the PHOTFLAM parameter. A formula is proposed by Holtzmann et al. (1995) to convert from observed count rates into physical fluxes. The knowledge of the system throughput at the wavelength of the emission line is required; these throughputs can be read from tables available via the WFPC2 homepage (in `/ftp/cdbs/cdbs6/synphot_tables/`). A major source of uncertainty is that these tables rely on the pre-launch filter transmission curves and on observation of continuum sources, as no known flux calibration with emission line sources has been carried out to date. This situation should change when the results of the proposal 6943, *Throughput verification for narrow band filters*, of the Cycle 6 calibration plan become available.

A last source of uncertainty in the calibration of narrow band filters is the possible contamination by neighbouring emission line(s). This problem has been recently considered in the flux calibration of WFPC2 images of BD +30°3639 (Harrington et al. 1997). The flux calibration of the F656N and F658N filters was corrected by 14% and 4% to account for the contamination by the [NII] (6548Å and 6584Å) and H $\alpha$  6563Å lines respectively. The quoted percentages were measured from the pre-launch filter transmission curves, and



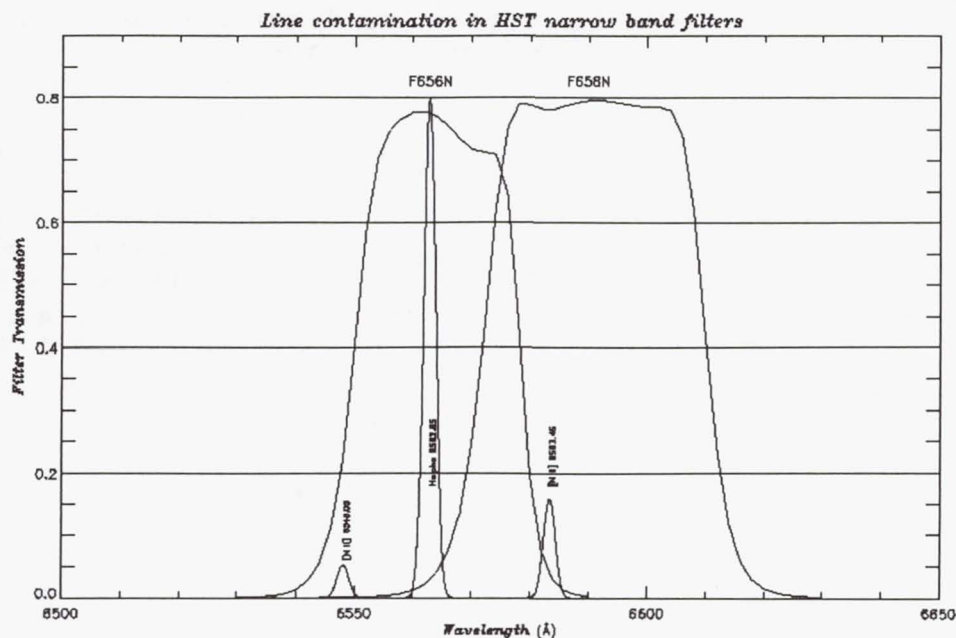


Figure 1. WFPC2 filter F656N and F658N bandpasses are shown with  $H\alpha$  and [NII] emission lines. F656N is contaminated by the [NII] 6548Å and 6584Å lines, at which its transmission is  $\sim 29\%$  and  $\sim 4\%$  respectively. The F658N filter is contaminated by the  $H\alpha$  6563Å line, transmission  $\sim 4\%$ .

since the contaminating lines lie on the steep shoulder of the filter passband (see Figure 1), additional inaccuracy can be expected from even a slight change in the transmission curves.

In Section 2, we present analytical formulae for the F502N, F656N and F658N narrow band filters that directly solve for the emission line nature of the object and for the possible contamination. The accuracy of the calibration is tested by comparing the total flux of four planetary nebulae (PNe) derived from HST images with ground-based measurements (Section 3) and brief conclusions are given in Section 4.

## 2. Calibration Formulae

An accurate absolute calibration of the HST  $H\alpha$  (F656N), [OIII] (F502N) and [NII] (F658N) narrow band filters was performed by comparing ground-based Orion Nebula images with the corresponding HST frames. The method described here is the application to WFPC2 narrow band filters of the method employed by Hu for the calibration of the WFPC narrow band filters (Hu 1997a, 1997b). The equations presented here were obtained for the WFPC2 filters by Wong (unpublished) and kindly provided to us by C. R. O'Dell. Several smooth regions of the ground-based Orion [OIII],  $H\alpha$  and [NII] images, obtained by R. J. Dufour, were used to calibrate the formulae relating the surface brightness of the emission lines to the measured counts in DN. The other quantities needed were obtained from the HST WFPC2 Instrument Handbook (Biretta et al. 1996).

Practical formulae give the surface brightness of lines in photons  $\text{cm}^{-2}\text{s}^{-1}\text{ster}^{-1}$  as a function of data number and exposure time. These formulae directly take into account the contamination of the  $H\alpha$ (F656N) filter by the [NII] 6548Å and 6584Å lines (and the contamination of the [NII](F658N) filter by the  $H\alpha$  6563Å line) and allow the correction of this effect on a pixel-to-pixel basis. This is particularly important as the [NII] emission

arises from low ionization regions that can be spatially different from the  $H\alpha$  emission (for example, low ionization knots in PNe).

The first three formulae also include a correction term for the continuum if F547M observations are available. This correction is more important for HII regions than for PNe. In HII regions, the scattered light continuum can be much stronger than the atomic continuum which dominates in PNe.

We applied a further multiplicative factor to the given equations to obtain the fluxes in units of  $\text{erg cm}^{-2}\text{s}^{-1}$ . Lastly, care must be taken of the analog to digital gain which was used for the HST observations. The final equations used for the  $H\alpha$ (F656N), [NII](F658N), [OIII](F502N) and  $H\beta$ (F487N) flux conversion are listed below. The formula for the F487N flux was obtained by directly comparing the total line flux in counts in BD+30°3639 (the continuum contribution inside the F487N filter was estimated and subtracted) to the total  $H\beta$  flux quoted in the ESO Strasbourg catalogue of PNe (Acker et al. 1992).

$$F_{502}(\text{ergs}^{-1}\text{cm}^{-2}) = \frac{N_{502} \times g}{t_{502} \times 8.71 \times 10^{13}} \times \frac{1}{1 + \frac{0.03 \times t_{502} \times N_{547}}{t_{547} \times N_{502}}} \quad (1)$$

$$F_{656}(\text{ergs}^{-1}\text{cm}^{-2}) = \frac{N_{656} \times g}{t_{656} \times 2.45 \times 10^{14}} \times \frac{1}{1 + \frac{0.15 \times t_{656} \times N_{658}}{t_{658} \times N_{656}} + \frac{0.05 \times t_{656} \times N_{547}}{t_{547} \times N_{656}}} \quad (2)$$

$$F_{658}(\text{ergs}^{-1}\text{cm}^{-2}) = \frac{N_{658} \times g}{t_{658} \times 2.64 \times 10^{14}} \times \frac{1}{1 + \frac{0.04 \times t_{658} \times N_{656}}{t_{656} \times N_{658}} + \frac{0.07 \times t_{658} \times N_{547}}{t_{547} \times N_{658}}} \quad (3)$$

$$F_{487}(\text{ergs}^{-1}\text{cm}^{-2}) = \frac{N_{487} \times g}{t_{487} \times 7.59 \times 10^{13}} \quad (4)$$

Where:

$F_{\text{filter}}$	Flux calibrated image in units of $\text{erg s}^{-1} \text{cm}^{-2}$
$N_{\text{filter}}$	Data Number (DN) counts in HST images
$t_{\text{filter}}$	HST image exposure time in second
$g=1$	if the analog to digital conversion factor of the observation is 7 (header keyword ATODGAIN = 7)
$g=2$	if the analog to digital conversion factor of the observation is 14 (header keyword ATODGAIN = 15)

### 3. Comparison with Other Observations

#### 3.1. HST Observations

In order to assess the validity and accuracy of the flux calibration formulae presented above, we performed a comparison of the total fluxes obtained from ground-based observations and from HST observations. From the HST archive, we obtained  $H\alpha$ (F656N), [NII](F658N) and [OIII](F502N) HST images of four bright planetary nebulae, namely NGC 3242, NGC 6826, NGC 7009 and NGC 7662 (PI: B. Balick, proposal number 6117). The data were pipeline calibrated with the most up-to-date calibration files (on-the-fly calibration). The calibration pipeline includes the bias subtraction, dark subtraction and flat fielding of the data. Images taken in the same filter were combined into one equivalent exposure; the data reduction further included a linear interpolation over bad pixels and the cosmic ray cleaning process. The mosaic image of NGC 7009 was built by combining the PC and WF images. The other PNe were all exposed within the field of the PC camera. We then applied the flux calibration formulae (1)–(4) to obtain images in units of  $\text{erg cm}^{-2} \text{s}^{-1}$ .



The last contamination to take into account and subtract is the nebular continuum emission in the filter passband. Using the DIPSO package (Howarth et al. 1995), the nebular continuum spectrum was calculated for each nebula, based on the observed total  $H\beta$  flux, the extinction and the nebular conditions. Using the CALCPHOT task of the IRAF SYNPHOT package, the continuum contribution in counts per second was estimated inside each filter passband. As an example, the continuum contribution in the  $H\alpha$ (F656N) filter for NGC 3242 was found to represent 1.5% of the line flux, and the flux in this image was reduced correspondingly. The same calculation was made for the other filters and the continuum removed as a fraction of the  $H\alpha$  image.

### 3.2. Ground-based Observations

We adopted total  $H\beta$  fluxes for the above mentioned PNe from Acker et al. (1992). We then compiled the logarithmic redenning parameter,  $c$ , from the literature. For NGC 3242 a reddening value of  $c = 0.11$  was adopted from radio measurements. For NGC 7662,  $c = 0.23$  was adopted from the study of Harrington et al. (1982). Finally, the value of the redenning parameter for NGC 6826 and NGC 7009 was 0.16 and 0.12 respectively, adopted from the work of Barker (1983, 1988). Using the theoretical case B dereddened line ratio value of 2.83 between  $H\alpha$  and  $H\beta$  (representative of the mean nebular conditions  $N_e = 4000 \text{ cm}^{-3}$ ,  $T_e = 11000 \text{ K}$  of these PNe), we derived the total  $H\alpha$  observed flux for each of the PNe. The error on the observed  $H\beta$  fluxes is 0.02 dex, the error on the theoretical line ratio is no more than 1%, and an  $\pm 0.05$  error on the redenning parameter  $c$  can contribute up to 0.02 dex. We then estimate the error on the observed  $H\alpha$  flux to be 0.04 dex in total.

We also obtained the global [OIII] fluxes for the nebulae from the literature (see footnotes to Table 1). These [OIII] observations were always obtained together with  $H\beta$  ones, and the [OIII] flux was rescaled if ever these  $H\beta$  fluxes were different from the one in the Acker et al. (1992) catalogue. The error on the [OIII] flux hence encompasses the 0.02 dex error on the observed  $H\beta$  flux of the Acker catalogue and the one of the observations, usually 0.03 dex. We hence adopt a total [OIII] error of 0.04 dex.

Table 1 summarizes the comparison between the [OIII] and  $H\alpha$  ground-based measured fluxes and the HST fluxes obtained from our calibration. (There were no HST  $H\beta$  images taken of these PNe.) The total  $H\alpha$  fluxes measured from HST compare very well with the ground-based estimate. The mean difference between  $H\alpha$  fluxes for the 4 objects is only of 0.02 dex. Comparing this value to the error on the ground-based  $H\alpha$  measurements of 0.04 dex, we conclude that the flux calibration formula for the  $H\alpha$  images is probably correct to 0.02 dex (or 5%). There is also no indication of a systematic error on the measurement.

Imaging spectrophotometry was recently performed on NGC 7009 and NGC 7662 (Lame & Pogge 1996). The flux calibration method relied on the comparison with flux calibrated long slit spectra at well-determined positions. However, the quoted total  $H\beta$  line fluxes within a  $40''$  diameter circular aperture are underestimated by 0.16 and 0.14 dex for NGC 7009 and NGC 7662 respectively, compared to the values from the Acker et al. (1992) catalogue. Nevertheless, rescaling their [OIII] total flux accordingly, we obtained a total logarithmic [OIII] flux of  $-8.71$  for NGC 7009 and  $-8.89$  for NGC 7662. For NGC 7009, a previous measurement of Webster (1983) gave a total logarithmic [OIII] flux of  $-8.73$ . Using the rescaled measurements of Lame & Pogge (1996) reduces the discrepancy with our HST determination to 0.04 dex for NGC 7009, while leaving it unchanged for NGC 7662. This also illustrates the difficulty in obtaining a good calibration from the ground for extended emission line objects.

The mean difference between the ground based and the HST [OIII] fluxes however reaches 0.04 dex. The errors appear to be correlated with the error on the  $H\alpha$  fluxes, and for 3 out of 4 objects, the HST [OIII] fluxes are  $\sim 0.04$  dex higher than the ground-based ones. The flux calibration formula for the [OIII] images is probably correct to 0.04 dex (or 10%).

Table 1. Comparison of H $\alpha$  and [OIII] absolute logarithmic fluxes

Object	H $\beta^a$	<i>c</i>	H $\alpha$	HST H $\alpha$	[OIII]	HST [OIII]
NGC 3242	-9.79	0.11	-9.30	-9.33	-8.63 <sup>b</sup>	-8.66
NGC 6826	-9.98	0.16	-9.48	-9.46	-9.12 <sup>c</sup>	-9.05
NGC 7009	-9.78	0.12	-9.29	-9.26	-8.71 <sup>d</sup>	-8.67
NGC 7662	-9.99	0.23	-9.46	-9.46	-8.89 <sup>c,d</sup>	-8.85

<sup>a</sup>log H $\beta$  flux in erg cm<sup>-2</sup> s<sup>-1</sup> from Acker et al. (1992)

<sup>b</sup>Collins et al. (1961)

<sup>c</sup>Capriotti & Daub (1960)

<sup>d</sup>Lame & Pogge (1996)

#### 4. Conclusions

We have presented formulae for the flux calibration of WFPC2 H $\alpha$  (F656N), [OIII] (F502N) and [NII] (F658N) narrow band filters. A 5% absolute accuracy for the H $\alpha$  emission line (10% for the [OIII] line) is achievable using this method. The accuracy for the [NII] emission line cannot be assessed from available global flux measurements. Further progress towards an accurate flux calibration for other narrow band filters is expected from the results of the proposal 6943 (Throughput verification for narrow band filters) of the Cycle 6 calibration plan.

**Acknowledgments.** We are grateful to C. R. O'Dell for providing the document describing the derivation of the formulae for the flux calibration of HST WFPC2 data.

#### References

- Acker, A., Ochsenbein, F., Tyllenda, R., & Marcout, J., 1992, *The Strasbourg ESO Catalogue of Galactic Planetary Nebulae*
- Barker, T., 1983, ApJ, 267, 630
- Barker, T., 1988, ApJ, 326, 164
- Biretta, J. A., et al., 1996, *WFPC2 Instrument Handbook*, Version 4.0 (Baltimore: STScI)
- Capriotti, E. R., & Daub, C. T., 1960, ApJ, 132, 677
- Collins, G. W., Daub, C.T., & O'Dell, C. R., 1961, ApJ, 133, 471
- Holtzmann, J. A., Burrows, C. J., Casertano, S., Hester, J. J., Trauger, J. T., Watson, A. M., & Worthey, G. 1995, PASP, 107, 1065
- Harrington, J. P., Seaton, M. J., Adams, S., & Lutz, J. H. MNRAS, 1982, 517
- Harrington, J. P., Lame, N. J., & White, S. M., 1997, AJ, 113, 2147
- Howarth, I. D., Murray, J., Mills, D., & Berry, D. S., 1995, *DIPSO(V3.2) - A friendly spectrum analysis package*, Starlink User Note 50.17
- Hu, X., 1993, Rev. Mex. Fis, 27, 153
- Hu, X., 1993, Space Telesc. Sci. Inst., Newsl. , 28
- Lame, N. J., & Pogge, R. W., 1996, AJ, 111, 2320
- Webster, B. L., 1983, PASP, 95, 610



## HST, uvby Photometry and System Calibration

P. Linde, A. Ardeberg, T. Bensby and R. Snel

*Lund Observatory, Box 43, S-221 00 Lund, Sweden*

### Abstract.

Galactic evolution is studied in a field in the centre of the LMC Bar. We obtain data of high quality with the HST WFPC2 and uvby photometry. To match the photometric accuracy and make use of the potential of the uvby system in terms of evolutionary parameters and chemical abundance, we need adequate calibration of the data observed. Conversion of the observing system into that of the international uvby system is made from observations of reference stars in cluster fields. These fields are first observed with a ground based telescope together with selected sets of standard stars for the uvby system. This way, the cluster field reference stars are tied into the international uvby system. Subsequently, the reference stars are observed with the HST WFPC2 used with its set of uvby filters, thus providing final system conversion. We here discuss the observations and present some initial results.

### 1. Introduction

In a study of star formation history and chemical evolution in the Large Magellanic Cloud (LMC), we use the HST to get detailed information concerning conditions at centre of the Bar (Ardeberg et al. 1997).

The LMC is a favourable platform for studies of stellar and galactic evolution. It has a distance allowing accurate detailed studies of individual main sequence stars. Also, it shows considerable variation in stellar ages and has an orientation and a structure favouring identification of stellar populations and their large scale structural features. Further, the LMC is a galaxy of an interesting type, different from that of the Galaxy.

Even with the best grounds based telescopes, and with excellent atmospheric turbulence conditions, only the brightest LMC stars can be studied for individual stellar characteristics. Thus, our understanding of the nucleosynthesis and massive star formation in the LMC has been limited to its most recent history. For the youngest generations of stars, large scale star formation processes in the LMC have shown rapid and violent bursts.

### 2. Programme

Targets of our programme are large scale star formation history, chemical evolution and the initial mass function of the stellar populations being dominant in the LMC Bar. For this purpose, we make use of stars with ages and chemical compositions that can be determined with optimum accuracy and reliability. At the same time, in order to make such studies of individual stars possible, we have to observe stars with reasonable brightnesses, although not too evolved with respect to the main sequence. In consequence, we have chosen to study stars close to the turn off point in the HR diagram. In the LMC Bar, these stars are of spectral type F. Their V magnitudes fall in the range 20.5 to 22.0.



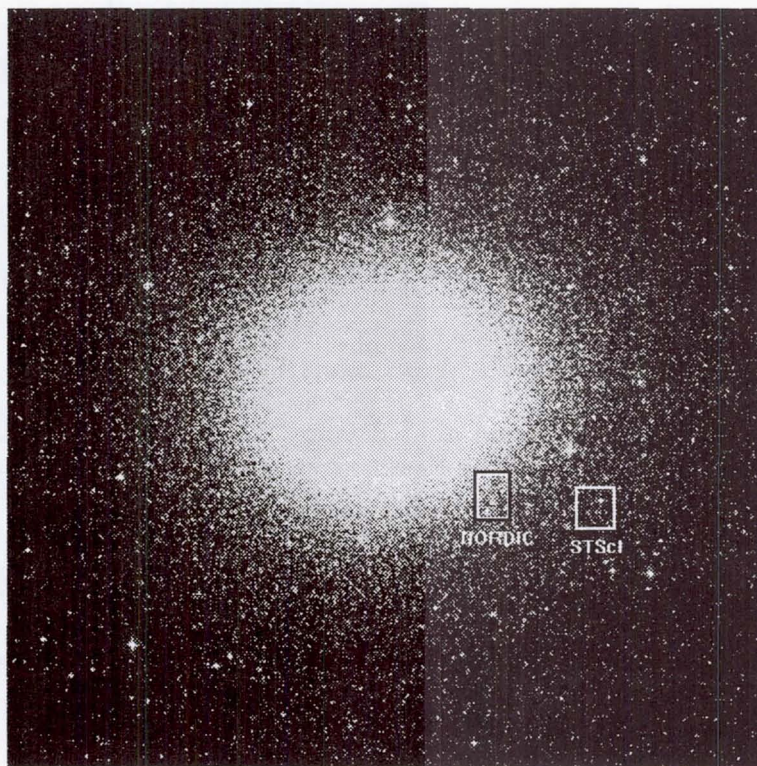


Figure 1. The  $\omega$  Cen cluster. The two fields chosen for calibration purposes are marked.

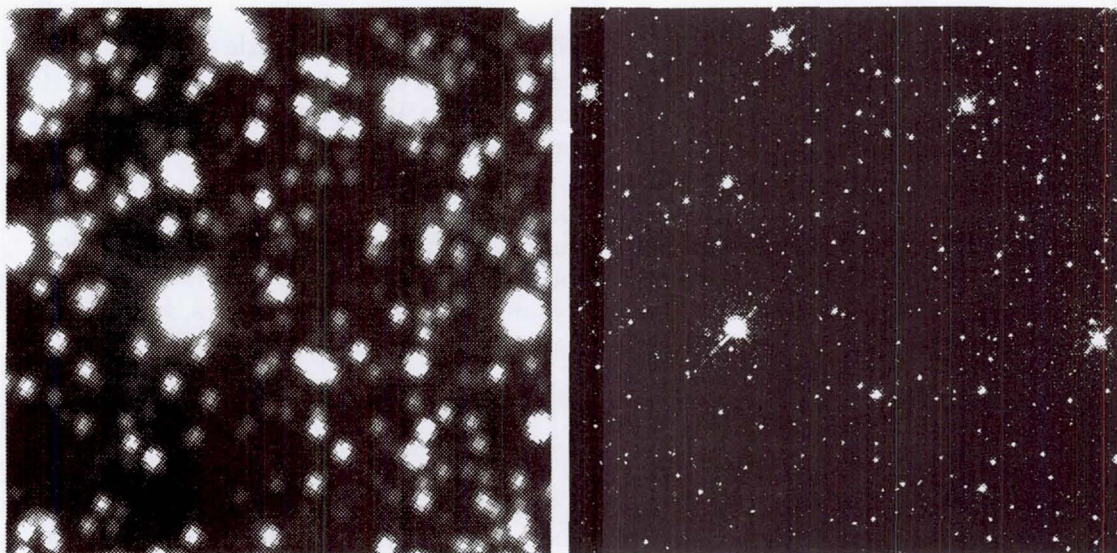


Figure 2. Left: The Nordic field as observed with the ESO 2.2m telescope. The image shown is a 5 min exposure through the  $y$  filter. The field size is  $35 \times 35$  arcsec<sup>2</sup>. Right: The same field, observed with the HST PC. The image shown is a 50 s exposure through the  $y$  (547M) filter.



### 3. The uvby System and its Astrophysical Relevance

For our work, we have chosen the uvby system (Strömgren 1963). The reasons for this choice are several. The system was designed and is ideally suited for exactly the type of studies defining our programme. Correctly employed, it delivers data of high accuracy having pass bands narrow enough to avoid the problems weakening broad band photometric systems. At the same time, its light collecting power is high enough to allow studies also of stars with modest brightness.

Field	Year	y <sub>eso</sub>	b <sub>eso</sub>	v <sub>eso</sub>	u <sub>eso</sub>	y <sub>wfpc</sub>	b <sub>wfpc</sub>	v <sub>wfpc</sub>	u <sub>wfpc</sub>
Targets:									
NORDIC	1986	62 (3)	94 (4)	93 (3)	229 (6)				
NORDIC	1996					9 (2)	30 (3)	30 (2)	80 (3)
STSCI	1996				30 (1)	24 (8)	70 (6)	130 (7)	135 (5)
Reference fields:									
M67A	1986	6 (3)	9 (3)	7 (3)	13 (3)				
M67B	1986	4 (2)	5 (2)	5 (2)	8 (2)				
NGC3680A	1986	4 (2)	6 (2)	6 (2)	12 (3)				
NGC3680B	1986	3 (2)	2 (2)	2 (2)	4 (2)				
IC4651A	1986	9 (3)	13 (3)	15 (3)	24 (3)				
IC4651B	1986	9 (3)	15 (3)	15 (3)	32 (4)				
3 single star fields:	1986	(8)	(5)	(4)	(5)				
M67A	1996				12 (3)	5 (13)	16 (12)	22 (12)	51 (13)
M67B	1996				22 (4)	2 (7)	9 (7)	14 (7)	33 (7)
NGC3680A	1996				5 (1)	2 (5)	7 (5)	12 (5)	28 (6)
NGC3680B	1996				10 (2)	2 (5)	7 (5)	13 (6)	27 (5)
17 single star fields:	1996				(5)	(41)	(30)	(31)	(32)

Table 1. Summary of ground based calibration observations. For each observed field, the following is given: year of observation; uvby for ESO filters; uvby for WFPC2 filters; for each filter total exposure (min) and number of exposures.

Field	Year	y <sub>wfpc</sub>	b <sub>wfpc</sub>	v <sub>wfpc</sub>	u <sub>wfpc</sub>
NORDIC	1997	3 (4)	27 (8)	40 (8)	53 (8)
STSCI	1996	3 (7)	5 (2)	24 (5)	412 (77)
M67-FIELD1	1996	2 (4)	13 (4)	24 (4)	32 (4)
M67-FIELD2	1996	2 (4)	13 (4)	24 (4)	32 (4)

Table 2. Summary of space based calibration observations. For each observed field, the following is given: year of observation; uvby for WFPC2 filters; for each filter total exposure (min) and number of exposures are given. Notes: Some exposures are only partly overlapping, due to position offsets and detector rotation. The STSCI field has been observed by the STScI WFPC2 group.

From our experience with the uvby system as applied to stars in the solar neighbourhood, we know that it can give data on the abundance of heavy elements, expressed in

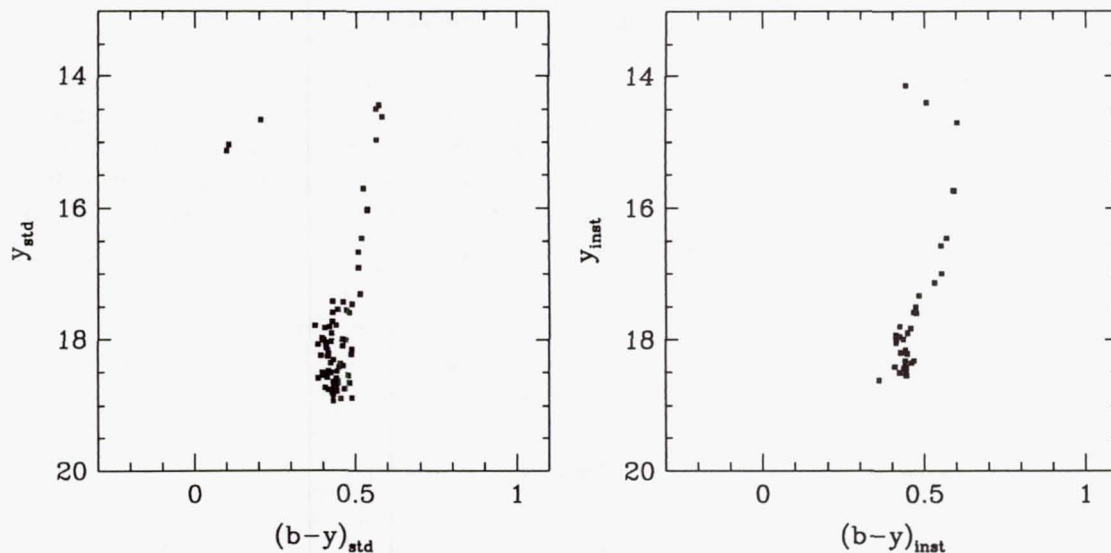


Figure 3. Left: Colour-magnitude diagram for  $\omega$  Cen for the brighter stars in the ESO 2.2m observations. Right: Colour-magnitude diagram for the brighter stars in the HST PC observations.

terms of  $[\text{Me}/\text{H}]$ , with an accuracy between 0.1 and 0.2 dex. Correspondingly, the accuracy obtainable in relative stellar ages is around 25 % or better. For our programme stars in the Bar of the LMC, we want to derive effective temperature, abundance of heavy elements and surface gravity or absolute (bolometric) magnitudes. Using these effective temperatures and absolute magnitudes, or their equivalents, we can, from comparisons with isochrones, determine ages of our programme stars.

The high quality of stellar parameters discussed above refers to observational data on the international uvby system. A prerequisite for solid analysis is, thus, adequate conversion of our observations from the instrumental system to corresponding data on the international uvby system. Such a system conversion must rely on a set of standard or reference stars with physical parameters, the ranges of which enclose those of our programme stars, and for which we have secured reliable and accurate data tied into the international uvby system. The present paper describes this procedure.

#### 4. Observations

Our LMC programme observations were made with the HST and its WFPC2 instrument, used with uvby filters. For our system conversion observations, we use both this instrumentation and the 2.2 m telescope at the European Southern Observatory (ESO). Although our main concern is calibrating the Planetary Camera, we will also attempt calibration of the wide field (WF2, WF3, WF4) cameras.

##### 4.1. Ground-based Observations

We have made two observing runs with the ESO 2.2 m, covering the two fields marked in Figure 1 as NORDIC and STSCI, respectively. The STSCI field is the same as used by Holtzman et al (1995) for Johnson photometry calibration. Table 1 gives a summary of the obtained data. The reference field in  $\omega$  Cen is shown in detail in Figure 2. It measures  $35 \times 35 \text{ arcsec}^2$ . To the left is seen a 5 min exposure in  $y$  obtained with the ESO 2.2 m telescope. A corresponding 50 sec  $y$  exposure made with the HST is shown to the right.

During the 1986 run, the NORDIC field was observed using ESO uvby filters. The 1986 data are reduced and have previously been reported (Linde et al. 1995).



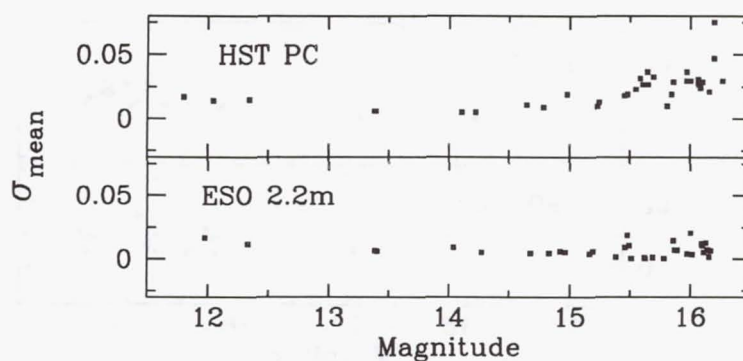


Figure 4. Photometric accuracy for the y filter.

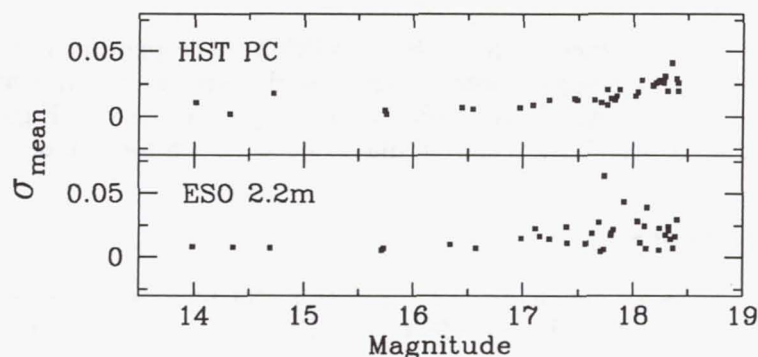


Figure 5. Photometric accuracy for the b filter.

In the 1996 run main emphasis was given to the STSCI field, while some images were also taken of the NORDIC field. Replicas of the uvby filters installed in the HST WFPC2 were used. Observations of the fields were alternated with observations of a generous amount of uvby standard stars. These observations and subsequent reductions give us a number of uvby system reference stars in  $\omega$  Cen tied into the uvby system. Their colour indices covers the intervals defined by our programme stars in the LMC Bar as well as stars somewhat cooler.

#### 4.2. Space-based Observations

The same fields in  $\omega$  Cen were then observed with the HST and the WFPC2. Further, with the HST, we observed two fields in the old open cluster M67. Here, we selected stars that were somewhat hotter than those in our LMC Bar programme field and that had been observed photoelectrically and tied into the standard uvby system. These observations are summarised in Table 2.

### 5. Current Status and Some Results

Detailed conversion of our recently acquired HST uvby data is now in progress. Meanwhile, we have been able to test our data in some different ways. The result of one of these tests can be seen in Figure 3. For the brighter reference stars situated in the  $\omega$  Cen field, the left figure shows a colour magnitude diagram as defined from our observations made with the ESO 2.2 m telescope. Right is displayed the corresponding diagram resulting

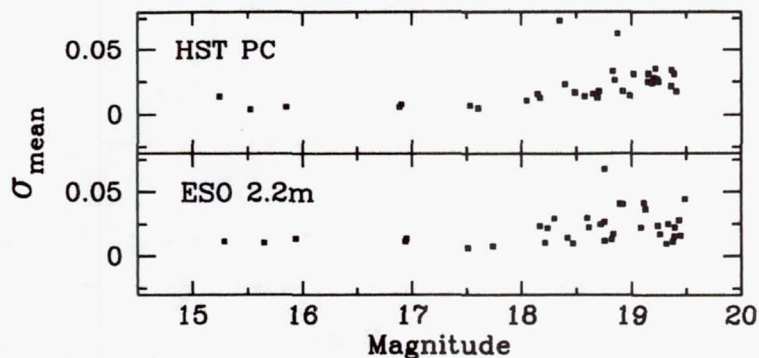


Figure 6. Photometric accuracy for the v filter.

from our observations obtained with the HST WFPC2. The photometric accuracy of our observations for system conversion may be estimated from Figures 4, 5 and 6. Here, the standard deviation of average  $y$  magnitudes are displayed versus  $y$  in Figure 4. In Figures 5 and 6, corresponding standard deviation diagrams are given for  $b$  and  $v$ , respectively.

## 6. Some Conclusions

From initial reductions we conclude that the data so far analysed look satisfactory. They indicate that a system conversion should be possible to adequate accuracy. This work is continued.

## References

- Ardeberg, A., Gustafsson, B., Linde, P., Nissen, P.-E. 1997, *A&A*, 322, L13  
 Linde, P., Ardeberg, A., Gustafsson, B., Nissen, P.-E., 1995, in *Calibrating Hubble Space Telescope*, eds. A. Koratkar & C. Leitherer, (Baltimore: STScI), 334  
 Strömgren, B. 1963. *QJRAS*, 4, 8



## Associations of WFPC2 Exposures

A. Micol

*Space Telescope European Coordinating Facility, ESA/SSD/SA, ESO*

P. Bristow

*NATO SACLANT, Undersea Research Centre*

B. Pirenne

*Space Telescope European Coordinating Facility, ESO*

**Abstract.** Unlike NICMOS and STIS, where a dataset might be constituted of a set of exposures, the WFPC2 data set's structure was thought to be a repository of all the files belonging to a single exposure. Lacking higher level of abstraction, there is no simple way of tracing back which observation strategy (e.g., cosmic ray rejection, dithering) a WFPC2 PI decided to employ.

Building *associations* of WFPC2 exposures can therefore be considered an important step towards a comprehensive description of the HST archive contents.

ST-ECF has started a project to build such associations and to store them into a database. Knowing what are the shifts among the exposures belonging to an association will allow the ST-ECF Archive to provide its users not only with on-the-fly recalibrated exposures, but also with cosmic ray-rejected and resolution-enhanced mosaics of WFPC2 images.

### 1. Introduction

The ST-ECF (Space Telescope European Coordinating Facility) HST archive stores each of the files generated by individual exposures (raw data, calibration files, calibrated data, auxiliary data), but does not store cosmic ray-cleaned or co-added exposures, nor does it currently have the capacity to handle these problems. The process of cosmic ray (hereafter CR) removal can be rather time consuming, requiring the identification of the relevant exposures, application of CR removal algorithms to only those exposures which are appropriately aligned and further combination possibly involving complex techniques such as "dithering" and "drizzling" (see Dickinson & Fosbury 1995, Hook 1995, and the Web page by Fruchter at URL <http://www.stsci.edu/~fruchter/dither/>).

Ideally one would prefer a more user-friendly situation whereby users can request the "product" of any given observation. A similar system is currently being prepared for the upcoming set of HST instruments (NICMOS and STIS) where the ground system will actually produce "observation products" rather than individual exposures in a semi-finished state as is currently the case.

To tackle this problem and provide a more complete service to archive researchers, the ST-ECF embarked upon a project which aimed to firstly group together into "associations" those WFPC2 images which "belonged" together for CR removal and co-addition and secondly combine these exposures and make the resultant products available, thereby retrofitting existing and future WFPC2 exposures into observation products. Determin-

ing (in an automatic way) which exposures belonged together turned out to be a rather intractable problem for three reasons.

- The primary parameter influencing the grouping is obviously the pointing. Unfortunately existing tabulated values were either not sufficiently accurate or (more worryingly) unreliably recorded. The same applied to the values appearing in the headers of the exposure fits files.
- A variety of observing strategies have been adopted by PIs so that we must consider associations which contain any number of exactly registered exposures and any number of shifted exposures.
- Ultimately, the decision of whether to include or reject an exposure from a group depends upon the scientific demands upon the resultant image. Some users may want good photometry, some good astrometry, in some cases low fluxes or sky variations are vitally important, in others high resolution.

Section 2 below discusses the restrictions automated data reduction techniques place upon this grouping, Section 3 explains how accurate pointing information was obtained, Section 4 describes the grouping criteria, Section 5 describes the relational scheme, and the automated CR removal and stacking is discussed in Section 6.

## 2. Requirements of Automation

Whilst the various steps in the “on the fly recalibration” are well suited to automation, this is not the case with CR rejection and co-addition. An interactive user may select and reject exposures for inclusion in co-addition according to his judgement and scientific goals, while here we must find an automatic way of grouping exposures. This involves taking into account the likely observing strategy of the PI whilst only grouping suitable exposures for CR removal.

### 2.1. Observing Strategies

In order to reproduce the CR rejection and co-adding procedures of real observers in an automatic way, we need to consider the strategy they are likely to adopt for their exposures. Of course, if the standard practice were to make several integrations with precisely the same pointing, then the co-addition and CR removal would be trivial. However, the real situation is more complicated for two reasons.

Firstly, in order to reduce the influence of hot pixels or bad columns, a shift of several pixels is made between the pointing of exposures of one target. Secondly, a further sub-pixel shift allows the true spatial resolution of HST, which is under-sampled by even the PC pixels, to be substantially recovered (Hook 1995). Consequently, a non-integer pixel shift, for example 5.5 pixels (along each axis), is likely to be present between the exposures of one target. In principle there may be just one exposure at each pointing, as tasks that can remove cosmic rays from exposures shifted by non-integral pixel offsets are now being investigated, but their eventual reliability and date of availability are not yet known. At the moment therefore the recommended strategy is to obtain multiple exposures at a single pointing (Leitherer et al. 1995). CR-cleaned exposures can then be shifted and added or “drizzled” together for higher resolution.

The problem we face here therefore is to recover the intentions of the PI by finding how many exposures are exactly registered so that we can combine them with a CR rejection algorithm, and how many of these “subgroups” belong together as part of a dithering strategy.



## 2.2. Cosmic Ray Removal

The most straightforward, and therefore most reliably automated, algorithms for CR rejection perform a comparison of corresponding pixels in several well registered exposures. If a pixel from one exposure contains an anomalously high flux then it is disregarded and replaced by a scaled average derived from the other exposure(s). Hence it is essential that the input exposures are very closely aligned to avoid degrading the PSF. Moreover, a small shift in the position of the pixel grid with respect to the centroid of a star may confuse the comparison for the pixels involved. Therefore we need to know which exposures are precisely registered and which are offset for dithering.

For interactive data reduction this does not pose such a problem, a user can select several bright point sources in each exposure, find their centroids and thus establish whether they are registered accurately enough for CR rejection (or measure the offset for dither combination, see Section 6). This problem can be tackled automatically with auto-correlation algorithms of course, however not all exposures have enough features to make auto-correlation reliable. Moreover, we must first establish what the members of the group are by comparing the position of each exposure with any potential companions, auto-correlation would obviously not be a practical solution for such a large number of comparisons. Therefore we need to find pre-recorded pointing information for all exposures.

## 3. Accurate Pointing Information

Initial attempts to group exposures involved searching the WFPC2 database for exposures well enough registered with one another to allow CR rejection (what constitutes "well enough registered" is discussed in Section 4). It soon became apparent however that associations obtained in this way often in fact contained exposures that were offset from one another, in contradiction to the tabulated co-ordinates<sup>1</sup>. This discovery prompted an examination of the co-ordinates recorded in the FITS file headers. In some cases these were indeed more reliable, but by no means always. The problems appear to arise for two reasons;

- A set of consecutive exposures are carried out for a given target and dithering is requested for some of this set. In some cases, exactly the same co-ordinates are recorded in the headers for all of the exposures and no indication as to the dithering offset is recorded.
- A target is re-acquired at a later epoch for further examinations, the re-acquisition may not be precise, but the recorded co-ordinates reflect the desired position (i.e., that of earlier exposure), not the actual position.

It is important to realise that the problems do not stem from some intrinsic lack of precision, in principle *relative* offsets can be accurately measured to within a fraction of a PC pixel (see STScI on-line Observation Logs documentation, M. Lallo 1996), but from inconsistently recorded positions<sup>2</sup>.

The information required must exist, at least in the HST engineering data. Since October 20, 1994, observation logs (often referred to as "jitter" files) for all exposures have been

---

<sup>1</sup>The are in fact several possible tabulated co-ordinates that can be considered (eg. the V1 axis co-ordinates in the HST science table or the "crval" co-ordinates in the "wfpc2.primary\_data" table) but none proved to be reliable

<sup>2</sup>A related problem here is that the CD matrices, which allow, for instance, SAOimage to convert pixel co-ordinates to RA and DEC given a reference pixel, recorded in the headers suffer the same problems as the pointing information. Hence measurements which depend upon the CD matrices are not necessarily reliable when very high precision is required.

produced by the Observatory Monitoring System, an automated software system which interrogates the HST engineering telemetry and correlates the time-tagged engineering stream with the scheduled events data. These logs contain tabulated pointing information as a function of time, from which we may calculate the mean and standard deviation, along with other diagnostics which give an indication as to the quality and reliability of the exposure.

Hence the *jitter co-ordinates* (RA, DEC and ROLL ANGLE) for all exposures were extracted along with other useful information (see associations tables). The provision of this information alone should greatly assist archive users carrying out data reduction. The ST-ECF has also undertaken to generate jitter files for exposures pre-dating October 20, 1994, so that jitter co-ordinates will exist for all WFPC2 exposures.

## 4. Grouping with Jitter Information

### 4.1. Member Types

Before an exposure can be considered as a group member it has to be assigned a "member flag". This is necessary because we only want to process those exposures for which we are confident that the pointing information is accurate (and there are no other anomalies). These exposures are flagged "P". The remainders are mostly flagged "G" (Groupable) except in those cases where there are indications that it is not even meaningful to group the exposures, in which case they are flagged "B" (Bad).

There are a number of other flags which indicate whether an exposure is suitable for automatic processing. The following conditions lead to an exposure being considered to be unprocessable (i.e., they have flag "G" or "B").

A "G" flag is assigned when:

- The exposure was taken in parallel mode.
- The exposure was not taken in "FINELOCK" mode.
- There was a loss of lock during the exposure.

A "B" flag is assigned when:

- Slewing occurred during the exposure.
- The aperture field is null in the jitter file.
- No mean RA, DEC, or ROLL can be extracted from the jitter file.

A restriction was also placed upon the standard deviation in RA, DEC and ROLL derived from the jitter files (which reflects the movement of the reference pixel during the observation and will effect the PSF. It is required that the RA and DEC have  $\sigma < 0.1$  PC pixels ( $\sim 0''.005$ ); exposures with larger jitter cannot satisfy the subgrouping criteria and are assigned a "G" flag. Similarly for ROLL,  $\sigma < 7''.2$  is required.

### 4.2. Grouping Criteria

We have adopted a very conservative approach: where there is any uncertainty in the extracted jitter information we do not set the member flag to "P".

As discussed in section 2.1, we anticipate most exposures to be arranged according to some kind of dithering strategy. Therefore we proceed by firstly grouping together all those exposures -taken within the same HST "visit", in the same filter and by the same PI— which are offset from one another by a distance of less than  $\sim 25$  PC pixels, which should be large enough to account for most dithering strategies (in fact the association may be



much larger than 25 PC pixels in diameter, it is only necessary that the nearest neighbour of each exposure is within this distance).

We then identify those exposures which are exactly registered (within  $\sim 0.10$  PC pixels) and place them in subgroups for CR removal. Tests show that CR rejection is reliable and the PSF is not degraded for exposures which are aligned to within 0.1-0.2PC pixels of one another.

The roll angle is restricted so that no two frames in the same association have a difference in roll angle<sup>3</sup> large enough to cause a shift in pixel position of more than 0.1 PC pixels in the pixels most distant from the roll axis (which works out at  $\sim 3''.6$ ).

#### 4.3. Association Types

As a result of the above, associations may contain varying numbers of subgroups and "lone" exposures. The existence of lone exposures has implications for the processing of the association as they cannot easily be CR cleaned. Moreover, if there is only one subgroup (i.e., no dither strategy was apparent) then no higher resolution image can be obtained via drizzling (see Section 6). We have therefore identified a number of different association types depending on the grouping:

Table 1. Association types.

Asn Type	Exposures	WFPC2 pipeline
0	a single "B" exposure or 1 or more "G" exposures	OTF <sup>a</sup> of all the exposures
1	1 Single "P" exposure <sup>b</sup>	OTF of all the exposures
2	$N$ perfectly aligned "P" exposures <sup>b</sup>	OTF + CR Rejection
3	$N$ groups of $M$ perfectly aligned "P" exposures <sup>b</sup>	OTF + CR Rejection and Coaddition (Drizzling) of all the exposures
4	$N'$ groups of $M$ perfectly aligned + $N''$ sparse "P" exposures <sup>b</sup>	OTF + CR Rejection and Coaddition (Drizzling) of the $N' \times M$ exposures and OTF of the $N''$ sparse exposures
5	$N''$ sparse "P" exposures <sup>b</sup>	OTF of all the exposures

<sup>a</sup>OTF stands for On The Fly Recalibration, a service already available at ST-ECF and CADC (Canadian Astronomy Data Center)

<sup>b</sup>plus 0 or more "G" exposures logically belonging to the association and for which really accurate pointing information is not available

#### 5. The WFPC2 Associations Relational Scheme

All the jitter information, extracted keywords and computed values (like the RA, DEC and ROLL averages and standard deviations), are stored in a relational database table called *jitter\_member*.

The resulting associations, built using the information stored both in the *jitter\_member* table and in other HST database tables, are stored in two tables:

<sup>3</sup>The V3 angle in the jitter files.

- the *hst\_associations* table, containing the association identifier, the total exposure time, the total number of "P" exposures within the association, the pointing coordinates of the leader<sup>4</sup> as required by the PI, and other fields describing the association (e.g., filter, proposal id, etc.).
- *hst\_association\_members* table, containing information relevant to the single exposure, the association identifier, the pointing information as computed from the jitter files, and, most importantly, the computed shifts in terms of X and Y PC pixels of the current exposure with respect to the so called "association leader" exposure.

## 6. The Automatic Pipeline

The WFPC2 pipeline is driven by an association file, which is built on-the-fly at the time of the archive request submission by a simple query to the *hst\_association\_members* table. The association file is composed of the dataset names, the member flags, the shifts (X and Y), and the sub-group number of all the exposures belonging to the association.

The WFPC2 pipeline consists of the following steps:

1. Run the On-The-Fly Recalibration on all exposures in the association
2. Run the *crrej* STSDAS IRAF task on any sub-group with at least 2 members
3. Run the *drizzle* IRAF task to co-add all the cosmic ray free images obtained with the previous step—if there are at least 2 such images. The shifts to be applied are provided by the association file.

## 7. Results/Conclusions

The jitter files proved to be a reliable source of pointing information for the Hubble Space Telescope.

It was therefore possible to define and compute associations of WFPC2 exposures. That is, the ST-ECF Archive User no longer needs to download all the exposures in a certain field to be able to work out, after hours of tedious work, what the shifts within such observations are, and which exposures can undergo the cosmic ray rejection algorithm. The shifts and the orientation are pre-computed for him/her.

ST-ECF has now a pipeline in place to automatically produce a final product out of any WFPC2 association. Such a product consists of OTF recalibrated, cosmic ray cleaned exposures co-added in a resolution-enhanced mosaic, according to the type of association selected.

Indeed, the output products of the WFPC2 association pipeline show in all their extent, especially for long total exposure times, the beauty of any high signal to noise ratio image, revealing faint objects otherwise invisible on a single, cosmic ray-covered, image.

## References

- Dickinson, M., & Fosbury, R., 1995, *ST-ECF Newsletter*, 22, 14  
Hook, R. N., 1995, *ST-ECF Newsletter*, 22, 16  
Leitherer et al., 1995, *HST Data Handbook*, Version 2.0 (Baltimore: STScI)

---

<sup>4</sup>The leader being defined as the exposure with the maximum number of neighbours within a limiting radius of around 0.15 PC pixels



## Drizzling Dithered WFPC2 Images—A Demonstration

Max Mutchler and Andrew Fruchter

*Space Telescope Science Institute, 3700 San Martin Drive, Baltimore, Maryland  
21218; e-mail mutchler@stsci.edu, fruchter@stsci.edu*

**Abstract.** The IRAF/STSDAS package **dither** and its primary task **drizzle** were created by Andrew Fruchter and Ivo Busko to reconstruct dithered WFPC2 images, and remove cosmic rays from singly-dithered images. Drizzling is akin to shifting-and-adding with a variable pixel size. The **drizzle** task was initially developed for the Hubble Deep Field project. Here, its use is demonstrated cookbook-style, using archival images of the edge-on galaxy NGC 4565 from Hubble Space Telescope (HST) program 6092.

### 1. Introduction

Although the HST and WFPC2 optics now provide an excellent PSF, the CCDs under-sample the images. On the three WF chips, the width of a pixel equals the FWHM of the PSF in the near-infrared, and greatly exceeds it in the blue. The image quality can be improved by combining sub-pixel dithered images. If the dithers are particularly well-placed, the pixels from each image can simply be interlaced on a finer grid. But in practice, imperfect offsets and the geometric distortion can make interlacing impossible.

For purposes of combining the dithered images of the Hubble Deep Field, Richard Hook and Andrew Fruchter developed a new technique known as variable-pixel linear reconstruction, or “drizzling”. Drizzling can be thought of as a continuous set of linear functions that vary smoothly from the optimum linear combination technique—interlacing—to the old standby, shift-and-add. The degree to which one must depart from interlacing and move towards shift-and-add is determined by the nature of the input data. Drizzling naturally handles both missing data and geometric distortion, and can largely remove the effect on photometry produced by the geometric distortion of the WFPC2. For more background, see the articles listed in the reference section.

This paper shows how these tasks can be used to remove cosmic rays from singly-dithered images (i.e., in which only one exposure is taken at each dither position). The **dither** package in IRAF/STSDAS contains the following tasks:

<b>precors</b>	- Remove cosmic rays prior to cross-correlation
<b>crossdriz</b>	- Builds 1-group cross-correlation image (shift + rotation)
<b>offsets</b>	- Builds 4-group cross-correlation image (shift only)
<b>shiftfind</b>	- Finds x and y shifts in a cross-correlation image
<b>avshift</b>	- Averages the shifts measured on 4 WFPC chips
<b>rotfind</b>	- Finds rotation angle from a set of cross-correlation images
<b>drizzle</b>	- Perform linear image reconstruction
<b>blot</b>	- Inverse of drizzle
<b>invert</b>	- Inverts the weight masks
<b>deriv</b>	- Takes derivative of blotted images
<b>drizcr2</b>	- Combines cosmic ray masks and removes bad pixels

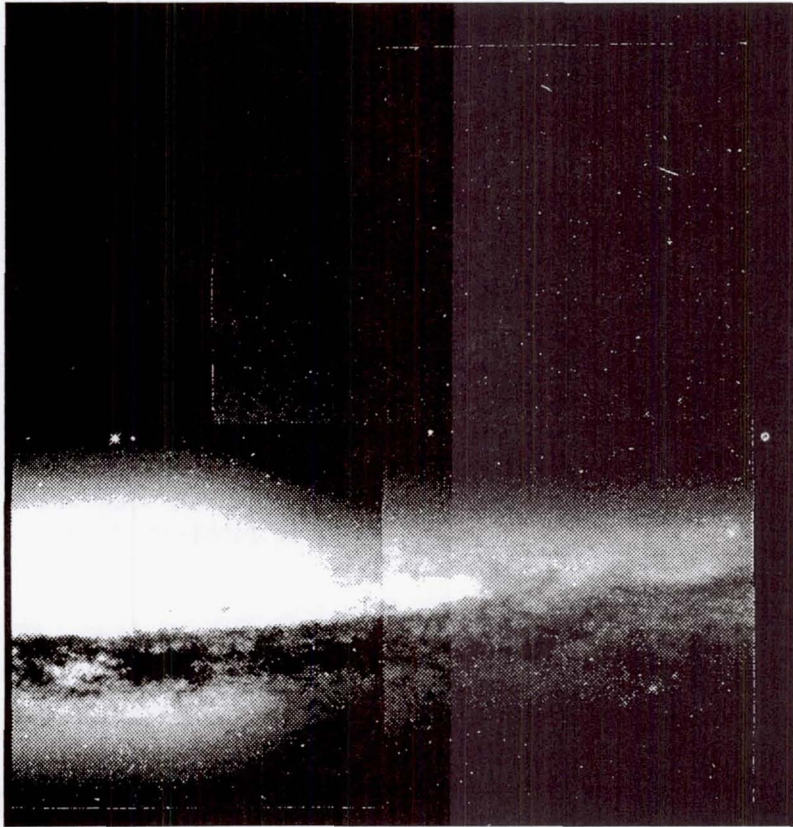


Figure 1. Mosaicked F814W image of NGC 4565 prior to drizzling—note the abundance of cosmic ray contamination. We will process only the WF2 chip in this example.

Note that the last three tasks listed above will not be available in IRAF/STSDAS until the next release. Also, the scripts `cosmic.calc` and `cosmic2.calc` must reside in your working directory for use by `drizcr2`. Scripts named `run*.cl` were used to ensure proper parameter settings at critical steps.

## 2. Measuring Shifts Between Dithered Images

The drizzling process is very sensitive to the accuracy of the shifts used, so we begin by carefully measuring the shifts between the dithered exposures. Our sample dataset is three singly-dithered WFPC2 images of the edge-on galaxy NGC 4565 from HST program 6092 by Keith Ashman (archival rootnames U31S0101T, U31S0102T, and U31S0103T). We will only work on the WF2 part of the image here.

### 2.1. Clean the Input Images

The measurement of shifts is often improved if some attempt to remove cosmic rays from the input images is made. Remove cosmic rays from the input images with `precor`. The clean images produced by `precor` should be used only for creating the cross-correlation images and measuring shifts, and NOT used as the input images in later stages.

```
di> precor *.hhh
```



## 2.2. Cross-correlate the Dithered Input Images

Create cross correlation images with the `crossdriz` task. We will use the first image as our reference image, and cross-correlate it with the 2nd and 3rd images:

```
cl> cl < runcrossdriz.cl
crossdriz.coeffs ="drizzle$coeffs/trauger"
crossdriz.lambda=814
crossdriz ../102[2] ../101[2] 2x1
crossdriz ../103[2] ../101[2] 3x1
```

If we were measuring shifts for all four WFPC2 groups at the same time, the `offsets` task would be used instead of `crossdriz`.

## 2.3. Measure the Shifts Using the Cross-correlation Images

Use `shiftfind` to measure the shifts using the cross-correlation images (\*x1.hhh). The output is written to a file named `shifts.out`. The shifts must be used consistently while running the `drizzle` and `blot` tasks later in this procedure:

```
cl> shiftfind *x1.hhh shifts.out
cl> more shifts.out
2x1.hhh    4.9714 0.0326    5.0206 0.0253
3x1.hhh    -5.0258 0.0330   -5.0148 0.0257
           x shift      y shift
```

In this example, we are measuring the shifts between WF2 images only. If we were measuring shifts on all four WFPC2 chips, we would run the `avshift` task at this point to average the shifts measured over all four chips:

```
cl> avshift shifts.out 0 > avshifts.out
```

## 3. Begin the Drizzling Procedure

Now that we have measured accurate shifts, we can begin drizzling. Create a subdirectory where we will work on one group (WF2 in this case) at a time. Then we `drizzle` the input images onto a finer grid, and unshift them. The output drizzled images are named \*p1.hhh here to indicate that they were drizzled with `pixfrac=1.0` and to distinguish them from the final drizzled image (which will have `pixfrac=0.6` and be named \*p06.hhh). Remember to set `stdimage=imt2048` to display the drizzled images on their new finer grid:

```
cl> cl < rundriz1.cl
drizzle.lambda=814
drizzle.wt_scl="exptime"
drizzle.expkey="exptime"
drizzle.pixfrac=1.0
drizzle.scale=0.5
drizzle.outnx=1600
drizzle.outny=1600
drizzle.coeffs=""
drizzle ../101.hhh[2] 101_p1 outweig=101_p1w xsh=0.0 ysh=0.0
drizzle ../102.hhh[2] 102_p1 outweig=102_p1w xsh=4.971 ysh=5.021
drizzle ../103.hhh[2] 103_p1 outweig=103_p1w xsh=-5.026 ysh=-5.015
```

#### 4. Create a Median Image to Remove Cosmic Rays

Now we will combine the unshifted images from the previous step such that the median pixel value is used. The highest pixel values will be rejected, thereby removing cosmic rays.

##### 4.1. Invert the Weight Images

Before we can combine the images, we must invert the output weighting images produced by `drizzle` (\*plw.hhh), since `gcombine` expects pixel values where good=0 and bad=1:

```
cl> invert
Mask(s) to be inverted: *plw.hhh
```

##### 4.2. Combine the Images

Use `gcombine` to create the median image from the WF2 I images (wf2i\_med.hhh) using the inverted weight masks (\*plw\_inv.hhh):

```
fo> gcombine *p1.hhh wf2i_med groups=1 masks=*plw_inv.hhh
      reject=minmax combine=median weight=none scale=exposure
      expname=EXPTIME nlow=1 nhigh=1 rdnoise=5.2 gain=7.5
```

#### 5. Blot the Median Image Back to the Input Plane

Use `blot` to make copies of the median image that are shifted back to the positions of the original input images. The output blotted images will be scaled to the input image exposure times and named \*bl.hhh:

```
cl> cl < runblot.cl
blot.lambda=814
blot.scale=0.5
blot.outnx=800
blot.outny=800
blot.expout=600
blot.coeffs=""
blot wf2i_med 101_bl xsh=0.0 ysh=0.0
blot wf2i_med 102_bl xsh=4.971 ysh=5.021
blot wf2i_med 103_bl xsh=-5.026 ysh=-5.015
```

##### 5.1. Take the Derivative of the Blotted Images

Take the spatial derivative of each of the blotted images in preparation for the following step. Make sure you have loaded ALL the tasks called by `deriv`.

```
di> deriv
Image(s) for cosmic ray cleaning (@inlist-deriv): *_bl.hhh
```





Figure 2. A section of one of the three dithered F814W images of NGC 4565 with cosmic rays (above), and the final drizzled image with cosmic rays removed (below).



## 6. Combine Cosmic Ray Masks and Remove Bad Pixels

The `drizcr2` task compares the original images to their blotted counterparts. Any pixels that show a significant difference are flagged as bad pixels in the mask it creates. This task iterates to find bad pixels adjacent to others it has already found, since most cosmic ray hits involve many adjacent pixels. It uses the files `cosmic.calc` and `cosmic2.calc`, which must reside in your working directory. Compare the original images with their corresponding output masks to check that only truly bad pixels are being flagged:

```
cl> more cosmic.calc
if (abs(im1-im2) .gt. 0.4*im3+3.5*sqrt(7*abs(im2)+(7*2)*(7*2))/7) then 0 else 1

cl> more cosmic2.calc
if (im4 .lt. 9) then 0 else 1

cl> drizcr2
Image(s) for cosmic ray cleaning: ../10*.hhh
Group being cleaned: 2
```

## 7. Final Drizzling of the Input Images

Finally, re-drizzle the input images with the masks you have created, with a smaller `pixfrac` on a finer grid, with the geometric distortion coefficients applied:

```
cl> cl < rundriz2.cl
drizzle.lambda=814
drizzle.wt_scl="exptime"
drizzle.expkey="exptime"
drizzle.pixfrac=0.6
drizzle.scale=0.5
drizzle.coeffs="drizzle$coeffs/wf2-trauger"
drizzle.fillval=0
drizzle.outnx=1600
drizzle.outny=1600
drizzle ../101.hhh[2] wf2i_p06 outweig=wf2i_p06w in_mask=101_cr
xsh=0.0 ysh=0.0
drizzle ../102.hhh[2] wf2i_p06 outweig=wf2i_p06w in_mask=102_cr
xsh=4.971 ysh=5.021
drizzle ../103.hhh[2] wf2i_p06 outweig=wf2i_p06w in_mask=103_cr
xsh=-5.026 ysh=-5.015
```

The final output image is then `wf2i_p06.hhh`—the WF2 part of the F814W (I) image drizzled with a pixel fraction of 0.6. The process described here could now be repeated for each CCD and each color.

## References

- Adorf, H., 1995, ST-ECF Newsletter, 23, 19
- Dickinson, M., & Fosbury, R., 1995, ST-ECF Newsletter, 22, 14
- Hook, R., & Fruchter, A., 1997, ST-ECF Newsletter, 24, 9
- Leitherer, C. (ed.), 1995, HST Data Handbook, version 2.0, Ch. 41, 520



## Calibrating the WFPC2 Astrometry for MDS

Kavan U. Ratnatunga, Eric J. Ostrander, and Richard E. Griffiths

*Department of Physics, Carnegie Mellon University, Pittsburgh, PA 15213*

### Abstract.

The HST Medium Deep Survey has optimized an automated procedure to associate and stack WFPC2 data. The coordinates listed in HST WFPC2 image and/or jitter file headers are often found to be insufficient to stack images for cosmic ray removal. We discuss results from software developed for the HST Medium Deep Survey (MDS) pipeline to evaluate these shifts by cross-correlation of the images. We will also discuss the distortion of the pre-cool-down WFPC2 field and attempts to derive absolute coordinates for MDS WFPC2 observations using the USNO-A1.0 half billion object catalog.

## 1. Introduction

The Hubble Space Telescope (HST) Medium Deep Survey (MDS) Key Project (Griffiths et al. 1994) includes pure parallel observations of a large number of random fields extending over multiple years and focuses on the statistical properties of all measurable objects. The processed MDS database in September 1997 is about 500 fields (one square degree) with well over one hundred thousand objects. The MDS database has been made available on the MDS web-site in the HST archive (<http://archive.stsci.edu/mds>) and also mirrored at the Canadian Astronomy Data Center CADC (<http://cadwww.dao.nrc.ca/mds>). Much effort in the MDS project was devoted to developing a pipeline for associating and stacking WFPC2 data (Ratnatunga et al. 1995). An automated procedure was required, not only for practical considerations of processing a very large number of both pure parallel and archival fields, but also to maintain uniformity in the statistical properties of the MDS database. These improvements are particularly important for quantitative analysis of the faintest extended sources with low signal-to-noise.

Images were originally stacked using WFPC2 image header information or jitter files when available. However some of the resulting stacks which looked acceptable to the "eye", gave unexpected results when the images were analyzed using the 2-dimensional image analysis procedure developed for the MDS (Ratnatunga et al. 1997). In a well stacked field, jitter and any small errors in the tinytim PSF used in the analysis results in a "half-light radius" estimate for stellar images which are typically about 20 mas or 0.2 of a WFC pixel. Stellar images were well resolved from extended galaxy images with half-light radius larger than about half a pixel. However, in few of the fields stellar images yielded a half-light radius estimate of about one WFC pixel. Comparison of magnitudes in such a field with another overlapping field also highlighted a serious problem in the stacking.

## 2. Estimating Shifts Between Images

A study of these stacks showed that the problem was caused by errors of order one WFC pixel in the shifts derived from the jitter file headers (.jih). The jitter file information was assumed to be more reliable since they are derived from the engineering telemetry

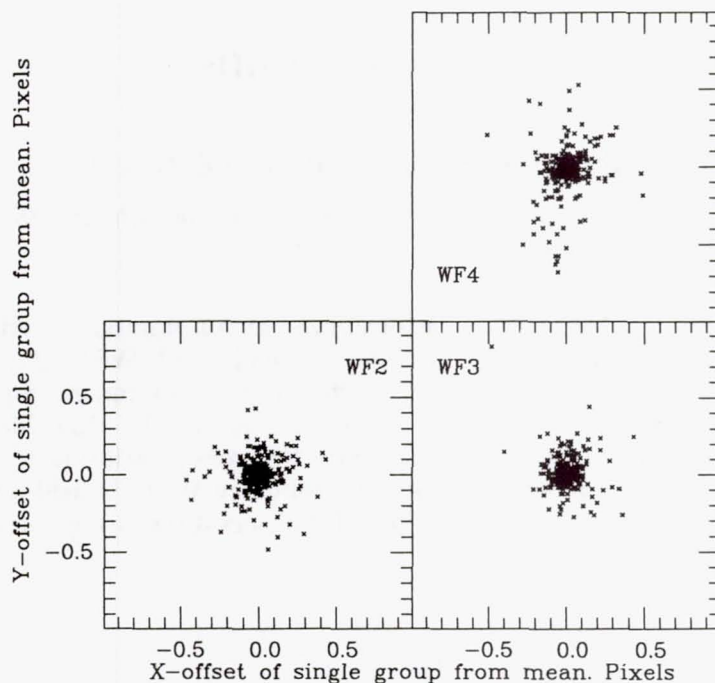


Figure 1. Consistency of shifts estimated for individual WFPC2 chip relative to the mean for datasets in dithered stacks. The slightly larger vertical scatter in WF4 maybe caused by the many bad columns in that CCD. The size of the region shown is one pixel.

taken during the observation, rather than from the requested coordinate which is put in the WFPC2 raw data file (.d0h) header.

It was not practical to determine the shifts interactively for a very large number of fields using IRAF/STSDAS. Cross-correlation was the only hope of determining these shifts by an automated procedure. The image cross-correlation algorithm needs to operate on unstacked, calibrated data, allowing for the presence of cosmic rays which outnumber and are much brighter than the faint galaxy and stellar images in the pure parallel fields. Also of concern are masked columns of bad pixels, hot pixels and the occasional saturated stellar images which could distort the cross-correlation.

A cross-correlation is derived independently for each of the three WFC CCD chips rotated to the WFC-4 orientation. Cross-correlations with very poor signal are ignored. The weighted sum of the acceptable cross-correlation is used to derive the adopted shift for the dataset. Consistency between the shifts for each the individual groups in comparison to the total gives measure of reliability. All stacks in the full MDS database have been checked and any field that may have suffered from poor stacking has been reprocessed.

We will not go into the details of the algorithm (any interested reader should contact the first author), but illustrate the results. The difference between the adopted shift for the dataset and the shift from each individual WFPC2 chips is less than half a pixel with an rms of under a tenth of a pixel as shown by the crosses in figure 1.

We can investigate the magnitude of the shift errors by considering only the most reliable datasets which gave consistent (within half-pixel) shift for all groups. We see in figure 2 that only the information from the jitter files for non-dithered primary observations can be assumed to be reliable. Shift errors for dithered observations are significantly larger



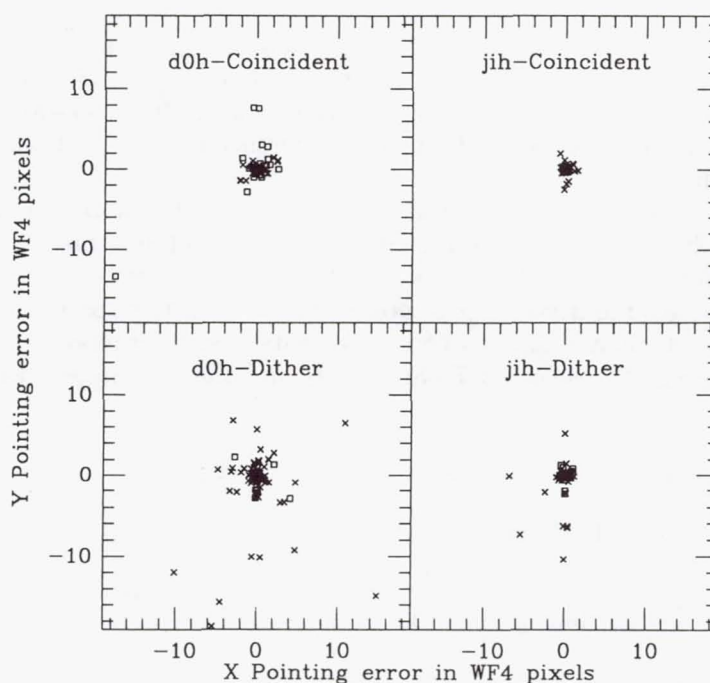


Figure 2. The relative shift errors between WFPC2 Datasets. Symbols indicate observation type: Parallel (cross); Primary (square)

than for coincident observations (see table-1). The error is also larger for pure parallel observations over similar primary observations.

Table 1. RMS shift errors between HST WFPC2 Datasets.

Type of Observation		.d0h header Info.			.jih jitter Info.		
		Number of datasets	x rms Pixels	y rms Pixels	Number of datasets	x rms Pixels	y rms Pixels
Parallel	Coincident	893	0.22	0.15	552	0.17	0.23
Primary	Coincident	330	1.28	1.50	55	0.08	0.10
Parallel	Dither	193	4.32	4.53	116	1.09	1.75
Primary	Dither	170	0.51	0.51	113	0.28	0.39

These errors, which result from coordinate errors in the guide stars and the mapping of the FGS, are not unexpected. Dithered images require the guide stars to be at different location of the FGS, and the derived coordinates then suffer from any error in the mapping of the FGS. "Peakups" in the primary observation could give unpredictable pointing shift in the related pure parallel observation. These errors would need to be recognized when stacking STIS and particularly NICMOS pure-parallel observations. This would be a harder task than for WFPC2 to solve by cross-correlation since the number of observed objects in the limited field of view is much smaller. If a broad-band WFPC2 observation is available in parallel, it could probably be used to constrain the shifts in the primary pointing during the observation.

### 3. WFPC2 Pre-cool-down Distortion Map

The largest strip of uniformly observed WFPC2 fields (Groth et al. 1994) was taken before the detector was cooled down from  $-78^{\circ}\text{C}$  to  $-88^{\circ}\text{C}$  on April 23, 1994. The WFPC2 distortion mapping derived from F555W observations taken after cool-down was found to be inadequate for these pre-cool-down data. The difference is most probably caused by the change in temperature.

The IDT WFPC2 distortion map derived from globular cluster  $\omega$  Cen observations has 20 coefficients for each CCD giving a total of 80 for the camera (Holtzman et al. 1995). Since these coefficients don't represent physical parameters it is not easy to correct or investigate to determine the changes required for pre-cool-down data. In the absence of sufficient pre-cool-down data to constrain a mapping of 80 coefficients, a simpler model with 7 parameters for each CCD was used. The selected 7 parameters and the parameter identification used in Table 2 are:

- (1) [g2] The pixel scale in arc seconds
- (2) [s2] Coefficient of the main quadratic term in the distortion.
- (3,4) [xc,yc] coordinates of the center of the distortion map in pixels. This is close but not exactly at the central [400,400] pixel of each WFPC2 CCD chip.
- (5,6) [x0,y0] coordinates the CCD chip origin from metric reference in arc seconds.
- (7) [th] Orientation of the CCD in degrees. These are the differences from the nominal rotation angles, multiples of  $90^{\circ}$ , and are less than  $0.5^{\circ}$ .

The adoption of the Cartesian metric aligned with the orientation of the PC chip and using reference pixel WF3 [133,149] as the origin removes three parameters. The MDS WFPC2 distortion model has therefore only 25 free parameters, rather than the 80 coefficients used in the Holtzman et al. (1995) distortion map.

To derive the coefficients we selected the 28 Groth-Westphal strip fields and 5 other fields observed before April 1994 which overlap. The selection and orientation of the overlap are not ideal for deriving the distortion, but we had to use what was readily available. To constrain the relative pointing on a scale larger than the WFPC2 an iterative procedure was used to identify objects in each field which have coordinates in the USNO-A1.0 catalog of a half billion objects in the sky. This catalog is very useful since it is currently the only catalog which will ensure at least a few objects in each WFPC2 field. On average one could expect 25, but the number will clearly be strongly dependent on Galactic latitude. At Galactic latitude  $+60^{\circ}$ , corresponding to the Groth-Westphal, strip we found on average 3 objects in each WFPC2 field. In addition to the reference stars we cross-identify objects in the MDS catalogs in the overlapping regions of the fields.

A global maximum likelihood solution was derived. The model included the 25 parameters for the WFPC2 distortion map and 3 free parameters for each WFPC2 field included in the solution. For example, when 33 fields are used there are a total of  $25 + 3 \times 33 = 124$  free parameters. The likelihood function assuming Gaussian errors is integrated over the USNO-A reference stars and the coordinates of cross-identified object in the field-overlap regions. The errors of the WFPC2 centroids was provided by the MDS Maximum Likelihood image analysis software (Ratnatunga et al. 1997). We adopt a  $0.3''$  rms error for the USNO-A1.0 coordinates (Monet et al. 1996).

Preliminary solutions with error estimates for both before and after the WFPC2 cool-down in wide band filters F606W and F814W are given on Table 2. A single iteration is used to reject any cross-identification which shows a very large ( $> 5\sigma$ ) residual and could be suspected to be a false identification. Hardly any of the USNO-A identifications are



Table 2. MDS WFPC2 distortion model coefficients

		Pre-cool-down				Post-cool-down			
		F814W-78c		F606W-78c		F814W-88c		F606W-88c	
WFPC2 Fields		33		30		31		20	
USNO-A stars		135( 135)		84( 84)		582( 582)		285( 287)	
MDS Crosssids		1416(1525)		1399(1441)		6159(6576)		3474(3603)	
G	id units	+/-		+/-		+/-		+/-	
1	[1] g2 mas	45.422	0.028	45.330	0.035	45.498	0.013	45.449	0.020
2	[1] s2 5.E-9	6.49	0.90	6.76	0.82	8.52	0.69	7.71	1.05
3	[1] xc pixel	365.0	13.7	375.1	18.9	376.7	8.2	396.3	18.5
4	[1] yc pixel	364.0	15.7	350.0	14.1	391.1	7.4	386.4	11.1
F	[1] x0 arcsec	8.214		8.327		8.031		8.054	
F	[1] y0 arcsec	7.947		8.066		7.721		7.804	
F	[1] th degree	0.000		0.000		0.000		0.000	
5	[2] g2 mas	99.451	0.053	99.237	0.075	99.480	0.013	99.441	0.022
6	[2] s2 5.E-9	6.71	0.68	6.81	1.12	7.05	0.14	7.90	0.19
7	[2] xc pixel	334.2	10.5	320.5	14.8	385.2	1.7	382.3	2.0
8	[2] yc pixel	408.2	8.8	416.6	30.3	408.7	2.1	440.2	5.1
9	[2] x0 arcsec	12.766	0.020	12.879	0.033	12.625	0.007	12.664	0.019
10	[2] y0 arcsec	5.207	0.010	5.339	0.009	5.089	0.006	5.099	0.017
11	[2] th degree	0.505	0.009	0.506	0.009	0.500	0.007	0.504	0.010
12	[3] g2 mas	99.288	0.050	99.070	0.067	99.450	0.013	99.380	0.022
13	[3] s2 5.E-9	7.52	0.67	7.57	1.08	6.90	0.13	7.04	0.20
14	[3] xc pixel	425.7	8.2	420.3	28.1	408.7	2.0	453.3	5.6
15	[3] yc pixel	453.9	10.2	454.1	18.4	399.7	1.6	391.9	2.3
16	[3] x0 arcsec	13.348	0.046	13.315	0.069	13.347	0.006	13.384	0.019
17	[3] y0 arcsec	14.856	0.043	14.823	0.066	14.829	0.006	14.811	0.017
18	[3] th degree	0.189	0.008	0.194	0.008	0.186	0.007	0.200	0.011
19	[4] g2 mas	99.455	0.066	99.168	0.086	99.462	0.014	99.376	0.039
20	[4] s2 5.E-9	8.87	1.24	7.63	1.47	6.62	0.15	6.91	0.26
21	[4] xc pixel	413.1	12.5	419.2	15.8	393.8	1.5	392.6	3.2
22	[4] yc pixel	378.2	7.3	367.8	31.9	403.8	1.8	395.6	8.9
23	[4] x0 arcsec	5.556	0.067	5.683	0.091	5.234	0.006	5.272	0.013
24	[4] y0 arcsec	14.557	0.071	14.675	0.118	14.587	0.007	14.739	0.012
25	[4] th degree	-0.280	0.047	-0.368	0.102	-0.369	0.007	-0.376	0.014

The metric coordinates (xm,ym) in arc-seconds for [G][xobs,yobs] from reference pixel [3][133,149] is given by the FORTRAN code

```

theta = mod(G-1,4)*pi/2. - th(G)/(180./pi)
x = xobs - xc(G)
y = yobs - yc(G)
r2 = x*x + y*y
xt = g2(G)*(xc(G)+(1.0d0 - 5.E-9*s2(G)*r2)*x)
yt = g2(G)*(yc(G)+(1.0d0 - 5.E-9*s2(G)*r2)*y)
xm = x0(G) + xt*cos(theta) - yt*sin(theta)
ym = y0(G) + xt*sin(theta) + yt*cos(theta)

```

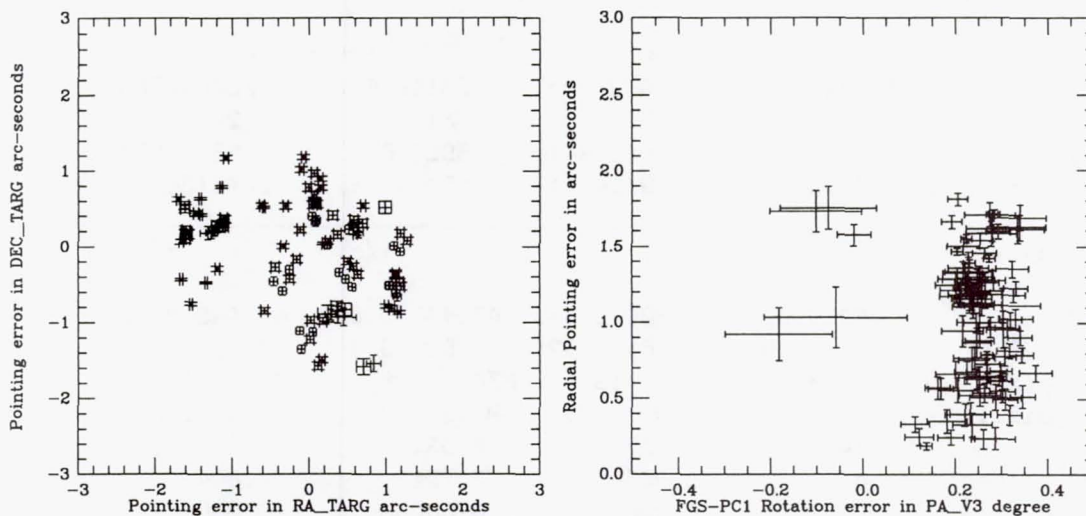


Figure 3. Accuracy of HST pointing.

rejected. However about 2% of the MDS cross-identifications are rejected. The number before rejection is given in parenthesis in Table 2.

We note that the plate scale has changed significantly between post and pre-cool-down models. A small decrease in the plate scale is also apparent between F814W and F606W filters.

The pre-cool-down solution decreases the  $\chi^2$  by a factor of 10 over using the standard Holtzman et al. (1995) solution on these data. The comparable accuracy post-cool-down solution is 20% better than the  $\chi^2$  derived adopting the Holtzman solution *for these data*. This was unexpected, considering the large decrease (80 to 25) in the number of parameters used in the distortion model. However, in order to avoid image analysis close to regions with rapid changes to the PSF and image distortion, the MDS catalogs filtered out objects with centroids within 10 pixels of edges of the pyramid and CCD. The more flexible Holtzman distortion map is probably required in these regions. The model would need to be used on the original  $\omega$  Cen data used to derive the Holtzman et al. (1995) calibration for an objective comparison. Our simpler model, with physically understandable parameters, will anyway be useful to monitor any changes in the distortion over time. This has not been done yet, and the software is available to the STScI or any other user interested in following up on this issue.

#### 4. Accuracy of HST Pointing

The solutions discussed above also provides an estimate for the correction to the HST coordinates of the WFPC2 pointing and orientation (PA\_V3). The coordinate differences are shown on the left in Figure 3. On the right we show the radial error and the error in the PA\_V3 orientation. The mean pointing error is about 1 arc-second. There appears to be a systematic relative difference of 0°3 between the adopted standard (PA\_V3-135.0) from the FGS and the orientation of the PC1 chip of the WFPC2. This error is comparable to the difference from right-angle rotations of the WFPC2 CCD chip orientations. The FGS system appears to be closer to the orientation of WF4 chip.

Estimates will be made for all of the HST pointings after the USNO-A2.0 or the GSC2 catalogs are made available referenced to the new global HIPPARCOS coordinate frame (Perryman et al. 1997). The current systems referenced to the much smaller FK5 catalog



are known to have systematic errors of order 1.0 arc seconds in few regions of the sky, comparable to the random errors of the HST pointing. Accurate absolute coordinates are needed for spectroscopic follow-ups and are useful to cross-identify objects in overlapping fields and ensure they are assigned the same coordinate identification.

## 5. Conclusion

WFPC2 image cross-correlation software was developed to derive relative shifts between WFPC2 observations. The shifts are derived independently for each WFPC2 group and are consistent to within 0.1 pixels rms.

We find that dithered observations and parallel observations have larger pointing errors relative to coincident and primary observations.

A simple, 25-parameter WFPC2 distortion map has been derived for pre-cool-down observations at  $-78^{\circ}\text{C}$ , and yields a  $\chi^2$  10 times smaller than the post-cool-down solution of Holtzman et al. (1995) on these data. Post-cool-down solutions have also been obtained for both F814W and F606W.

The mean pointing accuracy of the HST WFPC2 using the GSC1.1 catalog and the current FGS mapping appears to be about  $1''$ . A systematic difference of  $0.3''$  is measured between the FGS (PA\_V3-135) and the PC1 orientation.

**Acknowledgments.** This paper is based on observations with the NASA/ESA Hubble Space Telescope, obtained at the Space Telescope Science Institute, which is operated by the Association of Universities for Research in Astronomy, Inc., under NASA contract NAS5-26555. The Medium Deep Survey is funded by STScI grant GO2684 and daughters. We also thank USNO and CADC for making the large USNO-A catalog searchable over the World Wide Web.

## References

- Griffiths, R. E., et al., 1994, *ApJ*, 437, 67
- Groth, E. J., Kristian, J. A., Lynds, R., O'Neil, E. J., Balsano, R., & Rhodes, J., 1994 *BAAS*, 26, 1403
- Holtzmann, J. A., et al., 1995 *PASP*, 107, 156
- Monet, D., et al., 1996 in *USNO-A 1.0* Flagstaff: USNO
- Perryman, M. A. C., et al., 1997, in *The Hipparcos and Tycho Catalogues* (Noordwijk: ESA), 1, 311
- Ratnatunga, K. U., Griffiths, R. E., Neuschaefer, L. W., & Ostrander, E. J. 1995, *Proc. HST Calibration Workshop II*, eds. A. Koratkar and C. Leitherer (Baltimore: STScI), 351
- Ratnatunga, K. U., Griffiths, R. E., & Ostrander, E. J., 1997, in preparation

## HST Observations of the Gravitational Lens Systems HE 1104–1805 and J03.13

M. Remy, J.-F. Claeskens,<sup>1</sup> and J. Surdej<sup>2</sup>

*Institut d'Astrophysique, Université de Liège, Belgium*

**Abstract.** High angular resolution PC1 images of the gravitational lens systems HE 1104–1805 and J03.13 are presented. Using a method described in Remy et al. (1997a), optimal TinyTim PSFs are constructed to fit at best the lensed point-like components. The derived photometry of the GL components and the detection of the lens galaxy for HE 1104–1805 are discussed. *Textbook case* FOS spectra of J03.13 A and B clearly show that this double QSO is a cosmic mirage.

### 1. Introduction

The quasar HE 1104–1805 was discovered to be a gravitational mirage candidate with a redshift  $z = 2.303$  by Wisotzki et al. (1993, 1995). Prominent absorption lines in the spectrum of this quasar indicate the possible presence of galaxies at redshifts  $z = 1.6616$  (damped Ly $\alpha$ , FeII, MgII) and  $z = 1.320$  (MgII) along the line-of-sight (Smette et al. 1995). From the observed spectral variability, these authors report the signature of both intrinsic variations and changes due to microlensing. They stress the importance of direct observations of the lensing galaxy in order to model the macro-lensing configuration in detail.

On the basis of observations obtained with the NOT in February and March 1994, Grundahl et al. (1995) were the first to report the presence of a very red object between A and B at a distance of  $1''.15$  from A with  $I_c \sim 20.6$ , the probable lensing galaxy. This detection was subsequently confirmed on the basis of one single ESO NTT 3.5 m frame also obtained in February 1994. A full description of these ground-based NTT and NOT observations is given by Remy et al. (1997b).

Following this first set of observations, we have included HE 1104–1805 as a priority target in the framework of a study of gravitational lensing with HST. The corresponding direct imaging, data reduction, analysis and interpretation are briefly described.

In a search for gravitational lensing within a sample of highly luminous quasars (hereafter HLQs, Surdej et al. 1993), Claeskens et al. (1996) have reported the identification of a new candidate for the quasar J03.13.

Multiple direct CCD frames of J03.13 were taken in November 1995 through the F555W and F814W filters with the WFPC2 camera onboard HST. In addition, good S/N, low-resolution FOS spectra of J03.13 A and B were obtained in October 1996. A summary of all these data and their interpretation is also presented.

### 2. PC1 Direct Imaging of HE 1104–1805

One HST orbit was allocated to the planetary camera (PC1) observations of HE 1104–1805, which took place on November 23, 1995. Based on the photometry already reported for this

---

<sup>1</sup>Research Assistant (FNRS, Belgium)

<sup>2</sup>Research Director (FNRS, Belgium)



system from ground-based observations, our strategy was to obtain 2 exposures of 100 s with the F555W filter (nearly Johnson  $V$ ), 4 exposures of 200 s with F814W (nearly Kron-Cousins  $I_c$ ) and 2 additional 100 s exposures with F814W. We chose the ADC channel with  $14\text{ e}^-/\text{ADU}$  gain. Offsets by  $\simeq 1''.6$  were introduced between the exposures in order to optimally dither the QSO images and to more easily detect faint structures at small angular scales.

Composite F555W and F814W images of the quasar, made after proper re-centering and coaddition of the single PC1 frames, are shown in the upper panels of Figure 1. We immediately notice on the composite F814W image a diffuse object between A and B, identified as the lensing galaxy G. This object is not detected in the composite F555W image. The projected position of its peak is distant from A by about one third the angular separation ( $3''.193$ ) between A and B. Note that the galaxy is not exactly co-aligned with A and B.

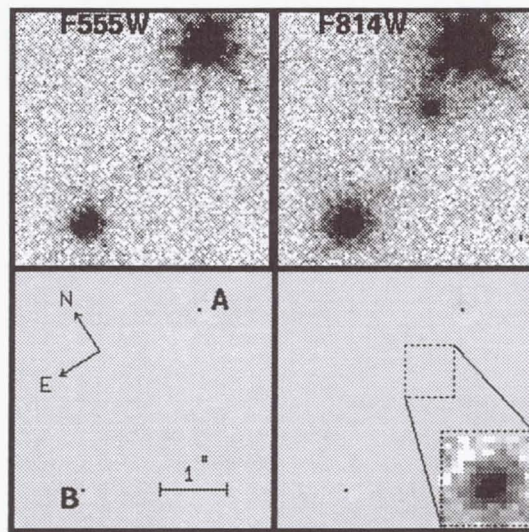


Figure 1. Composite F555W (upper left panel) and F814W (upper right panel) PC1 CCD frames of HE 1104–1805. From the F555W data, we only observe the two quasar components; the complex structure of the HST PSF is well seen. From the F814W observations, we detect the lensing galaxy G near the brightest component A. The lower panels correspond to the results of PLUCY deconvolutions using appropriate simulated TinyTim PSFs. An inset (zoomed by a factor 2) illustrates the deconvolved image of the galaxy with low cuts in the lookup table.

A set of approximately 100 simulated PSFs was computed by means of the TinyTim program (Krist 1997) for different values of the focus (Zernicke parameter  $Z_4$ ) and of the jitter of the telescope. These numerical PSFs were then fitted to the images of HE 1104–1805 A and B with an automatic procedure described in Østensen et al. (1997). Optimal values for the  $Z_4$  and the “jitter” parameters were then derived for each individual CCD frame. Due to the breathing of the telescope, excursions of up to  $7\text{ }\mu\text{m}$  were found for the focus ( $Z_4$ ) during the F814W observations. The optimal PSF was subsequently built with an oversampling factor of 10. An iterative procedure was used to address the problem of fitting the HST PSF peak after proper re-centering and re-binning of the final TinyTim PSF. Finally, the 2-channel PLUCY application program (Hook and Lucy 1994) was fed with those PSFs to deconvolve each single CCD frame of HE 1104–1805. The combined results of those deconvolutions are presented for the F555W and F814W filters in the lower panels of Figure 1. We also decomposed all images of HE 1104–1805 with two point-like components (their relative positions and brightnesses being the only free parameters) and one

additional exponential or gaussian profile with elliptical isophotes. After subtraction of the optimal model, we only observe insignificant residuals around the point-like components.

We have then followed the standard HST photometric procedure of integrating the flux of point sources in the classical  $0''.5$  aperture (Whitmore 1997) and rely upon the values of the PHOTFLAM keyword appearing in the header of the PC1 frames. We derived the individual magnitudes of HE 1104–1805 A, B in the Johnson *V* and Kron-Cousins *I<sub>c</sub>* systems (see Table 1) from the F555W and F814W in-flight magnitudes taking color corrections into account (Holtzman et al. 1995). The magnitude for the galaxy is derived in two steps. First we fit the images with two numerical PSFs and an exponential model for the galaxy. The measurements for the galaxy then result from the integration of the flux, remaining after the removal of the two fitted quasar components, using two apertures with radii  $0''.95$  and  $1''.35$ .

Object	A	B	G( $0''.95$ )	G( $1''.35$ )	B–A
<i>V</i>	16.74	18.48	>23	>23	1.74
<i>I<sub>c</sub></i>	16.33	17.93	20.93	20.88	1.60
$\theta$	$0''.0$	$3''.193$	$1''.03$	$1''.03$	$3''.193$

Table 1. Photometry and relative angular separation ( $\theta$ ) of the A & B components of HE 1104–1805 and of the lensing galaxy G. The photometric calibration is accurate to  $\pm 0.05$  mag. Radii of the aperture used to evaluate the magnitudes of the galaxy are given in parentheses. The error bars for the galaxy magnitude are estimated to be 0.1 mag.

### 3. PC1 Direct Imaging of J03.13

Following the ground-based identification of two resolved point-like images for the quasar J03.13 (see Claeskens et al. 1996), we proposed to image this interesting system with the WFPC2 planetary camera (PC1) through two wideband filters in order to search for possible structure of the QSO images at  $\simeq 0''.1$  angular scales and also to possibly set additional constraints on the lensing model. Based on the photometry reported for this system by Claeskens et al. (1996), we chose the ADC channel with  $14\text{ e}^-/\text{ADU}$  gain and integration times of 160 (resp. 400 and once 300) seconds, to avoid the saturation of the brightest QSO image through the F555W (resp. F814W) broadband filters. Given the two orbits allocated to this HST direct imagery program (ID 5958), our strategy has been to obtain 5 (resp. 6) such PC1 exposures with the F555W (resp. F814W) filters on November 28, 1995. Each of these exposures has been offset by  $\simeq 1''.6$  in order to optimally dither the QSO images and possibly detect faint structures at small angular scales.

Composite F555W and F814W images of J03.13 made after proper recentering and coaddition of the single PC1 frames are shown on the left panels of Figure 2.

On these composite and on each single CCD frames, J03.13 appears to be resolved as two point-like components. No trace of a third compact image or of a faint intervening galaxy is visible. The somewhat extended core and knotty-like structures seen for each single image component are essentially due to the complex shape of the combined “HST + WFPC2 + filters” point spread function (PSF). These images have been analysed using the same procedure as for the case of HE 1104–1805 discussed above.

Combined results of the PLUCY deconvolutions are presented for the F555W (resp. F814W) filters in the upper (resp. lower) right panels of Figure 2. Given that TinyTim PSFs are not more accurate than a few tenths of a percent, the very faint residuals seen near J03.13 A and B on the deconvolved images turn out to be non significant. Using the PLUCY deconvolution algorithm, the magnitude difference between the two unresolved components is found to be  $2.14 \pm 0.03$  and  $2.16 \pm 0.03$  mag for the F555W and F814W filters, respectively.



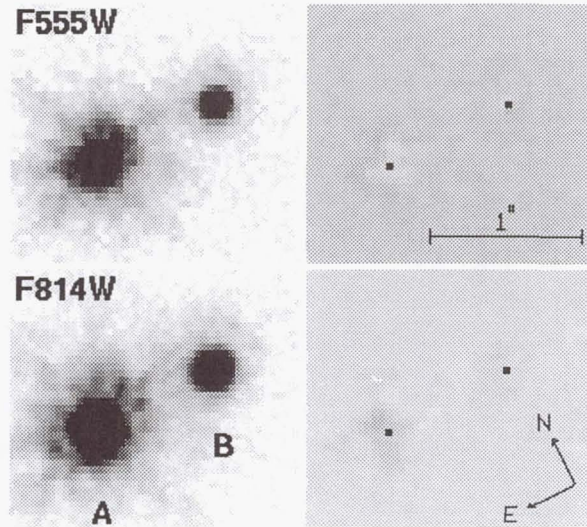


Figure 2. Composite F555W (upper left panel) and F814W (lower left panel) CCD frames of J03.13 A and B. The right panels correspond to the results of PLUCY deconvolutions using appropriate simulated TinyTim PSFs (see text). All four subimages have been normalized to the peak maximum of the A component. The faint residuals seen on the deconvolved images are well below 0.3%.

We also used the optimal TinyTim PSFs selected above and the automatic photometric fitting technique described in Østensen et al. (1997) to decompose all images of J03.13 with two point-like components, their relative positions and brightnesses being the only free parameters. After subtraction of the best fitted double PSFs, no significant residuals are seen. The angular separation between the two components is found to be  $0''.849 \pm 0''.001$  and the magnitude difference  $\Delta m = 2.14 \pm 0.03$  mag for both I and V.

We have derived the integrated magnitudes of J03.13 to be  $V = 17.3$  and  $I = 16.8$  mag, each  $\pm 0.1$ .

#### 4. FOS Observations of J03.13

To definitely prove the spectral similarity between the J03.13 A and B images ("to be or not to be lensed"), we have taken on October 28, 1996 FOS spectra at the positions of these two components, and at a third position C, symmetric from B with respect to A. These FOS/RD spectra were obtained with the grating G650L (central wavelength of  $4400 \text{ \AA}$ , FWHM  $\simeq 30.5 \text{ \AA}$ , COSTAR deployed) and the small  $0.5$  (actually  $0''.43$ ) circular aperture. The spectra of J03.13 A and B are shown in Figure 3.

We find that, apart from a multiplicative constant of  $7.5 \pm 0.7$  (corresponding to a magnitude difference  $\Delta m = 2.2 \pm 0.1$ ), the spectra of J03.13 A and B are identical. We have also reproduced in Figure 3 the residual spectrum  $A - B \times 7.5$  showing that, apart from a few datapoints near the emission line peaks—which are undersampled by the FOS—and the MgII absorption lines at  $z = 1.085$ , the spectra of J03.13 A and B do indeed look quite similar. Spectrum of C probes for the possible contamination of component B by A, which turns out to be absolutely negligible. We confirm the emission-line redshift  $z_{\text{em}} = 2.545$  reported by Claeskens et al. (1996) as well as the two absorption line systems at  $z_{\text{abs}} = 2.344$  and  $z_{\text{abs}} = 1.085$  (the latter one being only detected from its MgII resonance lines in the spectrum of image A).

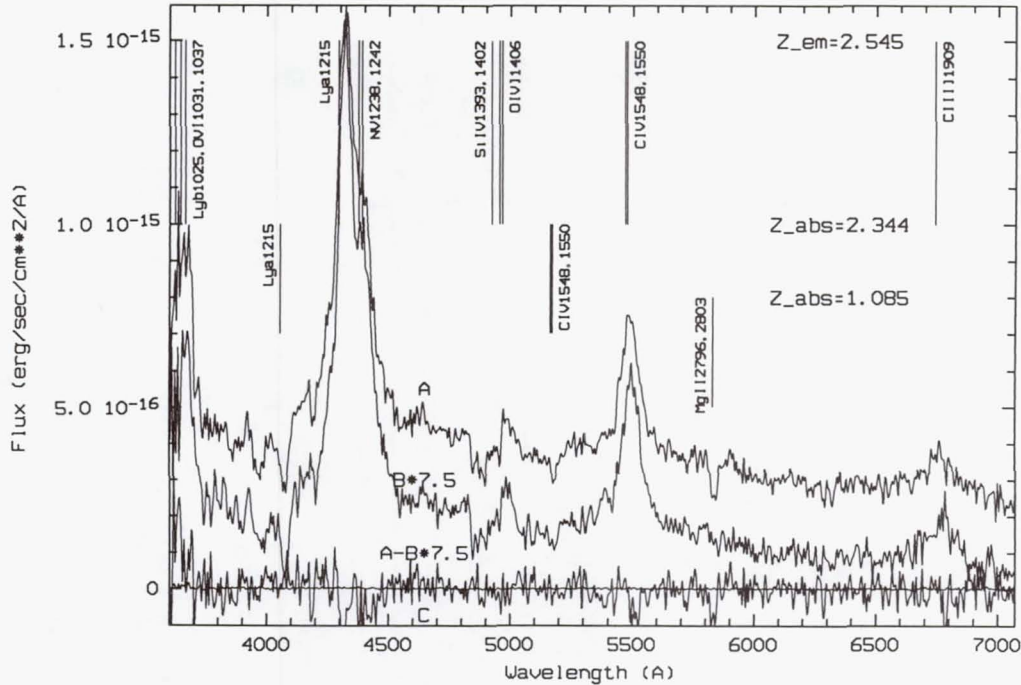


Figure 3. FOS spectra of (A) J03.13 A, (B) J03.13 B after multiplication of its flux by 7.5 and a vertical offset by  $-2.010^{-16}$  erg/sec/cm<sup>2</sup>/Å, (C) a fiducial target at the symmetric position of B with respect to A for probing light contamination from the latter component and (D) the residual spectrum of  $A - B \times 7.5$ . The QSO emission and two intervening absorption line systems are identified with vertical lines and labels at different redshifts (see text).

## 5. Conclusions

### 5.1. The Gravitational Lens of HE 1104–1805 A and B

The detection of a very red galaxy located between the two components of HE 1104–1805 proves the validity of the gravitational lensing hypothesis to explain this interesting object. The claim that a microlensing event is occurring for image A, proposed to explain the color differences between A and B (Wisotzki et al. 1993, 1995), is fully consistent with a more detailed analysis reported elsewhere (Remy et al. 1997b).

Combining the present HST data with ground-based IR and optical observations (Remy et al. 1997b), the lens is most likely found to be an elliptical galaxy with redshift  $0.95 < z < 1.4$ . This leads to a coherent scenario in which one can also explain the two main absorption line systems observed in the spectra of the quasar components. The  $z = 1.32$  absorption is produced in the spectra of A and B by the deflector (a bright elliptical with  $\mathcal{L} \approx 4.6\mathcal{L}^*$ ). Nevertheless, a smaller value for the redshift of the lens cannot be excluded. The hypothesis of a lensing galaxy at  $z = 1.66$  is poorly supported by the present observations. The  $z = 1.66$  absorption system is probably produced by absorbing gas in an yet unrevealed disk galaxy.

A singular isothermal sphere lens model with an additional shear term can easily explain the observed flux ratio between A and B (Remy et al. 1997b). The galaxy is found to be very massive. Its mass-to-light ratio does not much depend on redshift. For a deflector at  $z = 1.32$ , this ratio is estimated to be  $\mathcal{M}/\mathcal{L} \sim 11 h_{50} \mathcal{M}_{\odot}/\mathcal{L}_{\odot}$ , a typical value for an elliptical lensing galaxy. An excess of dark matter is not required to account for this system.



The physical origin of the additional shear is unknown. It may originate in an asymmetry of the galaxy gravitational potential or in the combined effect of several foreground galaxies located near the projected position of the quasar.

## 5.2. The Gravitational Lens System J03.13

Direct imagery of J03.13 with the PC1 camera clearly reveals that this bright and distant quasar consists of two point-like components having an angular separation of  $0''.849 \pm 0''.001$  and a magnitude difference  $\Delta m = 2.14 \pm 0.03$  mag in V and I.

Low resolution FOS spectra of J03.13 A and B show that these two components are lensed images of a same quasar at redshift  $z_{\text{em}} = 2.545$ , with a common absorption line system at  $z_{\text{abs}} = 2.344$ ; the MgII absorption resonance lines at  $z_{\text{abs}} = 1.085$  are only detected in the spectrum of the A component.

## Acknowledgments

This paper is based on observations made with the NASA/ESA Hubble Space Telescope, obtained at the Space Telescope Science Institute, which is operated by the Association of Universities for Research in Astronomy, Inc., under NASA contract NAS 5-26555. Part of this work has been supported by the SSTC/PRODEX (HST observations of gravitational lenses) project and a belgian FNRS grant (travel support for JS).

## References

- Claeskens J.-F., Surdej, J., & Remy, M., 1996, *A&A*, 305, L9  
 Grundahl, F., Hjorth, J., & Sørensen, A.N., 1995, *Highlights of Astronomy*, 10, 658  
 Holtzman, J. A., et al., 1995, *PASP*, 107, 1065  
 Hook, R. A., & Lucy, L. B., 1994, in *The restoration of HST images and spectra—II*, R. Hanisch & R. White (eds.), p. 86  
 Krist, J., 1997, *WFPC2 ghosts, scatter and PSF field dependence*, postscript document available via the STScI WWW page  
 Østensen, R., Remy, M., Lindblad, P. O., Refsdal, S., Stabell, R., et al., 1997, *A&AS*, in press  
 Remy, M., Surdej, J., Baggett, S., & Wiggs, M., 1997a, this volume  
 Remy, M., Claeskens, J.-F., Surdej, J., Hjorth, J., Refsdal, S., Wucknitz, O., Sørensen, A. N., & Grundahl, F., 1997b, *New Astronomy*, submitted  
 Remy, M., Claeskens, J.-F., & Surdej, J., 1998, in preparation  
 Smette, A., Robertson, J. G., Shaver, P. A., Reimers, D., Wisotzki, L., & Köhler, T., 1995, *A&A*, 113, 199  
 Surdej, J., Claeskens, J.-F., Crampton, D., Filippenko, A. V., Hutsemékers, D., et al., 1993, *AJ*, 105, 2064  
 Surdej J., Claeskens J.-F., Remy, M., Refsdal, S., Pirenne, B., Prieto, B., & Vanderriest, Ch., 1997, *A&A*, in press  
 Whitmore, B., 1997, *Photometry with the WFPC2*, postscript document available via the STScI WWW page  
 Wisotzki, L., Köhler, T., Kayser, R., & Reimers, D., 1993, *A&A*, 278, L15  
 Wisotzki, L., Köhler, T., Ikonoumou, M., & Reimers, D., 1995, *A&A*, 297, L59

## WFPC2 Photometry from Subtraction of TinyTim PSFs

M. Remy, J. Surdej,<sup>1</sup>

*Institut d'Astrophysique, Université de Liège, Belgium*

S. Baggett, M. Wiggs

*Space Telescope Science Institute*

### Abstract.

Based upon the subtraction of TinyTim PSFs from PC1 point-like objects, a method has been developed to determine the optimal values for the telescope jitter and the Z4 relative focus during calibration or science observations. Using these jitter and focus values, an optimal TinyTim PSF, computed over a resampled grid, is then iteratively fitted to the object, yielding an improvement in the PSF centering, more accurate photometric results and a better detection of underlying structures. Preliminary results seem to indicate that appropriate synthetic TinyTim PSFs perform as well as observed PSFs.

### 1. Introduction

Subtraction of scaled PSFs from direct CCD images of quasars (or stars) not only offers the possibility of detecting the presence of host or foreground galaxies (or companions like brown dwarfs or planets) but also provides a means of deriving accurate photometry for the primary objects.

In order to address the problem of fitting the undersampled point-like object peak on the PC1, a higher resolution PSF is necessary. A high resolution PSF is also necessary in order to use some new generation deconvolution algorithms (e.g. the 2-channel PLUCY algorithm, Hook & Lucy 1994). The TinyTim application program (Krist 1996) offers us the possibility of computing synthetic PSFs with a large range of resolution. Finally, synthetic PSFs are also needed when no observed PSFs are available. In addition, a good knowledge of the Z4 relative focus and jitter (among other TinyTim parameters) during the exposure, are very important in order to derive a useful PSF.

The observations used for the tests described here were taken from the WFPC2 photometric monitoring programs. The present analysis is based on the F555W PC1 mosaic of PSFs presented by Surdej et al. (1997). Please refer to that paper for a full description of the data set.

In the MIDAS environment, Remy (1996) has developed a general, automatic procedure to derive the best photometric measurements of (multiple) point source(s). For each single observation, PSFs are derived with TinyTim for different values of the jitter and Z4 parameters. The best PSF is identified with that giving the smallest fitting residuals in terms of  $\chi^2$ . The final PSF is then computed on a finer grid ( $10 \times 10$ ) with the derived optimum values for the parameters. Photometric measurements of single observations are then determined by iteratively fitting in flux and position the target with the above rebinned

---

<sup>1</sup>Research Director (FNRS, Belgium)



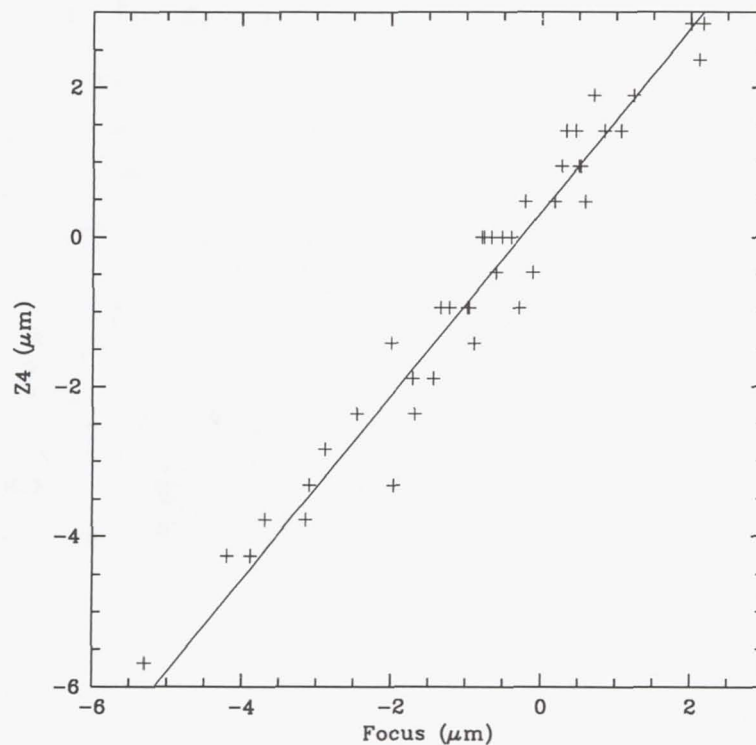


Figure 1.  $Z_4$  determined by our method versus focus measured with the phase retrieval method of Krist and Burrows (1995).

PSF (which is recentered at each iteration), using a  $\chi^2$  minimization method. A description of this automatic procedure may also be found in Østensen et al. (1997).

## 2. The Method

### 2.1. Determination of the $Z_4$ and Jitter Parameters

As a baseline for comparison, the  $Z_4$  and jitter parameters were determined with our technique using the 43 individual F555W images of a single object (characterized by different defocussing values).

The ( $Z_4$ , jitter) domain has been sampled with a rectangular grid of  $32 \times 6$  points around the nominal values of these parameters; each point of the grid corresponds to a different TinyTim PSF. The sampling steps correspond to  $0.42 \mu\text{m}$  ( $Z_4$ ) and to 3 milli-arcseconds (jitter). As this method is time consuming, the PSF grid has only been computed once, taking the average position in the individual frames ( $X=423$   $Y=427$ ), which is not far from the observed positions in most cases. Hence we avoided of constructing  $32 \times 6$  TinyTim PSFs for each of the 43 object positions. We then selected the optimum values corresponding to the PSF which best fits a given object.

All the optimal jitter parameters were found to be compatible with zero, as could be expected from the very short exposure times (typically  $< 5$  sseconds) used for the observations of the star GRW+70D5824.

We have plotted in Figure 1 the  $Z_4$  values in  $\mu\text{m}$  determined by our method versus the real focus in  $\mu\text{m}$ . The strong correlation indicates that our method is well suited to determine the focus to better than  $1 \mu\text{m}$ , even with very approximate values used for the position of the object. The best fitting line has also been plotted.

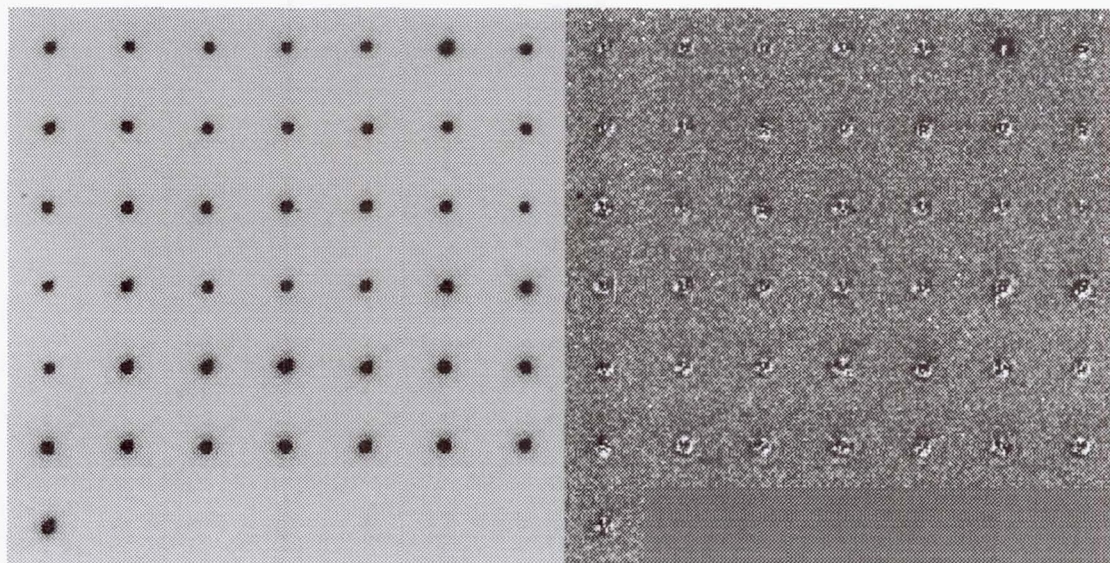


Figure 2. Mosaic image of the 43 test frames (left) and their corresponding residuals after an optimal subtraction of a resampled TinyTim PSF (right).

## 2.2. Iterative Fitting of Optimum PSFs

On the basis of the optimal values for the Z4 and jitter derived above, a PSF was constructed with TinyTim and an oversampling factor of 10. At each iteration, a fitting procedure gives a precise position for one chosen object (the “target”) on the CCD grid. The derived fractional coordinates of the target are used so that the resampled optimum PSF matches these fractional coordinates. To get a good precision and a stable resampled PSF, the process is iterated 2 or 3 times.

We present in Figure 2 the residuals of the subtraction of the optimum PSFs derived with our method. The residuals are still significant at the  $5\text{-}\sigma$  limit but less significant than those derived from direct subtraction of observed PSFs as discussed by Surdej et al. (1997). The map of the residuals is significantly “cleaner”. This should allow for better discrimination of real objects from artifacts near a point-like object.

## 2.3. The Photometry

Finally, we show in Figure 3 the observed magnitudes of the target as a function of the focus derived with the phase retrieval method. This graph can be directly compared with Figure 2 in Surdej et al. (1997) based on the same data set.

Our results are very similar to those of Surdej et al. (1997). If we exclude the frames with large coma, the frames for which the object positions are far from nominal and the frames with CLOCK=ON, there remain 34 objects. We derive a dispersion of 0.017 for the magnitudes of this subset of 34 objects, as compared to a value of 0.014 derived from the subtraction of observed PSFs.

## 3. Future Prospects

The tests presented here are still very preliminary, as the precise positions for the object were not input to TinyTim. We expect that by introducing these positions, the dispersion in the magnitude and the residuals of Figure 2 will be slightly reduced. TinyTim PSFs constructed with this method (including accurate input positions) have been used to analyse



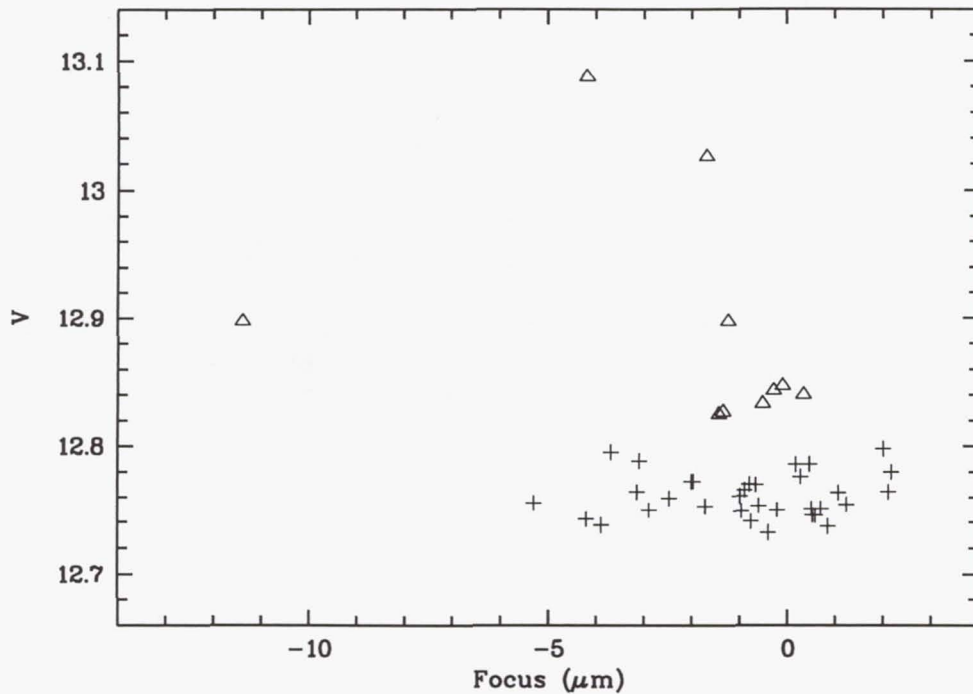


Figure 3. V magnitude of the target derived with our method versus phase retrieval focus. The triangles correspond to rejected measurements (see text).

PC1 images of the double quasars HE 1104–1805 and J03.13. A description of these studies are presented elsewhere in these proceedings (Remy et al. 1997).

### Acknowledgements

This paper is based on observations made with the NASA/ESA Hubble Space Telescope, obtained at the Space Telescope Science Institute, which is operated by the Association of Universities for Research in Astronomy, Inc., under NASA contract NAS 5-26555. This work has been supported by the SSTC/PRODEX (HST observations of gravitational lenses) project. We would like to thank Jean-François Claeskens for a careful reading of the manuscript.

### References

- Hook, R. A. & Lucy, L. B., 1994, in *The restoration of HST images and spectra-II*, Hanish, R. and White, R. (eds), p. 86
- Krist, J., 1996, *Tiny Tim manual*, at <http://scivax.stsci.edu/~krist/tinytim.html>
- Krist, J. & Burrows, C., 1995, *Appl.Optics*, 34, 4951
- Østensen, R., Remy, M. et al., *A&AS*, in press
- Remy, M., 1996 (Ph. D. thesis)
- Remy, M., Claeskens, J.-F., & Surdej, J., 1997, this volume
- Surdej, J., Baggett, S., Remy, M., & Wiggs, M., 1997, this volume

## Aperture Corrections for WFPC2 Stellar Photometry

A. Suchkov and S. Casertano<sup>1</sup>

*Space Telescope Science Institute, Baltimore, MD 21218*

**Abstract.** We examine the impact of the long term and short term focus position variations on small aperture photometry of WFPC2 images and present aperture corrections phased with the HST focus drift, as well as mean aperture corrections to large aperture radii ("infinity").

### 1. Introduction

Photometry of point sources in WFPC2 data is usually accomplished using one of two methods: aperture photometry or PSF fitting. PSF fitting has two major advantages: the ability to deal with crowded conditions, by iteratively fitting and subtracting point sources, and the ability to minimize the noise in the flux measurements and the influence of the background by weighting the fitting. Properly optimized, PSF fitting is a desirable avenue for accurate photometry of faint sources.

However, PSF fitting requires good knowledge of the shape of the PSF, either *a priori* or from the data themselves. It is well known that the WFPC2 PSF is very difficult to characterize perfectly, being a function of position in the field of view, wavelength, and also of focus position. PSF fitting is made more complex by the undersampling of both the PC and the WF cameras, which necessitates careful handling of the subpixel centering for the model PSF (see for example Remy et al. 1997). Specialized software, such as the DOPHOT package and the DAOPHOT routines, can deal with these difficulties and produce accurate photometry if enough well-exposed stars are available. If not, the resulting photometry can have slight zero-point errors due to an imperfectly known PSF. Note that properly weighted PSF fitting is optimal with respect to maximum S/N extraction.

Aperture photometry is a much simpler procedure which is commonly employed by many astronomers. It is much less sensitive than fitting to PSF variations and pixel-centering problems, and can produce good results for well-exposed images. The size of the aperture used should be large enough to reduce any edge effects due to centering and PSF variations, but not so large as to include an undue amount of background signal, which will increase the shot noise and produce additional uncertainty if the background estimate is uncertain. Of course, the zero point of aperture photometry depends on the aperture used; for example, the published zero points of Holtzman (1995b) refer to an aperture radius  $r$  of  $0''.5$  (see also Casertano 1997 for more details).

However, there are a number of situations in which this aperture is impractical, and smaller apertures need to be used, with the consequent need for aperture corrections. Here are a few examples:

- *Photometry of crowded stellar fields.* The light from a star in a large aperture may be directly contaminated by the light from neighboring stars in the wings of the PSF. Also the sky background, being measured from an even larger aperture, would be

---

<sup>1</sup>on assignment from the Space Sciences Division of the European Space Agency



impacted to a great extent by the background light of unevenly distributed nearby stars. Thus the resulting magnitudes and colors will be compromised. Use of small apertures obviously enables one to reduce both effects.

- *Photometry of stars and globular clusters in external galaxies.* For these targets, an uneven background light of the parent galaxy is often a substantial source of errors in the sky background to be subtracted from the target flux in the aperture. Small apertures may be the last resort in this case too.
- *Photometry of faint sources, especially in the case of a background-dominated noise.* The major adverse effect of large apertures in this case comes from background subtraction. The very fact of quantization of data numbers (DN), especially at GAIN =  $15 e^-$ , can introduce significant errors into the total flux in the aperture if the aperture is large. In this case the count numbers in the peripheral pixels are small, hence errors in the background will have a large effect upon them. Since the number of such pixels goes up quadratically with increasing aperture radius, their contribution to the flux error will also rapidly go up, resulting in progressively increasing error in the flux collected from the aperture area. Thus we are pushed again toward small apertures.

The advantages of small aperture photometry do not come for free. A number of factors are responsible for errors which become more important as the aperture radius decreases. For WFPC2, perhaps the most important are focus drift and focus "breathing". So, before we can comfortably use small aperture photometry, we need to examine these factors and find ways to correct for their impact.

The HST focus position,  $d$ , has changed systematically at a rate slightly less than  $1 \mu\text{m}/\text{month}$  since 1994. The change is believed to be due to the OTA shrinkage induced by desorption of water in the metering truss (Hasan et al. 1993, Casertano 1995), and appears to have slowed significantly in the last year or so (Biretta et al. 1997). In addition to this secular drift, there are short-term focus position variations with an amplitude of  $\sim 2 \mu\text{m}$  which presumably result from temperature variation during the HST orbit (Hasan & Bely 1994). The secular defocusing makes it necessary to correct the focus position by moving the secondary mirror twice a year (see Table 1). These focus moves enable us to maintain the PSF quality within limits which are satisfactory for most observational programs. However, programs which require especially accurate absolute photometry data can be substantially compromised by the amount of focus drift accumulating in between focus corrections. In this report, we analyze the impact of the focus drift on small aperture photometry and present aperture corrections phased with the secular focus change, as well as aperture corrections to large radii ("infinity") averaged over focus variations.

Table 1. History of focus adjustments

date (days)	$t_i^a$	adjustment ( $\mu\text{m}$ )	$d_i^b$ ( $\mu\text{m}$ )
3/04/94	63	minor change	+1.0
6/29/94	180	5	+1.5
1/15/95	380	5	+1.5
8/28/95	604	6.5	+2.5
3/14/96	803	5.5	+3.5

<sup>a</sup> $t_i$  is the day number starting January 1, 1994

<sup>b</sup> $d_i$  is the focus position after the second mirror move, assuming position of  $+1.5 \mu\text{m}$  on 6/29/94 and focus drift rate of  $-0.025 \mu\text{m}$  per day

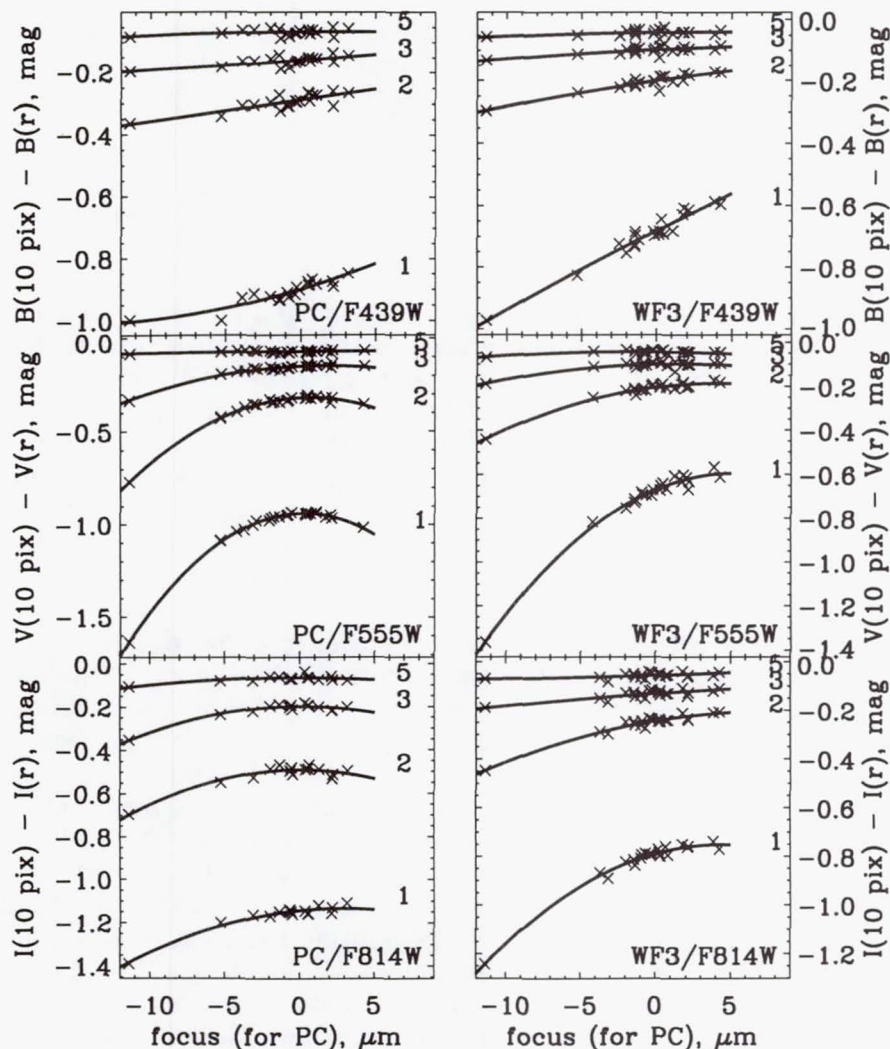


Figure 1. Phased aperture corrections for F439W, F555W, and F814W magnitudes normalized to aperture radius  $r = 10$  pixel. The solid curves represent the best quadratic fit to the data points; the fit coefficients are given in Table 2

## 2. Phased Aperture Corrections

The focus position monitoring based on phase retrieval solutions for the WFPC2 images of the spectrophotometric standard star GRW +70D5824 (Casertano 1995) has accumulated substantial amount of data to analyze the impact of the focus drift on photometry. The focus position measurements were done with the data obtained from exposures through the filter F555W on PC. In this report, we will use these data to study how the measured stellar magnitudes in F555W, F439W, and F814W from the standard star images on PC and WF3 correlate with the focus drift.

To derive the magnitudes of the standard star, we used the `phot` task from the `noao.daophot` package. The magnitudes were measured in aperture radii of 1, 2, 3, 5, and 10 pixels. Sky subtraction was performed using the annulus of 15 pixels, with the parameter `dannulus` set to 5 pixels. Aperture corrections computed from these data for the above aperture radii are plotted against focus position in Figure 1.



Inspection of Figure 1 shows that magnitude corrections for finite aperture size (aperture corrections) should take into account the focus position at the time of observation if small apertures are used for accurate absolute photometry. In other words, aperture corrections for small apertures should be phased with the focus change. Since the dependence of aperture magnitudes on focus becomes negligible for apertures of 10 pixel or larger, we normalize magnitudes to this aperture,

$$m_{r,10} = m_r - m_{10}. \quad (1)$$

Table 2. Coefficients to calculate phased aperture corrections from equation (2)

$r$ (pixel)	$\Delta_{10}m_{r,H}^a$ (mag)	$\Delta_{10}m_r(0)$ (mag)	$A$ (mag $\mu\text{m}^{-1} \times 10^{-2}$ )	$B$ (mag $\mu\text{m}^{-2} \times 10^{-2}$ )
F439W (PC)				
1	-0.91	$-0.90 \pm 0.04$	$-1.35 \pm 0.42$	$-0.04 \pm 0.05$
2	-0.30	$-0.29 \pm 0.02$	$-0.83 \pm 0.25$	$-0.01 \pm 0.03$
3	-0.16	$-0.16 \pm 0.02$	$-0.48 \pm 0.18$	$-0.01 \pm 0.02$
5	-0.07	$-0.06 \pm 0.01$	$-0.09 \pm 0.13$	$0.01 \pm 0.01$
F439W (WF3)				
1	-0.73	$-0.68 \pm 0.06$	$-2.47 \pm 0.50$	$0.03 \pm 0.07$
2	-0.23	$-0.20 \pm 0.02$	$-0.76 \pm 0.18$	$0.01 \pm 0.02$
3	-0.11	$-0.10 \pm 0.01$	$-0.27 \pm 0.10$	$0.01 \pm 0.01$
5	-0.04	$-0.04 \pm 0.01$	$-0.10 \pm 0.08$	$0.01 \pm 0.01$
F555W (PC)				
1	-1.02	$-0.94 \pm 0.02$	$-0.31 \pm 0.18$	$0.51 \pm 0.03$
2	-0.38	$-0.32 \pm 0.01$	$-0.27 \pm 0.11$	$0.32 \pm 0.02$
3	-0.19	$-0.15 \pm 0.01$	$-0.27 \pm 0.07$	$0.12 \pm 0.01$
5	-0.07	$-0.07 \pm 0.01$	$0.03 \pm 0.05$	$0.01 \pm 0.01$
F555W (WF3)				
1	-0.77	$-0.67 \pm 0.06$	$-2.65 \pm 0.46$	$0.29 \pm 0.06$
2	-0.24	$-0.21 \pm 0.02$	$-0.86 \pm 0.18$	$0.10 \pm 0.02$
3	-0.11	$-0.10 \pm 0.02$	$-0.29 \pm 0.13$	$0.04 \pm 0.02$
5	-0.06	$-0.05 \pm 0.01$	$-0.11 \pm 0.12$	$0.01 \pm 0.02$
F814W (PC)				
1	-1.17	$-1.15 \pm 0.04$	$-0.62 \pm 0.39$	$0.12 \pm 0.05$
2	-0.52	$-0.50 \pm 0.02$	$0.03 \pm 0.22$	$0.16 \pm 0.03$
3	-0.22	$-0.21 \pm 0.02$	$-0.02 \pm 0.17$	$0.11 \pm 0.02$
5	-0.08	$-0.07 \pm 0.01$	$-0.04 \pm 0.12$	$0.02 \pm 0.01$
F814W (WF3)				
1	-0.84	$-0.79 \pm 0.04$	$-1.94 \pm 0.32$	$0.19 \pm 0.04$
2	-0.28	$-0.24 \pm 0.02$	$-1.03 \pm 0.19$	$0.07 \pm 0.02$
3	-0.14	$-0.13 \pm 0.01$	$-0.33 \pm 0.12$	$0.02 \pm 0.02$
5	-0.06	$-0.05 \pm 0.01$	$-0.13 \pm 0.08$	$0.00 \pm 0.01$

<sup>a</sup>  $\Delta_{10}m_{r,H}$  are aperture corrections based on Table 2 of Holtzman et al. (1995a), normalized to aperture radius  $r = 10$  pixel. They are to be compared to "nominal" aperture corrections,  $\Delta_{10}m_r(0)$ , defined by equation (2)

Phased aperture corrections are then defined as a quadratic fit to  $m_{r,10}(d)$ :

$$\Delta_{10}m_r(d) = \Delta_{10}m_r(0) + Ad + Bd^2, \quad (2)$$

The coefficients of the fit are given in Table 2. The negative values of  $B$  for WF3/F439W are unphysical, but the errors are large, exceeding the estimates of  $B$ . Thus  $B$  is just indeterminate in this case.

Strictly speaking, the coefficients in Table 2 are valid only for the centers of the PC and WF3 cameras, because the standard star in the photometric monitoring program was always placed in the center of the CCD detector. In general, phased aperture corrections may vary across the CCD in each of the WFPC2 cameras to the extent to which the focus itself varies across the chips.

Focus position at any particular date of observation can be estimated from equation

$$d = d_i - 0.025(t_{94} - t_i), \quad (3)$$

where  $d_i$  is the focus position right after focus adjustment,  $t_{94}$  is the day number starting January 1, 1994, and  $t_i$  is the day when the previous adjustment was done (also starting January 1, 1994). The coefficients  $d_i$  and  $t_i$  given in Table 1. Substituting  $d$  from equation (3) in equations (2), we obtain phased aperture corrections for any particular day of observation from April, 1994, through October, 1996. The aperture corrections at  $d = 0$ ,  $\Delta_{10m_r}(0)$ ,

Table 3. Predicted range of flux variations at focus excursions of  $\delta d = \pm 2 \mu\text{m}$  around different average focus positions

$r$ (pixel)	$\bar{d}^a = +1$	range of flux variation (%)			
		$\bar{d} = 0$	$\bar{d} = -1$	$\bar{d} = -2$	$\bar{d} = -3$
F439W (PC)					
1	5.3	5.0	4.7	4.3	6.4
2	3.2	3.0	2.9	2.8	4.2
3	1.9	1.8	1.7	1.6	2.4
5	0.3	0.3	0.4	0.4	0.6
F439W (WF3)					
1	9.1	9.1	9.1	9.1	13.6
2	2.7	2.8	2.9	3.0	4.5
3	0.9	1.0	1.0	1.1	1.7
5	0.3	0.4	0.4	0.4	0.7
F555W (PC)					
1	4.0	3.7	5.1	8.3	13.1
2	2.5	2.4	3.4	5.6	8.9
3	0.6	1.0	1.8	2.7	4.2
5	0.2	0.1	0.0	0.1	0.1
F555W (WF3)					
1	7.7	9.7	11.5	13.1	20.0
2	2.4	3.2	3.9	4.6	7.0
3	0.8	1.1	1.4	1.7	2.6
5	0.3	0.4	0.5	0.5	0.8
F814W (PC)					
1	1.4	2.3	3.1	4.0	6.2
2	1.5	1.1	1.4	2.1	3.5
3	1.0	0.8	1.1	1.7	2.7
5	0.2	0.2	0.3	0.5	0.8
F814W (WF3)					
1	5.8	7.1	8.3	9.5	14.4
2	3.3	3.8	4.3	4.7	7.2
3	1.1	1.2	1.4	1.5	2.3
5	0.4	0.5	0.5	0.5	0.8

<sup>a</sup> $\bar{d}$  is the average focus position ( $\mu\text{m}$ ) on the PC focus scale

can be regarded as “nominal” corrections. They can be compared to aperture corrections obtained by Holtzman et al. (1995a) from observations of a field in  $\omega$  Cen soon after the First Servicing Mission. These corrections,  $\Delta_{10m_r,H}$ , are given in Table 2 alongside with the coefficients of equation (2). The comparison reveals a good agreement between the “nominal” and Holtzman’s corrections. The correction in Holtzman et al. (1995a) is slightly larger than ours for the smallest apertures, a difference easily understood assuming that the observations used in that paper were done at a focus position  $d \sim -2 \mu\text{m}$  rather than at the optimal position,  $d = 0$ . Given the high degree of consistency between  $\Delta_{10m_r}(0)$  and  $\Delta_{10m_r,H}$ , one can use Table 2(a-b) in Holtzman et al. (1995a) to translate the normalized



corrections from equation (2) to the ones corresponding to an "infinite" aperture radius,<sup>1</sup> if desired.

### 3. Effect of "Focus Breathing"

Table 2 can be used to estimate uncertainties in measured magnitudes caused by focus "breathing". Relative flux variation due to focus excursions of  $\pm\delta d$  from the average focus position  $\bar{d}$  can be written as

$$\epsilon_r(\bar{d}, \delta d) = \frac{f_r(\bar{d} \pm \delta d) - f_r(\bar{d})}{f_r(\bar{d})} = 10^{-0.4[A(\bar{d} \pm \delta d) + B(\bar{d} \pm \delta d)^2]} - 1. \quad (4)$$

The above equation gives an idea on the amount of photometric error that can be introduced by focus "breathing" during the orbital period. As seen from equation (4), the magnitude of the error strongly depends on the average focus position. Table 3 presents flux variations calculated from equation (4) with coefficients from Table 2 for a range of average focus positions and a typical breathing amplitude of  $\pm 2 \mu\text{m}$ . The numbers in Table 3 imply that focus breathing appears to be an important factor limiting accuracy that one can achieve with small aperture photometry. Therefore, until better understanding of focus breathing is reached and ways to correct for its effects are found, observers are recommended either to use apertures of 5 pixel or larger, or to determine aperture corrections from the brightest star in each observation if high absolute photometric accuracy is desired. Breathing may be less of an issue for relative photometry of stars in the same frame, although this issue has not been investigated here.

Further details on phased aperture corrections can be found in Suchkov and Casertano (1997).

Table 4. Mean aperture corrections (in magnitudes) and their errors for the WFPC2 photometric filter set at the center of WF3

pix	f336w	err	f439w	err	f555w	err	f675w	err	f814w	err
1	-1.071	0.002	-0.984	0.002	-1.203	0.002	-1.024	0.003	-1.115	0.002
2	-0.237	0.002	-0.194	0.002	-0.284	0.002	-0.243	0.003	-0.242	0.002
3	-0.128	0.002	-0.097	0.002	-0.130	0.002	-0.103	0.003	-0.109	0.002
4	-0.080	0.002	-0.059	0.002	-0.083	0.002	-0.060	0.003	-0.055	0.002
5	-0.053	0.002	-0.039	0.002	-0.054	0.002	-0.041	0.003	-0.037	0.002
6	-0.038	0.002	-0.027	0.002	-0.037	0.002	-0.028	0.003	-0.026	0.002
7	-0.029	0.002	-0.019	0.002	-0.026	0.002	-0.019	0.003	-0.017	0.002
8	-0.022	0.002	-0.015	0.002	-0.018	0.002	-0.013	0.003	-0.012	0.002
9	-0.016	0.002	-0.011	0.002	-0.014	0.002	-0.009	0.003	-0.008	0.002
10	-0.012	0.002	-0.009	0.002	-0.011	0.002	-0.006	0.003	-0.005	0.002
11	-0.008	0.002	-0.007	0.002	-0.009	0.002	-0.005	0.003	-0.004	0.002
12	-0.005	0.002	-0.005	0.002	-0.007	0.002	-0.004	0.003	-0.003	0.002
13	-0.003	0.002	-0.004	0.002	-0.006	0.002	-0.003	0.003	-0.002	0.002
14	-0.002	0.002	-0.003	0.002	-0.004	0.002	-0.002	0.003	-0.001	0.002
15	-0.001	0.002	-0.002	0.002	-0.003	0.002	-0.002	0.004	-0.001	0.002
16	-0.001	0.002	-0.001	0.002	-0.003	0.002	-0.001	0.004	-0.001	0.002
17	-0.000	0.002	-0.001	0.002	-0.002	0.002	-0.001	0.004	-0.001	0.002
18	-0.000	0.002	-0.001	0.002	-0.001	0.003	-0.001	0.004	-0.000	0.002
19	-0.000	0.002	-0.000	0.002	-0.001	0.003	-0.001	0.004	-0.000	0.002
20	-0.000	0.002	-0.000	0.003	-0.001	0.003	-0.000	0.004	-0.000	0.002
21	-0.000	0.002	-0.000	0.003	-0.000	0.003	-0.000	0.004	-0.000	0.003
22	-0.000	0.002	-0.000	0.003	-0.000	0.003	-0.000	0.004	-0.000	0.003
23	-0.000	0.003	-0.000	0.003	-0.000	0.003	-0.000	0.004	-0.000	0.003
24	-0.000	0.003	-0.000	0.003	-0.000	0.003	-0.000	0.004	-0.000	0.003
25	-0.000	0.003	-0.000	0.003	-0.000	0.003	-0.000	0.004	-0.000	0.003

<sup>1</sup>The largest radii in Holtzman et al. (1995a) are  $r = 130$  pixel for PC and  $r = 60$  pixel for WF cameras.

#### 4. Mean aperture corrections to large radii

The data accumulated since 1994 allow a better determination of the aperture correction to large radii than could be obtained in Holtzman et al. (1995). These new corrections were obtained from composite images of the primary standard GRW+70d5824 at the center of WF3. For the composites, we used 41 individual images in f336w, 31 images in f439w, 38 images in f555w, 31 images in f675w, and 37 images in f814w. We performed aperture photometry on each composite image, with the results shown in Table 4 and in Figure 2. The sky background was calculated in the annulus 26 to 30 pixels; the uncertainty in the sky value dominates the uncertainty in the aperture correction, and therefore the errors are highly correlated from one radius to the next. As seen in the Table, the corrections appear to be smaller than 0.001 mag, and actually vanish within the measurement error, at radii of approximately 20 pixels. The data thus suggest that the WFPC2 aperture corrections to large radii should be typically smaller than a few millimagnitudes for aperture radii larger than 20 pixel ( $\sim 2''$ ).

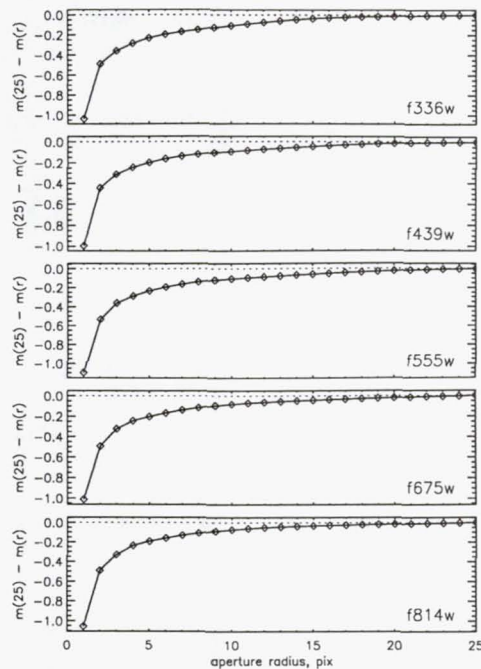


Figure 2. Mean aperture corrections, in magnitudes, for WF3, normalized to aperture radius  $r = 25$  pixel.



**References**

- Biretta, J., et al., 1997, Instrument Science Report WFPC2 97-09 (Baltimore: STScI)
- Casertano, S., 1995, Instrument Science Report OTA 18
- Casertano, S., 1997, this volume
- Hasan, H., & Bely, P.Y., 1994, in *The Restoration of HST Images and Spectra II*, eds. R.J. Hanish & R.L. White (Baltimore: STScI), p. 157
- Hasan, H., Burrows, C.J., & Schroeder, D.J., 1993, PASP, 105, 1184
- Holtzman, J., et al., 1995a, PASP, 107, 156
- Holtzman, J., et al., 1995b, PASP, 107, 1065
- Remy, M., Surdej, J., Baggett, S., & Wiggs, M., 1997, this volume
- Suchkov, A., & Casertano, S., 1997, Instrument Science Report WFPC2 97-01
- Whitmore, B., 1995, in *Calibrating Hubble Space Telescope: Post Servicing Mission*, eds. A. Koratkar & C. Leitherer, p. 269

## WFPC2 Photometry from Subtraction of Observed PSFs

J. Surdej,<sup>1,2</sup> S. Baggett,<sup>3</sup> M. Remy,<sup>1</sup> and M. Wiggs<sup>3</sup>

**Abstract.** Based on observed PSFs from the WFPC2 calibration programs, a series of PSF subtraction tests have been performed and the resulting photometry analyzed. We find that using a composite observed PSF, constructed from optimally selected PSFs based on location and breathing values, yields single photometric values affected by an RMS dispersion of about 0.01–0.02 mag. While resampling does not appear to have much of an effect on the photometric results, the color of the PSF employed is important.

### 1. Introduction

Subtraction of scaled PSFs from direct CCD images of quasars (or stars) not only offers the possibility of detecting the presence of host or foreground galaxies (or companions like brown dwarfs or planets) but also provides a means of deriving accurate photometry of the primary objects.

The observations used for the tests described here were taken from the WFPC2 photometric monitoring programs; primarily F555W in the PC was used, although separate independent tests were also done with a subset of the F814W and F439W, in PC and WF3, images. The target in all cases was the spectrophotometric standard GRW+70D5824, a DA3 white dwarf ( $V = 12.77$ ,  $B - V = -0.09$  mag). Details of the F555W images are provided in the table in Appendix A; tabulated are the image rootname, the PSF positions on the original chip, the row and column position of the PSF in the mosaic frame (see Figure in Appendix A), the date and MJD for the start of the observations, the exposure time (in seconds), the relative defocus of the secondary mirror (in  $\mu\text{m}$ ) and finally, the X,Y components of coma (in  $\mu\text{m}$ ) of wavefront error. The relative focus was determined using the phase retrieval code of Krist & Burrows (1995) to reproduce the detailed shape of the observed PSFs; the derived focus positions are illustrated in Figure 1 as a function of Modified Julian Date (MJD). Appendix A, Figure 4, provides a greyscale mosaic of the 43 observed PSFs.

In the MIDAS environment, Remy (1996) has developed a general, automatic procedure to derive optimal photometric measurements of (multiple) point sources. A composite PSF is determined by summation of the selected images of the spectrophotometric standard regularly observed with WFPC2, after recentering at the same position by bi-quadratic interpolations. Photometric measurements of single observations are then determined by fitting in flux and position the above composite PSF, using a  $\chi^2$  minimization method. A description of this automatic procedure may also be found in Remy et al. (1997).

---

<sup>1</sup>Institut d'Astrophysique, Université de Liège, Belgium

<sup>2</sup>Research Director (FNRS, Belgium)

<sup>3</sup>Space Telescope Science Institute



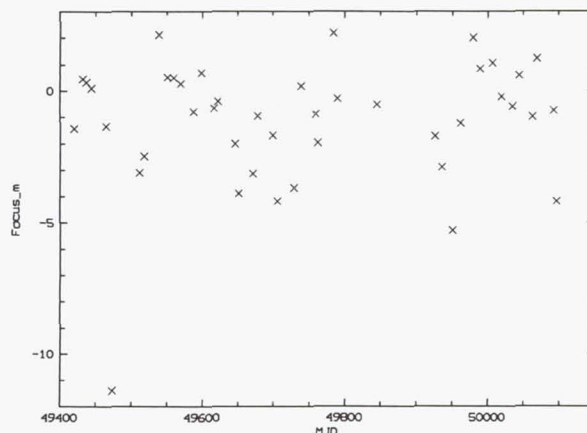


Figure 1. Relative focus positions (in  $\mu\text{m}$ ) as a function of Modified Julian Date (MJD).

## 2. The Photometry

### 2.1. Single Star—F555W, PC

As a baseline for comparison, photometry using a single PSF star (characterized by various defocussing values) was performed on the 43 individual F555W images. Depending upon the precise focus value of the observed PSF used, the final average magnitudes ranged from 12.79 to 12.85 mag, with scatter typically around 0.02 mag (somewhat higher, 0.04 mag, for the highest focus PSF, about  $0.5\mu\text{m}$ ). These tests indicate that using a single PSF leads to adequate results provided that it is close in location and focus to the target. However, the use of an observed PSF whose relative focus position differs by  $6\mu\text{m}$  or more may result in a systematic photometric error that exceeds 0.1 mag.

### 2.2. Composite of 42 Observed PSFs—F555W, PC

A composite PSF image constructed from 42 of the observed F555W PSFs was subtracted from each of the 43 original observations; a greyscale representation of the subtraction results is illustrated in Figure 4 in Appendix A. Because of the PC image undersampling, concentric rings are indicative that the centering may be slightly different from the center of the composite; fainter features around the periphery are probably due to focus differences (breathing, i.e., the PSF variations seen over the timescale of an HST orbit). The photometry results achievable when using this 42-image composite PSF are plotted in Figure 2 in the form of magnitudes obtained as a function of focus. The scatter affecting the photometric results of the 34 reliable (see below) observations of GRW+70D5824 is 0.014 mag. Note that no systematic dependence of the derived V magnitude as a function of the relative focus position is noticeable. These good photometric results are certainly due to the high S/N of the composite PSF constructed from the 42 single observations.

### 2.3. Composite of 34 Observed PSFs—F555W, PC

Immediately apparent in the photometric results of the previous test (Figure 2, using the composite of 42) are eight outliers; five of these appear to be due to PSFs with larger coma or PSFs which are in a substantially different location on the chip, while three of the PSFs were taken under different conditions: CLOCKS=ON, and therefore the exposure time was slightly shortened (two in Dec 94), or at a warmer operating temperature (one in Feb 94). For these reasons, a second observed composite was constructed, omitting these questionable PSFs as well as the one PSF dropped earlier (very far from the average focus).

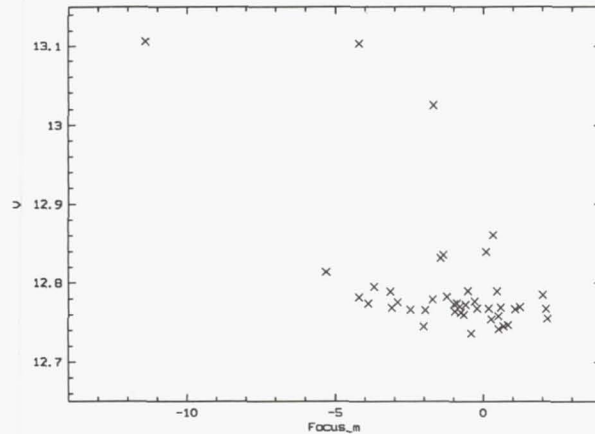


Figure 2. Magnitudes, obtained via PSF subtraction of the 42-image composite, as a function of focus (in  $\mu\text{m}$ ).

The photometry results using this composite of 34 images are also listed in Table 1. The photometric results derived from the 34 composite PSF are comparable (0.014 mag scatter) to those based on the 42 composite PSF.

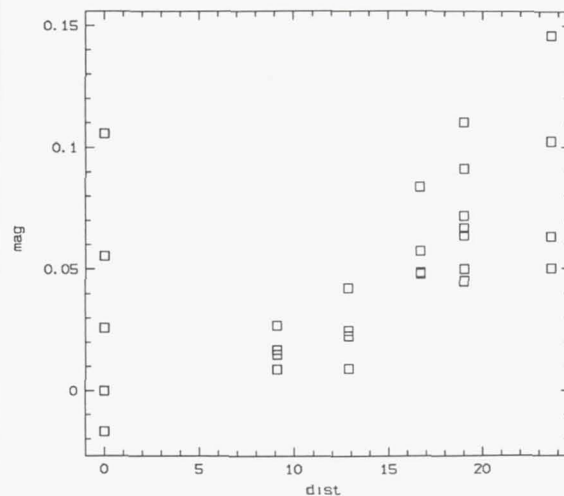


Figure 3. Changes in photometry as a function of radial distance from center (in arcsec). Additional data points at  $\text{dist} = 0$  are the results of using TinyTim PSFs of various spectral types ( $B - V = -0.297, -0.155, 0.126, 0.619$ , and  $1.590$ ; note: for  $\text{dist} > 0$ , magnitudes were computed using  $B - V = -0.155$  mag).

#### 2.4. Position and Spectral Type Dependence

Figure 3 demonstrates the scatter in the resulting photometry when TinyTim (Krist 1993, 1996) model PSFs at a range of angular distances away from the target are used. Also in the same figure (at distance = 0) are the results when using TinyTim PSFs of various spectral types. As can be seen, a mismatch in spectral type can result in nearly as much error as when using a PSF about 15–20'' away from the target.



### 3. Conclusions

Table 1 summarizes the average magnitude and scatter obtained from the PSF subtraction photometry of GRW+70D5824 when using the noted (composite or single) PSF type and focus range. These results indicate that the best PSF subtraction photometry is obtained when using a composite PSF close in relative focus to the target, originating from a location on the chip as close as possible to the target (typically less than  $10''$ ) and having a spectral type as similar to the target's type as possible, in that order of importance. Owing to the better S/N, a composite PSF fared better than a single PSF, however, the specific number of PSFs used in the composite was found to be relatively unimportant. In addition, resampling did not improve the resulting photometry. Additional tests were also done with a subset of F814W and F439W PC and WF3 images, corroborating the F555W PC results. A WFPC2 PSF Library has been established to enable users to carry out more experiments (see WWW page, under WFPC2 Software Tools). An investigation of photometric measurements based upon subtraction of TinyTim model PSFs has been performed by Remy et al. (1997).

Table 1. Summary of the F555W PSF subtraction photometry results. The average magnitudes and scatters were calculated from the 34 reliable observations (see text); columns 3 and 4 are results for a composite PSF, columns 5 and 6 are results using a resampled composite PSF. Focus (in  $\mu\text{m}$ ) is that of the composite PSF.

test case	relative focus	mag	scatter	mag	scatter
observed PSF, single	$F \geq 0.492$	12.806	0.042	12.826	0.087
	$0.492 > F \geq -0.820$	12.809	0.022	12.750	0.065
	$-0.820 > F \geq -2.459$	12.849	0.024	12.826	0.050
	$-2.459 > F$	12.792	0.024	12.746	0.049
observed PSF, composite of 42	$2.295 > F > -11.311$	12.736	0.014	12.770	0.016
observed PSF, composite of 34	$2.295 > F > -11.311$	12.769	0.014	12.767	0.021

### References

- Casertano, S., 1995, Instrument Science Report OTA 18.
- Hasan, H., & Bely, P.Y., 1994, in *The Restoration of HST Images and Spectra II*, eds. R.J. Hanish & R.L. White (Baltimore: STScI), p. 157
- Krist, J., 1993, in *Astronomical Data Analysis Software and Systems II*, eds. R. J. Hanisch, R. J. V. Brissenden, & J. Barnes, (San Francisco: Astronomical Society of the Pacific), p. 530.
- Krist, J., and Burrows, C., 1995, *Appl. Optics*, 34, 4951
- Krist, J., 1996, *Tiny Tim manual*, at <http://scivax.stsci.edu/~krist/tinytim.html>
- Remy, M., 1996 (PhD thesis)
- Remy, M., Surdej, J., Baggett, S., & Wiggs, M., 1997, this volume
- Wiggs, M., Baggett, S., Surdej, J., and Tullos, C., 1997, Technical Instrument Report

## Appendix A: Table and Figure of Images

Table 2. Log of PC1 F555W images used for tests described in this paper.

rootname	x	y	ix	iy	obsdate	MJD	expt	focus	x-coma	y-coma
u2a70305t	472	458	1	1	8/03/94	49419.1328	1.6	-1.4333	0.0029	-0.0029
u2a70605t	417	428	2	1	20/03/94	49431.6602	1.6	0.4610	0.0054	0.0005
u2a70905t	402	444	3	1	25/03/94	49436.6875	1.6	0.3345	0.0023	-0.0023
u2a70c05p	431	477	4	1	1/04/94	49443.8555	1.6	0.1025	0.0043	-0.0044
u2a70i05t	355	496	5	1	21/04/94	49463.7852	1.6	-1.3445	0.0055	-0.0066
u2a70l05t	345	486	6	1	1/05/94	49473.3750	1.6	-11.3925	0.0017	-0.0103
u2a70o05t	331	420	7	1	8/06/94	49511.1367	1.6	-3.0977	0.0149	-0.0104
u2a70r05t	329	432	1	2	14/06/94	49517.3555	1.6	-2.4649	0.0088	-0.0061
u2a70u05t	357	385	2	2	4/07/94	49537.6523	1.6	2.1136	0.0045	-0.0047
u2a70x05t	369	372	3	2	16/07/94	49549.9766	1.6	0.5301	0.0078	-0.0072
u2a71005p	381	363	4	2	25/07/94	49558.8164	1.6	0.5056	0.0093	-0.0056
u2a71305t	367	340	5	2	4/08/94	49568.8477	1.6	0.2755	0.0090	-0.0070
u2a71605t	395	361	6	2	23/08/94	49587.1289	1.6	-0.7914	0.0091	-0.0048
u2a71905t	412	356	7	2	2/09/94	49597.9805	1.6	0.7010	0.0099	-0.0080
u2a71c05t	452	325	1	3	21/09/94	49616.0547	1.6	-0.6605	0.0035	-0.0048
u2a71f05t	458	328	2	3	26/09/94	49621.5391	1.6	-0.3941	0.0056	-0.0066
u2a71i05t	483	345	3	3	20/10/94	49645.2461	1.6	-2.0015	0.0084	-0.0069
u2a71l05t	489	352	4	3	25/10/94	49650.8750	1.6	-3.8875	0.0087	-0.0050
u2a71o05t	504	379	5	3	14/11/94	49670.7617	1.6	-3.1423	0.0045	-0.0063
u2a71r05t	507	388	6	3	21/11/94	49677.9805	1.6	-0.9612	0.0077	-0.0052
u2a71u05t	511	423	7	3	12/12/94	49698.8633	1.0	-1.6872	0.0080	-0.0078
u2a71x05t	522	462	1	4	20/12/94	49706.0312	1.0	-4.1893	0.0168	-0.0088
u2a72605t	509	497	2	4	11/01/95	49728.6172	1.6	-3.6870	0.0051	-0.0096
u2a72905t	498	513	3	4	21/01/95	49738.8750	1.6	0.1799	0.0119	-0.0085
u2a72c05t	465	504	4	4	11/02/95	49759.3242	1.6	-0.8905	0.0060	-0.0070
u2a72f05t	459	505	5	4	13/02/95	49761.8711	1.6	-1.9657	0.0086	-0.0097
u2n10203p	409	593	6	4	7/03/95	49783.5586	3.5	2.1728	0.0133	-0.0083
u2n10403t	392	590	7	4	13/03/95	49789.7695	3.5	-0.2908	0.0122	-0.0092
u2o00501t	332	504	1	5	7/05/95	49844.9141	1.2	-0.5168	0.0113	-0.0087
u2s61101t	406	419	2	5	27/07/95	49925.2930	3.5	-1.7113	0.0098	-0.0053
u2s61201t	405	419	3	5	6/08/95	49935.1953	3.5	-2.8893	0.0115	-0.0067
u2s61301t	427	436	4	5	21/08/95	49950.0586	3.5	-5.2985	0.0132	-0.0122
u2s61401t	408	451	5	5	31/08/95	49960.9609	3.5	-1.2288	0.0092	-0.0082
u2s61501t	418	410	6	5	18/09/95	49978.4453	3.5	2.0072	0.0126	-0.0066
u2s61601t	419	411	7	5	28/09/95	49988.5430	3.5	0.8492	0.0123	-0.0071
u2s61701t	418	415	1	6	16/10/95	50006.0664	3.5	1.0692	0.0094	-0.0096
u2s61801t	417	417	2	6	29/10/95	50019.1992	3.5	-0.2110	0.0108	-0.0049
u2s62101t	416	410	3	6	13/11/95	50034.7266	3.5	-0.5944	0.0133	-0.0050
u2s62201t	416	412	4	6	22/11/95	50043.9023	3.5	0.5878	0.0116	-0.0050
u2s62301t	416	413	5	6	12/12/95	50063.0547	3.5	-0.9875	0.0126	-0.0053
u2s62401t	416	415	6	6	18/12/95	50069.2031	3.5	1.2373	0.0098	-0.0060
u2s62501t	417	416	7	6	10/01/96	50092.9648	3.5	-0.7580	0.0132	-0.0024
u2s62601t	448	429	1	7	15/01/96	50097.0508	3.5	-4.2018	0.0084	-0.0054



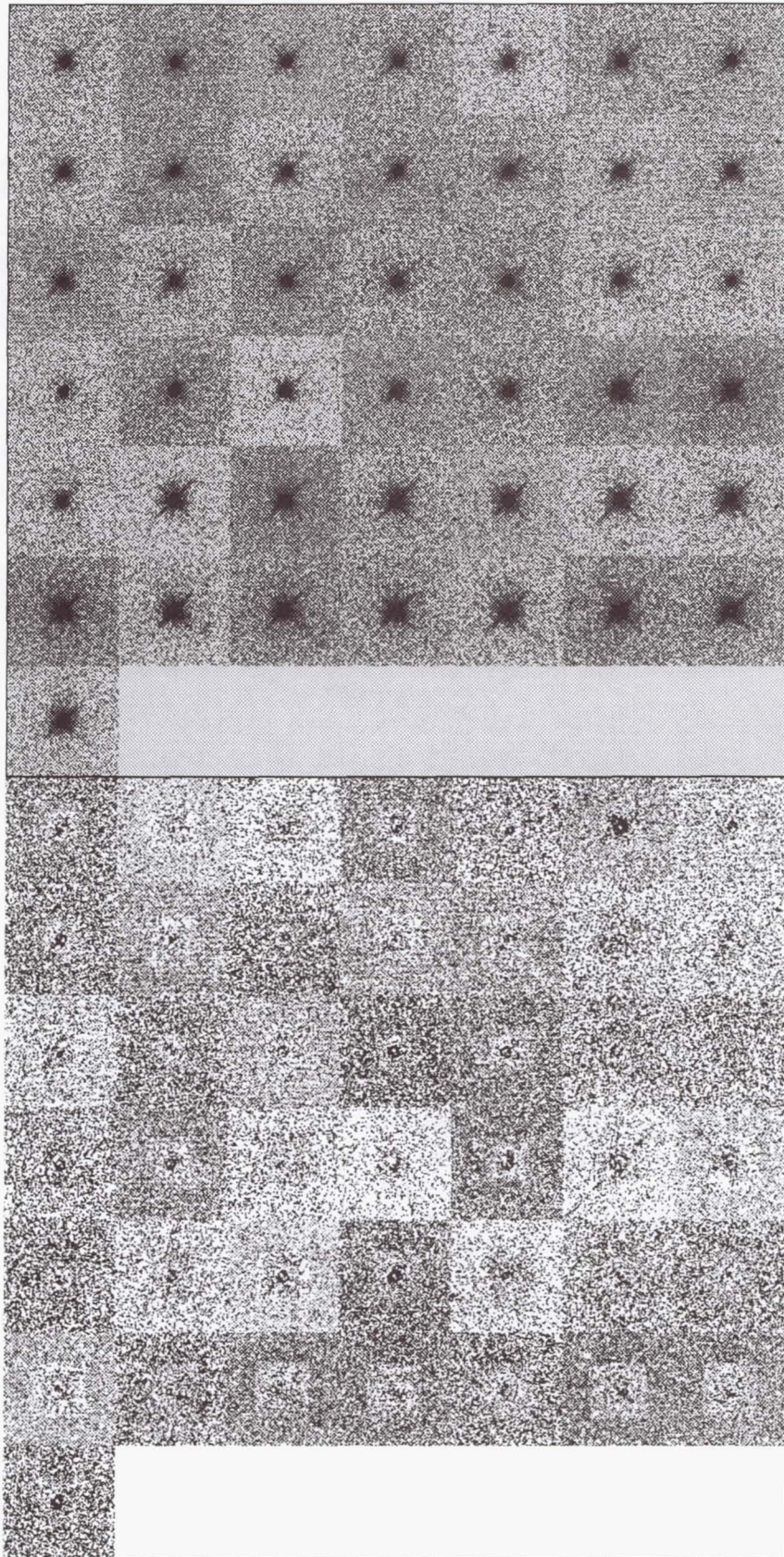


Figure 4. Greyscale representation of the 43 GRW+70D5824 observed PSFs (top) and residuals after subtraction of the composite observed PSF (bottom).



## The WFPC2 PSF Library

Michael S. Wiggs,<sup>1</sup> Sylvia Baggett,<sup>1</sup> Jean Surdej,<sup>2,3</sup> and Calvin Tullios<sup>1</sup>

**Abstract.** We describe the development of the WFPC2 PSF Library. The extraction of observed Point Spread Functions from standard calibration observations, as well as the creation of their associated header files are discussed. We then describe the development of the WWW-based PSF Library Search Tool, and use of the Tool.

### 1. Introduction

The WFPC2 PSF Library is designed to provide observers with easy access to a selection of observed PSFs, taken in most WFPC2 filters, and in various positions across each chip. Many of the PSFs were extracted from images of the clusters  $\omega$  Centauri and M67, which were imaged as part of STScI's ongoing WFPC2 Calibration Observations. These observations provided stellar images of various intensities, saturation levels, and positions across the chips. Only isolated, non-overlapping PSFs were selected.

In the future, we plan to extract PSFs from the calibration observations of the single white dwarf stars A+81D266, BD+75D325, GRW+70D5824, and Feige110, from selected, public GO data, as well as from the remaining observations of the clusters mentioned previously.

### 2. Generation of the PSFs

The PSF images were extracted from archival, pipeline processed WFPC2 images, with no further processing, and generally no cosmic-ray rejection. To identify PSF candidates, the observations were examined by eye. The PSF stars had to be well separated from other stars and have a peak intensity of no less than 150 DN; there was no imposed upper limit on any star's intensity.

For all stars meeting these simple selection criteria, the IRAF tool *imexamine* was used to fix the star's position and calculate the peak intensity (a Gaussian fit, in DN). An estimate was made of the background level on the chip by determining the average within 3  $20 \times 20$  pixel regions, free from cosmic rays. The resulting estimate is given in the *BACKGND* keyword in the PSF header.

The PSF positions and intensities were used to:

1. Determine the DN value of the peak pixel from image statistics (not the fit from *imexamine*), and then define the size of the extracted image. For peak intensities less than 3500 DN, the extracted image is  $64 \times 64$  pixels, centered on the PSF; greater than 3500 DN, the image is  $128 \times 128$  pixels.

---

<sup>1</sup>Space Telescope Science Institute

<sup>2</sup>Institut d'Astrophysique, Université de Liège, Belgium

<sup>3</sup>Research Director (FNRS, Belgium)



2. Extract the image sections as separate images with individual headers, comprised of the original WFPC2 header, plus new PSF specific keywords, listed in the table below.

3. Recompute the minimum and maximum data values and the "good" minimum and maximum data values, and update the PSF headers.

Table 1. Keywords added to PSF image headers.

KEYWORD	DEFINITION
ORIGIN	Data Source (HST, TINYTIM, or COMPOSITE)
XCENTER	X coordinate of PSF center on chip
YCENTER	Y coordinate of PSF center on chip
XCORNER	X pixel of (1,1) corner in PSF image
YCORNER	Y pixel of (1,1) corner in PSF image
RA_PSF	RA of PSF star (deg, J2000)
DEC_PSF	DEC of PSF star (deg, J2000)
PEAKINT	Peak intensity at xcenter, ycenter
PEAKFIT	Peak of Gaussian fit
SATURATD	Is PSF saturated? (Y or N)
BACKGND	Background (DN)
SPECTRAL	Spectral type of source, if known
REFSPEC	Reference spectrum, if known
T306	Secondary mirror temperature (degrees Celsius)
T307	Secondary mirror temperature (degrees Celsius)
T308	Secondary mirror temperature (degrees Celsius)
T309	Secondary mirror temperature (degrees Celsius)
V2_RMS	V2 Axis RMS (milli-arcsec)
V2_P2P	V2 Axis peak to peak (milli-arcsec)
V3_RMS	V3 Axis RMS (milli-arcsec)
V3_P2P	V3 Axis peak to peak (milli-arcsec)
GUIDEACT	Actual guiding mode at end of GS Acquisition
RELFOCUS	Relative focus ( $\mu$ m)

Any PSF image with saturated pixels (bitflag = 8, in the original calibration image's data quality (.c1h) file), had those pixel values replaced with a value of -100. This will allow users to quickly identify saturated pixels within the PSF.

### 3. Status of the PSF Library

To date there are 2701 PSF images available in the PSF Library. The table below lists the current distribution of PSFs by filter and chip.

Table 2. Status of the PSF Library by filter and chip.

FILTER	PC	WF2	WF3	WF4
F300W	8	9	14	9
F336W	40	81	86	50
F380W	1	3	3	0
F410M	1	1	1	0
F439W	60	93	122	73
F450W	2	4	1	0
F467M	1	3	3	1
F547M	10	17	26	11
F555W	80	102	132	89
F569W	12	18	20	11
F606W	38	25	50	30
F675W	40	14	18	10
F702W	12	27	18	17
F785LP	22	24	29	23
F814W	218	277	334	277

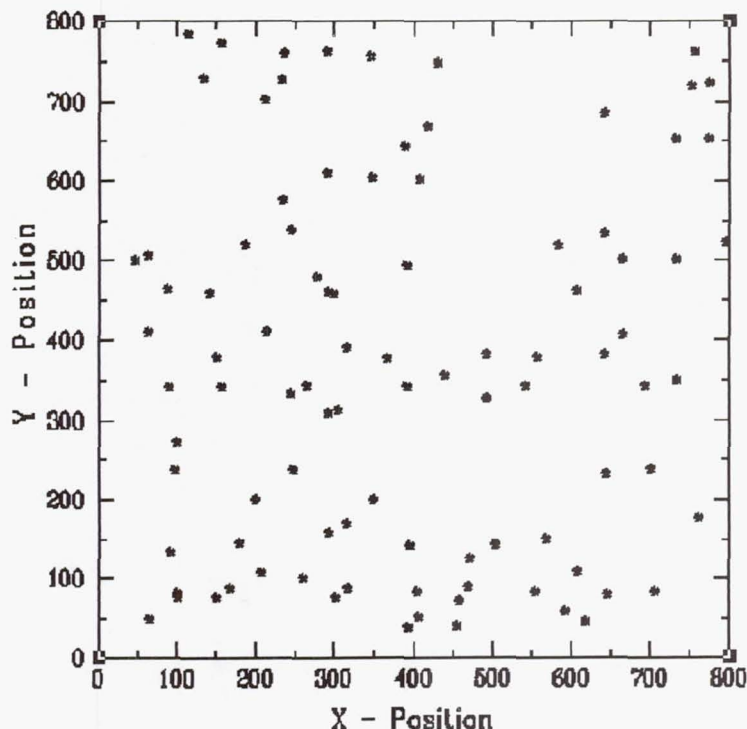


Figure 1. Positions of all PSFs available for F555W on the WF2 chip.

#### 4. PSF Relative Focus Information

One of the new PSF header keywords provides a value for the relative focus (RELFOCUS). This was done to provide users with a general idea of the focus of HST at the time of the PSF observation. Thus, users can use PSFs at or near the same focus as their own observations.

Presently, nearly half of the PSFs in the Library have RELFOCUS values determined from an average fit of the focus monitoring data based on the "phase-retrieval" method, with no correction for orbit-to-orbit variations in the focus (known as "breathing"). No breathing correction could be performed because the observations were made prior to July 1995, when temperature data became readily available. The other half of the PSFs were taken after July 1995, and have the "breathing" correction applied to the averaged phase-retrieval focus values. See Instrument Science Report OTA-18 for details on the focus history of HST and the "breathing" correction (Casertano, 1995). The rms scatter around the average fit is roughly  $\pm 2\mu\text{m}$ , while the scatter for points with the breathing correction applied is close to  $\pm 1.3\mu\text{m}$ .

Within the headers of the PSFs, we have also included the secondary mirror temperatures (T306, T307, T308, and T309 keywords), if known. Thus, if a particular PSF has a value other than 0.00, the breathing correction has been applied.

Also available from the PSF Library Help Page is a table containing the Modified Julian Date (MJD), and the averaged phase-retrieval focus values (with no breathing correction applied), to provide users with an estimate for the focus of their science image.

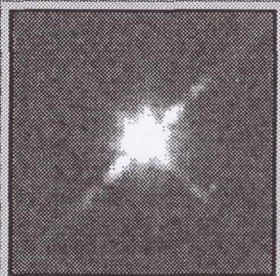
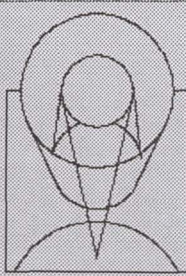


## 5. PSF Library Search and Retrieval Tool

In order to make the PSF images easily accessible to WFPC2 users, we opted for a Web-based search and retrieval tool, with the PSF images stored and available on-line. The tool was designed to be as flexible as possible, allowing the user to search for desired PSFs using virtually any combination of criteria. The output of this search can also be sorted according to the user's needs.

There are four basic steps to using the tool:

1. Define a subset of PSFs using qualifiers on the main page.
2. Select for retrieval a subset (or all) PSFs from the tabular output.
3. Request generation of an ftp command file for retrieval of the selected PSFs.
4. Save the command file to local disk, and run it at the user's leisure.

  **SPACE  
TELESCOPE  
SCIENCE  
INSTITUTE**

**WFPC2 PSF LIBRARY SEARCH TOOL:**

[How to use this form.](#)   [Status of the PSF Library.](#)

• **Image Data:**

Detector:    AtoD Gain:    Serials:

Filtname1:    Filtname2:

Sort Output By:

1: <input type="text" value="rootname"/>	2: <input type="text" value="detector"/>	3: <input type="text" value="atodgain"/>
<input type="button" value="CLEAR FORM"/>	SEARCH: <input type="text" value="DEFAULT OUTPUT"/>	SEARCH: <input type="text" value="FULL OUTPUT"/>

Figure 2. A portion of the WFPC2 PSF Library Web Page.



The Tool is accessible at the following WWW address:

[www.stsci.edu/ftp/instrument\\_news/WFPC2/Wfpc2\\_psf/wfpc2-psf-form.html](http://www.stsci.edu/ftp/instrument_news/WFPC2/Wfpc2_psf/wfpc2-psf-form.html)

The page has an extensive help file as well as a status page, listing the number of PSFs per filter and chip, and also plots showing the X-Y positions of the PSFs on the original images (see Figure 1). The PSF files can be retrieved in either FITS or GEIS formats.

**PSF's Found Satisfying Search Criteria : 10**

To preview individual PSF's, simply 'click' on the highlighted dataset name.

You may select all datasets by marking the 'Select All' checkbox, or select only those you wish by marking the appropriate checkboxes in the table below. Afterwards, select the 'Generate...' button of your choice. This will display an FTP command on the Netscape window. Use the 'Save As...' option and save this file to your disk, giving it any filename.

At your unix prompt issue the command: `ftp -n ftp.stsci.edu < yourfilename`  
and the desired PSF's will be written to your local disk.

Select All: ☐

select	det	filt-1	gain	clks	orig	xcenter	ycenter	obsdate	exptime (secs)	dataset name	sat	peakfit	dimension	prop id
<input type="checkbox"/>	1	F547M	15	OFF	HST	212.29	662.73	23/01/94	26	<u>gcj1339kn</u>	NO	242.36	64,64	4749
<input type="checkbox"/>	1	F547M	15	OFF	HST	79.25	428.05	23/01/94	26	<u>gcj13403u</u>	NO	1275.97	64,64	4749
<input type="checkbox"/>	1	F547M	15	OFF	HST	294.24	198.4	23/01/94	26	<u>gcj1340du</u>	NO	355.95	64,64	4749
<input type="checkbox"/>	1	F547M	15	OFF	HST	212.53	663.28	27/01/94	26	<u>h181432ti</u>	NO	328.05	64,64	4749
<input type="checkbox"/>	1	F547M	15	OFF	HST	79.5	428.54	27/01/94	26	<u>h181432mu</u>	NO	1061.34	64,64	4749
<input type="checkbox"/>	1	F547M	15	OFF	HST	294.47	198.86	27/01/94	26	<u>h181432qu</u>	NO	404.38	64,64	4749
<input type="checkbox"/>	1	F547M	15	OFF	HST	725.82	475.25	28/05/94	26	<u>h231604lu</u>	NO	234.01	64,64	5572
<input type="checkbox"/>	1	F547M	15	OFF	HST	154.5	407.44	22/09/94	26	<u>h2a14457u</u>	NO	1418.27	64,64	5572
<input type="checkbox"/>	1	F547M	15	OFF	HST	731.34	464.42	22/09/94	26	<u>h2a1445bu</u>	NO	336.79	64,64	5572
<input type="checkbox"/>	1	F547M	15	OFF	HST	643.78	490.14	28/08/95	35	<u>gat1607su</u>	NO	208.4	64,64	6182

Figure 3. Output from a search of the PSF Library.

Figure 2 displays a portion of the PSF page, with parameters set to search for all PSFs for filter F547M, in the PC, with any gain, and both serials. There are many other keywords that can be used as qualifiers, such as observation date, exposure time, whether the PSF is saturated, peak intensity, X,Y position (with search radius), as well as jitter. The user can sort the output according to any criteria; in this example the output will be sorted by dataset name, detector, and gain. The result of this search is in the "default output" format and is illustrated in Figure 3.

The output page allows the user to preview the PSF image, by "clicking" on the highlighted dataset name. It also allows for the selection of either all or just a few PSFs to be marked for retrieval. The PSFs can then be downloaded to the user's machine in either GEIS or FITS format.

The PSF Library is being continually updated with new PSFs. However, some users may find no appropriate PSFs in the Library. In this case we recommend using archival



data, either calibration or public GO data as a source of observed PSFs. Another alternative is to use TinyTim, a program to generate theoretical PSFs. Tiny Tim can be accessed at:

<http://scivax.stsci.edu/~krist/tinytim.html>

**Acknowledgments.** We would like to thank the following people for useful comments and suggestions: Stefano Casertano, Calvin Tullos, Matt Lallo, and Tim Kimball.

## The WFPC2 Clearinghouse

Michael S. Wiggs, Brad Whitmore, and Inge Heyer

*Space Telescope Science Institute*

**Abstract.** We discuss the development and use of the WFPC2 Clearinghouse, a Web-based search tool designed to provide WFPC2 users with a listing of astronomical publications which report results based on the use of WFPC2 data. The database can be searched on a variety of WFPC2 calibration related topics, ranging from astrometry to UV throughput.

### 1. Introduction

The WFPC2 Clearinghouse was designed to provide users of the Wide Field and Planetary Camera 2 with a searchable listing of all known journal articles, STScI documentation and reports, as well as user submitted documents on all aspects of the performance, calibration, and scientific use of WFPC2.

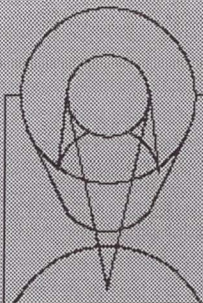
Table 1. WFPC2 Clearinghouse Topics.

Aperture Corrections	Object Identification
Aperture Photometry	Observation Planning
Astrometry	Photometric Transformations
Bias Frames	Photometric Zeropoint
Bias Jumps	Pipeline Calibration
Calibration Observations	Polarization
CCD Characteristics	PSF Characterization
Charge Transfer Traps	PSF Fitting Photometry
Chip-to-Chip Normalization	PSF Subtraction
Completeness Corrections	Quad Filters
Cosmic Rays	Recalibration
CTE Losses	Red Leaks
Darks	Residual Images
Data Quality	Saturated Data
Deconvolution	Scattered Light
Dithering	Serial Clocks
Drizzle	Size Measurements
Field Distortion	Software
Flats	Surface Photometry
Focus	SYNPHOT
Hot Pixels	T=77 Observations
Image Anomalies	UV Throughput
Linear Ramp Filters	Vignetting
Long vs. Short Exposures	Woods Filters
Narrow Band Photometry	1997 Servicing Mission

The Clearinghouse has two basic goals:

1. To make it easier for WFPC2 users to take advantage of the fact that there are hundreds of astronomers reducing and analyzing WFPC2 data, and learning much that may be of interest to other users.
2. To keep the WFPC2 Group at STScI aware of how people use WFPC2, and what they consider to be the main concerns regarding the instrument.





# SPACE TELESCOPE SCIENCE INSTITUTE

## THE WFPC2 CLEARINGHOUSE:

The WFPC2 Clearinghouse is designed to provide easy reference to a wide variety of WFPC2 related information. It includes references to:

- STScI documentation.
- Publications from the astronomical literature.
- User submitted documentation.

Please note that inclusion in the WFPC2 Clearinghouse does not necessarily mean that the WFPC2 Instrument Scientists at STScI endorse the results of a given reference, due to the fact that there are simply too many items for detailed review.

To search for articles pertaining to a specific topic, select a keyword from the menu below, and then hit the search button to generate a list of relevant documents.

An alphabetized listing of all references contained in the Clearinghouse database is also available.

### STScI's WFPC2 Reference Library:

<a href="#">WFPC2 Homepage</a>	<a href="#">WFPC2 Instrument Handbook</a>	<a href="#">WFPC2 KR's</a>	<a href="#">HST Data Handbook</a>
--------------------------------	---	----------------------------	-----------------------------------

### Related Search Engines:

<a href="#">STScI Homepage</a>	<a href="#">HST Papers (STScI)</a>	<a href="#">HST Papers (ST-ECC)</a>	<a href="#">Journals</a>	<a href="#">ADS</a>
--------------------------------	------------------------------------	-------------------------------------	--------------------------	---------------------

Figure 1. The WFPC2 Clearinghouse Web Page. In this example a user has selected to search for all articles which contain references to SYNPHOT

## 2. Description

Once a suitable article has been identified, it is added to our database, which is accessible through the WFPC2 Clearinghouse Web-page. Each article is entered into the database with its specific WFPC2 calibration related topics and an attempt is made to estimate how important the information on that topic may be to general users of WFPC2.

Please note that inclusion in the WFPC2 Clearinghouse does not necessarily mean that the WFPC2 Instrument Scientists at STScI endorse the results of a given reference, due to the fact that there are simply too many items for detailed review.



## WFPC2 CLEARINGHOUSE SEARCH RESULTS:

The results of this search are given in the following sample format:

Author: Holtzman, Mould, Gallagher, et al.  
 Title: *Stellar Populations in the Large Magellanic Cloud: Evidence for a...*  
 Year: 1997  
 Reference: AJ 113,656  
 Science Keyword: IMF, LMC  
 Calibration Keyword(3): *psf\_fitting\_photometry*(3)  
 Calibration Keyword(2): *bias*(2)  
 Calibration Keyword(1): *photometric zeropoint*(1)  
 Comment: Comparison of aperture and PSF fitting photometry.

Where the category number following each keyword stands for the following:

- (3) = One of the fundamental references on this topic.
- (2) = Some new information on this topic.
- (1) = General information on the subject.

## STScI Documents on synphot:

### References in Category #3:

Bushouse  
*SYNPHOT Users Guide*  
 1995  
[ra.stsci.edu/documents/SyG/SG\\_1.html](http://ra.stsci.edu/documents/SyG/SG_1.html)  
 None  
*synphot*(3)  
*observation\_planning*(2)  
 None  
 None

Baggett, Wiggs  
*Index of SYNPHOT Tables*  
 1997  
[www.stsci.edu/ftp/cdbs/cdbs6/synphot\\_tables/](http://www.stsci.edu/ftp/cdbs/cdbs6/synphot_tables/)  
 None  
*synphot*(3)  
 None  
 None  
 None

Figure 2. A small portion of the Clearinghouse Search Results Page, showing 2 important references regarding SYNPHOT.

### 3. An Example

Figure 1 shows a portion of the WFPC2 Clearinghouse Search Tool available through the World Wide Web. The user can select from a large list of WFPC2 calibration related topics (see Table 1). In this example a user has decided to search for all articles on SYNPHOT. Figure 2 shows the results of the search. At the top is a descriptive example of each database entry. Below that is the beginning of the listing, which starts with STScI Documentation on the subject, then on to references in the astronomical literature. Note that each reference line is linked to the appropriate STScI document. For journal articles, the reference is linked to its entry in the ADS Abstract Database, so that users can quickly determine if that particular article is relevant to his/her needs. The entire database listing is also



downloadable. A handy section providing links to other useful astronomical search engines is also included.

The Clearinghouse can be found at the following URL:

[http://www.stsci.edu/ftp/instrument\\_news/WFPC2/Wfpc2\\_clear/wfpc2\\_clrhs.html](http://www.stsci.edu/ftp/instrument_news/WFPC2/Wfpc2_clear/wfpc2_clrhs.html)





## Part 4. Other Instruments





## FOC Status and Overview

R. Jedrzejewski

*Space Telescope Science Institute, Baltimore, MD 21218*

**Abstract.** The calibration status of the Faint Object Camera is described. The best reference files to be used with COSTAR-corrected data are given, along with some discussion of the accuracies to be expected when these files are used. Finally, some discussion of the calibration of polarimetric and objective-prism spectroscopic observations is given.

### 1. Introduction

The Faint Object Camera is the only one of the original complement of prime science instruments that is still on HST, having been working for over seven years. In that time, our knowledge of the characteristics of the instrument has grown, while at times our understanding has lagged behind. In this paper, the most up-to-date summary of the characteristics of the FOC is given, concentrating on changes from the time of the last Calibration Workshop, in May 1995. This review will concentrate on the F/96 camera only; the F/48 relay will be covered in the next presentation.

### 2. Calibration Pipeline Overview

The automatic calibration pipeline performs at most four tasks to calibrate FOC data:

1. Dezooming (if the data were taken in zoom mode)
2. Computing photometric parameters
3. Geometric correction
4. Flatfielding

Along with these steps are some capabilities that were originally envisioned as necessary, but have since been found to be either pointless, or else impractical to implement. These are:

1. Background subtraction
2. ITF correction

The former step is not used, since the FOC background defies predictive modelling, and most users can just determine the background locally from the data themselves. The latter step was originally included as a means of correcting nonlinearity (ITF stands for Intensity Transfer Function), but is now being considered as a way to apply a format-dependent flatfield. A review of all FOC calibration products was undertaken in 1994 (Instrument Science Report FOC-082); this paper extends that work to the mid-1997 timeframe.

The currently applied calibration steps are now described in more detail:

## 2.1. Dezooming

There really isn't much to say about this. No reference files are harmed in performing this step. Each zoomed pixel is merely replaced by two pixels containing half of the zoomed intensity.

## 2.2. Computing Photometric Parameters

The 5 FOC photometry keywords in the FOC data header are:

1. PHOTMODE—this is the string describing the components that are required to determine the sensitivity
2. PHOTFLAM—this is the computed (by synphot) flux (in  $\text{erg}/\text{cm}^2/\text{sec}/\text{\AA}$ ) that gives rise to a total count rate of 1 count/sec (in an aperture of radius 1 arcsecond)
3. PHOTZPT—the ST magnitude zeropoint; this is always  $-21.10$  mag by definition.
4. PHOTPLAM—the pivot wavelength, as defined in Equation 1 below
5. PHOTBW—the rms bandwidth of the filter+detector

The critical parameter is PHOTFLAM. However, users usually don't want to know the flux in  $\text{ergs}/\text{cm}^2/\text{sec}/\text{\AA}$  that gives rise to a unit count rate, they want to know, for example, the  $V$  magnitude of a G2V star that gives 1 count/sec total. Fortunately, the STSDAS SYNPHOT package makes this calculation relatively simple:

```
calcphot obsmode='band(v)' \
>>> spectrum="rn(crgrid$bz77/bz_26.tab,band(foc,f/96,costar,f430w),1.0,counts)" \
>>> form="vegamag"
```

will work out the  $V$  magnitude for a star from the Bruzual spectral atlas with a G2V spectrum (bz\_26.tab), renormalized so that the FOC F/96 camera with F430W filter gives 1.0 count/sec. The answer is  $V = 22.62$  mag.

The sensitivity is derived by integrating over wavelength the product of the various throughputs and sensitivities in the light path. A typical FOC observing configuration has 7 components, plus 1 for each filter used. For the example given above (F/96, F430W filter), the components are:

Table 1. Components used in deriving FOC sensitivity

Throughput table	Explanation
hst_ota.005.tab	OTA throughput
foc_96_m1m2.001.tab	COSTAR throughput
foc_96_rflpri.002.tab	FOC primary ( $\equiv 1.0$ )
foc_96_rflsec.002.tab	FOC secondary ( $\equiv 1.0$ )
foc_96_f430w.002.tab	F430W filter
foc_96_rflfocus.002.tab	FOC refocus mirror ( $\equiv 1.0$ )
foc_96_n512.001.tab	Format-dependent sensitivity
foc_96_dqe.004.tab	FOC/96 detector sensitivity

The OTA throughput reference file is unlikely to be updated unless an identical change in performance is noticed by users of all HST instruments. Similarly, the COSTAR throughput is combined with the FOC sensitivity in such a way that there is no point in trying to determine each separately. The FOC primary, secondary and focus mirror terms are set



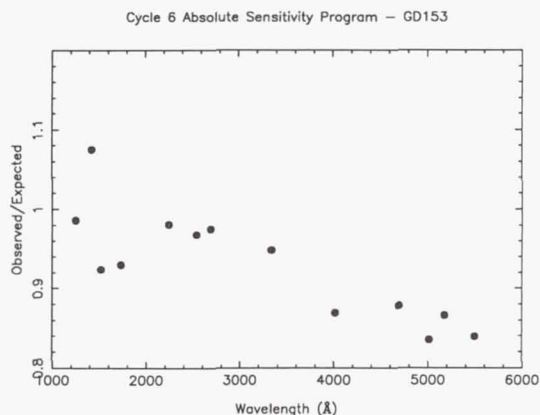


Figure 1. FOC Photometry of the primary standard GD153

to 1.0 and absorbed into the FOC detector sensitivity. The filter transmission curves were determined from ground test measurements, and will not be modified unless an individual filter is found to behave significantly differently from other filters in the same wavelength region.

Thus, the only throughput components that are subject to revision as a result of improved calibration are the FOC detector sensitivity and the format-dependent sensitivity. There are two parts to the calibration; setting the absolute value by observation of standard stars with known flux, and determining any changes in this value. The first must be done by observing a spectrophotometric standard star, while for the second, the only requirement is that the spectrum of the star not vary.

In practice, the calibration of the detector sensitivity has been done by observing spectrophotometric standards. Typically, these are the faintest of the IUE standards (BPM16274 at  $V = 14.20$ , HZ4 at  $V = 14.52$  and LB227 at  $V = 15.34$  mag). BPM16274 has absolute IUE flux calibration in the UV, but no visible spectrophotometric calibration. HZ4 and LB227 have both IUE UV spectrophotometry and Oke visible spectrophotometry. Observations during 1994 showed good agreement between the UV measurements of BPM16274 and HZ4 (see Instrument Science Report FOC-085), but 1996 observations of HZ4 showed some disagreement from observations of LB227, at the 10–20% level, while agreeing with the Cycle 4 observations of HZ4. Note that none of the faint standards used have FOS spectroscopy.

To try and overcome the confusion between standards, the 1997 absolute calibration program used the PRIMARY standard GD153 as the target. This white dwarf standard, described in Bohlin et al. (1995), has FOS spectrophotometry that agrees with the model atmosphere prediction to better than 1–2% everywhere, so there is no doubt as to the reliability of the absolute flux levels.

Comparison of the measured count rates with the SYNPHOT predictions showed a surprising trend with wavelength; in the UV, the measured count rates were close to the predictions, with large ( $\sim 5\%$ ) scatter, while in the visible, the measured count rates were down by 10–15% from the prediction. As can be seen from Figure 1, there is a roughly linear relation between the observed/expected count rates and wavelength.

The observed behavior is not just a reflection of the fact that the previously observed standard stars have larger spectrophotometric errors than the primary standard; it has been noticed that the FOC sensitivity is changing with time. We can rule out significant changes between 1994 and 1995, because monitoring of a standard star with a variety of filters over that timeframe did not show any changes at the 5% level or so. However, later observations (mid-late 1996 and 1997) have shown that the throughput of the FOC is declining slowly, at

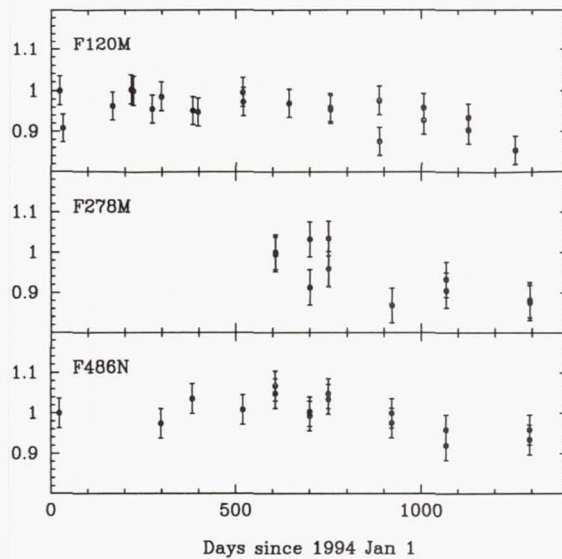


Figure 2. FOC Sensitivity Trends, 1994–1997

approximately 10%/year, with little or no dependence of the sensitivity drop on wavelength. The relative sensitivities of observations in three filters (F120M, F278M and F486N) are plotted in Figure 2.

Observations made just after the Second Servicing Mission (when COSTAR was retracted) showed that the sensitivity drop is confined to the FOC, and not due to any degradation in COSTAR or the OTA. It is not clear at this point whether it is possible to “tune” the FOC to restore this sensitivity. Currently, we are working on trying to characterize this sensitivity drop using all available data. In the meantime, users are advised to assume that the error on the absolute sensitivity can be as large as 15%.

Until the recent sensitivity changes have been characterized reliably, users should use the `foc_96_dqe_004.tab` instrumental sensitivity file for absolute calibration. This was installed as the default sensitivity file in October 1994, so observations taken before then will have used the earlier file, with possible errors of up to 20–30% in the UV.

### 2.3. Geometric Correction

The geometric correction for the F/96 camera has been improved by use of images of a crowded field to sample the geometric distortion pattern on a finer scale than is provided by the reseau marks etched onto the photocathode. The method has been used to derive geometric correction files for the 512×1024(z), 512×512, 256×256 and 128×128 formats. For details, consult the Instrument Science Reports FOC-086 and FOC-087.

The optimum geometric correction files are given in Table 2.

On a more global scale, it is known that the overall plate scale and rotation angle of an FOC image change over short timescales; this can be seen by blinking well-exposed images of a diffuse source taken shortly after the camera is switched on. Unfortunately, there is no strong repeatable pattern to the variation. However, plate scale changes are generally limited to  $\pm 0.1\%$ , and rotation angle to  $\pm 0.1^\circ$ .

We hope to develop a simple method to apply low-order corrections to the geometric correction files to be used; this will allow more reliable co-addition of multiple images when the geometric distortion changes significantly from image to image. Interested users should keep an eye on the FOC WWW pages.



Table 2. Best Geometric Reference Files for COSTAR-corrected FOC data

Format	Best GEO file
512×512	f371529ex.r5h
512×1024(z)	f371531ox.r5h
256×256	f3715276x.r5h
128×128	f371524px.r5h
512×1024	ga10937nx.r5h
256×1024	f371522ex.r5h

## 2.4. Flatfielding

The FOC flatfield is mainly the manifestation of photocathode sensitivity variations. These exist on all scales, from the pixel-to-pixel scale to that of the whole detector. However, unlike the case with CCDs, the flatfield response varies only slowly with wavelength. This is fortunate, since the process of acquiring flatfield data of sufficient signal-to-noise is extremely time-consuming. In practice, flatfields have been taken for a few select wavelengths where a suitable celestial target exists (the Orion nebula in the ultraviolet) or else where the internal LED lamps are active (4800–6500Å).

Because of the count-rate limited nature of the FOC, it is not practical to obtain enough counts to provide a signal-to-noise per pixel of 1% or so. When the full 512×1024(z) format is used, the maximum allowable count rate for which the response is still reasonably linear is about 0.03 counts/pixel/s, so to obtain the necessary 10000 counts/pixel would require exposure times of  $3 \times 10^5$ s or so, or over 3 days of continuous illumination. Instead, the flatfields are smoothed over scales of 15 pixels or so to improve the global accuracy, at the expense of fine-scale precision. The geometric distortion is not stable enough to ensure that small-scale features will remain in the same place in the image such that fine-scale flatfielding would work.

Overall, there is not a huge difference between the flatfields from the UV to the visible. Typically, the amplitude of any differences are 10% or so, with an rms variation of 3%. Near the red end of the FOC response (for wavelengths  $> 5600\text{\AA}$ ), the global sensitivity variations are somewhat enhanced, but this is an extremely rarely-used wavelength region for the FOC. Similarly, the small-scale features are more pronounced in the ultraviolet.

The best current flatfields were derived from pre-COSTAR flatfields, with the geometric correction adjusted to reflect the difference between the pre-COSTAR and COSTAR-corrected geometric distortion. The best flatfields are given in Table 3 below:

Table 3. Best Flatfield Reference files for COSTAR-corrected FOC data

Wavelength Range (Å)	Best Flatfield
$\lambda < 2555.0$	f3716027x.r2h
$2555 < \lambda < 5184.6$	f3716029x.r2h
$5184.6 < \lambda < 6079.5$	f371602cx.r2h
$\lambda > 6079.5$	f371602dx.r2h

Here the wavelength is the pivot wavelength, defined as

$$\lambda_P(P) = \sqrt{\frac{\int P(\lambda) \lambda d\lambda}{\int P(\lambda) d\lambda / \lambda}} \quad (1)$$

where  $P(\lambda)$  is the instrumental sensitivity. These flatfields are the "best" for all COSTAR-corrected data, until superior versions are delivered. Users are advised to check the FOC WWW pages to learn of any new developments in the area of reference files.

The large gap in the wavelength coverage of the flatfields will be closed somewhat with the completion of the Cycle 6 calibration program. Here, images of the Orion nebula will be taken using the F220W filter to provide a near-UV flatfield. Analysis of some of the data which were taken as part of the Cycle 4 calibration program showed small but significant differences from the F140W flatfield that had been acquired before COSTAR was inserted.

Finally, there is a component of the flatfield response that appears to be associated with the TV camera rather than the photocathode. Normally, when the flatfield for a format other than the full  $512 \times 1024(z)$  format is required, the appropriate subsection of the full-format flatfield is used. It has been found that the ratio of a small-format flatfield to the subsection of the full-format flatfield is not constant, with variations of 10–20% or so on the right-hand edge, where the scanning beam starts up. It had been suspected that this was merely a result of the rapidly-changing geometric distortion in that part of the image, and that if the distortion were modelled correctly, the apparent sensitivity variations would disappear. Recent work by Greenfield (FOC Instrument Science Report FOC-086) has shown that this is not the case; even when the improved geometric correction is applied, the sensitivity variations remain. Users should be aware that the sensitivity in the 100-pixel wide region on the right-hand side of the image may be different from that over the rest of the image by up to 10–20%, until this effect is corrected in the FOC pipeline.

### 3. Expected Accuracies

It is always difficult to try and summarize the performance of the FOC with a table of the accuracies you can expect; one always feels that it is necessary to include disclaimers or "your mileage may vary" warnings. Still, such a table can at least highlight the capabilities of the instrument and warn users away from projects that require precision well beyond that which the FOC can deliver. Table 4 gives a summary of the accuracies you can expect to achieve from FOC observations.

### 4. Special Modes: Objective Prisms and Polarizers

#### 4.1. Objective Prisms

The F/96 camera has two objective prisms that provide low dispersion spectroscopic capability with high throughput. The calibration of the prisms has been improved recently, and a set of data analysis programs have been incorporated into the STSDAS `focprism` package. The Near-UV prism provides coverage from 1600Å to 6000Å, with a dispersion that goes from about 0.6Å/pixel at 1600Å to 81Å/pixel at 6000Å. Typically, spectrophotometry is possible to approximately 0.1–0.2 mag accuracy, and the wavelength calibration is good to about 1.8Å at 1600Å and 17Å at 2500Å. The red end of the wavelength calibration is less accurate, but a planned Cycle 6 calibration program has been designed to address this. Results will be posted on the FOC WWW pages when they are available.

The Far-UV prism covers all the way down to 1200Å, but the dispersion is very low in the visible. At 1200Å the dispersion is 1.7Å/pixel, but at 5000Å it is more than 500Å/pixel, such that the entire 3000–6000Å range is covered in only 10 pixels in the dispersion direction! Typical spectrophotometric accuracies are again in the 10–20% range, and wavelength uncertainties range from approximately 1.3Å at 1200Å, to ~16Å at 1800Å.

Interested parties should refer to FOC Instrument Science Report FOC-092 for more details.



Table 4. Accuracies you can expect from FOC observations

Procedure	Estimated Accuracy	Notes
Calibration:		
Flat fielding	< 5% rms large scale 5–10% rms small scale Up to 90%	"Clean" areas On reseau marks, scratches
Geometric Correction	0.3 pixel rms	
Relative Photometry		
Repeatability:	~2–3% rms	As long as statistical errors are not important, target in same place on detector.
Background determination	~1–2%	Depends on aperture size, but generally not a dominant contributor to overall error
PSF/focus effects, small apertures	Up to 50%	1 pixel aperture, UV wavelengths
PSF/focus effects, large apertures	~2–3%	Aperture size >10 pixels radius
Absolute photometry		
Sensitivity	~10% for most filters	But beware of recent changes
Astrometry		
Relative	0''.005 rms	After geometric correction
Absolute	1'' rms (estimated)	Guide star uncertainty

#### 4.2. Polarizers

The FOC F/96 camera is equipped with three polarizers with pass directions at  $0^\circ$ ,  $60^\circ$  and  $120^\circ$  to the image  $x$  axis. They consist of double Rochon prisms cemented together, so that the ordinary rays are transmitted undeviated, while the extraordinary rays are shifted off the detector. The transmission of the pass direction and rejection of the perpendicular polarization are very good, much better than the performance of most polaroids. Also, since most of the reflections in the FOC+COSTAR optics are at small angles of incidence, very little instrumental polarization is induced ( $<1\%$ ).

However, it is not easy to obtain accurate polarization values, especially for point sources. This is partly because the polarizing prisms modify the point-spread function (especially the POL60 prism) in such a way as to introduce an unknown (and uncalibratable) aperture correction to the measured flux whose value does not become unimportant until the aperture radius is as large as 7–10 pixels (0.1–0.15 arcsec).

Secondly, the FOC is not exactly a precision photometric instrument. Repeated observations of the same target through the same filters typically show an rms deviation of 2–3% even when the Poisson noise associated with each observation is 1% or less. The fundamental limit to the accuracy of FOC photometry is believed to be small-scale features in the flatfield, which are not removed in the flatfielding process. (Recall that the flatfields used are heavily smoothed to give adequate signal-to-noise ratio). Acquiring such flatfields would be prohibitive.

To show how the polarization analysis depends critically on the aperture size, Figure 3 shows the apparent degree of polarization for multiple observations of an unpolarized star through the three polarizer filters and the F342W filter. The eight observations (3 in POL0, 2 in POL60 and 3 in POL120) were combined with each other in all possible combinations to give a total of 18 polarization "observations". The PSF was observed to change slightly

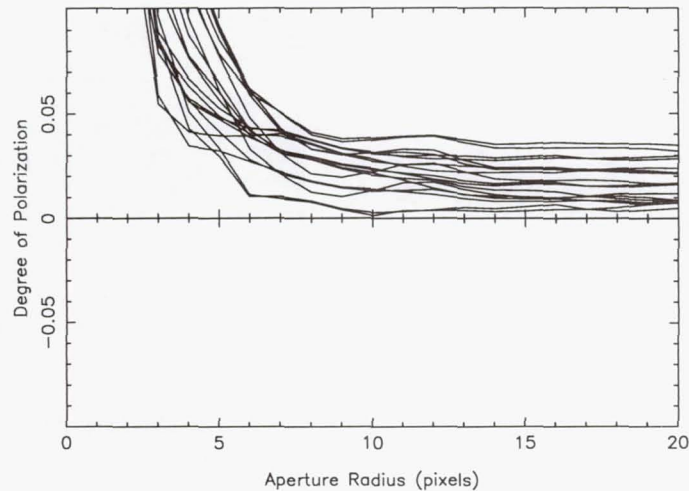


Figure 3. Effect of aperture size on measured point-source polarization

from observation to observation, even for images using the same polarizer, due to small focus effects. It is easy to see that the apparent “polarization” does not settle down to its small value until the aperture radius is 7 pixels or larger. However, users should also note that 7 FOC F/96 pixels correspond to 1 WFC pixel, so the loss in resolution is not too bad.

It can also be seen that the individual observations converge to values between 0 and 3% or so. This is about as well as the polarization can be measured for a well-exposed, isolated point source. Users who are careful to try and overcome some of the sources of systematic error (for example, by dithering between multiple images to lessen the effects of the small-scale flatfields) can, in principle, reach these levels of accuracy. However, a program that simply gathers three images, one in each polarizing filter, is much less likely to be able to achieve this level of accuracy for point sources.

For extended sources, one can do better, since the effects of PSF differences are lessened and the flux is in general averaged over areas that mitigate the influence of the small-scale flatfields. However, here one has the problem of trying to determine the background; extended objects are less likely to have “empty” areas of the image to be used for background determination.

In summary, polarization accuracies of 1–2% are achievable if care is taken in the observations or if extended sources are observed.

**Acknowledgments.** Many people who have contributed to the continuing success of the FOC. In particular, Perry Greenfield, Warren Hack and Mark Voit and Antonella Nota did much of the analysis reported here.

## References

Bohlin, R., et al., 1995, *AJ*, 110, 1316



## F/48 Slit Spectroscopy

R. Jedrzejewski & M. Voit

*Space Telescope Science Institute, Baltimore, MD 21218*

**Abstract.** The calibration of the FOC F/48 long-slit spectrograph is described. The time-varying and nonlinear geometric distortion makes both target acquisition and spectral rectification difficult. Here we describe the methods developed to ensure adequate calibration accuracy, and present our best understanding of the precision achievable with this instrument.

### 1. Introduction

The F/48 long-slit spectrograph was designed to allow spatially resolved spectroscopy of extended, high surface brightness objects at a wavelength resolution that provides accuracies of tens of km/s or so. However, the difficulties of accurately locating the narrow ( $0''.1$  pre-COSTAR) slit and the subsequent problems of the F/48 detector experiencing a coronal discharge and tripping its high voltage power supply meant that this powerful facility saw little use before the First HST Servicing Mission in 1993. The installation of COSTAR made the slit even narrower ( $0''.062$ ), and at the time of the Servicing Mission it was not clear what the long-term prospects for reliability of the F/48 camera were. However, cautious attempts to use the relay were initially successful, so work was started to try and locate the spectrograph slit and characterize the properties of the spectrograph in order to enable a science program of FOC IDT observations, and to allow GO use in Cycle 6 at the proposer's risk. Despite the fact that the F/48 longslit spectrograph introduced a unique facility to the observatory, only one Cycle 6 GO proposal was accepted. The FOC IDT reserved a significant amount of its guaranteed time for spectroscopic observations, giving a total usage of about 40 orbits.

### 2. F/48 Spectrograph Characteristics

The main characteristics of the F/48 spectrograph are given in Table 1. In all respects (sensitivity, choice of gratings and slits), STIS is a superior instrument, but the F/48 spectrograph had the unique position of being the only long-slit spectrograph on HST before the Second Servicing Mission.

### 3. Calibration

In order to enable the science program, it is necessary to locate the slit on the OTA focal plane or else generate a robust method of acquiring targets onto the slit. Then a first order characterization is necessary to ensure that the performance is close to expectations, so that the science data has the signal-to-noise ratio and other characteristics assumed by the proposers.

Table 1. Characteristics of the F/48 Spectrograph

Slit length:	12.5"
Slit width:	0.062"
Wavelength range:	3600–5400 Å first order 1800–2700 Å second order 1200–1800 Å third order 1150–1350 Å fourth order
Dispersion:	1.7 Å/pixel first order
Wavelength resolution:	3 pixels FWHM = 5.1 Å = ~400 km/s @ 3727 Å
Spatial resolution:	2–3 pixels = 0''.05–0''.08
Detector Background:	~ 0.3–1 × 10 <sup>-2</sup> counts/pixel/sec
Sensitivity:	$B = 14.6 \text{ mag} \Rightarrow \sim 0.3 \text{ count/sec peak @ } 4200 \text{ Å}$ ~ 1 count/sec total @ 4200 Å

### 3.1. Slit location

The design of the spectrograph does not make target acquisition easy. The slit is etched into the F/48 aperture plate, offset from the central clear imaging aperture. Light that passes through the slit normally misses the detector. However, when the spectrograph mirror is inserted, the direct light is blocked out and the light through the slit is directed onto a grating, where it is dispersed and fed back onto the detector. The only clue as to the location of the slit is the slit finger, a small opaque protrusion that blocks some direct light at the edge of the F/48 512×1024(z) field of view. Once the shadow of the slit finger is known, in principle the slit can be located provided that one knows the angle that the aperture plate makes with the (V2, V3) system. Unfortunately, the geometric distortion is quite severe at the edge of the field where the image of the slit finger is, so that the slit finger appears to be bent, and this uncertainty in the orientation of the slit finger translates into a large (~ 1'' or so) uncertainty in the location of the slit.

Early attempts to locate the slit involved scanning an astrometric standard star over the slit finger (to locate the (V2, V3) coordinates of the finger), and then scanning an astrometric star across the slit. Unfortunately, successive scans failed to give a consistent answer to the location of the slit.

After COSTAR was installed (and the focal plane metrology changed too!), a different method was used. It was realized that it is not necessary to know the absolute location of the slit in (V2, V3) space, only the offset from a reference point in the imaging field. Choosing the reference point to be close to the center of the field, where the changes in geometric distortion are small, should provide some insurance against changes in the distortion that acquisitions in the area close to the slit finger would have been prone to. The offset was determined by scanning a complex target (the AGN NGC 4151) across the slit, and comparing the structure of spectrum of the narrow-line region with narrow-band images taken with the F/96 camera. Having located the offset of the slit, the Project Data Base Science Instrument Aperture File was updated to reflect this knowledge.

But there remains the problem of being able to reliably acquire targets onto the slit. There is no onboard target acquisition facility in the F/48 camera. Actually, that's not quite true. There *is* an onboard target acquisition facility, but the acquisition aperture (63 × 63 pixels) is so small (1''.8), that it would require an interactive acquisition to reliably place a target in the acquisition aperture. So it is necessary to use an interactive target acquisition (a so-called "Mode-1 Target Acquisition").



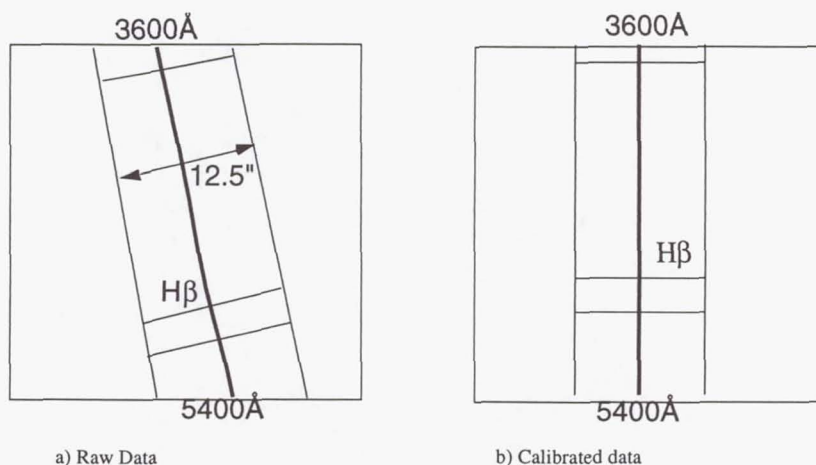


Figure 1. Geometric Distortion in Spectrograph Data

Unfortunately, the geometric distortion is quite nonlinear. This means that the OPUS target acquisition software, which uses a linear distortion model, is not accurate enough to calculate the offset required to move a target to the reference point; the error from using a linear approximation to the distortion can amount to many pixels, or rather larger than the width of the slit.

To overcome this, the geometric distortion of the F/48 imaging camera was measured in the same way as was done for the F/96 camera, by observing a crowded field with multiple pointings. This gives us a detailed model of the geometric distortion stored as a bicubic spline, and an IDL procedure was written to use this spline to calculate the slew required to move the target from the position in the acquisition image to the slit acquisition reference point. This procedure is now routinely used instead of the standard OPUS target acquisition software for interactive acquisitions onto the F/48 slit, and occasionally for F/96 interactive acquisitions when very accurate pointing is required.

Typically, the accuracy of this acquisition method is slightly better than the width of the slit; the main source of residual error is the fact that the geometric distortion is time dependent, so the pixel location of the slit acquisition reference point changes slightly from program to program. A slight improvement can be obtained by scanning the target across the slit, but this is expensive in terms of telescope time.

More details about the procedure for acquiring targets onto the F/48 slit can be found in FOC Instrument Science Report FOC-095.

#### 4. Wavelength Calibration and Rectification

The geometric distortion of the F/48 camera makes analysis of the longslit spectroscopic data difficult. Both the wavelength and the position along the slit are complex functions of pixel location, whereas "calibrated" data would have wavelength a linear function of pixel location in one dimension, and position along the slit a linear function of pixel location in the perpendicular direction. This is exemplified in Figure 1. The F/48 spectrograph does not have an internal emission-line source which could be used for wavelength calibration and wavelength rectification. Nor does it come with a slit mask, which would be useful for determination of the paths traced by point continuum sources. Instead, celestial targets must be used for this type of calibration.

For the wavelength calibration, the high surface brightness planetary nebula NGC 6543 was used. This has many strong first-order lines and fills the spectrograph slit. Using tasks

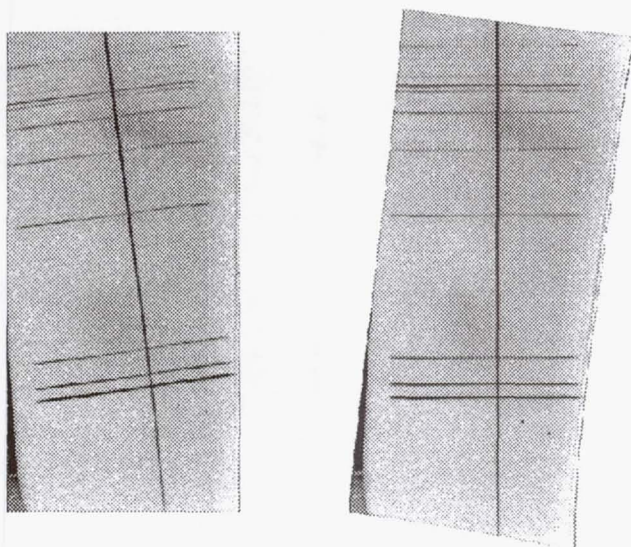


Figure 2. Result of the rectification process applied to calibration data. Left: Raw data, before geometric correction; Right: Rectified data

in the `noao.twodspec.longslit` package, the transformation between pixel position  $([i,j])$  and wavelength can be found.

In the perpendicular direction, along the slit, nature does not provide us with convenient linear arrangements of stars. The only way to overcome this is to take spectra of a single star at many different positions along the slit, an expensive proposition. In practice, a single star was positioned close to the center of the slit (to allow measurement of the trace of a star), and then moved approximately  $3''$  along the slit. The spectrum was geometrically rectified to make the central spectrum come out straight and vertical. The other spectrum was then examined to look for deviations from verticalness. Any deviations show, to first order, that the scale along the slit is a function of wavelength. No significant deviations were found, so it was assumed that the same regularizing function can be applied to all positions along the slit.

Having created polynomial functions that convert from wavelength and position along the slit to pixel position  $[i,j]$ , we can create a reference file that, for each pixel in the rectified image, contains the coordinates of the corners of the quadrilateral that the pixel maps into in the raw data. Summing the contributions of the partial pixels covered by the quadrilateral (weighted by the intersection of the areas of raw pixels and mapped quadrilateral) gives the flux in the geometrically corrected pixel, calculated in a fashion that is rigorously flux-conserving. The HST Data Handbook gives an illustration of this process.

The result of geometrically correcting F/48 longslit data is shown in Figure 2, where a raw spectrum (actually the sum of a planetary nebula and a continuum point source) is shown before and after rectification.

This is all straightforward, but the time-dependence of the geometric distortion means that, in general, the reference files derived from calibration data are not quite applicable to science data. The error can amount to a few pixels at the extremes of the wavelength range, making any wavelength (or redshift) measurements incorrect at the few Å (or few hundred km/s) level.

Since there is no facility to take calibration line spectra, the only monitor of the geometric distortion is the reseau marks. Most science images are not exposed enough to show the reseau marks, but fortunately all proposals were written to include internal flatfield



exposures during the occultation part of the orbit. Similarly, the calibration programs also included internal flatfield exposures to provide a snapshot of the geometric distortion at the time the calibration exposures were taken.

Using these internal flatfield exposures, it is relatively straightforward to create "custom" geometric correction reference files for each science exposure. We use the fact that the reseau marks have unique locations in the correctly geometrically corrected spectra (i.e., the geometrically corrected calibration spectra). The polynomial transformation applied to the reseau positions from the raw calibration flatfields gives the positions of the reseau marks in the geometrically corrected calibration images. Then all that is required is to determine the transformation required to go from the observed reseau mark positions in the flatfield appropriate to the science data to these reference reseau mark positions. There are tools in the `stdas.hst.calib.foc.focgeom` package to assist in the locating of reseau marks (task `rfindx`) and fitting one set of reseau marks to another (task `rfitx`).

In practice, this method is relatively simple, convenient and robust. Typically, a  $5 \times 5$  polynomial fit with cross terms is required to give r.m.s residuals of the fit between raw and reference reseau positions of approximately 0.3 pixels. Generating reference files and geometrically correcting the data is then straightforward using the `p2geo` and `newgeom` tasks in the `focgeom` package.

It is possible to get small offsets between geometrically corrected spectra, both in the wavelength direction and in the direction along the slit. These can amount to a few pixels in each dimension, and is believed to be due to small differences in the way the spectrograph fold mirror is deployed from observation to observation. The difference is a pure shift, with no difference in dispersion or plate scale. Users should be aware of this possibility when combining multi-orbit observations.

The wavelength calibration and geometric rectification processes are described more fully in Voit (1997a, 1997b).

## 5. Spectrophotometric Calibration

The spectrophotometric calibration is performed by taking a spectrum of a spectrophotometric standard star. Comparison of the measured counts/second in the stellar spectrum with the known flux from the star gives the total sensitivity of the F/48 spectrograph in counts/( $\text{erg cm}^{-2} \text{ \AA}^{-1}$ ), or counts/photon.

Unfortunately, most of the spectrophotometric standard stars in the HST calibration reference library are too bright for the F/48 spectrograph to observe in first order without significant nonlinearity or saturation. Only the faintest standard star, LDS749B, is faint enough to be used in the linear regime. The reference spectrum uses the most recent corrections to the flux for both the UV spectrum (from IUE) and the visible (from Oke Double Spectrograph measurements), and is probably accurate to 10-20% or so in the UV and 5% or so in the visible.

Since we are trying to give an absolute calibration, it is very important to make sure that the star is accurately centered in the slit. An error of a few hundredths of an arcsecond in the centering can make a difference of more than 25% in the absolute calibration. For this reason, the calibration star was scanned across the slit in steps of  $0''.04$ , allowing a centering accuracy of  $0''.01$ – $0''.02$ . In practice, the spectrum with the highest throughput was sandwiched between two spectra with almost identical count rates, making interpolation of the maximum throughput straightforward.

Analysis of the point source profile along the slit direction shows that the FWHM is approximately 2 pixels, and that the slit transmits about 60% of the total flux of a point source if the flux along the slit is summed over a 10 pixel aperture. Conversion from measured flux to absolute flux depends on whether one is considering a point source or an extended source, and however the reference files are defined is sure to confuse some people.

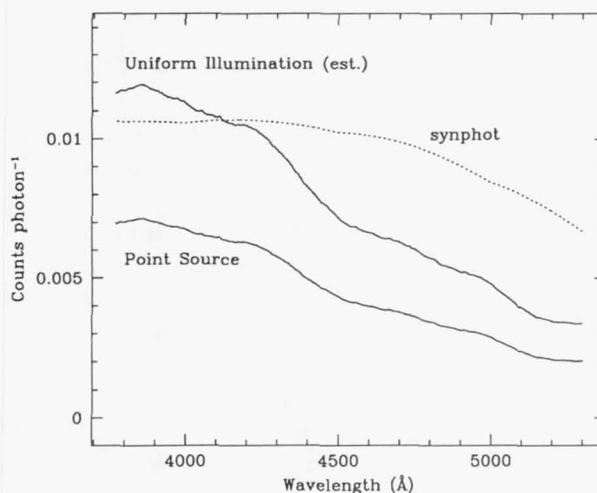


Figure 3. Spectrograph efficiency in counts/photon for first order spectra.

One could either keep all sensitivities in terms of “per pixel”, and advise users that when converting from measured fluxes to absolute fluxes for a point source, they should apply an aperture correction of  $1/0.6$  to account for the fact that only 60% of the flux from a point source passes through the slit. Alternatively, one could define the absolute sensitivity reference files to assume that point sources are observed, and advise users that when looking at an extended source, they should multiply the absolute calibrated fluxes by 0.6 to back out the aperture correction that is included in the reference files.

Comparison of the measured count rates with the known flux from the standard star gives the spectrograph efficiency curve shown in Figure 3. The two curves (for point and extended source) refer to the fact that the initial pre-launch calibration of the sensitivity of the spectrograph used an extended source. It can be seen that the sensitivity agrees with the pre-launch expectations reasonably well.

In a similar way, the sensitivity of the spectrograph in third order was measured by observing the same star with the F150W filter in place as an order extracting filter. This effectively cuts out all of the 1st and 2nd order flux and a large part of the fourth order flux, allowing a relatively clean measurement. The result of the sensitivity check is shown in Figure 4, where it is seen that the sensitivity agrees with the pre-launch estimates to within a factor of 2 over most of the wavelength region of interest.

Full details of the spectrophotometric calibration can be found in Voit & Jedrzejewski (1997).

## 6. Accuracies

If the rectification is performed using custom-generated reference files, the absolute wavelength accuracy is limited by the repeatability of the deployment of the spectrograph mirror, to about  $5 \text{ \AA}$ . However, relative wavelength measurements are much more accurate, amounting to approximately 0.5 pixels rms for both wavelength-to-wavelength comparisons and for comparisons at the same wavelength but different positions on the slit.

For spectrophotometry, the first-order accuracy is approximately 20% or so, while for third order the error is probably closer to 50%.

**Acknowledgments.** Richard Hook and Sperello di Serego Alighieri did some of the original work on the wavelength calibration of the F/48 spectrograph.



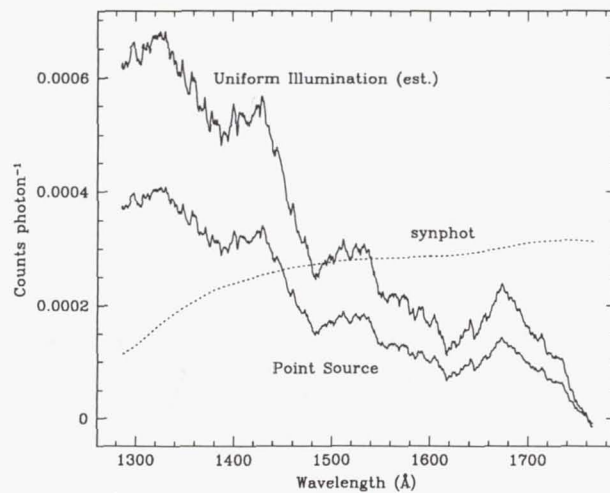


Figure 4. Spectrograph efficiency in third order

### References

- Voit, M., 1997a, Instrument Science Report FOC-96 (Baltimore: STScI)  
Voit, M., 1997b, Instrument Science Report FOC-97 (Baltimore: STScI)  
Voit, M., & Jedrzejewski, R., 1997, Instrument Science Report FOC-98 (Baltimore: STScI)

## The Closeout State of the Faint Object Spectrograph

Charles D. (Tony) Keyes

*Space Telescope Science Institute, 3700 San Martin Drive, Baltimore MD 21218*

**Abstract.** The Faint Object Spectrograph (FOS) was one of the original HST instruments and was removed from the spacecraft in February, 1997. We present a summary of the state of FOS calibration accuracies as of fall 1997. Modest background information about each of the various calibrations and instrumental operating conditions that limit calibration accuracy is also provided. We also reference other useful documentation for more in-depth discussion of these topics.

### 1. Introduction

This presentation will focus on a summary of the calibration status of the FOS as of fall, 1997. Much of what is presented here is based directly upon the results of the FOS Closeout Calibration re-analysis of on-orbit data performed since the de-commissioning of the instrument in February, 1997.

The primary recommendation of this presentation is that *all FOS data, no matter when or how they were obtained, should be re-calibrated* with the closeout reference files and current *calfos* algorithms in order to achieve the highest degree of calibration accuracy and data quality. Secondly, you should refer to the FOS WWW page (under the STScI page at <http://www.stsci.edu>) for the latest calibration information.

For a thorough technical-level description of the FOS instrument please refer to the FOS Instrument Handbook version 1.1. For descriptions of typical on-orbit usage and operating concerns see FOS Instrument Handbook version 6. Volume II of the forthcoming *HST Data Handbook* (DH) version 3, to be issued in January, presents much of the following material with greater elaboration. The new DH is the primary reference for all questions pertaining to FOS calibration and analysis.

The Faint Object Spectrograph (FOS) was one of the five original instruments on HST. The FOS was a single-pass spectrometer with six high-dispersion ( $R = 1300$ ) and two low-dispersion ( $R = 250$ ) blazed, ruled gratings and one sapphire prism. Two separate Digicon detectors were available to provide coverage of the entire wavelength range from 1150 to 8400 Å with redundancy between the detectors in the range 1650-5400 Å. The FOS/BL detector was sensitive between 1150 and 5400 Å and the FOS/RD between 1650-8400 Å. FOS/RD was more sensitive at all wavelengths longward of 1700 Å, but also had a higher detector background, more substantial photocathode changes, and less effective magnetic shielding. The spectra were recorded by 512 diodes each of which were 0.35 arcsec wide (x-coordinate parallel to dispersion) and 1.43 arcsec in height in the pre-COSTAR setup. Post-COSTAR dimensions were 0.31 arcsec wide by 1.29 arcsec in height.

Not all FOS data, particularly those from the pre-COSTAR era, were acquired with optimal target acquisition procedures or with optimal instrumental settings. Although the effort is not as intrinsically interesting as interpretation of the science data, we strongly urge you to analyze the quality of the target acquisition for your data and, based upon the following information and that in the DH, understand its impact on your science exposures.

As we shall see, the quality of all FOS data is governed by the location of the target in the aperture (determined by the target acquisition employed), the location of the target



image on the photocathode (most strongly affected by filter-grating wheel positioning), and the location of the photocathode image on the diode array (controlled by the Y-base). Therefore, you should assess the limitations that each may place on your observational material.

Target acquisition centering affected

- the amount of light transmitted by the aperture, hence the photometric accuracy of the observations,
- the degree to which calibrated photocathode granularity was sampled, hence the limiting S/N after flatfield correction,
- the centering of the beam on the grating parallel to dispersion, hence the wavelength accuracy, and
- for larger apertures the positioning of the image on the photocathode with respect to those portions of the photocathode that were sampled by the diode array.

The position of the target on the photocathode affected

- wavelength calibration and
- the correct sampling of photocathode granularity.

Incorrect sampling of the output photocathode image for larger apertures affected both

- the absolute photometric accuracy of the observations and, especially
- the shape of the spectrum.

In the following we will assess the ranges of variation associated with the instrumental effects that limit FOS calibration accuracies and will then discuss the various calibration accuracies themselves.

## 2. Instrumental and Operational Limitations

### 2.1. Y-bases

The FOS Y-base is the amount of magnetic deflection required to ensure that the photocathode output image is directed onto the diode array. Depending upon the changing magnetic environment of the detector, differing amounts of deflection may have been required at different times to direct phototelectrons from a particular place on the photocathode to a particular place on the Digicon detector. The Y-base was measured in ybase units of which 256 were always defined to equal the diode height (1.29 arcsec post-COSTAR and 1.43 arcsec pre-COSTAR).

Repeated independent observations of the same Y-base yield an external  $\pm 25$  ybase scatter (0.14 arcsec pre-COSTAR; 0.12 arcsec post-COSTAR) which is attributable to residual geomagnetic image motion (GIM) and filter-grating wheel position non-repeatabilities. The internal measurement error associated with any Y-base measurement is  $\pm 5$  ybases.

The images of FOS spectra were curved on the photocathode. These so-called *s-curves* typically ranged  $\pm 20$  ybases about a midrange value. The nature of the FOS design required that an average Y-base be used for the entire spectrum. If curvature were substantial, and the target were displaced toward the edge of an aperture, the diode array might not sample all of the dispersed image.

Clear temporal trending existed for the nominal position of FOS/BL Y-bases, while the trending was less clear for FOS/RD. Y-bases were updated approximately every six months so that installed values were usually within 10 ybases of the nominal trend line. In certain cases, notably FOS/BL G130H between February and November, 1994, considerably larger deviations existed which had noticeable color-dependent photometric effects.

The photometric impact of an erroneous Y-base depended upon the size of the error, the aperture involved, and the detector-disperser combination employed. On the average, for post-COSTAR point sources observed with the 1.0 and larger apertures, an error of 20 ybases could produce a 3-5% general light loss and up to 10% at certain wavelengths where the s-curvature was substantial - typically near the edges of the spectral regions. The light loss was larger, but harder to simply quantify, for pre-COSTAR point sources and all observations of extended sources.

Y-base uncertainties have essentially no photometric impact for observations with apertures smaller than 1 arcsec in size as the displacements required to place these aperture images off the diode array are simply much larger than the observed uncertainties.

*Summary:* For large aperture (1 arcsec and larger) observations, Y-base uncertainty is a prime contributor to photometric, especially spectral shape, uncertainties in FOS data. There is little or no photometric effect for apertures smaller than 1 arcsec.

## 2.2. Mechanism Stability and Image Motion

The positions of the FOS filter-grating wheel (FGW) were stabilized by notches or detents. There was some mechanical non-repeatability of the wheel position on separate visits to the same notch. The x-component of any FGW positioning uncertainty caused an offset in the observed wavelengths from the calibrated dispersion relation. An offset in either x or y added a small uncertainty to the flat field calibration.

The FOS aperture wheels could also suffer some non-repeatability of their positional alignments, but the sizes of aperture wheel non-repeatability were an order of magnitude smaller than FGW non-repeatability. As such, aperture wheel non-repeatability had no significant impact on any FOS calibration uncertainty.

FOS image motion could be produced by the combined effects of GIM motions and guiding errors. In the pre-COSTAR period before routine onboard GIM motion correction was implemented (5 April 1993), typical image motion was of the order of 0.15 arcsec. A post-observation correction for the x-component of this motion was made in standard pipeline calibration, which was accurate to the nearest pixel (0.044 arcsec or, at high dispersion, 30 km/sec). No post-observation correction was possible for the y-component of this motion, which could be up to 25 ybases in size.

Following the implementation of an onboard correction, residual peak image motions were reduced to approximately 0.02 arcsec. The one sigma uncertainty in x was 0.06 diodes (0.25 pixel or about 15 km/sec at high dispersion). The one sigma residual in y was about 5 ybases.

## 2.3. Target Acquisition

Pre-COSTAR FOS ACQ/BINARY target acquisition accuracies were typically 0.12 arcsec (one sigma) in addition to 0.15 arcsec due to GIM (prior to 5 April 1993). Post-COSTAR ACQ/BINARY one sigma accuracies were 0.08 arcsec for FOS/BL and 0.12 arcsec for FOS/RD. ACQ/PEAK accuracies were always determined by the photon statistics and the step-size of the last pattern employed in the acquisition sequence. The worst-case pointing accuracy of the finest pattern used in FOS acquisitions was 0.025 arcsec in each coordinate.



### 3. FOS Calibration Results

#### 3.1. Flux Calibration Accuracy

The overall limiting FOS photometric calibration accuracy is approximately 3% (one sigma). This overall accuracy is composed of the following components:

- 2% or smaller systematic residuals for comparison of FOS fluxes with the white dwarf pure hydrogen model atmospheres that define the HST flux system.
- <1% (one sigma) residuals in Landolt visible photometry used to normalize the flux system.
- 1% (one sigma) internal FOS repeatability, which is the ultimate limiting accuracy of the determination of spectral shape.

Additional factors may limit the accuracy of individual FOS observations, in particular:

- Absolute and relative accuracies are limited by Y-base uncertainties for apertures 1 arcsec and larger. These effects depend upon aperture, grating, and target acquisition.
- Precision absolute spectrophotometry required precise pointing (<0.06 arcsec or better).
- Precision relative spectrophotometry required precise pointing (<0.06 arcsec or better) for apertures larger than 0.5 arcsec.
- FOS/RD G780H accuracy is somewhat worse (about 4% one sigma) due to lower S/N in the fewer observations of standard stars and more uncertainty in flatfields.
- Small aperture throughput could be affected by breathing. Documented smooth trends of as much as 3-4% have been seen for well-centered targets in the post-COSTAR small apertures. Pre-COSTAR small aperture photometry was affected to a greater degree (perhaps as much as 7%) and was further compromised by the effects of jitter and guiding.

Many early pre-COSTAR programs did not utilize precise acquisitions. As a result, the photometric quality of these observations is diminished (see Koratkar and Evans, this volume). It is essential that the impact of the target acquisition on any FOS observation be assessed, and especially for pre-COSTAR data,

The influence of Y-base errors on FOS photometry is not fully characterized at this writing. FOS calibration program 6916 contains two visits of data obtained in December 1996 and January 1997 that may be helpful to GOs who wish to assess the impact of Y-base uncertainty on their data. These observations consist of RAPID mode readouts of FOS standard star BD+28D4211 as it was drifted perpendicular to dispersion across the 1.0 and 4.3 apertures at pre-determined rates.

#### 3.2. Flatfield Calibration

FOS flatfields are designed to remove photocathode irregularities with typical dimensions of 10 pixels or less. Our cumulative experience with the FOS detectors has shown that the amount of photocathode structure or granularity varies as a function of time, spectral element, and photocathode location. As a result it is important to use flatfields taken as nearly contemporaneously as possible with the exposure to be calibrated. The FOS calibration observations from which flatfields are produced always used the highest precision acquisition available, namely 0.025 arcsec or better accuracy in each coordinate. In order

to achieve optimum flatfield correction it was necessary to sample the same portion of the photocathode as was used for the flatfield calibrating exposures, hence the same high degree of pointing accuracy was required.

Two different techniques have been used to produce FOS flatfields: the superflat method and the continuum-fit method. Please refer to the *HST Data Handbook* and FOS ISRs 088 and 134 for details on the methods, but we note that superflats are much more objective and are the superior product.

*FOS flat field status:* Post-COSTAR aperture-dependent flatfields have been prepared for all standard star observations of standards G191B2B and BD+28D4211. All post-COSTAR FOS flatfields are based on or derived from superflat observations. The apertures include 4.3, 1.0, 0.3, 1.0-PAIR, and 0.25-PAIR. Pre-COSTAR flatfields for the 4.3 aperture are available for 1992-93, but flats for earlier periods are not based on superflats. In the pre-COSTAR epoch few flats for apertures other than 4.3 are available, but given the larger PSF, this is not a serious problem for the single apertures. The relative lack of paired aperture pre-COSTAR flatfields is a limiting factor, however, as photocathode granularity can be quite different at the paired aperture locations.

New flatfields delivered as part of the FOS closeout calibration increase the accuracy of correction for temporally variable features, particularly in the FOS/RD G190H 1950 and 2150 Å, FOS/RD G400H 4475 Å, and FOS/BL G160L 1550 Å regions.

High S/N observations ( $S/N > 30$ ) always required pointing accuracy of 0.06 arcsec or better.

Some x-shifting of the granularity (typically  $\pm 1$  pixel) relative to the standard star epoch did occur with the FOS due to residual GIM and other magnetic effects. If a persistent feature is not adequately removed by flatfielding with the closeout flats, we recommend shifting the spectrum by  $\pm 1$  or 2 pixels and re-flatfielding. This procedure typically shows little improvement for  $S/N < 30$ , but can be of use in higher S/N situations. As a related item, we note that arbitrary shifting of highly accurate standard star observations by only 1 pixel prior to flatfielding introduces obvious pattern noise at the 1-2% level. Fractional pixel shifts, caused by residual image motion effects will likewise introduce similar noise in nearly any FOS exposure.

*FOS flatfielding accuracies:*

- 1% limiting RMS can be achieved with post-COSTAR superflat-based flats, high photon statistical S/N, precise aperture centering, and excellent x-coordinate alignment with the flatfield. Accuracies of 2-3% are more typical for precisely centered observations. .
- input calibration data typically had counting statistics S/N of 40:1 to 200:1
- substantial improvement (5-25%) is achieved relative to the original pipeline flats in certain wavelength regions for tracking of flatfield features (e.g., at 1950, 2150, 4475, and 1550 Å),
- Time-sampling frequency is variable. Some trends (e.g., 5% changes at FOS/RD G400H 4475 Å between June 1995 and April 1996 are not sampled well).

*Flatfield suggestions:* Remember that FOS flatfields are not interpolated between standard star epochs and USEAFTER dates are chosen to represent midranges of time periods. As we have recommended in previous workshops and in the *HST Data Handbook*, detailed comparison of your data with the nearby (before and after) standard star observations and their attendant flatfields can be very helpful in determining the veracity of any particular feature.



### 3.3. Wavelengths

FOS pipeline wavelengths should be considered only an approximation to the actual wavelength scale appropriate to any exposure due to the influence of a variety of instrumental and observing effects. Some of these sources of error can be removed if a contemporaneous WAVECAL was taken immediately before or after the science exposure *without* any motion of the FOS filter-grating wheel between the exposures.

Since the FOS pipeline wavelength solution is based upon a single set of dispersion fits made at one epoch of observation, a potentially large systematic wavelength offset may be present in the calibrated wavelengths for any observation that does not have a contemporaneous WAVECAL. A recent re-examination of the pipeline fits has indicated that the filter-grating wheel position for several of the defining WAVECAL observations may have been near an extremum of its range (one sigma filter-grating wheel uncertainty is of the order of 0.12 diodes).

The net effect is that a systematic offset of up to 1 diode width (250 km/sec at high dispersion) may be present in many calibrated wavelength sets. This offset can be removed by forming a mean set of wavelength coefficients that are more representative of the actual range of filter-grating wheel motion for each disperser. This update is currently in progress and will be reported on the FOS WWW page when available.

In the meantime, for those observations with a contemporaneous WAVECAL, FOS wavelength accuracies are affected by the following contributions to the error budget:

- target centering: (worst-case for best acquisition scenario is 0.025 arcsec or 0.08 diode). All observers must assess for their particular case.
- residual image motion (GIM or other): 0.06 diode (one sigma)
- line-measurement: 0.02 diode (typical one sigma).
- dispersion fit rms: typically 0.04 diode
- spacecraft orbital motion: 0.034 diode (upper limit)

Remember that no correction is made in the pipeline for any motion of the spacecraft, so that heliocentric motion may also be important.

### 3.4. Polarimetry

The pre-COSTAR polarimetry calibration stands as provided by the 1994 reference files. The post-COSTAR calibration is being re-worked at this writing to include a special correction for the influence of COSTAR-induced instrumental polarization. This new correction will be included in the next release of *calfos*.

All FOS polarimetry fluxes are on the white dwarf reference system. At this writing, all polarimetry data in the HST Archive must be re-calibrated.

*Polarimetry accuracies:* Pre-COSTAR polarization accuracies were limited by the effects of residual GIM motion, filter-grating wheel positioning, and jitter on the fraction of the large PSF s-curve that was actually recorded by the diode array. Variations in these quantities produced scatter in total polarization of the order of 0.5% and occasionally somewhat worse. The uncertainty in the retardation calibration also contributed a systematic instrumental polarization equal to 2% of the linear polarization. Actual observing limits were often imposed by the photon statistics of the data.

Post-COSTAR total polarization residuals of approximately 0.1% may be achieved after correction for instrumental polarization throughout most of the 1600-3300 Å region. In the 1800-2100 Å region the limit is approximately 0.2%. Again the uncertainty in the retardation calibration contributes an additional systematic uncertainty of 2% of the linear

polarization. Although all FOS polarimetry calibrations were taken with 16 polarizer rotation steps and a minimum of 8 steps was recommended, some polarimetry observations used only 4 rotation positions. These cases contain an additional 0.4% uncertainty in total polarization. Again, photon statistics are nearly always the limiting factor in individual polarimetry measurements.

### 3.5. Aperture Locations and Plate Scale

No precise measurement of the pre-COSTAR FOS aperture locations was attempted. The absolute location of the 4.3 aperture was determined with approximately 1 arcsec accuracy. Each single aperture was assumed to be concentric with the 4.3; an assumption not borne out by post-COSTAR measurement.

Post-COSTAR aperture locations were more precise. The absolute location of the 1.0 aperture was determined with 1 sigma accuracies of 0.24 arcsec and 0.30 arcsec for FOS/BL and FOS/RD, respectively. All relative aperture locations, except for that of the 4.3, were determined with 0.02 arcsec (1 sigma) accuracy. The accuracy of the relative position of the 4.3 was approximately 0.1 arcsec. All single apertures but the 4.3 were concentric as were all paired apertures except the 1.0-PAIR. Details may be found in FOS ISRs 137 and 139.

Pre-COSTAR plate scale was 0.0896 arcsec per pixel in each coordinate. Post-COSTAR plate scale (arcsec per pixel) values were  $x=.0774$ ,  $y=.0786$  (FOS/BL) and  $x=.0752$ ,  $y=.0812$  (FOS/RD). All post-COSTAR one sigma uncertainties were  $\pm .001$  arcsec per pixel.

### 3.6. Background

FOS detector background was produced by high-energy particle events within the detector. Cerenkov radiation produced light as particles hit the faceplate and occasionally the particles themselves hit the detector and produced spurious counts. Variations in mean rates of up to a factor of 1.5 were correlated with geomagnetic latitude, but no longitude, solar position angle, or solar cycle effects were seen. The pipeline model background deviates from fits to the dark observations by up to 20% at high latitudes.

*Mean detector background:*

- FOS/BL = 0.007 counts/sec/diode;
- FOS/RD = 0.01 counts/sec/diode

Mean particle-induced background levels were scaled by the ambient geomagnetic field to produce the pipeline background correction. Since the dark contribution in short exposures was dominated by individual events that usually affected individual diodes, many FOS exposures - and all readouts - were not lengthy enough to allow a uniform dark distribution to build up at sufficiently high S/N for the pipeline mean correction to have high accuracy. Random excursions of at least a factor of two about the mean level were often seen. Examination of the paper products is useful in assessing the quality of background correction. For more details please refer to the *HST Data Handbook*.

### 3.7. Dead and Noisy Diodes

Over the lifetime of the FOS diodes occasionally began to perform spuriously and, in some cases, to quit working altogether. The FOS team followed the general rule of disabling any diode that exhibited three separate dead or noisy occurrences. Upon the disabling of the diode, a new dead diode reference file was produced that contained an effective date of the first reported occurrence of anomalous activity by the diode.

As part of the closeout, the dead diode files are now complete. Naturally, any unreported earlier occurrences of a disabled diode will not be corrected by the final reference



files. As well, several diodes had fewer than three anomalous events over the lifetime of the FOS. Such events are also not tagged by the closeout dead diode reference files.

### 3.8. LSF/PSF

A detailed series of pre-COSTAR computed PSFs and LSFs is available from CDBS (see FOS ISRs 104 and 105 for details of these models). No post-COSTAR theoretical LSFs or PSFs are available, but observational dispersed light LSFs were examined from comparison arc lines and in spectra with nominally unresolved emission lines.

These post-COSTAR LSFs display typical Voigt profiles. For  $S/N < 10$  only a Gaussian core is evident, but at higher  $S/N$  with the 4.3 and 1.0 apertures Lorentzian wings develop at approximately 20% of peak intensity. The FOS/RD G270H has the narrowest core (FWHM approximately 1 diode) whereas FOS/BL G270H was the widest (FWHM approximately 1.25 diodes). All FOS/BL profiles have broader wings than those in equivalent FOS/RD spectra. The different profiles are attributable to different magnetic and optical focus qualities in the two detectors as well as possible grating alignment differences. The FOS/RD G270H profile most nearly matches the FOS/RD white light profile and the FOS/BL G130H comes closest to the FOS/BL white light profile.

### 3.9. Observation Timing

The details of precise FOS exposure timing are too complex for a short presentation here. FOS header exposure start times, found in keyword FPKTTIME, contain an uncertainty of at least 0.125 sec. Further, it is not possible to determine the start times of readouts later than the first in a time-series by simple algebraic manipulation of readout times and header keyword entries. Please refer to the *HST Data Handbook* and contact [help@stsci.edu](mailto:help@stsci.edu) if you require timing information more accurate than 0.125 sec.

### 3.10. Unfinished or Additional Calibration Analyses:

- incorporation of post-COSTAR instrumental polarization correction algorithms into calfos
- update dispersion fits to remove possible FGW positional offset systematic errors
- analyze standard star drift scan observations in program 6916 to provide measure of photometric effect of Y-base error as a function of mis-centering and wavelength; also provide measure of granularity changes as function of position perpendicular to dispersion.
- produce superflat-derived flatfields for all pre-COSTAR standard star observation epochs; may improve paired aperture flatfields.
- complete analysis of post-COSTAR dispersed light LSFs
- update FOS ISR 148 description of white-light LSF/PSF

## 4. FOS Documentation

*HST Data Handbook:* As noted earlier, the *HST Data Handbook* version 3 volume II for Retired Instruments is intended to be the definitive document on calibration and analysis of FOS data. This edition replaces all previous versions. It contains a technical instrument overview, summaries of important calibration results presented in Instrument Science Reports, and a discussion of the accuracies of the closeout calibration. The document is available in both electronic and hardcopy versions. Please contact [help@stsci.edu](mailto:help@stsci.edu) or refer to the FOS WWW page for additional information.

*Instrument Science Reports:* FOS Instrument Science Reports (ISRs) contain technical detail pertaining to all aspects of instrument calibration and operation. Typically ISRs are intended to provide low-level and background information that is not frequently required by GOs. All important ISRs are available online for researchers who require this additional information.

*Instrument Handbooks:* Version 6 (June 1995 - cycle 6) is the best description of the state of the instrument as used in the post-COSTAR era. Version 1.1 (May 1990 - immediately post-launch) provides the best technical description of the instrument available. All other versions of the FOS Instrument Handbook contain no information not found in these two editions and should be considered obsolete.

*WWW Resources:* The FOS WWW homepage, accessible via the STScI WWW page (<http://www.stsci.edu>) also contains a number of other useful documents and additional items. Information pertaining to any updates to the FOS calibration will be posted on the FOS WWW page first.

## 5. The FOS Asterism

The FOS functioned for more than five years in HST without a major system failure. Its legacy of more than 20,000 exposures and at least 187 refereed papers (to date) is the tangible result of years of effort by the many individuals in the FOS Investigation Definition Team, Martin Marietta Aerospace Division, Goddard Space Flight Center, STScI, and elsewhere who defined, built, refined, calibrated, and explained the instrument. At the considerable risk of omitting many who are unknown to us, we wish to thank all of the following individuals who have contributed so much of their time and talent over the past 20 years to yield the bounty of the FOS found in the HST Archive:

*FOS Investigation Definition Team (IDT):* R. Harms PI, R. Angel, F. Bartko, E. Beaver, R. Bohlin, M. Burbidge, A. Davidsen, H. Ford, B. Margon

*STScI FOS Group:* G. Hartig, A. Kinney, T. Keyes, I. Evans, A. Koratkar, M. Dahlem, J. Hayes, A. Storrs, R. Downes, E. Smith, B. Bhattacharya, C. Taylor, J. Christensen, S. Holfeltz, S. Martin

*ST-ECF FOS Support:* M. Rosa

*FOS design, support, and calibration:* D. Lindler, R. Lyons, M. Sirk, V. Junkkarnen, E. Rosenblatt, R. Cohen, R. Hier, R. Allen, G. Schmidt, J. Wheatley, J. Koorneef, A. Uomoto, G. Kriss, W. Blair, W. Baity, J. Linsky, L. Dresser, R. Ciardullo, Z. Tsevetanov, G. Neill, S. Caganoff, L. Armus, K. Horne, M. Eracleous, W. Welsh, K. Korista, J. Caldwell, C. Cunningham, D. Chance, M. Reinhart, T. Wheeler, J. Fitch, J. Skapik, J. Bacinski, J. Eisenhamer, S. Hulbert, H. Bushouse, J.C. Hsu, W. Hack, M. de la Peña, A. Berman, D. Manning, K. Peterson, D.C. Taylor, T. Roman,

**Acknowledgments.** In closing, I want to express my gratitude to all of the above and others at STScI and elsewhere who have made working on the FOS the professional experience of a lifetime.

## References

Allen, R.G. and Smith, P.S. 1992, Instrument Science Report CAL/FOS-078 (Baltimore:STScI)



- Evans, I.N., Koratkar A., Taylor, C.J., and Keyes, C.D. 1995, Instrument Science Report CAL/FOS-139 (Baltimore:STScI)
- Evans, I.N., Koratkar A., Keyes, C.D., and Taylor, C.J. 1995, CAL/FOS-137 (Baltimore:STScI)
- Evans, I.N. 1993, Instrument Science Report CAL/FOS-104 (Baltimore:STScI)
- Evans, I.N. 1993, Instrument Science Report CAL/FOS-105 (Baltimore:STScI)
- Ford H. C. and Hartig, G. 1990, *FOS Instrument Handbook*, Version 1.1, (Baltimore:STScI)
- Keyes C. D., Koratkar A. P., Dahlem M., Hayes J., Christensen J., Martin S. 1995, *FOS Instrument Handbook*, Version 6.0, (Baltimore:STScI)
- Keyes C. D. ed., 1998, *HST Data Handbook*, Vol. II, (Baltimore:STScI)
- Koratkar, A.P and Evans, I.N. 1997, this volume.
- Kriss G.A., Blair W.P., Davidsen A.F. 1992, Instrument Science Report CAL/FOS-070 (Baltimore:STScI)
- Kriss G.A., Blair W.P., Davidsen A.F. 1991, Instrument Science Report CAL/FOS-067 (Baltimore:STScI)
- Lindler, D. et al. 1993, Instrument Science Report CAL/FOS-088 (Baltimore:STScI)
- Lindler, D. Bohlin, R., and Keyes, C. 1995, Instrument Science Report CAL/FOS-134 (Baltimore:STScI)

## Average Inverse Sensitivity Recalibration of Pre-COSTAR Faint Object Spectrograph Data and Comparison with International Ultraviolet Explorer Data

Anuradha Koratkar

Space Telescope Science Institute, 3700 San Martin Drive, Baltimore, MD 21218

Ian Evans

Smithsonian Astrophysical Observatory, 60 Garden Street, MS-27, Cambridge, MA 02138

### Abstract.

We have recalibrated all pre-COSTAR archival Faint Object Spectrograph (FOS) UV and optical spectrophotometry of active galaxies and quasars in order to extract uniformly calibrated spectrophotometric data for further detailed scientific investigations. In this paper we present results of the average inverse sensitivity (AIS) recalibration of this large dataset. The fluxes derived from the recalibrated data are significantly different from the original pipeline calibrations, as expected, because of the revision of the photometric reference scale. We use this dataset to present statistics of the photometric accuracy in the grating overlap wavelength regions for observations spanning multiple gratings.

Where possible we have combined multiple observations to produce a single spectrum for each object with the highest possible signal-to-noise (S/N) ratio and covering the widest wavelength range. The recalibrated spectra will be published shortly as atlases and will be available also in electronic form.

As the *International Ultraviolet Explorer* (IUE) satellite data archive is an important source of historical UV spectroscopic information, combining FOS and IUE spectra obtained at different epochs is often necessary. Consequently, understanding how the measurable quantities depend on the individual instrumental calibrations, and how any conclusions derived from modeling the observations may vary depending on the source of the UV data, is critical. Here we present a comparison of typical FOS and IUE spectra.

### 1. Introduction

The *Hubble Space Telescope* (HST) Faint Object Spectrograph (FOS) data archive is a rich source of excellent high quality UV and optical spectrophotometric data that can be used for various scientific problems associated with individual objects or classes of objects. To effectively use these spectra to obtain meaningful scientific results, it is essential that the data be compared consistently and be calibrated as uniformly as possible. Several of our scientific investigations require a large database of uniformly calibrated spectra of active galactic nuclei (AGNs) that can be intercompared. Therefore we have recalibrated all pre-COSTAR archival FOS UV and optical spectrophotometry of AGNs, and are in the process of doing the same for the post-COSTAR data. In this paper we present the results of the recalibration of the large number of datasets from the pre-COSTAR era.

Although the FOS UV archive is important for the study of AGNs, the vast majority of UV reference data were obtained using the *International Ultraviolet Explorer* (IUE)



satellite. These data remain important since they provide historical information about the intensities of the UV continua and emission lines that is needed to constrain models of the active nucleus. Here we present a comparison of FOS and *IUE* data, so that the two UV archives can be used effectively for comparative studies.

## 2. Why recalibrate pre-COSTAR FOS data?

As mentioned in the introduction, consistently and uniformly well calibrated spectrophotometric data are fundamental for any observationally analyzed problem. At present, datasets retrieved from the *HST* archive are not necessarily consistently and uniformly calibrated. This problem is especially acute for pre-COSTAR data and all spectropolarimetric data. The FOS archival data are not uniformly calibrated for the following reasons.

1. The FOS pipeline calibrations used early in the *HST* mission did not consider many instrumental effects that were later identified and quantified.
2. Although the FOS pipeline used the best calibration data available at the time, further analysis enabled these calibration data to be refined, thus rendering the prior pipeline calibrations obsolete.
3. Time varying calibrations are required to correctly model the behavior of the instrument. However, earlier versions of the *FOS* pipeline did not incorporate such capabilities.
4. The FOS pipeline photometric reference scale was changed from the mean UV reference flux system to a white dwarf model for G191B2B in 1994. This change affects the photometry dramatically.

To obtain the best calibrated spectrum per object, the datasets in the *HST* archive must be recalibrated, at least for the pre-COSTAR era. For our recalibration we have used the latest pipeline calibration called the average inverse sensitivity (*AIS*) calibration.

## 3. What is average inverse sensitivity (*AIS*) calibration?

The latest pipeline calibration technique uses an inverse sensitivity reference file that is generated by a spline fit to the inverse sensitivities derived from an average of many observations of a number of standard stellar spectra. This "average inverse sensitivity" reference file (hence the name of the technique) is supported by many other tables and reference files that are used to account for (amongst others) temporal, wavelength dependent, and aperture dependent variations that are seen in the instrumental response. These observed variations are readily characterized and parameterized using the *AIS* calibration framework. In comparison, the previous calibration technique required reference files that were time stamped and that were to be used only for observations obtained during a specific time interval. This method did not permit accurate calibration of a temporally smoothly varying instrumental response. The *AIS* method allows us to calibrate data to a higher level of accuracy than was possible with the older calibration technique. An added advantage to the *AIS* calibration is enhanced statistical photometric accuracy, since the inverse sensitivity reference file is generated from a large number of observations. The *AIS* calibration technique was developed over several years, with improvements applied progressively to correct for deficiencies and/or photometric discrepancies identified in the recalibrated data. Indeed, the *AIS* reference files incorporate corrections in the wavelength overlap regions of adjacent gratings derived based on inconsistencies discovered while generating the AGN atlases (Evans, Koratkar, & Pesto, 1998; and Koratkar, Evans, Blitz, & Pesto, 1998).

The *AIS* method for flux calibrating FOS data incorporates four major improvements when compared to the previous flux calibration technique.

1. Normalizing count data from all apertures to the 4.3'' aperture.
2. Correcting wavelength dependent aperture throughput to account for changes in aperture throughput as a function of the optical telescope assembly focus;
3. Correcting the data for time-dependent detector sensitivity degradation;
4. Scaling the data to the white dwarf photometric reference scale.

Below we discuss how these changes affect the final recalibrated output data.

#### 4. The sample and the overall changes seen in the data due to recalibration

We have obtained all *HST* pre-COSTAR (UV and optical) *FOS* spectrophotometric archival data for AGNs. This sample consists of 933 datasets and 263 objects. Of these, 112 targets have observations with only one grating. These 933 datasets are *AIS* recalibrated using the latest pre-COSTAR reference files adopted in March 1996.

##### 4.1. Photometry

Figure 1 shows for a typical observation the differences between an *AIS* recalibrated spectrum and the spectrum available from the *HST* data archive. For most pre-COSTAR data recalibration changes the photometry by 10–40%. The most dramatic changes occur in the UV because of the difference between the old and new photometric reference scales.

##### 4.2. Grating overlap statistics

Where possible, the recalibrated spectra are combined carefully to produce a single high quality, complete wavelength coverage UV-optical spectrum for each object. From Figure 1 we see that the *AIS* recalibration improves the photometry at the ends of each grating, and provides improved photometry in the grating overlap regions (around 1600Å and 2300Å). Before combining any spectra the observational consistency of the datasets is investigated. Figure 2 shows a typical spectrum produced by combining multiple observations and spectra obtained using several gratings.

Such multiple grating observations were obtained for only 151 objects in the present sample from which we have generated the overlap statistics (see Table 1 and Figures 3, 4, and 5).

As can be seen from Table 1, the photometric consistency between spectra from adjacent gratings in the grating overlap regions is no greater than  $\sim 5\%$ . In general, the spline fits to the inverse sensitivity data near the ends of the grating wavelength regions are not as well constrained as the fits in the center of the grating wavelength regions. Consequently, the photometric accuracy near the edges of the grating is worse than near the center of the grating. Thus, an error of 5% in the grating overlap region photometry does not imply that the photometric accuracy at the grating center is as bad as 5%. The latter may be significantly better. We find that the grating overlap statistics for our sample are slightly worse than expected from observations of calibration standard stars, but routine (non-calibration) observations often employ less accurate target acquisition procedures, and scattered light corrections may be less well determined for many AGN with strong continua.



Figure 1. A comparison of the *AIS* calibrated spectrum with the *HST* archival spectrum for a typical AGN observation. The lower panel shows the ratio of the recalibrated spectrum to the archival spectrum.

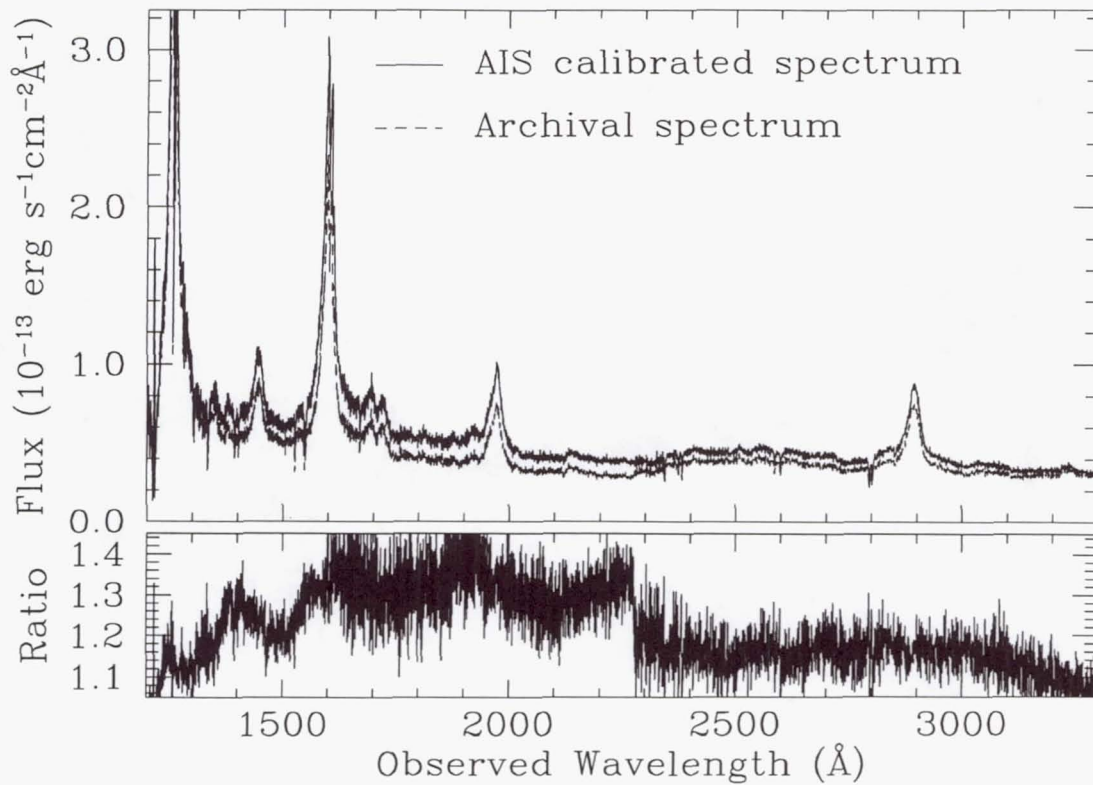


Table 1. Grating Overlap Statistics

Grating Type	Mean <sup>a</sup>	Median <sup>a</sup>
High Resolution	0.99	0.98
High Resolution Red-Blue	0.92 (1.31)	0.92 (0.88)
High Resolution Blue-Blue	0.99 (0.98)	0.99
High Resolution Red-Red	0.98 (0.99)	0.97 (0.98)
High Resolution-Low Resolution <sup>b</sup>	1.00 (1.35)	1.02
NGC 5548 <sup>c</sup>	1.00	1.00

<sup>a</sup>The values in parentheses are for the entire sample, while the quoted values are for the "good" overlaps which range from 0.8 to 1.25.

<sup>b</sup>The low resolution grating is the G160L.

<sup>c</sup>This is for a uniform sample of 39 overlaps between the blue detector G130H and G190H gratings. The  $1\sigma$  for this distribution is 0.18, and is dominated by the two points at 1.3 in Figure 5.

Figure 2. A typical spectrum that is a coaddition of a number of gratings, from the AGN atlas.

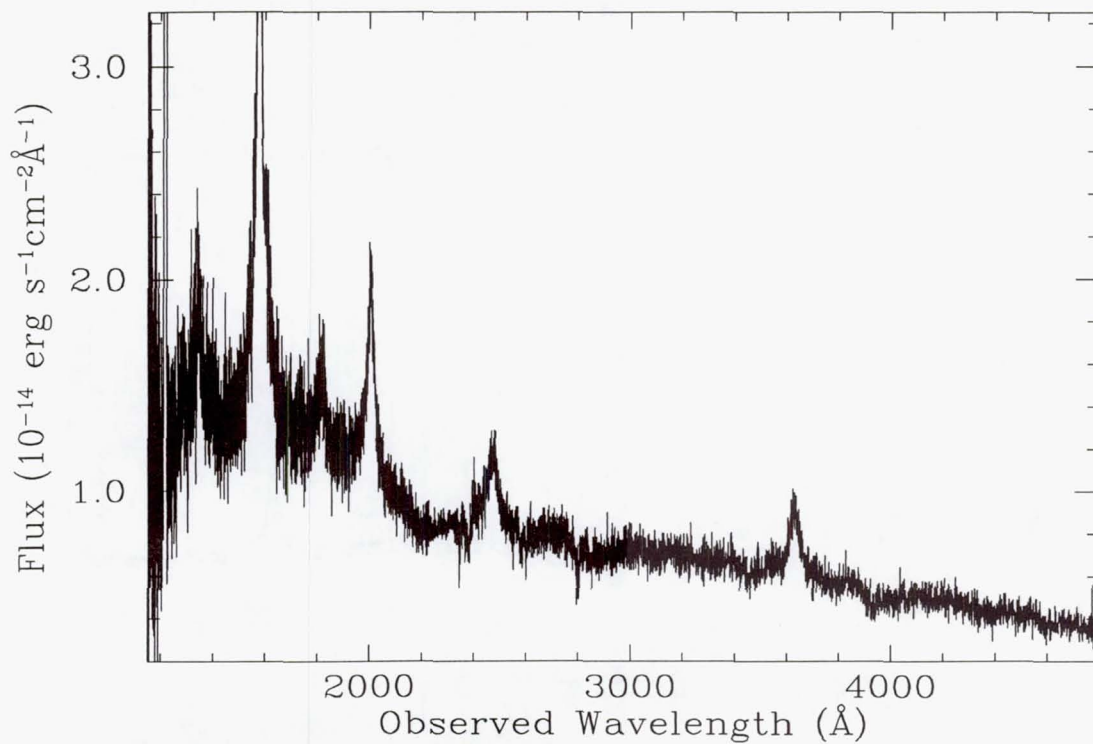


Figure 3. Grating overlap statistics for all the high resolution gratings.

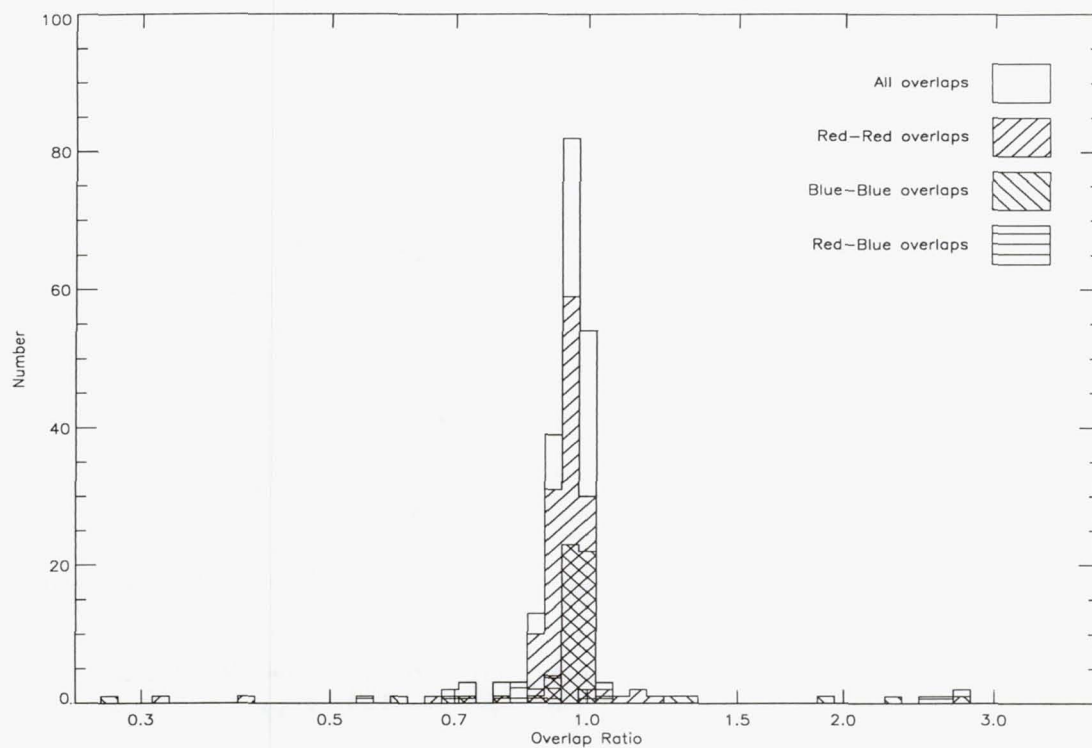




Figure 4. As Figure 3, but for the limited range of overlap ratios centered around unity.

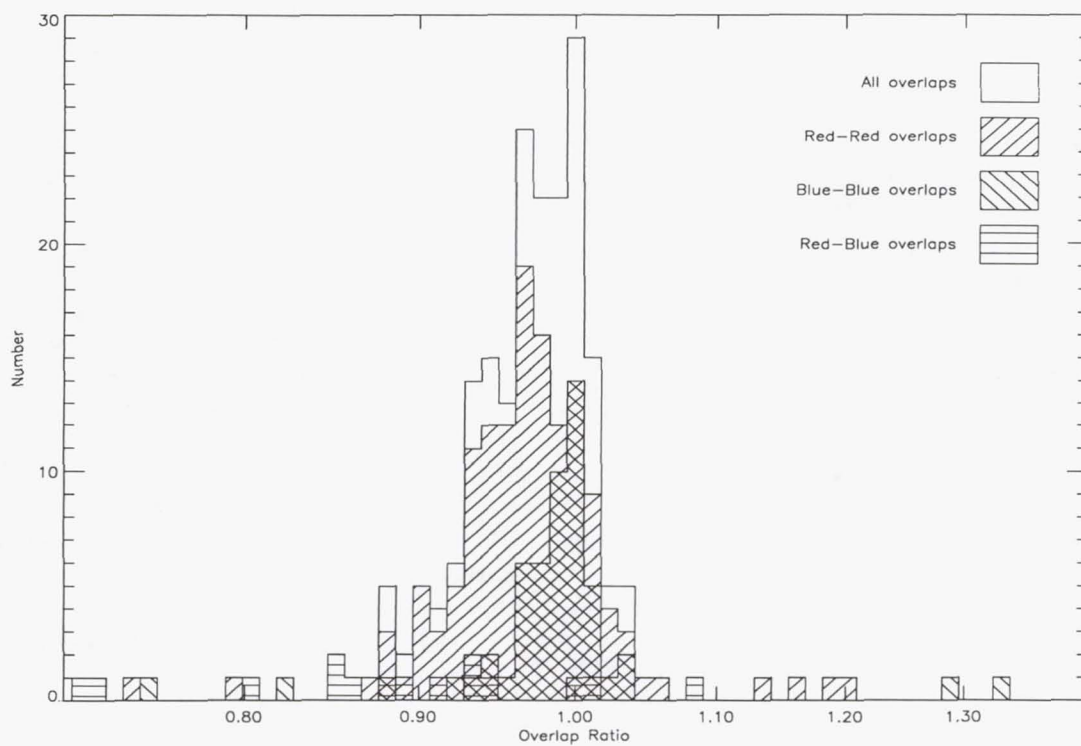
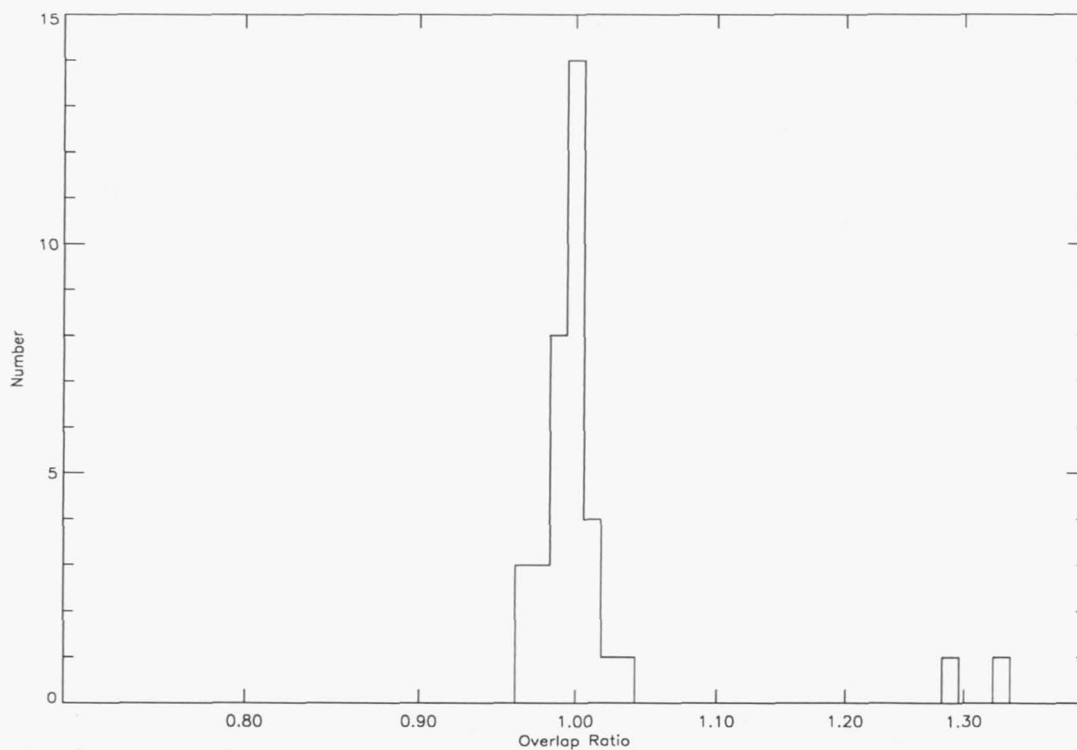


Figure 5. Grating overlap statistics for the Blue G130H and G190H observations of NGC 5548.



## 5. Comparison of AIS calibrated FOS data with NEWSIPS calibrated IUE data

Comparison of FOS and *IUE* UV spectra of three spectrophotometric standard stars (Colina & Bohlin 1994) shows that there is a difference of  $\sim 6\%$  between the absolute flux calibrations of the two instruments, with the FOS yielding larger measured fluxes. Their investigation shows further that the difference in the photometry is independent of wavelength. The differences between the photometric calibrations of the two instruments may arise from small differences between the white dwarf model temperatures used to fit the observed spectrophotometric standard star data.

Although comparison of standard star spectrophotometry is important because it allows us to evaluate the limiting photometric accuracies of the two instruments, such a comparison does not allow us to assess the photometric compatibility of the two archival databases for typical observations that often have poorer data quality than the standard star observations. The FOS standard star observations are not typical of all FOS observations because the former utilize precision target acquisition sequences and the spectra have very high S/N ratios. To assess the differences between spectrophotometry that might be expected for more typical AGN observations, we have compared FOS and *IUE* spectra of three Seyfert galaxies with near-simultaneous (within 24 hours) observations. These observations are more representative of typical FOS archival data because "standard" target acquisition sequences are used, and the spectra have adequate but not outstanding S/N ratios. The FOS spectra were recalibrated with the *AIS* technique discussed above and the *IUE* spectra were calibrated using the NEWSIPS calibrations (Nichols & Linsky 1996). Details of the analysis can be found in Koratkar et al. (1997).

### 5.1. Wavelength comparison

We have shifted linearly the wavelength scale of the FOS grating data so as to place the interstellar absorption lines seen in these spectra at their rest vacuum wavelengths. This procedure is necessary because the FOS filter-grating wheel assembly is non-repeatable and can produce a shift in the wavelength zero-point. Since the interstellar lines are not well defined in the *IUE* spectra we have not applied any zero-point wavelength shifts to these data.

The wavelength calibration accuracy generally quoted for FOS spectrophotometry is 0.1 diode. This translates to a  $1\sigma$  FOS wavelength calibration error of 0.1 Å for the G130H grating, 0.15 Å for the G190H grating, and 0.22 Å for the G270H grating. Although the formal  $1\sigma$  *IUE* wavelength calibration errors are  $\sim 0.4$  Å for the SWP and  $\sim 0.6$  Å for the LWP, the wavelength linearization solution can introduce non-Gaussian calibration errors of order 2–3 Å in individual spectra.

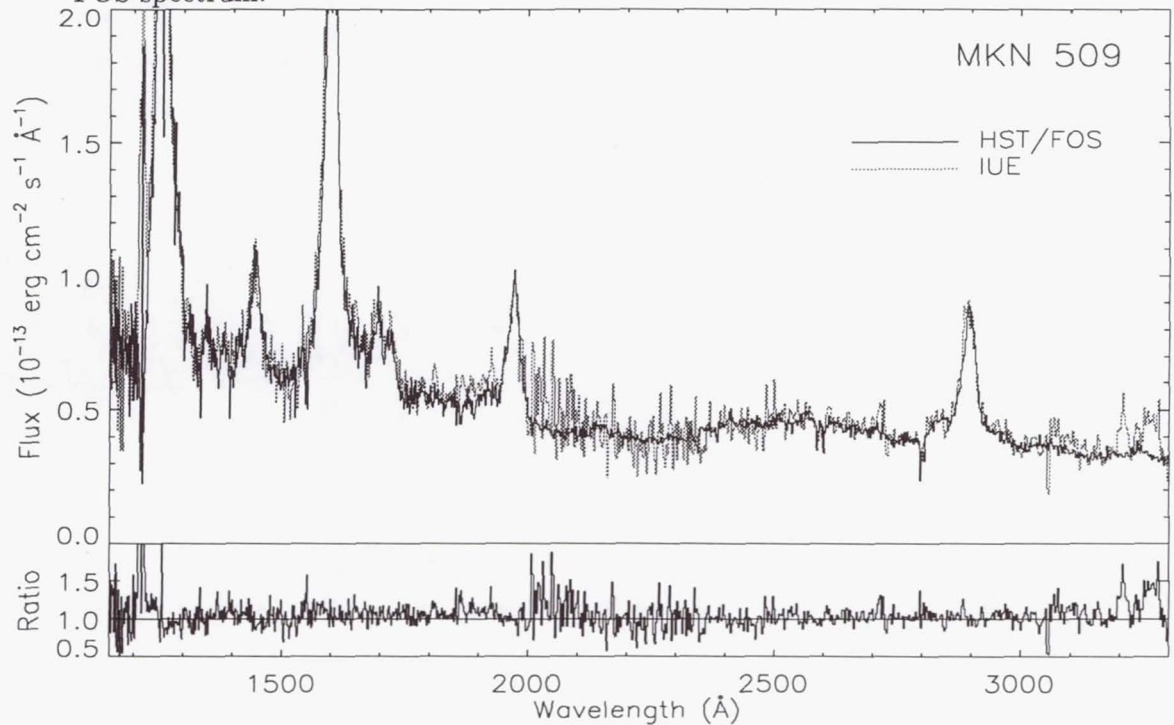
Cross-correlating the strong emission lines visible in both the *FOS* and *IUE* spectra indicates that the wavelength calibrations of both instruments agree to within the errors expected for the *IUE* wavelength calibration. We therefore conclude that no zero-point shift or non-linear correction is required to align the *IUE* and FOS wavelength scales.

### 5.2. Photometric comparison

Figures 6, 7, and 8 compare the FOS and *IUE* spectra. In these figures, the recalibrated FOS spectra are resampled to the *IUE* wavelength grid and resolution. The figures demonstrate that the absolute photometric calibrations of the *FOS* and *IUE* show some differences, even for this limited set of observations. Globally, for MKN 509 and NGC 3783 the absolute photometry of the FOS and *IUE* agree within  $5 \pm 3\%$ . A detailed inspection shows that this photometric agreement is independent of wavelength. Since the  $1\sigma$  absolute flux calibration errors in FOS and *IUE* are 3% and 5% respectively, the photometric calibrations of



Figure 6. Comparison of the FOS and *IUE* spectra for Mkn 509. In this figure, the recalibrated FOS spectra are resampled to the *IUE* wavelength grid and resolution. The lower panel in the figure shows the ratio of the *IUE* spectrum to the FOS spectrum.



these observations are consistent with each other. However, for NGC 5548 the photometric differences are  $\sim 50\%$ .

For the spectra included in our comparison, the photometric calibrations do not produce the 6% larger apparent flux values for the FOS data seen in standard star spectra (Colina & Bohlin 1994). The photometric differences may be due to (1) inadequate aperture corrections, (2) target miscentering in the FOS aperture, or (3) non-linearity of the *IUE* flux scale. A detailed analysis of each of these effects (see Koratkar et al. 1997) indicates that non-linearity in the *IUE* detectors can account for most of the difference seen in the NGC 5548 data. Further, any one of the above effects by themselves or in combination could account easily for the negligibly small differences between the FOS and *IUE* absolute photometry of MKN 509 and NGC 3783.

### 5.3. Line measurements

The accuracy with which line fluxes can be measured depends strongly on both the ability to properly position the underlying continuum and on the ability to distinguish cleanly the line from the continuum. This in turn depends on both the spectral resolution and the S/N ratio of the data. For low S/N data, weak emission lines or emission-line complexes such as Fe II may artificially raise the continuum. Line measurements that employ profile fitting techniques can be affected adversely by low S/N and low spectral resolution, since the widths of the best fitting profiles increase as the resolution degrades and the weak lines become less well distinguished from the noisy continuum. Consequently, we should expect that for weak lines there may be significant differences between flux measurements from the FOS and *IUE* spectra. To quantify these effects, the intensities of a number of emission lines of different strengths are measured.

Figure 7. As Figure 6, except for NGC 3783.

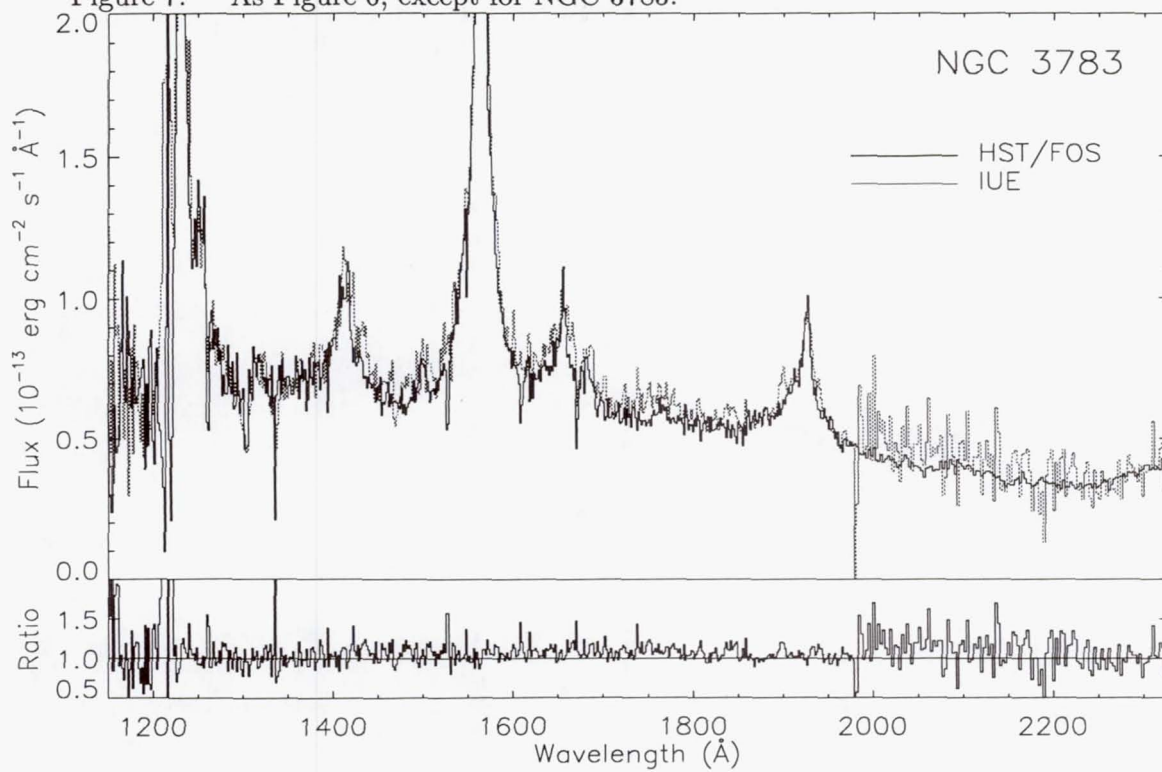
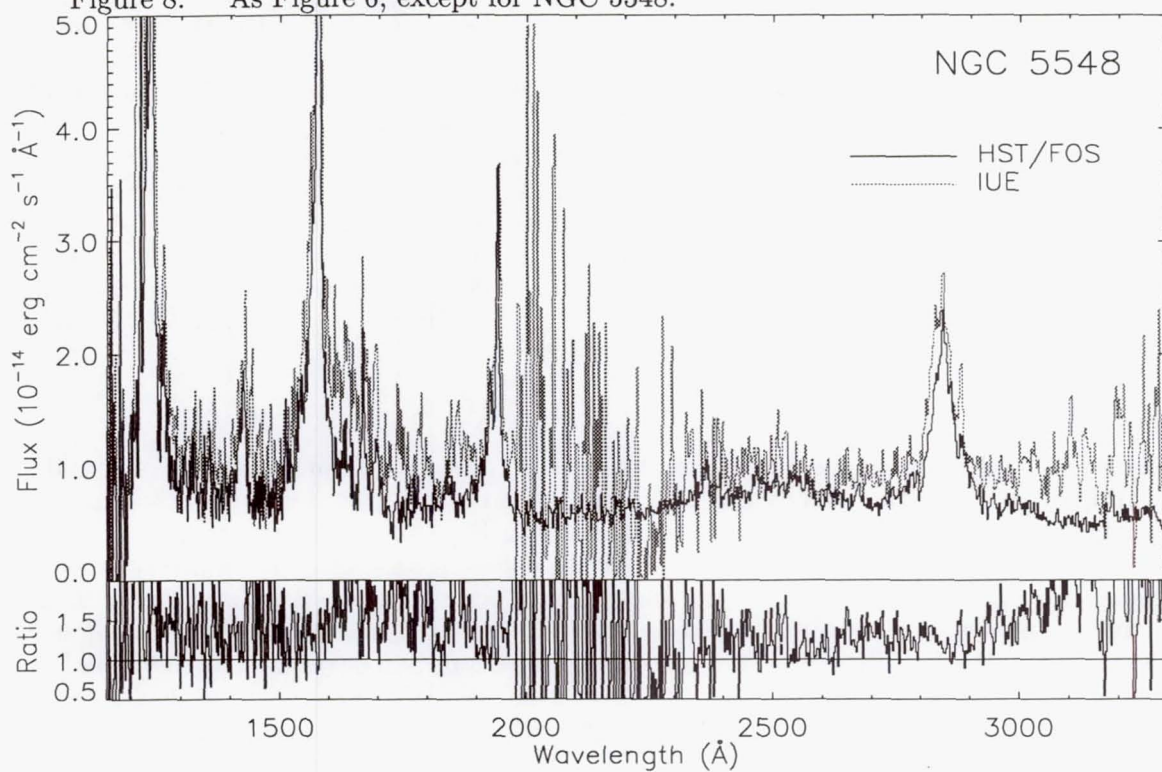


Figure 8. As Figure 6, except for NGC 5548.





A comparison of the emission line intensities show that the agreement between the line intensity measurements depends on the strength of the line. The strong emission lines such as Ly $\alpha$  and C IV agree to within 15%. Moderately strong lines (e.g., N V, Si IV/O IV, He II, and C III]) agree to within  $\sim 30\%$  ( $1\sigma$ ). When detected in the *IUE* spectra, weak lines (e.g., O I, C II, N IV], O III], N III]), could have disagreements as large as a factor of six.

## 6. Conclusions

Because of the changes in the calibration techniques over the life time of the FOS it is necessary to recalibrate archival data to obtain a consistent, uniformly calibrated sample. *AIS* recalibration of AGN spectra shows the expected dramatic rise in UV photometry because of the change in the photometric reference scale. The *AIS* calibration presently adopted for pre-COSTAR data improves significantly the photometric calibration of FOS spectra when compared to the previous calibration technique.

A complete set of recalibrated pre-COSTAR FOS AGN spectra will be published shortly in atlas form (Evans, Koratkar, & Pesto, 1998; Koratkar, Evans, Blitz, & Pesto, 1998), and will soon be available electronically also. We are in the process of recalibrating the complete set of post-COSTAR FOS AGN spectra.

A comparison of a limited set of FOS and *IUE* data shows that the photometric differences observed may be due to (1) inadequate aperture corrections, (2) target miscentering in the FOS aperture, or (3) non-linearity of the *IUE* flux scale.

**Acknowledgments.** We thank C. Imhoff and M. Garhart for NEWSIPS reprocessed *IUE* data and for answering numerous questions, and H. Bushouse for helpful discussions about the *IUE* wavelength calibration procedure. We also thank R. Bohlin and C. Keyes for energetic discussions on *FOS* calibration.

## References

- Colina, L. & Bohlin, R. C. 1994, Instrument Science Report CAL/SCS-003 (Baltimore:STScI)
- Evans, I. N., Koratkar, A., & Pesto, S., 1998, in preparation.
- Koratkar, A., Evans, I. N., Blitz, E., & Pesto, S., 1998, in preparation.
- Koratkar, A., Evans, I. N., Pesto, S., & Taylor, C., ApJ, 1997, in press.
- Nichols, J. & Linsky, J. L. 1996, AJ, 111, 517

## Estimating Scattered Light in the FOS

Jeffrey J.E. Hayes and Charles D. (Tony) Keyes

*Space Telescope Science Institute, 3700 San Martin Drive, Baltimore, MD 21218*

### Abstract.

We quantitatively assess the impact of grating scatter within the FOS as a function of intrinsic target spectrum and spectral element employed. *bspec*, the FOS scattered light optical modeling code of Micheael Rosa, has been used for this analysis. In this poster we present an example from an atlas of spectra (published in FOS ISR 151) illustrating the amount of predicted scattered light for all high dispersion gratings with both FOS detectors for a representative range of colors and object types. As has been qualitatively noted previously, we find that the intrinsic color of the observed object can affect the amount of scattered light detected and that this scattered light is, in most cases, wavelength independent. For the limited number of spectral elements to which it can be applied, the standard FOS pipeline scattered light correction is, therefore, a good approximation. The figures included in the above mentioned ISR can be used as a guide in estimating the degree of scattered light contamination in spectral regions for which the standard pipeline algorithm can not be applied.

### 1. Background

The Faint Object Spectrograph (FOS) is a single pass spectrometer with blazed, ruled gratings. Both the FOS/BL and FOS/RD detectors are sensitive to wide spectral ranges. Therefore, the FOS is subject to "scattered" light which originates primarily in the diffraction patterns of the gratings and the entrance apertures, as well as in the microroughness of the gratings due to their ruled surfaces. These characteristics are due to basic physical principles, which we assume throughout this paper can be utilized to model the practical impact of grating-scattered light on routine FOS observations.

Additional scattering due to the contamination of optical surfaces or unbaffled stray light may worsen the situation. Fortunately, the analysis of laboratory and on-orbit Science Verification (SV) FOS data (Uomoto *et al.* 1989, Bartko *et al.* 1992) shows that the actual instrument performance is very close to that expected from ideal optical surfaces and that the HST primary mirror is essentially smooth at UV wavelengths. The SV analysis, based upon measures of white dwarf BD+75°325 with FOS/BL and G130H, G190H and G160L gratings, verified that detected scattered light was limited by grating-scatter and was within pre-launch specifications.

In an examination of on-orbit science data for targets of a wide range of known color, E. Kinney and R. Gilmozzi (1994) pointed out that FOS grating-scatter contamination is particularly obvious for observations of late type stars in the UV range ( $\lambda \approx 1150\text{--}2100\text{\AA}$ ). This scattered light appeared to be wavelength independent, and to depend on the magnitude and color of the target object only. This result was confirmed by the parallel study of Rosa (1993).

The result of all these analyses was that A. Kinney and Bohlin (1993) recommended that the calibration pipeline for FOS data be modified to correct for grating-scattered light when possible. The correction algorithm determines the mean detected signal for those



diodes that are insensitive in a given dispersed spectrum and uses this mean as a measure of the wavelength-independent scattered light for the entire spectral range of the grating. This scattered signal is subtracted as a constant from all diodes in the spectrum. We note that not all FOS data can be so corrected as all diodes are illuminated by dispersed light in some FOS detector/disperser combinations. This procedure was implemented in the calibration pipeline in March 1994, and subsequently modified in February 1996 to use the median, rather than the mean, with the additional proviso that all deviations from the mean greater than  $4\sigma$  are eliminated in order to remove the impact of particle hits from the determination of the correction.

To further aid the observer, Bushouse *et al.* (1995) incorporated into the STSDAS software package a pair of tasks that would allow one to *estimate* the amount of scattered light in any type of observation carried out with the FOS (the so-called “*bspec*” package (Rosa 1994a)). We have used *bspec* to model the predicted grating-scatter for a representative sample of stellar types and object types that have been observed with the FOS. This report announces an atlas of these *bspec* predicted spectra that will allow users of FOS exposures to estimate the degree to which their FOS data is affected by grating-scattered light.

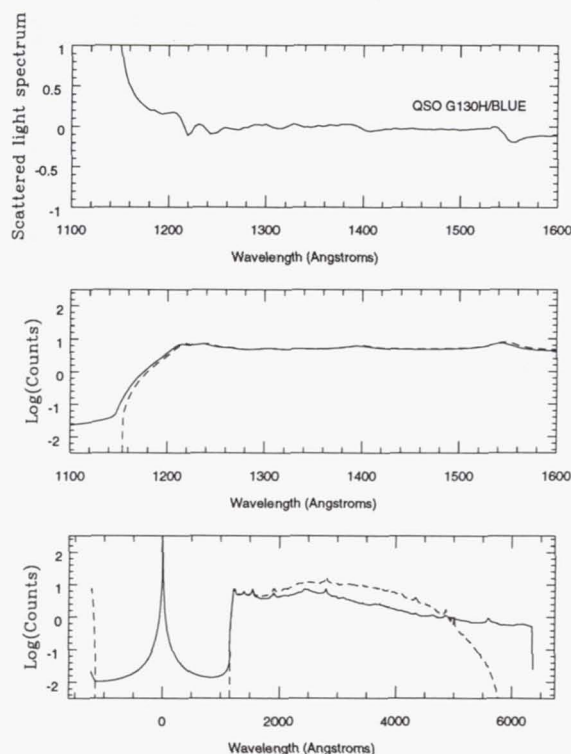


Figure 1. The lower two panels display scattered+intrinsic light (solid line) and the intrinsic light (dashed line) for a QSO as dispersed by the FOS/BL G130H grating. The upper panel indicates the ratio of scattered to scattered+intrinsic light in the spectral region of interest.

## 2. Example

We present a sample from FOS ISR 151: a QSO with the FOS/BL G130H grating. The reference spectrum was re-normalized to  $V = 15$  (at the fiducial wavelength of  $5556\text{\AA}$ ), through the  $1.0''$  aperture, and with COSTAR inserted in the optical path using the Synphot

task `calcspec`. We then ran the data through the task `countspec`, which takes a re-normalized spectrum and produces an FOS countrate spectrum. The task convolves the observed absolutely calibrated flux spectrum with the throughput functions of the FOS optical components to produce a corresponding spectrum that is in units of counts per second per pixel. The last step in the procedure is to run the result through the task `bspec`. Details are left to the ISR, but the result is that an *estimate* is made of the amount of scattered light in a given target from `bspec` by plotting some of the output of that task: the quantities of most interest are "gwav" (wavelength); "ablg" (the total of intrinsic+scattered light countrate spectrum); and "benv" (the total intrinsic light countrate spectrum). Figure 1 shows a sample of the results as presented in FOS ISR 151 to which we refer the reader for a more complete and thorough discussion of all these points.

## References

- Bartko, F., Burks, G., Kriss, G., Davidsen, A., Cohen, R., Junkkarinen, V., & Lyons, R., 1992, Instrument Science Report CAL/FOS-073 (Baltimore: STScI)
- Bushouse, H., Rosa, M., & Mueller, Th., 1995 in "*ADASS IV Proceedings*" eds. R. Shaw, H. Payne & J. Hayes, 345 (San Francisco:ASP)
- Hayes, J.J.E., & Keyes, C.D., 1997, Instrument Science Report CAL/FOS-151 (Baltimore: STScI)
- Kinney, A.L., & Bohlin, R.C., 1993, Instrument Science Report CAL/FOS-103 (Baltimore: STScI)
- Kinney, E., & Gilmozzi, R., 1994, Instrument Science Report CAL/FOS-101 (Baltimore: STScI)
- Rosa, M., 1993 "*Correcting for FOS background*" in *ST-ECF Newsletter* (Garching:ESA), 16
- Rosa, M., 1994, Instrument Science Report CAL/FOS-127 (Baltimore: STScI)
- Uomoto A., Blair, W.P., & Davidsen A.P., 1989, Instrument Science Report CAL/FOS-059 (Baltimore: STScI)



## The HST/FOS Wavelength Scale

Roeland P. van der Marel<sup>1</sup>

*Space Telescope Science Institute, 3700 San Martin Drive, Baltimore, MD 21218*

**Abstract.** I analyze the accuracy of the FOS pipeline wavelength calibration for the FOS/RD detector with the G570H grating. I use observations of arc spectra and external targets that I obtained in the context of studies of galactic nuclei, complemented with an observation of the planetary nebula NGC 6833 obtained by the FOS Instrument Science Team. The combined data were obtained in five visits spread over the period August 1995 to January 1997. I find that the absolute wavelength calibration generated by the pipeline for these visits is in error by 0.2–1.2 diodes, in the same direction for all visits. The mean of the errors is 0.62 diodes, where 1 diode = 4.37 Å. The error is largest for the two visits that used the paired apertures. These results indicate that the grating-wheel non-repeatability is larger than believed, or that (some of) the dispersion solutions in the pipeline may need to be modified by a constant offset. There are variations in the S-distortion between visits at the level of  $\sim 0.1$  diodes. The RMS shift between arc spectra obtained in the same visit, as a result of residual GIM errors, is  $\lesssim 0.04$  diodes. The average internal/external offset determined from these data is consistent with the constant value that has been used by the pipeline since 1992. No dependence is found on aperture or epoch. However, there is an indication that the internal/external offset varies systematically by 0.15 diodes between the blue and the red ends of the grating. If true, this translates directly into a systematic error in the relative wavelength scale for all G570H FOS/RD data in the HST Data Archive.

### 1. Introduction

The FOS pipeline calibration assigns a wavelength  $\lambda$  to each pixel  $x$  in a spectrum. The dispersion relations  $\lambda(x)$  for all detector/grating combinations were determined from an analysis of internal arc lamp spectra. The underlying principle is that the dispersion relation must place the centroid of each arc emission line at its known vacuum wavelength, plus an offset. The offset accounts for the fact that the light from the internal arc lamps traverses a different path in the instrument than the light from an external target. This offset is conventionally expressed as  $X_{\text{off}} \equiv X_{\text{internal}} - X_{\text{external}}$  in detector diodes; I will refer to it as the internal/external offset. This quantity must itself be calibrated, which can be done from observations of any target with known radial velocity. Kriss, Blair & Davidsen (1992) used pre-COSTAR observations of an M star with strong emission lines, obtained in September 1991. They found  $X_{\text{off}} = +0.176$  diodes for FOS/RD and  $X_{\text{off}} = -0.102$  diodes for FOS/BL, in either case with only a small dependence ( $\lesssim 0.05$  diodes) on the choice of grating. The observations were done with the 0.3 aperture, and a possible dependence on the choice of aperture was not tested for. These internal/external offsets have been used in the pipeline since 1992, and have not been updated after the installation of COSTAR.

---

<sup>1</sup>STScI Fellow



visit	#	date	galaxy	aperture(s)	$D$ diodes	$\text{RMS}(d_j)$ diodes	$X_{\text{off}}$ diodes
5847/1	9	08/22/95	M32	0.1/0.25	1.40	0.03	$0.16 \pm 0.02$
5848/2	7	09/07/95	NGC 7052	0.3	0.38	0.03	$0.19 \pm 0.10$
5848/4	7	08/17/96	NGC 7052	0.3	0.42	0.02	$0.19 \pm 0.10$
6537/2	6	11/30/96	IC 1459	0.1/0.25	1.02	0.04	$0.49 \pm 0.30$

Table 1. The first five columns list the project-ID/visit-number, number of orbits in the visit, date of the observations, name of the galaxy that was studied, and aperture(s) that was (were) used; '0.1/0.25' refers to the upper paired apertures of the given size. The next two columns list characteristics of the wavelength scale. The quantity  $D$  is the offset between the inferred wavelength scale for the visit, and the wavelength scale generated by the pipeline;  $\text{RMS}(d_j)$  is the RMS shift in the wavelength scale during the visit as a result of residual GIM errors. The last column lists the estimate of the internal/external offset  $X_{\text{off}}$  for the FOS/RD detector with the G570H grating, obtained from the galaxy spectra as discussed in Section 3; the two NGC 7052 visits were combined to yield a single estimate.

The accuracy of the FOS wavelength scale provided by the pipeline is limited by several effects (see, e.g., Keyes et al. 1995). (1) Non-repeatability in the positioning of the filter-grating wheel. Koratkar & Martin (1995) measured maximum deviations of  $\sim 0.35$  diodes, more-or-less independent of the choice of either the grating or the detector; the RMS deviation was  $\sim 0.1$  diodes. Grating wheel non-repeatability is believed to be the dominant uncertainty in the pipeline wavelength scale. However, it can be fully corrected in projects where arc lamp spectra were obtained in addition to the spectra of external targets, with no grating wheel motion in between. (2) Target acquisition uncertainties. The centering of the target in the aperture affects the accuracy of the wavelength scale. Errors are minimized by the choice of an accurate acquisition strategy, and can be corrected post-hoc if the position of the target in the aperture is known, e.g., from an FOS/ACQ image taken in the same orbit. (3) Residual errors in the on-board correction for the geomagnetically induced image motion problem (GIM). These have not been reported to exceed 0.1 diodes (HST Data Handbook 1995). Residual GIM errors can be corrected if the spectra of the external target are interspersed with frequent arc lamp spectra. (4) Errors in the internal/external offset. The measurements by Kriss et al. (1992) had a  $1\sigma$  uncertainty of 0.1 diodes. The offset may also depend on epoch, or may have changed with the installation of COSTAR. (5) Uncertainties in the dispersion solutions. The dispersion solution to an arc spectrum generally fits individual lines with a RMS of 0.01–0.08 diodes, depending on the choice of grating (HST Data Handbook 1995). The dispersion solutions may also depend on epoch.

In the context of the Cycle 5 and Cycle 6 projects GO-5847, 5848 and 6537, I analyzed FOS/RD spectra with the G570H grating of the nuclear regions of the galaxies M32, NGC 7052 and IC 1459 (see Table 1). The goal of these projects was to infer the nuclear mass distribution from the observed stellar and/or gas kinematics, and to determine the mass of possible black holes. The spectra for GO-5847 and 6537 were obtained in one visit each (5847/1 and 6537/2), while the spectra for GO-5848 were obtained in two visits (5848/2 and 5848/4), separated by one year. The first two orbits in each visit were used for target acquisition. There were no grating-wheel motions after the acquisition. In each orbit, arc lamp spectra were obtained during occultation to allow the construction of an optimally accurate wavelength scale. The galaxies have known systemic velocities, and the FOS/RD G570H internal/external offset could therefore be measured from the data. The scientific results from these projects are discussed elsewhere (van der Marel, de Zeeuw & Rix 1997; van der Marel & van den Bosch 1998; van der Marel, Carollo et al. 1998). Here I use the data to study the accuracy of the FOS pipeline wavelength scale.



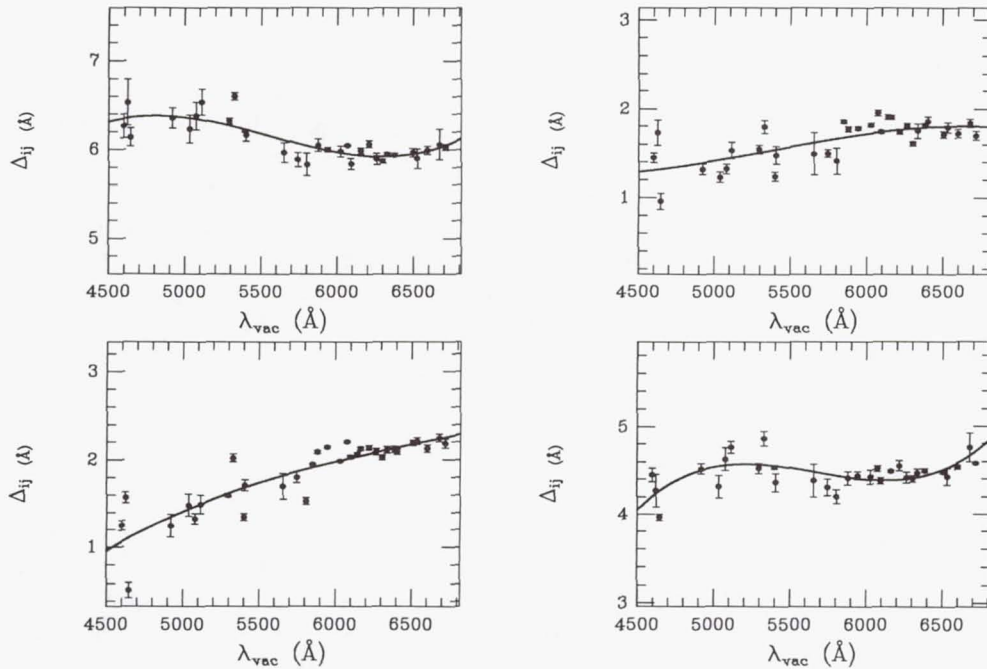


Figure 1. Wavelength calibration results for 5847/1 and 5848/2 (top row) and 5848/4 and 6537/2 (bottom row). Data points show for each arc emission line  $i$  at wavelength  $\lambda_{\text{vac},i}$  (plotted along the abscissa), the mean  $\Delta_{ij}$  averaged over the arc spectra  $j$  in the given visit; the quantity  $\Delta_{ij}$  is the difference between the vacuum wavelength, and the central wavelength of the line measured on the wavelength scale provided by the pipeline. The scale along both axes is in Å. The size of each panel along the ordinate is the same, but the range of displayed values is different. The curve in each panel is the best-fitting third order polynomial ( $D + P_3(\lambda_{\text{vac},i})$ ). Arc lines at larger wavelengths have higher signal-to-noise ratio, and their centroids therefore have smaller errors.

## 2. Wavelength calibration

I wrote fortran software to perform the wavelength calibration for these projects. The centroids of non-blended lines in the arc lamp spectra were determined through Gaussian fits. This yields for each spectrum  $j$ , and for each line  $i$  with vacuum wavelength  $\lambda_{\text{vac},i}$ , the observed wavelength  $\lambda_{ij}$  on the scale provided by the pipeline. For each visit I fitted the observed offsets  $\Delta_{ij} \equiv \lambda_{\text{vac},i} - \lambda_{ij}$  as

$$\Delta_{ij} = D + d_j + P_3(\lambda_{\text{vac},i}). \quad (1)$$

The quantity  $D$  is a constant offset. It is expected to be equal to +0.176 diodes (the internal/external offset in the pipeline; by convention, the pipeline scale is tailored to be correct for external targets, and hence to be offset for the internal lamps), plus an unknown offset that is different for each visit, due to grating wheel non-repeatability. The  $d_j$  represent shifts of the wavelength scale between arc spectra within the same visit (i.e., on a time scale of orbits), and are expected to be non-zero due to residual GIM errors. The third order polynomial  $P_3$  (with zero mean, by convention) accounts for differences between the actual S-distortion of the wavelength scale, and that part of the S-distortion that is already corrected by the pipeline.

Table 1 lists  $D$  and the RMS of the  $d_j$  for each visit, expressed in diodes (1 diode = 4.37 Å for the G570H grating). Figure 1 shows the results as function of wavelength,

averaged over the multiple arc spectra in a given visit. The shifts in the wavelength scale during a visit as a result of residual GIM errors are small,  $\text{RMS}(d_j) \lesssim 0.04$  diodes. The residual S-distortion varies from visit to visit, but is also small,  $|P_3| \lesssim 0.1$  diodes. The inferred values of  $D$  are surprising. They are not randomly distributed around  $+0.176$  diodes, as would have been expected. Instead,  $D - 0.176$  ranges from  $0.2$ – $1.2$  diodes, and has the same sign for all visits. The error is particularly large for the two visits that used the upper paired apertures. These results indicate that the grating-wheel non-repeatability is larger than believed, or that (some of) the dispersion solutions in the pipeline may need to be modified by a constant offset. The quantities  $D - 0.176$  provide a direct comparison between the dispersion solutions from my data and the dispersion solutions used by the pipeline. Both are based on arc spectra, and the inferred discrepancy is therefore independent of the internal/external offset.

### 3. The internal/external offset

I used the dispersion solutions for the arc spectra to generate an optimal wavelength scale for each of the galaxy spectra in each visit, initially assuming that there is no internal/external offset. Residual GIM errors were corrected by shifting the wavelength scale for each galaxy spectrum by the (small) amount  $d_j$  determined for the arc spectrum (spectra) obtained in the same orbit. The absorption and/or emission lines in the galaxy spectra were analyzed to determine the mean velocities of the stellar and/or gaseous components. The distribution of light within the aperture was modeled for each observation, and the small velocity shifts resulting from a possible asymmetric distribution of light within the aperture were corrected for. Rotation curves were generated using the results from spectra obtained at various distances along the major axis, and the mean velocity at the position of the nucleus (obtained by interpolation) was adopted as the inferred systemic velocity. The systemic velocity for each galaxy was compared to literature values available from ground-based observations. The difference  $\Delta V \equiv V_{\text{obs}} - V_{\text{lit}}$  provides a measurement of the internal/external offset. For the FOS/RD with the G570H grating,  $X_{\text{off}} = (\Delta V/c) \times (\lambda_{\text{obs}}/4.37\text{\AA})$ , where  $c$  is the speed of light and  $\lambda_{\text{obs}}$  is the wavelength (or the mean of the wavelength region) used to derive the velocity.

For M32 only absorption lines are available. However, the spectra have very high signal-to-noise ratio, and the apertures sampled the nuclear region densely. The systemic velocity and the internal/external offset are therefore accurately determined. The result,  $X_{\text{off}} = 0.16 \pm 0.02$  is entirely consistent with the value of  $0.176$  diodes (with a quoted  $1\sigma$  error of  $\sim 0.1$  diodes; Kriss et al. 1992) that has been used for years by the pipeline. The NGC 7052 and IC 1459 observations were aimed at a determination of the gas kinematics; the absorption lines have too little signal for an accurate determination of  $X_{\text{off}}$ . The emission lines have sufficient signal, but their kinematics are more difficult to interpret. The gas near the nucleus need not move at the systemic velocity, and the presence of dust in both galaxies provides additional uncertainties. For IC 1459 there are also differences of up to  $100$  km/s in the systemic velocities quoted in the literature. The errors in  $X_{\text{off}}$  listed in Table 1 for NGC 7052 and IC 1459 provide my assessment of the possible importance of these complicating factors, based on extensive tests. The  $X_{\text{off}}$  determinations for these galaxies are less accurate than for M32, but as for M32, the results are consistent with the internal/external offset that is used by the pipeline.

### 4. Analysis of a planetary nebula spectrum

Galaxies are not the most convenient targets to determine the internal/external offset of the FOS. Planetary nebulae are more suitable, because of their pronounced emission lines and lack of intrinsic kinematic gradients. The FOS instrument team has observed the planetary



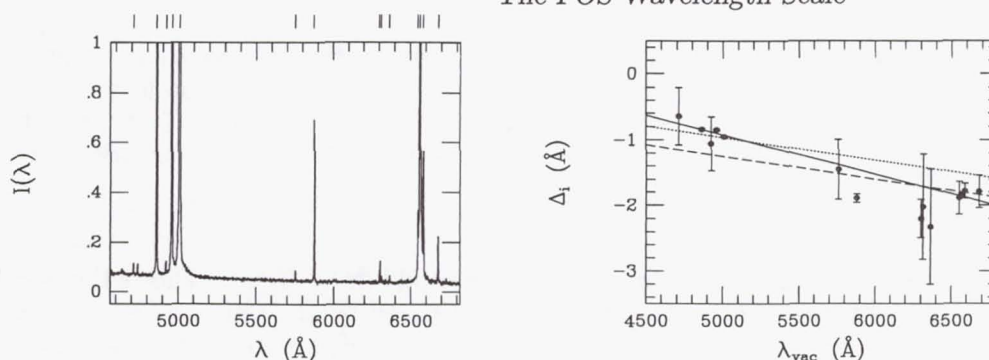


Figure 2. The left panel shows a spectrum of the planetary nebula NGC 6833. Bars indicate the emission lines that were identified and fitted: HI ( $\lambda_{\text{air}} = 4861.33$ ,  $6562.82\text{\AA}$ ), He I ( $4713.20$ ,  $4921.93$ ,  $5875.67$ ,  $6678.15$ ), [OI] ( $6300.30$ ,  $6363.78$ ), [NII] ( $5754.64$ ,  $6548.03$ ,  $6583.41$ ), [OIII] ( $4958.91$ ,  $5006.84$ ) and [SIII] ( $6312.10$ ). The vacuum wavelengths follow from  $\lambda_{\text{vac}} = \lambda_{\text{air}} n_{\text{air}}$ , where the index of refraction for air  $n_{\text{air}} \approx 1.000279$ . The right panel shows the residuals  $\Delta_i$  between the measured and the vacuum wavelength of the emission lines, as a function of  $\lambda_{\text{vac}}$ . The scale along the ordinate is in  $\text{\AA}$ . These data allow an accurate determination of the internal/external wavelength offset. The linear fits are discussed in the text.

nebula NGC 6833 as part of its calibration program. To verify the results reported in Sections 2 and 3, I analyzed a spectrum (y3kk010ct) of NGC 6833 and a contiguous arc spectrum (y3kk010dt), obtained on 01/12/97 with the 0.3 aperture and G570H grating on the FOS/RD detector. These spectra were taken as part of proposal 6918 (PI: Keyes), and were kindly provided to me by E. Smith. These and more spectra of the same target are also available from the HST Data Archive.

The arc spectrum was analyzed as described in Section 2. The offset  $D$  was found to be 0.76 diodes; as before, significantly larger than the expected value of 0.176 diodes, and too large to be attributable to grating wheel non-repeatability. The wavelength solution for the arc spectrum was used to calibrate the NGC 6833 spectrum, initially assuming that there is no internal/external offset. The spectrum is shown in the left panel of Figure 2. Gaussians were fitted to all detectable emission lines (indicated in the Figure and listed in the caption), yielding for each line  $i$  the observed wavelength  $\lambda_i$ . The right panel of the figure shows the inferred residuals  $\Delta_i \equiv \lambda_i - \lambda_{\text{vac},i}$  as a function of  $\lambda_{\text{vac}}$ .

The observed and vacuum wavelength for a line are related according to

$$\Delta = 4.37 X_{\text{off}} + (V/c)\lambda_{\text{vac}}, \quad (2)$$

where  $V$  is the line-of-sight velocity of NGC 6833 with respect to the earth at the time of the observation, and 4.37 is the scale in  $\text{\AA}/\text{diode}$  for the G570H grating on the FOS/RD detector. This is a linear relation between  $\Delta$  and  $\lambda_{\text{vac}}$ ; the velocity  $V$  determines the slope, and the internal/external offset determines the intercept. The heliocentric velocity of NGC 6833 from the literature is  $-109.8 \text{ km/s}$ . This implies  $V = -104.0 \text{ km/s}$ , taking into account the annual velocity of the earth as calculated with the IRAF task `rvcorrect`. The dotted line in Figure 2 shows the best fit line for this velocity when the individual  $\Delta_i$  are weighted by their errors. The inferred internal/external offset,  $X_{\text{off}} = 0.177$ , is then determined primarily by the three strong lines near  $5000\text{\AA}$ . The dashed line shows the fit if the  $\Delta_i$  are all weighted equally, which yields  $X_{\text{off}} = 0.111$  diodes. These results are in satisfactory agreement with both the pipeline value and the results of Section 3, indicating that there is no appreciable dependence of  $X_{\text{off}}$  on either epoch or aperture.

Neither the dotted nor the dashed line in Figure 2 fits the data on both the blue and the red ends of the spectrum. If one assumes that this is due to an error in the literature

value for the heliocentric velocity, one must also assume that the internal/external offset in the pipeline (and verified in Section 3) is wrong. This is not a plausible explanation. It is more likely that the internal/external offset is not a pure constant, but is of the form  $X_{\text{off}} = A + BX$ . This still yields a linear relation between  $\Delta$  and  $\lambda_{\text{vac}}$ , but now of the form

$$\Delta = [-sA + B(\lambda_1 - s)] + [(V/c) - B]\lambda_{\text{vac}}, \quad (3)$$

where  $\lambda_1$  is the wavelength at the first diode. The solid line in Figure 2 shows the best linear least squares fit of this form, when the  $\Delta_i$  are weighted by their errors. It has  $A = 0.080$  and  $B = 2.53 \times 10^{-4}$ . A similar fit, but with all data weighted equally, yields  $A = 0.036$  and  $B = 3.24 \times 10^{-4}$ . The internal/external offset at the first diode (on the red end) is  $A + B \approx A$ . At the last diode (number  $N$ ; on the blue end), it is  $A + NB = 0.210$  or  $0.202$ , depending on whether the data points are weighted in the fit or not. Thus, it appears that the internal/external offset varies from  $X_{\text{off}} \approx 0.21$  diodes on the blue end to  $X_{\text{off}} \approx 0.06$  diodes on the red end. The addition of a linear term in  $X_{\text{off}}$  decreases the  $\chi^2$  of the fit from 438 to 70 (for 12 degrees of freedom), and is thus highly significant. The relatively low values of the  $\Delta_i$  for the emission lines in the range 5800–6500 Å may indicate that even second- or higher-order terms should be invoked for an accurate description of the internal/external offset.

## 5. Conclusions

The results presented here show that the pipeline wavelength calibration for the FOS/RD detector with the G570H grating is somewhat less accurate than has been believed. The results of Section 2 suggest that there are errors in the *absolute* scale that are both systematic and surprisingly large, and that can therefore not be attributed to the usual grating wheel non-repeatability. The results of Section 4 show that the internal/external offset may not be a simple constant, but may have a systematic variation of  $\sim 0.15$  diodes between the two sides of the detector. If so, this translates directly into a systematic error in the *relative* wavelength scale for all G570H FOS/RD data in the HST Data Archive. Improvements in the pipeline calibration parameters may be feasible, and should be followed by a recalibration of all impacted data in the Archive.

**Acknowledgments.** This work benefited from discussions with FOS Instrument Scientists Tony Keyes and Ed Smith. They are currently studying the FOS wavelength calibration in a more systematic fashion, and kindly shared with me both their data (on NGC 6833) and their insights. The FOS spectra of M32, NGC 7052 and IC 1459 were obtained in collaborations with Tim de Zeeuw, Hans-Walter Rix, Frank van den Bosch, Marcella Carollo and Marijn Franx.

## References

- Keyes C. D., Koratkar A. P., Dahlem M., Hayes J., Christensen J., Martin S. 1995, *FOS Instrument Handbook*, Version 6.0, (Baltimore:STScI)
- Koratkar A., Martin S. 1995, Instrument Science Report CAL/FOS-145 (Baltimore:STScI)
- Kriss G.A., Blair W.P., Davidsen A.F. 1992, Instrument Science Report CAL/FOS-070 (Baltimore:STScI)
- van der Marel R. P., de Zeeuw P. T., Rix H.-W. 1997, ApJ, 488, in press
- van der Marel R. P., van den Bosch F. C. 1998, in preparation
- van der Marel R. P., Carollo C. M. C., de Zeeuw P. T., Franx M. 1998, in preparation



## Astrometry with the FGS in POSITION Mode and TRANSFER Mode: Observing Strategies, Pipeline Processing and Data Reduction

Ed Nelan, Olivia Lupie, and Laretta Nagel

*Space Telescope Science Institute, 3700 San Martin Drive Baltimore, MD 21218*

**Abstract.** We present an overview of HST astrometry, data analysis techniques, calibrations, errors, and pipeline processing steps for FGS astrometry data.

### 1. Introduction

Each Fine Guidance Sensor (FGS) on the HST is an optical-mechanical white-light interferometer that can sense 1–3 milliarcsec (mas) angular displacements of a point source over a large dynamic range:  $3 < V < 15$ . For fainter objects down to  $V < 17$ , the accuracy degrades to more than 2 mas. The FGS can also resolve structure in non-point sources at the 15 mas level. The light gathering power of the HST and the dynamic range of the FGS make it an unparalleled science instrument for many important astronomical investigations. Detecting and resolving multiple star systems and planetary companions, delineation of objects in crowded fields, measuring angular diameters, parallax, proper motion, positional surveys, occultation studies and photometry are among its many uses. FGS3 is currently serving as the HST astrometer. For many scientific endeavors, the FGS continues to exceed ground-based efforts in sensitivity and resolution.

The optical path through an FGS is complex because the beam must pass through multiple optical elements. The relative alignment of all these components and the wavelength dependencies introduced by their refractive or reflective properties limits the resolution and magnitude sensitivity of the FGS. Most of the FGS calibration procedure consists of empirical and semi-empirical subtraction of the instrument signature necessitating observations of standard stars in all modes and various spectral ranges.

This paper briefly describes the modes of the FGS and discusses the data analysis techniques and pipeline, calibrations, and the removal of instrument signatures.

### 2. Instrument Overview

Three Fine Guidance Sensors on the HST each have a total field of view that extends radially 10 arcminutes to 14 arcminutes; each is a quarter annulus in the HST focal plane with a total area of 69 square arcminutes. The instantaneous field of view (IFOV) is smaller,  $5 \times 5$  arcsec. Only photons in this  $5 \times 5$  arcsec aperture fall on the PMTs at any one time. The IFOV can be placed at any position in the annulus.

For extensive detail of the optical components and light path of the FGS, we refer the reader to the latest version of the HST Data Handbook (Voit 1997), Chapters 9, 10, 11, and 12, to be released later this year. Here, we briefly review those pertinent aspects of the instrument which will be important in discussions of instrument effects discussed later in this paper.

At the heart of the FGS are the polarizing beam splitter (PBS), the 2 Koesters prisms, and the four photomultiplier tubes (PMTs). The optical elements upstream from the PBS narrow the IFOV to  $5'' \times 5''$  and present to the PBS a collimated beam. The PBS performs

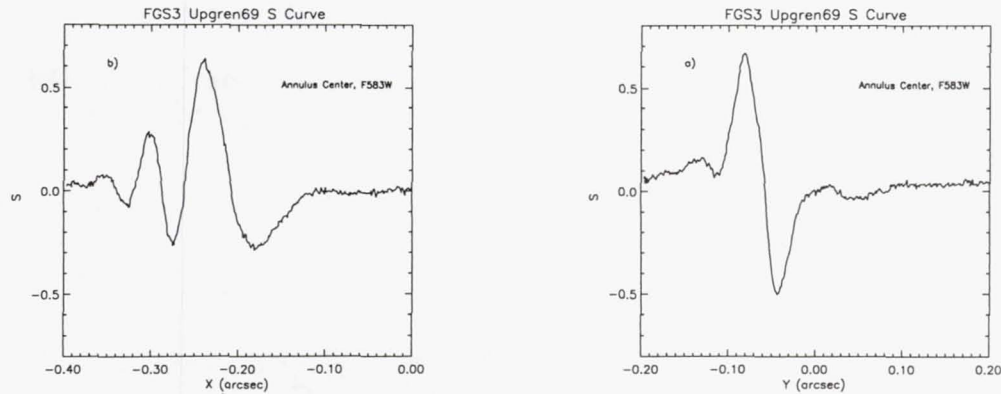


Figure 1. The X and Y Axes S-Curves of the single standard star Uggren 69 at the center of the FGS3 annulus and acquired in filter f583W.

a 50/50 intensity division of the incident light and emits two mutually orthogonal plane polarized beams. These beams fall upon the face of the appropriate Koesters prism.

The Koesters prism is a fused silica pyramid with two halves separated by a dielectric interface. The prism senses tilt about an axis which is in the plane of the dielectric and parallel to the entrance face of the prism. Small rotations of the Star Selector A and B assemblies vary the tilt of the wavefront. When the component of the wavefront's propagation vector which is perpendicular to the plane of the dielectric is zero, a condition of interferometric null results and the relative intensities of the two emergent beams are ideally equal. Two Koesters prisms are needed for sensing the tilt of the wavefront in orthogonal directions. For a star at a given position in the FGS detector space, there is a unique set of SSA and SSB rotation angles which brings that star's wavefront to zero tilt at the face of each Koesters prism. Therefore, the position of the star in detector space can be measured with high precision.

### 3. The S-Curve

The relative intensities of the beams emerging from the Koesters prism assembly correlate with the wavefront tilt angle and therefore respond to the rotations of the SSA and the SSB assemblies that cause the IFOV to scan across a star. The PMT output during such a scan provides the characteristic interferometric pattern. The normalized difference of the PMTs on a given channel against the IFOV position produces a figure called the S-Curve. For each point along the X axis, the S-Curve is given by the following with a similar expression for Y:

$$S_x = (A_x - B_x) / (A_x + B_x)$$

where  $A_x$  and  $B_x$  are the PMT counts from PMTs A and B on the X channel integrated over 25 milliseconds. When the IFOV is more than 100 mas from the location of the interferometric null, the PMTs record nearly equal intensities. A zero point crossing between the peaks of the S-Curve occurs near interferometric null. But, because of slight differences in the PMT sensitivities and in the paths traversed by the two beams, the zero point crossing is slightly shifted from the true null. A correction is made in the data reduction pipeline for this effect.

The S-Curve in FGS3 of a single standard star Uggren 69 is shown in Figure 1. The Y axis S-Curve is nearly perfect as can be seen from the morphology and amplitude. The



X axis however is degraded, a result of misalignment of Koesters prism with respect to the wavefront's tilt axis.

#### 4. Modes of Observing

The two observing modes of the FGS are POSition mode and TRANSfer mode. An FGS in Position mode acquires an object in fine lock and tracks it for an extended period of time. An FGS in Transfer mode acquires an object and scans the IFOV back and forth along a 45 degree diagonal path in detector space to sample the interference pattern and generate an S-Curve.

**Position Mode Observing:** This mode can be used to determine the parallax, proper motion, and/or reflex motion of a given object. A typical Position mode observing program, regardless of the scientific goal, measures the (x,y) detector space positions of several objects concurrently observable in the FGS's total FOV. An FGS can observe only one object at a time, so each of the objects are visited and tracked in a sequence specified in the proposal. To begin the visit, the IFOV is slewed to the predicted position of the first target. The target acquisition phases are initiated and once the interferometric null is located, Fine lock tracking ensues (described below) and data are obtained according to the exposure time in the proposal. This process repeats until the FGS has observed all stars in the visit.

**Transfer Mode Observing:** This mode can be used to resolve the components of multi-star systems and measure the angular dimensions of extended objects. In a Transfer mode observation the FGS acquires the object, but instead of attempting to keep the FGS's IFOV at or near interferometric null as in a Position observation, the FGS steps its IFOV back and forth across the object along a 45 degree diagonal path in detector space to sample the entire S-Curve and its immediate vicinity. Each swath across the object is referred to as a scan. The number of scans, size of each step, and length of each scan are specified in the proposal. Typically, a Transfer mode observation will consist of 20 or more scans, each 1''4 long, with a STEP\_SIZE of 1 mas.

**Mixed Mode Observing:** It is sometimes possible to determine the parallax, proper motion, and/or reflex motion of a multiple star system resolvable by the FGS in Transfer mode. If the FGS can both resolve a binary system and measure its parallax, then the absolute masses of its components would be determined. To accomplish this task, the FGS observes the target in Transfer mode and other nearby stars in Position mode. A mixed mode observing strategy would include a series of Position mode observations of the reference stars and a Transfer mode observation embedded somewhere in the sequence. Although the post-observation analysis of mixed mode observing data can be challenging, the potential scientific returns have made it an increasingly popular way to use the FGS as an astrometer.

#### 5. A Note About Target Acquisition

The target acquisition phases are described in detail Voit (1997). The stages are briefly discussed here because the target acquisition data are included in the data set delivered to the general observer and also because some of those data are used for background subtraction and calibration of the science data. The target acquisition consists of three stages: Search, Coarse track, and Fine lock.

**Search:** This phase consists of an outward spiral of the IFOV from the expected location of the target which proceeds until the PMT counts from a 5×5 arcsec patch of sky falls within a specified range. When this occurs, the instrument proceeds to the next phase.

**CoarseTrack:** The FGS determines the photocenter of the light by comparing the photon counts from the four PMTs as the IFOV nutates in a 5 arcsec circular path around the

target. The position of the nutation circle is continuously adjusted to improve the centering of the target.

**FineLock:** Upon completion of the Coarse track phase, the FGS attempts to acquire the target in Fine lock. This activity involves two distinct phases, acquisition and tracking. Both make use of the interferometric signal (the S-Curve) to achieve success. The acquisition phase is termed the WalkDown. The IFOV is commanded to a position offset or "backed-off" from the object's photocenter (determined by Coarse track). The IFOV is held fixed while the FGS electronics performs an integration to calculate a DIFF and SUM in order to compensate for any difference in the response of the two PMTs on a given axis. During the WalkDown, the IFOV creeps towards the photocenter in a series of equal steps, approximately 0".006 in x and y, and is held fixed for while the PMT data are integrated to compute the fine error signal on each axis. If the fine error signal satisfies a threshold criteria, the FGS begins fine lock tracking of the object, constantly adjusting the IFOV to null the fine error signal and track the interferometric null. The fine error signal on the X-channel is given as:

$$Q_x = (A_x - B_x - DIFF_x) / SUM_x$$

## 6. POS Mode Pipeline Processing

This section describes how FGS data are calibrated. Unlike the data from other HST instruments, FGS astrometry data are not calibrated automatically. Observers now require the assistance of the Space Telescope Astrometry Team (STAT, specifically Barbara McArthur at the University of Texas) and the FGS team at STScI to process astrometry science data through the pipeline; however, we are currently working to make FGS calibration more automatic. We are developing IRAF/STSDAS tools that will calibrate the data conveniently and efficiently using the current best set of calibration reference files and algorithms, and these tools may ultimately evolve into a routine data processing pipeline that generates and archives calibrated FGS data. Check the FGS Web pages for updates.

### 6.1. Individual Observations

The pipeline will calibrate Position Mode data in two distinct stages. The first stage processes each single observation in a stand-alone fashion, ignoring the other observations belonging to the same HST visit. The second stage relates all the individual observations to one another so that an astrometric "plate" can be produced.

The dataset for a given observation includes the slew to the target, the Search, the CoarseTrack, the WalkDown, and the FineLock Tracking, as well as guide star data over the same interval of time. These data provide information used by the pipeline algorithms to determine backgrounds, to locate the interferometric null, and ultimately, to pinpoint the position of the star relative to the other stars observed in the visit. The Slew portion of the observation is used to measure the background.

The processing steps for each individual observation in the visit are:

1. inspect flags
2. convert the Star Selector rotation angles into FGS detector X,Y coordinates using parameters determined by the long term stability monitor analysis (McArthur et al. 1997)
3. gather photon statistics at various stages of the acquisition and observation
4. determine the centroid of the IFOV taken to be the median of the instantaneous x,y positions during the FineLock tracking



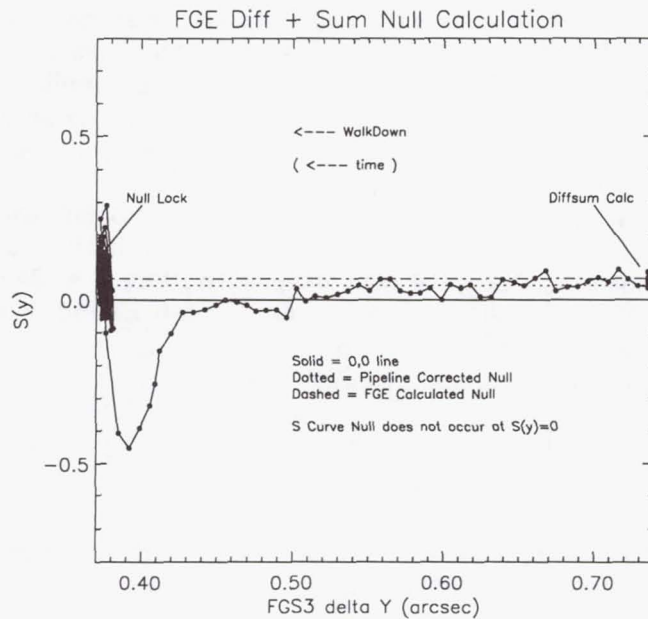


Figure 2. The DIFF and SUM values calculated by the FGS onboard processor for the Walkdown to FineLock algorithm requires adjustment in the pipeline.

5. improve the FGS's calculation of the DIFF and SUM using the photometry from the WalkDown (see Figure 2)
6. apply calibrations to remove optical field angle distortions and correct for differential velocity aberration (McArthur et al. 1997)

The pipeline produces output files that log these corrections, the associated standard deviations about the centroids, and the photometry data from the four PMTs.

## 6.2. The Visit

The goal of this segment of the Position pipeline is to map all of the positional measurements of the individual targets onto a common coordinate system. This is necessary since the observations are made in a sequence rather than simultaneously and it is known the detector jitters and drifts on the sky during the course of the visit. Defining the common coordinate system involves de-jittering and application of the drift correction.

**Jitter:** The pipeline accounts for spacecraft jitter during the visit by establishing a fixed but arbitrary reference frame determined by the positions of the guide stars within the guiding FGSs. The output products of the pipeline for individual observations include the x,y centroids of the guide stars' positions evaluated over the same time interval as the astrometer centroids. During the course of the visit any change in the x,y centroids of the guide stars within the guiding FGSs are interpreted to be HST jitter (translational and rotational) and is removed from the data. Typically, the size of the dejittering correction is less than a millisecond of arc when averaged over the visit but can be as large as 3–5 mas during times when HST transitions from orbit night to day.

**Drift:** After the FGS data have been de-jittered, there will remain an apparent motion of those astrometry targets, called check stars, which have been observed more than once within the observing sequence. The drift correction model assumes that the astrometer is a rigid body which both translates and rotates in the HST focal plane during the course of

the visit, and it corrects the measured positions of the stars in the visit for contamination by this motion. The time-tagged positions of the check stars are used to generate a model for this drift and the time-tagged positions of all the stars in the visit are adjusted by application of the model. Three separate models can be applied: Linear, Quadratic, and Quadratic + Roll. The choice of model depends upon the number of check stars available and the number of times each is observed. The pipeline applies all three models, providing three sets of corrected centroids. It is the responsibility of the general observer to decide which set is best from the residuals and the chi squares of subsequent plate overlays. The amount of drift is loosely correlated with a target's inclination. Those in the plane of the HST's orbit demonstrate the most drift, (typically 10 mas) while those at high inclination have the least drift (as small as 3–4 mas). On the other hand, if guiding of the spacecraft is handled with only one FGS, the telescope is not roll constrained and a drift of up to 70 mas can be seen in the astrometric check star sequence.

### 6.3. Proposal Level Processing

Plate overlays are necessary to measure the parallax, proper motion, or reflex motion of a given object with respect to the reference field stars. To generate a plate overlay, you must collect pipeline calibrated data from several visits, which might span years, and map them onto a common reference frame or "virtual" plate. You can then determine whether the object of interest moves in a systematic, time-dependent way with respect to the reference field. The Space Telescope Astrometry Science Team (STAT) has developed a very useful algorithm for constructing plate overlays and has made it available to STScI for development into a publicly-accessible tool.

The plate overlay tool derives a virtual plate using either a four parameter or six parameter plate solution. The four parameter model adjusts for translation, rotation, and relative scale, while the six parameter model also adjusts the relative scales along the x and y axis independently. Formally, the six parameter model requires at least three common reference stars in each plate, but in order to avoid over-constraining the plate solution, you should not apply the six parameter model with fewer than five reference stars.

The four-parameter model has been the workhorse for obtaining FGS astrometric plate solutions because the reference fields around the scientific targets have frequently been too sparse for a six-parameter model. Formally only two reference stars are needed to apply the four-parameter model, but obviously such a solution is highly constrained and vulnerable to motions of the reference stars and errors in their measured positions. Figure 3 shows the residuals from two visits to an astrometric field relative to their common virtual plate. The small residuals ( $< 1\text{ mas}$ ) are impressive considering that one of the visits suffered from 25 mas of drift (detected by the check stars and taken out by application of the drift model).

## 7. Sources of Position Mode Errors

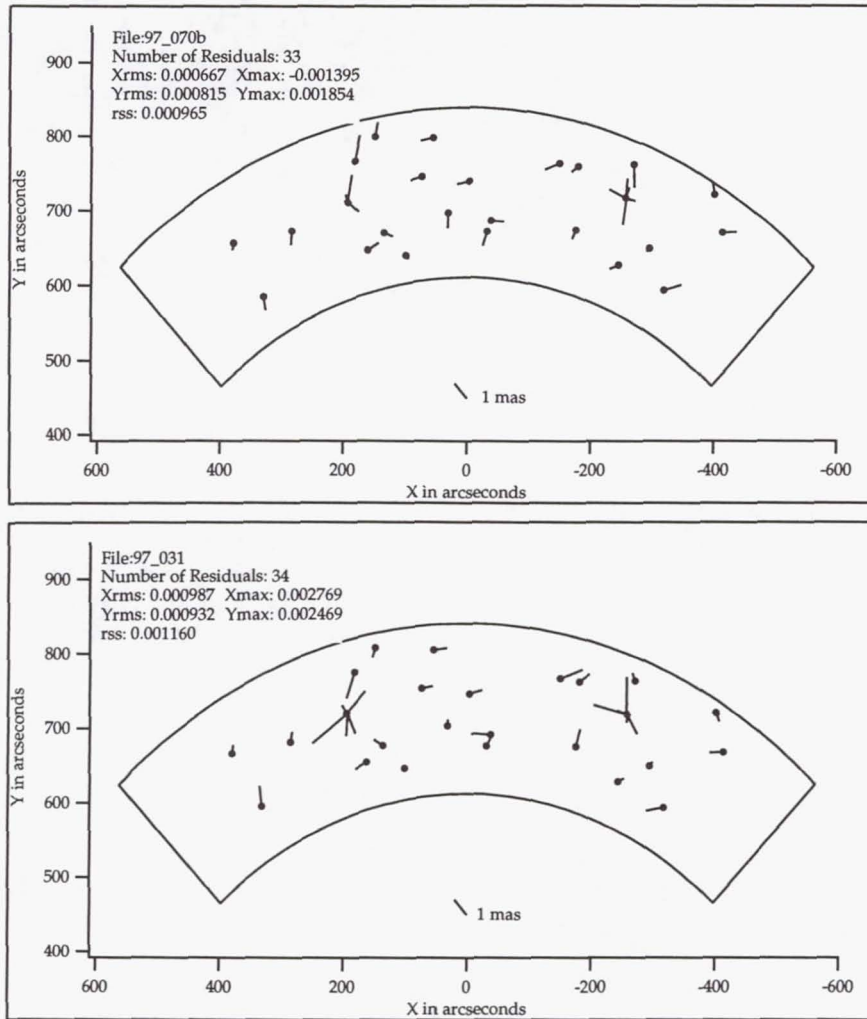
Here, we address the errors remaining after the pipeline corrections and calibrations are performed.

### 7.1. Centroiding Errors

During nominal FineLock tracking of an object, the instantaneous field of view of the FGS will jitter and drift about the (x,y) median. The standard deviation of these excursions depends upon the magnitude of the target and HST vehicular jitter. Because the FGS tracks an object by computing and implementing corrections to the current position of the IFOV on the basis of the fine error signal, noise in the PMT counts can introduce errors in the corrections. To compensate for the increase of the photometric noise with a target's magnitude, the integration time is increased and hence the number of independent samples is decreased. As targets become fainter, the FGS applies increasingly unreliable DIFF and



Spring 1997 LTSTAB, pre and post servicing mission  
4 prm plate solution



Scale Difference: 1.0259E-05

BMC9703

Figure 3. Residuals from two visits to an astrometric field. Before drift correction, one of the visits contained 25 mas of drift in the check stars.

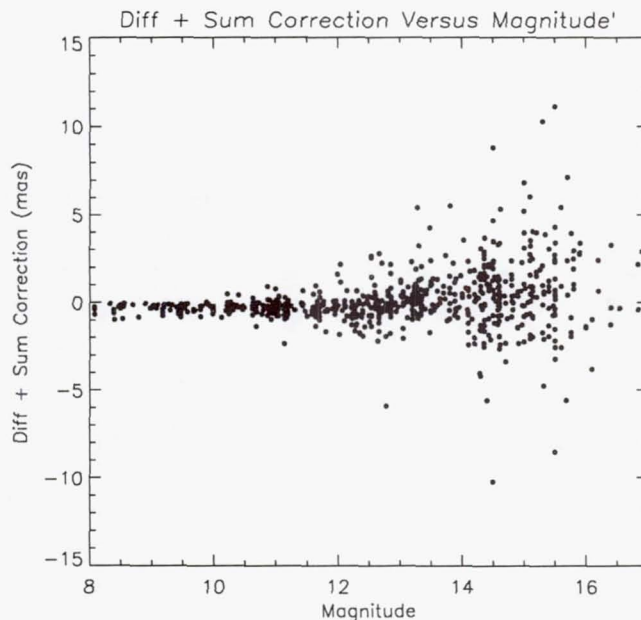


Figure 4. The DIFF and SUM corrections as a function of magnitude.

SUM values in its calculation of the fine error signal and therefore risks locking onto a region of the S-Curve which is not the true interferometric null. To compensate for this uncertainty, the calibration pipeline attempts to derive better values of DIFF and SUM. For more information, see Chapter 12 in Voit (1997). The size of the correction computed by the pipeline is small for bright stars but can be large for faint ( $V > 15$ ) stars, up to 5 mas. This is shown in Figure 4.

### 7.2. Optical Field Angle Distortion

Optical field angle distortion (OFAD) alters the apparent relative angular separations of stars distributed across the FGS's pickle (annulus) as the FGS translates and rotates on the sky. This distortion originates from both the FGS/OTA optical train and errors in the readout of the star selector encoders. Correcting for the distortion is absolutely necessary for all Position mode observing programs that visit the target field at a variety of HST orientations (roll angles). The Space Telescope Astrometry Science Team has made extensive efforts to calibrate optical field angle distortion and to maintain this calibration. The relative distortions appear to change slowly as a function of time. A Long Term Stability Monitor test (LTSTAB) obtains data which are used to update or maintain the current OFAD calibration. The absolute size of the OFAD correction is on the order of 4 arcsec, nearly 2000 times the overall error budget (McArthur et al. 1997). The updates derived from the LTSTAB data are on the order of 100 mas across the annulus, nearly 50 times the error budget.

### 7.3. Lateral Color

The chromatic response of the five element corrector group, the polarizing beam splitter, the filter, and Koesters prism, introduces a slight color dependence into the tilt of a wave front measured by the FGS. This chromatic effect results in a displacement of the target's position in the FGS's field of view. But the size and sign of the positional shift as a function of color difference are not well understood. It is suspected to be important only when the



color differences exceed one magnitude, where it is estimated to be about 1 mas (McArthur et al. 1997). The lateral color effect, not corrected for in the pipeline, will manifest itself as an HST roll-dependent motion of an object with respect to stars of different color.

#### 7.4. Cross Filter Effect

The cross filter calibration addresses the apparent change in the measured position of an object observed in Position mode as function of the filter selected for the observation. As with the lateral color effect, any shift, if unaccounted for, will result in an apparent HST roll-dependent motion of the object relative to those stars measured through a different filter. Unfortunately, the cross filter effect is known to be field dependent and is well calibrated at only three locations within FGS3. The cross filter effect contributes only about 1 mas to the residual of targets requiring this correction provided the observations are made at a calibrated position.

#### 7.5. Visit-Level Position Errors

FGS measurements are sensitive to temporal variations that might occur during the observing sequence. The challenge is to assemble an astrometric plate by defining a common coordinate system onto which the individual observations are mapped. Observers must assume that the telescope's yaw, pitch, and roll might be slightly different for each observation, causing the sky to wobble about in FGS3's detector space. Such motions can be detected and eliminated using guide star data and check star measurements. The size of the corrections are typically 2 to 6 times the overall astrometry error budget but can be as large as 30 times.

### 8. Transfer Mode Pipeline Processing

The dataset for a Transfer Mode observation includes of all the acquisition phases described in section 5. Automatic pipeline processing of Transfer mode data is limited to locating each scan in the astrometer's data file, editing out bad data arising from garbled telemetry, and determining the median position and standard deviations of the guide stars within the guiding FGSs during each scan. The guide stars' positions are not corrected for differential velocity aberration. The pipeline generates three ASCII files for every scan, one for each FGS. Each file contains the raw star selector A,B encoder values and the photon counts/25msec of the four PMTs. The guide star data are provided for (optional) de-jittering of the astrometer's IFOV.

A future enhancement to the Transfer mode pipeline will support Mixed-mode observing to map the S-Curve results onto Position mode plates.

### 9. Resolving Structure with Transfer Mode

Transfer mode observations with the FGS can resolve the individual components of multiple star systems and measure the angular diameters of extended objects. These observations scan the IFOV of the FGS across an object to accumulate the necessary data for a post observation reconstruction of the x and y axis S-Curves. The general observer compares the observed S-Curves to those from a reference star, presumed to be single, in the calibration database to deconvolve the contribution from each component of a multi-star system or each cord of an extended object. Such an analysis can reveal the magnitude difference and relative separation in x and y of a binary star system or the apparent angular diameter of an extended object in both the x and y directions.

If the angular separation of the stars is greater than the characteristic width of an S-Curve, two distinct S-Curves will be apparent, but the modulation of each will be diminished

relative to that of a single star by an amount depending on the relative intensity of each star. On the other hand, if the angular separation is sufficiently small, the S-Curves will be superimposed, and the morphology of the resulting blend will be complicated. In either case, provided the separations are not too small ( $< 15\text{mas}$ ) and the magnitude difference not too large ( $> 4$  magnitudes), the composite S-Curve can be deconvolved using reference S-Curves from point sources. To be more precise, by fitting the observed double star S-Curve with two appropriately weighted, linearly superimposed reference S-Curves from single stars, one can determine the angular separation and magnitude difference of the binary's components. The resolving power of the FGS is ultimately determined by the modulation and morphology of its point-source S-Curves. Figure 5 compares the S-Curves from a single star, a binary (separation = 50 mas, and delta magnitude = 0) and an extended source (80 mas in diameter).

## 10. Transfer Mode Data Reduction

After the astrometry pipeline locates and extracts the individual scans of a transfer mode observation, the resulting data files are ready for further analysis. Currently, the steps involved in routine Transfer mode data reduction are:

1. Visual inspection of the S-Curves from each scan to identify and disqualify those corrupted by vehicular jitter or data dropouts
2. Dejittering of the astrometry data at 40 Hz using the instantaneous position of the dominant guide star in its FGS, if desired. (This step may re-qualify scans that would otherwise be deleted from further consideration.)
3. Cross-correlation of each scan, in order to detect any drift of the FGS across the sky during the course of the observation
4. Shifting of each scan by the amount determined necessary in step (3) so that all scans are mapped to a common reference frame
5. Binning and co-adding of the individual scans to generate a high signal-to-noise composite S-Curve
6. Fitting of a piecewise third order polynomial fit to the binned and co-added S-Curve
7. Selection of an appropriate set of reference S-Curves from the calibration library on the basis of the target color (or colors) and the dates of observation of both the binary system and the calibration stars. These dates should be as close as possible to minimize the impact of temporal variations.
8. Fitting the binary system's composite S-Curves with the reference S-Curves by iteratively determining the angular separation and magnitude difference. This fitting is done on both the x and y axis. The quality of the fit can be assessed by comparing the magnitude differences determined independently along each axis.

Whether the observation be of a calibration star, a binary system, or an extended source, the STScI will be producing publicly-available software packages to support the analysis of these data. Please consult the STScI Web pages for updates.

## 11. Uncertainties in Transfer Mode Data

The following limits the accuracy and resolution of the Transfer Mode.



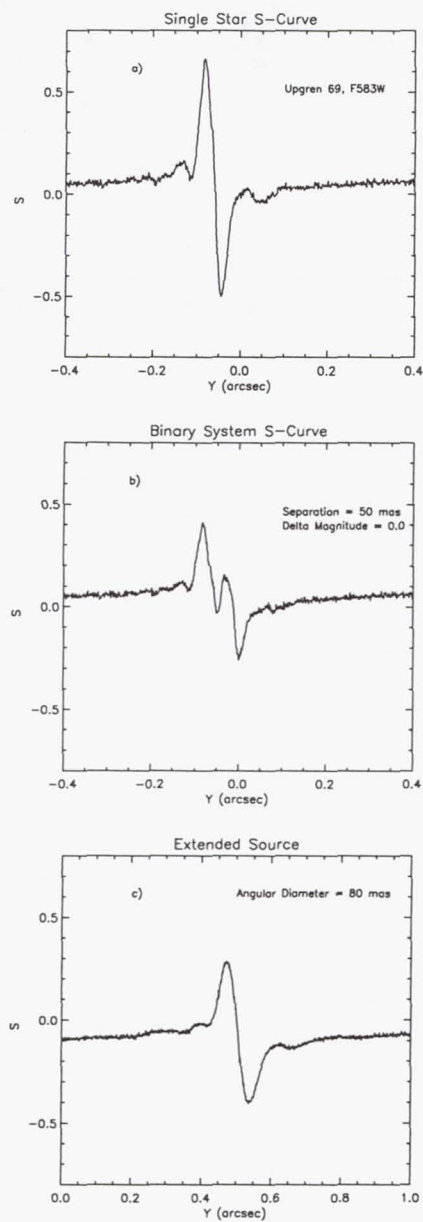


Figure 5. S-Curves from a single star (upper panel), a binary system with a separation of 50 mas and relative magnitude difference of 0, and an extended target with a diameter of 0.08 arcsec.

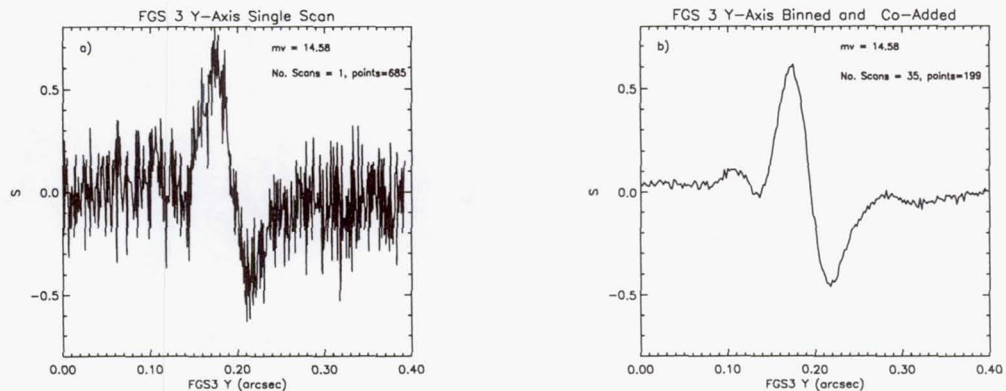


Figure 6. FGS3 Signal-to-Noise: A single Transfer function scan (a) is compared to a co-added data set of 35 scans (b). Data were obtained using filter F583W.

### 11.1. Jitter

Periods of extreme spacecraft jitter or telemetry dropouts can compromise the data from an individual scan. Mild jitter of the spacecraft, at the level of 20 mas peak-to-peak, is repairable by using the guide star data to remove the apparent wobble of the sky in the astrometer's aperture. In the most extreme cases, it may be necessary to disqualify the S-Curve from further analysis.

To obtain high signal-to-noise S-Curves, the single scans must be binned and co-added. Any small, unaccounted for spacecraft motion that occurs during each scan will effectively blur the boundaries of the binning procedure, ultimately causing the co-added S-Curve to suffer some loss of spatial resolution. Figure 6 shows the advantage of co-adding single scans to boost the S/N.

### 11.2. FGS Drift

The cross-correlation of S-Curves prior to binning and co-adding automatically accounts for drift in Transfer mode observations. Each single-scan S-Curve is shifted so that the particular feature of the S-Curve used for the cross correlation coincides with that of the fiducial S-Curve. The reliability of implicitly removing the drift is only as good as the accuracy of the cross-correlation procedure.

### 11.3. Temporal Variability of S-Curves

Measurements of the standard star Upgren69 over the lifetime of FGS3 have indicated 1–2% temporal variability of the shapes and the peak-to-peak amplitude of its S-Curves. The magnitudes of these changes can have important consequences in the reduction of binary star data when the separations of the binary components are less than 20 mas and the magnitude difference exceeds 0.6. These temporal changes also affect analyses of extended source observations. There are three ways to minimize the effects of temporal S-Curve instability: (1) obtain reference standard star data near the time of the observation, (2) select from a library of calibration S-Curves taken over the course of the cycle the one obtained closest in time to the target's observation and (3) determine a correction algorithm which interpolates from the library of S-Curves.

Because of the temporal variability of the S-Curves, calibration standards for multiple component systems with small separations and large magnitude differences may have to be observed in the same epoch as the target as part of the proposed observing program. For less constrained programs, selection of reference S-Curves close in time to the observation



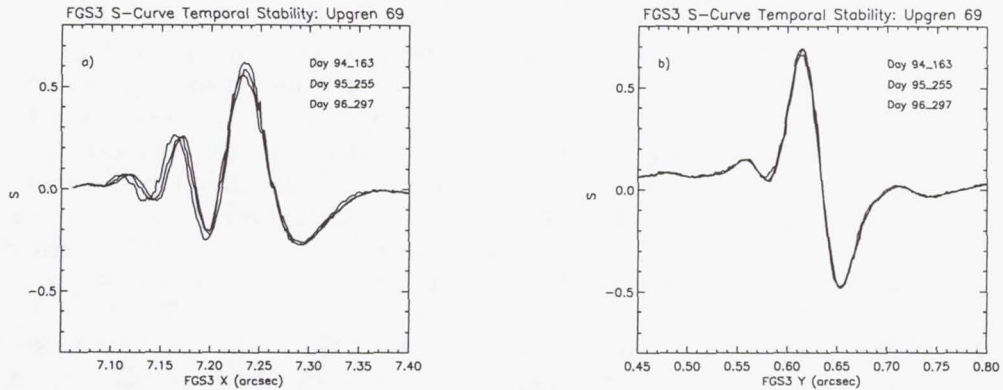


Figure 7. FGS3 Monitoring: The S-Curve as a function of 3 dates over two years.

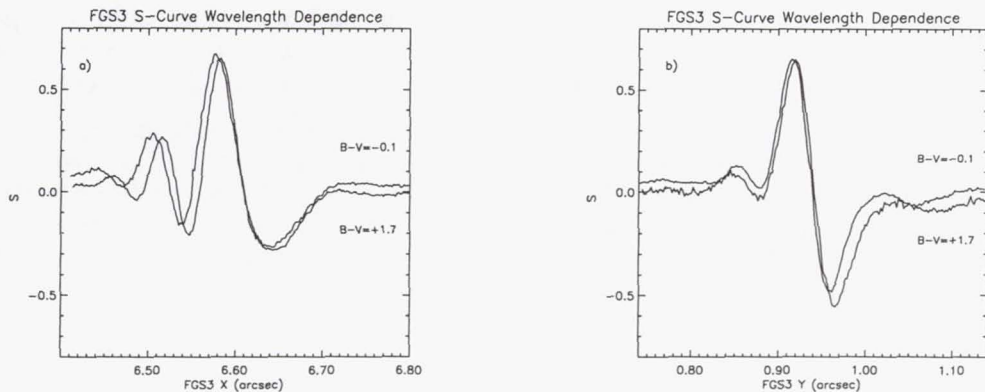


Figure 8. FGS3 S-Curve Wavelength Dependence.

should be adequate. The STScI Cycle 7 program contains a monitoring program which will allow us to establish the size of the S-Curve variability and to assess its timescale coarsely. We will determine whether or not we can derive a correction algorithm as these data accumulate. Figure 7 shows the changes in the S-Curves over a 2.5 year period. Note that the X-axis appears less stable than the Y-axis.

#### 11.4. Wavelength Dependence of S-Curves

S-Curves are also wavelength dependent. Semi-empirical modeling has shown that when the difference between a standard reference star color and the target star color,  $\Delta(B-V)$ , exceeds 0.2-0.3 magnitudes, the residuals of the deconvolution begin to degrade the reliability of the binary star analysis. To deconvolve a binary system, reference scans of the appropriate colors, scaled by the relative brightnesses, are required. Models and extrapolations have yet to reproduce this wavelength dependence of the FGS S-Curves with acceptable accuracies. Also, the data base of reference transfer functions to date is not comprehensive. The current STScI calibration program includes observations of single reference stars whose colors are comparable, within 0.2-0.3 magnitudes, to the targets in the general observer programs. Figure 8 shows the spectral response of the S-Curves for a large color difference.

### 11.5. Transfer Mode Plate Scale and HST Roll

Several observing programs have revealed that the measured separation of a binary system is sensitive to its orientation relative to the FGS interferometer axis. The impact of this dependence on the HST roll angle is to introduce systematic variations into the derived binary's orbit. In some cases, these variations could masquerade as perturbations by massive dark companions. Hughes Danbury Optical Systems has developed a model for this effect. The theory is that the Koesters prism has a rotation error about an axis which is perpendicular to the entrance face of the prism, resulting in cross-talk between the X and Y axis measurements. The model's predicted effect depends upon the separation of the binary's components and their orientation in detector space (Crout 1997).

The presence of a 1 degree rotational error in the FGS3 Y-axis Koester prism has been verified by statistical analysis of the WalkDown to FineLock data from ~5000 position mode observations. This roll error does not impact position mode observations of single stars but it must be taken into account to make transfer mode observations compatible with position mode measurements in the same visit. For the binary star analysis, the error is about 2% of the separation, scaling linearly with separation of the components. Thus binaries with large separations (>200 mas) are affected more than those with small angular separations. The Cycle 7 calibration program incorporates a test that will be used to verify and scale this model, and the results will be made generally available as an STSDAS calibration tool.

**Acknowledgments.** We wish to thank the Space Telescope Astrometry Team (STAT) for their advice and support, especially Otto Franz, Fritz Benedict, and Barbara McArthur. We also express appreciation to Linda Abramowicz-Reed and Kevin Chisolm (HDOS) for their expertise with FGS1R, Gary Welter and Ed Kimmer (GSFC) for their support of SMOV, and Denise Taylor, Vicki Balzano, Antonella Nota, and John Hershey (STScI) for their help with the alignment and FGS efforts.

### References

- Crout, B., 1997, HDOS Internal Memo OS-97-005, B16-ST-0340.  
McArthur, B. , Benedict, G.F., 1997, this volume.  
Voit, M., 1997, *HST Data Handbook*, Version 3.0 (Baltimore: STScI).



## FGS1R: Potentially HST's Astrometry Science Workhorse

Olivia Lupie, Ed Nelan and Lauretta Nagel

*Space Telescope Science Institute, 3700 San Martin Drive Baltimore, MD 21218*

**Abstract.** We review the enhancements to the flight spare FGS (called FGS1R) which was installed in the Second Servicing Mission in February 1997, and present the latest results of the FGS1R monitoring program. The performance of FGS1R and the current astrometer, FGS3, are compared and we present simulations of expected performance of FGS1R once the instrument reaches in-orbit stability.

### 1. Introduction

The Second Servicing Mission to HST in 1997 included the installation of FGS1R, an enhanced flight spare, to replace the original FGS1 whose mechanical bearings were beginning to wear. In this paper, we review the enhancements to FGS1R and present the latest results of the FGS1R monitoring program. The performance of FGS1R and the current astrometer, FGS3, are compared and we present simulations of expected performance of FGS1R once the instrument reaches in-orbit stability.

Over the past 7 years, in-orbit evaluations of the FGSs have shown that proper alignment of the FGSs' complex array of internal optics is absolutely essential to its performance. Comparison of pre-launch performance with initial in-orbit operation shows that alignments are not preserved during the launch stresses and continuously evolve as the instrument outgasses. Hughes Danbury Optical Systems, the manufacturer of the FGS, prepared a refurbished FGS with a commandable articulating adjustment optic that recenters the light beam onto the critical component of the interferometer, the Koesters prism. The replacement FGS in radial bay #1 contains the AMA, an Articulating Mirror Assembly (also referred to as FF3, Folding Flat 3, in other documentation).

A centered beam on the prism results in an FGS with more dynamic range and resolving power than the current FGS3 astrometer. Simulations indicate that FGS1R will be able to *detect* and *resolve* multiple systems with separations of 5 and 10 mas, respectively.

### 2. Instrument Overview and the Articulating Folding Flat Mirror

In order to emphasize the benefits of the adjustable transfer mirror, called the Articulating Mirror Assembly (AMA), a brief discussion of the FGSs optical train is in order. Additional detail may be found in Voit (1997).

#### 2.1. The Koesters Prism and FGS Optical Train

The heart of the FGS white-light interferometer consists of a beam splitter followed by two Koesters prisms. The prism is a fused silica pyramid consisting of two halves with a dielectric interface. The beauty of the prism is that it senses the tilt of a wavefront presented to it. As the tilt varies, the signal from the Koesters prism responds in a way that correlates with the angle of tilt. To sense the displacement of the wavefront in two dimensions, each FGS contains two Koesters prisms, oriented orthogonally with respect to one another. The dielectric in the prism divides the beam into two equal parts, with a 90

degree phase difference between the reflected and transmitted portions of the beam, the latter lagging the former. The beam reflected from one side of the prism, when joined with the transmitted beam from the other side, constructively or destructively interferes to a degree depending upon the angle between the incoming wavefront and the entrance face. Each Koesters prism thus emits two collimated exit beams whose relative intensities depend upon the tilt of the incident wavefront. Each beam is focussed and passed through a field stop to illuminate the surface of a photomultiplier tube (PMT), which records the number of photons. A schematic diagram of the Koesters prism is shown in Figure 1.

The entire annulus of the FGS is sampled by the combined motion of the Star Selector Assemblies, A and B (abbreviated SSA and SSB). The SSA, a rigid assembly of mirrors and a five element corrector group, and SSB consisting of four mirrors, can be commanded to rotate about the HST optical axis and transfer the beam to the beam splitter and Koesters prisms. Due to the presence of spherical aberration from the telescope's primary mirror, the modulation and morphology of the S-Curve depends critically upon the precision of the optical alignment of the Koesters prism with respect to the wavefront's axis of tilt. FGS1R has been upgraded from the original design by a substitution of an articulating flat mirror mirror for a previously static mirror. This movable mirror can be commanded to align the wavefront on the face of the Koesters prism and thereby restore the S-Curve to the optimal modulation.

### 3. The S-Curve

The relative intensities of the beam emerging from the Koester's prism correlates with the wavefront tilt, which is in fact controlled by the SSA and SSB rotation. We refer the reader to Voit (1997) for greater detail. The normalized difference of the PMTs versus the position of the IFOV in arcsec produces an *S-Curve*. The S-Curve is the interferometric transfer function. Its morphology and modulation are a direct diagnostic of the performance of the FGS. The X-axis S-curve at each X position is given by the following with a similar expression for Y:

$$S_x = (A_x - B_x)/(A_x + B_x)$$

where  $A_x$  and  $B_x$  are the PMT counts from PMTs A and B on the X channel. When the IFOV is more than 100 mas from the location of the interferometric null, the PMTs record nearly equal intensities. The zero point crossing between the peaks of the S-Curve occurs near interferometric null in the ideal case (slight differences in the PMT sensitivities and in the optical paths shift the zero-point crossing from the null and have to be adjusted in data reduction). Figure 2 displays a series of FGS1R S-Curves. The solid line is the S-Curve obtained when the FGS1R was accurately aligned. The theoretical modulation amplitude is 1.4 peak-to-peak. Thus the solid-line S-Curve in Figure 2 demonstrates that the performance is very close to specification.

### 4. Alignment Issues

Figure 1 illustrates a perfect alignment of the Koesters prism with respect to the HST optical axis, i.e., the wavefront's tilt axis is in the plane of the prism's dielectric surface. The S-Curve will be degraded if the tilt axis of the collimated beam from the beamsplitter does not fall on the center of the Koesters prism face. The amount of offset from optimal alignment is termed "decenter". A decentered beam would be illustrated as a shift of position "B" (in that figure) with respect to the center of the face of the prism and the dielectric. The AMA can be adjusted to re-position that beam.

Another adverse effect can occur when the alignment of the optics in the star selectors is not perfect. HDOS believes that a misalignment of the SSB reflective optics and the



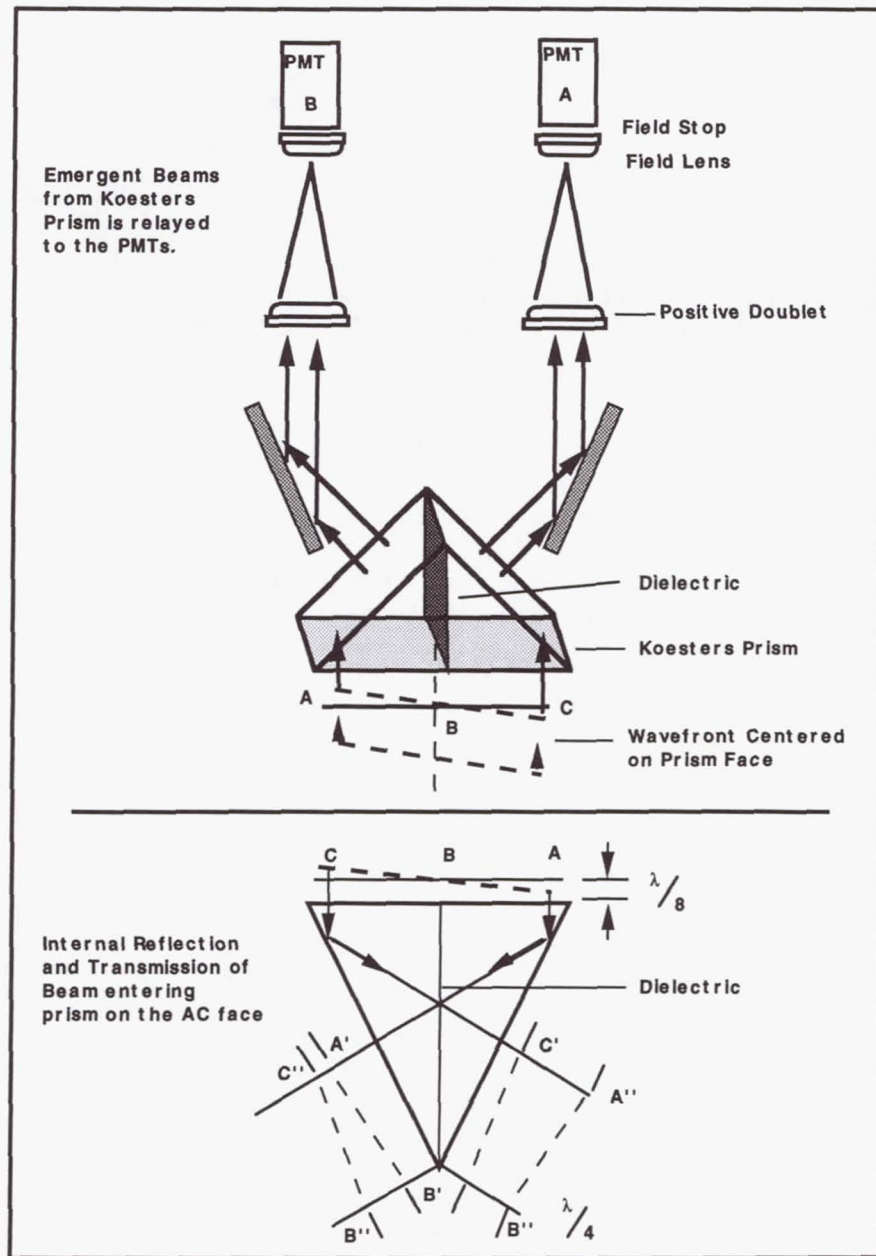


Figure 1. Emergent Beams from the Koesters Prisms are relayed to the PMTs. The Koester prism is sensitive to tilt of the wavefront about an axis which is normal to the page at point B. If the axis of tilt is not at point B, the beam is said to be "decentered."

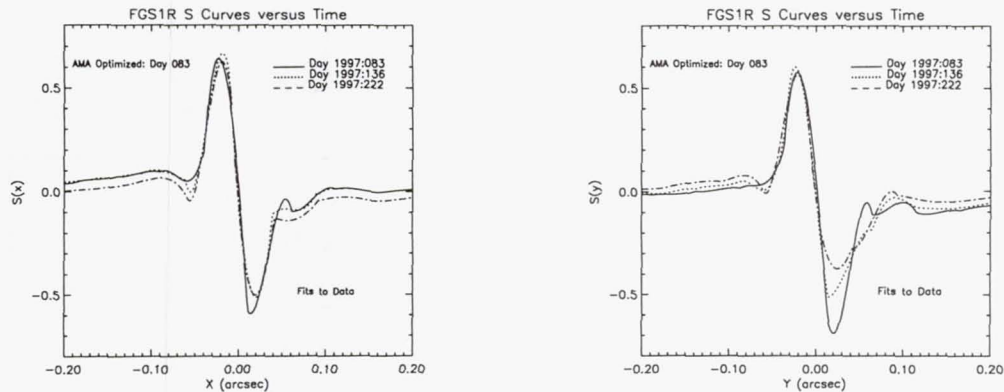


Figure 2. The temporal evolution due to desorption of the FGS1R S curves during Science Mission Orbital Verification. The AMA was re-positioned on day 083.

Koesters prism causes a decentering of the wavefront as the Star Selectors are rotated. The effect gives rise to S-Curve characteristics which vary as a function of location in the annulus. The AMA can optimize the S-Curve at any one place but does not eliminate the field dependence.

The spherical aberration from the HST's misfigured primary mirror presents to the Koesters prism a wavefront with curvature. Consequently, any misalignment in the FGS which results in a decenter of the beam at the Koesters prism will spawn optical aberrations that degrade the S-Curve morphology and modulation. In Figure 2, the Y-axis S-Curve from 1997 day 222 demonstrates this sensitivity. Here, the Koesters prism is decentered by about 0.25 mm and the S-Curve has lost  $\sim 25\%$  of its peak-to-peak amplitude relative to the optimal observation from day 083.

## 5. The In-Orbit History of FGS1R to Date

The alignment of the FGS1R was measured in-orbit a few weeks after the Servicing Mission and the data revealed that zero gravity effects had altered a near-perfect ground alignment. Several stages in the AMA optimization process were implemented during the Servicing Mission Observatory Verification by the HDOS team with support from GSFC and STScI. A single star (verified by an earlier HST test) and later, the standard (single) star Upgren69 were observed at various places within the annulus and at varying intervals during the verification period. Final optimization of the mirror on day 83 yielded the near-perfect S-Curves in the center of the annulus.

The internal alignment changes as the instrument slowly outgasses. The X and Y S-curves in Figure 2, obtained on three dates (day 083 when the AMA alignment was optimized, and days 136 and 222), clearly reveal an evolving morphology.

The change in modulation amplitude (peak-to-peak) as a function of 1997 day number is plotted in the upper panel of Figure 3 (these data are courtesy of L. Abramowicz-Reed and K. Chisolm, HDOS). HDOS used these data and the morphology signatures to model the corresponding decenter of the beam on the Koesters prism. These results are plotted in the lower panel of Figure 3. A direct correlation between the S-Curve shape (and hence the FGS1R overall performance) and the centering of that beam is clear in these plots. The most recent results of the cycle 7 FGS1R monitoring programs reveal that the FGS1R is still outgassing and its environment is not yet stable but the changes appear to be slowing down with time. In fact, the most recent monitoring data obtained during this '97 Calibration



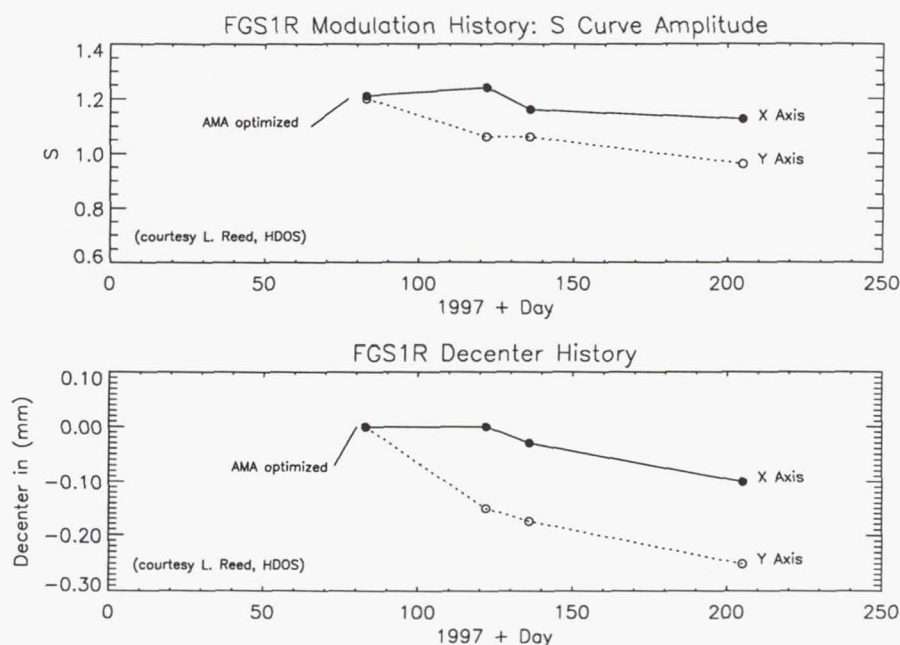


Figure 3. The upper panel contains measurements of the peak-to-peak amplitude of the S-Curves at the center of the annulus (filter F583W) as a function of day number. The lower panel is the corresponding decenter of the beam on the face of the Koesters prism, modelled by HDOS. The data was provided by Abramowicz-Reed and Chisolm, HDOS.

workshop indicate that the stability could occur within the next few months (Abramowicz-Reed 1997). Models of desorption evolution are simple at best because temporal histories of the previous FGSs shortly after orbit insertion are not available.

When the cycle 7 monitoring data indicate FGS1R's stability, the AMA will be adjusted via ground command to optimize the S-Curves. Detailed performance assessment tests and calibrations will ensue.

S-Curve data obtained across the annulus of FGS1R indicate a spatial or field dependence, probably due to small alignment errors in the optical components of the movable star selectors. Although the performance is degraded at the extreme ends of the FGS1R pickle, the overall capabilities of FGS1R exceeds that of the other FGSs.

## 6. A Brief Review of the FGS1R Cycle 7 Monitoring Program

The cycle 7 calibration plan for FGS1R is primarily a monitoring and assessment program and contains the following tests. If so justified by the results of the cycle 7 program, FGS1R will be calibrated as an astrometric instrument starting in Cycle 8.

1. Proposal 7678, *FGS1R Long Term Stability Monitor for Position Mode* — A 6-orbit (total) test, distributed over cycle 7, monitors the Position Mode stability using a field in M35.
2. Proposal 7597, *FGS1R Long Term Stability Monitor for Transfer Mode* — This 7-orbit test obtains S-Curve data over the course of cycle 7 on standard star Upgren 69. It will establish a baseline of performance, and provide an indication of stability and thereby FGS1R's readiness to be used as a science instrument.

3. Proposal 7684, *HST Astrometry Angular Resolution Test* — is designed to compare the angular resolution of FGS1R and FGS3 in Transfer Mode (S-Curve data). A 9th magnitude known binary (component separation of 0.352 arcsec and relative magnitude of 0.6) will be observed at several (small) angular increments with both instruments. This test will not be performed until FGS1R stability is established and its S-Curves are re-optimized.
4. Proposal 7680, *FGS3 and FGS1R Transfer Mode Plate Scale Calibration* — used to check for any systematic effects, caused by misalignment of certain optical components, which may introduce spurious results in binary orbit programs.

## 7. Comparison of FGS3 and FGS1R

In order to illustrate the performance capabilities of FGS3 and FGS1R, we have generated a series of synthetic S-Curves of binary systems. A simple schematic of a binary orbit and resulting S-Curves are given in Figure 4. *The composite S-Curve of a multiple system is a linear superposition of the S-Curves from the individual components, scaled by their relative brightnesses.* If the components are widely separated, unique S-Curves are clearly in evidence as illustrated by the Y-axis S-Curve in Figure 4. Smaller separations yield a merged S-Curve with a morphology that differs from that of a single star (depending on the resolution of the instrument and the binary separation) as shown by the X-Axis S-Curve. The delineation of multiple components in the composite transfer function is accomplished by modelling the composite using a linear superposition of reference S-Curves from a single star, scaled by relative magnitude and shifted by the separation of the components.

The single star S-Curves of the current astrometer, FGS3, are shown in the upper two panels of Figure 5. These data were obtained at the center of the FGS, using the F583W filter on the standard star Upgren69. Clearly, the FGS3 Y-axis (left upper panel) exhibits a near-perfect S-Curve in morphology and modulation, but the X-axis S-Curve is somewhat degraded in both amplitude and shape. If one compares these two panels with the solid-line S-Curves of FGS1R in Figure 2, it is evident that the FGS1R X and Y axes are nearly perfect and are comparable to the Y-axis of FGS3. The FGS3 X axis performance is what limits the FGS3's resolution and sensitivity and ultimately its ability to resolve binary systems with small separation and large brightness differences. Panels B and C in Figure 5 are composite S-Curves of binary systems that were synthetically generated from the FGS3 X and Y S-Curves: panel B is a 50 mas binary with a relative magnitude difference of 0 and panel C is a 50 mas binary with a delta magnitude of 2. From these figures it is clear the FGS3 can more easily resolve a binary along its Y-axis than along its X-axis. In panel c, for example, the morphology of the X-axis S-Curve more closely resembles that of a single star than do the Y-axis transfer functions. Please note however, the binary parameters used in these plots were chosen for visual graphical demonstration. In reality our data analysis tools would have no trouble resolving the binary in panel C's X-axis.

In anticipation of the enhanced performance of FGS1R, a study to assess and predict its expected performance was carried out at Lowell Observatory (Franz & Wasserman 1996). Since the Y-axis performance of FGS3 is near ideal it is a good representation of what can be expected from both axis of FGS1R. As stated earlier, the X-axis of FGS3 suffers from internal misalignments and therefore this axis is the limiting factor of FGS3's performance. The simulation study compared the X-axis performance of FGS3 to the Y-axis, with the X-axis representing FGS3, the Y-axis FGS1R. In essence, actual FGS3 data were used to generate both a table of synthetic binary observations and to provide a calibration database by which to de-convolve the simulated binaries.

For the simulation, the Lowell group used the data from a TRANSfer mode observation of a standard single star which was scanned 18 times. In order to avoid any possible correlation of the photometric noise from the individual scans, the observation was divided



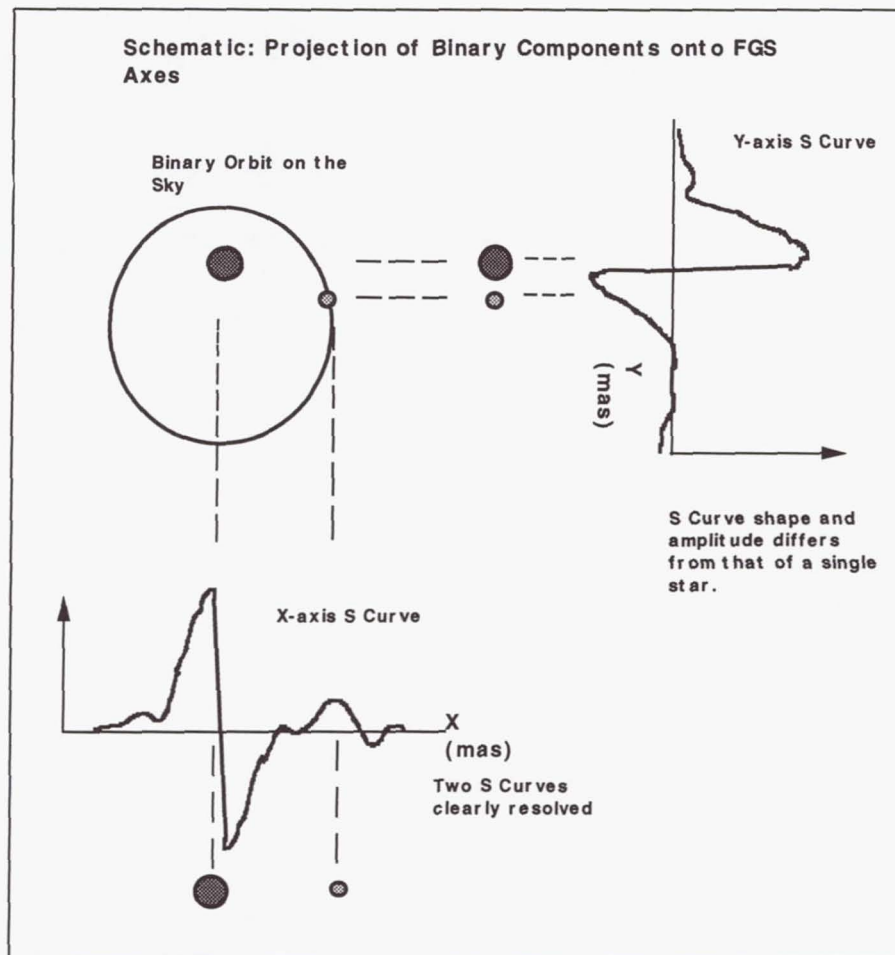


Figure 4. A schematic of a binary system projected onto the FGS X and Y axes. The separation of the components is large enough that the projection onto the FGS X-axis clearly shows two S-Curves. The Y-axis separation is much smaller and the composite S-Curve, although still noticeably different from a single S-Curve, will have to be modelled to deconvolve the components.

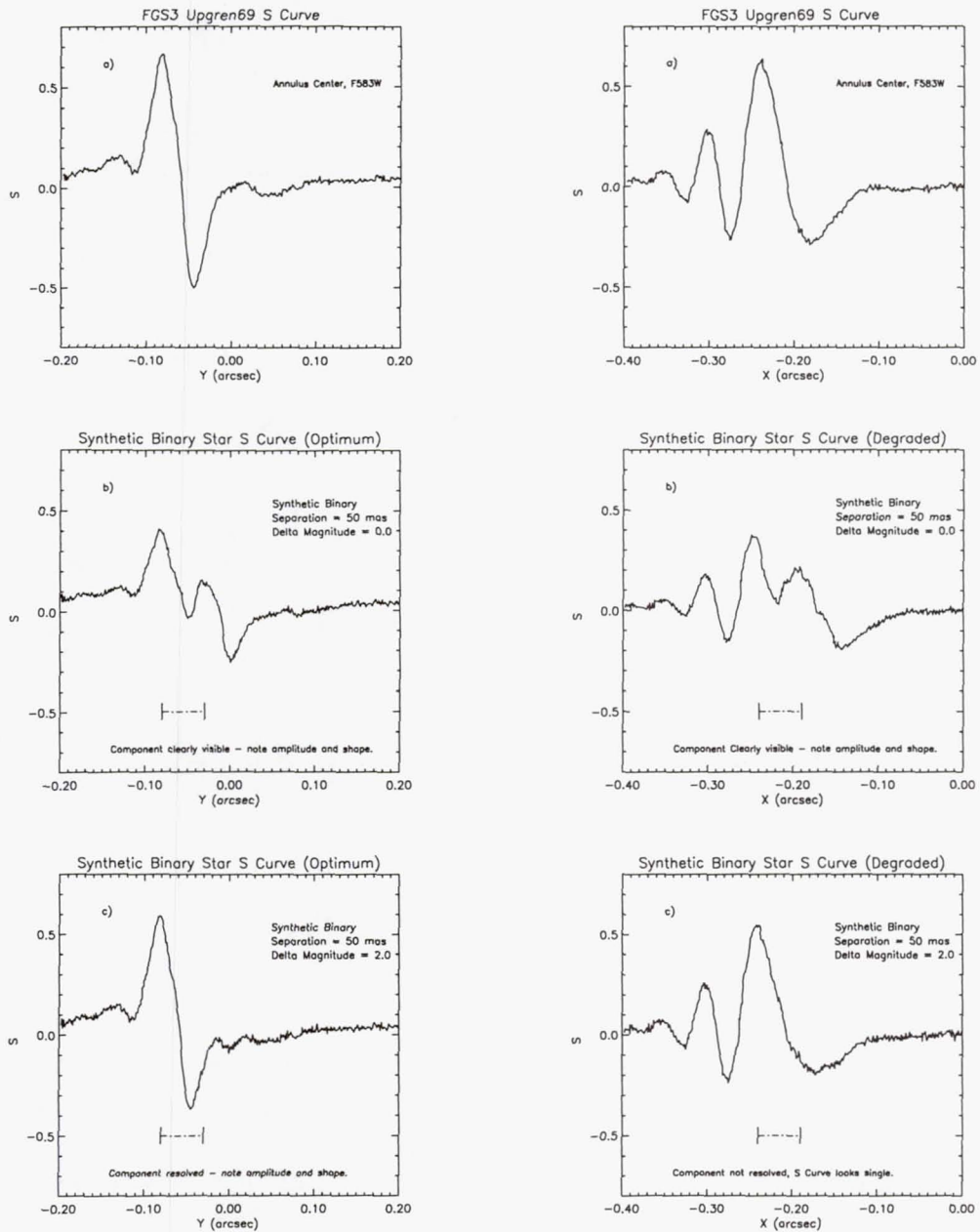


Figure 5. FGS3 S-Curves (panels "a") and synthetic composite S-Curves of binaries. The FGS3 Y-axis exhibits a near-perfect S-Curve and is representative of the S-Curves on both axes of FGS1R.



into 3 segments, one for each of the binary's two "components", and one for the calibration star. X and Y axis S-Curves were generated for a grid of binary star parameters, namely separations of 5, 10, 20, 30, and 80 milli-seconds of arc (mas) and with magnitude differences ( $\delta M$ ) of 0.44, 1.51, 2.39, and 3.20 at each of the separations.

The results indicated that along the X-axis in FGS 3 the binary systems were not resolvable for these magnitude differences when the angular separation was less than 20 mas, and also at 20 mas the  $\delta M = 3.20$  was not resolved. Along the Y-axis however, the "binary" was resolved when the separation was 10 mas for all but the  $\delta M = 3.2$ , and encouragingly, the non-singularity of the binary was "detected" at separation = 5mas for  $\delta M = 0.44$  and 1.51, although it is not clear that it was actually "resolved".

This study was limited by considerations of signal to noise since each synthetic "observation" contained only 6 individual scans. This is also true for the calibration observations. Actual TRANSFER mode observations usually have between 15 and 35 scans and therefore yield significantly better S/N.

In summary, since the FGS3 y-axis S-Curve is about as good as those expected in both axis of FGS1R, these results suggest that FGS1R will be able, if stable and properly calibrated, to resolve multiple component star systems with angular separations as small as 10 mas, and to detect non-singularity at even smaller separations.

## 8. Summary

Initial results from the testing of FGS1R during the observatory verification period and initial months of Cycle 7 indicate that its performance exceeds that of FGS3 for astrometry science, that the articulating mirror adjustment works as planned and is crucial for achieving the original FGS design goals for astrometric resolution and sensitivity. Cycle 7 monitoring programs will provide the data needed for assessing the ultimate capabilities of the instrument and, if supported by the data, FGS1R will be calibrated as the HST astrometer in cycle 8. We have provided a temporal history of FGS1R and compared its capabilities with that of FGS3. Simulations show that when properly calibrated (and stable), FGS1R should be able to resolve multiple component star systems with angular separations as small as 10 mas, and to detect non-singularity at even smaller separations.

**Acknowledgments.** We wish to thank Otto Franz and Larry Wasserman (Lowell Observatory) for their kindness, expertise, and for contributing many models and targets used for this manuscript and in the cycle calibration plans. We thank Linda Abramowicz-Reed and Kevin Chisolm of HDOS for their expertise on FGS1R and data analyses. We also express gratitude to Ed Kimmer and Gary Welter (GSFC) and Sherie Holfeltz, John Hershey, Denise Taylor, and Vicki Balzano for their expertise and help during SMOV, and Harry Payne, Antonella Nota (STScI), Barbara McArthur and Fritz G. Benedict (Univ. of Texas), and the Space Telescope Astrometry Team.

## References

- Abramowicz-Reed, L. and Chisolm, K., 1997, private communication.
- Franz, O., and Wasserman, F. 1996, Minutes from the Space Telescope Astrometry Team Meeting, April 1996.
- McArthur, B., and Benedict, G.F., 1997, this volume.
- Voit, M., 1997, *HST Data Handbook*, Version 3.0 (Baltimore: STScI).

## Maintaining the FGS3 Optical Field Angle Distortion Calibration

B. McArthur, G.F. Benedict and W.H. Jefferys

*Astronomy Department, University of Texas, Austin, Texas 78712*

E. Nelan

*Space Telescope Science Institute, Baltimore, Maryland 21218*

**Abstract.** To date four OFAD (Optical Field Angle Distortion) calibrations have been performed on FGS3 in M35 and analyzed by the Astrometry Science Team. Two have been performed since the last HST (Hubble Space Telescope) Calibration Workshop. The ongoing Long Term Stability Tests have also been analyzed and incorporated into the calibration. A lateral color calibration has been derived from calibration and science data. Descriptions of these tests and the results of our analysis of the resulting data are given. The astrometric science supported by these calibrations is briefly reviewed.

### 1. Introduction

The largest source of error in reducing star positions from observations with the Hubble Space Telescope (HST) Fine Guidance Sensors (FGSs) is the Optical Field Angle Distortion (OFAD). Description of past analyses can be found in Jefferys et al., (1994), and Whipple et al., (1994, 1996). The precise calibration of the distortion can only be determined with analysis of on-orbit observations. The Long Term STABility tests (LTSTAB), initiated in fall 1992, are an essential component of the OFAD calibration, and provide information on temporal changes. They also provide indicators that a new OFAD calibration is necessary. The lateral color correction has been redetermined with Science Verification data from 1994 and with new analyses of GTO and GO science data. This paper reports the results of the continuing OFAD and LTSTAB tests and the Lateral Color calibration. The astrometric science enabled by the maintenance of these calibrations is briefly reviewed.

### 2. Motivation and Observations

A nineteen orbit OFAD (Optical Field Angle Distortion) was performed in the spring of 1993 for the initial on-orbit calibration of the OFAD in FGS3. The First Servicing Mission made no changes to the internal optics of the three Fine Guidance Sensors (FGS) that are used for guiding and astrometry on HST. However, the subsequent movement of the secondary mirror of the telescope to the so-called "zero coma" position did change the morphology of the FGS transfer functions (Ftaclas et al. 1993). Therefore, a five orbit post servicing mission delta-OFAD calibration plan was designed and executed. After detection by the LTSTAB of increasing incompatibility with the spring 1994 delta-OFAD calibration, an 11 orbit OFAD was performed in the fall of 1995 to recover the error budget for astrometry. In the spring of 1997 a five orbit OFAD was performed on FGS3 after the second servicing mission. Thirty-five LTSTABS (Long Term Stability Tests) have been performed to assess time-dependent changes. A current list of the OFAD and LTSTAB tests is shown in Table 1.



Table 1. LTSTAB and OFAD Observations.

Orbit	Julian Date	Year	Day	Observation	Coefficient Set
1	2448959.340822	1992	337	FALL LTSTAB	1
2	2448971.061435	1992	349	FALL LTSTAB	1
3-21	2448997.782164	1993	10	SPRING OFAD	1
22	2449082.954086	1993	95	SPRING LTSTAB	1
23	2449095.742836	1993	108	SPRING LTSTAB	1
24	2449096.613044	1993	109	SPRING LTSTAB	1
25	2449226.341817	1993	238	FALL LTSTAB	1
26	2449255.529236	1993	268	FALL LTSTAB	1
27	2449283.771053	1993	296	FALL LTSTAB	1
28	2449309.341898	1993	321	FALL LTSTAB	1
First Servicing Mission					
29	2449379.838241	1994	27	SPRING LTSTAB	2
30	2449408.794850	1994	56	SPRING LTSTAB	2
31	2449437.560417	1994	85	SPRING LTSTAB	2
32	2449468.662153	1994	116	SPRING LTSTAB	2
33-37	2449469.602118	1994	117	SPRING DELTA-OFAD	2
38	2449593.554884	1994	241	FALL LTSTAB	2
39	2449624.182975	1994	271	FALL LTSTAB	2
40	2449652.274942	1994	299	FALL LTSTAB	2
41	2449683.371435	1994	330	FALL LTSTAB	2
42	2449711.665382	1994	359	FALL LTSTAB	2
43	2449749.996910	1995	32	SPRING LTSTAB	2
44	2449780.160903	1995	62	SPRING LTSTAB	2
45	2449811.662894	1995	94	SPRING LTSTAB	2
46	2449838.070301	1995	120	SPRING LTSTAB	2
47	2449990.553542	1995	273	FALL LTSTAB	3
48	2450018.625255	1995	301	FALL LTSTAB	3
49	2450042.360197	1995	324	FALL LTSTAB	3
50-60	2450052.674838	1995	335	FALL DELTA-OFAD	3
61	2450112.122350	1996	29	SPRING LTSTAB	3
62	2450133.837824	1996	51	SPRING LTSTAB	3
63	2450158.835440	1996	76	SPRING LTSTAB	3
64	2450174.716192	1996	92	SPRING LTSTAB	3
65	2450199.778704	1996	117	SPRING LTSTAB	3
66	2450321.550822	1996	239	FALL LTSTAB	3
67	2450353.777465	1996	271	FALL LTSTAB	3
68	2450377.443275	1996	294	FALL LTSTAB	3
69	2450416.366701	1996	333	FALL LTSTAB	3
70	2450480.031933	1997	31	SPRING LTSTAB	3
Second Servicing Mission					
71	2450518.768090	1997	70	SPRING LTSTAB	3
72-76	2450560.517523	1997	112	SPRING DELTA-OFAD	4

### 3. Optical Field Angle Distortion Calibration and Long Term Stability Test

The Optical Telescope Assembly (OTA) of the HST (Hubble Space Telescope) is a Aplanatic Cassegrain telescope of Ritchey-Chrétien design. The aberration of the OTA, along with the optics of the FGS comprise the OFAD. The largest component of the design distortion, which consists of several arcseconds, is an effect that mimics a change in plate scale. The magnitude of non-linear, low frequency distortions is on the order of 0.5 seconds of arc over the FGS field of view. The OFAD is the most significant source of systematic error in position mode astrometry done with the FGS. We have adopted a pre-launch functional form originally developed by Perkin-Elmer (Dente, 1984). It can be described (and modeled to the level of one millisecond of arc) by the two dimensional fifth order polynomial:

$$\begin{aligned}
 x' = & a_{00} + a_{10}x + a_{01}y + a_{20}x^2 + a_{02}y^2 + a_{11}xy + a_{30}x(x^2 + y^2) + a_{21}x(x^2 - y^2) \\
 & + a_{12}y(y^2 - x^2) + a_{03}y(y^2 + x^2) + a_{50}x(x^2 + y^2)^2 + a_{41}y(y^2 + x^2)^2 \\
 & + a_{32}x(x^4 - y^4) + a_{23}y(y^4 - x^4) + a_{14}x(x^2 - y^2)^2 + a_{05}y(y^2 - x^2)^2
 \end{aligned}$$

$$\begin{aligned}
 y' = & b_{00} + b_{10}x + b_{01}y + b_{20}x^2 + b_{02}y^2 + b_{11}xy + b_{30}x(x^2 + y^2) + b_{21}x(x^2 - y^2) \\
 & + b_{12}y(y^2 - x^2) + b_{03}y(y^2 + x^2) + b_{50}x(x^2 + y^2)^2 + b_{41}y(y^2 + x^2)^2 \\
 & + b_{32}x((x^4 - y^4) + b_{23}y(y^4 - x^4) + b_{14}x(x^2 - y^2)^2 + b_{05}y(y^2 - x^2)^2
 \end{aligned}
 \tag{1}$$

where  $x, y$  are the observed position within the FGS field of view,  $x', y'$  are the corrected position, and the numerical values of the coefficients  $a_{ij}$  and  $b_{ij}$  are determined by calibration. Although ray-traces were used for the initial estimation of the OFAD, gravity release, outgassing of the graphite-epoxy structures, and post-launch adjustment of the HST secondary mirror required that the final determination of the OFAD coefficients  $a_{ij}$  and  $b_{ij}$  be made by an on-orbit calibration.

M35 was chosen as the calibration field. Since the ground-based positions of our target calibration stars were known only to 23 milliseconds of arc, the positions of the stars were estimated simultaneously with the distortion parameters. This was accomplished during a nineteen orbit calibration, executed on 10 January 1993 in FGS number 3. GaussFit (Jefferys, 1988), a least squares and robust estimation package, was used to simultaneously estimate the relative star positions, the pointing and roll of the telescope during each orbit (by quaternions), the magnification of the telescope, the OFAD polynomial coefficients, and these parameters that describe the star selector optics inside the FGS:  $\rho_A$  and  $\rho_B$  (the arm lengths of the star selectors A and B), and  $\kappa_A$  and  $\kappa_B$  (the offset angles of the star selectors). Because of the linear relationship between  $\rho_A, \rho_B, \kappa_A$  and  $\kappa_B$ , the value of  $\kappa_B$  is constrained to be zero. A complete description of that calibration, the analysis of the data, and the results are given in Jefferys et al. (1994).

In late fall 1992, just prior to the 1993 OFAD calibration, a series of one orbit long-term stability tests (LTSTAB) was initiated. These tests had two seasonal orientations, a spring orientation taken from an orbit of the OFAD, and a fall orientation, which was a 180 degree flip of the spring orientation. LTSTABs have been performed several times in each of the orientations, spring and fall, every year.

The LTSTAB is sensitive to scale and low order distortion changes. It is an indicator of the validity of the current OFAD coefficients and the need for recalibration. The LTSTAB series immediately showed that the scale measured by the FGS was changing with time. The indication of this change was seen in the large increase with time in the post-fit residuals from a solution that solved for a constant sets of star positions, star selector encoder (SSE) parameters, and OFAD parameters. The amount of scale change is too large to be due to true magnification changes in the HST optical telescope assembly. These changes could be due to water desorption in the graphite-epoxy components within the FGS. Initially the scale-like change was modeled by allowing a variation in the star-selector-A effective lever arm ( $\rho_A$ ). Since 1995, the change has been modeled by allowing a change in both  $\rho_A$  and  $\kappa_A$  (the offset angle of the star selector).

A five orbit delta-OFAD was performed on 27 April 1994 after the first servicing mission to assess the distortion changes caused by the secondary mirror movement to the zero coma position. Significant effects in the OFAD (in addition to the scale-like changes) at the level of 10 mas were found. The LTSTAB tests have revealed continued permutations in the FGS. In addition to the scale changes, in mid-1995 we began to recognize higher order distortion changes. These changes manifested themselves as something that looks like a radial scale variation and is fairly well modeled by alterations in the third order terms in Eq. (1). We had also noted that the residuals from the fall orientation LTSTABs are consistently higher than for the spring.

An eleven orbit delta-OFAD was performed in the late fall of 1995, to analyze temporal changes, and upgrade the y-axis coverage. Initially puzzling poor results were the result of deterioration of the S-curve in the negative X region of the pickle, causing locks on the wrong zero-crossings. These incorrect locks produced an island of large negative residuals



in the negative X region of the pickle (Figure 1). With the removal of these observations, the delta-OFAD was successfully completed.

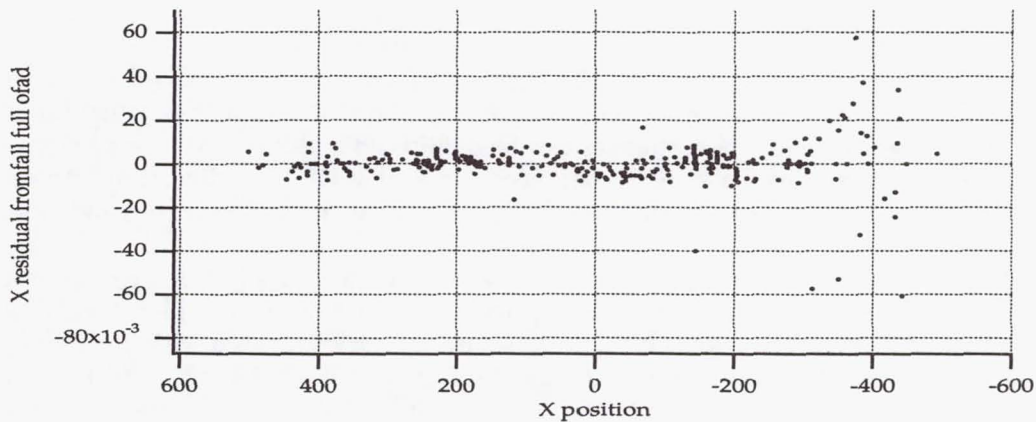


Figure 1. Large residuals in negative X pickle region indicate deterioration of S-curves in that area.

Further analysis suggested redetermining the star catalog, which was done with input from the three OFAD experiments of 1993, 1994 and 1995. This was done to minimize the OFAD distortion that could have been absorbed by the catalog positions.

In the spring of 1997 a Second Servicing Mission replaced FGS1. A five orbit delta-OFAD was performed in FGS3, repeating the orientation of spring 1994. Two LTSTABS were performed in Spring 1997, one before and one after the second servicing mission. With scale and offset removed, a comparison yielded an rms of 0.965 mas, indicating stability of FGS3 across the servicing mission.

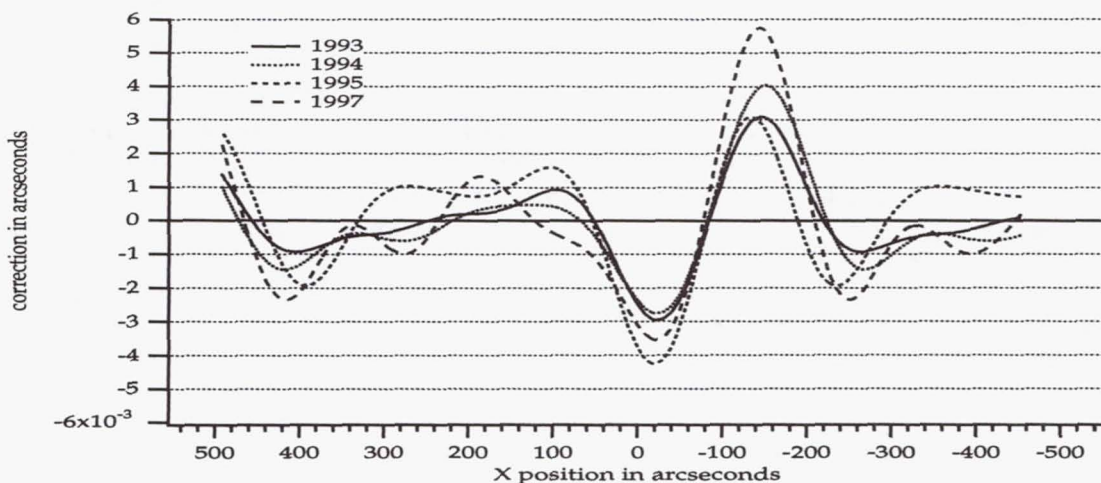


Figure 2. Four frequency Fourier series correction of systematic signature in X Residuals

A systematic signature in the X residuals from the four OFAD analysis remains. This appears as a very distinctive curve in the x component residuals as a function of position angle in the FGS field of view (Figure 2). The curve cannot be modeled by the fifth order polynomial. We have used a four frequency Fourier series to remove this effect. The size of this effect, in an RMS sense over the entire field of view of the FGS, is about one millisecond of arc. However, the peak-to-peak values near the center of the field of view can be as large

as 8 mas. The source of this unexpected distortion is not yet known but it may be due to the way the FGS responds to the spherically aberrated HST beam.

A small signature in the Y residuals of the  $\rho_A \kappa_A$  fit of the LTSTAB to the OFAD coefficients has also been found. It appears as a quadratic. This signature is not found in the OFAD residuals. Currently it is not removed from the data.

On the basis of almost five years of monitoring the distortions in FGS 3 we have concluded that at the level of a few milliseconds of arc, the optical field angle distortion in HST FGS 3 changes with time. These changes can be monitored and modeled by continuing the LTSTAB tests, which also alerts us to the need for a new OFAD calibration. There remains some dichotomy between the OFAD calibration data taken in the spring and that taken in the fall.

Four sets of OFAD coefficients (Eq. 1) and star selector parameters ( $M$ ,  $\rho_A$ ,  $\rho_B$ ,  $\kappa_A$  and  $\kappa_B$ ) have been derived for reductions of astrometry observations. The average plate residuals for these determinations are listed in Table 2. Comparisons of grids created with each set of OFAD coefficients and distortion parameters indicate that the OFAD has changed around 10 milliseconds of arc in non-scalar distortion between calibrations (which have spanned 12–18 months). These changes in the OFAD with x and y scale and offset (a 6 parameter plate fit) removed can be seen in Figures 3, 4 and 5.

Table 2. OFAD Residuals.

OFAD	Xrms	Yrms	RSS	Number of Residuals	Orbits
Spring 1993	0.0020	0.0024	0.0027	548	19
Spring 1994	0.0020	0.0020	0.0024	144	5
Fall 1995	0.0019	0.0022	0.0026	354	11
Spring 1997	0.0025	0.0026	0.0029	121	5

Each LTSTAB is associated with a specific set of coefficients Table 1. In the boundary area between two OFAD experiments, the LTSTAB observations are reduced with both sets of OFAD separately to determine which coefficients produce the best  $\rho_A \kappa_A$  fit of the LTSTAB.

The values of  $\rho_A$  and  $\kappa_A$  determined by the LTSTABS and OFADS are illustrated in Figure 6 and Figure 7. The error bars for these determination are smaller than the symbols. The rms errors of these determinations are shown in Figure 8.  $\rho_A$  and  $\kappa_A$  initially appeared to be smooth exponential changes over time. Since the fall of 1995,  $\rho_A$ , the scale-like sse parameter has been less predictable. Therefore, for reduction of science astrometry data, the  $\rho_A \kappa_A$  parameters are determined by interpolation of the two nearest LTSTABS in time. The 1997 Spring OFAD shows a dramatic drop in  $\rho_A$ , evidence of a significant scale change occurring. Interestingly, the Spring 1997 OFAD shows approximately the same value of  $\rho_A$  as the Spring 1994 OFAD. These two OFAD observation proposals were almost identical.



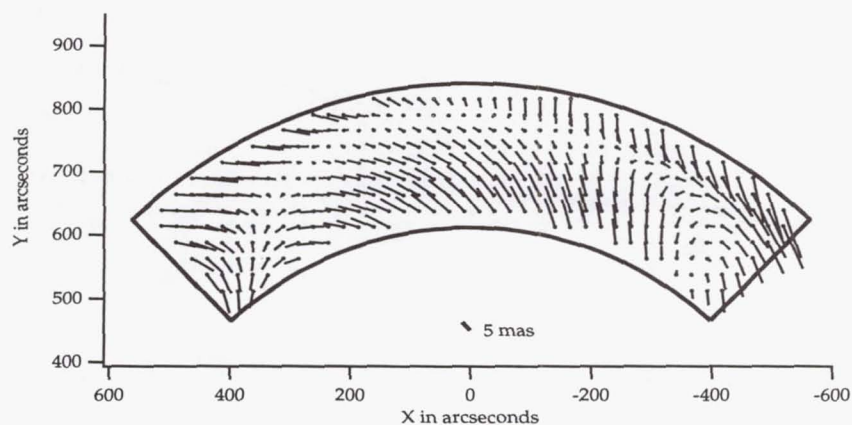


Figure 3. OFAD change between Spring 1993 and Spring 1994. The rss of the change is 10.6 milliseconds of arc.

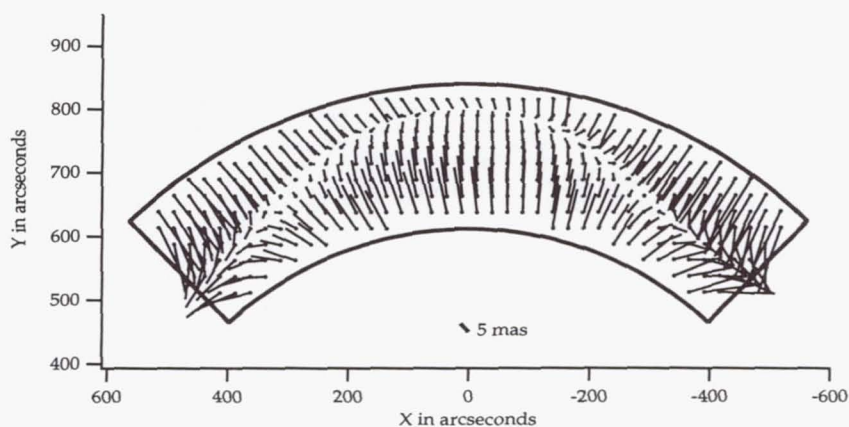


Figure 4. OFAD change between Spring 1994 and Fall 1995. The rss of the change is 17.5 milliseconds of arc

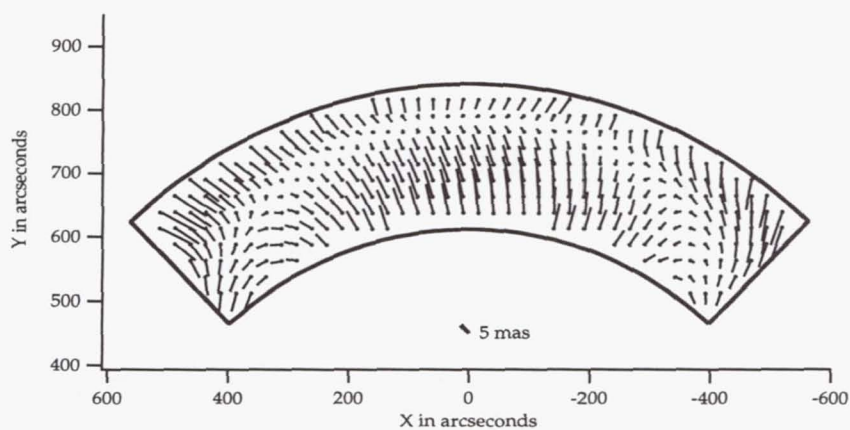
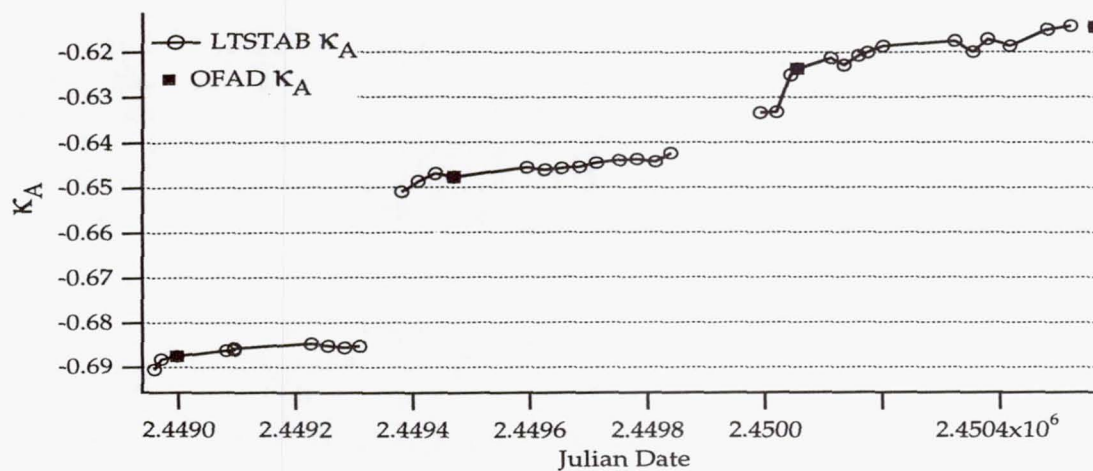
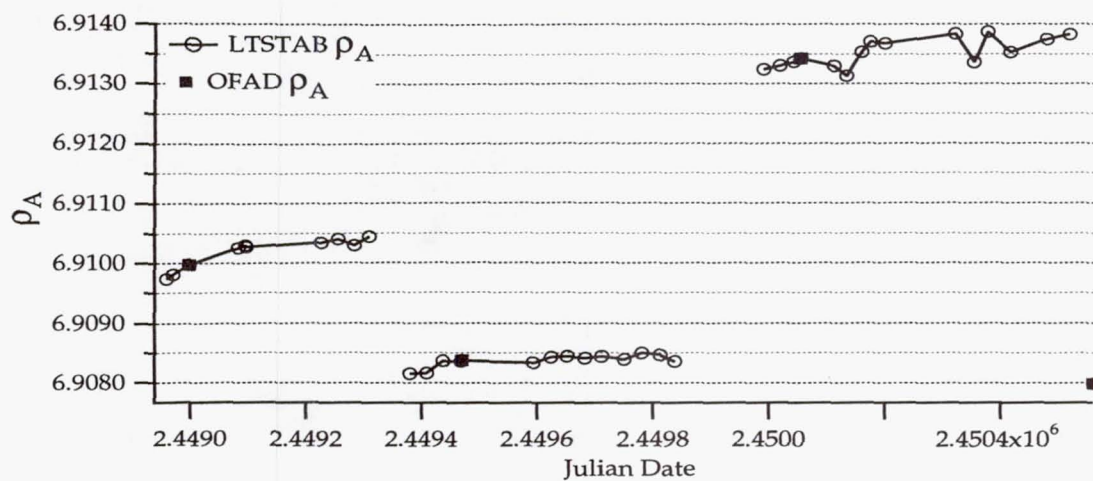
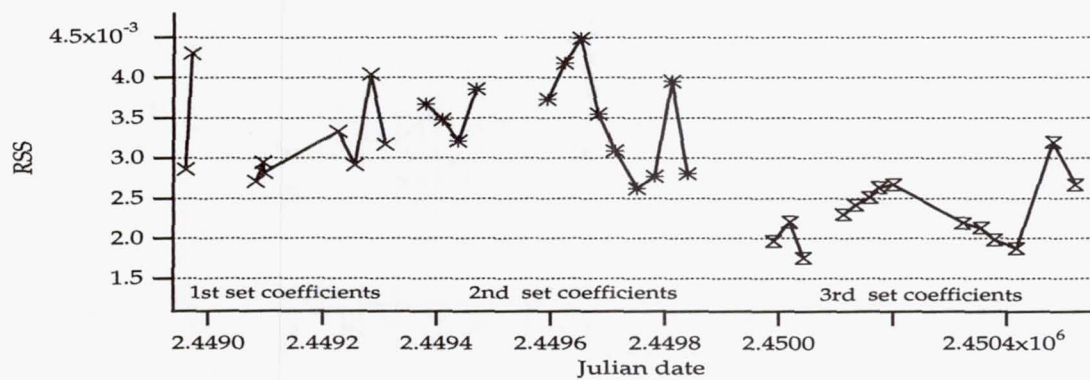


Figure 5. OFAD change between Fall 1995 and Spring 1997. The rss of the change is 9.3 milliseconds of arc.

Figure 6.  $\kappa_A$  fit of the LTSTABSFigure 7.  $\rho_A$  fit of the LTSTABSFigure 8. RSS of  $\rho_A$   $\kappa_A$  fit of LTSTABS



#### 4. Lateral Color

Since each FGS contains refractive elements (Bradley et al. 1991), it is possible that the position measured for a star could depend on its intrinsic color. Changes in position would depend on star color, but the direction of shift is expected to be constant, relative to the FGS axes. This lateral color shift would be unimportant, as long as target and reference stars have similar color. However, this is not always the case (e.g., Proxima Centauri, Benedict et al. 1993), hence our interest. Pre-launch ground testing indicated for FGS 3 a lateral color effect predominantly in the x direction, with magnitude a few milliseconds of arc per unit change in B-V color index. The effect is modeled (for example in X)

$$X' = X + ctx * (B - V) \quad (2)$$

We have recently completed the lateral color calibration. This two-pronged attack consisted of a reanalysis of the Science Verification Lateral Color Test data (acquired in late 1994) and an analysis of the Proxima Cen reference frame (a mix of SV, GTO and GO data acquired 1992-1997). The SV Lateral Color field was chosen to have a very wide range of stellar colors ( $\Delta B - V \sim 2$ ). The Proxima Cen reference frame makes up in sheer volume of data (68 data sets) what it lacks in color range ( $\Delta B - V \sim 1$ ). Neither approach is ideal, since the original SV test was exceedingly sparse. From the 1994 SV test we obtain  $ctx = -0.0009 \pm 0.0002$  and  $cty = -0.0002 \pm 0.0003$ . The Proxima Cen data yield  $ctx = -0.0010 \pm 0.0005$  and  $cty = +0.0003 \pm 0.0004$ . We adopt as the Lateral Color calibration a weighted average of the two results:  $ctx = -0.0009 \pm 0.0002$  and  $cty = -0.0000 \pm 0.0002$

#### 5. Ongoing Astrometric Science with FGS 3

FGS 3 is being used to obtain many series of data from which trigonometric parallaxes will be derived. Targets include distance scale calibrators ( $\delta$ Cep, RR Lyr), interacting binaries (Feige 24), a central star of a planetary nebula (NGC 6853), an old Nova (RW Tri), and several dwarf novae (e.g., SS Cyg). It is also involved in an intensive effort to obtain masses and mass ratios for a number of very low-mass M stars (for example, GJ 22, GJ 791.2, GJ 623, and GJ 748). We have completed parallax determinations for Proxima Cen and Barnard's Star and obtained 0.5 mas precisions (Benedict et al. 1997). For most of the targets mentioned above we will have far fewer sets of observations. Our recent analyses of Hyades parallax data sets, containing a similarly small number of epochs (van Altena et al. 1997), suggest that we will obtain parallax precisions of 1 mas for most of these targets. A continued program of LTSTAB monitoring and OFAD updates is essential to the success of these ongoing, long-term investigations.

#### 6. Conclusions

We have shown that continued OFAD calibration of the Fine Guidance Sensors can reduce this source of systematic error in positions measured by the FGSs to the level of 2 mas. However, changes in the FGS units continue to occur, even seven years after launch. These changes require periodic updates to the OFAD to maintain this critical calibration. The OFAD calibration is an ongoing process, every new observation set is used to not only expand the timeline, but re-evaluate the previous calibrations. A lateral color calibration in FGS 3 has been determined using Science Verification and GTO data.

**Acknowledgments.** The Astrometry Science Team is supported by NASA NAG5-1603. We are grateful to Q. Wang for the initial modeling of the OFAD and D. Story and A.L. Whipple for their earlier contributions to this calibration. We thank L. Reed for

her long-term contribution to our knowledge of FGS3. We thank Gary Welter and Keith Kalinowski for their interest and assistance at Goddard Space Flight Center. We thank all the members of the STAT, past and present for their support and useful discussions. We thank Melody Brayton for assistance in the preparation of this manuscript.

## References

- Benedict, G.F., McArthur, B., Whipple, A., Nelan, E., Story, D., Jefferys, W.H., Shelus, P.J., Hemenway, P.D., Duncombe, R., van Altena, Wm.F., Franz, O.G., Fredrick, L.W. 1997, in *28th meeting of the Division on Dynamical Astronomy*, to appear in BAAS.
- Benedict, G.F., Nelan, E., McArthur, B., Story, D., van Altena, W., Ting-Gao, Y., Hemenway, P.D., Shelus, P.J., Whipple, A.L., Franz, O.G., Fredrick, L.W., and R.L. Duncombe. 1993, PASP, 105, 487.
- Bradley, A., Abramowicz-Reed, L., Story, D., Benedict, G., and W. Jefferys. 1991, PASP, 103, 317.
- Dente, G. and Abramowitz-Reed, L., 1984, *Space Telescope Optical Field Angle Distortion Calibration Algorithm*, Perkin-Elmer ST-SE-3336.
- Ftaclas, C., Nonnenmacher, A., Weindling, F., Story, D., and E. Nelan. 1993, Appl.Optics, 32, 1696.
- Jefferys, W., Fitzpatrick, J., and McArthur, B., 1988, Celest. Mech. 41, 39.
- Jefferys, W.J., Whipple, A., Wang, Q., McArthur, B., Benedict, G.F., Nelan, E., Story, D., and L. Abramowicz-Reed, 1994, in *Calibrating Hubble Space Telescope*, eds. J.C. Blades and S.J. Osmer (Baltimore:STScI), 353.
- van Altena, W.F., Lu, C.-L., Lee, J.T., Girard, T.M., Guo, X., Deliyannis, C., Platais, I., Kozhurina-Platais, V., McArthur, B., Benedict, G.F., Duncombe, R.L., Hemenway, P.D., Jefferys, W.H., King, J.R., Nelan, E., Shelus, P.S., Story, D., Whipple, A., Franz, O.G., Wasserman, L., Fredrick, L.W., Hanson, R.B., Klemola, A.R., Jones, B.F., Mendez, R., Tsay, W.-S., Bradley, A., 1997, ApJ, 486, 123.
- Wang, Q., and Jefferys, W., 1990, in *Statistical Analysis of the Optical Field Angle Distortion of the Hubble Space Telescope Using the Bootstrap Method*, (Austin:University of Texas), 1.
- Whipple, A., Jefferys, W., Wang, Q., McArthur, B., Benedict, G.F., Nelan, E., Story, D., and L. Abramowicz-Reed. 1994, in *Calibrating Hubble Space Telescope*, eds. J.C. Blades and S.J. Osmer, (Baltimore: STScI), 375.
- Whipple, A., McArthur, B., Wang, Q., Jefferys, W., Benedict, G.F., Lalich, A.M., Hemenway, P.D., Nelan, E., Shelus, P.J., and Story, D.. 1995, in *Calibrating Hubble Space Telescope:Post Servicing Mission*, eds. A. Koratkar and C. Leitherer, (Baltimore: STScI), 119.



## Stability of FGS Photometry

R. Kuschnig, W.W. Weiss, K. Zwintz

*Inst. f. Astronomy Univ. Vienna, Austria*

### Abstract.

The three Fine Guidance Sensors produce time series photometry of thousands of stars while providing a pointing reference to the HST. In 1993 we started a project focused on the search for variable Guide Stars by performing a time series analysis of all accessible data sets. This project requires a detailed knowledge of the photometric stability and systematic effects of FGS time series photometry. We found that the photometric accuracy in general is limited by photon noise with an average noise level for our sample of about  $10^{-4}$  and the highest accuracy presently obtained being 30 ppm. About 15% of all data sets are influenced by the South Atlantic Anomaly and by stray light from the Moon and/or the Sun. The two FGS data sets obtained during the Deep Field program of the HST in December 1995 are perfectly suited for an investigation of these effects.

## 1. Introduction

The three Fine Guidance Sensors are the kernel of the HST pointing control system. They measure the brightness of pre-selected Guide Stars with high time resolution. These photometric time series are stored as engineering data in the HST archive (DADS) without further scientific treatment. In general two FGS instruments are simultaneously locked on two different stars. Since the start of the HST mission more than 7000 objects distributed over the whole sky have been measured photometrically.

The main goal of our project which we started in 1993, is to discover variable Guide Stars by performing a time series analysis of all accessible FGS data sets. In the past only astrometric properties of the FGS', particularly for "the Astrometer" (FGS3), have been studied in great detail, but not the photometric characteristics. An essential part of our work is therefore devoted to an analysis of the photometric stability and of systematic effects in FGS data. First results have been already published by Kuschnig et al. (1997) and are summarized in the following section.

In addition we present our investigation of two systematic effects which influence about 15% of all analyzed data sets. The first one is caused by the South Atlantic Anomaly (SAA), a region where the photometric signal dramatically increases. The second effect could be identified as stray light from bright celestial objects, such as the Moon and the Sun (Section 4).

## 2. Photometric Properties

Based on time series analyses of more than 4500 data sets obtained in the years from 1992 to 1996 for about 3500 Guide Stars, we summarize the photometric properties of the FGS instruments:

- The FGS photometry is photon noise limited

- the noise spectrum is not frequency dependent (white noise)
- the number of individual measurements and the mean intensity are sufficient parameters to estimate the mean noise level for a given data set
- the average noise level for the 4500 hitherto analyzed data sets is about  $10^{-4}$
- the lowest noise level found up to now is 30 ppm

The long term stability over months or years needs further investigation, because only few Guide Stars have yet been repeatedly used over such time scales.

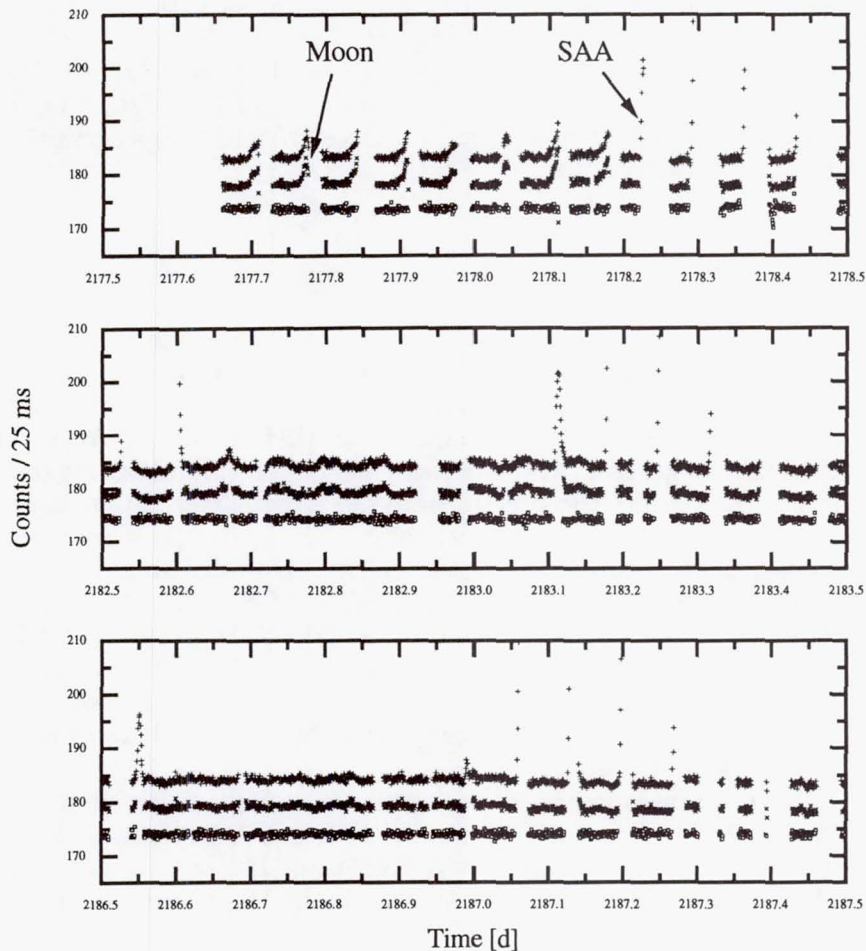


Figure 1. The light curve of GS 0416200075 is plotted for the 1st day (top layer), the 5th day (middle) and the 10th day (bottom) of the HDF program. In each layer the upper curve corresponds to the “raw” data extracted from DADS, the middle curve is cleaned for the SAA effect and the lower light curve is the result from our stray light correction. Each data point is a an average of 1200 individual FGS measurements with 25 msec integration time. Constant offsets of 5 counts are introduced for better visibility of the light curves.



### 3. Decorrelation of Systematic Effects

About 15% of all data sets are severely distorted by systematic effects which are mainly caused by the South Atlantic Anomaly and by variable stray light contamination from the Sun and/or the Moon.

Perfect test samples for an investigation of these effects are the two FGS data sets obtained in December 1995 during the Deep Field program (HDF) of the HST. Continuous guiding during 10 days was done by FGS2, locked on GS 0416200075 ( $m_v = 13.05$ ), and by FGS3 (GS 0416200054,  $m_v = 11.87$ ).

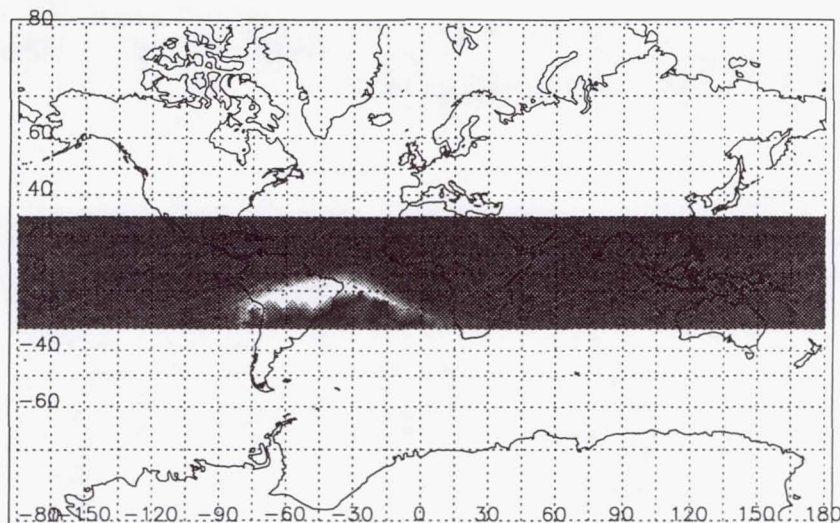


Figure 2. Intensities measured for GS 0416200075, correlated with the geographic positions of the HST. The northern border of the bright region, where the count rates exceed one sigma relative to the mean, coincides with published SAA maps. The grey shade inside the SAA is an artefact due to our graphic routine.

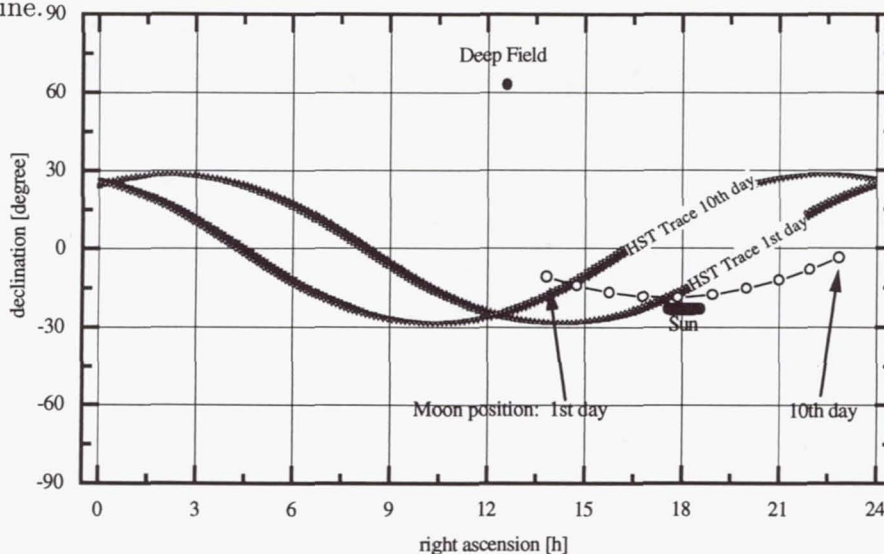


Figure 3. The celestial positions of the Moon, the Sun and the HST for the first and the last day of the HDF program, as well as the location of the Deep Field.

The "raw" light curve of GS 0416200075 for the 1st, 5th and 10th day can be inspected in Figure 1. Strong variations are present, in particular spikes. When plotting the intensity values versus the geographic position of the HST a clear correlation was found between the increase of the count rates and the SAA region (Fig. 2). The light curve can be cleaned by eliminating data points which are obtained at times when the HST passed close to the SAA (Fig. 1, middle curve in each layer).

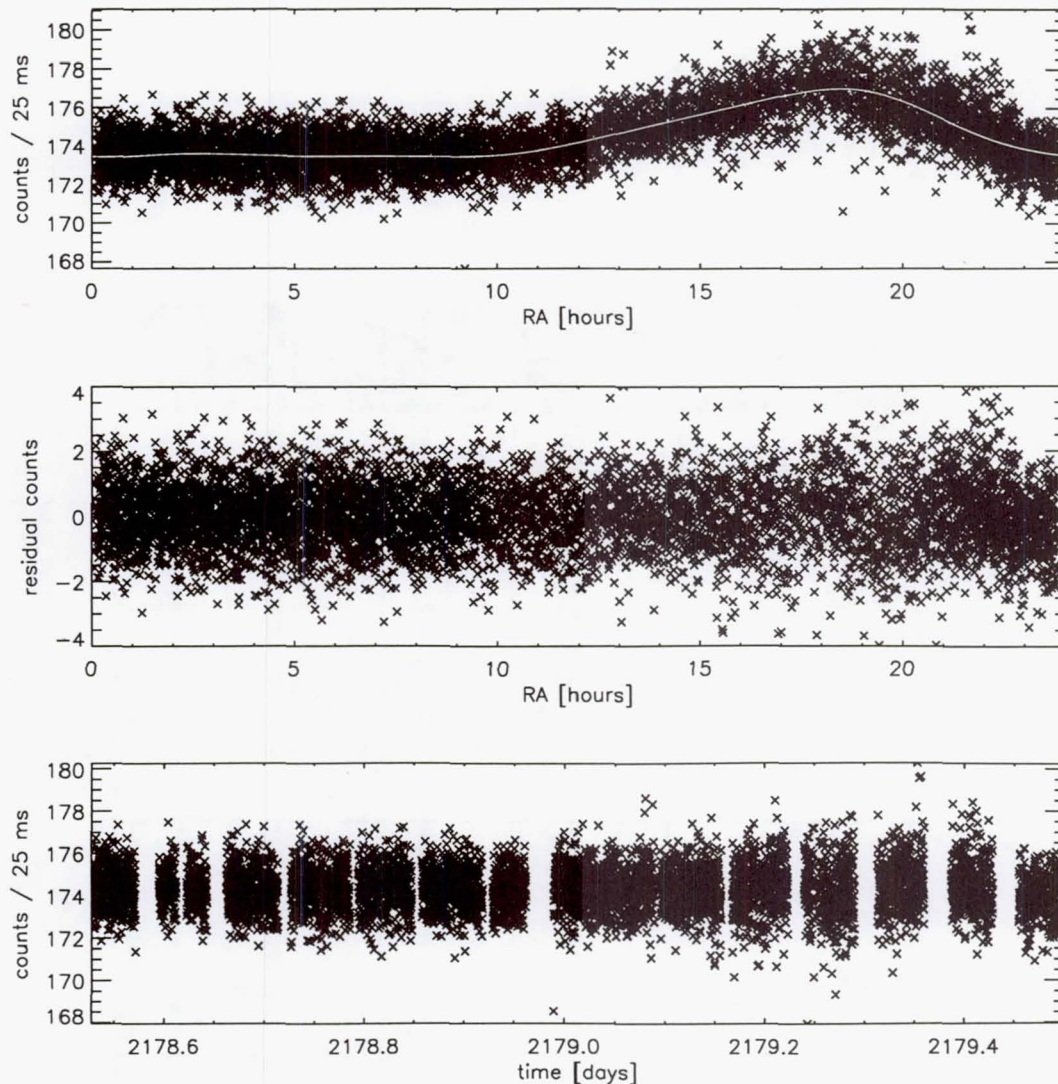


Figure 4. Correlation between right ascension and counts obtained for GS 0416200075 during day 2 of the HDF (upper layer). The white line is a cubic spline fit to the data. The residual signal to this fit (intensities as function of RA) is presented in the middle layer. The rectified light curve (intensities as function of observing time) is plotted at the bottom.

But still, a periodic variation of the signal with a decreasing amplitude remains. Furthermore, a frequency analysis of this data set reveals a dominant peak in the amplitude



spectrum exactly at the orbital period of the HST. Figure 3 shows the celestial positions of the Moon, the Sun and the HST for the first and the last day of the HDF program, as well as the location of the Deep Field. During the first few days the waning Moon illuminates the HST entrance aperture for a significant fraction of each orbit (at right ascensions between 12 and 24 hours), hence introducing variable scattered light. This can be seen in a plot of the photometric signal versus the right ascension of the HST for each day (Fig. 4). In comparison, the influence of the Sun appears not to be critical. The white line in Fig. 4 is a cubic spline fit to the data which was obtained for each day individually. The residual light curve to this fitting procedure is shown in Fig. 1 (bottom curve in each layer), where all systematic effects were eliminated.

Finally, we obtained a noise level in the frequency spectrum for the decorrelated data of GS 0416200075 of 50 ppm and for GS 0416200054 of 30 ppm.

**Acknowledgments.** The project is supported by the Digital Equipment Corp. (European External Research Program, project *STARPULS*) with computer hardware, and funded by the Austrian Academy of Science (project *FGS-Präzisionsphotometrie*).

## References

Kuschnig, R., Weiss, W.W., Gruber, R., Jenkner, H., 1997, A&A, in press.

## The Goddard High Resolution Spectrograph

David R. Soderblom and Lisa E. Sherbert

*Space Telescope Science Institute, 3700 San Martin Drive, Baltimore MD 21218*

**Abstract.** The Goddard High Resolution Spectrograph (GHRS) was on *HST* at the time of its launch in 1990, and was withdrawn from *HST* during the second servicing mission in 1997. This paper summarizes key events during the operational history of the GHRS and provides a recapitulation of results from the many calibrations that have been done.

### 1. Introduction

This paper will provide a brief look at the state of calibrations for the GHRS. By the time the present volume appears, a new version of the *HST Data Handbook* will have been completed, and that volume has all the details that are only referenced here. Before we begin, we wish to emphasize two important statements: First, for up-to-date information, you should go to the GHRS web page, under the STScI home page. Second, if you select GHRS observations from the *HST* Data Archive, always recalibrate them to ensure you are using the best possible calibration reference files.

The GHRS was a spectrograph built to address a number of scientific goals through ultraviolet spectroscopy. Two detectors were used, one for far-UV work and one for near-UV. "Side 1" incorporated a detector optimized for the far ultraviolet, having a faceplate of CeI with a LiF window. This made Side 1 blind to photons above about 1800 Å but sensitive down to almost 1100 Å.

Side 1 included a low-resolution mode for faint objects, realized with grating G140L, with a resolving power  $R = 2,000$ . This mode was more sensitive than the FOS at many far-UV wavelengths and had less background as well. Medium resolution capabilities ( $R = 20,000$ ) were provided with grating G140M. High resolution ( $R = 80,000$ ) was achieved with Echelle-A.

"Side 2" worked in the near-UV, and had a faceplate of CeTe on a MgF window. This made it sensitive down to Lyman- $\alpha$ , and it was best from about 1700 to 3300 Å. Side 2 was also solar-blind, and had three medium-resolution gratings ( $R = 20,000$ ): G160M, G200M, G270M, as well as a high resolution mode ( $R = 80,000$ ) with Echelle-B.

#### 1.1. Instrument Operation

The GHRS had two entrance apertures for celestial targets. The Large Science Aperture (LSA) was 2 arcsec square (1.74 arcsec square after COSTAR), and was designed to get good fluxes. The LSA mapped onto 8 diodes of the Digicon in width, and one in height, and it passed 95% of light post-COSTAR.

The Small Science Aperture (SSA) was intended for getting good wavelengths, and it was 0.25 arcsec square (0.22 after COSTAR), and it mapped onto one diode. The SSA had 50 to 60% of throughput of the LSA (post-COSTAR), depending on wavelength and the quality of the centering of a star.

There were also two wavelength calibration lamps (SC1 and SC2), and they had their own apertures.



A typical observing procedure was:

1. DEFCAL: to find the aperture
2. Acquire target into LSA: find the object
3. Acquisition IMAGE (optional): where was the object?
4. Move to SSA and peak-up if that aperture was used.
5. SPYBAL: SPectrum Y BALance to center spectrum in the cross-dispersion direction.
6. Wavelength calibration exposure (optional).
7. One or more ACCUMs.
8. RAPID mode for time-resolved spectra.

Some items were optional steps, while the other steps were usually present. The types of data produced and their structures are described in the Data Handbook (DH). DEFCALs and SPYBALs were calibrations internal to the GHRs. SPYBALs are especially useful to an archival researcher as a means of improving the default wavelength calibration (see below).

### 1.2. Key Events During the Life of the GHRs:

1. Most important of all was the launch inside HST in April, 1990!
2. The Side 1 low-voltage power supply (LVPS) had repeated problems in the summer of 1991, eliminating access to both low- and high-dispersion modes in the far-UV (G140L and Ech-A). Prior to this loss, Ech-A was the most-requested GHRs grating, but deconvolution techniques were developed that allowed G160M (Side 2) observations to approach Ech-A resolution. Some of this science was done with Side 2 during Cycles 2 and 3.
3. The LVPS problem was fixed during SM1, restoring important capabilities and leading to greater GHRs usage.
4. The failure of lamp SC1 eliminated redundancy for wavelength calibration, also in 1991. Fortunately, the specifications for the lamps were very conservative and SC2 had ample lifetime to meet observer needs.
5. Acquisitions during the early years had to specify BRIGHT and FAINT limits, leading to failed ACQs and wasted telescope time. The implementation of BRIGHT=RETURN eliminated this problem. Also, BRIGHT=RETURN used 32 bits, preventing register overflow, which had been a problem with very bright stars.
6. Other flight software changes were made to improve acquisitions and overall operation.
7. The installation of COSTAR during SM1 changed the net throughput of the LSA very little (two extra reflections offset the better PSF), but the contrast of the PSF changed enormously, resulting in reliable fluxes. SSA throughput improved too, by about a factor of two.
8. Prior to COSTAR, *HST*'s spherical aberration was sometimes a "feature" for acquisitions in that the algorithm could find the wings of the PSF even when the initial centering was poor.
9. A major failure occurred one week before SM2, resulting in the complete shutdown of the GHRs. The most important loss was some special observations that were to be made with the COSTAR mirrors withdrawn to try to determine the origin of far-UV sensitivity losses.

## 2. GHRS Calibration Results

The dimensions of a GHRS spectrum include:

- Flux, with several components of uncertainty on different wavelength scales:
  - Overall spectrum level (scale  $\sim 100 \text{ \AA}$ ).
  - Shape of the spectrum (scale  $\sim 50 - 100 \text{ \AA}$ ).
  - Noise and structure in spectra (scale  $\sim 1$  diode).
- Wavelength, both in zero-point and scale (dispersion).
- Position and imaging quality (acquisition, PSF, LSF).
- Timing (start, stop, interrupts, doppler compensation and correction).
- Other (instrument and spacecraft errors).

### 2.1. About Fluxes and Flux Calibrations

The flux calibration is established by observing a standard star and then comparing the observations to a reference spectrum, which is taken to represent "truth." The result is the sensitivity function, in (flux units) per (count rate) at a given wavelength.

The first major problem is that the response of the instrument depends of the position of the spectrum on the photocathode. Also, structure in the spectrum of the standard star makes analysis more difficult and partly resolution-dependent.

"Sensitivity" describes the overall response function, while "vignetting" refers to effects that depend on position on the detector. The components of the "flux" calibration (everything that goes into determining the vertical scale of the spectrum) include:

1. Spectrum level:
  - The sensitivity function for the grating + detector.
2. Spectrum shape:
  - The vignetting function, to correct for photocathode position.
  - The echelle blaze function, for the echelle gratings only.
3. Level and shape:
  - Time-dependent corrections to sensitivity functions.
4. Noise and structure ("flatfields")
  - Granularity function, available only for G140L.
  - Granularity determination, accomplished with FP-SPLITS or other means.
  - Corrections for bad diodes.
  - Corrections for diode-to-diode response.



## 2.2. Flux I: Spectrum Level and the Sensitivity Function

"Sensitivity" and "vignetting" are intertwined, and at some level the distinction is arbitrary. That distinction is made by defining the vignetting function at the center of a spectrum to be 1.

Some issues of determining sensitivity can be seen by comparing the observed spectrum of a standard star to its reference spectrum (see the DH). To separate sensitivity from vignetting, a series of spectra are obtained spaced by half the bandwidth, so each wavelength is observed twice. The calculation is iterated to convergence.

The presence of major spectrum features – especially Lyman- $\alpha$  – is a major problem, exacerbated by these being astrophysically important wavelengths. Also, the observed spectrum below 1140 Å has few counts and much curvature, making the fitting difficult. (At any rate we had no reference spectrum defined below 1140 Å anyway.)

Recent work in this area includes:

1. ISR085 on G140L sensitivity and vignetting. The G140L sensitivity file installed post-COSTAR was shown to be wrong, probably because of incorrect allowance for the new white dwarf flux scale. The correct calibration reference files are now in CDBS and the time-dependent sensitivity is provided for in CDBS.
2. ISR088 on redetermining sensitivity for G140M and Echelle-A. The problems are similar to those for G140L.
3. ISR089, on time-dependent sensitivity for Side 2 first-order gratings and ISR090, a check on Ech-B sensitivity.

## 2.3. Flux II: Sensitivity Monitoring and Time-Dependent Effects

Sensitivity monitoring of the GHRS was done separately for Side 1 and Side 2. For the Side 2 observations, gratings G160M (centered at 1200 and 1500 Å), G200M (2000 Å), and G270M (2500 and 3000 Å). This sequence was repeated approximately every three months.

*Pre-COSTAR* Prior to the installation of the COSTAR mirrors, the GHRS LSA had the same overall absolute throughput as post-COSTAR, but the blurred PSF put significant power into the wings. The result was that the quality of flux measurements was very sensitive to the centering of the star in the LSA.

Pre-COSTAR observations (ISR036, ISR038) showed excellent reproducibility of count rates for acquisitions and spectra of standard stars, consistent with no change in sensitivity. (Several different stars were observed, primarily BD+28D4211 and  $\mu$  Col.)

ISR042 confirmed that no changes were seen for the pre-COSTAR GHRS (Side 2), even below 1200 Å. ISR051 showed that Side 2 pre-COSTAR was stable to within better than 3.6%, consistent with effects of focus and centering.

*Post-COSTAR* The Side 1 post-COSTAR monitor contained a series of visits of the UV standard BD+28D4211, done with an identical instrumental configuration each time, except that exposure times were increased at later dates to achieve better signal to noise. Grating G140L was used at two wavelengths: 1200 and 1500 Å.

After the Servicing Mission, we could see distinct declines in sensitivity with time, especially on Side 1 below Lyman- $\alpha$ . This was suspected to be due to contamination on the COSTAR mirrors, and a special measurement was planned for just before the second Servicing Mission to verify this. Unfortunately, the GHRS experienced a catastrophic failure one week before SM2 so these measurements were not done.

Declines in the post-COSTAR sensitivity of the GHRS are now well-characterized, and provision has been made by providing calibration reference files that apply to specific time periods. These time periods are three months in length, which is short enough that



significant changes did not occur on shorter time scales. This is described in detail in the DH.

Time-dependent effects may be slightly different at different wavelengths. We have ignored this because we have inadequate information to fully characterize it.

*Short Time-Scale Effects: Decreasing Counts During an Orbit* A series of short-exposures of a star showed a regular decline of observed counts of  $\sim 10\%$  over each orbit for a star observed in SSA. This was described in ISR073, together with some possible explanations. Our best hypothesis is that this phenomenon is due to telescope "breathing." This effect can contribute to flux uncertainty, obviously. However, similar observations through LSA appear unaffected.

Single FGS observations in SSA have shown a similar effect, due to drift of the object out of the aperture.

## 2.4. Flux III: Other Flux Scale Effects

*Flux Correction for Extended Sources* `calhrs` assumes that a point source has been observed when reduction to flux is made. If an extended source has been observed, then the flux calibration from `calhrs` will be inappropriate.

To obtain an estimate of specific intensity, multiply the post-COSTAR observed flux by  $0.95 \pm 0.02$  for observations taken through the LSA, and divide by the area of the aperture in square arcsec. This assumes the extended source completely and evenly fills aperture. For pre-COSTAR observations, the correction factor is 0.725 (ISR061).

*Correction for Background Counts* The background level, or dark current, for both GHRS detectors was very low: about 0.01 counts per second per diode when well away from the South Atlantic Anomaly (SAA). However, for very faint objects the dark level could dominate the signal, and accurate correction for the background is vital.

Because of this, some provision was made in the GHRS commanding software for features that would allow for lower net noise rates compared to standard observing modes. One of these modes used the CENSOR option (ISR045), and the other used a parameter called FLYLIM (ISR054). These are described in previous workshops.

For archival data, there are several options for correcting for the background. ISR070 discusses measurements of the background for Side 2 in detail, and ISR085 describes a model used for estimating background counts, recently implemented. This uses accumulated flight experience to estimate dark counts and works especially well for short exposures.

Results from dark noise calibrations are presented in ISR041 and ISR070. These have been very consistent over instrument lifetime.

## 2.5. Flux IV: Spectrum shape

*Shape Effects from the Sensitivity Function: G140L* For most GHRS observations, the bandpass samples only a small portion of the spectrum produced by the grating. Undulations in the sensitivity function, which have length scales of  $\sim 100$  Ångstroms, at most have a small linear effect across a spectrum.

G140L is the exception to this rule because it produces spectra nearly 300 Å long. Therefore spectra from grating G140L may have modest shape effects that have their origin in the sensitivity function. These can be especially pernicious near Lyman- $\alpha$  because the breadth of that feature in the standard stars we observed prevented a good determination of the shape of the underlying sensitivity function at those wavelengths.

Time-dependent sensitivity functions help mitigate this, but this leaves residual uncertainty of  $\sim 2\%$  in flux at one wavelength relative to another wavelength more than 50 to 100 Å away in same spectrum, and  $\sim 4\%$  in the worst case. These shape effects are probably due to comparing BD+28 to  $\mu$  Col, and the fact that  $\mu$  Col is a secondary standard.



Intercomparisons of different stars used as standards often show systematic effects at the  $\sim 2\%$  level (R. Bohlin).

*Light Falling Off the Diode Array* Temperature changes during an observation caused spectrum to move on the photocathode, so the GHRS used SPYBALs to properly center the spectrum on the diode array. A SPYBAL was performed every time a new spectrum element was used (i.e., the first use of a different grating), and approximately every two orbits thereafter. (Sometimes SPYBALs were suppressed to avoid carousel movement.)

This centering can be important because a given spectrum is tilted across the diode array, and a lack of proper centering could result in the ends of the spectrum falling off the array. Again, this is routinely corrected for, and only becomes a problem if SPYBALs were suppressed for long exposures (i.e., for several orbits).

The worst case is for an extended object uniformly filling the LSA. In this case, the width of the spectrum cannot be ignored. The width is equal to the size of the aperture, or about 64 deflection units. For the case of a G140L observation of an extended object in the LSA, we start out with a loss of light. The spectrum is already falling off the array with the ends experiencing about 30% light loss. In the time it takes to drift 25 deflection units, some part or all of the spectrum may fall off the array, resulting in a significant reduction in signal. This effect produces an apparent drop-off in flux at ends of spectrum, similar in form to vignetting.

*G270M Vignetting Errors* The pre-COSTAR sensitivity calibration used in the pipeline processing between 1991 Nov 11 and 1994 Apr 14 was wrong shortward of 2300 Å for grating G270M. The pre-COSTAR vignetting correction for G270M was inadequate shortward of 2300 Å, and the post-COSTAR vignetting correction shortward of about 2150 Å was not handled properly by *calhrs* because the  $y$ -deflection not been measured below 2300 Å. The program which was to correct this failed, and the issue was judged to be not important enough to warrant further work. This is documented in ISR077.

*The Echelle Blaze Function* The echelle blaze function relates relative fluxes to those observed at the center of a given spectrum order. This function was determined by observing  $\mu$  Col at different wavelengths in different orders, and then relating those observations to others made with first-order gratings. It is impossible to cover fully a free spectral range or to sample every echelle order, so the blaze function is meant to be a reasonable approximation to the true function. An underlying, but unstated, assumption is that observers used the echelles to measure the strengths or positions of weak spectrum features and were therefore not primarily concerned about the absolute flux level in the final, reduced spectrum.

*Inappropriate Background Subtraction* In some cases the shape of a spectrum can be distorted if the background is improperly calculated and subtracted. This was seen in the first couple of years of GHRS operation because the background subtraction software fitted a polynomial to the background before subtracting it from the source spectrum. This was done to preserve shape in the background spectrum, but often the background had very few counts so that the fit was spurious. Modification of the procedure to fit to a single value removed the problem.

## 2.6. Flux V: Spectrum Noise and Structure

The first-order diode-to-diode response variations are removed in *calhrs*. These are independent of the grating, wavelength, etc.

*Granularity* There are also granularity effects produced in the photocathode faceplates of the detectors. No calibration provided for these because the scope of the task of determining them is impractical. However, grating G140L has been so characterized because its bandpass

is large (see ISR076 for details on how this was derived). For the other gratings, FP-SPLIT was provided to allow for improved signal to noise in the final spectrum.

*Dead or Noisy Diodes* Each diode was independently monitored. Diodes could exhibit anomalous behavior or fail. These diodes are grouped together into the "Dead or Noisy Diode" category. Use of the COMB parameter helped to work around these. Diodes that showed anomalous behavior over an extended time were turned off for science observations. In practice, the threshold voltage was set to a high value so that it did not detect electrons from the photocathode. The GHRS calibration software corrects for known anomalous diodes.

*Spikes* Large spikes and unrealistic flux levels were found in a subset of Fall 1995 calibrated GHRS data. The affected observations were all made using the Ech-A grating in orders 35 and 36. Fortunately, this problem only affected a handful of observations in a few proposals. The PIs of the affected programs were notified of the problem, and, in any case, recalibration of the observations solves the problem.

*Blemishes* Scratches, pits, and other microscopic imperfections in the detector window and on the photocathode surface are "blemishes." The magnitude of these blemishes depended on how the spectrum illuminated the photocathode near a blemish. Many blemishes have spatial structures and depths that make them difficult to distinguish from real stellar or interstellar features. Therefore, it is difficult to automatically correct data for the effect of blemishes.

In the absence of independent information, individual subexposures can be displayed in diode space to identify non-real spectrum features. The calibration code does not correct for blemishes, but the data quality file (.cqh) contains DQ values marking which pixels are affected by known blemishes. The use of FP-SPLITS aided in blemish removal.

*Flaky Diodes* These were seen in some Side 2 CVZ RAPID-mode observations. They were attributed to increases in the pre-amp temperature, producing non-linear amplification of input from diodes. They were also seen in some non-CVZ observations, but were not seen on Side 1.

## 2.7. Flux VI: Summary

The quality of the flux calibration depends on the question asked:

- For absolute flux of a given observation, the work of Bohlin et al. shows internal consistency of 2%, agreement with ground-based to 3%, and systematic external errors less than 15%.
- For the pre-COSTAR instrument, there is no evidence for time-dependent sensitivity changes, but the intrinsic uncertainty of relative fluxes is fairly large due to PSF effects and centering:  $\sim 4\%$ . This increases with time after initial acquisition of an individual object.
- Post-COSTAR, if same star is reobserved at the same wavelength with the same grating, relative fluxes can be compared to 1% or better. (PSF has sharp peak, so sensitivity to centering is greatly reduced.)
- If the same star is observed, but at different wavelengths, then modest systematic effects enter, and limit is 3 to 4% in worst case, 2% typically. Worst case arises from shape effects mentioned above, and is an upper limit.



- All of the above are for LSA observations. SSA fluxes need to include effects over an orbit, which can be as much as 10% as a relative effect and more than that if initial centering in SSA was poor.

## 2.8. Wavelength Calibrations

*Aperture offsets* This is the apparent shift in wavelength between light from different apertures due to different angles for entering light. The convention is to refer all GHRS wavelengths to SSA. The post-COSTAR offsets reported in ISR080.

*Doppler compensation* The onboard doppler compensation moved spectra on the photocathode to oppose the motions induced by orbital speed of spacecraft. Some early observations had wrong compensation applied, leading to significant errors. This was fixed in April, 1993. Moving target observations before July, 1994, are incorrect. Observers were notified at time error detected. ARs should use obsnum task to check for this.

*Using wavecalcs and SPYBALs* The wavelength calibration program shows that the default wavelength scale (dispersion) is highly reliable and needs no correction. Default zero point can be off by 60 mÅ (typical, for medium-resolution gratings), as determined from wavecalcs. A SPYBAL can correct to 19 mÅ or better (ISR053). (A SPYBAL is a SPectrum Y BALance exposure taken with same grating as science observation but at a standard wavelength.)

## 2.9. Spatial Uncertainty and Target Acquisition

*Acquisitions* ISR079 discusses GHRS target acquisitions and problems encountered and has been incorporated into the latest DH. Paper products provide a graphical check on pointing (jitter ball).

Acquisitions in early years could not use BRIGHT=RETURN and needed explicit BRIGHT and FAINT limits. This led to some acquisition problems that are documented.

*Line Spread Functions (LSFs)* These are documented in ISR063.

*The Far Wings of the PSF* See ISR083.

## 2.10. Timing Uncertainty

The actual times of observations are not recorded, and must be inferred from when the observation ended.

*Exposure start time* The packet time (PKTTIME) of first group in UDL is the closest estimate to start time of observations, except for RAPIDs. The UDL was always created prior to start of exposure, and PKTTIME is good to within 1/8 sec. For RAPIDs, PKTTIME in calibrated science headers represents when data left GHRS.

*Exposure end time* For ACCUMs, another UDL was generated at the end of observations, so use the PKTTIME in second group of UDL. For multiple readouts (e.g., FP-SPLITS), UDLs come in pairs that bracket the science. For RAPIDs, the second UDL was not dumped until the end of the observing sequence.

*Exposure duration* This is in EXPTIME keyword. Exposure per pixel is calculated for reduced data.

*Interruptions* GHRS was HST's only interruptible instrument, making scheduling flexible, although limiting in some ways. Precise interrupt information is not possible to determine except with detailed examination of OMS data.

### 2.11. Instrument and Spacecraft Errors

*Carousel resets* This was a frequent problem that increased over life of instrument. Some flight software changes were made to mitigate the effects of resets, especially for acquisitions. Resets could lead to early termination of ACCUMs; this is revealed through FINCODE in header since about 1995.

*Data transmission errors* Reed-Solomon checking is used for data transmission. If an error is detected, it goes into the data quality file as quality value = 1. Data losses and other situations can lead to fill data with quality value = 16.

## 3. GHRS Documentation

### 3.1. Primary document for archival researchers (ARs)

All ARs will need to refer to:

*Data Handbook (DH97):* It is fully up-to-date as of October 1, 1997. It incorporates recent ISRs. It is available as paper or on-line. It will be issued as part of volume 2 of DH97 in January.

### 3.2. Other documents

These are described and enumerated in ISR090. They are important in certain circumstances during program preparation, but should be only rarely needed by ARs.

*Instrument Handbook v6 (IH6):*

- Proposer-oriented description of instrument design and operation.
- Useful for understanding structure and strategy of Phase II proposals.
- Explains operating modes and options.
- Available on-line (as is IH5).
- Essential portions for ARs incorporated into DH.

*Instrument Science Reports*

- Primary content has been distilled into DH97.
- Some ARs may wish to read full text.
- Most ISRs since SMOV available on-line.

*Earlier Instrument Handbooks:* These may sometimes be needed to understand observations obtained in a particular mode or time. They will be maintained to record state of instrument at the time they were written in case that cannot be reconstructed from other documents.



*Ball Technical Documents* Should not be needed by ARs.

- Science Verification Report (9202)
- Ball System Engineering Reports (SERs; 134 plus 10 during SMOV; 9011 to 9404)
- SE-01 ("SI System Description...") (8510)
- Pre-Launch Calibration Report (8603)
- HRS Intermediate Calibration Report (8401)
- Orbital Verification Test Report (9205)
- Orbital Verification Data Analysis Plan (9005)
- A&V Thermal Vacuum Test Report (8611)

*Related documents:*

- Phase II Proposal Instructions
- TRANS Scripting Guide
- A User's Guide to the GHRS Software (IDT at GSFC)

A set of archival documentation is being saved at STScI.

#### 4. Program Status

*Calibration program:* The calibration program has been reported in Calibration Plans and ISRs.

- Formal close-out exist for Cycles 4, 5, and 6.
- Plans for Cycles 3 through 6 are in ISRs.

*Unanalyzed calibrations:*

- Echelle wavelength monitors:
  - First-order gratings showed no problems.
  - Previous echelle analyses showed no problems (ISR058).
- Echelle-B sensitivity being checked.

*Documentation close-out:*

- Available documentation has been evaluated.
- Copies of paper-only documents to go to library; these have been set aside.

## 5. A Few Last Words...

...from the last Instrument Scientist for the GHRS during the last week of a GHRS Group at STScI on the last day of this calibration workshop, to the many who will not be the last users of GHRS data.

The GHRS was a well-designed and well-constructed instrument that showed its productivity by the time observers that requested – typically about 25% of HST time in Cycles 4 to 6, second only to WFPC2. The quality of the observations will be further shown through use of the archive.

Productivity is also shown by the record of publications that were based on GHRS observations. Those known to us that appeared in refereed journals are:

1992: 6

1993: 21

1994: 34

1995: 54

1996: 45

1997+: 55+

These numbers are based on papers sent as preprints to the STScI library, and so are lower limits. In particular, papers in European journals are probably underrepresented.

### 5.1. The GHRS Lineage:

When installed in *HST* in 2002, the HRS parts within COS will be the only remnants of the five launch instruments.

The success of the GHRS is a credit to the many people in the Investigation Definition Team (IDT), and at Ball Aerospace, Goddard Space Flight Center, and STScI who helped to build and calibrate it.

I wish to acknowledge the contributions of all these individuals, at the risk of forgetting some. They include:

*GHRS Investigation Definition Team:* J. Brandt PI, E. Beaver, A. Boggess, K. Carpenter, D. Ebbets, S. Heap, J. Hutchings, M. Jura, D. Leckrone, J. Linsky, S. Maran, B. Savage, A. Smith, L. Trafton, F. Walter, R. Weymann

*GHRS Experiment Development Team:* GSFC: R. Melcher, F. Rebar, H.D. Vitagliano, J. Shannon, V. Krueger, J. Yagelowich, E. Devine, K. Flemming, W. Fowler, J.K. Kalinowski  
Ball: G. Yurka, W. Meyer, J. Chodil, I. Becker, M. Bottema, H. Eck, T. Kelly, S. Koby, H. Garner, J. Kinsey, V. West

*GHRS Science Team:* T. Ake, F. Bruhweiler, J. Cardelli, D. Crenshaw, D. Lindler, E. Malumuth, C. Randall, R. Robinson, J. Sandoval, M. Snow, S. Shore, R. Stencel, G. Wahlgren

*GHRS@ST-ECF:* J. Walsh

*GHRS@STScI:* J. Bacinski, W. Baggett, A. Berman, M. de la Peña, D. Duncan, J. Eisenhamer, L. Ferrarese, R. Gilliland, A. Gonnella, S. Hulbert, M. Lallo, H. Lanning, C. Leitherer, J. Mack D. Manning, M. McGrath, K. Peterson, A. Schultz, L. Sherbert, J. Skapik, D. Soderblom

Finally, we would like to thank R. Williams, K. Long, R. Gilliland, and H. Jenkner for their leadership in improving support to GO/ARs, and all others within and without STScI who have made working on the GHRS a pleasure.



## GHRs Calibration Changes since February 1997

L. E. Sherbert

Space Telescope Science Institute, 3700 San Martin Drive, Baltimore, MD 21218

### 1. Introduction

The STScI GHRs Group has made some changes relating to GHRs calibration since the instrument was removed from HST in February 1997. These changes include an alternative method for calculating and removing background from observations, updates to most of the sensitivity files based on updates to the reference star data, and improvements and corrections to other Calibration Database (CDBS) files. This poster highlights 9 improvements that have been or could be made.

### 2. CALHRS Enhancement

In March 1997, CALHRS was enhanced to provide the option of calculating and subtracting a model background count rate for the two GHRs detectors. CALHRS v.1.3.11, (and later versions, if there will be any) expect 3 new keywords in the raw science header: SAAHFILE, CCRE, and BMD\_CORR. The STSDAS task `hst_calib.ctools.chcalpar` can be used to add these keywords and their values to the raw science header. The model uses a mean relation determined for the FOS, scaled appropriately for Sides 1 and 2 of the GHRs. Geomagnetic longitude and latitude are used to predict the background count rate at the time of the observation, which must be outside of the South Atlantic Anomaly. Please see GHRs-ISR-084 for more details.

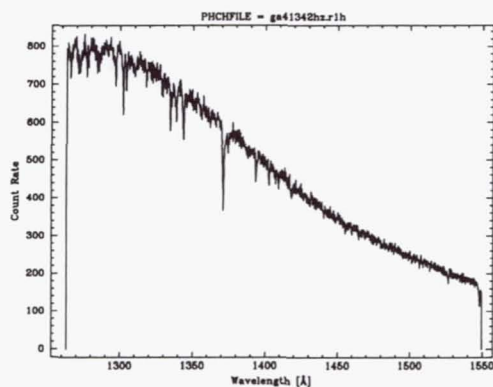


Figure 1. Data flat-fielded with ga41342hz.r1h containing INDEFs

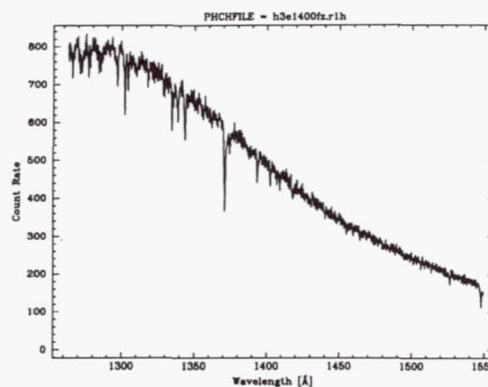


Figure 2. Same data flat-fielded with h3e1400fz.r1h with no INDEFs

### 3. CZZ File Update

A new, post-COSTAR Small Science Aperture Wavelength Offset (CZZ) file is being added to CDBS. The CZZ file is used only by the `zwavecal` task in `stsdas.hst_cal.hrs` to create a new wavelength dispersion based on a GHRs wavelength calibration observation. The table is now being updated for the new post-COSTAR Side 1 carousel positions.

#### 4. Minor changes to G140L flat-fields (PHCHFILES) to fix accidental INDEFs

The INDEFs in the g\*.r1h tables cause the first and last points of flat-fielded (photocathode nonuniformities removed) GHRS data to be 0, as illustrated in Figure 1. The problem is fixed by the h\*.r1h tables, as shown in Figure 2. For more information about when to use G140L flat-fields, see GHRS-ISR-076.

Table 1. Image statistics for ga41342hz.r1h (Columns 2-5) and the corrected h3e1400fz.r1h (Columns 6-9)

GROUP	MEAN	STDDEV	MIN	MAX	MEAN	STDDEV	MIN	MAX
1	1.6000E35	5.0584E36	0.918745	INDEF	1.00001	0.0131494	0.918745	1.04787
2	1.6000E35	5.0584E36	0.848478	INDEF	1.00004	0.0202133	0.848478	1.15366
3	1.6000E35	5.0584E36	0.946298	INDEF	1.00003	0.0133674	0.946298	1.03758
4	1.6000E35	5.0584E36	0.952967	INDEF	1.00004	0.0130505	0.952967	1.037
5	1.6000E35	5.0584E36	0.953588	INDEF	1.00001	0.0122881	0.953588	1.03679
6	1.6000E35	5.0584E36	0.956037	INDEF	1.00001	0.0131402	0.956037	1.03792
7	1.6000E35	5.0584E36	0.954318	INDEF	0.999982	0.0135689	0.954318	1.04381
8	1.6000E35	5.0584E36	0.951942	INDEF	0.999992	0.0142112	0.951942	1.0458
9	1.6000E35	5.0584E36	0.936251	INDEF	0.999999	0.0158543	0.936251	1.06082
10	1.6000E35	5.0584E36	0.916761	INDEF	1.00001	0.0188566	0.916761	1.07989

#### 5. New CCR8 table containing updated LSA incidence angle offsets available 18 Feb 97

Figures 3 and 4 illustrate the differences in G160M wavelengths when old (e3t1250lz.cz8) and new (h2615285z.cz8) CCR8 tables are applied. Note that no update was made to the G140L incidence angle correction. For more information, please read GHRS-ISR-080.

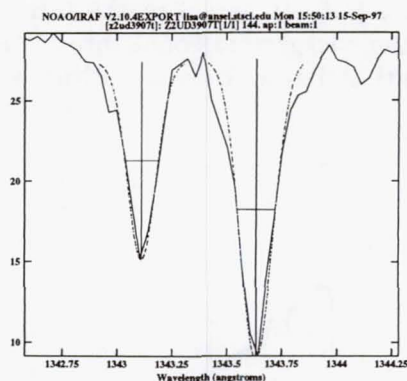


Figure 3. Positions of lines using old LSA incidence angle offsets

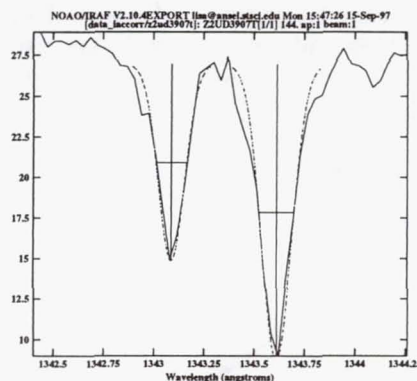


Figure 4. Positions of lines using new LSA incidence angle offsets

Table 2. Comparison of new and old LSA incidence angle offsets

GRATING	A	B	Old CCR8 A value
G140L	0.	0.	0.
G140M	-0.0065	0.	0.
G160M	-0.0448	0.	-0.022±0.023
G200M	-0.057	0.	-0.037±0.012
G270M	-0.06	0.	-0.036±0.007
ECH-A	-0.0076 × m	0.	0.
ECH-B	-0.0078 × m	0.	0.



## 6. G140L post-COSTAR baseline and time-variable sensitivity files available 22 May 97

The top plot in both Figures 5 and 6 shows GHRs data flux-corrected with the appropriate time-variable sensitivity file divided by the reference star; the bottom plot in each set is the same ratio for data calibrated by the OPUS pipeline. Figure 5 shows data from Jan 95; and Figure 6 shows data from Jan 97. GHRs-ISR-085 gives more information.

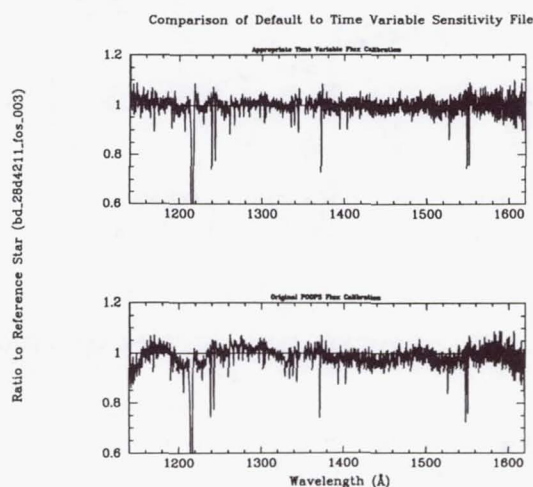


Figure 5. Jan 95 G140L data, before and after sensitivity file update

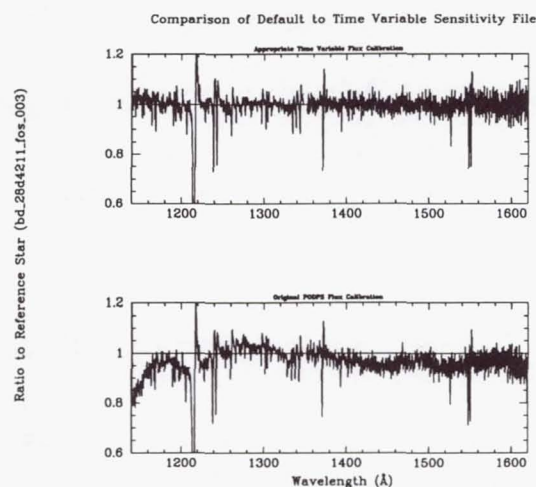


Figure 6. Jan 97 G140L data, before and after sensitivity file update

Table 3. New G140L post-COSTAR sensitivity files in CDBS

ABSHFILE	NETHFILE	GRATING	DATE	USEAFTER	PEDIGREE
h5m10094z.r3h	h4s1130qz.r4h	G140L	22 May 97	14/06/94	INFLIGHT
h5m10095z.r3h				01/08/94	
h5m10096z.r3h				21/10/94	
h5m10097z.r3h				14/01/95	
h5m10098z.r3h				17/04/95	
h5m10099z.r3h				25/06/95	
h5m1009az.r3h				17/09/95	
h5m1009bz.r3h				04/01/96	
h5m1009cz.r3h				02/05/96	
h5m1009dz.r3h				30/08/96	
h5m1009ez.r3h				22/11/96	
h5m1009fz.r3h				24/01/97	

## 7. New G140M and Ech-A post-COSTAR sensitivities available 10 Sep 97

The improvement in G140M and Ech-A sensitivity is based on reference file *mu\_col\_006.tab*, updated 5 Oct 95, which is almost a year and a half after the original post-COSTAR sensitivity files (*e5v0936qz.r3h* and *e5v0936nz.r3h*) were placed in CDBS. Please read GHRs-ISR-088 for more details.

The top plot in Figure 7 shows reference IUE spectrum for *mu Col* is plotted with the merged G140M data using the most current reference files (*e5v0936qz.r3h*).

The middle plot in Figure 7 shows the ratio of G140M to the reference spectrum fit with a linear function for use in correcting the sensitivity.

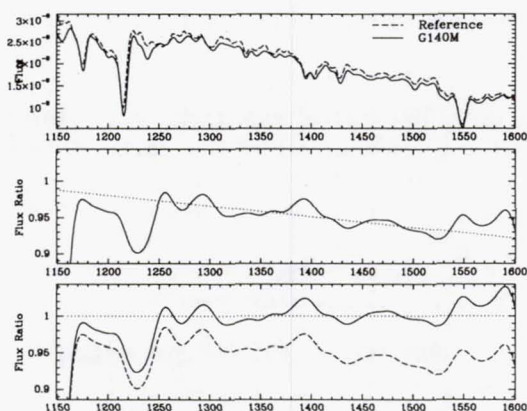


Figure 7. G140M data compared to  $\mu$  Col before and after sensitivity file update

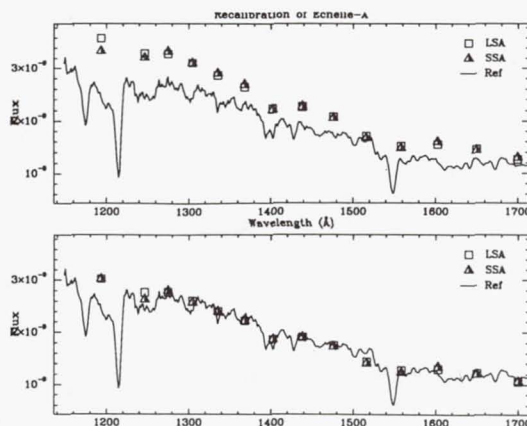


Figure 8. Ech-A data compared to  $\mu$  Col before and after sensitivity file update

Applying the linear correction to the current sensitivity function improves the ratio dramatically, as shown in the bottom plot of Figure 7.

Figure 8 shows the reference flux for  $\mu$  Col plotted with the calculated values from Ech-A. In the top plot, both LSA and SSA show an excess flux of 19% using the old sensitivity file (e5v0936nz.r3h). In the bottom plot, measured and reference flux values agree once a constant factor is applied.

Table 4. New G140M and Ech-A sensitivity files in CDBS

ABSHFILE	NETHFILE	GRATING	DATE	USEAFTER	PEDIGREE
h9a11401z.r3h	e5v09367z.r4h	ECH-A	10 Sep 97	04 Feb 94	INFLIGHT
h9a11402z.r3h	e5v09369z.r4h	G140M			

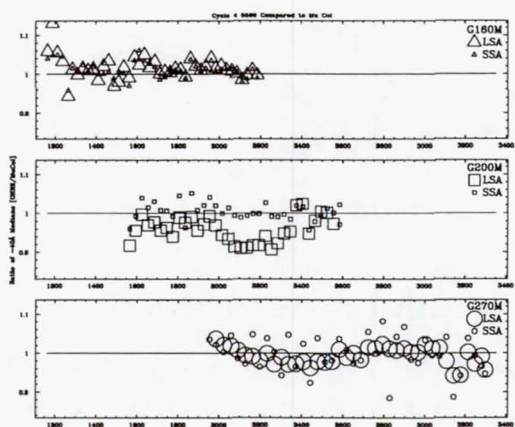


Figure 9. Side 2 first-order data compared to  $\mu$  Col before using sensitivities from 31 May 94 (e5v\*.r3h)

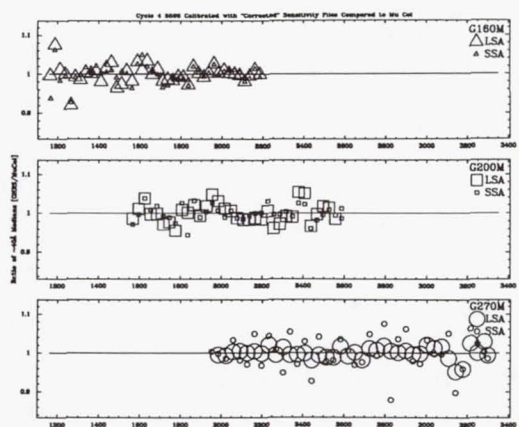


Figure 10. Same data after correcting sensitivity files for shape seen in Figure 9



## 8. Review of Side 2 medium resolution baseline sensitivities

Figure 9 shows the ratio of Cycle 4 Side 2 Sensitivity Calibration program 5596 to  $\mu$  Col reference file (mu.col.006.tab, updated since post-COSTAR Side 2 sensitivity files were put into CDBS). These results were fit with 3rd order cubic splines and applied to the 31 May 94 sensitivity files in an attempt to correct them. Figure 10 shows the same ratio after using the "corrected" sensitivity files. Although the peak-to-peak variation is suppressed, the underlying structure is still evident. Perhaps a complete recalibrating may get rid of the underlying structure, but the current GHRs group may not have time to do the calibrations. These sensitivities also could be corrected for about a 2% decrease per year.

## 9. Review of Side 2 Ech-B baseline sensitivity

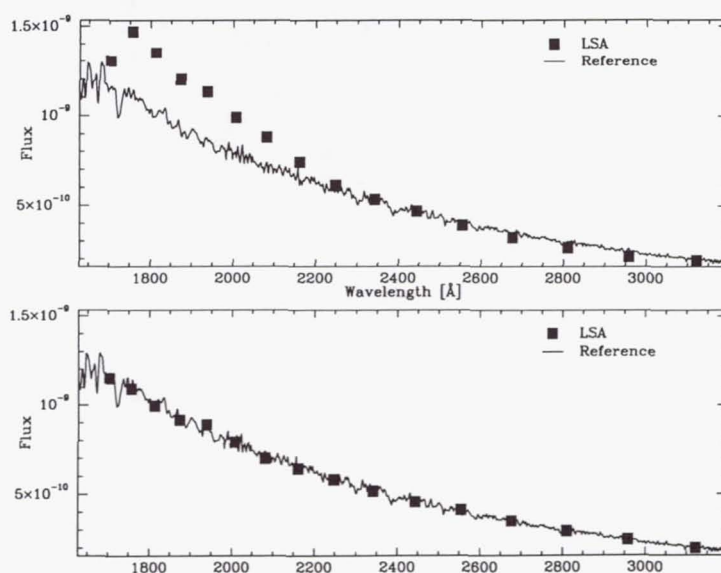


Figure 11. Ech-B data compared to  $\mu$  Col before and after LSA sensitivity file update

The top of Figure 11 shows average values of the Cycle 4 Echelle-B Sensitivity Calibration program 5597 against the  $\mu$  Col reference file (mu.col.006.tab, updated since post-COSTAR Side 2 sensitivity files were put into CDBS). The Ech-B LSA sensitivity was then completely recalculated and applied to the same data. The bottom of Figure 11 shows the same data after applying the "corrected" sensitivity files. The SSA sensitivity is proving a little more difficult, so a corrected Ech-B sensitivity file has not yet been put into CDBS.

**Acknowledgments.** We are grateful to J. Mack for doing the G140M, Ech-A, and Ech-B reductions and CDBS updates.

## References

- De La Peña, M., 1996, Instrument Science Report GHRs-084 (Baltimore: STScI)
- Schultz, A., 1996, Instrument Science Report GHRs-076 (Baltimore: STScI)
- Schultz, A., 1996, Instrument Science Report GHRs-080 (Baltimore: STScI)
- Sherbert, L., 1997, Instrument Science Report GHRs-085 (Baltimore: STScI)
- Mack, J., 1997, Instrument Science Report GHRs-088 (Baltimore: STScI)





## Part 5. General





## The New HST FITS Format, the FITS Kernel and OpenIRAF

P. Greenfield

*Space Telescope Science Institute, Baltimore, MD 21218*

**Abstract.** The pipeline calibration of STIS and NICMOS involves a number of changes from how previous HST instrument data were calibrated in the pipeline. These changes include a change in the data formats, what software language and libraries were used to write the programs, and the methods used to access the new data format. This paper will summarize the new STIS and NICMOS data formats, how to access these files using the new FITS kernel in IRAF, and the changes in how the software is written.

### 1. Introduction

The pipeline calibration of STIS and NICMOS data involves many changes from previous HST calibration pipelines for both the software and the data files. This paper will review what those changes are, particularly those that affect HST users most directly. The most obvious change is the data format used. Previous instrument data has been processed in GEIS (Generic Edited Information Set)—often referred to as ST format—and then converted to FITS format for the archive. STIS and NICMOS data files are now being processed as FITS files directly. The raw and processed results are stored directly in the archive with no conversions in the format. The new format and conventions will be described in detail.

Changes to the IRAF image kernel (the interface that handles image input and output) were necessary to recognize the FITS format directly. The new IRAF fits kernel is used by the calibration pipeline tasks to access the image files. The same fits kernel allows IRAF users to directly access the data products without converting them into other formats. While adding much power, some complications result that IRAF/STSDAS users should be aware of. This paper will describe some of these.

The new pipeline tasks have been written in the C programming language using aspects of the OpenIRAF effort. A brief description of what this entails and means for future STSDAS and TABLES development is included.

### 2. STIS and NICMOS Data Formats

Four basic reasons drove the decision to use multi-extension FITS files as the basic processing format. The first is that the FITS format is machine independent. The products can be moved from one computer to another without requiring the user to convert the file as is currently required for GEIS files. An added benefit is that, should the type of computer the pipeline is run on change, the software used to generate the raw data files will not have to be modified (the software producing the raw data files for WFPC2 and FOC would need to be modified).

The second reason is that no conversion is needed to store the data products in the HST archive, nor is one needed to convert retrievals of STIS or NICMOS data from the archive to a format useful for processing. The third reason is related; current GEIS files are converted to FITS for the archive, but the FITS files that result are not easily used by

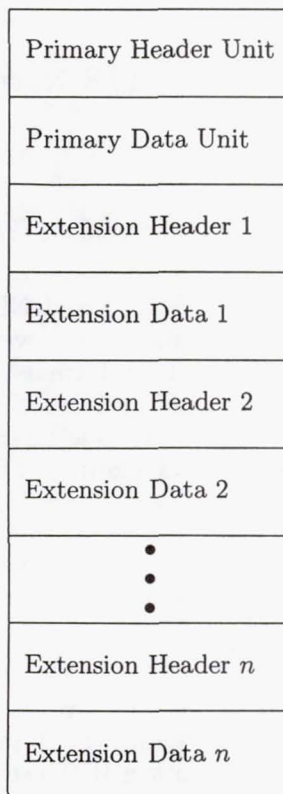


Figure 1. Organization of FITS files containing extensions.

other systems since the data have been encoded in a odd way so as not to lose information on conversion back to GEIS format. For example, the FITS file for WFPC2 contains a three dimensional array where the four images have been combined into a data cube. All the group parameters are stored in a table extension making their access very inconvenient. None of these problems exist with the use of the multi-extension FITS files. No rearranging of the data is required.

Lastly, unlike GEIS files, it is possible to group data of different type or size in the same file. This allows much more flexibility in the content of data files.

Figure 1 illustrates the general layout of multi-extension FITS files. It essentially consists of repeated Header/Data Units (HDU). The first is referred to the Primary HDU and all subsequent ones as Extension HDUs. It is allowable that some of the Data Units are absent (or 'null' in our terminology) as long as that is indicated in the corresponding header by setting the required keyword NAXIS equal to 0. There are currently three standard types for extensions: IMAGE, TABLE (otherwise referred to as ASCII tables), and BINTABLE (binary tables). The PDU (Primary Data Unit) is always assumed to be of type IMAGE.

STScI has adopted some local conventions regarding its use of multi-extension FITS files.

- Use of associated data (IMSETS).
- Extension naming (using EXTNAME and EXTVER).
- Null Primary Data array, all data in image extensions.
- Keyword inheritance.



		Primary Header (Null Data Array)
EXTNAME =	SCI	Science Image (float)
	ERR	Error Image (float)
	DQ	Data Quality Image (16-bit integer)
	SAMP	Samples Image (16-bit integer)
	TIME	Exposure Time Image (float)

Figure 2. Schematic outline of NICMOS data file containing one IMSET.

- Associated arrays with constant values represented by null arrays.

Extension naming and keyword inheritance are an integral part of the IRAF FITS kernel. Each of the above conventions will be described in turn.

STIS and NICMOS data consists of groups of arrays called 'IMSETS.' Each IMSET consists of a standard set of arrays, always present. STIS IMSETS consist of a science image, an error image, and a data quality image. NICMOS IMSETS consist of these three plus an additional two: a samples array and an integration time array. Figure 2 shows a schematic example of a NICMOS data file. STIS or NICMOS files may contain multiple IMSETS.

Extension naming means that the FITS file extensions can be referred to by name (the Primary HDU cannot be named under this scheme). We felt this necessary since requiring users to remember the numerical place of an extension in a file placed too great a burden on them, particularly when different types of extensions were combined in a data file. The scheme uses a name and number to identify unique extensions. In our scheme, the name is used to identify a component of an IMSET (e.g., SCI for science image), and the number to identify which IMSET (not to be confused with the extension number). The IMSET number does not necessarily—though usually does—reflect the order of the IMSET in the file. The FITS kernel will choose the first extension which matches the specified name. If the EXTVER (number component) is not specified, the kernel will match the first extension that matches the name component only. Extensions names are saved with the case as typed, but case is ignored when matching (e.g., Sci will match SCI).

So that all data elements can be referred to by name, STIS and NICMOS data files always leave the PDU null.

Keyword inheritance is a mechanism that allows the keywords in the Primary Header to be logically applied to all extension image headers. There are various rules about when keyword inheritance can be used that won't be detailed here, but all STIS and NICMOS

Row	SPORDER	NELEM	WAVELENGTH	...	NET	FLUX	ERROR	DQ
1	66	1024	< array >	...	< array >	< array >	< array >	< array >
2	67	1024	< array >	...	< array >	< array >	< array >	< array >
3	68	1024	< array >	...	< array >	< array >	< array >	< array >
...	...	...	...	...	...	...	...	...

Figure 3. Structure of a STIS extracted spectra table. Two columns, GROSS and BACKGROUND, are not shown to reduce the printed size.

data make use of this feature. The FITS kernel, unless instructed otherwise, will combine the Primary Header with the Extension Header when accessing an extension. If the same keyword exists in both, the value from the extension header is used.

In a number of cases, particularly for NICMOS, some of the associated arrays in an IMSET may consist of a constant value for all the pixels. To save space, these extensions consist of a null data array. The necessary information to reconstruct the array is contained in the corresponding extension header. While some STSDAS tasks may recognize this convention, in general IRAF tasks will not.

For the time being, the data format for the old instruments (WFPC2 and FOC) is unchanged. That is to say, files are processed in GEIS format and converted to FITS. The possibility of converting the processing format to one using multi-extension FITS files is being considered, but no decisions have been made. Such a change requires significant system work so that existing WFPC2 tasks would continue to work.

Both STIS and NICMOS are using FITS BINTABLE format to store extracted 1-D spectra. They do so using the so called '3-D table' format where each 1-D array is stored in a table cell rather than a table column. Thus, each row of the table contains a complete spectrum, as well as other associated arrays such as wavelength, error, and data quality. Figure 3 shows an example of a STIS extracted spectra table. Such FITS table extensions are accessed using the same naming convention as used for images. The TABLES package can now directly access FITS tables though many tasks do not yet deal with 3-D tables except for a few (they all will eventually). There are a number of tasks to translate 1-D data to and from 3-D tables so that such data may be used with existing IRAF tasks that do not handle 3-D tables.

### 3. IRAF/STSDAS/TABLES support for the New Data Formats

#### 3.1. FITS image kernel

The IRAF FITS image kernel allows all existing IRAF tasks to directly access FITS image data in the same way it can access .imh or .hhh files—no conversions are necessary. However, with this convenience and power come some disadvantages.

The internals of the FITS kernel are quite complicated and hence, the initial versions are somewhat buggy. Since FITS files may now contain many image (or table) objects, users may become confused about the contents of the file. Because there are now multiple objects to worry about, there are unavoidable complications to the user interface. Finally, certain operations, such as inserting images into the middle of a FITS file with many large extensions, may trigger lengthy file rewrites. The potential problems will be discussed in more detail in the following discussions on how to use the FITS kernel.



First, certain IRAF environmental variables affect the behavior of the FITS kernel. For details on their use, refer to the IRAF 2.11 release notes:

<http://iraf.noao.edu/iraf/web/v211revs.html>

**imtype** —specify a default image type. The behavior is changed from older versions of IRAF. Previously, IRAF would only use the value of **imtype** when creating new files from scratch. When producing output files based on modified input files (such as **imcopy** or **imcalc**), it would instead use the input file type to set the output file type unless the output filename explicitly specified a different image file format. Now it will by default always use the value of **imtype**, regardless of the input file format unless the **inherit** option for **imtype** is specified. This **inherit** option has nothing to do with keyword inheritance.

**imextn** —This variable is used to identify the image format of a file corresponding to the file's extension name. This can be used to override IRAF's defaults for identifying which format it should assume for a given filename extension convention. For example, it would be possible to tell IRAF to treat all files ending in **.f** as fits files. Wildcards are permitted.

**imclobber** —If this is set to yes, then IRAF will overwrite output files if they already exist; the default setting is no, in which case an error results.

**fkinit** —This is used to set default behavior for the FITS kernel

FITS image extensions may be selected in a number of ways. The simplest is to specify the extension by extension number (0=Primary, 1=first extension, etc.)

```
infile.fits[3]
```

Selecting by extension name:

```
infile.fits[SCI,2]
```

In any case, selecting the specific extension is required by IRAF for multi-extension files. All HST FITS file are multi-extension, including those made from GEIS files.

Unfortunately, the task of filename specification has become more complicated for three reasons. First, an extension must be specified; second, for output files, guidance must be given about how or where to write the extension (start a new file, or append or overwrite an extension in an existing file?); and finally, how keyword inheritance should be handled. To handle these and other issues there are the following options that can be used when specifying filenames.

**(no)inherit** —combine Primary Header keywords with Extension Header keywords (or not) regardless of the default implied.

**append** —append output FITS image to an existing FITS file.

**overwrite** —overwrite an existing FITS image extension in an existing file.

**ehulines** —preallocate some number of blank lines in headers to allow room for future growth.

**padlines** —add extra blank lines to header on copy of header.

Plus some others that most should never need.

Note that keyword inheritance introduces some problems of its own. While it is useful for the original set of data, any operations on that set of data that propagate the extensions *en masse* to a new output image will effectively defeat the careful separation of the global keywords (those in the primary header) and the local ones (those in the extension header) since IRAF will combine them before writing the image out. Thus, the primary keywords will appear repeated in each of the output extensions. It is possible to keep them segregated by using only tasks that do this specifically (e.g., `calstis` or `calnic`) or by using the `noinherit` option on the input files and the `inherit` option on the output file. This last method can be quite tedious and error prone though. Most users should not bother trying to keep the global and local keywords separate.

Another potential problem with keyword inheritance is confusion about what is being changed. An example is editing a keyword that affects `calstis` or `calnic` processing in one of the science images not realizing that the keyword is a global one. A new one will appear in the extension header and then be ignored by the calibration pipeline task as it uses its old value which is still in the primary header.

IRAF keeps an internal cache of where the file extensions are located within a file. Use of non-IRAF or non-image file utilities (such as using the Unix `rm` command or IRAF's `del`) command may confuse the kernel and lead to errors. Expanding a header or overwriting an existing extension with a larger one (or even smaller one) will lead to the rewriting of the file and possibly long delays. The current kernel prevents updating multiple extensions simultaneously. It is necessary for tasks needing to do so to read in to memory all such arrays or create temporary output files in order to get around this limitation.

### 3.2. Some Examples

Use of the FITS kernel can be comparatively simple as the following couple of examples illustrate.

```
imcopy infile.fits[1] outfile.fits
```

Here the first extension is copied to a new file if one does not already exist or overwrites the old one if `imclobber=yes`.

```
imstatistics infile.fits[sci,1]
```

This prints image statistics for the image extension that has `EXTNAME=sci` (or `SCI`) and `EXTVER=1`.

But one can see quite complicated examples as well:

```
imcopy in.fits[SCI,5] [noinherit] [100:400,*]
      out.fits[6] [overwrite,inherit]
```

This copies a section of an image extension with `EXTNAME=SCI` and `EXTVER=1` without inheriting the keywords from the primary to the 6<sup>th</sup> extension of an existing FITS file, overwriting the existing extension, and setting it to inherit the primary keywords from the output file.

```
imsum in.fits[1],in.fits[2],in.fits[3] out.fits[sum123, append,inherit]}
```

This computes the sum of the first 3 extensions of `in.fits` and append the result in the existing `out.fits` file, and sets the extension to inherit the keywords from the primary header of the output file.



### 3.3. Tools for dealing with multi-extension FITS files.

**stdas.fitsio.catfits** —Use this to list the contents of a FITS file.

**stdas.toolbox.imgtools.mstools** —This package contains tasks that can handle imsets.

**ecdel** —Delete an entire class of FITS extensions from a FITS file (e.g., all NICMOS TIME extensions).

**ecextract** —Select all extensions of one selected 'type' from a FITS file (e.g., all SCI extensions).

**extdel** —Delete single extensions from a FITS file.

**msarith** —Image arithmetic with STIS and NICMOS files which uses and updates the data quality and error extensions.

**mscombine** —Combine NICMOS or STIS files using gcombine and appropriately using the data quality and error extensions.

**msdel** —Remove one entire IMSET from a FITS file.

**mssort** —Sort a FITS file to order extensions by EXTVER number.

**msjoin** —Join files containing single IMSETS into one file.

**mssplit** —Splits multi IMSET NICMOS or STIS files into separate files containing one IMSET each.

**msstatistics** —An extended gstatistics for .imh, .hhh, and .fits files which can take data quality and error arrays into account.

In addition, NOAO is developing a package of FITS utilities (**fitsutil**, currently an external package). However, they generally do not recognize our IMSET conventions.

**fxcopy** —Copy FITS files or FITS extensions to an output FITS file.

**fxdelete** —Delete FITS extensions in place.

**fxinsert** —Insert FITS files or extensions into another MEF file.

**fxheader** —List one line of header description per FITS unit.

**fxsplit** —Split a multiple extension FITS file into single FITS files.

**fxdummyh** —Create a dataless single FITS file.

The external package is in: <ftp://iraf.noao.edu/pub/fitsutil.tar.Z>

### 3.4. Sources of information about the FITS kernel

STScI User's Guide to the IRAF FITS kernel

[http://ra.stsci.edu/stdas/fits\\_userguide.html](http://ra.stsci.edu/stdas/fits_userguide.html)

NOAO's Fits Kernel User's Guide

[ftp://iraf.noao.edu/iraf/docs/fits\\_userguide.txt](ftp://iraf.noao.edu/iraf/docs/fits_userguide.txt)

IRAF 2.11 Release Notes

<http://iraf.noao.edu/iraf/web/v211revs.html>

STSDAS manuals are being updated; the new versions will be available in 1997.

### 3.5. Using FITS BINTABLEs

A row selector mechanism is available for some tasks (**tscopy**, **sgraph**, **igi**) to allow the selection of specific rows so that 1-D data in 3-D tables can be used with tasks that accept 1-D data. The row selector mechanism will be incorporated into the TABLES interface in the next release so that all tasks can incorporate the row selector mechanism though not all tasks may use 3-D tables by then.

Tasks that provide a means to convert 3-D tables to and from other forms or formats include:

**tiimage** —Insert images into rows of a 3-D table.

**titable** —Insert 2-D tables into rows of a 3-D table.

**tximage** —Extract images from rows of 3-D tables.

**txtable** —Extract 2-D tables from rows of 3-D tables.

**tscopy** —Copy row/column subsets of tables using selectors.

**stdas.hst.calib.ctools.tomultispec** —Convert spectra from rows of a fits 3-D binary table to an IRAF multispec image.

Further information on row and column selectors can be obtained by typing **help selectors**.

#### 4. Elements of OpenIRAF

OpenIRAF represents an effort to make it easier to import outside software into IRAF as well as making it easier to use IRAF tasks outside the usual IRAF environment. One of the first steps in this direction has been the development of a C language interface to the IRAF libraries. Such C bindings have been developed for the major IRAF libraries and are distributed with STSDAS v2.0.

All the STIS and NICMOS calibration pipeline tasks are written in ANSI C with no dependence on vendor extensions. In general, these C tasks can be compiled as traditional native IRAF tasks (runnable from the CL or host level) or as standalone tasks that are linked with the host LIBC. Currently, the pipeline tasks are compiled as standalone tasks.

All the image file I/O is handled by a higher level library—HSTIO—which is layered on the IRAF imio library. This serves to minimize the dependence on the software environment. All image data are mapped into C data structures which correspond to all important data objects from data arrays (of various types), image extensions, IMSETS, and files. This library provides convenient routines to read and write to such data structures—high level and low level—as well as accessing sections of arrays. A more generalized version is being developed to handle accessing other data formats (e.g., GEIS) and incomplete IMSETS so that programs written using the library can be used for general purpose analysis.

Documentation on the C interface and the HSTIO library may be found in the STSDAS v2.0 subdirectories **lib/cvos/doc** and **lib/hstio/doc**.

**Acknowledgments.** The work described here involved the efforts of many people including all of the Science Software Group (Phil Hodge, Howard Bushouse, Allen Farris, Ivo, Busko, J. C. Hsu, Michele de la Pena, Warren Hack, Bernie Simon, Ray Williamson, Eric Wyckoff, and Rick White) as well as considerable contributions from the STScI instrument groups, NICMOS and STIS IDT's, OPUS, Hubble Data Archive, and the NOAO IRAF group.



## New Calibration Systems Projects at STScI

Stephen Lubow

*Space Telescope Science Institute, Baltimore, MD 21218*

**Abstract.** STScI has continued the development of systems for HST data calibration. The calibration database system (CDBS) tracks information about all HST calibration files. CDBS has been rebuilt to be more automated and provide some additional capabilities for users. We have also begun investigating the requirements for an on-the-fly calibration system. This system would allow users to retrieve data that are automatically calibrated at STScI with the most recently recommended calibration files and software.

### 1. Introduction

HST raw data are initially calibrated in a pipeline system at STScI. The raw and calibrated data are currently stored in the DADS archive and can be accessed remotely by GOs through the Starview user interface. In addition, users can obtain datasets plus newly recommended calibration files via Starview, and then recalibrate the data at their own sites using STSDAS software. The current system has met many user needs. However, some improvements are underway. The new calibration systems projects will provide better capabilities for managing calibration data at STScI and will offer more calibration services to GOs.

We describe below two projects for improving the STScI calibration systems: the rebuilt calibration database system (CDBS) and the on-the-fly calibration (OTFC) system.

### 2. CDBS

#### 2.1. Description

The calibration database system (CDBS) plays a key role both in the initial calibration and in data recalibration by GOs. CDBS is a separate database system that maintains a record of all calibration files ever delivered for HST. It provides information to the calibration pipeline about which files should be used to calibrate an observation. In addition, it provides information to users via the Bestref system in Starview about the reference files that are currently recommended for each observation. (The Bestref screen is found by selecting "HST Instrument Searches" followed by "Reference" in Starview.) The CDBS system was recently completely redesigned and rebuilt. The new system is currently operational.

#### 2.2. Data Flow

Calibration data files are prepared by instrument groups at STScI. The instrument groups also create load files that describe the contents of the calibration files. The data and load files are delivered to CDBS by the instrument groups. CDBS processes the load files and stores this information on a Sybase database system. Information about all calibration files ever used for HST is stored in this database. CDBS also undertakes several consistency checks (about a dozen) for possible errors in creating the load file or in processing the data.

CDBS generates code for updating a database in the calibration pipeline. The pipeline database contains a list of the currently recommended files to be used in the STScI initial calibration of observations. The data and code files are delivered to the pipeline system. The pipeline informs CDBS of when those data were loaded into the pipeline and into its database.

CDBS delivers the calibration data files to the DADS system for archival storage. The DADS system informs CDBS of when the data are archived.

The Bestref system in Starview provides GOs with information about which reference files are the currently optimal for calibrating a given observation. The Bestref system uses the CDBS database as the source of information for determining the recommended files. This selection involves considerations of the observation mode, the date of the observation, and the date of use (useafter date) for each possible calibration file.

### 2.3. New Capabilities

CDBS was redesigned and rebuilt in part to handle the greater complexity of the NICMOS and STIS instruments (Lubow et al. 1997). The CDBS data processing has been fully automated to minimize operator errors. The new database design is simpler and makes system maintenance and software development much easier than had been the case with the old system.

The new CDBS automatically determines whether a new file being delivered replaces some existing file currently in use. If so, the existing file is marked as out of use in the CDBS database and code is generated to remove that entry from the pipeline database. The information about the old file is kept in the CDBS database for tracking purposes.

Bestref was redesigned to use a new algorithm for determining the recommended files for each HST observation. The previous algorithm recomputed the recommended files for all HST observations every night. The computational demands of the system were rapidly exceeding the capacity of the hardware and the SM2 (second servicing mission) instruments would considerably worsen the situation. The new Bestref system each night recomputes the recommended files for only a small subset of HST observations, namely, those that can be affected by the newly delivered calibration files. As a result, the Bestref performance has been radically improved. The NICMOS and STIS data are being easily processed by Bestref.

The new CDBS database stores comment and level of change information about each data file. The following levels of change can appear on the Bestref screen

- N/A - No original or recommended file
- NO CHANGE - exactly the same files
- UNKNOWN - level of change not determined (only for preSM2)
- TRIVIAL - not important
- MODERATE - maybe important
- SEVERE - definitely important (recalibrate)

Levels TRIVIAL, MODERATE, and SEVERE are determined by CDBS software, based on information supplied by STScI instrument groups. Specifically, for each calibration file delivered, the instrument groups designate in a accompanying load file its level of change relative to some previously delivered related file, called the comparison file. The comparison file name is determined by CDBS. In the case of calibration files that are images, the level of change is specified by the instrument groups for the entire file. However, in the case of calibration files that are tables, the level of change is specified for each row of the



table. This row-level specification permits Bestref to determine whether a newly delivered calibration table contains of change of importance to an observation that uses a particular row of that table. In the case of deliveries of large tables with a small number of significant row changes, this capability becomes quite useful.

CDBS stores these change levels internally in its database by using *equivalence classes*. This method permits a rapid level of change determination between any two calibration files without following a chain of change levels among related files (i.e., transitivity problem, see Lubow et al. 1997).

## 2.4. New Features for Users

As a result of the new capabilities described above, some new features have been provided in the Bestref screens of Starview. Bestref now indicates the level of change for each recommended calibration file, relative to the file used to carry out the original calibration. In general, if one or more indications of SEVERE changes are listed, then recalibration is warranted. In practice, the level of change information is highly incomplete for pre-SM2 (before the second HST servicing mission of Feb '97) calibration files. A default change level of UNKNOWN is applied to such cases where incomplete change level information is available. Post SM2 calibration files, including all those for NICMOS and STIS, should have proper level of change determinations. The MODERATE change level suggests that recalibration may be needed, while the TRIVIAL change level usually indicates that recalibration is not necessary.

Important information about calibration files is now being stored as calibration comments in the CDBS database. These comments can be accessed through Starview. In general, complete comments are found in calibration files delivered after SM2. Currently, calibration file comments are available through Starview by selecting the "HST Instrument Searches", followed by "CALIBRATION" and by specifying the name of the calibration file. This feature is useful, though awkward for the purposes of most users, who would want a comprehensive historical list of comments for reference files that are relevant to some particular observation dataset. Such a capability is under development and should soon be available in the Starview Bestref screen. For a given observation, a user will be able to obtain all comments that were provided by instrument groups. These comments are selected from the database based on the date of observation, the types of files used to calibrate the observation, and the relevant mode of observation. The comments listed will include those for the original calibration files and those for the currently recommended files, as well as comments that may be found in several intervening files.

## 3. On-The-Fly Calibration

An on-the-fly calibration (OTFC) system at STScI would allow users to obtain data from the DADS archive which are calibrated with the most up-to-date calibration files and software. In most cases, this capability requires that data be automatically calibrated at STScI when the data are requested by a user. An OTFC system has been successfully developed for HST data by the CADC/ST-ECF (Crabtree et al. 1995). The requirements for an OTFC system at STScI are somewhat different from the CADC/ST-ECF, but their pioneering efforts provide STScI with a basis for development.

To date, we have conducted a preliminary investigation of the design issues and requirements for an OTFC system at STScI. Some of the main points are described below.

### 3.1. Advantages of OTFC

The HARP report (Hanisch et al. 1997) recommended that STScI pursue development of an OTFC system to reduce the level of data storage in the DADS archive. It may be possible to store only uncalibrated data in DADS and thereby not need the storage space



that would have been required for the calibrated data. WFPC2 calibrated data are a factor of ten larger than the uncalibrated data. Furthermore, the uncalibrated WFPC2 data compress very well (by a factor of ten), while the calibrated data do not compress well. The HARP report recommended that uncalibrated data be stored in compressed form and that calibrated data not be stored. The storage requirements for DADS are rapidly increasing with STIS and NICMOS and will become even greater with the Advanced Camera (ACS). The large advantages of OTFC for WFPC2 would likely be realized for ACS.

Another motivation comes from the scientific need to recalibrate data. About 2/3 of GOs recalibrate their data prior to analysis. Cameras such as WFPC2 produce dark files that typically should be retroactively used to calibrate observations taken in the prior week. Unfortunately, this means that the original calibration carried out in the STScI pipeline is not optimal. Furthermore, this less than optimal calibration is stored in the DADS archive. An OTFC system would help solve this problem by providing users with the calibration having the appropriate dark, as soon as it is available.

Currently, instruments that undergo evolution of calibration files or calibration software require users to carry out their own recalibrations at their home sites. It may well be easier for both the users and the STScI support groups to have STScI carry out the recalibration.

### 3.2. Design

The OTFC system should work closely along the lines of the current STScI calibration pipeline, so that both systems will produce nearly the same results. Users should be able to request OTF calibrated data electronically, much in the manner that data requests are currently carried out.

The OTFC system would handle each request for calibrated data by obtaining the raw data from the DADS archive. The raw data could then be calibrated using the appropriate STSDAS routines. Headers in the calibrated data will be updated to reflect the processing. The calibrated data will then be sent to the user.

To coordinate the processing activities, the OTFC system should employ the OPUS blackboard technology (Rose 1996). This system allows for parallel processing of tasks distributed over multiple cpus.

The system will need to function in a highly automated manner. The number of datasets calibrated per day in the OTFC system will greatly exceed the number of datasets calibrated by the current calibration pipeline system. The OTFC system will need to be robust and be able to automatically recover from problems with calibration processing. Possible problem datasets will be identified in advance of OTF calibration so that the system will be able to process them as best as is possible. In some cases, no calibration may take place, but the user will need to be informed of that outcome. The system will also need to handle cases where the calibration procedures have evolved over time and data might be missing from the headers that is needed to carry out processing with current software.

There are several approaches that can be taken to identify and resolve the above problems and special situations. One possibility is to store information about all problem observation datasets in a database, which the OTFC system would check before carrying out its calibration. This approach would require that appropriate parameters be identified to describe all such problems. Another approach would be to use a set of rules in a decision tree, as has been adopted by the CADCE/ST-ECF (Crabtree et al. 1995). This approach works well when the rules can be simply stated with few exceptions.

### 3.3. Plans

In the near-term we expect to develop a prototype which will be heavily tested. We believe that it would be beneficial to have an OTFC system in place for the ACS, before SM3.



Our initial goal will be to produce a calibration system that will provide calibrations that are as good as would be obtained by users today who recalibrate manually. Beyond that, various improvements and customizations are possible.

**Acknowledgments.** I thank Colin Cox, Lee Hurt, Shaw-Hong Kao, Bernie Simon, Rick Whitman, for their assistance in CDBS development. I greatly benefited from the OTFC Working Group discussions with Faith Abney, Andy Fruchter, Lee Hurt, Robert Jedrzejewski, Marc Postman, Daryl Swade, Jay Travisano, and Rick White.

## References

- Crabtree, D. R., Durand, D., Gaudet, S., & Hill, N., 1995, *Astronomical Data Analysis Software and Systems V*, ASP Conf. Ser., Vol. 101, eds. G. H. Jacoby & J. Barnes (San Francisco: ASP), 505
- Hanisch, R. J., Abney, F., Donahue, M., Gardner, L., Hopkins, E., Kennedy, H., Kyprianou, M., Pollizzi, J., Postman, M., Richon, J., Swade, D., Travisano, J., & White, R., 1996, *HARP: The Hubble Archive Re-Engineering Project Summary Report* (Baltimore: STScI)
- Lubow, S., Cox, C., Hurt, L., & Simon, B., 1997, *Redesign of CDBS* (Baltimore: STScI)
- Rose, J. F., 1996, *Astronomical Data Analysis Software and Systems VI*, A.S.P. Conf. Ser., Vol. 125, eds. G. Hunt & H. E. Payne (San Francisco: ASP), 38

## A Package for the Reduction of Dithered Undersampled Images

A. S. Fruchter<sup>1</sup>, R. N. Hook<sup>2</sup>, I. C. Busko<sup>1</sup> and M. Mutchler<sup>1</sup>

<sup>1</sup>*Space Telescope Science Institute, 3700 San Martin Drive, Baltimore, MD 21210*

<sup>2</sup>*Space Telescope European Coordinating Facility, D-85748 Garching, Germany*

**Abstract.** We present a set of tasks developed to process dithered undersampled images. These procedures allow one to easily determine the offsets between images and then combine the images using Variable-Pixel Linear Reconstruction, otherwise known as “**drizzle**”. This algorithm, originally developed for the combination of the images in the Hubble Deep Field (Williams et al. 1996, Fruchter & Hook 1997), preserves photometry and resolution, can weight input images according to the statistical significance of each pixel, and removes the effects of geometric distortion both on image shape and photometry. In this paper, the method and its implementation are described, and measurements of the photometric accuracy and image fidelity are presented. In addition, we describe ancillary tasks developed for determining offsets between images, and discuss the use of drizzling to combine dithered images in the presence of cosmic rays.

### 1. Why Dither?

Although we have all observed the usefulness of dithering throughout our social lives, the attendees at this conference may find it surprising that a technique so important to politicians should also improve the quality of one’s Space Telescope data. However, dithering or spatially offsetting the telescope detector between exposures has several benefits.

- Large scale dithering allows one to reduce the effects of flat field errors or spatially varying detector sensitivity on the final image.
- Shifts of a few pixels allow one to remove small scale defects such as hot pixels, bad columns, and charge traps from the image.
- Non-integral dithers allow one to recover some of the information lost to undersampling.

The latter reason is particularly important in the case of Hubble Space Telescope (HST) imaging, for while the telescope now provides the superb images for which it was designed, the detectors on HST are frequently unable to take full advantage of the resolving power of the optics. This is particularly true of the Wide Field Camera (WF) of WFPC2 and Camera 3 of NICMOS (NIC3). The width of a WF pixel equals the full-width at half maximum of the optics in the near-infrared, and greatly exceeds it in the blue. The NIC3 similarly undersamples the image over much of its spectral range. The effect of undersampling on WF images is illustrated by the “Great Eye Chart in the Sky” in Figure 1.

Fortunately, much of the information lost to undersampling can be restored. In the lower right of Figure 1 we display a restoration made using one of the family of techniques we refer to as “linear reconstruction.” The most commonly used of these techniques are shift-and-add and interlacing. The image in the lower right corner has been restored by interlacing dithered images. However, due to the occasional small positioning errors of



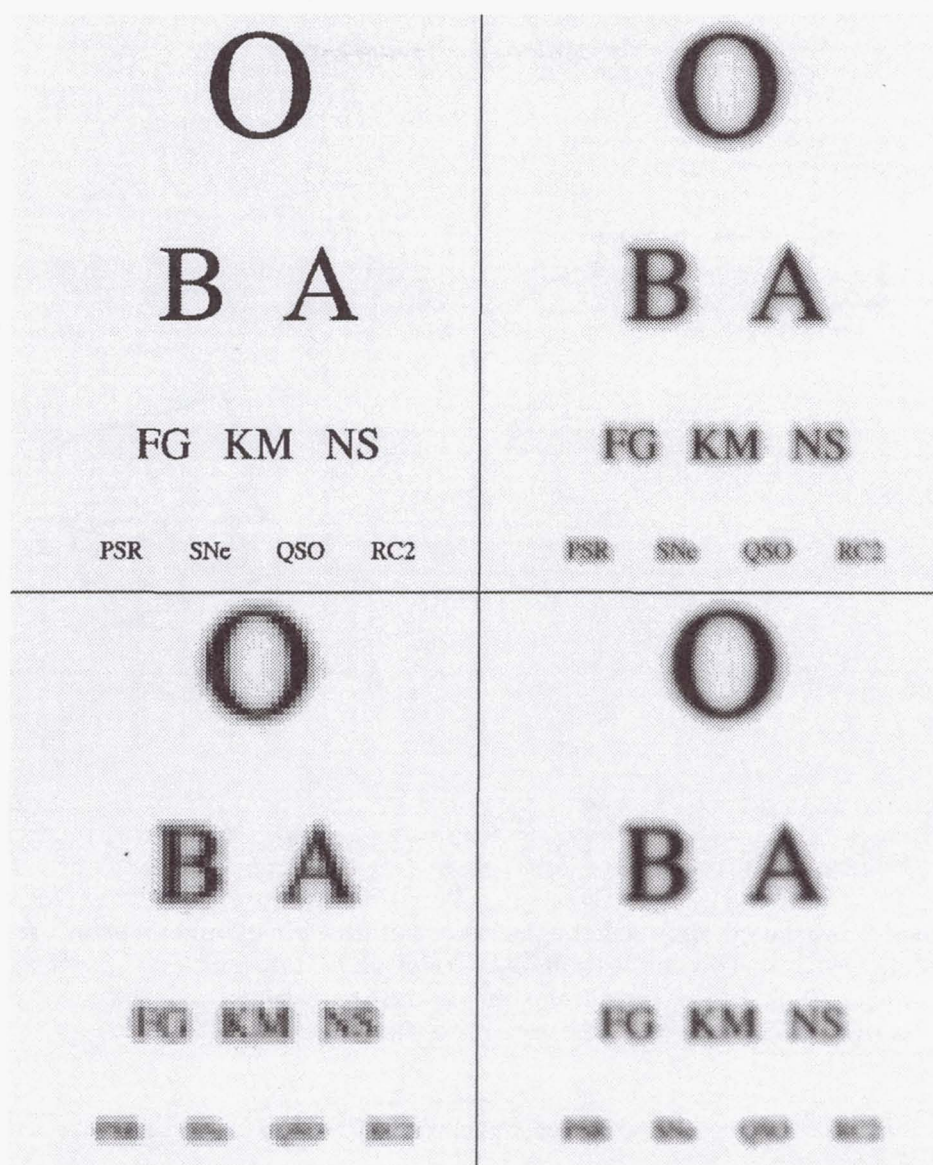


Figure 1. In the upper left corner of this Figure, we present the “true image”, i.e., the image one would see with an infinitely large telescope. The upper right shows the image after convolution with the optics of the Hubble Space Telescope and the WFPC2 camera—the primary wide-field imaging instrument presently installed on the HST. The lower left shows the image after sampling by the WFPC2 CCD, and the lower right shows a linear reconstruction of dithered CCD images.

telescope and the non-uniform shifts in pixel space caused by the geometric distortion of the optics, true interlacing of HST images is often infeasible. The other standard linear reconstruction technique, shift-and-add, can easily handle arbitrary dither positions, but it convolves the image yet again with the original pixel, adding to the blurring of the image and to the correlation of the noise. The importance of avoiding unnecessary convolution of the image with the pixel is emphasized by comparing the upper and lower right hand images in Figure 1. The deterioration in image quality is due entirely to convolution of the image by the WF pixel. In the next Section we present a new method, **drizzle**, which has

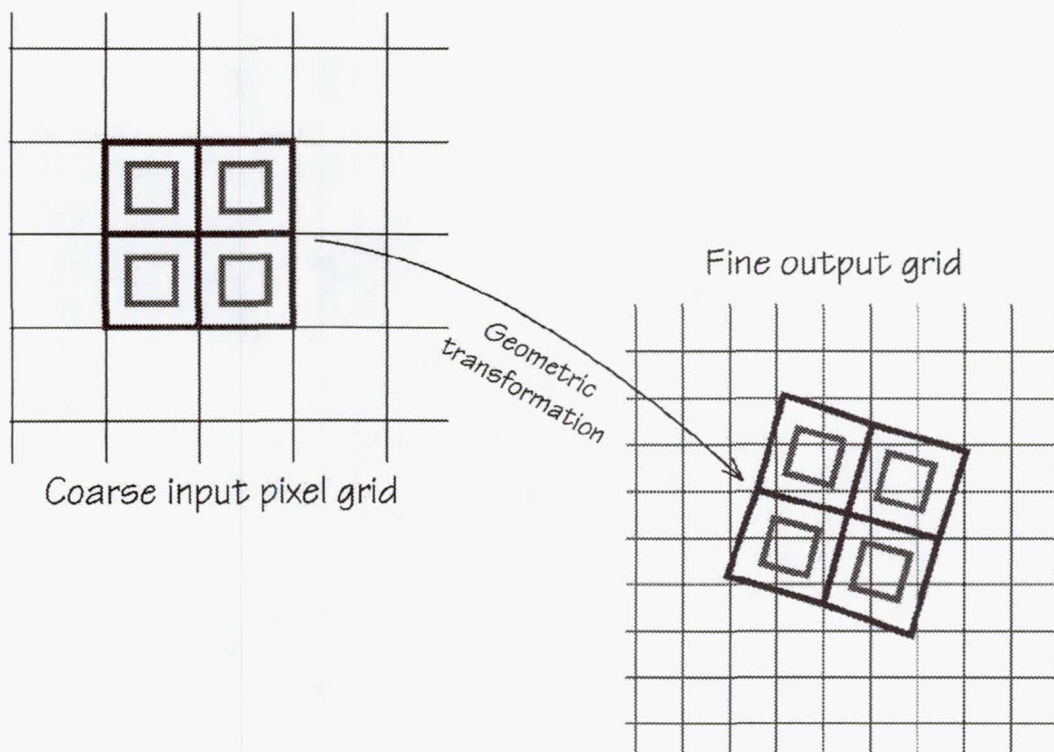


Figure 2. A schematic representation of drizzling. The input pixel grid (shown on the left) is mapped onto a finer output grid (shown on right), taking into account shift, rotation and geometric distortion. The user is allowed to “shrink” the input pixels. We refer to these shrunk pixels as drops (faint inner squares). A given input image only affects the output image pixels under drops. In this particular case, the central output pixel receives no information from the input image. Therefore, the dropsize (*pixfrac*) shown here would only be appropriate were many more images to be drizzled onto the output.

the versatility of shift-and-add yet largely maintains the resolution and independent noise statistics of interlacing.

## 2. The Method

The **drizzle** algorithm is conceptually straightforward. Pixels in the original input images are mapped into pixels in the subsampled output image, taking into account shifts and rotations between images and the optical distortion of the camera. However, in order to avoid convolving the image with the large pixel “footprint” of the camera, we allow the user to shrink the pixel before it is averaged into the output image, as shown in Figure 2.

The new shrunk pixels, or “drops”, rain down upon the subsampled output. In the case of the Hubble Deep Field (HDF), the drops used had linear dimensions one-half that of the input pixel—slightly larger than the dimensions of the output subsampled pixels. The value of an input pixel is averaged into an output pixel with a weight proportional to the area of overlap between the “drop” and the output pixel. Note that, if the drop size is sufficiently small, not all output pixels have data added to them from each input image. One must therefore choose a drop size that is small enough to avoid degrading the image, but large enough so that after all images are “drizzled” the coverage is fairly uniform.



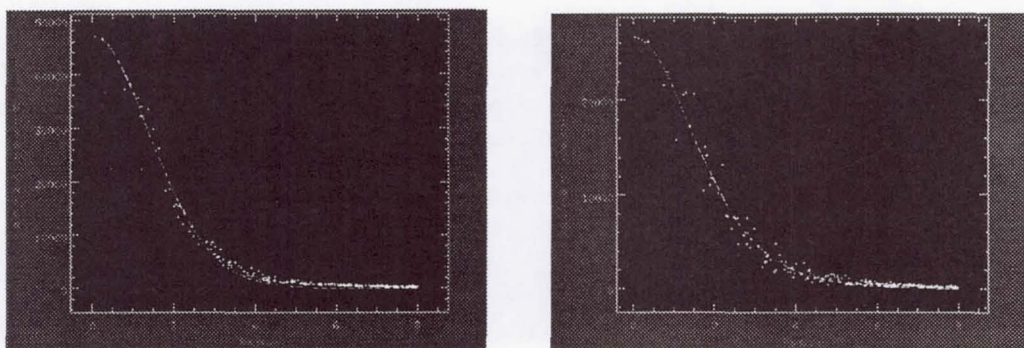


Figure 3. A comparison of two PSFs from the HDF. Note that one of these PSFs shows substantial noise about the Gaussian. Although some noise is expected as a result of the interpolation performed by **drizzle**, WFPC2 images occasionally show more noise than simulations would predict. This may be the result of defects in the detector, and could be related to the known charge transfer errors in WFPC2. A pixel in the processed HDF image has a linear size of  $0''.04$ .

The drop size is controlled by a user-adjustable parameter called *pixfrac*, which is simply the ratio of the linear size of the drop to the input pixel (before any adjustment due to the geometric distortion of the camera). Thus interlacing is equivalent to setting *pixfrac* = 0.0, while shift-and-add is equivalent to *pixfrac* = 1.0.

When a drop with value  $i_{xy}$  and user-defined weight  $w_{xy}$  is added to an image with pixel value  $I_{xy}$ , weight  $W_{xy}$ , and fractional pixel overlap  $0 < a_{xy} < 1$ , the resulting value of the image  $I'_{xy}$  and weight  $W'_{xy}$  is

$$W'_{xy} = a_{xy}w_{xy} + W_{xy} \quad (1)$$

$$I'_{xy} = \frac{a_{xy}i_{xy}w_{xy} + I_{xy}W_{xy}}{W'_{xy}} \quad (2)$$

This algorithm has a number of advantages over standard linear reconstruction methods presently used. Since the area of the pixels scales with the Jacobian of the geometric distortion, **drizzle** preserves both surface and absolute photometry. Therefore flux can be measured using an aperture whose size is independent of position on the chip. As the method anticipates that a given output pixel may receive no information from a given input pixel, missing data (due for instance to cosmic rays or detector defects) do not cause a substantial problem, so long as there are enough dithered images to fill in the gaps caused by these zero-weight input pixels. Finally, the linear weighting scheme is statistically optimum when inverse variance maps are used as weights.

### 3. Image Fidelity

**Drizzle** was designed to obtain optimal signal-to-noise on faint objects while preserving image resolution. These goals are unfortunately not fully compatible. For example, non-linear image restoration procedures, which attempt to remove the blurring caused by the point-spread function (PSF) and the large pixel by enhancing the high frequencies in the image (such as the Richardson-Lucy (Richardson 1972, Lucy 1974, Lucy & Hook 1991) and maximum entropy methods (Gull & Daniell 1978, Weir & Djorgovski 1990)), directly exchange signal-to-noise for resolution. In the drizzling algorithm no compromises on signal-to-noise have been made; the weight of an input pixel in the final output image is entirely

independent of its position on the chip. Therefore, if the dithered images do not uniformly sample the field, the “center of light” in an output pixel may be offset from the center of the pixel, and that offset may vary between adjacent pixels. The large dithering offsets which may be used in WFPC2 imaging, combined with geometric distortion, can produce a sampling pattern that varies across the field. The output PSFs produced by the combination of such irregularly dithered datasets may, on occasion, show significant variations about the best-fit Gaussian. Fortunately this does not noticeably affect aperture photometry performed with typical aperture sizes. In practice the variability about the Gaussian appears larger in WFPC2 data than our simulations would lead us to expect. Examination of recent dithered stellar fields leads us to suspect that this excess variability results from a problem with the original data, possibly caused by charge transfer errors in the CCD (Whitmore & Heyer 1997).

#### 4. Photometry

The WFPC2 optics geometrically distort the images: pixels at the corner of each CCD subtend less area on the sky than those near the center. However, after application of the flat field, a source of uniform surface brightness on the sky produces uniform counts across the CCD. Therefore point sources near the corners of the chip are artificially brightened compared to those in the center.

In order to study the ability of **drizzle** to remove the photometric effects of geometric distortion, we have created a sub-sampled grid of artificial stellar PSFs and adjusted their counts to reflect the effect of geometric distortion—the stars in the corners are up to  $\sim 4\%$  brighter than those in the center of the chip. This image was then shifted and down-sampled onto four simulated WF frames and the results combined using drizzling with typical parameters. Aperture photometry on the grid of stars after drizzling reveals that the effect of geometric distortion on the photometry has been dramatically reduced: the RMS photometric variation in the drizzled image is 0.004 mags.

#### 5. The Dither Package

In order to effectively use the **drizzle** algorithm, one must know the offset and rotation between input images. We have therefore developed a package of tasks to assist the user through the entire process of combining dithered images. This STSDAS package is known as “**dither**” and presently contains the following tasks:

- **precors**: determines regions of the image containing astrophysical objects and nulls the remainder of the image, thereby substantially reducing the effect of cosmic rays and chip defects on the offset measurement. The output from **precors** is only used for offset determination and not final image creation.
- **offset**: cross-correlates all four images in a WFPC image, creating output cross-correlation images with names that can be appropriately grouped by later tasks. **Offset** employs the task **crossdriz** to perform the cross-correlation.
- **crossdriz**: cross-correlates two images, after preprocessing which includes trimming, and, if requested, drizzling to remove geometric distortion or rotation. **crossdriz** will also perform a loop over a range of test rotation angles.
- **shiftfind**: locates the peak in a cross-correlation image and fits for sub-pixel shift information. The search region and details of the fitting can be adjusted by the user.



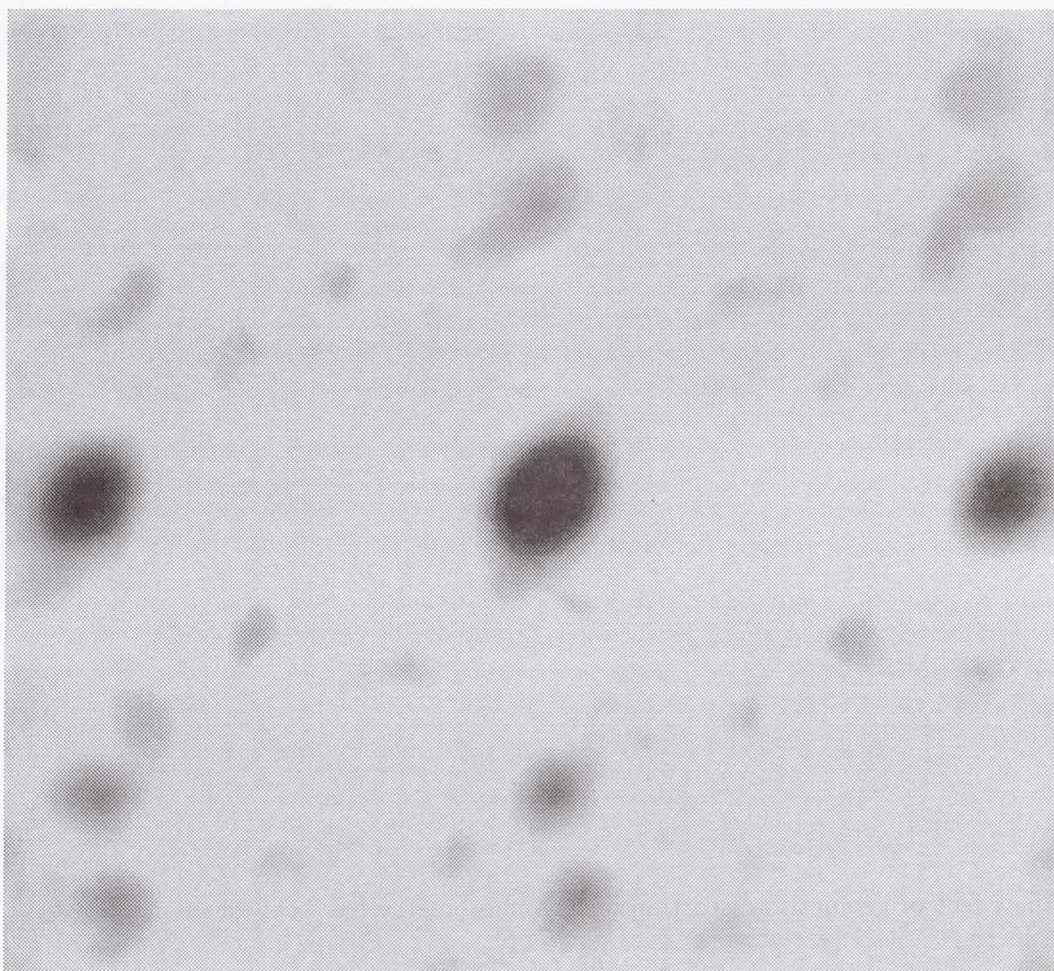


Figure 4. The cross-correlation image of one of the WF chips from two dither positions in the HDF. Note that the cross-correlation is symmetric about the maximum, and reflects the dominant objects in the image. In this case, a bright elliptical galaxy, rather than a star, dominates. Nonetheless, one can determine the shift between these two chips to about  $1/20$ th of a pixel. The shift between the images is equal to the offset between the peak of the cross-correlation and the center of the image.

- **rotfind**: fits for the rotation angle between two images. **rotfind** is called when **crossdriz** has been used to loop over a range of test rotation angles between two images.
- **avshift**: determines the shifts between two WFPC2 images by averaging the results obtained on each of the groups after adjusting for the rotation angles between the four groups. **avshift** can also be used to estimate the rotation angle between two different WFPC2 images, when the rotation angle is a small fraction of a degree.
- **blot**: maps a drizzled image back onto an input image. This is an essential part of the tasks we are developing for removing cosmic rays from singly-dithered images.

Although a detailed exposition of all of these tasks is beyond the present review, here we will describe a number of the **dither** tasks and typical results from their use.



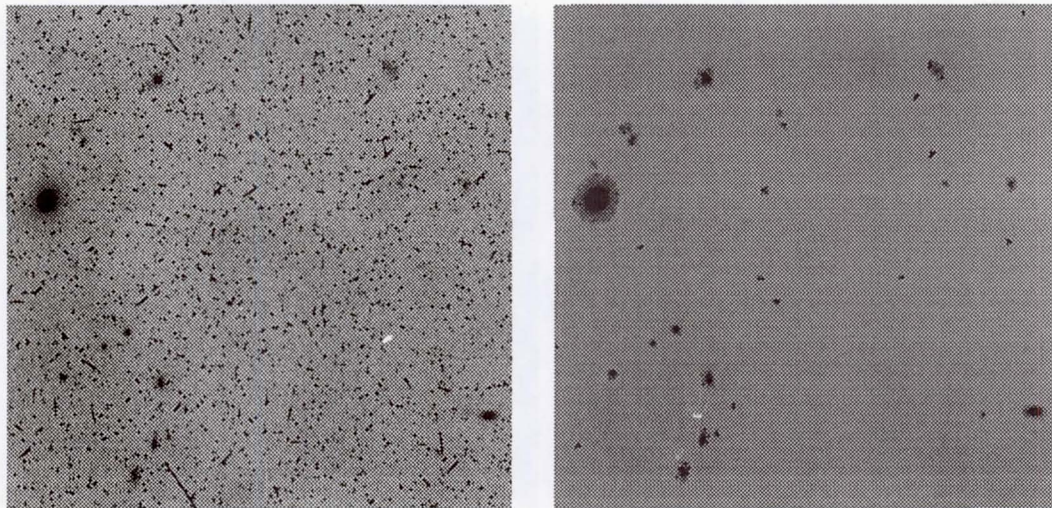


Figure 5. A comparison of a raw image and the output image from **precor**. The sky is set to zero, while true objects are preserved. As a result, essentially all cosmic rays, with the exception of those on top of detectable astronomical objects, are removed.

The major engine for determining the offset between two images in the **dither** package is cross-correlation. The following equations explain the reason for the choice of this algorithm. Assume that one has a known template image,  $T(x_{i,j})$ , and an observed image,  $I(x_{i,j})$ , and one wishes to know the offset between the observed and template images. Then

$$\sum_{i=1,j=1}^{N,N} (I(x_{i,j}) - T(x_{i,j}))^2 =$$

$$\underbrace{\sum_{i=1,j=1}^{N,N} I(x_{i,j})^2 + \sum_{i=1,j=1}^{N,N} T(x_{i,j})^2}_{\text{These terms invariant under shifts and rotations}}$$

$$- 2 \sum_{i=1,j=1}^{N,N} I(x_{i,j})T(x_{i,j}) .$$

Thus minimizing the difference of the sum of squares under shifts and rotations of  $I(x_{i,j})$  is equivalent to maximizing the cross-correlation between the two images! If the errors in the images are Gaussian, then this is equivalent to minimizing  $\chi^2$ . In practice, of course, images are a mixture of Gaussian and Poisson noise as well as, in many cases, very highly skewed noise additions such as cosmic rays and hot pixels. These can be largely removed by a task we call **precor**. This task separates objects from hot pixels and cosmic rays, by determining whether the fraction of pixels above the sky in a given box is above a user defined threshold. **precor** is not perfect, but is able to distinguish the vast majority of these defects from true objects. The regions of the sky-subtracted images containing objects are kept; other areas are set to zero. The image can also be converted from counts to signal-to-noise ratio, thus removing the distinction between Gaussian and Poisson noise in the minimization of  $\chi^2$  (in practice this step also appears to help reduce the errors



introduced by the spatial undersampling of images). Figure 5 shows an HST image before and after the application of *precor*.

After the cross-correlation image has been created, *shiftfind* determines the shift by locating the peak of the image. In the case of a single image (with no rotation) one is now done. However, in the case of WFPC, all four chips have been shifted (and rotated) by the same physical amount, and therefore one can average the shift values determined from each of the individual chips to obtain a better estimate of the shift. The script *avshift* performs this task, taking into account the (fixed) rotations between the four chips. Furthermore, in the case of a rotation between the template image and the observed image of significantly less than one degree, one can use *avshift* to estimate the rotation.

Below is an example of applying *avshift* to two dither positions of the HDF. In acquiring the second of these dither positions, the fine guidance sensors locked up on a secondary null, and as a result the pointing of the telescope was off by about an arc second, and was rotated with respect to the desired orientation by a few arc minutes. In the first use of *avshift* the user puts in a suggested rotation of 0.00 degrees, and a large error is found in the shift determination. However, in the second attempt the user (correctly) guesses the correct orientation and the error becomes a small fraction of a pixel. In practice, it only takes a few tries with *avshift* to home in on the rotation angle.

```
di> avshift pos2x11.out 0.00
Assumed angle of rotation = 0. degrees
Weights: 1. 1. 1. 1.
#
# Image      xsh_in  ysh_in best_xsh best_ysh tot_sh_in delta_xsh delta_ysh
pos2x11_g1   45.068  31.945  45.709  31.410  55.461  -0.641  0.536
pos2x11_g2   14.095 -20.226  14.559 -20.780  25.372  -0.464  0.553
pos2x11_g3  -21.278 -14.065 -20.858 -14.446  25.372  -0.420  0.381
pos2x11_g4  -14.839  21.432 -14.245  20.996  25.372  -0.594  0.436
# RMS error (all chips on WF scale): 0.6187
# RMS error (WF only): 0.6795
# weighted RMS error (all chips on WF scale): 0.6187
# weighted RMS error (WF only): 0.6795
di> avshift pos2x11.out 0.08
Assumed angle of rotation = 0.08 degrees
Weights: 1. 1. 1. 1.
#
# Image      xsh_in  ysh_in best_xsh best_ysh tot_sh_in delta_xsh delta_ysh
pos2x11_g1   45.068  31.945  45.068  32.066  55.311  0.000  -0.121
pos2x11_g2   14.095 -20.226  14.105 -20.231  24.663  -0.011  0.005
pos2x11_g3  -21.278 -14.065 -21.289 -14.018  25.490  0.012  -0.047
pos2x11_g4  -14.839  21.432 -14.821  21.416  26.044  -0.018  0.016
# RMS error (all chips on WF scale): 0.0392
# RMS error (WF only): 0.0322
# weighted RMS error (all chips on WF scale): 0.0392
# weighted RMS error (WF only): 0.0322
di>
```

In cases where the rotation angle is large, or where one only has one image, we use a different approach. We apply test rotations to the template and cross-correlate after each test rotation. We then find the best rotation angle by finding the maximum of the cross-correlation in this three-dimensional space of shifts and rotations. This is done by fitting for the rotation angle that produces the highest cross-correlation, and then interpolating for the precise shift using the shifts determined by the cross-correlation of the two best template



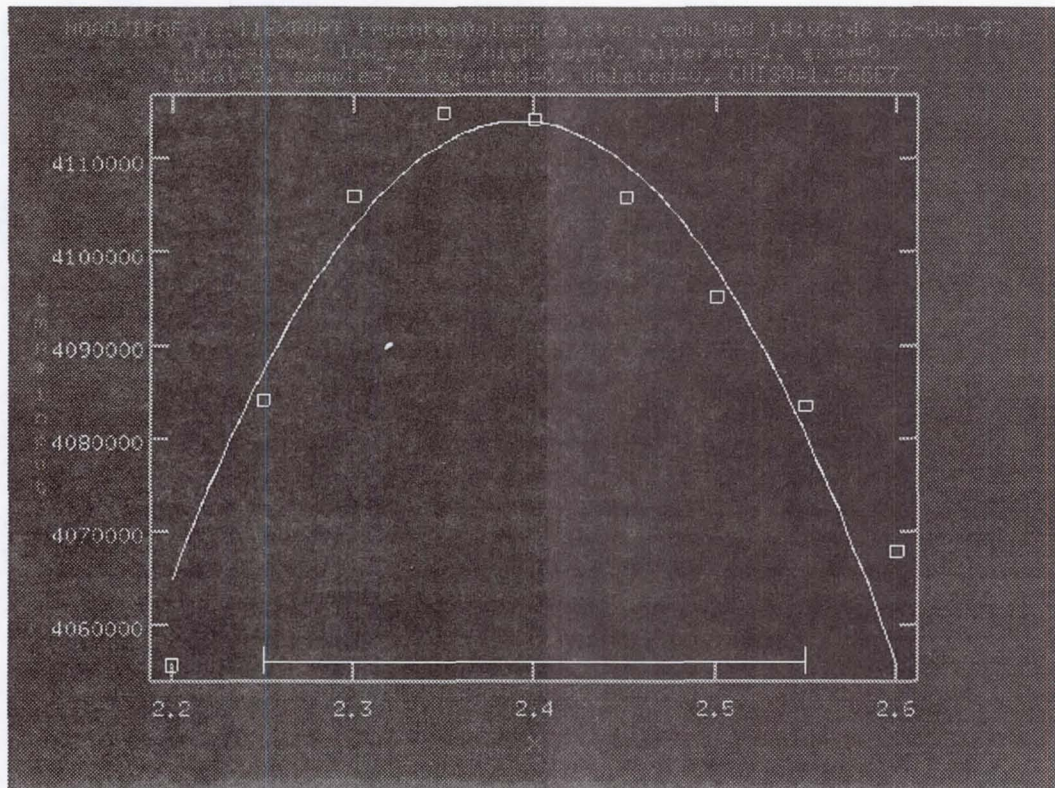


Figure 6. The graphical output of the task `rotfind`, used in this case two determine the rotation angle between two WFPC2 images of GRB 970228. According to the header, the change in orientation between these two images was 2.4 degrees. An error of 0.01 degrees is typical in measuring the rotation between two WFPC images.

rotations. The task `rotfind` is used to fit the rotation angle; an example of its graphical output is shown in Figure 6. Comparison of single group images produces a measurement which agrees with that in the header to 0.01 degrees. This level accuracy is typical for the comparison of two single group WFP2 images, and would result in an error of about 0.1 pixels at the very edge of the chip. Some of this error undoubtedly comes from the difficulty of attempting to interpolate an undersampled image. Higher accuracy should be obtainable (though is probably rarely required) by comparing the image with a first pass drizzled output of many dithered images of the same field.

## 6. Cosmic Ray Detection

Few HST observing proposals have sufficient time to take a number of exposures at each of several dither positions. Therefore, if dithering is to be of wide-spread use, one must be able to remove cosmic rays from data where few, if any, images are taken at the same position on the sky. We have therefore begun to adapt `drizzle` to the removal of cosmic rays.

A technique which appears quite promising is described below. We are presently working on creating a suite of robust scripts to perform these procedures. At present one of the authors (ASF) has a suite of very fragile scripts to do these operations. It is possible that some version of these scripts will be made publicly available in an unofficial, caveat-emptor release. Information will be posted on the web pages mentioned below.



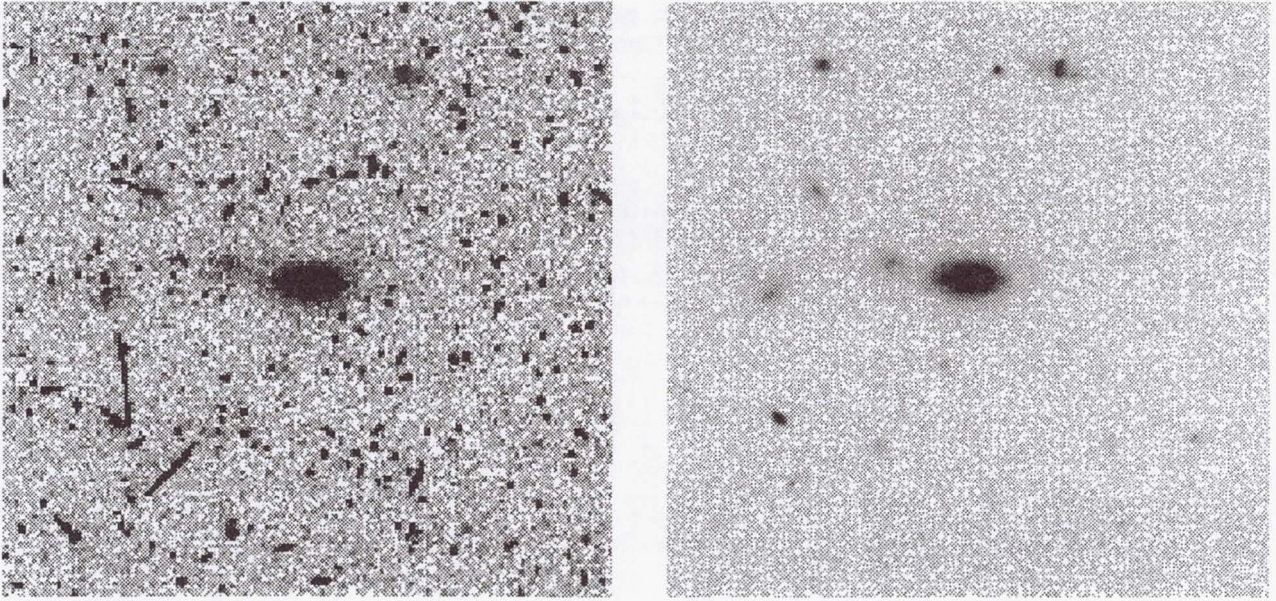


Figure 7. The image on the left shows a region of one of twelve 2400s archival images taken with a wide near-infrared filter on WFPC2. Numerous cosmic rays are visible. On the right is the drizzled combination of the twelve images, no two of which shared a dither position.

1. *drizzle* each image onto a separate sub-sampled output image using  $pixfrac = 1.0$
2. Take the median of the output drizzled images.
3. Map the median image back to the input plane of each of the individual images, taking into account the image shifts and geometric distortion. This is now done by interpolating the values of the median image using a program we call "blot".
4. Take the spatial derivative of each of the blotted output images.
5. Compare each original image with the corresponding blotted image. Where the difference is larger than can be explained by noise statistics, or the flattening effect of taking the median, or perhaps an error in the shift (the magnitudes of the latter two effects are estimated using the image derivative), the suspect pixel is masked.
6. Repeat the previous step on pixels adjacent to pixels already masked, using a more stringent comparison.
7. Finally, *drizzle* the input images onto a single output image using the pixel masks created in the previous steps.

Figure 7 shows the result of applying this method to data originally taken by Cowie and colleagues (Cowie, Hu, & Songaila 1995), which we have reprocessed using *drizzle*.

## 7. Additional Information

*Drizzle* was originally developed for the Hubble Deep Field, a project whose purpose was to image an otherwise unexceptional region of the sky to depths far beyond those of previous

astronomical images. The resulting images are available in the published astronomical literature(Williams et al. 1996) as well as from the Space Telescope Science Institute via the World Wide Web at <http://www.stsci.edu/ftp/science/hdf/hdf.html>. This web page provides access both to the final drizzled image, and to the stacks of images at each of the 11 dither positions. These images are excellent material for those who would like to try out the tasks in the `dither` package.

The `dither` package is scheduled to be released shortly by STScI as an IFAF STS-DAS package. However, additional, unofficial tasks may become available from time-to-time, before they are officially released. Interested IRAF users should occasionally examine <http://www.stsci.edu/~fruchter/dither> for more information.

## References

- Cowie, L. L., Hu, E. M., & Songaila, A., 1995, *AJ*, 110, 1576
- Fruchter, A., & Hook, R. N., 1997, *A novel image reconstruction method applied to deep Hubble Space Telescope Images*, ed. A. Tescher, Vol. 3164 (S.P.I.E.), in press
- Gull, S. F., & Daniell, G. J., 1978, *Nature*, 272, 686
- Lucy, L. B., 1974, *AJ*, 79, 745
- Lucy, L. B., & Hook, R. N., 1991, in *Astronomical Data Analysis Software and Systems I*, A.S.P. Conf. Ser., Vol. 25, eds. D. M. Worrall, C. Biemesderfer, & J. Barnes (San Francisco: ASP), 277
- Richardson, B. H., 1972, *J. Opt. Soc. Am.*, 62, 55
- Weir, N., & Djorgovski, S., 1990, in *The Restoration of HST Images and Spectra*, eds. R. L. White & R. J. Allen (Baltimore: STScI), 31
- Whitmore, B., & Heyer, I., 1997, Instrument Science Report WFPC2 97-08
- Williams, R. E., et al., 1996, *AJ*, 112, 1335



## Deconvolution of Substepped 1-D and 2-D HST Data

Nailong Wu and John Caldwell

*Dept. of Physics and Astronomy, York University, 4700 Keele St., North York,  
Ontario, M3J 1P3, Canada*

**Abstract.** Substepping is a technique in which data are acquired in steps smaller than the normal pixel size, such that resolution after restoration will be comparable to the subpixel size. Substepped data have been acquired by first generation HST instruments in both one-dimensional (spectroscopic) and two-dimensional (imaging) modes. In this presentation, we first introduce the principle of the substepping technique and then demonstrate numerical examples of MEM (Maximum Entropy Method) deconvolution of an FOS ACQ image of a star as well as of an FOS stellar spectrum.

### 1. Introduction

Substepping is a technique in which data are acquired in steps smaller than the spatial or spectral resolution element defined by an instrument's hardware. It may be done in two dimensions for imaging or in one dimension for spectroscopy. Substepped data may be restored by direct combination methods or deconvolution. The ultimate resolution may be comparable to the subpixel size (Wu & Caldwell 1997).

Substepping may be useful when the instrumental resolution is significantly worse than the inherent resolution of the optics of the telescope. It has been successfully applied to WFPC2 imaging (dithering). In data acquisition, this is achieved by small HST slews, of order 10 mas. For restoration methods, see Hook & Fruchter (1997) and Adorf (1995).

Substepped FOS imaging and spectroscopic data have also been taken, but very little attention has been paid to reconstructing these data optimally.

For FOS ACQ imaging we present a comparison of two reconstruction techniques, MEM deconvolution and the IRAF/STSDAS task `tarestore`. For FOS spectroscopy we present, apparently for the first time, MEM deconvolution of a substepped spectrum.

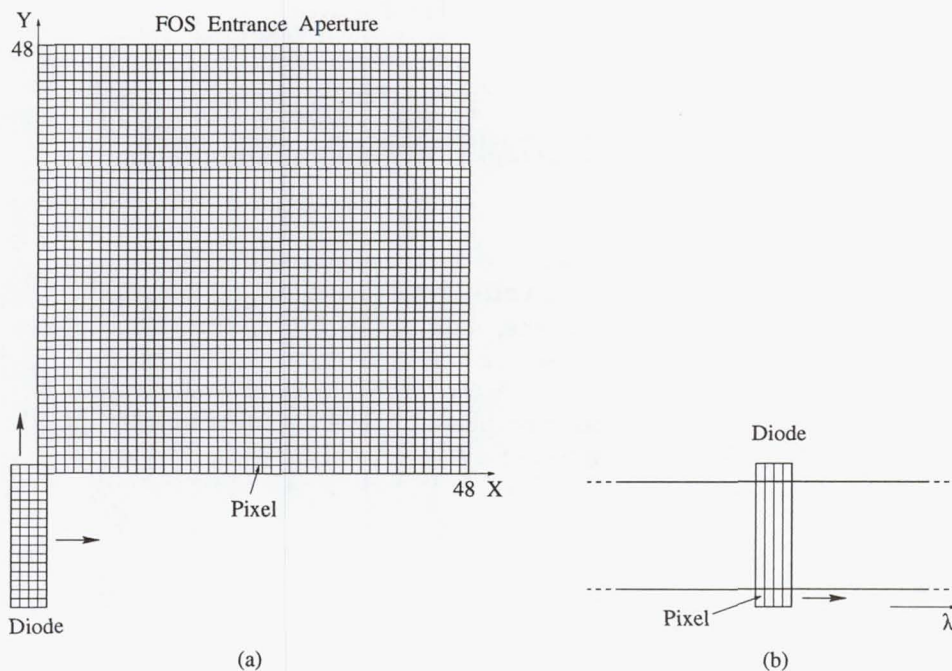
It should be emphasized that deconvolution here is used to eliminate the "moving-sum" effect in substepping to improve resolution, but does not address the problem of the effect of the HST PSF (point spread function, in imaging) or LSF (line spread function, in spectroscopy) on resolution.

### 2. Application of Substepping to FOS ACQ Imaging

#### 2.1. Data Acquisition

As shown *schematically* in Fig. 1a, the FOS entrance aperture is divided into  $48 \times 48$  "pixels". (They would have been named "subpixels" according to standard substepping terminology.) The diode footprint has a size of  $4 \times 16$  "pixels". (The diode footprint would have been named "pixel" in standard terminology.) Starting from position (1, 1), the diode (used to collect photoelectrons) moves in a raster scan. The step in each direction (pixel size) is equal to one quarter of the diode width, or equivalently, one sixteenth of the diode height. (In reality, the substepping is achieved electronically, i.e., photoelectrons are

Figure 1. Schematic substepping with FOS. (a) ACQ imaging. (b) Spectroscopy.



deflected magnetically and the diodes are fixed in position.) Therefore, in each step the photoelectrons collected by a diode are the sum of the photoelectrons in 64 ( $= 4 \times 16$ ) pixels.

## 2.2. Task tarestore for Reconstruction

The task tarestore in IRAF/STSDAS was written based on the moving-sum model of data acquisition (Oegerle 1989). As shown in Fig. 1a, in each of the diode's positions,  $(i, j)$ , the number of photoelectrons collected by the diode is

$$D_{i,j} = \sum_{k=p}^q \sum_{l=r}^s P_{k,l}$$

where  $P_{k,l}$  is the number of photoelectrons in pixel  $(k, l)$ ;  $1 \leq i \leq 48 + 4 - 1$ ,  $1 \leq j \leq 48 + 16 - 1$ ;  $p = \max(1, i - 4 + 1)$ ,  $q = \min(48, i)$ ,  $r = \max(1, j - 16 + 1)$ ,  $s = \min(48, j)$ .

The above linear equations can be solved by the generalized inversion of a matrix to reconstruct the photoelectron distribution  $P_{k,l}$  (an image).

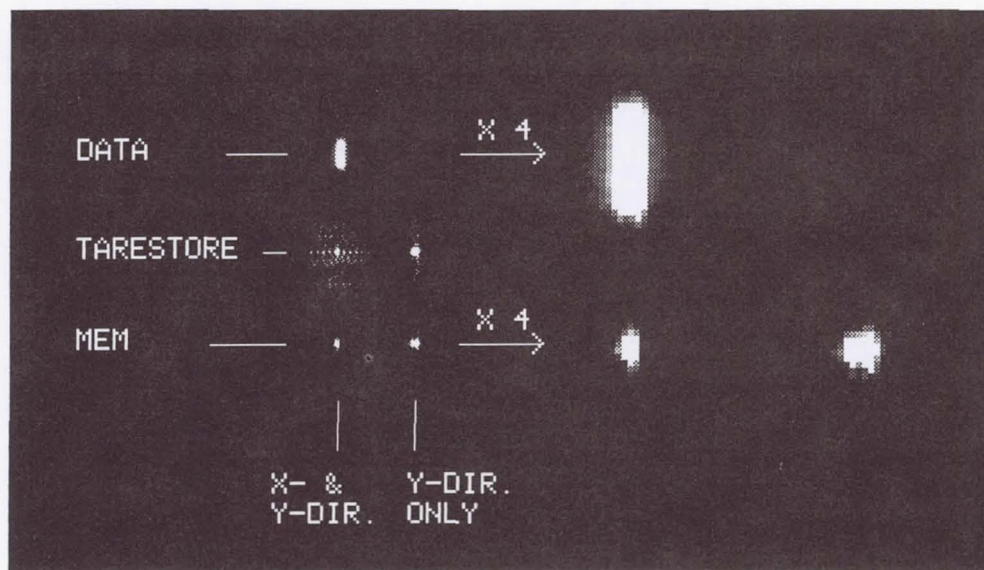
As a direct inversion method, the above algorithm cannot handle the high frequency components in the signal correctly, and is extremely sensitive to noise. Consequently, reconstruction is usually done only in the Y-direction. The moving-sum effect in the X-direction is not removed, i.e., the summation for  $k$  from  $p$  to  $q$  is not inverted. Otherwise the reconstructed image would have excessively high level sidelobes (rings) and noise. As a result, it would be nearly impossible to extract useful information from the reconstructed image.

## 2.3. Convolution Model and Deconvolution

If the area outside the aperture is also divided into pixels (without photoelectrons), then the limits  $p, q, r, s$  in the above moving-sum model can be set arbitrarily, and a crosscorrelation model and hence a convolution model may be applied. Consequently, deconvolution can be



Figure 2. FOS ACQ images of the star Wolf 359. X 4 means magnified by a factor of 4; X- & Y-DIR. means reconstructed in both X- and Y-directions; and Y-DIR. ONLY means reconstructed only in the Y-direction.



used to reconstruct the image  $P_{k,l}$ . In principle, any deconvolution program can be used for this purpose. In particular, the tasks `mem` and `lucy` in IRAF/STSDAS are most convenient, and give very good results.

## 2.4. Numerical Example

Figure 2 shows FOS ACQ images of the star Wolf 359. The image before reconstruction (`DATA` in the top row) is essentially the shape of the diode.

The images reconstructed by the task `tarestore` (especially the one reconstructed in both X- and Y-directions) in the middle row have high resolution, and strong sidelobes (rings) and high level noise. In practice, only the image reconstructed in the Y-direction only can be used for analysis.

In contrast, the images reconstructed by `mem` in the bottom row have high resolution and insignificant sidelobes and noise. The price paid is the computational complexity.

## 3. Application to FOS Spectroscopy

### 3.1. Data Acquisition

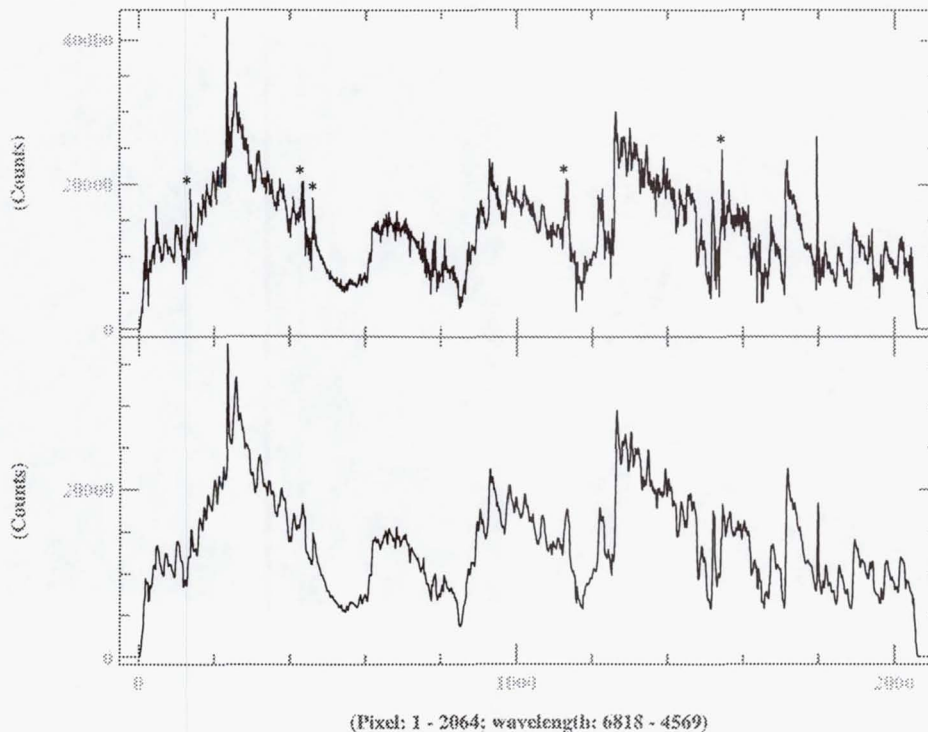
Because the diode's width along the dispersion ( $\lambda$ ) direction in spectral data acquisition is too large, the substepping technique is used to improve spectral resolution (Fig. 1b). The substepping factor is 4, i.e., the diode moves in steps of a quarter of the diode width.

### 3.2. Convolution Model

The output data from the diode is a moving-sum of 4 pixel values in the  $\lambda$  direction. Therefore, the spectral data acquisition can be modelled as convolution, and, potentially, the resolution in spectra can be improved by deconvolution.

Only the task `mem` in IRAF/STSDAS is available for this purpose. The task `tarestore` was written specifically for reconstructing FOS ACQ images, and `lucy` contains bugs in the 1-D case.

Figure 3. FOS spectra. Lower: data. Upper: mem.



### 3.3. Numerical Example

Deconvolution by `mem` was attempted on a spectrum of Proxima Centauri (G570H,  $\lambda\lambda$  4569–6818). As shown in Figure 3, the resolution seems to be improved. There is more fine structure (indicated by asterisks) in the `mem` spectrum.

Before applying this deconvolution technique, the following questions must be answered by computer simulation and real data tests: Are the extra peaks in the `mem` spectrum real? Is it worth doing deconvolution at all for a signal whose bandwidth is limited by the optical system?

### References

- Adorf, H.-M., 1995, in *Astronomical Data Analysis Software and Systems IV*, A.S.P. Conf. Ser., Vol. 77, eds. R. A. Shaw, H. E. Payne & J. J. E. Hayes (San Francisco: ASP), 456
- Hook, R. N., & Fruchter, A. S., 1997, in *Astronomical Data Analysis Software and Systems VI*, A.S.P. Conf. Ser., Vol. 125, eds. G. Hunt & H. E. Payne (San Francisco: ASP), 147
- Oegerle, B., 1989, STScI internal technical reports, February 28 and March 14
- Wu, N., & Caldwell, J., 1997, *Substepping Technique and its Applications to HST Imaging*, in *Astronomical Data Analysis Software and Systems VII*, A.S.P. Conf. Ser. (in press)



## Calibrating Echelle Spectra using Instrument Models

M. R. Rosa<sup>1</sup>

*Space Telescope European Coordinating Facility, European Southern Observatory,  
Garching, D 85748, Germany*

P. Ballester

*European Southern Observatory, Garching, D 85748, Germany*

**Abstract.** We have developed a generic model of echelle spectrographs, based on first optical principles, fully treating 3-dimensions. The geometrical part of it is capable of predicting detector positions for wavelength calibration spectra within 0.2 pix (1 sigma), solely using engineering parameters such as focal lengths, grating constants and configuration angles. First results are also available from the modeling code for grating efficiencies (blaze functions) for any given polarization, surface accuracy and random or periodic groove errors. Combined these tools allow one to carry calibrations of well observed modes into less well or even uncalibrated modes of operation.

### 1. Introduction

Current and future instruments provide astronomers with large amounts of high signal-to-noise, multi-dimensional observational data. In order to exploit optimally these data, the entire chain of the observation process from instrument configuration control through calibration, analysis and archival has to be tailored towards very high standards. In contemporary data calibration and analysis, very little has been done so far to relate the optical layout and its engineering parameters with the performance on scientific targets and calibration sources. Even less use has been made of the physical principles underlying the characteristics of a given instrument in predicting its performance to such a degree of accuracy, that it will allow to support and even substitute classical (i.e., empirical) calibration and analysis (cf. Rosa 1995).

One of the most demanding cases of data calibration and analysis are 2D echelle spectra. Traditionally, they require complex data reduction procedures to cope simultaneously with both the geometrical distortion of the raw data introduced by order curvature and line tilt, and the spread of the signal across the tilted lines and between successive orders respectively (cf. Hensberge & Verschueren 1988). We have studied (Ballester & Rosa 1997) the principles governing the accurate form of the echelle relation for off-plane echelle spectrographs, and have applied software models based on these equations to several echelle spectrographs at a ground based observatory (ESO's CASPEC, UVES) and to HST's STIS.

In the present paper we summarize the salient points of the above analysis, then discuss the potentials for application in model based calibration and analysis, and finally address the steps required to implement these techniques.

---

<sup>1</sup>Affiliated to the Astrophysics Division, Space Science Department, European Space Agency

## 2. Modeling Optical Principles in Echelle Spectrographs

The elements of a model for echelle spectrographs are mirrors, lenses, gratings, prisms, grisms. For the moment we will focus solely on the geometric aspects, i.e., the relations producing the spectral formats at the detectors. Luminosity aspects brought about by the interference terms, e.g., the echelle blaze function, line spread functions, as well as geometrical vignetting, reflectivity and transmissivity of materials, are remarked upon in Section 5.

Following the discussion in Ballester & Rosa (1997), the optical elements are placed into the 3D geometry of the instrumental layout, and then optical rays are followed through the system (here from slit to detector) using rotational matrices to change back and forth between the 3D instrumental geometry and the optical surfaces. This procedure allows one to write very compact code while retaining full visibility of the optical equations at each surface, a necessary requirement for studying the merits of first principle models in observation simulation. For example, all STIS modes can be completely described by the following operations at each reflective surface: 3 matrix rotations at entry, 1 matrix multiplication at the surface, and 3 matrix rotations on exit from the surface (collimator, X-disperser or mirror, Echelle or mirror, camera). A final rotation and projection deals with the detector.

In a complete optical train, the above strictly applies only for on-axis rays and does not take into account field distortions, camera aberrations and the like. In instruments like UVES (as described below) these effects can amount to discrepancies of several pixels at the detector. Distortions are specific to the optical elements and layout, and are usually predictable and stable in time. As was shown by Ballester & Rosa (1997), a model for a given instrument and mode will typically match 99% using the physical description as developed above. For most applications it will not pay off to develop further the description by introducing fully general off-axis optical equations. Instead, these percent-level effects can be accounted for by inserting at the proper location (eg. during projection onto the detector) low order polynomial functions whose coefficients can for example be produced with the help of a ray tracing program.

## 3. Comparison of Simulated and Observed Spectral Formats

The model represents adequately all effects for off-plane spectrographs, including line curvature with an accuracy close to one pixel. Because it is mostly based on linear algebra, it is straightforward to produce high performance code. Such code can be used to generate accurate simulations of lamp exposures through various slits (wavelength calibration observations). We have used such simulations to "re-find" the engineering parameters of CASPEC (ESO), which has been in operation for over a decade. We ran automatic feature line centering algorithms on the data frames to obtain  $x, y$ -location tables of about 560 Th-Ar lines. Optimization of the configuration parameter sets used the simulated  $x, y$ -positions on the basis of the catalogued wavelengths. The residuals between the measured and predicted positions are typically 0.4 pixel (3 sigma), where 1 pixel represents 0.5 true resolution elements. This result is excellent, since we can attribute most of the scatter to the difficulties generalized (Gaussian fitting, edge detection etc.) line centering techniques have in locating the centers of the tilted and curved emission line segments in the observed 2D echellograms.

As detailed in Ballester & Rosa (1997), we could show that the incident angle on the echelle grating remained very stable between 1984 and 1991 ( $71^\circ 2 \pm 0^\circ 7$ ). A dataset from epoch April 1994 produces a configuration solutions with a value of  $71^\circ 6 \pm 0^\circ 7$  for this angle. Although the shift of  $0^\circ 4$  seems to be insignificant in the nominal error margin, it coincides with an overhaul and reassembly of the instrument in 1992, and may indicate that our



conservative quotations of nominal errors are actually surpassed by the predictive power of the instrument simulation software.

#### 4. Application: Wavelength Calibration and Order Extraction

The model technique described above represents adequately all effects for off-plane spectrographs including line curvature with an accuracy better than an actual resolution element. Because it is mostly based on linear algebra, it is straight forward to produce high performance code. Such code can for example be used to generate accurate initial solutions of the dispersion relation using the grating positions as provided by encoders. This allows to implement fully automatic, boot-strapping wavelength calibration procedures, considerably easing the chore of generating calibration reference data.

One of the most demanding cases for the implementation of un-supervised pipeline data reduction is the target extraction and wavelength calibration of high resolution, large field 2D echellograms. Typically (e.g., the *calstis* software package for STIS), a complex structure of code segments is supported by a large number of tables to define expected "average" solutions and to provide the capability to adjust to shifts, tilts and rotations of the actual spectral format. Underlying is the assumption that two spectral formats with only small deviations in one or more of the angles defining their generating optical paths can be affinely transposed into one another. Unfortunately, the various features of an off-plane echelle spectral format (e.g., order separation, order curvature, line tilt and line curvature) cannot easily be predicted simultaneously to the same accuracy by simplistic transformations and scaling laws.

In the classical schemes it is therefore necessary to provide a dense coverage of the actually observed range of spectral formats (e.g., shifts induced by non-repeatability of grating mechanisms or off-center location of target on extended slits) with reference data from empirical calibrations. Also required is a mechanism to align the nearest solution with the actually observed case and then to translate predicted dispersion solutions and order locations using linear offsets. Typically one uses correlation techniques to find these shifts—the result on an actual scientific dataset being insecure in the case of low S/N, or even undetermined in the case of, e.g., pure emission line spectra. Also, the requirement of finding and following the ridge of a spectral order for optimal extraction schemes is most demanding exactly where the scientific (target) signal is low compared to the background (e.g. in the valleys of deep and broad P-Cygni absorption profiles).

It is obvious that predictive algorithms based on first optical principles can provide more exact solutions for any observed situation. Empirical calibration exposures in this scheme are used to optimized configuration parameter sets. The classical "alignment" task then reverts into, e.g., estimating the actual value of a grating tilt angle, and predicting a new full dispersion solution, instead of estimating a zero point shift only for a prefabricated "approximate" solution.

#### 5. Implementation Requirements and Current Activity

This concludes the exploratory stage, in which we developed from first principles the formalism of optical equations for spectral formats in echelle spectrograms, suitable for high performance code. Lately we have successfully configured models for a broader range of instruments, and the list now includes FOS, STIS (HST), CASPEC, UVES (ESO), and all 8 "modes" of IUE (SW, LW; Primary and Redundant cameras; low and high resolution).

Current activity is concentrated on linking the spectral format code with multi-parameter non-linear optimization software, such as simulated annealing. This will yield software ready to be applied routinely for calibration purposes, e.g., to automatically produce optimized

configuration sets for the plentitude of STIS modes, and to apply our first principle predictive technique in a routine manner to the spectral extraction from STIS frames.

Up to now we have concentrated on instrument model code that deals exclusively with the geometrical aspects (spectral formats). In a next step we will include the luminosity aspects. As is well known, the basic textbook grating and echelle blaze function equations do not generally produce sufficiently accurate predictions of the efficiency curves from real spectrographs (excluding simple corrections such as vignetting or reflectivities of materials). The failure has its physical basis in the necessity to find a solution to a set of  $N$  Maxwellian equations, where  $N$  is equal to the total number of grooves illuminated by the beam. The simple equations work best for first order, low resolution gratings in near Littrow configuration, where groove shaping errors, and the permeability and conductivity of the coating and the substrate play a lesser role.

Therefore predictive code for the luminosity aspects will probably have to be based on a capability to simulate real gratings from the superposition of a large multitude of idealized textbook gratelets, and the goal is to find a compromise between accuracy and speed. Once this second aspect of spectrograph simulation can be predicted with the same success as in our geometrical code, a fully model-based predictive calibration will be a question of package implementation rather than principle.

Our work is closely linked with the calibration and data flow activities of instrument supported at two major observatories, namely HST and ESO's VLT, with a view towards next generation instrumentation. These two current instruments are well supported by "classical" calibration and data reduction techniques and therefore provide an ideal testbed for our predictive calibration and forward data analysis scenario (cf. Rosa 1995). We anticipate that user-friendly packages on the geometrical aspects of STIS and UVES will become available for the respective communities in mid-1998.

## References

- Ballester, P., & Rosa, M. R., 1997, A&AS, in press  
Hensberge, H., & Verschueren, W., 1990, A&A, 240, 216  
Rosa, M.R., 1995, in *Calibrating and Understanding HST and ESO Instruments*, ed. P. Benvenuti (Garching: ESO), ESO Conf. Proc. No. 53, p. 43



## Author Index

- Ardeberg, A., 343  
Axon, D., 267
- Baggett, S., 374, 386, 392  
Ballester, P., 533  
Barg, I., 277, 297  
Baum, S., 3, 52, 94, 100  
Beck, T., 65  
Benedict, G., 472  
Bensby, T., 343  
Bergeron, L., 171, 240, 308  
Bohlin, R., 29, 77, 150  
Bower, G., 70  
Bowers, C., 18, 132, 144  
Bristow, P., 349  
Brown, T., 114  
Bushouse, H., 223, 255, 287  
Busko, I., 245, 518
- Caldwell, J., 529  
Calzetti, D., 250, 255, 287  
Casertano, S., 327, 378  
Claeskens, J., 368  
Colina, L., 182, 259, 287  
Collins, N., 77, 94  
Cornett, R., 84  
Crenshaw, M., 39
- Daou, D., 171, 263, 267  
Downes, R., 39  
Dudziak, G., 338
- Evans, I., 430
- Ferguson, H., 52, 90, 94  
Ferro, A., 277, 297  
Fosbury, R., 94  
Freudling, W., 207  
Fruchter, A., 355, 518  
Ftacalas, C., 84
- Galas, G., 308  
Gardner, J., 94  
Gilliland, R., 94  
Goudfrooij, P., 52, 100  
Green, R., 70, 94  
Greenfield, P., 505  
Griffiths, R., 361  
Gruszczak, A., 84  
Gull, T., 94, 106, 138
- Hayes, J., 52, 440
- Heap, S., 84, 94, 114  
Heyer, I., 398  
Hill, R., 94, 106, 120  
Hines, D., 217  
Hodge, P., 47  
Hook, R., 192, 518  
Hulbert, S., 47, 52, 138
- Jedrzejewski, R., 405, 413  
Jefferys, W., 472  
Joseph, C., 126
- Kaiser, M., 29  
Katsanis, R., 39  
Keyes, C., 420, 440  
Kimble, R., 8  
Koratkhar, A., 430  
Kraemer, S., 39, 138  
Krist, J., 192, 271  
Kuschnig, R., 481
- Landsman, W., 65, 120, 132  
Leitherer, C., 52  
Linde, P., 343  
Lindler, D., 29, 70, 94, 120, 138  
Lubow, S., 513  
Lupie, O., 449, 463  
Lytle, D., 217, 277, 297
- Malumuth, E., 94, 144  
McArthur, B., 472  
McGrath, M., 39, 52  
McLeod, B., 281  
Micol, A., 94, 349  
Mutchler, M., 355, 518
- Nagel, L., 449, 463  
Nelán, E., 449, 463, 472
- Ostrander, E., 361
- Pirenne, B., 349  
Pirzkal, N., 94  
Plait, P., 150
- Ratnatunga, K., 361  
Remy, M., 368, 374, 386  
Rieke, M., 182  
Ritchie, C., 287  
Robinson, R., 39, 106  
Rosa, M., 533

- Sahu, K., 52  
Sandoval, J., 94  
Schmidt, G., 217  
Shaw, R., 52, 106, 120  
Sherbert, L., 486, 497  
Skinner, C., 171, 233, 240, 263, 267, 287  
Snel, R., 343  
Soderblom, D., 486  
STIS IDT, 70  
Stobie, E., 277, 297  
Stolovy, S., 202  
Storrs, A., 259, 287, 303  
Suchkov, A., 308, 378  
Surdej, J., 368, 374, 386, 392  
  
Taylor, M., 106  
Thompson, R., 163  
Tolstoy, E., 94  
Tullos, C., 392  
  
van der Marel, R., 443  
Voit, M., 413  
  
Walsh, J., 94, 100, 156, 338  
Weiss, W., 481  
Whitmore, B., 317, 398  
Wiggs, M., 374, 386, 392, 398  
Woodgate, B., 60, 84, 94  
Wu, N., 529  
  
Zwintz, K., 481



## Index

- absolute calibration
  - WFPC2, 338
- absolute photometry
  - WFPC2, 327
- annealing
  - STIS, 65
- archive, 349
- astrometry
  - FGS, 449
  - FGS OFAD, 472
  - FGS1R, 463
  - infrared, 163
  - WFPC2, 361
- background
  - GHRS, 497
  - NICMOS, thermal, 267
- blaze function
  - STIS, echelle, 114
- blot, 355
- calibration
  - echelle spectra, 533
  - FGS, 449
  - FOC, 405, 413
  - NICMOS, 223, 233, 250, 259, 297
  - STIS, 47, 52, 100
  - systems development, 513
  - wavelength, 443
- CCD, 8
  - cosmic ray, 120
  - STIS, annealing, 65
- clearinghouse
  - WFPC2, 398
- coronagraphs
  - STIS, 84
- cosmic ray
  - removal, CCD, 120
- cosmic rays, 355
- CR-SPLIT, 349
- CRL 2688, 217
- darks
  - NICMOS, 240
- data analysis
  - NICMOS, 163, 297
- data formats, 505
- data handbook
  - NICMOS, 255
- data processing
  - NICMOS, 245
- data quality
  - NICMOS, 287
- deconvolution, 529
- detectors
  - MAMA, 29
  - NICMOS, 171
  - NICMOS darks, 240
- dither, 355
- dithering, 529
- drizzle, 349, 355
- Ech-A, 497
- Ech-B, 497
- echelle, 132
  - spectrographs, 533
  - STIS, 114
- emission lines, 202
  - WFPC2, 338
- FGS
  - FGS1R, 463
  - photometry, 481
- file formats
  - NICMOS, 277
- FITS
  - file formats, NICMOS, 277
- FITS kernel, 505
- flatfielding
  - STIS, 90
- FOC
  - calibration, 405
  - F/48 slit spectroscopy, 413
- focus
  - NICMOS, 308
- FOS
  - closeout, 420
  - scattered light, 440
  - wavelength scale, 443
- fringe correction
  - STIS, 100
- fringing, 150
- FUV, 29
- G140L, 497
- G140M, 497
- G160M, 497
- G200M, 497
- G270M, 497
- galaxies

- M84, nuclear ionized gas, 70
- geometric distortion
  - STIS, 144
- GHRSL
  - description, 486
  - sensitivity, 497
- gravitational lensing, 368
- grism mode
  - NICMOS, 207
- gui, 297
- IDL, 297
- image processing, 368, 374
- image reconstruction, 518
- imaging
  - STIS, 84
- infrared astrometry
  - NICMOS, 163
- instrument models, 533
- instrumentation, 463
- ionized gas
  - M84, 70
- IRAF
  - FITS format, 505
- IRC +10216, 217
- long-slit spectrometry, 156
- MAMA, 8, 132
  - STIS, stability, 126
- MAMA detectors, 29
- maps, 303
- maximum entropy, 529
- mosaic, 349
- mosaics, 303
- Mu Col, 497
- MULTIACCUM
  - reduction, 281
- narrow band emissions
  - NICMOS, 202
- narrow band filters
  - WFPC2, 338
- NIC3 campaign, 259
- NICMOS
  - calibration, 223, 233, 250, 259
  - darks, 240
  - data handbook, 255
  - data quality, 287
  - detectors, 171
  - emission lines, 202
  - file formats, 277
  - focus, 308
  - grism mode, 207
  - imaging, 202
  - infrared astrometry, 163
  - maps, 303
  - mosaic, 202
  - MULTIACCUM data, 281
  - narrow band emissions, 202
  - narrow band filters, 202
  - NIC3 campaign, 182
  - persistence, 263
  - photometry, 182, 202
  - photometry, differential, 182
  - photometry, errors, 182
  - photometry, stability, 182
  - pipeline, 223
  - polarimetry, 217
  - PSF, 182, 192, 271
  - software, 245, 297
  - standards, 182
  - thermal background, 267
- NICRED
  - MULTIACCUM data, 281
- NUV, 29
- OMC-1, 202
- optical bench
  - motion, STIS, 106
- optical field angle distortion
  - FGS, 472
- optical modeling, 192
- paper products
  - NICMOS, 287
- parallel survey
  - STIS, 94
- patterns, 303
- persistence
  - NICMOS, 263
- photometric calibration
  - STIS, 77
  - WFPC2, 343
- Photometric errors, 182
- photometry
  - FGS, 481
  - magnitude systems, 182
  - NICMOS, 182
  - stability, 182
  - standards, 182
  - WFPC2, 374, 378, 386
  - WFPC2, calibration, 327
- pipeline
  - NICMOS, 223, 233
- pixels
  - hot, STIS, 120



- STIS, annealing, 65
- point source extraction, 156
- polarimetry
  - NICMOS, 217
- POS-TARG, 349
- POSITION mode
  - FGS, 449
- PSF
  - NICMOS, 192, 271
  - STIS, 84
  - WFPC2, 374, 392
  - WFPC2, photometry, 386
- quasars
  - HE 1104–1805, 368
  - J03.13, 368
- restoration
  - image, 518
- scattered light
  - FOS, 440
- sensitivity
  - GHRS, 497
- sensitivity curves
  - STIS, 77
- signal-to-noise
  - MAMA, 29
- software
  - NICMOS, 245
- spectral reduction, 150
- spectrograph
  - STIS, 8
- spectroscopy
  - FOC F/48, 413
- ST-ECF, 349
- stellar photometry
  - WFPC2, 378
- STIS
  - calibration, 47, 52
  - capabilities, 60
  - CCD, 8
  - echelle, 114
  - flatfielding, 90
  - fringe correction, 100
  - fringing, 150
  - future, 60
  - geometric distortion, 144
  - hot pixels, 120
  - MAMA, 8, 132
  - MAMA stability, 126
  - parallel survey, 94
  - performance, 18
  - spectrometry, 156
  - target acquisition, 39
  - thermal motion, 106
  - TIME-TAG, 138
  - STIS:overview, 3
  - STSDAS
    - NICMOS software, 245
  - substepping, 529
  - target acquisition
    - STIS, 39
  - thermal background
    - NICMOS, 267
  - thermal motion
    - STIS, 106
  - time-resolved spectroscopy, 138
  - TIME-TAG
    - STIS, 138
  - TinyTim, 374
  - tools
    - software, NICMOS, 297
  - TRANSFER mode
    - FGS, 449
  - undersampled images, 518
  - UV, 29
  - uvby system, 343
  - variable stars, 481
  - wavelength scale
    - FOS, 443
  - WFPC2
    - associations of exposures, 349
    - astrometry, 361
    - calibration, 338
    - clearinghouse, 398
    - drizzle, 355
    - overview, 317
    - photometric calibration, 327
    - photometry, 343, 374, 378, 386
    - PSF, 392